Production and processing of graphene and related materials

Claudia Backes, Amor Abdelkader, Concepción Alonso, Amandine Andrieux, Raul Arenal, Jon Azpeitia, Nilanthy Balakrishnan, Luca Banszerus, Julien Barjon, Ruben Bartali, et al.

PRODUCTION AND PROCESSING OF GRAPHENE AND RELATED MATERIALS

Claudia Backes[1,2], Amor M. Abdelkader[3], Concepción Alonso [4], Amandine Andrieux [5], Raul Arenal [6, 7], Jon Azpeitia [8], Nilanthy Balakrishnan [9], Luca Banszerus [10], Julien Barjon [11], Ruben Bartali [12], Sebastiano Bellani [13], Claire Berger [14, 15], Reinhard Berger[16], M.M. Bernal Ortega [17], Carlo Bernard[18], Peter H. Beton[9], André Beyer [19], Alberto Bianco [20], Peter Bøggild [66], Francesco Bonaccorso [13], Timoth J. Booth [66], Gabriela Borin Barin [21], Cristina Botas [22], Rebeca A. Bueno [8], Daniel Carriazo [23, 22], Andres Catellanos-Gomez [8], Meganne Christian[24], Artur Ciesielski [25], Tymoteusz Ciuk[26], Matthew T. Cole[27], Jonathan Coleman [2], Camilla Coletti [28, 13], Luigi Crema [12], Huanyao Cun[18], Daniela Dasler[29], D. De Fazio[3], Noel Díez [22], Simon Drieschner [30], Georg S. Duesberg[31], Roman Fasel [33, 21], Xinliang Feng[16], Alberto Fina [17], Stiven Forti [28], Constantine Galiotis [34, 35], Giovanni Garberoglio[36], Jorge M. García [65], Jose Antonio Garrido[38], Marco Gibertini [39], Armin Gölzhäuser [19], Julio Gómez [40], Thomas Greber [18], Frank Hauke[29], Adrian Hemmi[18], Irene Hernandez-Rodriguez [8], Andreas Hirsch [29], Stephen A. Hodge[3], Yves Huttel [8], Peter U. Jepsen [66], Tommi Kaplas[32], HoKwon Kim [41], Andras Kis [41], Papagelis Konstantinos[42, 35], Kostas Kostarelos [43], Aleksandra Krajewska [26], Kangho Lee[31], Changfeng Li [44], Harri Lipsanen [44], Andrea Liscio [45], Martin R. Lohe [46], Annick Loiseau[47], Lucia Lombardi [3], Maria Francisca López[8], Oliver Martin[29], Cristina Martín [48], Lidia Martínez[8], Jose Angel Martin-Gago[8], Nicola Marzari [39], Álvaro Mayoral [7], Manuela Melucci [45], Javier Méndez [8], Cesar Merino [49], Pablo Merino [8], Andreas P. Meyer [14], Elisa Miniussi[18], Vaidotas Miseikis [28,50], Neeraj Mishra [28], Vittorio Morandi [24], Carmen Munuera [8], Roberto Muñoz [8], Hugo Nolan [2], Luca Ortolani [24], Anna K. Ott [3], Irene Palacio [8], Vincenzo Palermo [51, 24, 45], John Parthenios [35], Iwona Pasternak [52, 26], Amalia Patane [9], Maurizio Prato[53, 23, 54], Henri Prevost[47], Vladimir Prudkovskiy [14], Nicola Pugno[55, 56, 57], Teófilo Rojo [22, 58], Antonio Rossi[28], Pascal Ruffieux[21], Paolo Samorì [25], Léonard Schué [47], Eki Setijadi [12], Thomas Seyller [59], Abhay Shivayogimath [66], Giorgio Speranza [56, 12], Christoph Stampfer [10], Ingrid Stenger [11], Wlodek Strupinski [52, 26], Yuri Svirko[32], Simone Taioli[36, 37], Kenneth B.K. Teo[60], Matteo Testi [12], Flavia Tomarchio[3], Mauro Tortello[61], Emanuele Treossi[45], Andrey Turchanin[62], Ester Vazquez [48], Elvira Villaro [63], Patrick R. Whelan [66],Zhenyuan Xia [45], Rositza Yakimova [64], Sheng Yang [46], G.Reza Yazdi [64], Chanyoung Yim[31], Duhee Yoon [3], Xianghui Zhang [19], Xiaodong Zhuang [46], Andrea C. Ferrari [3], Mar Garcia-Hernandez [8,*]

*Corresponding author

1. Physikalisch-Chemisches Institut, University of Heidelberg, Im Neuenheimer Feld 253, 69120 Heidelberg, Germany
2. School of Physics, Centre for Research on Adaptive Nanostructures and Nanodevices (CRANN) and Advanced Materials and BioEngineering Research (AMBER), Trinity College Dublin, Dublin 2, Ireland
3. Cambridge Graphene Centre, 9 JJ Thomson Avenue, University of Cambridge, CB3 0FA, United Kingdom
4. Dept. Applied Physical Chemistry, Autonomous University of Madrid, 28049 Madrid, Spain
5. ONERA, Département Physique, Instrumentation, Environnement et Espace - Université Paris Saclay - 29 Avenue de la Division Leclerc, 92320 Chatillon, France
6. ARAID Fundation, Calle Mariano de Luna, 50018 Zaragoza, Spain
7. Laboratorio de Microscopias Avanzadas (LMA) Instituto de Nanociencia de Aragon (INA), Universidad de Zaragoza, Calle Mariano Esquillor, 50018 Zaragoza, Spain
8. Materials Science Factory, Instituto de Ciencia de Materiales de Madrid, Consejo Superior de Investigaciones Científicas, C/ Sor Juana Ines de la Cruz 3, Madrid, E-28049, Spain
9. University of Nottingham. School of Physics and Astronomy, University Park,Nottingham,NG7 2RD,UK
10. JARA-FIT and 2nd Institute of Physics, RWTH Aachen University Germany
11. Groupe d'Etude de la Matière Condensée (GEMaC), CNRS – Université Versailles ST Quentin – Université Paris Saclay, 45 Avenue des Etats Unis, Versailles France

12. Fondazione Bruno Kessler, via Sommarive 18, 38123 Trento, Italy
13. Graphene Labs, Istituto Italiano di Tecnologia, Via Morego 30, 16163 Genova, Italy
14. Institut Néel, CNRS – University Grenoble, 25 rue des Martyrs, 38042 Grenoble, France
15. Georgia Institute of Technology, School of physics, Atlanta, USA
16. Center for Advancing Electronics Dresden (cfaed) & Department of Chemistry and Food Chemistry, Technische Universität Dresden, 01062 Dresden (Germany)
17. Politecnico di Torino, Dipartimento di Scienza Applicata e Tecnologia, Alessandria Campus, Viale Teresa Michel 5, 15121 Alessandria, Italy
18. Physik-Institut, University of Zürich, Winterthurerstrasse 190, CH-8057 Zürich, Switzerland
19. Physics of Supramolecular Systems, Bielefeld University, Universitätsstr. 25, 33615 Bielefeld, Germany.
20. Institut de Biologie Moléculaire et Cellulaire, CNRS, UPR3572, Immunopathologie et Chimie Thérapeutique, Strasbourg, France
21. Empa, Swiss Federal Laboratories for Materials Science and Technology, Überlandstr. 129, 8600 Dübendorf, Switzerland
22. CIC EnergiGUNE. Parque Tecnológico de Álava, 01510-Miñano, Álava, Spain
23. IKERBASQUE, Basque Foundation for Science, 48013-Bilbao, Spain
24. National Research Council (CNR) Institute for Microelectronics and Microsystems (IMM), via Gobetti 101, 40129 Bologna, Italy
25. Université de Strasbourg, CNRS, ISIS, 8 alleé Gaspard Monge, 67000 Strasbourg, France
26. Instytut Technologii Materiałów Elektronicznych, Wólczyńska 133, 00-001 Warszawa, Poland.
27. Department of Electronic and Electrical Engineering, BA2 7AY, Bath, UK
28. Center for Nanotechnology Innovation @NEST, Istituto Italiano di Technologia, P.zza S. Silvestro 12, 56127, Pisa, Italy
29. Chair of Organic Chemistry II & Joint Institute of Advanced Materials and Processes, Nikolaus-Fiebiger-Str. 10, Friedrich-Alexander Universität Erlangen-Nürnberg, 91058 Erlangen
30. Walter Schottky Institut Technische Universität München,Am Coulombwall 4,D-85748 Garching,Germany.
31. Institute of Physics, Universität der Bundeswehr München, 85577 Neubiberg, Germany
32. Institute of Photonics, University of Eastern Finland, Yliopistokatu 7, 80100 Joensuu, Finland
33. Department of Chemistry and Biochemistry, University of Bern, 3012 Bern, Switzerland
34. Department of Chemical Engineering, University of Patras, Patras 26504, Greece
35. Institute of Chemical Engineering Sciences, Foundation for Research and Technology- Hellas (FORTH/ICE-HT), Patras 26504, Greece
36. European Centre for Theoretical Studies in Nuclear Physics and Related Areas (ECT*-FBK), 38123, Trento, Italy and Trento Institute for Fundamental Physics and Applications (TIFPA-INFN), 38123 Trento, Italy
37. Faculty of Mathematics and Physics, Charles University, Praha 8, 180 00 Prague, Czech Republic
38. Instituto Catalán de Nanotecnologia ICN2, UAB Campus, Bellaterra, (Barcelona) 08193, Spain
39. Theory and Simulation of Materials (THEOS), and National Centre for Computational Design and Discovery of Novel Materials (MARVEL), École Polytechnique Fédérale de Lausanne, CH-1015 Lausanne, Switzerland
40. Avanzare Innovacion Tecnologica S.L., Avda Lentiscares 4-6 Navarrete,Spain
41. EPFL, Electrical Engineering Institute and Institute of Materials Science and Engineering, École Polytechnique Fédérale de Lausanne (EPFL), CH-1015 Lausanne, Switzerland
42. Department of Physics, University of Patras, Patras 26504, Greece
43. University of Manchester United Kingdom
44. Department of Electronics and Nanoengineering, Aalto University, Tietotie 3, 02150 Espoo, Finland
45. Institute of Organic Synthesis and Photoreactivity - National Research Council (CNR) Bologna, Italy.
46. Technical University of Dresden, Mommsenstr. 4, 01069 Dresden, Germany
47. Laboratoire d'Etude des Microstructures (LEM), CNRS – ONERA, Université Paris Saclay, 29 Avenue de la Division Leclerc, 92320 Chatillon, France
48. Instituto Regional de Investigación Científica Aplicada (IRICA), Universidad de Castilla-la Mancha, Avda Camilo Jose Cela, 13071, Ciudad Real, Spain49. Grupo Antolin Ingenieria, S.A., Ctra. Madrid-irun, Km. 244,8 Burgos, Spain
50. Consorzio Nazionale Interuniversitario per le Telecomunicazioni, Via Moruzzi 1, 56124, Pisa, Italy
51. Chalmers University of Technology, Department of Industrial and Materials Science, Horsalsvagen 7A, SE-412 96 Gothenburg, Sweden
52. Faculty of Physics Warsaw University of Technology Koszykowa 75 00-662 Warsaw Poland
53. Carbon Bionanotechnology Laboratory, CIC biomaGUNE, Paseo de Miramón 182, 20009 Donostia-San Sebastián, Spain

54. Dipartimento di Scienze Chimiche e Farmaceutiche, INSTM UdR Trieste, Università degli Studi di Trieste, Via Licio Giorgieri 1, 34127 Trieste, Italy
55. Laboratory of Bio-Inspired and Graphene Nanomechanics, Department of Civil, Environmental and Mechanical Engineering, University of Trento, Via Mesiano 77, 38123 Trento, Italy
56. Ket Lab, Edoardo Amaldi Foudation, Italian Space Agency, Via del Politecnico snc, 00133 Rome, Italy
57. School of Engineering and Materials Science, Queen Mary University of London, Mile End Road, London E1 4NS, United Kingdom
58. Universidad del País Vasco UPV/EHU, 48080-Bilbao, Spain
59. Technische Universität Chemnitz, Institut für Physik, Reichenhainer Str. 70, 09126 Chemnitz, Germany
60. Buckingway Business Park, Anderson Road, Swavesey, Cambridge CB24 4FQ, United Kingdom
61. Politecnico di Torino, C.so Duca degli Abruzzi 24, 10129 Torino, Italy
62. Institute of Physical Chemistry, Friedrich Schiller University Jena, Lessingstr. 10, 07743 Jena, Germany
63. Interquimica, C/ Antonio Nebrija , 8- Bajo. CP 26006 , Logroño, Spain
64. University of Linköping, IFM, 58183, Linkoping, Sweden.
65. Instituto de Micro y Nanotecnología, IMN-CNM, CSIC (CEI UAM+CSIC) Isaac Newton, 8, E-28760, Tres Cantos, Madrid, Spain.
66. Center for Nanostructured Graphene (CNG), Technical University of Denmark, Kongens Lyngby, 2800, Denmark.

TABLE OF CONTENTS

List of Acronyms

0d: Zero dimensional
1d: One dimensional
1L: One Layer
1LG: 1 Layer Graphene
2D: 2D Raman Peak of graphene
2d : Two dimensional
2LG: 2 Layer Graphene
3d: Three dimensional
3LG: 3 Layer Graphene
4LG: 4 Layer Graphene
AES: Auger Electron Spectrocopy
AFM - Atomic Force Microscopy
AGNR: GNRs with armchair edges
ALD: Atomic Layer Deposition
APS: Ammonium persulfate
ARGO: Reduced Graphene Oxide-based aerogels
ARPES: Angle Resolved Photoemission Spectroscopy
BHJ: Bulk Hybrid Junction
Bipy: 2,2'-Bipyridine
BL: Buffer Layer
BLG: Bilayer Graphene
BODIPY: 2,6-diiodo-1,3,5,7-tetramethyl-8-phenyl-4,4-difluoroboradiazaindacene
BP: Black phosphorus
BP3: 3-(Biphenyl-4-yl)propane-1-thiol
BPT: 1,1'-biphenyl-4-thiol
BZ: Brillouin Zone
BZ: Benzidine
CA: Cellulose Acetate
CCS - Confinement Controlled Sublimation

c-CVD: catalytical-Chemical Vapor Deposition
CE: Counter electrode
CES- Constant Energy Surface
CHP: *N*-Cycloxexyl-2-pyrrolidone
CL: Cathodeluminiscence
CMC: Critical micelle concentration
CMOS: Complementary Metal-Oxide Semiconductor
CMP: Conjugated microporous polymers
CNF: Carbon Nanofibre
CNM: Carbon nanomembrane
CNT: Carbon Nanotube
COD: 1,5-Cyclooctadiene
CPD: Critical Point Drying
CTAB: Cetyl trimethyl ammonium bromide
CVD: Chemical Vapour Deposition
D: D Raman Peak
DA: Diels-Alder
DAP: donor-acceptor pairs
db: dangling bonds
DBT: 4-docosyloxy-benzenediazonium tetrafluoroborate
DCM: Dichloromethane
DEA: Dissociative electron attachment
DES: Diethyl sulphide
DFT: Density Functional Theory
DGM: Density Gradient Medium
DGU: Density Gradient Ultracentrifugation
Dh: Decahedral
DI: Deionized water
DIC: Differential interference contrast microscopy
DMAc: *N*,*N*'-dimethylacetamide
DME: 1,2-dimethoxymethane
DMF: Dimethylformamide
DMSO: Dimethylsulfoxide
DOS : Density of states
DOTA: 1,4,7,10-tetraazacyclododecane-1,4,7,10-tetraacetic acid
DSSC: Dye-Sensitized Solar Cell
EA: Elemental Analysis
EBSD: Electron Back Scattering Diffraction
EC: Ethyl Cellulose
EDA: Ethylene-diamine (EDA)
EE: Electrochemical Exfoliation
EEG: Electrochemically Exfoliated Graphene
EG: Epitaxial Graphene
EVA: ethylene vinyl acetate
FCC: Face-centered Cubic
FESEM: Field Emission Scanning Electron Microscope
FET- Field Effect Transistor
FIB: Focused Ion Beam
FL: Few Layer

FLaT: Functional layer transfer
FLG: Few Layer Graphene
FoM: Figure of Merit
FS- Fermi Surface
FTIR: Fourier Transform Infra Red Spectroscopy
FWHM: Full Width Half Maximum
G: G Raman peak
G3DCN: Graphene-based covalent networks
GANF: Grupo Antolin Nano- Fibras
GFactor: Gauge factor
GF: Graphene Foam
GIC: Graphite intercalation compound
GnP: Graphene nanoplatelets
GNR: Graphene nanoribbons, nanometer wide graphene strips exhibiting a bandgap
GO: Graphene oxide
GOS- Graphene on Silicon
GRM: Graphene-related material
GRMs: Graphene and related materials
HAADF: High Angle Annular Dark Field
HATU:O-(7-azabenzotriazole-1-yl)-N,N,N,N'-tetramethyluronium hexafluorophosphate
HBC: Hexabenzocoronene
HBC-Br: 2-Bromo-11-(1'-[4'-(S-Acetylthiomethyl)phenyl]acetyl)-5,8,14,17-tetra(3',7'-dimethyloctyl)-hexa-peri-hexabenzocoronene
HBC-CN: 2-Cyano-11-(1'-[4'-(S-Acetylthiomethyl)phenyl]acetyl)-5,8,14,17-tetra(3',7'-dimethyloctyl)-hexa-peri-hexabenzocoronene
HIM: Helium Ion Microscope
hMDM: human monocyte macrophages
HOPG: Highly Oriented Pyrolytic Graphite
HMDS: hexamethyldisilazane
HOPG: Highly Oriented Pyrolytic Graphite
HPB: S,S'-(3',4',5',6'-Tetraphenyl-[1,1':2',1''-terphenyl]-4,4''-diyl) diethanethioate
HPL: Hot-press lamination
HREM - High Resolution Electron microscopy
HRP: Horseradish peroxidase
HRTEM - High Resolution Transmission Electron Microscopy
ICS: Ion cluster source
Ih : Icosahedral
IPA: Isopropyl Alcohol
JCNM: Janus carbon nanomembrane
KPM - Kelvin Probe Microscopy
LCC: Liquid Cascade Centrifugation
LEED: Low Energy Electron Difracction
LEEM: Low Energy Electron Microsocpy
LIB: Lithium ion battery
LM: Layered material
LMH- Layered Material Heterostructure
LMs: Layered Materials
LPCVD: Low Pressure CVD
LPE: Liquid Phase Exfoliation

LRI: Liquid Resin Infusion
μ: Carrier mobilities
μ-ARPES- Micro spot ARPES
MALDI-TOF: Matrix-assisted laser desorption/Ionization-time of flight
MBE: Molecular Beam Epitaxy
MC- Mecanically Clived
MEG- Multilayer epitaxial graphene
MICS : Multiple ion cluster source
mIPM : murine intraperitoneal Macrophages
ML- Monolayer
MLG: Multilayer Graphene
MNP: Metal Nanoparticle
MOCVD: Metalorganic Chemical Vapour Deposition
MP- Moire Pattern
MS: Mass spectrometry
MSCs: Micro Super Capacitors
MW: Microwave
M_W: Molecular Weight
N: Number of layers
NaCMC: Sodium Carboxymethylcellulose
NBE- Near Band Edge
n-BuLi: n-Butyllithium
NC- Nitrocellulose
Nc-AFM: Non-contact atomic force microscopy
NDI: Naphthalene Diimide
NMP: N-Methyl-2-pyrrolidone
NMR: Nuclear magnetic resonance
NP: Nanoparticle
NPTH: Naphtalene-2-thiol
ODCB: 1,2-dichlorobenzene
OPV: Organic Photovoltaics
ORR: Oxygen Reduction Reaction
Otf: Trifluoromethanesulfonate
P3HT:poly(3-hexylthiophene)
PAH: Polycyclic Aromatic Hydrocarbon
PANi: Polyaniline
PCBM: phenyl-C61-butyric acid methyl ester
PDI: Perylene Diimide
PDMS : Polydimethylsiloxane
PE: Polyethylene
PECVD: Plasma Enhanced Chemical Vapour deposition
PEDOT: poly(3,4 ethylenedioxythiophene)
PET: Polyethylene terephthalate
PhCN: Benzonitrile
PI: Polyimide
PL- Photoluminescence
PMMA: Polymethyl Methacrylate
PPF: Pyrolyzed Photoresist Film
PPP: Polu(p-phenylene)

PS: Polystyrene
PTCVD: Photo Thermal CVD
PTFE: Polytetrafluoroethylene
PVA: Polyvinyl acetate
PVC: Polyvinyl chloride
PVDF: Polyvinylidene difluoride
PVP: Polyvinylpyrrolidone
PVT: Physical Vapor Transport
QFBLG: Quasi free standing bilayer layer graphene
QFSLG: Quasi Free Standing Single Layer Graphene
r-(ECR-CVD): Remote Electron Cyclotron Resonance Plasma Assisted Chemical Vapor Deposition
RBLM: Radial-breathing-like mode
RCA1, RCA2: Standard sets of wafer cleaning steps which need to be performed before high-temperature processing steps
RE: Reference Electrode
RF: Radiofrequency
RGO : Reduced Graphene Oxide
RHEED: Reflection High Energy electron Diffraction RT: Room Temperature
RIE: Reactive Ion Etching
Rpm: revolutions per minute
RT: Room Temperature
RTM: Resin Transfer Moulding
RTP Rapid Thermal Process
RZS: Rate zonal centrifugation
SAED: Selectd Area Electron Diffraction
SAM: Self-assembled monolayers
SARPES: Spin Resolved ARPES
SAV: Single atom vacancies
SBS: Sedimentation based separation
SC: Sodium Cholate
SDBS: Sodium dodecyl benzene sulfonate
SDF: sodium deoxycholate
SDS: Sodium dodecyl sulfate
SEC: Size exclusion chromatography
SEM: Scanning Electron Microsocopy
SET: Single electron transfer
SL: Single-layer
SLG: Single Layer Graphene
Slm: Standard liter per minute
SOI: Silicon On Insulator
STEM: Scanning transmission electron microscopy (STEM)
SThM: Scanning Thermal Microscopy
STM: Scanning Tunnelling Microscopy
STS: Scanning Tunnelling Spectrocopy
SuMBE: Supersonic Molecular Beam Epitaxy
SWCNT: Single Wall Carbon Nanotube
T: Temperature
TAC: Thermally Assisted Conversion
Tb: temperature of the bubbler

TCB: 1,2,4-Trichlorobenzene
TCF: Transparent Conducting Film
TCNQ: Tetracyanoquinodimethane
TEM: Transmission Electron Microscopy
TEMPO: 2,2,6,6-Tetramethyl-1-piperidinyloxy
TGA: Thermogravimetric Analysis
THF: Tetrahydrofuran
THz-TDS: THz-Time Domain Spectroscopy
TLG- Trilayer Graphene
TMC : Transition Metal chalcogenide
TMD: Transition Metal Dichalcogenide
TOA: Tetraoctylammonium
TPT: [1'',4',1',1]-Terphenyl-4-thiol
Tr-ARPES: Time resolved ARPES
TRT: Thermal Release Tapes
UHV: Ultra High Vacuum
ULF: Ultra Low Frequency
UV: Ultraviolet
UVA: Ultra-violet adhesive
Uv-Vis: Ultravioleta-visible
vdW: van der Waals
VPE- Vapour Phase Epitaxy
WE: Working Electrode
XPS: X-ray Photoelectron Spectroscopy
Z: Reciprocal of the Ohnersorge number
ZGNR: GNRs with zigzag edges

ABSTRACT

We present an overview of the main techniques for production and processing of graphene and related materials (GRMs), as well as the key characterization procedures. We adopt an "hands-on" approach, providing practical details and procedures as derived from literature as well as from the authors' experience, in order to enable the reader to reproduce the results.

Section I is devoted to "bottom up" approaches, whereby individual constituents are pieced together into more complex structures. We consider graphene nanoribbons (GNRs) produced either by solution processing or by on-surface synthesis in UHV, as well carbon nanomembranes (CNM). Production a variety of GNRs with tailored band gaps and edge shapes is now possible. CNMs can be tuned in terms of porosity, crystallinity and electronic behaviour.

Section II covers to"top down" techniques. These rely on breaking down of precursor into its constituents. The main focus of this section is on various exfoliation techniques in a liquid media, either intercalation or liquid phase exfoliation (LPE). The choice of precursor, exfoliation method, medium as well as the control of parameters such as time or temperature are crucial. A definite choice of parameters and conditions yields a particular material with specific properties that makes it more suitable for a targeted application. We cover protocols for the graphitic precursors to graphene oxide (GO). This is an important material for a range of applications in biomedicine, energy storage, nanocomposites, etc. Hummers' and modified Hummers' methods are used to make GO that subsequently can be reduced to obtain reduced graphene oxide (RGO) with a variety of strategies. GO flakes are also employed to prepare three-dimensional (3d) low density structures, such as sponges, foams, hydro- or aerogels. The assembly of flakes into 3d structures can provide improved mechanical properties. Aerogels with a highly open structure, with interconnected hierarchical pores, can enhance the accessibility to the whole surface area, as relevant for a number of applications, such as energy storage. The main recipes to yield graphite intercalation compounds (GICs) are also discussed. GICs are suitable precursors for covalent functionalization of graphene, but can also be used for the synthesis of uncharged graphene in solution. Degradation of the molecules intercalated in GICs can be triggered by high temperature treatment or microwave irradiation, creating a gas pressure surge in graphite and exfoliation. Electrochemical exfoliation by applying a voltage in an electrolyte to a graphite electrode can be tuned by varying precursors, electrolytes and potential. Graphite electrodes can be either negatively or positively intercalated to obtain GICs that are subsequently exfoliated. We also discuss the materials that can be amenable to exfoliation, by employing a theoretical data-mining approach.

The exfoliation of LMs usually results in a heterogeneous dispersion of flakes with different lateral size and thickness. This is a critical bottleneck for applications, and hinders the full exploitation of GRMs produced by solution processing. The establishment of procedures to control the morphological properties of exfoliated GRMs, which also need to be industrially scalable, is one of the key needs. Section III deals with the processing of flakes. (Ultra)centrifugation techniques have thus far been the most investigated to sort GRMs following ultrasonication, shear mixing, ball

milling, microfluidization, and wet-jet milling. It allows sorting by size and thickness. Inks formulated from GRM dispersions can be printed using a number of processes, from inkjet to screen printing. Each technique has specific rheological requirements, as well as geometrical constraints. The solvent choice is critical, not only for the GRM stability, but also in terms of optimizing printing on different substrates, such as glass, Si, plastic, paper, etc., all with different surface energies. Chemical modifications of such substrates is also a key step.

Sections IV-VII are devoted to the growth of GRMs on various substrates and their processing after growth to place them in the surface of choice for specific applications. The substrate for graphene growth is a key determinant of the nature and quality of the resultant film. The lattice mismatch between graphene and substrate influences the resulting crystallinity. Growth on insulators, such as SiO2 typically results in films with small crystallites, whereas growth on the close-packed surfaces of metals yields highly crystalline films. Section IV outlines the growth of graphene on SiC substrates. This satisfies the requirements for electronic applications, with well-defined graphene-substrate interface, low trapped impurities and no need for transfer. It also allows graphene structures and devices to be measured directly on the growth substrate. The flatness of the substrate, results in graphene with minimal strain and ripples on large areas, allowing spectroscopies and surface science to be performed. We also discuss the surface engineering by intercalation of the resulting graphene, its integration with Si-wafers and the production of nanostructures with the desired shape, with no need for patterning.

Section V deals with Chemical Vapour Deposition (CVD) onto various transition metals and on insulators. Growth on Ni results in graphitised polycrystalline films. While the thickness of these films can be optimised by controlling the deposition parameters, such as the type of hydrocarbon precursor and temperature, it is difficult to attain single layer graphene (SLG) across large areas, owing to the simultaneous nucleation/growth and solution/precipitation mechanisms. The differing characteristics of polycrystalline Ni films facilitate the growth of graphitic layers at different rates, resulting in regions with differing numbers of graphitic layers. High-quality films can be grown on Cu. Cu is available in a variety of shapes and forms, such as foils, bulks, foams, thin films on other materials and powders, making it attractive for industrial production of large area graphene films. The push to use CVD graphene in applications has also triggered a research line for the direct growth on insulators. The quality of the resulting films is lower than possible to date on metals, but enough, in terms of transmittance and resistivity, for many applications as described in section V.

Transfer technologies are the focus of Section VI. CVD synthesis of graphene on metals and bottom up molecular approaches require SLG to be transferred to the final target substrates. To have technological impact, the advances in production of high-quality large-area CVD graphene must be commensurate with those on transfer and placement on the final substrates. This is a prerequisite for most applications, such as touch panels, anticorrosion coatings, transparent electrodes and gas sensors etc. New strategies have improved the transferred graphene quality, making CVD graphene a feasible option for CMOS foundries. Methods based on a complete etching of the metal substrate in suitable etchants, typically iron chloride, ammonium persulfate, or hydrogen chloride although reliable, are time- and resource-consuming, with damage to graphene and production of metal and

etchant residues. Electrochemical delamination in a low-concentration aqueous solution is an alternative. In this case metallic substrates can be reused. Dry transfer is less detrimental for the SLG quality, enabling a deterministic transfer.

There is a large range of layered materials (LMs) beyond graphite. Only few of them have been already mechanically exfoliated and fully characterized while others have been prepared by LPE. Section VII deals with the growth of some of these materials. Amongst them, h-BN, transition metal tri- and di-chalcogenides are of paramount importance. The growth of h-BN is at present considered essential for the development of graphene in electronic applications, as h-BN is ideal as capping layer or substrate. The interesting optical and electronic properties of TMDs also require the development of scalable methods for their production. Large scale growth using chemical/physical vapour deposition or thermal assisted conversion has been thus far limited to a small set, such as h-BN or some TMDs. Heterostructures could also be directly grown.

Chapter VIII discusses recent advances in GRM functionalization. A broad range of organic molecules can be anchored to the sp2 basal plane by reductive functionalization. Negatively charged graphene can be prepared in liquid phase (e.g. via intercalation chemistry or electrochemically) and can react with electrophiles. This can be achieved both in dispersion or on substrate. The functional groups of GO can be further derivatised. Graphene can also be noncovalently functionalized, in particular with polycylic aromatic hydrocarbons that assemble on the sp2 carbon network by π-π stacking. In the liquid phase, this can enhance the colloidal stability of SLG/FLG. Approaches to achieve noncovalent on-substrate functionalization are also discussed, which can chemically dope graphene. Research efforts to derivatize CNMs are also summarized, as well as novel routes to selectively address defect sites. In dispersion, edges are the most dominant defects and can be covalently modified. This enhances colloidal stability without modifying the graphene basal plane. Basal plane point defects can also be modified, passivated and healed in ultra-high vacuum. The decoration of graphene with metal nanoparticles (NPs) has also received considerable attention, as it allows to exploit synergistic effects between NPs and graphene. Decoration can be either achieved chemically or in the gas phase. All LMs, can be functionalized and we summarize emerging approaches to covalently and noncovalently functionalize MoS2 both in the liquid and on substrate.

Section IX describes some of the most popular characterization techniques, ranging from optical detection to the measurement of the electronic structure. Microscopies play a very important role, although macroscopic techniques are also used for the measurement of the properties of these materials and their devices. Raman spectroscopy is paramount for GRMs, while PL is more adequate for non-graphene LMs. Liquid based methods to produce GRMs result in flakes with different thicknesses and dimensions. The qualification of size and thickness can be achieved using imaging techniques, like scanning probe microscopy (SPM) or transmission electron microscopy (TEM) or spectroscopic techniques. Optical microscopy enables the detection of flakes on suitable surfaces as well as the measurement of optical properties. Characterization of exfoliated materials is essential to improve the GRM metrology for applications and quality control. For grown GRMs, SPM can be used to probe morphological properties, as well as to study growth mechanisms and quality of transfer. More generally, SPM combined with smart measurement protocols in various modes allows one to

get information on mechanical properties, surface potential, work functions, electrical properties, or effectiveness of functionalization. Some of the techniques described are suitable for “in situ” characterization, and can be hosted within the growth chambers. If the diagnosis is made “ex situ”, consideration should be given to the preparation of the samples to avoid contamination. Occasionally cleaning methods have to be used prior to measurement.

I. BOTTOM UP

I.1 Graphene nanoribbons

Graphene nanoribbons (GNRs) constitute an interesting family of materials combining aspect ratios allowing to bridge the range of (sub-) nanometer dimensions with ultimate structure-properties relationship (GNR width, below 5 nm) and mesoscopic dimensions (GNR length up to 500 nm). This makes GNRs accessible to established top-down contacting strategies and thus allows for their device integration. For GNRs with armchair edges (AGNRs), theory predicts the opening of sizable electronic bandgaps as soon as the AGNR width falls below ~2 nm [1-5]. This bandgap opening is due to quantum confinement and edge effects and can qualitatively be understood by slicing the graphene Dirac cone along *k*-lines in reciprocal space that are compatible with the hard-wall boundary conditions set by the finite AGNR width. The further these cuts of allowed electronic states are away from the *K* point of the Brillouin zone of graphene, the larger is their bandgap [6]. Armchair GNRs were predicted to show metallic to semiconducting behavior, depending on their width [2, 7-9]. Generally, armchair GNRs exhibiting widths smaller than 10 nm behave as semiconductors with non-zero bandgaps that increase as the GNRs become narrower [5, 7-11]. For instance, armchair GNRs as narrow as 2–3 nm are expected to possess a bandgap of ∼0.7 eV, which is comparable to that of germanium [5]. In contrast, early theoretical studies indicated that zigzag GNRs have metallic properties with zero bandgap irrespective of the width, showing strongly localized edge states at the zigzag sites [7], with ferromagnetic coupling along and antiferromagnetic coupling across the edges [12]. Thus, small differences in width and edge configuration lead to large variations in GNR properties [5, 10, 11], making it imperative to control the GNR structure on the atomic level to achieve the desired (opto)electronic and magnetic properties with high accuracy and reproducibility . While this is clearly beyond the level of what can be controlled by traditional top-down structuring methods, such as lithographic patterning or cutting of carbon nantoubes, recent advances in bottom-up fabrication have shown that GNRs with specific edge structure and width are indeed accessible [13]. But not only purely armchair- or zigzag edged graphene nanoribbons can be synthesized. Many other types in between named chevron- or necklace-type can be designed and prepared as well.

Solution synthesis of graphene nanoribbons

The concept of solution based bottom-up synthesis relies on the synthesis of large polycyclic aromatic hydrocarbons (PAHs), often referred to as nanographenes [14, 15] The reaction is based on the intramolecular oxidative cyclodehydrogenation of corresponding oligophenylene precursors and was extended from defined molecules to polymers, namely from PAHs to GNRs [15]. Since then, the synthesis of GNRs through intramolecular cyclodehydrogenation of polyphenylene polymers was

achieved, which are prepared through A2-B2 -type Diels–Alder, A2B2 type Suzuki [16-18] and AA-type Yamamoto [19] polymerizations.

The most critical issue in the solution-synthesis is to achieve high (>600000 $gmol^{-1}$on average by DA polymerisation) molecular weight of the precursor polymer. While the width of GNRs is determined by the dimension of monomer itself, themolecular weight is directly proportional to the number of repeating units and therefore directly proportional to the length of the resulting GNR after the cyclodehydrogenation -graphitization- step. For example, DA polymerization provides a molecular weight of >600000 on average corresponding to a length of 600 nm [15]. First, the preparation of precursor polymers by the different synthetic protocols based on the Suzuki, Yamamoto and Diels-Alder reaction with a focus on practical aspects is described. Then the protocol for the cyclodehydrogenation of precursor polymers into GNR is addressed along with details on how to maintain solubility or dispersability of the planarized GNR after the graphitization step and purification.

Preparation of polymer precursors by A2B2-polymerization

Here, an A2B2-Polymerization requires two monomers with complementary functional groups A and B .These can be A= Cl, Br, I, Otf in combination with B being a boronic acid or boronic acid ester. In this case, the underlying carbon-carbon bond formation is based on the Suzuki-reaction. In contrast, if A is a diene and B a dienophile, it belongs to the reaction class of a Diels-Alder reaction. The most prominent combination for a Diels-Alder reaction to form PAHs is the combination of a cyclopentadienone and a substituted acetylene [20, 21]. The benefit of this –inverse electron demand- Diels-Alder reaction is the tandem cycloaddition and carbon-monoxide-extrusion reaction. Therefore, both reaction classes require very different protocols. In all cases, the polymerization growth follows a step-growth mechanism and is defined by Carother's equation [22] . In this case, the functionalized monomers first react into monomers, dimers, trimer, oligomers and finally high molecular weight polymers. The exact stoichiometry of both monomers is of fundamental importance to achieve a high degree of polymerization and thus molecular weight. A small deviation imbalance in stoichiometry or impurity of at least one monomer of even 2% will not allow high molecular weight polymer formation. To ensure exact stoichiometry the purity of monomers as well as dryness is a critical issue. A balance used to weight the monomers must require an accuracy of 0.1 mg. In a theoretical example, an impurity of 2% at a degree of polymerization of 98%, will cut molecular weight to half [22].

A Suzuki reaction is a palladium catalyzed reaction. The active catalyst is a Pd(0) species which is oxygen sensitive. This protocol therefore requires the preparation of the reaction under inert condition. To exclude oxygen from the reaction, both monomers and a base (potassium carbonate) are usually evacuated in a Schlenk-type glassware. Afterwards, the solvents (a combination of toluene, ethanol and water, typically 3:1:1, is bubbled with Ar for at least 20 minutes when a total volume of solvent is in the range of 100-200 mL. It is recommended to apply high (~1200 rpm)

stirring during the bubbling to ensure a complete saturation of the solvent mixture with Ar. After the reaction apparatus is in contact with the preheated oil bath, the catalyst ($Pd(PPh_3)_4$) is added under Ar. During the reaction, it must be made sure that no oxygen can enter the reaction chamber. In addition, it is recommended to cover the reaction chamber with aluminum foil to protect from light. To track the reaction, samples can be taken in different intervals of 15 minutes to several hours, always under Ar protection. These samples (0.1 mL) can be quenched by adding a drop of water and extracted with an organic solvent such as dichloromethane or chloroform and are required for tracking the molecular weight increase by mass spectrometry. Matrix-Assisted Laser Desorption/Ionization-Time of Flight (MALDI-TOF) [23] using Tetracyanoquinodimethane (TCNQ) as matrix is found to be suitable for the class of nanographenes and GNRs.

With prolonged reaction time in the order of hours to days, the molecular weight of the resulting polymer will continuously increase following the step growth mechanism. However, the solubility of the formed polymer will decrease. Before the polymer precipitates out of the solution, the residual terminal functional groups (halogen or boronic acid) must be “end-capped”, to avoid undesired atoms at the terminal positions of the GNR. The “end-capping” must be performed before precipitation of the polymer to ensure conversion of unreacted functional groups. This is achieved by adding a suitable end-capper for example bromo-benzene followed by excess of phenylboronic acid in the respective solvent. The reaction is continued for several hours (at least one) to ensure the full conversion of the terminal functional groups. Afterwards, the reaction is quenched by the addition of water. After extraction and precipitation into typically methanol, the crude polymer can be characterized by mass spectrometry (MS) and analytical site exclusion chromatography (SEC) using PS or PPP as internal standard, although the molecular weight values derived from SEC analyses are only rough estimations and the absolute molecular weights may be obtained by laser light scattering experiments [24] .

Nevertheless, the SEC data are useful for qualitative comparison of the molecular weights of different polymer samples and a crucial indicator for the resulting GNR’s length. At this stage, it is recommended to narrow the broad molecular weight distribution by gel permeation chromatography or centrifugation into fractions of a lower polydispersity index (<1.5). UV-Vis absorption spectroscopy can also provide a qualitative analysis of the polymer length since the wavelength of maximum absorption will shift bathochromic with extension of conjugation length

In contrast to the Suzuki and Yamamoto reaction, the Diels Alder reaction does not require a metal catalyst and can be performed only by the thermal treatment of both monomer [24].This is typically conducted in in either in diphenylether as solvent (reflux, 20-28) or in the pure melt of monomer at T~ 260-270 ºC during 5 hours. However, the constant solubility of the propagating chain must be ensured similar to the Suzuki polymerization.

Preparation of precursor polymers by AA-type polymerization

In contrast to the aforementioned A2B2-type polymerization, the AA-type Yamamoto polymerization is unrestricted by the stoichiometry problem and thus is intrinsically easier to handle than A2B2-type polymerization methods [25, 26]. Furthermore, the Yamamoto polymerization is known to be highly efficient reaction even in sterically demanding systems [27, 28] which can improve the molecular weights (M_W = 52.000 g/mol, M_n = 44.000 g/mol) of the resulting polyphenylene precursors over the ones obtained by Suzuki reaction.

It must be noted, that the catalytic Ni(0) is not as stable as the Pd(0) derivative. Therefore, for the preparation of the reaction mixture ($Ni(COD)_2$, COD, bipy in THF), precaution in avoiding both oxygen and light must be taken. As a general indication: The active catalyst system is deep purple. It will quickly turn dark in contact with traces of oxygen.

Cyclodehydrogenation of Precursor Polymer into final GNR

The cyclodehydrogenation of precursor polymers usually follows a similar protocol. The Scholl-reaction, a oxidative cyclodehydrogenation using Iron(III)chloride as both oxidant and Lewis acid is the most used. The handling of the reaction is similar for a broad variety of GNR.

In a typical procedure, the precursor polymer is dissolved in unstabilized dichloromethane (DCM), which was saturated with Ar by bubbling for 15 min. It is recommended to apply a continuous DCM saturated Ar stream through the reaction chamber. As a starting point for novel systems, usually 6 eq. of $FeCl_3$ per hydrogen to be removed are recommended as oxidant. The FeCl3 oxidant is added as suspension (~100 mg per ml) in nitromethane.

Samples can be taken in sequential time frames of 15 minutes to days and analyzed after quenching of methanol. Due to the very much decreased solubility of the planarized GNR compared to precursor polymers, it is recommended to use MALDI-TOF MS, as well as absorption and Fourier transform infrared spectroscopy (FTIR) for both qualitative and quantitative verification of the degree of cyclodehydrogenation. One of the most dominant side reactions is the formation of chlorinated species. The amount of chlorination can be controlled by the amount of $FeCl_3$ equivalents (6-12) as well as the reaction time, from minutes to days. The reaction is generally at RT.

<u>On surface production of graphene nanoribbons</u>

The on surface bottom-up synthesis concept relies on the use of specifically designed molecular precursor monomers that carry the full structural information of the final GNR together with leaving groups that can be activated on the surface, so that the target structure is built up by establishing covalent bonds between activated sites of adjacent precursor monomers. By this approach, selective growth of a single type of GNR is possible and depends solely on the choice of the precursor

monomer and an activation protocol that triggers the surface-assisted reaction steps under optimized conditions. Recent advances in GNR fabrication and characterization have been described in Ref. [29] .

Synthesis

The bottom-up synthesis of GNRs on surfaces critically depends on the atomic perfection of the used precursor monomers as well as control over the surface-assisted synthesis steps. In the case of one-dimensional target structures (such as for the case of GNRs) this is even more pronounced since any introduced defect profoundly changes the electronic properties or may act as a growth stopper. It is therefore crucial to start with ultrapure precursor monomer samples so that undesired coupling configurations arising from contaminations are minimized. We find that purity judged from nuclear magnetic resonance (NMR) spectroscopy is not sufficient in order to guarantee the lowest possible defect density and maximum GNR length, so that precursor monomer samples need to be further purified with up to eight recrystallization steps. Similarly important is the preparation of "clean" growth substrates: We use Au(111) single crystals (MaTecK.com) or Au thin films on mica (200 nm thickness, Phasis.ch) that are prepared under UHV conditions $< 2 \cdot 10^{-9}$ mbar by two or three sputtering (Ar^+ ions, 1 keV, 15 min.) and annealing (720 K, 10 min.) cycles. The subsequent surface-assisted synthesis steps are schematically depicted in Fig.I. 1.

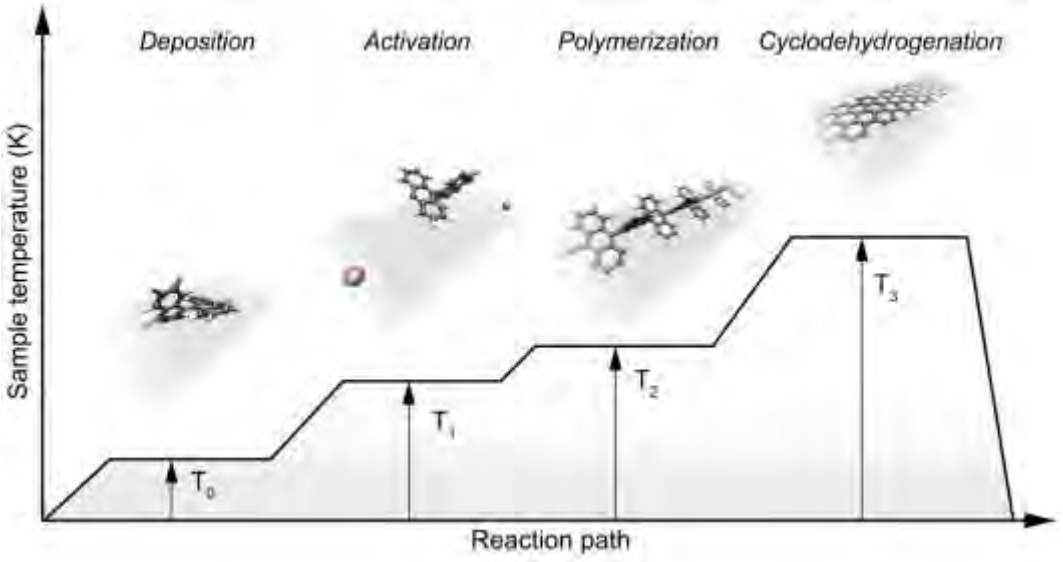

Fig. I.1: GNR bottom-up synthesis concept. GNR synthesis is achieved by deposition of halogen-substituted precursor monomers at a substrate temperature T_0, followed by their activation (halogen cleavage) at T_1, polymerization at T_2, and cyclodehydrogenation at T_3.

All steps are accomplished at a chamber pressure below $2 \cdot 10^{-9}$ mbar while heating the sample to a specific T. In the first step, precursor monomers are deposited on the clean substrate held at T_0.We use quartz crucibles that are resistively heated up to the T needed for maintaining a precursor

monomer flux of 0.1 nm per minute at the sample position, as determined with a quartz microbalance. The sample temperature is then raised to T_1 for the halogen cleavage (activation) and to T_2 for the polymerization of the activated precursors. Finally, GNR are achieved by triggering cyclodehydrogenation of the polymers by heating the growth substrate to T_3. While each of these steps is crucial for the GNR synthesis, not all of the intermediate products are easily accessible for structural characterization. For instance, monomer activation at T_1 ideally leads to doubly activated precursor monomers (biradicals) that coexist with the cleaved halogens at the surface. Practically, however, this phase is often not accessible because the activated species frequently undergo polymerization directly at these T.

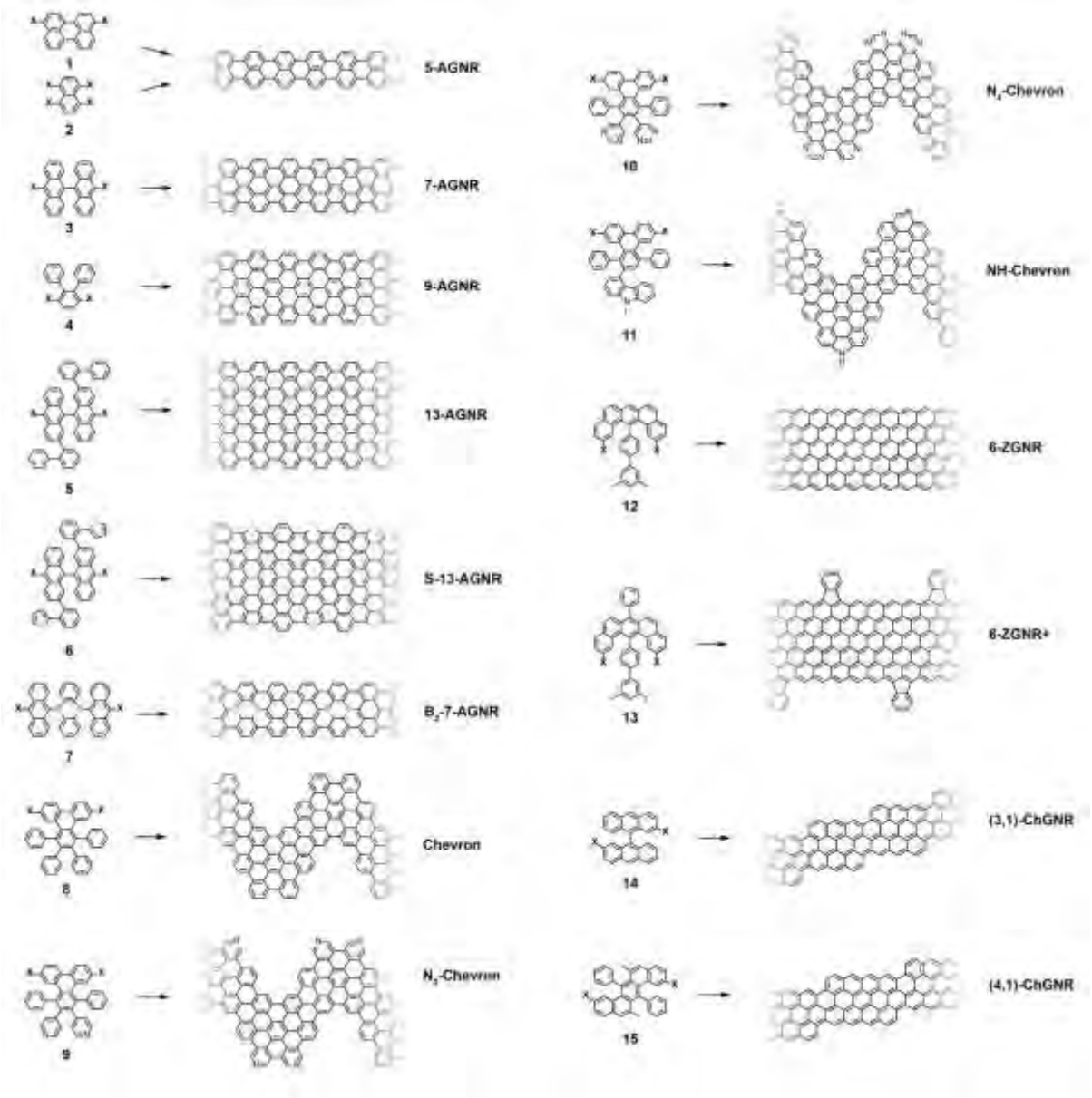

Fig. I.2: Overview of bottom-up synthesized GNRs. X marks the leaving group, which is typically a halogen atom (X = Br, I, Cl). References are: 5-AGNR: [30], 7-AGNR: [13]*, 9-AGNR: [31], 13-AGNR: [32], S-13-AGNR: [33], B_2-7-AGNR: [34, 35], Chevron: [13], N_2-Chevron: [36, 37], N_4-Chevron: [38], NH-*

*Chevron: [39], 6-ZGNR: [40], 6-ZGNR+: [40], (3,1)-ChGNR: [41], (4,1)-ChGNR: *O. Deniz et al., to be published**.

This implies that the activation barrier related to diffusion and covalent bond formation between the biradical species is smaller or equal to the energy barrier for halogen bond cleavage [42]. *Deposition*, *activation*, and *polymerization* steps can be combined into a single step by depositing precursor monomers directly at the polymerization temperature $T_2 = 450$ K. The characteristic time for this combined step is the deposition time (1 – 10 minutes, depending on target GNR coverage) plus 15 minutes hold time. This step is followed by the *cyclodehydrogenation* step, which is triggered by increasing the sample temperature to $T_3 = 630$ K and holding it for 15 minutes. It is crucial to not exceed this T in order to avoid further activation of the formed GNRs. For higher T($T_3 \approx 660$ K) we find covalent crosslinking of GNRs as well as the formation of GNRs of multiple width related to partial edge dehydrogenation of GNRs which triggers GNR fusion (cross-dehydrogenative coupling) to form seamless higher-order GNRs [43]. After the *cyclodehydrogenation* step, the sample is cooled down to RT and either transferred to a connected scanning tunneling microscope (STM) for *in situ* characterization or directly taken out of the UHV chamber for characterization and/or further processing under ambient conditions.

The above mentioned parameters are valid for the growth of GNRs on Au(111), for which the highest quality is achieved for all reported GNR types. An overview on published GNR structures is given in Fig. I.2. The most frequently used halogen atom is Br. The two main reasons for using Br is its better synthetic accessibility for most of the precursor monomers (as compared to I) and its lower reactivity with the growth substrates (as compared to Cl [44]) .

GNR characterization

The main method applied for developing new bottom-up synthesized GNR structures is *in situ* scanning tunneling microscopy (STM, see section IX.1.4). It allows accessing the growth at the surface-related synthesis steps by simply interrupting the growth protocol (Fig. I.1) after a specific step and, subsequently, transferring the substrate to the connected STM chamber. Beside the coverage determination, we use STM for the determination of polymer length after the *polymerization* step as well as for the determination of possible undesired coupling motifs that can occur by either not entirely purified precursor monomer batches or a not fully selective monomer design, which potentially allows for covalent coupling configurations that are not compatible with the envisaged final GNR structure. With the exception of 5-AGNRs, polymerization of the activated precursor monomers yields structures, where not all molecular subunits are planar with respect to the substrate surface. The related apparent height imaged by STM is for all monomers above 0.25 nm, which is clearly higher than the apparent height of the final GNR structure (~0.19 nm). Using this sensitivity, STM allows for a direct access to the onset T of the *cyclodehydrogenation* step by identifying polymer segments where lowered apparent height indicates the related planarization of

the polymer to the final GNR. For the investigation of individual GNRs, T below ~25 K are needed to suppress their mobility on the surface (Fig. I.3).

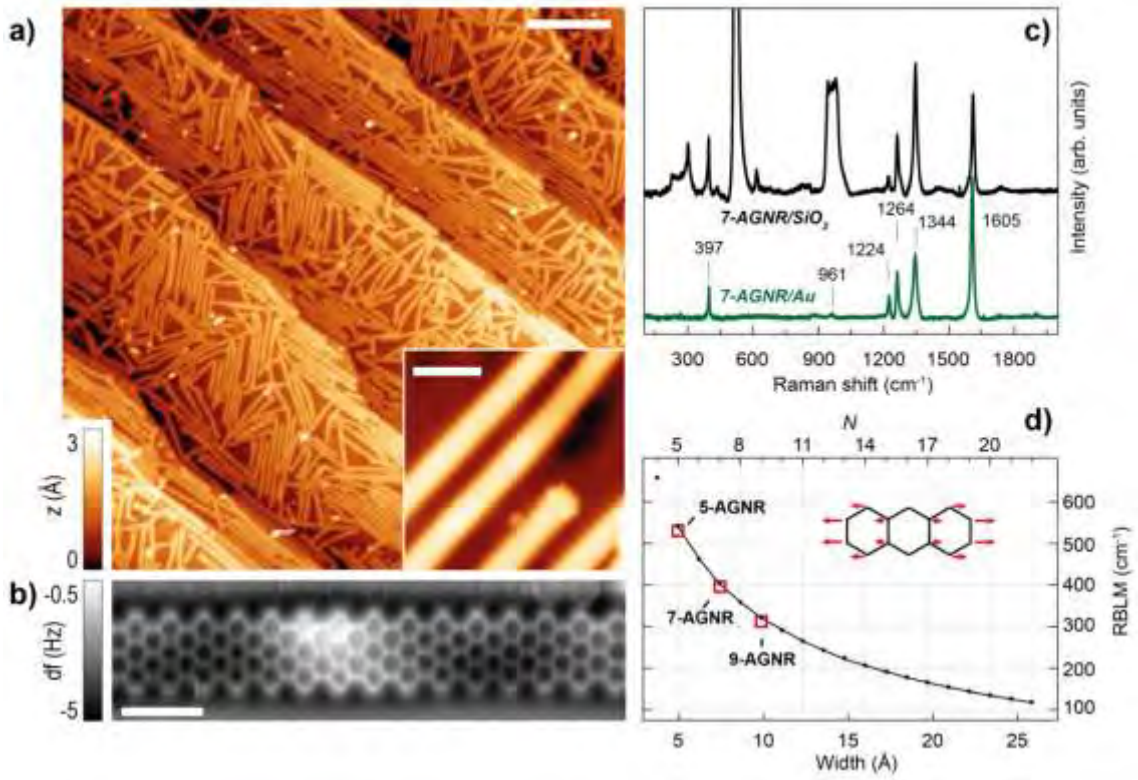

Fig. I. 3: Characterization of 7-AGNRs on their growth substrate and after substrate transfer. a) Large-scale STM topography image (Bias: -0.5 V; Current: 5 pA; T: 4.5 K; Scale bar: 30 nm) showing high coverage 7-AGNRs on Au(111). Inset: small-scale STM image (Bias: 0.1 V; Current: 30 pA; Scale bar: 3 nm). The apparent height of individual 7-AGNRs is 0.19 nm. (b) Constant-height nc-AFM frequency shift image (Bias: 2 mV; Oscillation amplitude: 0.3 Å; T: 4.5 K; Scale bar: 1 nm) taken with a CO-functionalized tip. (c) Raman spectra of 7-AGNR on Au(111) recorded under ambient conditions immediately after synthesis (green curve) with indicated peak positions of the main lines, and after transfer to Si/SiO_2 (black curve; laser 532nm, power of 2mW, 3 scans of 20 seconds). (d) RBLM peak position for 5-AGNRs, 7-AGNRs and 9-AGNRs (red markers), together with predicted width-dependent RBLM wavenumbers for AGNRs [45].

An even higher resolution is achieved by using non-contact atomic force microscopy (nc-AFM) where the tip apex can be decorated with specific molecules or atoms to yield unprecedented insight into the chemical structure of the synthesized carbon nanostructures [46]. Tungsten tips attached to a tuning fork sensor [47] have been used in a low-T STM (ScientaOmicron) which are functionalized with CO molecules by dosing CO onto the surface and a controlled pick-up procedure [48]. By recording the frequency shift image at constant height (Fig. I.3 b), the chemical structure of GNRs can be visualized with a resolution that is going down to individual chemical bonds. The sensitivity is high enough to resolve, for instance, additionally attached hydrogens at ZGNR edges (H_2- instead of H-termination) [40]. With this unique structural sensitivity, nc-AFM is complementary to STM, which is only indirectly sensitive to the investigated atomic structure by recording an apparent structure

defined by the local density of states near the Fermi level. The used constant-height imaging mode, however, can only be applied to the flat final GNR structures. Non-planar structures such as the used precursor monomers and the polymer intermediates are hardly accessible by nc-AFM due to the related 'constant height' imaging mode

The main *ex situ* characterization tool applied to GNRs is Raman spectroscopy. Owing to their atomically defined structure, GNRs present well defined excitations in Raman spectra (Fig. I.3 c). The main excitations observed are the so-called G-mode (~1590 cm^{-1}), D-mode (~1350 cm^{-1}) with overtones and the width-dependent radial-breathing-like mode (RBLM) (~396 cm^{-1} for 7-AGNRs) [49]. In contrast to graphene, where the intensity of the D-mode is linked to the defect density, this mode is intrinsic for GNRs due to the presence of edges. For this *ex situ* characterization conducted prior to further processing, we place the GNRs/Au or GNRs/substrate under a 50x or 100x objective lens and adjust the focus (for an optimized spectrum it is important to have a fine adjust of the focus in order to maximize Raman counts). For laser energies ranging from 457 to 633nm we use between 1-2mW power (higher power can result in thermal effects). For laser energies in the infrared range (785nm) a max of 10mW is used. In order to reach an optimized signal-to-noise ratio, at least 3 scans with 20 seconds integration time are recorded. These values need to be adjusted for each laser line. It is important to select the photon energy of the laser source close to one of the fundamental optical excitations of the GNRs since the GNR modes show a pronounced resonance behavior [31]. For 7-AGNRs with an optical band gap of 1.9 eV [50], all characteristic modes are efficiently excited using a green laser (532 nm, 2.33 eV). For 9-AGNRs with an optical band gap of 1.1 eV [51], all excitations are resolved with an infrared laser line (785 nm, 1.55 eV). Exchanging the two laser lines for both examples leads to a loss of resonance conditions and the width-characteristic RBLM mode cannot be resolved anymore.

GNR transfer

The on-surface synthesis of GNRs relies on the catalytic action of the metallic growth substrate, and therefore requires their transfer onto dielectric substrates for further exploration of their electronic or optical properties. The first successful transfer was achieved using a sacrificial PMMA layer deposited onto the as-grown GNRs [52], which is stripped off after GNR transfer to the target substrate. More recently, we have developed a transfer method allowing for the transfer of GNRs without PMMA deposition, which avoids possible contamination problems related to PMMA residues [38, 49]. The main strategy followed here is delamination of Mica from the Mica/Au/GNR stack in an hydrochloric acid from which the remaining Au/GNR stack is directly picked up with the target substrate. In a last step, the Au layer is then dissolved leaving a clean GNR film (without Au or iodine residues) on the target substrate. To do so, we use a small plastic container (3cm x 2.5 cm x 1.5 cm) where we add 4ml of concentrated (38%) hydrochloric acid (HCl). With the help of tweezers, the GNR/Au/mica stack is then placed on top of the HCl with the GNR/Au film facing up. After 15-20min the mica should detach from the Au (in case this does not happen, the cleaving off can be aided by

moving the container). Once the mica is detached, the acid is removed from the container in subsequent steps. First, we remove around 3ml of the acid. In order to prevent sticking of the Au film at the container walls, it is important to not remove the acid completely. After removing the acid, we slowly add 5ml of water using a pippete.Again, take ~4ml of water out and add 5ml. We repeat this process 4 or 5 times in order to substantially reduce the HCl concentration. In the last dilution step, we keep the container full of water for the pickup of the Au film with the target substrate. It is important that the target substrate is free of any impurities. To do so, we soak it in 10-15ml of acetone (if the substrate does not have sensitive fine structures it is also possible to sonicate for 10 min) and then soak it for 10 min in 10-15ml of ethanol (or sonication). The target substrate is then rinsed with 20-30 mL of water and dried with N_2.

With the help of tweezers, we approach the target substrate (facing down) and press it against the floating Au/GNR film until they stick together. The merged Au/GNR/substrate stack is then pulled out of the water. At this stage, the Au film is usually not completely flat on the substrate. In order to increase the contact between Au film and substrate we add 1-2 drops of pure ethanol and let it dry in ambient conditions (this takes around 10-15 min). Once dried, we put the Au/GNR/substrate stack on a hot plate at 100ºC for 10 min. This two-step process results in a flattening of the Au film on top of the target substrate. The Au film is then removed by adding 1-2 drops of Au etchant (KI/I_2, no dilution, CAS No. 7681-11-0) on top of the gold film and waiting until the Au film is completely etched away (around 5 minutes). Finally, to clean the GNRs/substrate, we soak it in water (5-10min), rinse it with 20-30mL of acetone/ethanol and water and finally dry it under N_2 flux.

Using this method, we so far successfully transferred 5-AGNRs, 7-AGNRs, 9-AGNRs and Chevron GNRs to SiO_2, CaF, Al_2O_3, glass slides and TEM grids (lacey carbon supported graphene, TedPella.com). The main characterization tool used to prove that the structure of the GNRs remains intact upon transfer is Raman. An example of Raman spectra taken before and after transfer of 7-AGNRs is shown in Fig. I.3 c). All the characteristic 7-AGNR lines are present in the spectrum taken after transfer. Most importantly, the sensitive radial breathing like mode (RBLM) observed at 397 cm^{-1} remains equally intense and does not show significant broadening.

I.2 Graphene- and carbon nanomembranes (CNM)

Carbon nanomembranes (CNM) with tunable properties can be grown by conversion of aromatic self-assembled monolayers (SAMs) and subsequently converted into GRM [53-60]. The process is schematically shown in Fig. I.4a. First, a SAM is formed on a solid substrate, then the monolayer is converted into a carbon nanomembrane [61], (CNM) *via* electron irradiation [62], and finally the CNM is transformed into GRM *via* annealing in vacuum (pyrolysis) or in an inert atmosphere. By tuning the structure of molecular precursors (Fig. I.4b), parameters of the self-assembly, substrate materials, electron irradiation and annealing conditions, GRM with adjustable crystallinity, thickness, porosity and electronic properties can be produced.

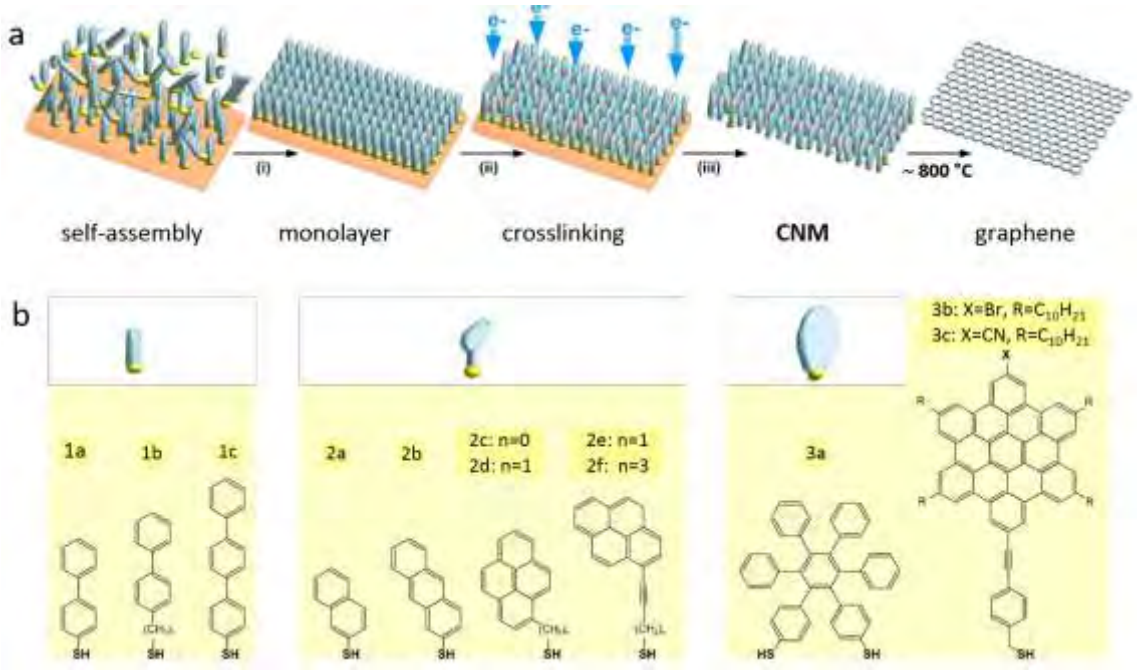

Fig. I.4: Formation of CNMs and GRM from aromatic self-assembled monolayers. a, Schematic illustration of the fabrication route for CNMs and graphene: Self-assembled monolayers are prepared on a substrate (i), then crosslinked by electron irradiation to form CNMs of monomolecular thickness (ii). The CNMs are released from the underlying substrate (iii), and further annealing at 900 °C transforms them into graphene or GRM. b, Chemical structures of the different precursor molecules used for synthesis of CNMs and graphene. Figure adapted from [53].

Molecular self-assembly

Molecular self-assembly of aromatic molecules can be flexibly performed from solvents [53, 63] or by vapor phase deposition [64, 65]. For the self-assembly on coinage metal substrates, typically thiol functional groups are employed providing a covalent binding of the molecules to the substrate [66]. The solvent-based self-assembly of 1,1'-biphenyl-4-thiol (BPT, **1a**, in Fig I.1.4b), an aromatic

precursor used for the production of single graphene layer [54, 59] on Au substrates can be conducted as follows [65]. The substrates (typically 300 nm Au/mica) are immersed into a 0.2 µM solution of BPT in dimethylformamide (DMF) at RT for about 3 days resulting in the formation of a densely packed and well-ordered BPT SAM. Alternatively, a BPT SAM can be prepared by vapor deposition. There, BPT powder is heated to 60 °C in vacuum and sputter-clean Au substrates are exposed the to a BPT vapor pressure of ~10^{-7} mbar for about 1 hour [65]. Both methods allow the formation of BPT SAMs with comparable structural quality, although the solvent-based preparation typically results in a slightly higher (~5 %) packing density of the formed SAMs. In case of the self-assembly from solvents the solvent/molecule interactions play an important role [66], and the packing density of the formed SAMs can be tuned by adjusting the solvent polarity and concentration of the precursor molecules [53]. In comparison to the solvent-based self-assembly, the self-assembly by vapor deposition requires high vacuum equipment but provides a significantly shorter time (~1h compared to 3 days) for the preparation of a SAM. For practical reasons, these different aspects have to be considered when designing the experiment. Furthermore, vacuum vapor deposition is preferred over solution deposition in the case of the formation of thiol-based SAMs on oxidative metal substrates (e.g., Cu or Ni), as the metal oxidation which hinders the self-assembly is avoided [64, 66].

Electron irradiation induced crosslinking of aromatic SAMs and formation of CNMs

Electron irradiation of aromatic SAMs results in lateral crosslinking of the constituting molecules and formation of carbon CNMs [53, 62, 67]. The mechanisms of the electron irradiation induced crosslinking are in detail discussed in [62] and have also recently been reviewed in [68]. Here only the essential features of this process and most recent experimental [69, 70] and theoretical results [71] are described. It is important to note that in aliphatic SAMs the electron irradiation results in significant up to 80-90% molecular decomposition and desorption [72, 73]. In contrast, in aromatic SAMs upon the same treatment a new 2d carbon material is formed. To induce the crosslinking in aromatic SAMs with low-energy electrons (50-100 eV), typically doses of ~50 mC/cm^2, corresponding to ~750 electrons per molecule, are used. Because of the electron irradiation, C-H cleavage takes place [70], which is the predominant process leading to a crosslinking between adjacent aromatic rings. As suggested by UV photoelectron spectroscopy, quantum chemical and molecular dynamics calculations of BPT SAMs on gold, the formation of single- and double-links (C-C bonds) between phenyl rings of the molecules is expected during crosslinking [62]. This picture is also supported by UV-Vis spectroscopy of the formed CNMs [56]. Recent molecular dynamic calculations suggest [71] that a partial dissociation of the aromatic rings can take place and play a role in the formation of a 2D carbon network. Such a mechanism would be in agreement with partial desorption of carbon in purely aromatic SAMs as observed by XPS. The XPS data also show that the irradiation and the subsequent molecular reorganization also affects the sulfur-gold bonds. These structural changes at

the molecule/substrate interface are in agreement with the recent LEED and STM results showing a loss of the long range (>5 nm) order in the SAMs upon electron irradiation [54].

Complete crosslinking of aromatic SAMs can be also achieved via He^+ ion irradiation [74] with exposuresrequires an exposure dose ~1 mC/cm^2, which is roughly 60 times smaller than the corresponding electron irradiation dose. Most likely, this effect is due to the energy distribution of secondary electrons that have a maximum at energies below 50 eV, which results in a more efficient dissociative electron attachment (DEA) process. The crosslinking can also be achieved employing UV/EUV [75] and potentially higher energy electrons (few keV) [76].

After the electron irradiation of the aromatic SAMs, the formed CNMs can be separated from the original substrates and transferred using the poly(methyl methacrylate) (PMMA) assisted transfer onto new solid or perforated substrates (e.g. grids, see section 6.1.1) [58], where they form large free-standing areas (up to 0.3 mm^2). Fig. I.5 shows helium ion microscope (HIM) images of free-standing CNMs from different types of aromatic molecular precursors [53]. These images shows unbroken membranes which demonstrates mechanically stable CNMs. CNMs with extremely large free-standing areas of up to approximately 0.3 mm^2 can be obtained in this way. Since the thickness of CNMs is determined by the size of the precursor molecules and their packing in the SAMs, it can be tailored by varying these parameters enabling nanomembrane engineering. Fig. I.5a-c shows examples of CNMs where the thinnest nanomembrane has a thickness of d=0.6 nm, while the thickest CNM had d=2.2 nm. Different CNMs have been fabricated and were investigated by HIM. A clear relation between the size and shape of the precursor molecule, the degree of order in its SAMs and the appearance of the ensuing CNM has been established. If the molecule forms a densely packed SAM (**1a-c**, **2a-c**, **2e** in Fig. I.4b), the corresponding CNM is homogeneous and free of holes above 1.5 nm diameter. Fig. I.2d shows a HIM image of such a CNM made from terphenylthiol (**1c**). Conversely, CNMs made from large molecules, i.e. hexabenzocoronenes (HBC, **3b-c** in Fig. I.4b) or S,S'-(3',4',5',6'-tetraphenyl-[1,1':2',1''-terphenyl]-4,4''-diyl) diethanethioate (HPB, **3a** in Fig. I.4b), form less ordered SAMs and exhibit pores, as presented in Fig. I.5e-f. Here the dark spots are pores with diameters of 2-10 nm. Note that these pores have a narrow size distribution (see histogram insets). In case of the HBC precursor the mean size of the nanopores is approximately 6 nm with the surface density of 9.1×1014 pores/m^2; the more compact HPB precursor shows a size of approximately 2.4 nm with a surface density of 1.3×1015 pores/m^2. The formation of nanopores in these CNMs can be attributed to the large lateral dimensions of HBC and HPB molecules in comparison to smaller molecular precursors (see Fig. I.4b) and in the case of HBCs to the tendency of the disk like molecules to intermolecular stacking which reduces the ordering in the respective SAMs. The average pore diameter correlates with the SAM thickness and decreases from 6.4 nm to 3.0 nm when the thickness increases from 1 to 2 nm [53].

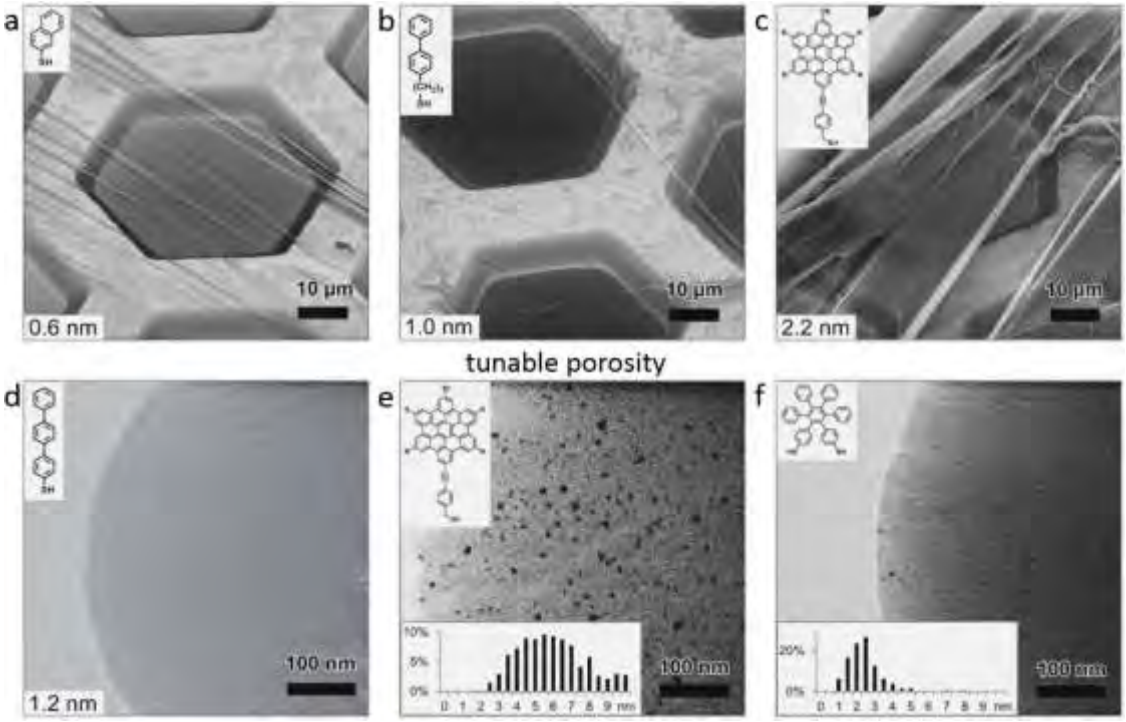

Fig. I.5: Helium Ion Microscope (HIM) images of free-standing CNMs. After crosslinking the nanomembranes were transferred onto transmission electron microscope (TEM) grids and images were taken at different magnifications (see scale bar). CNMs were prepared from: a) Naphtalene-2-thiol (NPTH, ***2a)****; b) 3-(biphenyl-4-yl)propane-1-thiol (BP3,* ***2b****). c) 2-Cyano-11-(1'-[4'-(S-Acetylthiomethyl)phenyl]acetyl)-5,8,14,17-tetra(3',7'-dimethyloctyl)-hexa-peri-hexabenzocoronene (HBC-CN,* ***3c****); d) [1'',4',1',1]-Terphenyl-4-thiol (TPT,* ***1c****); e) 2-Bromo-11-(1'-[4'-(S-Acetylthiomethyl)phenyl]acetyl)-5,8,14,17-tetra(3',7'-dimethyloctyl)-hexa-peri-hexabenzocoronene (HBC-Br,* ***3b****); f) S,S'-(3',4',5',6'-Tetraphenyl-[1,1':2',1''-terphenyl]-4,4''-diyl) diethanethioate (HPB,* ***3a****). The upper left insets show the precursor molecules. The CNMs in (a-c) are suspended over copper grids, CNMs in (d-f) over Cu grids with thin holey carbon film. The numbers in the lower left corners in a-d indicate the CNM thicknesses, as determined from XPS before the transfer. HIM images e and f show CNMs with nanopores, the lower insets show the respective distributions (in %) of pore diameters (in nm). Figure adapted from [53]*

Conversion of CNMs into Graphene and GRMs via pyrolysis

- *Formation of nanocrystalline graphene/GRMs*

CNMs possess an extremely high up to 800 K thermal stability [63], which enables their conversion into graphene/GRMs *via* pyrolysis in vacuum or in the inert atmosphere [53, 58]. The crystallinity of the produced GRM can be tuned by the annealing conditions, i.e. T and substrate material. The formation of nanocrystalline GRM sheets by annealing of free-standing CNMs [58] on TEM grids (Fig. I.6a) is described , on substrates like gold [59] or silicon oxide [56, 57]. Although sulfur

is initially present in the CNMs both, XPS (of supported sheets) and scanning Auger microscopy (of suspended sheets), indicate that after annealing above 800 K all sheets consist only of carbon [58, 62]. At this T, the structural transformation of CNMs into GRM sets in, which is most evident from appearance of the characteristic D-, G- and 2D peaks in the Raman spectra [77] at 1350, 1590 and 2700 cm^{-1}, [57-59] respectively. This transformation can also be directly visualized by HRTEM [53, 59]. As shown in Fig. I.6b, after annealing of a BPT CNM (chemical formula **1a** in Fig. I.4b), most of the sheet area (~70%) is single-layer graphene, which is clearly recognized by the hexagonal arrangement of carbon atoms. Randomly oriented nanocrystallites graphene domains are connected with each other *via* the typical heptagon-pentagon grain boundaries [78] (see inset to Fig. I.6b); a small fraction (~20%) of the sheet consists of graphene double-layer, which is recognized from the well-known Moiré pattern [79] and some of the sheet area (~10%) shows disordered carbon atoms forming a 2D amorphous phase [80].

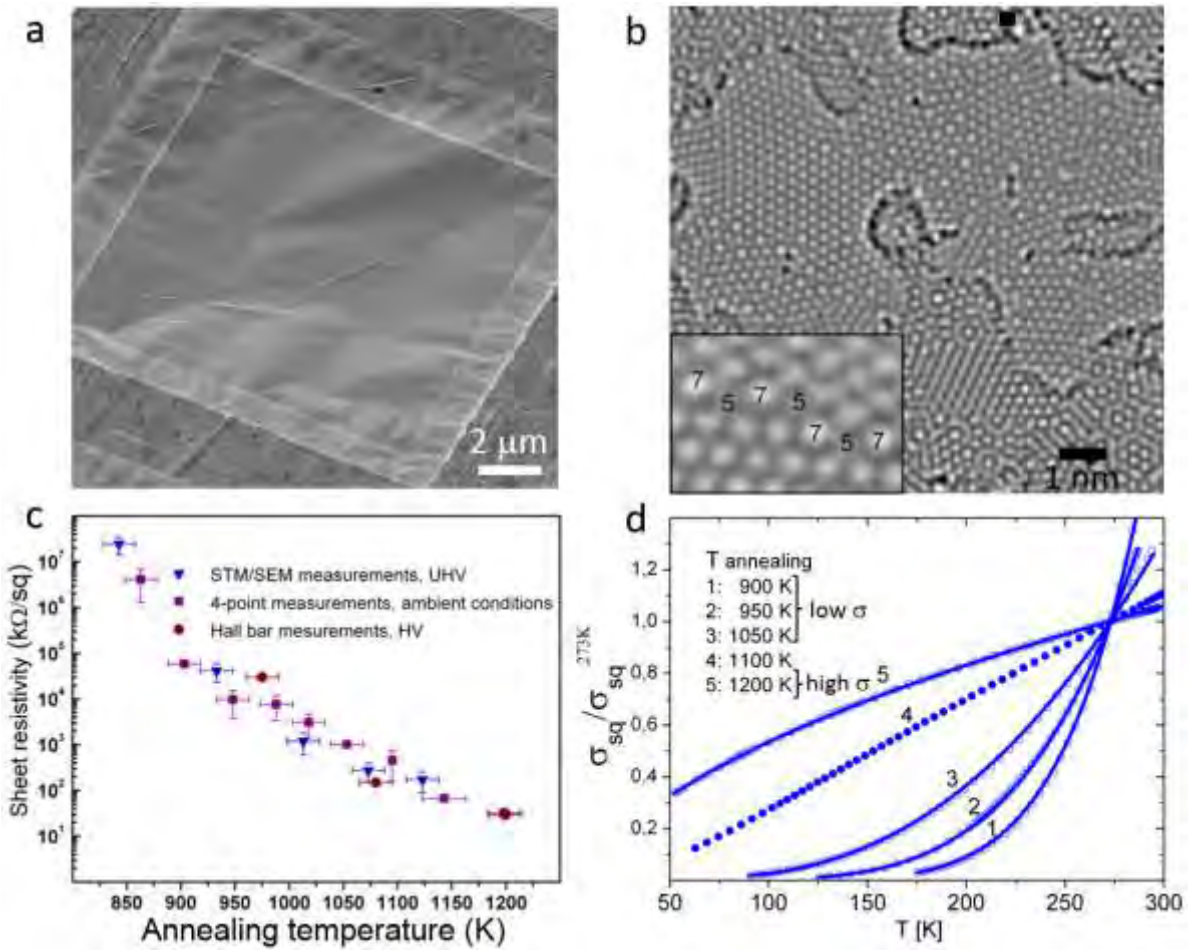

Fig. I.6: Conversion of 1,1'-biphenyl-4-thiols (BPT) CNMs into nanocrystalline GRM upon annealing. a) Helium ion microscope image of a BPT CNM annealed to 1000 K on a gold TEM grid. b) Atomic structure of a similar sample obtained by aberration-corrected high-resolution transmission electron microscopy (AC-HRTEM, 80 kV). The inset shows a magnified grain boundary where arrangements of carbon atoms into pentagons and heptagons are highlighted. c) RT sheet resistivity of the samples as a function of annealing T d) T dependencies of the normalized sheet conductivity

clearly demonstrates the change in electrical transport mechanism, i.e. insulator to metal transition. Fig. b adapted from [53],Fig. (c-d) adapted from [59].

The conversion of CNMs into graphene/GRM influences the electrical and optical properties [56, 58, 59]. Fig. I.6c shows the sheet resistivity of BPT CNMs as a function of annealing T. The measurements were conducted at RT by different methods after respective annealing steps on both supported and suspended GRM. The non-annealed CNMs are dielectrics do not show any measurable lateral conductivity, electrical conductivity was first detected after annealing at ~800 K. After annealing at higher T (~1200 K) the conductivity increases by six orders of magnitude approaching a value of ~10 kOhm/sq. To characterize the influence of this transformation on the electrical transport, the T dependencies of the electrical conductivity, $\sigma(T)$, and the electric field effect were studied in microfabricated Hall-bar devices [59]. Samples with lower annealing T (900, 950 and 1050 K), (1-3) in Fig. 6d, i.e. with lower degree of transformation into graphene, demonstrate insulating behavior with a positive curvature in T. Their T dependence can be well described by $\sigma(T) \propto \exp\left[-\left(\frac{T_0}{T}\right)^{\frac{1}{3}}\right]$ representing the Mott law, which is characteristic of the thermally activated variable range hopping in a 2d system with weak Coulomb interaction. For the sample with the highest degree of transformation into graphene, (5) in Fig. I.6d, $\sigma(T)$ shows a negative curvature with $\sigma(T) \propto T^{1/2}$, i.e. a semi-metallic state. Since the conductivity of nanocrystalline GRM in the insulating regime strongly depends on the density of states, a large ambipolar electric field effect was observed. It was found that the electron mobility in nanocrystalline GRM is approximately 50 cm^2/Vs at RT [59]. Note that the evolution of the electric transport characteristics upon the conversion of CNMs into nanocrystalline GRM is reminiscent to that observed upon the thermal reduction of graphene oxide (GO) into reduced graphene oxide (r-GO) sheets [81, 82]. In both cases the final material presents an interconnected network of graphene nanocrystallites, however, in case of the r-GO some amount of the oxygen containing groups is present [83] whereas nanocrystalline GRM sheets obtained by the conversion BPT CNMs consist only of carbon [53, 58, 59] .

The thickness of the formed graphene sheets depends on the structure of precursor molecules, their ability to form SAMs and to be crosslinked into CNMs. Thus, by varying precursors (see Fig. I.4b), the thickness of the formed nanocrystalline GRM sheets can be tuned by a factor of ~3 [53]. The resistivity correlates with the thickness of the GRM sheets, with lower resistivity for thicker sheets [53, 56]. An interesting opportunity is opened up by using nitrogen- or boron-containing precursors, as in this case, GRM sheets doped by these elements can be expected, which are of interest for applications in catalysis [84] or energy storage.[85]

Formation of polycrystalline graphene

Employing the conversion of CNMs into GRM by performing pyrolysis on catalytically active substrates like copper, graphene layers with high crystallinity and, therefore, high mobility above

2000 cm^2/Vs can be attained [54]. As a model system, we present the conversion of BPT SAMs (see chemical formula **1a** in Fig. I.4b) into graphene on copper foils. The Raman spectroscopy data (see Fig. I.7a) show an evolution of the characteristic D, G and 2D Raman peaks as a function of T. The conversion of a CNM into graphene with T is clearly observed. For the highest annealing T (830 °C), the same features as known for single-layer graphene prepared by mechanical exfoliation (G peak at 1587 cm^{-1} and a narrow Lorentzian 2D peak at 2680 cm^{-1} (FWHM=24 cm^{-1}) [86] are observed after the conversion. The grown sheets were transferred onto grids and onto oxidized highly doped Si-wafers and were characterized by HRTEM and by electric transport measurements. The HRTEM and selected area diffraction (SEAD) data unambiguously confirm formation of SLG [87], Fig. I.7b-c. The dark-field TEM imaging shows that the formed sheets consist of graphene single crystals with the lateral dimensions up to 1-2 μm [54].

Electric transport properties of the synthesized graphene films were studied by four-point measurements in the Hall bar geometry (see inset in Fig. I.7d-e) [54]. Fig. I.7d presents the observed ambipolar nature of graphene as measured in a FET device. The RT charge carrier mobility, □, extracted from the data at a hole-concentration of 1×10^{12} cm^{-2}, has a value of approximately 1600 cm^2/Vs. μ values at lower charge carrier concentrations, where electron-electron interactions can be neglected, are ~ 2300 cm^2/Vs. Further characterization of the transport properties at low T (T = 0.3 K) in a magnetic field of 15 T demonstrates that by varying the charge density with the back-gate voltage, Shubnikov - de Haas oscillations and resistivity plateaus of the quantum Hall effect specific for SLG are observed [88]. These results unambiguously confirm the high electronic quality of the grown sheets making them attractive for high performance electronic applications.

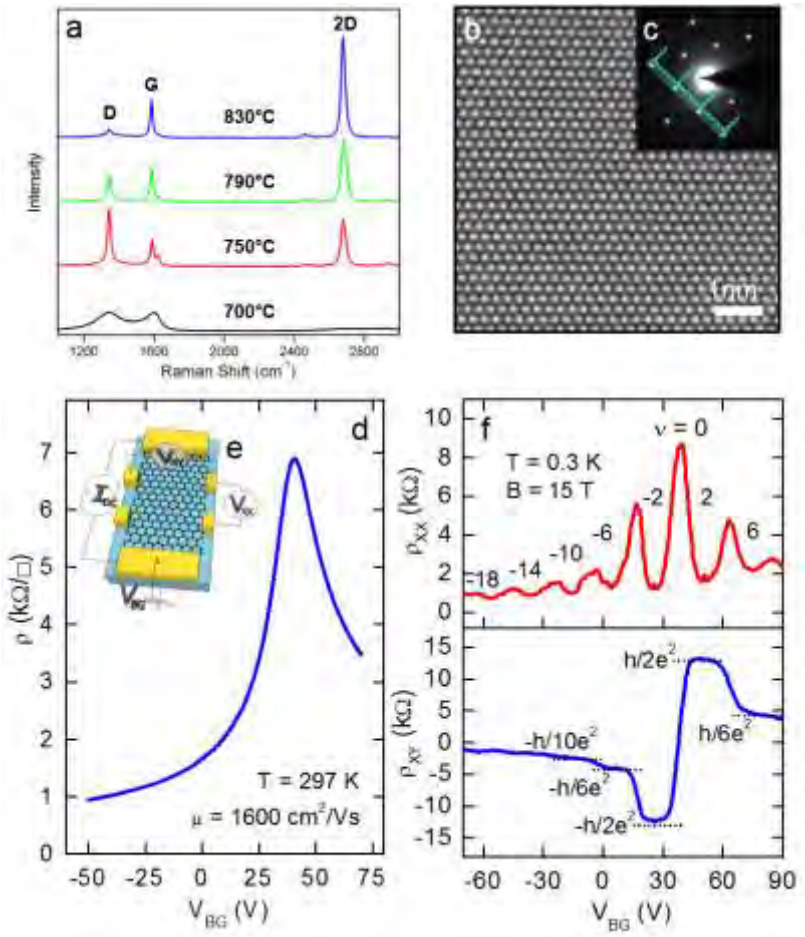

Fig. I.7: Conversion of 1,1'-biphenyl-4-thiols (BPT) CNMs into graphene on Cu foils. a) Raman spectra (λ_{exc} = 532 nm) of the conversion of BPT CNMs into graphene as a function of T. The sheets after annealing were transferred from copper foils onto silicon wafers with 300 nm of silicon oxide. b) HRTEM micrograph of the sheet clearly resolves the honeycomb lattice of graphene. The single layer nature of this film can be determined from the HRTEM image contrast; it was further verified by the selected area electron diffraction shown in (c). d) RT resistivity of the graphene measured in vacuum as a function of back-gate voltage using Hall bar devices schematically depicted in (e). f) Quantum Hall effect at 0.3 K and 15 T. The upper plot shows Shubnikov-de Haas oscillations with the corresponding filling factors and the lower plot shows the Hall resistance as a function of back gate voltage, i.e. varied charge carrier density. Figure adapted from [54].

Direct growth of graphene/GRM micropatterns

Since only the electron-beam irradiated areas of SAMs undergo conversion into graphene/GRM, both large-area up to 10 cm^2 and more graphene sheets and GRM of various architectures (e.g., nano-ribbon, dot, anti-dot patterns) can be fabricated from SAMs by employing either defocused electron flood exposures [54, 58] or exposures by focused electron beams [55]. Because only electron-irradiated (crosslinked) regions of aromatic SAMs are converted into graphene/GRM upon annealing, whereas non-irradiated (pristine) SAMs desorb from the surface [63], the suggested

approach provides a unique opportunity to directly grow graphene/GRM patterns by area-selective electron irradiation [60], Fig. I.8a. Therewith, at least four technological steps (spin-coating of photoresist, developing of photoresist, reactive ion etching, stripping of photoresist) employed in the conventional microfabrication of graphene electronic devices are omitted. Fig. I.8b shows a graphene pattern grown on a copper foil at 800 °C after a BPT SAM was locally crosslinked by a primary electron beam of 3 keV and doses ranging from 75 mC/cm² to 125 mC/cm². The successful transfer of this structure onto a 300 nm SiO_2/Si substrate is presented in Fig. I.8c. As can be seen by comparing the distances between the single structure elements in Fig. I.8b (on Cu) and 8c (on SiO_2/Si), the structural integrity is conserved during the transfer process. Only a few elements show folding defects or missing parts. In this case, the local adhesion to the substrate is too weak to withstand the forces occurring during the removal of the transfer medium in solvent [60]. More advanced transfer techniques, like electrochemical delamination [89] or a clean-lifting transfer [90] may be applied to avoid or minimize the creation of defects (see Section VI). The minimum size of the features in the grown graphene pattern correspond to approximately 1 µm. Note that the lateral resolution is defined in principle by the resolution of electron-beam lithography, which has been shown to be 7 nm for SAMs [91]. Another interesting opportunity is given by the fact that molecular self-assembly can be conducted on non-planar surfaces, thus it is also feasible to apply the developed methodology to create graphene/GRM structures on any three-dimensional shape.

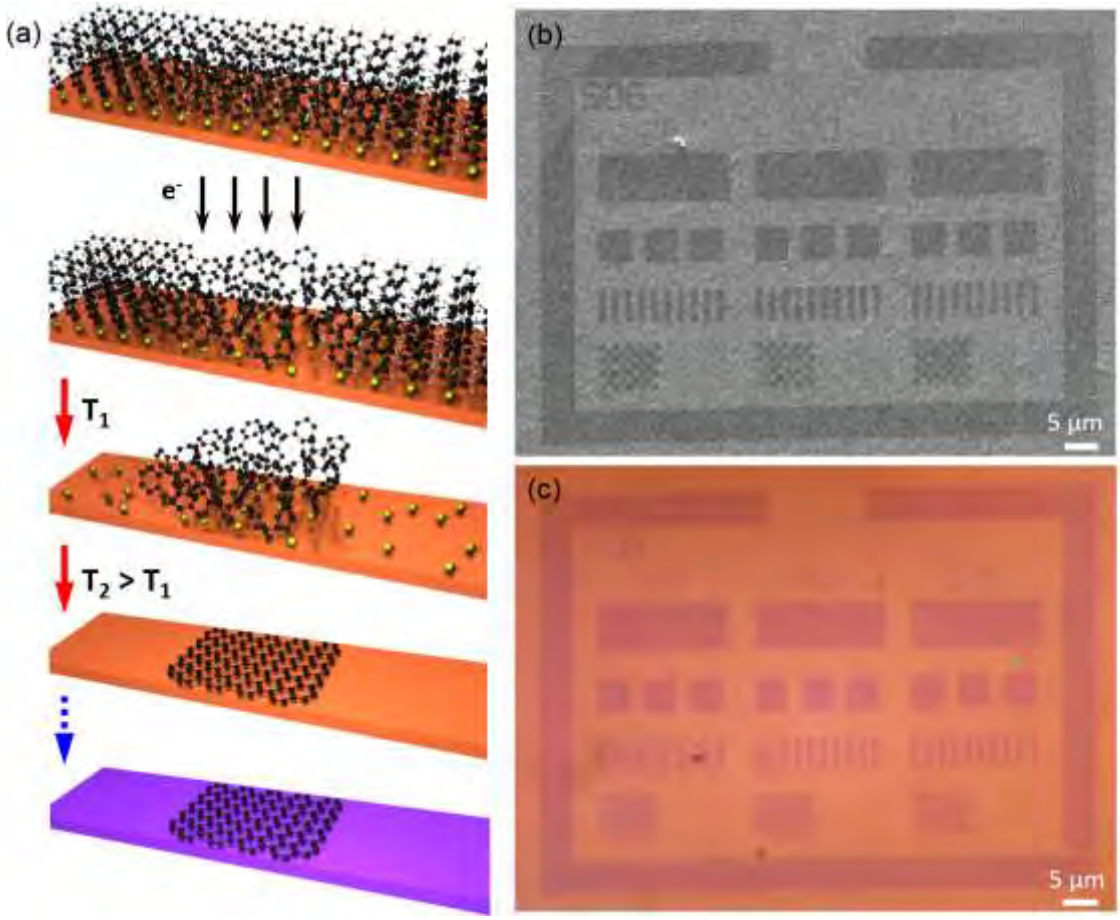

Fig. I.8: Direct growth of patterned graphene. a) Schematics of direct growth of patterned graphene. b) SEM image of graphene microstructures directly written on top of the copper surface by

irradiating a BPT SAM with a focused electron beam (3 keV, 75 mC/cm² (left) - 125 mC/cm² (right)) and subsequent annealing (800 °C). c) Same structure after transfer to a SiO2/Si wafer. Figure adapted from [60].

I.3 0d/2d Heterostructures from CNMs

Stacking of 2d sheets including graphene, hexagonal boron nitride, or metal chalcogenides into the layered vdW heterostructures have led to novel composite materials with a high potential for applications and in fundamental research [92, 93].The integration of other low dimensional materials into these heterostructures extending these borders even further. Here we present a modular and broadly applicable route to create hybrid vdW heterostructures made of individual approximately 1 nm thick Janus CNMs (JNM) [94] functionalized with other low-dimensional materials (see Fig. I.9).

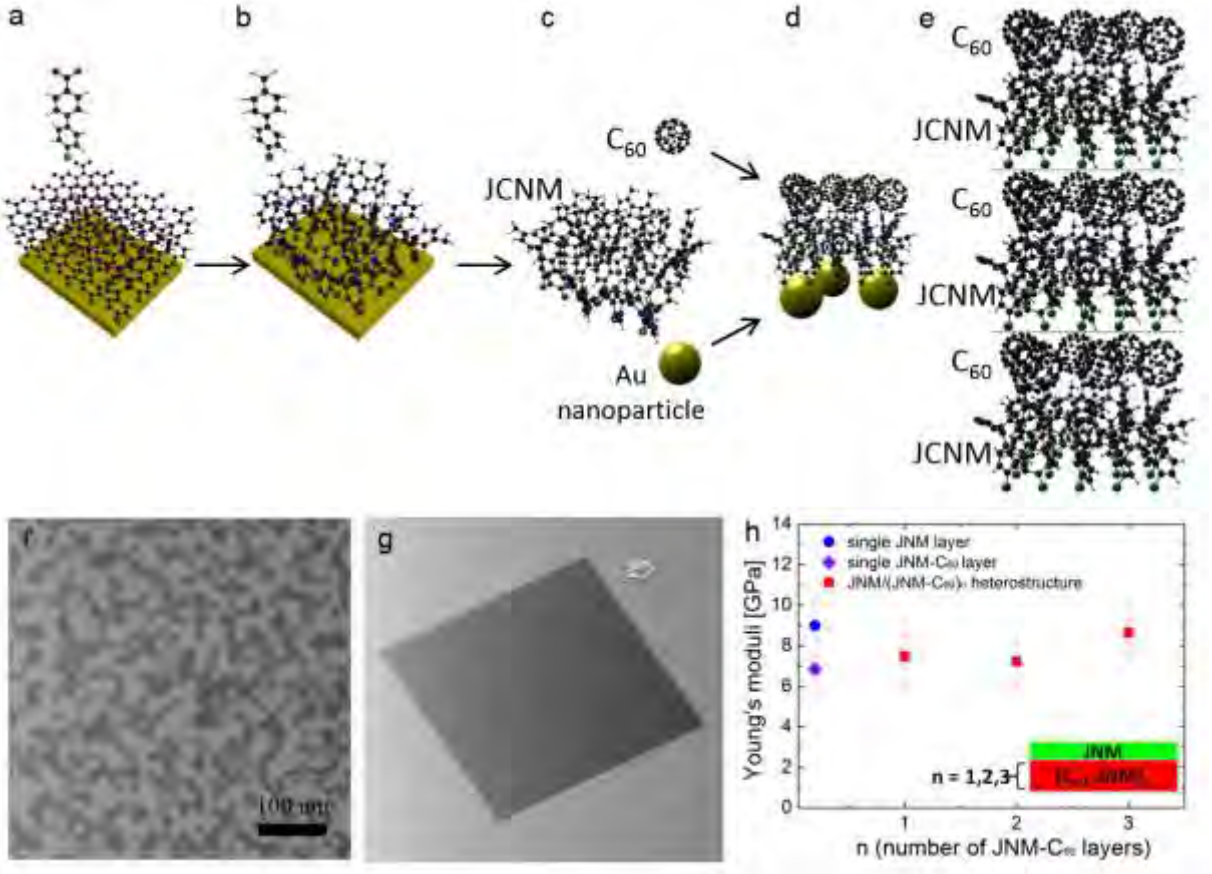

Figure I. 9: Hybrid van der Waals heterostructures of 0d and 2d carbons. a-e) Schematic representation of the heterostructure assembly. a) Formation of a NBPT SAM on a gold substrate. b) Electron irradiation induced crosslinking and reduction of the terminal nitro groups into amino groups. c) Formation of a free-standing JNM with the terminal N- and S-faces. d) Functionalization of the N- and S-faces with C_{60} and Au-NP, respectively. e) Assembly of a (C60–JNM)$_n$ (here n=3) hybrid heterostructure by mechanical stacking. Color code for atoms: black – carbon, grey – hydrogen, blue – nitrogen, green – sulfur, and red – oxygen. f) Helium ion microscope (HIM) images in the scanning transmission ion mode shows the immobilization of 16 nm Au NPs on a JNM which are uniformly

distributed with an coverage of approximately 50%. g) HIM image of an JNM-(C_{60}–JNM)$_3$ heterostructure spanning a Si window. h) Young's moduli of JNM, C60–JNM and JNM-(C_{60}–JNM)$_n$ (n =1, 2, and 3). Figure adapted from [94]

Janus CNMs are produced *via* electron irradiation induced crosslinking of 4'-nitro-1,1'-biphenyl-4-thiol self-assembled monolayers (SAMs) and have different chemical groups on their opposite faces, e.g. amino groups on the top side (*N*-side) and sulfur species on the lower side (*S*-side) [95]. They can be independently chemically functionalized with desired building blocks and assembled into hybrid vdW heterostructures *via* stacking, Fig. I.9a-e. Thus, 0D carbon, fullerene C_{60}, as a functional nanomaterial was covalently bound to the amino groups on the *N*-side of a Janus CNM [94]. To demonstrate that in the assembly of hybrid heterostructures also the *S*-side of Janus CNMs can be used, it was functionalized with gold nanoparticles (NP), Fig.I.9f. The possibility of bifacial chemical functionalization of Janus CNMs paves the way to hybrid vdW heterostructures with a variety of other 0d and 1d materials.

Zheng et al. fabricated cm^2-sized heterostructure stacks of hybrids with C_{60} coupled to Janus CNMs. They were characterized with respect to their structural, chemical and mechanical properties. The characterization by XPS shows that the chemical composition and effective thickness of the individual C_{60}/Janus CNM layers remains unaffected [94]. Individual C_{60}/Janus CNMs and their heterostructures were further studied by mechanical bulge tests to characterize their mechanical properties. To this end, the sheets were transferred onto a silicon substrate with an array of square shaped orifices. Fig. I.9g shows a HIM image of a homogeneous free-standing hybrid structure of three layers C_{60}/Janus CNM spanning over an orifice with dimensions of 40×44 μm^2. The free-standing vdW heterostructure can support its own weight and preserves its mechanical integrity. The Young's moduli of C_{60}/Janus CNM multilayer heterostructures were measured by mechanical bulge tests and are presented in Fig. 9h. Within the accuracy of the measurement, the Young's moduli have similar values demonstrating that the mechanical properties are not degraded upon the assembly of the hybrid.

II. TOP-DOWN

II.1. Precursors

A wide variety of GRMs with different characteristics can be obtained through liquid phase techniques [92, 96]. For a given approach, the selection of an appropriate precursor allows to tune the final features and properties of the GRM products in order to optimize their performance for each application. Graphite is the reference starting material to produce graphene, but it presents different characteristics like the particle size, crystal size or purity, which have to be considered. As an example, graphite with small crystal size will limit the maximum lateral size of the final graphene flakes. Other precursors, such as nanocarbons (i.e. carbon materials with nanoscale size, such as carbon nanotubes) [97-99] or pre-graphitic carbons (short ranged ordered amorphous carbons) [100, 101] have been also investigated as potential candidates for graphene production, as discussed below.

Graphite

Graphite consists of stacked graphene layers bonded by van der Waals (vdW) forces [102]. Carbon atoms are hexagonally arranged and the graphene layers are parallel to each other. Graphite has two main allotropic forms, hexagonal [103] (Fig. II.1a) and rhombohedral [104] (Fig. II.1b). In both cases the carbon hybridization is sp^2, the C-C distance in the basal plane is 0.1417 nm, and the distance between the layers is 0.3320 nm. The hexagonal form is the most stable thermodynamically, with layers stacked in an ABAB sequence (unit cell constants: a = 0.2456 nm, c = 0.6708 nm) [103]. In Rhombohedral graphite the sequence of the layers is ABCABC (unit cell constants: a = 0.2566 nm, c = 0.10062 nm) [104].

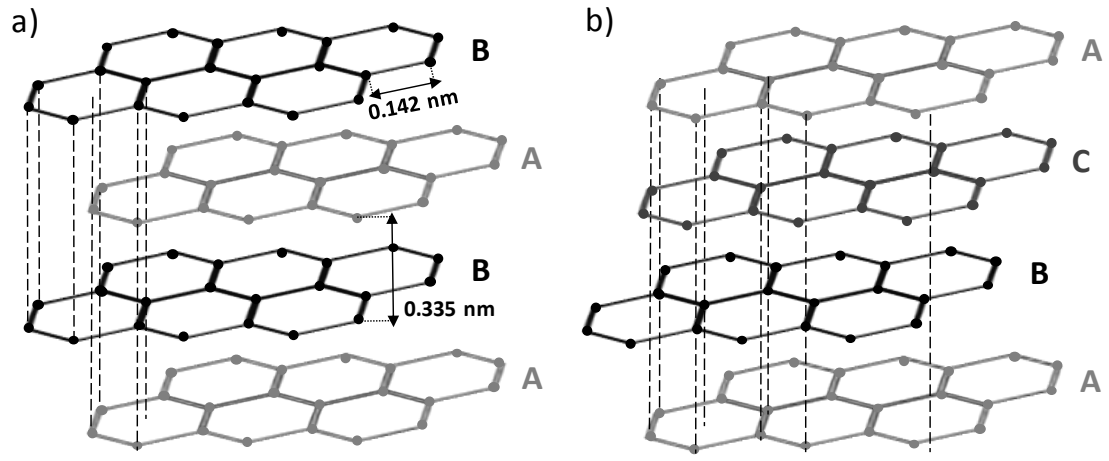

Fig. II. 1. a) Hexagonal and b) rhombohedral structures of graphite.

Graphite can be natural or synthetic. The latter can be obtained by subjecting nongraphitic carbons as pitches and cokes to high temperatures (1700-2700 ºC) in inert atmosphere or vacuum [105-107].This is the case of graphitizable carbons, non-graphitic carbons which, upon graphitization, convert into graphitic carbon, as the high temperature treatment promotes the creation of a graphitic structure [108]. The degree of graphitization, the amount of disordered phase effectively converted in their graphitic counterpart, can be further increased by performing the thermal treatment under high pressure (100-1000 MPa) [109]. Graphitic materials can also be obtained by Chemical Vapor Deposition (CVD) of some hydrocarbons, such as methane [110] or ethane [111] at T ~1200 ºC or by catalytic (c-CVD) and these synthetic methods are reviewed in full in Section V.

Graphene can be obtained by exfoliation of graphite [112], overcoming the vdW attractions between the carbon layers. Presence of defects in the layers leads to graphene with less conductivity [102, 113-116]. Graphite with large crystal size allows one to obtain bigger nanosheets [114]. The crystal boundaries of the pristine graphite have influence in the amount and type of oxygen functional groups introduced in the oxidation reaction resulting graphene oxide (GO) [114], influencing also the sonication time required to overcome the vdW interactions [115], as well as the chemical structure of the reduced graphene oxide (RGO) obtained after thermal [117] or chemical reduction [117]. The microstructure of graphite can be distinguished by polarized light microscopy [102], where the different crystalline domains are defined by the interference colours (Fig. II.2a). Fig. II.2b shows the scanning electron microscopy (SEM) image of graphite in which these features cannot be observed. The distribution of crystal size in the graphitic particles shall also influence the polydispersion in lateral size of the obtained graphene material, limiting the maximum lateral size attainable. The final average size of graphene is usually much smaller than the initial crystal size in graphite, and is mainly dictated by the mechanical process of exfoliation taking place at the meso- and nano-scale [118, 119].

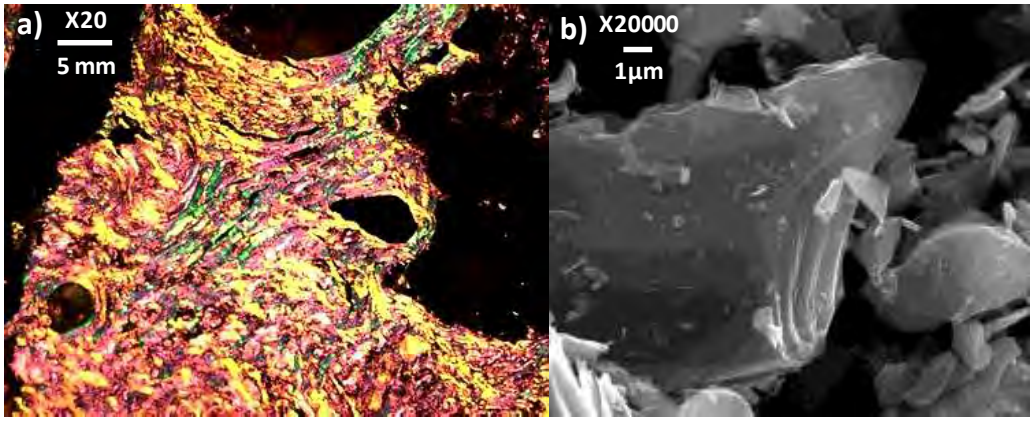

Fig. II.2: a) Optical micrograph acquired with an oil-immersion objective (20X) and an one-wave retarder to generate interference colours and b) SEM picture of the same graphite.

Graphene has been prepared from different natural graphites [120]: flaky, natural graphite conformed by finely powdered crystalline graphite with grain size smaller than 250 µm), lumpy, a

massive crystalline graphite with a walnut to a pea size, and amorphous, exhibiting only short range order [121, 122]. Lower crystallinity of the parent graphite (lumpy > natural > amorphous) leads to higher defects, smaller GO sheets' size and higher surface areas (Fig. II.3). Natural graphites can contain silicates and other mineral particles that can contaminate the final graphene materials, as detected by thermogravimetric (TGA) measurements [123].

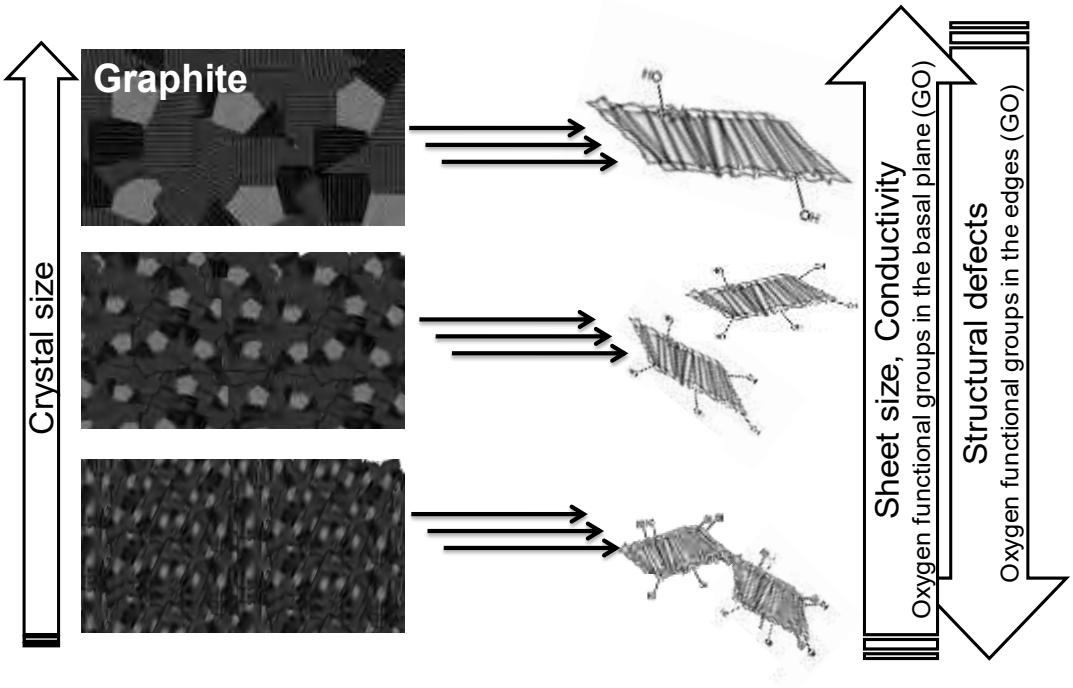

Fig. II.3. Schematic model of partially reduced GO and their parent graphites

Smaller particle size will result in higher content of oxygen functional groups in GO because of easier diffusion of reagents during oxidation. This influences the final electrical and thermal properties [124, 125]. Graphite with particle sizes>200 μm are adequate for the production of graphene-based materials to use in thermoset composites by infusion [126]. Particle size>600 μm are ideal for conductive thermoset composites [127].

It is worth mentioning here that the discrete particle size of graphite, as observed in the SEM pictures (see Fig. II.4), is different than the particle size determined by other techniques as laser diffraction, optical microscopy or granulometry.

Laser diffraction or granulometry techniques, due to the agglomeration of the discrete crystals graphite, increase the measured particle size of graphite. SEM without processing can distinguish between different or discrete crystal and allows the measurement of the particle size with more accuracy. In the case of optical microscopy, it is more difficult to separate the particle regarding SEM measurements.

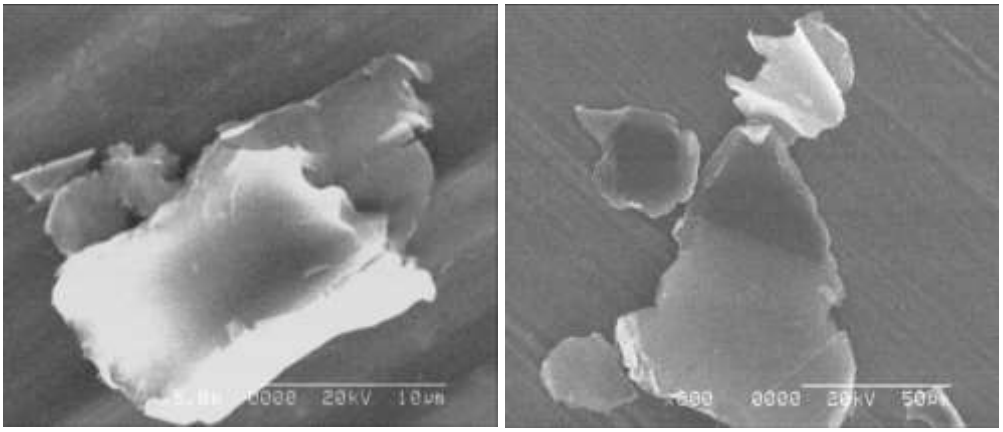

Fig. II. 4. SEM pictures of a graphite of a graphite 0-200 µm (>0.2 mm; 10% max) and a graphite 0-600 µm. Adapted from [128]

Expanded graphite is a graphite-derived material formed by a two-step oxidation-reduction process that retains the long-range-ordered layered structure of graphite, yielding a large interlayer distance. It can be used for the preparation of graphene flakes by liquid methods [129]. Typical expanded graphites used for the preparation of graphene flakes have a medium diameter D50, i.e. the value of the particle diameter at 50% in the cumulative distribution of particle size diameters, from 15 to 50 µm.

Non-graphitic carbons

Non-graphitic carbons have been also proposed [130, 131] as precursors for the synthesis of graphene by top-down techniques. E.g. petroleum and coal-tar pitches pass through a liquid or liquid-crystalline phase when subjected to heat treatment in inert atmosphere [132]. These materials are graphitizing and develop a graphitic microstructure upon heating to 3000 ºC [133]. When these precursors are carbonized at lower temperatures (1000 ºC) refs] they become cokes. A coke is a solid carbonaceous material derived from distillation of low-ash, low-sulphur bituminous coal or derived from oil refinery coke units or other cracking processes [134]. They exhibit a partially organized lamellar structure resulting from the parallel stacking of layers of sp^2-hybridized carbon atoms. Therefore, refs. [130, 131] suggested that these could be used for the preparation of graphene flakes. Since high T (up to 2500-3000 ºC) are required to obtain synthetic graphites, the direct use of cokes as precursors reduces the economy and the environmental impact of the whole process. Moreover, the broad range of microstructures and chemical compositions of cokes (as determined by the carbon source and the carbonization conditions) makes them a suitable starting material for the synthesis of graphene or graphene oxide with targeted structures and compositions.

Due to the different microstructure and chemical composition of cokes and graphites, the conditions for the synthesis of graphene materials should also be adjusted. Thus, compared to graphites, cokes require larger amounts of reactants during their oxidation by the Hummers´method; otherwise, its exfoliation into graphene oxide would have a much lower yield [130]. When cokes and

graphites were exfoliated in NMP, flakes from coke had a larger number of defects and smaller lateral size (~ 400 nm) than those from graphite (~ 1 μm) [130]. Similarly, as the crystallinity of cokes increases, its subsequent exfoliation yields flakes with larger lateral size and in higher yield [131].

Nanocarbons

Carbon nanotubes (CNTs) or nanofibres (CNFs), have also been explored as alternative precursors to produce graphene sheets and nanoribbons in liquid media [97-99]. Twisted ribbon-shaped carbon nanofibers (GANF®,Grupo Antolin Nano-Fibras) are helical carbon nanofibers comprising 5-6 stacked graphene layers [99, 135-137]. Two approaches have been proposed for the production of graphene flakes and sheets from GANF® [135, 138].The first is based on a mechano-chemical method, through melamine intercalation during ball milling in different solvents such as isopropanol, THF or DMF. Ref. [135] produced graphene suspensions in low [define numerically] boiling point solvents by a scalable and inexpensive method [135]. Refs. [138] obtained graphene flakes from GANF® using the Hummers' method [139] and different reduction techniques [138, 140, 141].

Graphene nanoribbons (GNRs) have been produced from CNTs as the starting material by solution-based oxidative processes[98, 99]. CNTs suspended in concentrated H_2SO_4 were oxidized by adding $KMnO_4$ (500 wt.% with respect to CNTs) at T<70 ºC [98].The resulting GNRs have straight edges and are dispersible in water and other polar solvents due to the presence of oxygen moieties. Unzipping single-wall carbon nanotubes (SWCNTs) [98] gives GNRs, but these are difficult to disentangle. Multi-wall carbon nanotubes (MWNTs) led to less entangled GNRs,that can be separated to single layers after sonication. Carbonyls, carboxyls and hydroxyl groups present in the GNRs can be reduced by treatment with aqueous hydrazine ($N_2H_4 \cdot H_2O$) after dispersing them in aqueous sodium dodecyl sulphate in order to prevent their re-aggregation. CNT unzipping by intercalation of lithium and ammonia and subsequent exfoliation was also reported [97]. However, this procedure yields a mixture of multilayer GNRs, partially open MWNTs, and graphene flakes, contrary to oxidation with $KMnO_4$, which allows a nearly 100% yield of nanoribbon with no presence of partially open MWCNT structures [99].

II.2 Liquid phase exfoliation

Various strategies have been developed to produce colloidally stable GRM dispersions. They can be classified into intercalation-based methods [142-144], and methods relying on mechanical exfoliation and further stabilisation by suitable solvents or surfactants (liquid phase exfoliation – LPE) [144-147]. Oxidative intercalation of graphite and subsequent delamination to yield GO, are amongst the oldest techniques [148].

We first discuss LPE, as it is probably the simplest and most versatile strategy to obtain colloidally stable dispersions from a broad range of layered materials (LMs). Energy form shear is

used to overcome the van der Waals attraction in the bulk LM. If this is done in a suitable liquid (solvents with matching solubility parameters, or additives that act as electrostatic and/or steric stabilizers [149]) reaggregation is prevented. The resulting flakes can have low defects, and can be further solution processed by a range of techniques [150]. LPE of MoS_2 and WSe_2 reported by Henglein in 1989 [151].

While LPE is a versatile method for producing large quantities of flakes from bulk powders, it has some disadvantages. The flakes are highly polydisperse with a range of sizes and thicknesses (lateral sizes ranging from tens of nanometres to tens of microns, N from 1-100s of layers). The dispersions can also have low monolayer content (Y_M < 1%). A precise, statistical analysis of size distribution due to exfoliation by ultrasound has been recently reported, but only for monoatomic GO sheets [118]. The dispersions can also have low monolayer content (<30%). For application areas where LPE flakes are well suited, such as printed optoelectronic and electrochemical devices, optimized performance is unlikely to arise through direct use of the native dispersions. This is especially true for those applications requiring the direct bandgap luminescence conferred by monolayers. Thus, size selection must be an integral part of the material production process.[152]

Many strategies exist for both exfoliation and size selection, depending on the starting material and the desired outcome. A number of review articles on exfoliation in liquid media have been published [144-147, 150, 152-157]. Here, questions such as which medium (*e.g.* solvent or surfactant) or exfoliation method (*e.g.* sonication or shear) is more suitable and how to size-select flakes using benchtop centrifuges are addressed.

Choice of medium

Solvents and detergents

In a typical LPE experiment, the bulk crystal is immersed into a liquid and subjected to sonication [113, 157-160], shear mixing [161, 162], microfluidization [163], ball milling [164] or similar [165, 166]. Prior to designing an experiment, thought needs to be given to the choice of medium. This can be crucial and will often depend on the starting material in combination with the exfoliation method and the purpose of production. Irrespective of the exfoliation method and/or medium, a purification step of starting materials (e.g. graphite flakes) is useful, since their powders may contain impurities that can destabilize the dispersion.

Aqueous surfactant solutions are widely used as stabilisers in LPE [156, 167-169]. Usually, the exfoliation, stabilisation and size selection is quite robust and reproducible giving access to long-term (weeks-months) stable, dispersions. In order to retain “pristine-like” optical properties, similar to those exhibited by mechanically exfoliated materials, aqueous surfactant solutions are of advantage. Photoluminescence (PL) of MoS_2 and WS_2 can be observed in single layer-enriched solutions in sodium cholate (SC) with emission dominated by excitons and at similar spectral positions as mechanically exfoliated dichalcogenides (TMDs) [170, 171]. SC is environmentally friendly because is

solubilized in water and does not require additional health precautions unlike other non-aqueous solvents, such as *N*-methy-2-pyrrolidone [172]. SC is compatible with many processing techniques such as vacuum filtration and spraying. However, printing from aqueous surfactant still remains challenging, as it is difficult to control the rheological properties [150]. In addition, there are two other downsides. First, some materials (such as GaS [173] or black phosphorus [174, 175]), can degrade in the presence of water/oxygen [174, 176] so that aqueous surfactant solutions cannot be used. Second, it is difficult to completely remove the surfactant from the resulting flake surfaces after processing, as it can be trapped between restacked flakes, potentially deteriorating the resulting network properties. A few systematic studies (see [144-147, 150, 152-157, 177]) exist on the impact of the chemical structure of the surfactant or its concentration on the degree of exfoliation, i.e. layer number or yield of single and few layer nanosheets as well as their lateral size, with detailed data mostly available for most commonly used surfactants such as sodium cholate (SC) or sodium dodecyl benzene sulfonate (SDBS). However, a comprehensive picture is still lacking due to the vast parameter space (materials, surfactants, concentrations of components, exfoliation techniques, centrifugation procedure). Systematic studies on the effect of more exotic surfactants, such as polycyclic aromatic hydrocarbons (PAH), have also been reported, correlating the adsorption energy of the single molecule on graphene to the overall exfoliation performance [178, 179]. Flakes produced in aqueous surfactants are smaller, but also thinner than in solvents such as *N*-methyl-2-pyrrolidone (NMP) and *N*-Cycloxexyl-2-pyrrolidone (CHP) [180].This is most likely related to the higher viscosity of these solvents compared to aqueous surfactant. This can on the one hand hinder intercalation of the solvent between the layers of the crystals during the exfoliation process and in addition lead to a slower sedimentation in the centrifugal field [181] and hence a larger population of larger/thicker nanosheets. Details on differences in sizes/thicknesses and yields of monolayers and few-layers strongly depend on the material, the exfoliation conditions and in particular the centrifugation conditions making it impossible to quantify this effects, as the literature data cannot be directly compared.

Solvent stabilisation can be described in the framework of solubility parameters [182]. Solvents or solvent blends can stabilize liquid-exfoliated nanosheets and prevent them from reaggregating, when solubility parameters, such as surface tension or Hansen parameters, of solvent and solute match [113, 180, 183-186]. Chemically unstable materials, such as black phosphorus, can be protected against degradation through a stabilising solvation shell [187]. In addition, it is easier to tune rheological properties for processing techniques such as inkjet printing [188] and solvent removal is typically easier than for surfactants. However, certain solvents such as NMP or *O*DCB solvents can degrade and polymerise [189, 190], changing the properties of the exfoliated material while also hampering subsequent spectroscopic and microscopic characterisation [191]. In such cases, the solvent can also remain on the flakes surfaces completely. In general, good solvents show a strong, yet noncovalent interaction with the flakes, altering optical properties as, e.g., manifested by PL shifts in TMDs [171]. Another consideration is that many suitable solvents, such as NMP, suffer from high boiling points (>200 °C) and are often toxic [192]. Some solvent blends have been

identified as promising (e.g. alcohols and water) [193, 194] to potentially overcome the limitation of the high boiling point solvents.

GRM dispersions in water can also be stabilized by using a wide range of polymers [167, 195-199], such as ethyl cellulose (EC) [196], cellulose acetate (CA) [195], lignin [198], polyvinylpyrrolidone (PVP) [197], and even more complex systems [167, 199]. The use of polymers as stabilizing agents in the LPE process works better than the use of small organic molecules in terms of the concentration of graphene dispersions. Yet, because of the strong polymer/graphene non-covalent interactions, flakes produced by exploiting this approach cannot be completely separated from the polymer/graphene composites [200].

Molecule-assisted LPE

Stable dispersions of graphene in water have also been obtained using small polyaromatic dyes as surfactants [179, 201, 202]. Thanks to their aromatic core, these molecules can adsorb strongly on the graphene surface (E_{ADS} ~ 15 Kcal mol^{-1}), forming also ordered layers [178]. They have also a strong (molar absorption coefficient ε>15000 L $g^{-1}m^{-1}$) and unique absorption and emission spectrum in the visible range, which allows to monitor easily their interaction with graphene in solution and in solid [203, 204]. Many of these molecules are low cost (<100 $/Kg) dyes, widely used in large-scale compounding of polymers, e.g. as industrial additives and colorants dyes [205]. While most of the work has been done with graphene- where a strong interaction of the aromatic core of the dye with the extended π-electron network of the flakes occurs- these molecules can also be used to exfoliate a wide range of LMs, such as BN [206] , WS_2 [206] and MoS_2 [206] , selenides and tellurides [206].

The use of properly selected small PAH organic molecules or polymers can enhance the exfoliation of graphite, in particular when the molecules/polymers possess a high (E_{ADS} ~ 15 Kcal mol^{-1}) energy of adsorption on the basal plane of graphene. However, these molecules or polymers do not act as graphene dispersants or graphite exfoliators, i.e., they do not trigger the exfoliation, as commonly misinterpreted in literature. These molecules/polymers mainly act as dispersion stabilizing agent *via* the non-covalent functionalization, i.e. through the physisorption of their hydrophobic moieties on the graphene surface during the process of exfoliation. Therefore, they can prevent re-aggregation and increase the stability of both aqueous and organic dispersions [207].

Using water as a LPE media is a natural choice because of its non-toxicity and offers potential for the formation of biocompatible graphene-based materials for biomedical applications [208]. Yet, the LPE of graphene in water is particularly challenging due to the hydrophobic nature of the sheets. This challenge can be overcome by using surfactants such as SC, which allow exfoliated flakes to remain suspended. Among various molecular stabilizers, PAHs [209, 210], substituted with numerous side groups, are the most studied compounds. Adsorption of PAHs onto the graphene surface occurs through π–π interactions between the planar π-conjugated surfaces. In these non-covalent interactions both PAHs and flakes surfaces share the π-orbital electrons, ultimately resulting in the reduction of the surface free energy of the dispersion[179]. i.e. derivatives have been used to

stabilize CNTs dispersions [211], and as in the case of NMP, they have been adopted for LPE of graphite [179, 212-214]. Nevertheless, not all stabilizers suitable for CNTs, having a curved surface, would be ideal for dispersing graphene with a flat surface. Because of the improvement of the exfoliation yield (the amount of solubilized material during LPE) and, in particular, increase in the number of SL in LPE in presence of small PAHs such as pyrenes, NDIs, [215] and PDIs [216], and other PAHs are also expected to be suitable to stabilize graphene produced by LPE.

Regardless of the exfoliation yields (% of SL, concentration) and the stability of graphene in aqueous dispersions, the use of water as an exfoliation medium is not recommended for electronic devices such as field-effect transistors (FETs). The presence of water at the interface with the dielectric substrate can enhance the charge-trapping [217]. Therefore, the use of stabilisers in organic solvents has also been explored [218-223]. For more details on the underlying specific noncovalent interaction, the reader is referred to Section VIII.

Exfoliation methods

Sonication and shear

We now discuss sonication [113, 158] and shear exfoliation [224-226]. The purity especially with respect to contaminations of the commercially available materials is often unpredictable, which creates problems for the reproducibility in the exfoliated product. Accordingly, the general recommendation is to perform a two-step exfoliation process.[170, 171, 227] In the first one, the material in the medium of choice is subjected to a short (~20% of the time of the total planned duration of the process) exfoliation. After this initial step, the dispersion should be subjected to centrifugation at intermediate centrifugal acceleration (~ 5000 *g*) after which the supernatant is decanted and discarded and the sediment collected in fresh solvent/surfactant. This can then be followed by a second, longer exfoliation. This approach allows most of the impurities (and very small flakes) to be removed. This is particularly needed when working with ionic surfactants, as the impurities are often ionic and therefore, can destabilise the surfactant dispersion via charge screening effects.

A higher initial concentration of the precursor bulk material will also give a higher concentration of exfoliated flakes, up to when the dispersed concentration saturates. This initial concentration is typically > 30 g/L of precursor concentration [173, 175, 180, 224-226, 228-230]. Similarly, longer processing times yield higher dispersed concentrations (but not linearly) [173, 175, 180, 224-226, 229-232]. While this can also change the length and thickness distributions in the as-obtained dispersion [231], this effect can be balanced by appropriate size-selection techniques [152].

The choice of the exfoliation method is material dependent. E.g. while graphite is readily exfoliated for all methods [224, 225, 228], this may not be the case for other materials. In particular for TMDs, the quality of exfoliation (as measured by the concentration/yield of single and few-layered (2-5 layers) nanosheets) is better when using tip sonication compared shear mixing [161,

233]. For GaS, bath sonication is the most effective approach [173]. When attempting to exfoliate a new material it is important to not only consider the stabiliser, but also to test various available exfoliation methods. In particular the role of the crystallite size of the starting material in combination with the exfoliation method is a parameter that has not been investigated systematically.

Sonication can be performed in tip or bath sonicators. In tip sonication, energy is imparted to the dispersion media directly [234], whereas in the sonic bath, the energy must travel through the tank and dispersion vial before reaching the flakes [234]. Although the scalability of sonication to produce few layer flakes has not been demonstrated (compared with shear exfoliation and ball milling), tip sonication remains useful as lab-scale technique, as the material quantity (100s of mg) is generally sufficient even to test size dependent properties in a range of application areas.

For layered inorganic materials, tip sonication is preferred over bath sonication due to the higher production rates, (*i.e*. more exfoliated material is produced in shorter times, with concentrations in the range of ~1 g/L in < 24 h for initial bulk material concentrations of 30-50 g/L [171, 180, 235]. In this case, various sonic tip configurations are available with different probe sizes and shapes and processors. In a typical protocol [170, 171, 236, 237], a solid flathead tip with a diameter~ 2 cm is immersed into 80 mL of a dispersion in a metal beaker. The sonic tip is lowered into the dispersion to the bottom of the beaker and then lifted up by 1-2 cm. It is recommended to set the sonication amplitude to 60% of the maximum power as the concentration of few-layered nanosheets seems to decrease linearly with the amplitude [237]. In addition, the mean layer number of WS_2 increased by ~1 (across eight size-selected dispersions) for sonication at an amplitude of 50% compared to 60% [237]. Higher amplitudes can damage the processor after prolonged (100s of hours) use. 500 and 750W do not give noticeable differences [237]. Since the sonic energy falls off exponentially from the probe [234], it is important to match the container to the probe size as recommended by manufacturers. Even though the dispersed concentration of (few-layered) nanosheets increases with sonication (or processing time) [173, 175, 180, 224-226, 229-232], 5-7h sonication provide a coμpromise between dispersed concentration and time. However, defects might be introduced on prolonged (>10 h) sonication. This is particularly the case when a fresh probe is used which delivers more energy into the dispersion. The probe should be exchanged after ~15-20 sonication runs of 5-7 h each, as it wears down significantly. To avoid cross-contamination from different samples, it is better to sacrifice some of the material to be exfoliated and clean the probe by a 15 min sonication in the respective powder water/surfactant or solvent mixture before starting a new exfoliation process.

It is crucial to prevent heating of the sample- especially in tip sonication, but also in bath sonication or shear exfoliation. This is not only because heating can deteriorate the properties of the material, but also because dispersed concentrations are lower. While cooling in tip sonication can be achieved by positioning the metal cup in an ice bath, it is far more ideal to install a chiller, as the ice must be replenished every 2 hours or so [236]. In addition, keeping the dispersion cool is facilitated by pulsing the sonication through the device controller, with 6s on and 2s off ratio. For a given combination of sonicator, operating conditions, cooling, sonication time and material, the outcome

of tip sonication appears rather reproducible both in terms of dispersed concentration and size distribution [170].

In general, bath sonication may offer a lower-cost alternative to tip sonication, and additionally, in some cases, such as for GaS [173], this is preferred because tip sonication can damage the exfoliated flakes. The energy input is lower in bath sonication [234], as it is less localised. Therefore, less material fragmentation is expected. However, longer processing times are required (depending on the material) to achieve an equivalent concentration of dispersed material compared to tip sonication. For TMDs, sonication times are longer by ~ a factor of 20 in bath compared to tip sonication. In general, bath sonication process is less reproducible than tip sonication and the outcome varies considerably depending on the specific bath used, the filling level of the bath and the positioning of the vial within the bath. Our recommendation is to use small vials and place them in hot spots (thermolytic centers, where the sonication induced cavitation bubbles of the water in the tank preferentially collapse). While more reproducible results can be obtained by rotating the sample in the bath during sonication, this will also result in a lower dispersed concentration for an equivalent sonication time. Again, it is important to prevent heating of the sample (at least for materials beyond graphene) by either installing a cooling system or exchanging the water every 30 min.

Alternatively to sonication, one can use shear exfoliation in rotor stator mixers [224] or in blenders with rotating blades [225, 226]. Even a kitchen blender can be used, offering a very low cost alternative to sonication [225]. However, the household kitchen blenders are not designed to operate in organic solvents and can be destroyed when doing so. In addition, continuous operation heats up both sample and mixer, so that the run has to be paused and mixer and sample cooled in an ice bath. The dispersed concentration of few-layered material is not strongly dependent on the processed volume, so that shear exfoliation is a scalable process with production rates of 0.15 g/h for graphene and 1.3 mg/min for MoS_2 [224, 225, 238]. The quality of the material produced in terms of dispersed concentration and mean layer number is comparable to sonication in the case of graphene [225].

Microfluidization

Microfluidization is a homogenization method that applies high pressure (up to 207MPa) [239] to a fluid forcing it to pass through a microchannel, Fig. II.5. The key advantage over other LPE methods is that high shear rates ($\dot{\gamma}>10^6$ s^{-1} [240, 241]) can be applied to the whole fluid volume [241], not just locally. Microfluidization was used for the production of polymer nanosuspensions [239], in pharmaceutical applications to produce liposome nanoparticles with diameters smaller than 80nm to be used in eye drops for drug delivery to the posterior segment tissues of the eye [242], or to produce aspirin nanoemulsions [243], as well as in food applications for oil-in-water nanoemulsions [244]. Microfluidization was also used for the de-agglomeration and dispersion of CNTs [245].

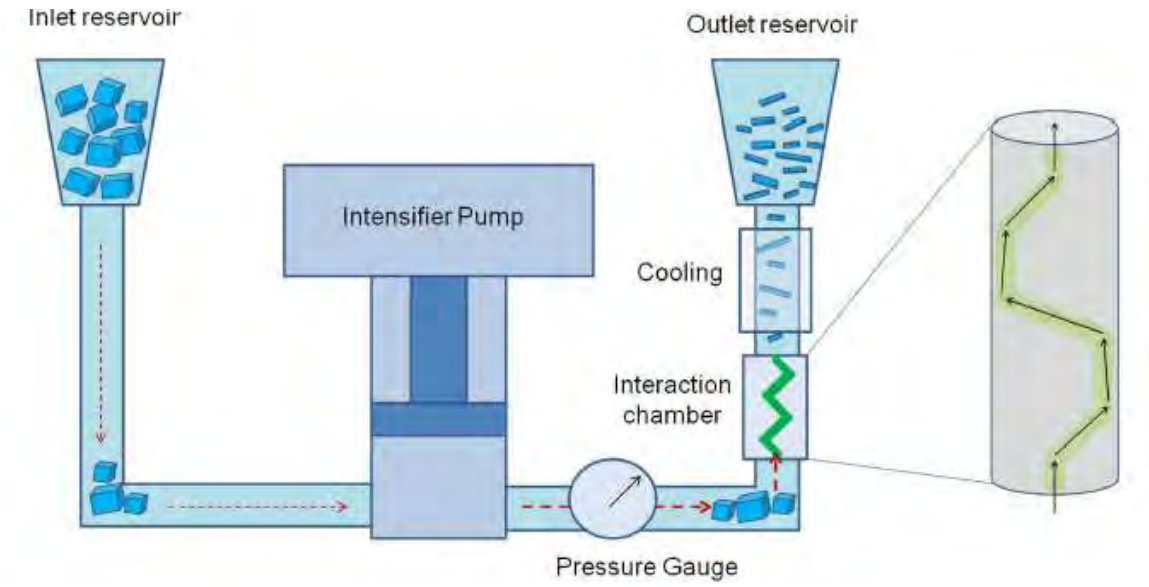

Fig. II.5: Schematic of microfluidization process. Graphite flakes in SDC/water are added in the inlet reservoir. An intensifier pump applies high pressure (207MPa) and forces the suspension to pass through the microchannel of the interaction chamber where intense $\dot{\gamma}$~9.2x10^{7}s^{-1} is generated. The processed material is cooled down and collected from the outlet reservoir. The process can be cycled several times [163]. Adapted from [163]

The main step of this process involves placing the graphite/solvent mixture into an inlet reservoir. An intensification pump, driven by electro-hydraulics, provides two motions - suction and compression, drawing a portion of sample into the processor through a one-way valve, and then pushing this sample fraction past the pressure gauge and through sub-millimetre sized channels within a diamond interaction chamber, where graphite exfoliation takes place [163].

Interaction chambers are typically based on two geometries, Y- and Z type. The Z-type chamber is preferred for graphite exfoliation, since the geometry consists of sharp turns and a narrow rectangular cross-section for optimal shear. The chamber G10Z is ~87 µm in diameter. The motion of the intensification pump creates mixing within these micro channels, generating pressures>30,000 psi (~2100 bar). The fluid dynamics of the process can be turbulent or laminar as defined by the Reynolds number, dependent on the kinematic viscosity and density of the solvent used [163].

Before processing material in the microfluidizer, it is good practice to ensure the system is clean and leak free. Cleaning can be performed using the solvent that will be used for the experiment. However, due to the system comprising many seals and joints where material can be trapped, it is useful to use a compatible high (>1 Pa.s) viscosity solvent to help push this material out of the system. Glycerol (1.4 Pa.s) is a good solvent due to its high viscosity, before flushing this out with the solvent to be used in the experiment. It is also useful while doing this flushing and cleaning, to ensure the system can flow at the desired experimental pressure to check for any possible leaks in the system. The entry of air into the microfluidic system should always be avoided; bubbles can cause the etching of the interaction chamber, thus, gradually increasing the chamber diameter.

Below are 2 typical recipes for the production of graphitic flakes without centrifugation (Method 1), or Isolated FLGs following centrifugation (Method 2). Due to the dimensions of the interaction chamber, microfluidic processing of large (>100 μm) graphite flakes may block the microfluidic channel. Instead, smaller powder sizes are advisable (typically, the particle diameter corresponding to 90% cumulative (from 0 to 100%) of the undersize particle size distribution (D90) , is less than 30μm).

Method 1: Production of graphene flakes

This method [163] refers to the production of high yield (100 wt.%), high concentration (up to 100 g/L) graphene-based inks that are not centrifuged.

Graphite powders (natural or synthetic) with a particle size<30μm are mixed at a concentration up to 100 g/L with SDC at a concentration 9 g/L in water and stir bar mixed for 5 min. A typical batch size is 250-500 mL. However, the microfluidic system has a dead space of 50 mL and is flushed through with the graphite mixture beforehand. 50 mL of the initial pre-mix will, therefore, be lost. Then the rest of the graphite mix is added to the inlet reservoir and microfluidized for 1 cycle whilst timing to calculate the length of each cycle. The material is collected in a beaker and placed back in to the inlet reservoir to cycle automatically for the desired length of time depending on the number of process cycles, *n* (where *n* is typically < 70). The final product is collected in a large beaker. It is important to measure the exact volume of ink collected as the microfluidic system has a dead space of ~50 mL, and so it may not be possible to recover all ink inserted. Sodium carboxymethylcellulose (NaCMC) (10 g/L) is added whilst stirring to adjust the viscosity to the required value. NaCMC is slowly added until fully dissolved in order to avoid the formation of clumps. Clumps that are formed should be ground with a spatula and the ink left to stir overnight.

Fig. II.6, shows SEM images of the coatings comprising the starting graphite (Fig. II.6a), after 5 (Fig. II.6b) and 100 cycles (Fig. II.6c). Flake size reduction and platelet-like morphology is observed after microfluidic processing.

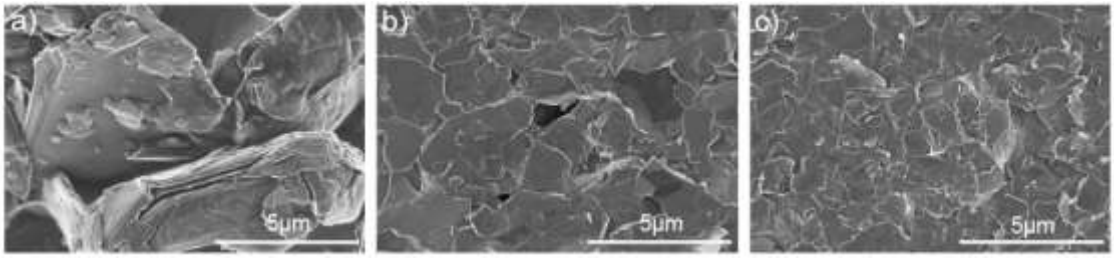

Fig.II.6 SEM images taken from coatings comprising a) starting graphite, b) after 5 cycles and c) after 100 cycles. Reproduced from ref [163].

Since we do not further process these inks by centrifugation, Y_W (yield by weight) is 100 wt.%. 4 wt.% of the exfoliated material consists of FLGs (<4 nm thick) that can be isolated using Method 2 below, and 96 wt.% are flakes in the 4 to 70 nm thickness range. The stabilized dispersion is used for blade coating and screen printing. Fig. II.7 plots the sheet resistance (R_S) and thickness of blade

coated films as a function of process cycles at a flake loading of 80 g/L (73 wt.%), highlighting that exfoliated materials produce thinner films with lower Rs. The bulk conductivity of films increases with loading with a plateau above 80 wt.%, and the critical thickness at which bulk conductivity is reached is less when loading is higher. After annealing (300°C-40 min), Rs reaches 2 Ω/☐ at 25 µm (conductivity, $\sigma=2x10^4$ S/m), suitable for electrodes in devices such as OPVs [246, 247], organic thin-film transistors (OTFTs)[248] or RF-IDs [249], The inks can then be deposited on glass and poly(ethylene terephthalate) PET flexible substrates using blade coating and screen printing to demonstrate the viability for these applications (OPVs, OTFTs, RFIDs). Screen printing is discussed in Section III.

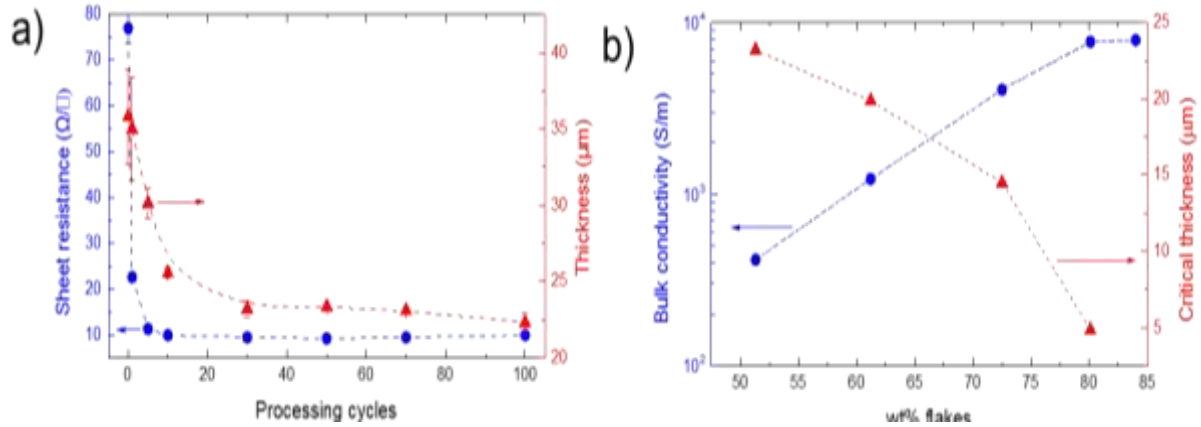

Fig. II.7: a) R_S and film thickness as a function of processing cycles for a formulation with 73 wt% flakes, b) bulk and critical thickness as a function of loading (70 cycles). All samples are dried for 10 min at 100°C. Reproduced from ref [163].

Method 2: Production of FLGs

Graphite powders (natural or synthetic) with particle size D90<30µm are mixed at a concentration 12 g/L with SDC at a concentration~0.5 g/L in water and stir bar mixed for 5 min. Then the dispersion is microfluidized for *n* process cycles (where *n* is typically < 100). Following processing, samples are centrifuged with a Thermo Scientific centrifugue with Sorvall TH-641 swinging bucket rotor typically at 10,000 rpm (17,000 g). Films obtained by vacuum filtration of the FLG ink have Rs~4.5 kΩ/□ at 90 nm thickness, significantly better than the equivalent sonication produced graphene films that have Rs~8.9 kΩ/□ at 160 nm. The effects of processing cycles, pressure, surfactant concentration, centrifugation speed and graphite loading on graphene concentration are shown in Figs. II.8a-f). AFM indicates that the exfoliated material consists of FLG with ~18% SLG (Fig. II.9).

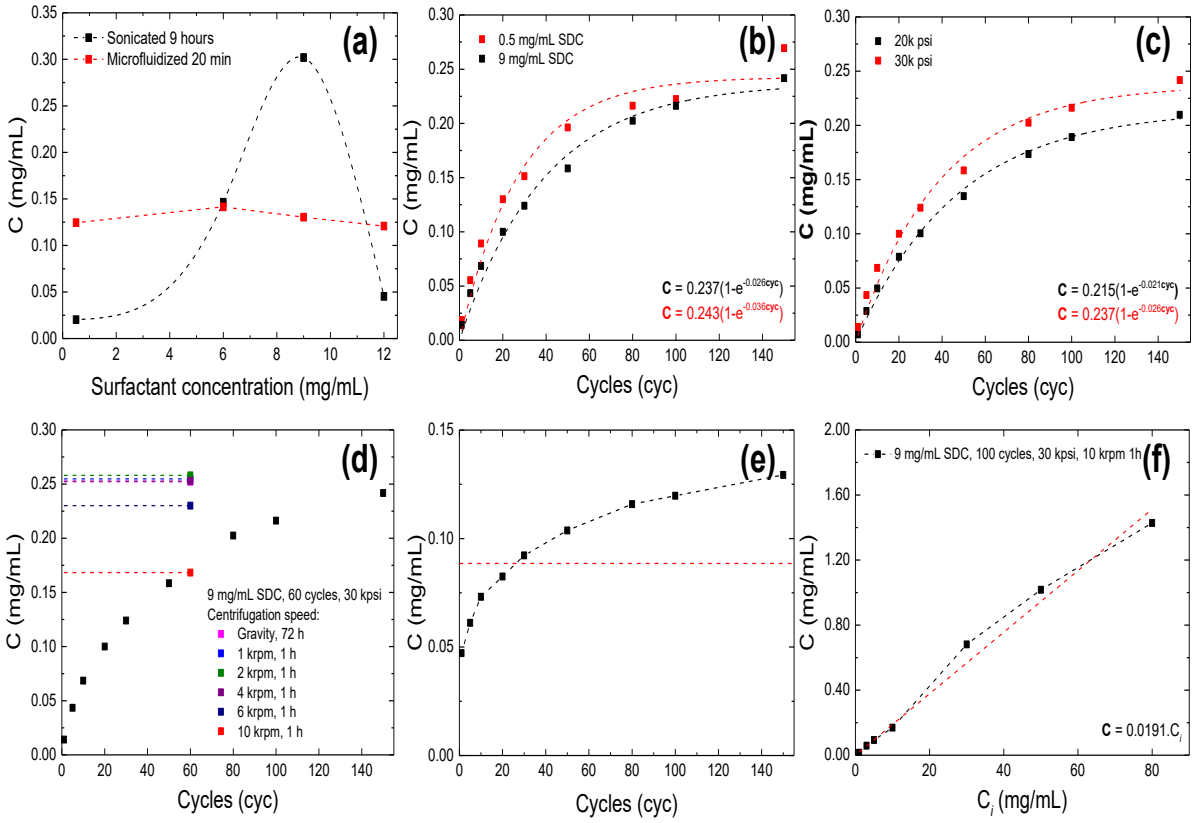

Fig. II.8: (a) Effect of SDC concentration at fixed processing cycles (~60 cycles , 20 minutes, red) compared to sonication processing (9 h,black). (b) Effect of surfactant concentration 0.5 mg/mL(red) and 9 mg/mL (black) and process cycles. (c) Effect of process pressure 20k psi (black) 30 k psi (red). (d) Effect of centrifugation parameters; (e) Effect of using NaCMC as a stabiliser. Dashed red line represents sonication processing using the same NaCMC loading. (f) Effect of increased graphite loading.

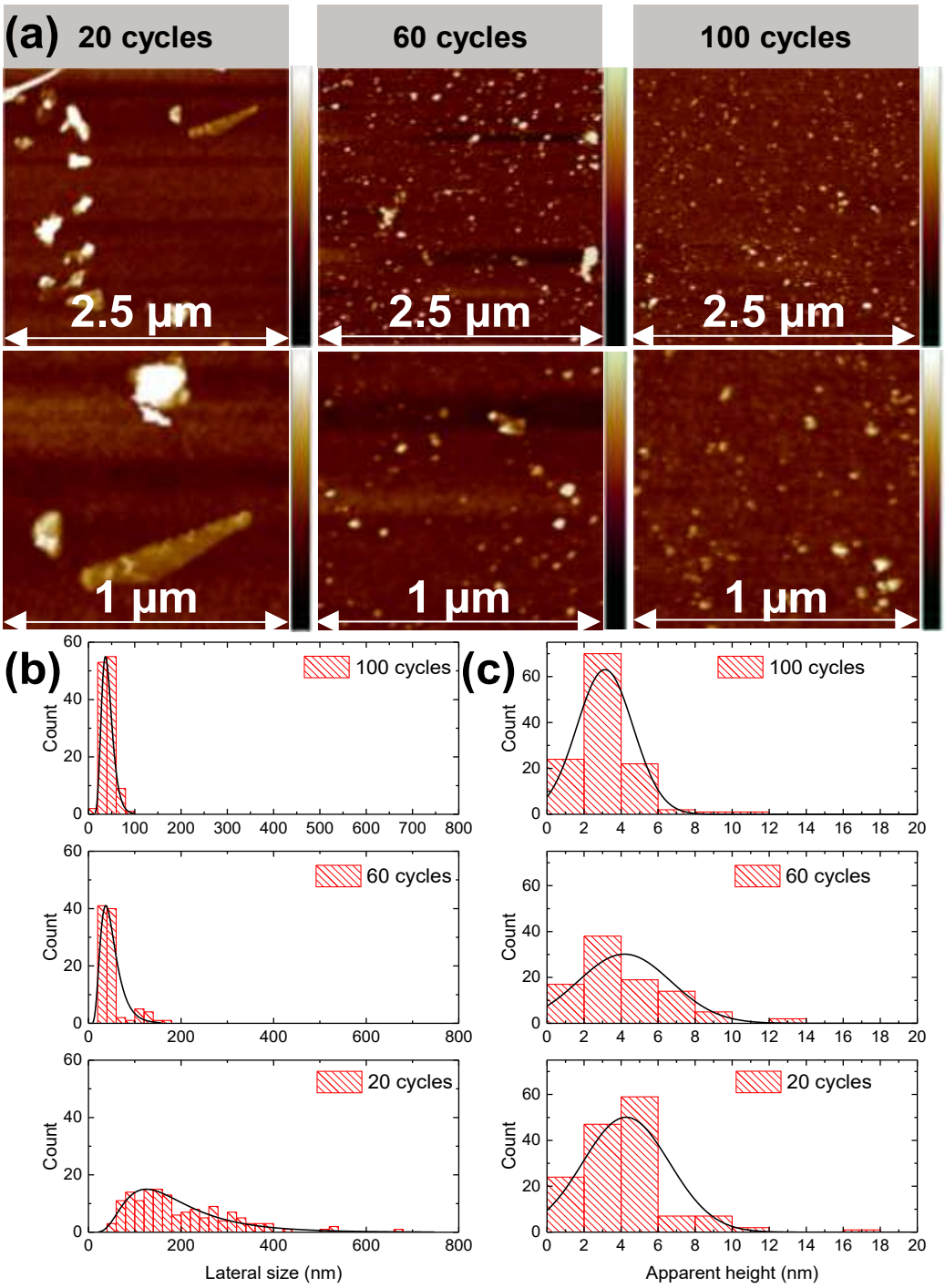

Fig. II.9: (a) AFM height scans of flakes microfluidized for 20, 60 and 100 cycles. (b) Histogram showing the lateral size distribution of flakes with increasing process cycles. (c) Histogram showing the AFM height distribution for increasing process cycles.

Ball milling

Ball milling can produce FLG at low-cost and under environmentally friendly conditions. It does not require solvents, avoiding the use of toxic organics, while increasing efficiency in terms of time and energy. Other green aspects also favour the scaling up of the process.

Two effects take place in ball milling [146]: the shear force, that promotes the synthesis of large-sized flakes, of the order of the starting graphite planes, and the vertical impacts applied by the balls during the rolling actions, which tend to deteriorate the flakes and must then be minimized in order to reduce the number of defects. Ref. [250] reported changes of graphite, during milling processes, through a nanocrystalline phase prior to amorphization. To avoid this and favour the shear force process, the use of solid exfoliating agents is recommended.

Exfoliating agents, including triazine derivatives, can be used to form multipoint interactions with the exfoliated flakes. Amounts around few grams of graphite and exfoliating agents, such as melamine (2,4,6-triamine-1,3,5-triazine), can be used to prepare FLGs, which, subsequently, can be dispersed in organic solvents, such as DMF or in aqueous media [164]. The lateral size of the resulting flakes can be modulated depending on the ball-milling conditions (atmosphere, revolutions, and time of treatment). Different triazine derivatives were tested, in relation to their ability to exfoliate graphite, not only experimentally but also by computational studies, which evidenced that melamine is the better option to favour exfoliation [251]. Melamine not only has an aromatic nucleus that can interact with the graphene π-system [251], but can also form an extended network on its surface, owing to the presence of hydrogen bonds (Fig. II.10). Melamine can then be washed away using hot water, leaving high quality graphene suspensions, with very small D band in the Raman spectrum.

In a typical experiment, 7.5 mg of graphite and 22.5 mg of melamine are ball-milled at 100 rpm for 30 minutes, under air atmosphere, in a stainless steel grinding jar containing ten stainless steel balls of 1 cm of diameter. The resulting solid mixture is dispersed in 20 mL of solvent, obtaining black suspensions. Filtration can remove melamine from the suspensions, giving rise to FLG dispersions in different solvents. If DMF is used as the solvent, a complete exfoliation can be estimated since no precipitate is observed. If water is used as a solvent, a concentration gradient appears, and some precipitation takes place after stabilization of the dispersion, at room temperature, for 5 days.

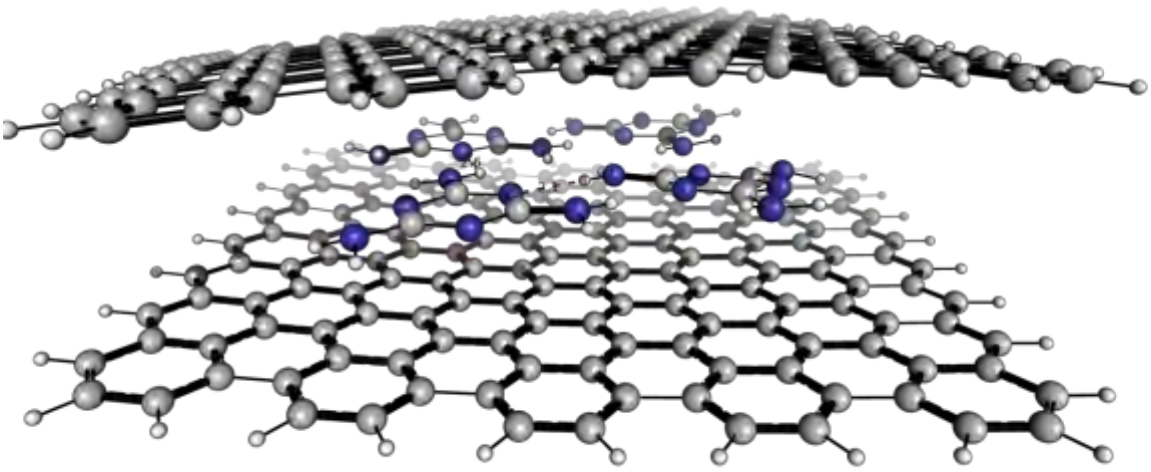

Fig. II.10. Supramolecular assembly of melamine between graphene sheets

When preparing dispersions in water, melamine can also be eliminated by dialysis, which is highly recommended, mainly because this technique allows keeping the flakes always in dispersion [200]. It is advisable to hand-shake the dialysis sack and to apply a pulse of mild (bath sonication for no more than 1 minute) if any precipitate appears in the black dispersion during dialysis. Once melamine is removed, the black dispersion is kept in the stabilization container at room temperature for 5 days, in order to obtain a concentration gradient. The liquid fraction with stable sheets in suspension needs to be carefully extracted, avoiding the meniscus and the precipitate, in which non-exfoliated graphite remains. The obtained aqueous dispersions, with concentration~0.1 mg/mL, are stable at room temperature for a few weeks. According to elemental analysis, these dispersions contain an amount of melamine lower than 1ppm, which is considered non toxic [252].

Characterization of the FLG shows a low number of defects, with D/G ratios ~ (0.2-0.6), confirming that no oxidation occurs during the preparation [164]. In reference [253], ab-initio calculations on graphene-melamine-water systems have been performed focusing on how small amounts of melamine molecules tune the adsorption of few water layers on graphene. These reveal that melamine acts as a non-covalent anchor, keeping some water molecules near the graphene sheets, providing a quantitative estimation of the non-covalent interactions (dispersion and hydrogen-bonding), which provide the required driving force to stabilize the graphene-water systems.

A further advantage of the above-mentioned method is that the aqueous suspensions can be lyophilized after having been frozen [254]. A very soft and low-density black powder, consisting of FLGs, is produced this way. This solid can be safely stored and shipped, being easily dispersed in water, culture media or other solvents, using mild sonication combined with shaking with no change in its structure (Fig. II.11). The mass yield of the entire process, starting from graphite, is~30%.

Fig. II.11. FLG powder (left) and its dispersion in cell culture medium (right).

Powders are characterized with elemental analysis (EA), thermogravimetric analysis (TGA), X-ray photoelectron spectroscopy (XPS), transmission electron microscopy (TEM) and Raman spectroscopy. EA resulted in average values of of 94.3 wt %C, 0.4 wt %H, 0.4 wt %N and 4.9 wt %O.

TGA showed a weight loss, in agreement with EA, confirming the non-oxidative nature of the milling treatment. This feature was also corroborated by XPS, as deconvoluted plots confirmed the presence of small amounts of oxygenated groups, from the C 1s and O 1s core level spectra and traces of melamine. Raman spectra showed in Fig. II.12 that 15 min of ultrasonication does not add a significant number of defects. TEM analysis was used to determine the lateral flake sizes. concluding that the FLG have a wide size distribution around 200-2000 nm.

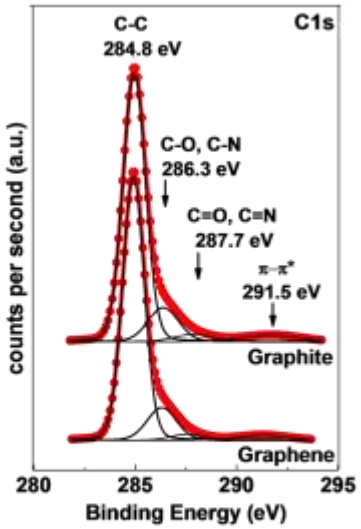

	C1s		N1s	
Graphite	284.93	C-C		
	286.31	C-O		
	287.78	C=O		
	291.48	π-π*		
Graphene	284.93	C-C	399.04	N-H
	286.29	C-O	400.16	N=C
	287.67	C=O		
	291.33	π-π*		

Fig. II.12. XPS spectrum of graphene powders produced by ball-milling graphite.

There is an increasing interest in the use of GRMs in biological applications. Dispersions in water and culture media allow the preparation of hydrogels for drug delivery [251], the study of synaptic functions in culture brain cells [255, 256] as well as the development of environmental toxicity studies [254], among others.

The addition of small amounts of solvent during the milling treatment was reported to improve the exfoliation process [135]. Solvent drop grinding was shown to be an effective technique to accelerate mechanochemical reactions [257]. The addition of catalytic amounts of a liquid phase facilitates the molecular mobility, inducing reactivity in normally inactive systems. Therefore, wet milling conditions have been probed, and ball milling exfoliation of GANF® carbon nanofibers was reported [135]. Melamine was used as the exfoliating agent: 0.5 mL of solvent was added to 30 mg of GANF®/melamine mixture. The Hansen solubility parameters of each material in dispersion were studied in order to discriminate SLG from the rest of materials (FLG, poorly exfoliated carbon fibres and melamine) after the milling treatment. This allows one to select a suitable solvent to disperse mainly SLGs [135]. The quality of exfoliation was measured by Raman spectroscopy. Although there is a compromise between exfoliation quality and graphene concentration, these wet conditions follow the same trend established by the Hansen solubility parameters permitting SLG dispersion [135].

To achieve larger particle sizes in the range of microns), mechanical exfoliation by ball milling or high-shear mixing can be combined with chemical intercalation. Intercalating lithium and

ammonium-based ions (such as tetraethylammonium,Et_4N^+, ions) between layers in the graphite crystals weakens the van der Waal forces that holds the flakes together [258]. Ball milling supplies shear forces high enough to decompose the intercalated compounds into flakes. Using ionic liquid or ammonium based deep eutectic solvents as the milling liquid accelerates the kinetics of the intercalation because it increases the activity of ammonium ions [258]. Also, deep eutectic solvents are green solvents having the advantages of non-flammability [259], high thermal stability (> 150 ^oC) [259], wide liquid phase range (usually over a range of 200-500 ^oC) [260], negligible vapour pressure (< 10 Pa at room temperature) [261] and easy recycling [262]. These properties eliminate the safety problems associated with typical organic solvents. An eutectic mixture of urea and choline chloride (2:1) can be produced by stirring the two components until clear liquid is formed. The liquid can be then charged into the grinding chamber with 2g of graphite, 4 g of battery grade lithium chips, and yttria stabilized zirconia milling media. The ball milling runs under a flow of N_2 gas inside a glovebox. It is better to pause the grinding process for 30 min every 2 h to allow the system to cool. To recover the exfoliation product, the samples are then washed with dimethylsulfoxide (DMSO), and centrifuged at 1500 rpm to remove thick flakes. The milling speed should be controlled to below 500 rpm to avoid extensive heating and to minimize defects in the produced flakes.

II.3 Graphene oxide and reduced graphene oxide

Graphene oxide

GO has itself a number of properties that are advantageous for several applications. Due to its oxygenated surface groups, it can undergo complete exfoliation in water [263-265], yielding colloidal suspensions individual sheets [265-267], that can be further functionalized, deoxygenated or dispersed in polymeric matrixes to give new multifunctional materials and composites [268]. This, combined with chemical tailoring [203, 204, 269] and biofunctionalization [270-274]makes GO a promising candidate for biomedical applications where water compatibility is crucial, e.g. in tissue engineering, drug delivery, cancer treatment and biosensing [272-280].

GO can be prepared by oxidation of graphite using highly oxydant reactants such as H_2SO4, $KMnO_4$, H_2O_2 [139, 140]. The preparation method strongly influences the surface chemistry and related chemo-physical properties, ultimately affecting its functionalities. In 1859, Brodie first reported the synthesis of GO by adding potassium chlorate ($KClO_3$) to a slurry of graphite in fuming nitric acid (HNO_3) in a single portion [281]. In 1898, Staudenmaier improved Brodie method by replacing about two thirds of fuming HNO_3 with concentrated H_2SO_4 and by adding $KClO_3$ in multiple portions during the course of reaction rather than in a single portion. Such slight modification had the same oxidation efficiency of reiterative Brodie oxidations (achieving high oxygen contents, up to C:O= 2: 1) but in a single synthetic step. However, the Brodie and Staudenmaier method was not widely used because of the potential risk of explosions [282]. In 1958 Hummers and Offeman proposed a safer approach, currently widely adopted and known as Hummers method [139], consisting the replacement of $KClO_3$ by $KMnO_4$ and $NaNO_3$ in concentrated H_2SO_4. Ref. [283] reported

that excluding $NaNO_3$, increasing $KMnO_4$ and a mixture of H_2SO_4/H_3PO_4 can improve the oxidation process. In these conditions the reaction is not exothermic and no toxic gas is produced.

The method proposed in Ref. [283] and ref [264] allows one to prepare highly soluble (>4 mg/ml) water-soluble GO for studying the biological and toxicology effects on living cells [277-279]. In this way, GO sheets could be prepared with constant surface chemistry but varying lateral size, spanning from 100 μm down to less than 100 nm [279].

The synthesis was as follows: graphite flakes (purchased from Aldrich, maximum particle diameter 500 μm, 5g) and 3.8 g of $NaNO_3$ were introduced in a 2 L flask equipped with a mechanical stirring apparatus. Then, H_2SO_4 (375 mL) was added at 0°C (ice bath), and the solution was stirred until homogeneous. $KMnO_4$ (25 g) was slowly added over 1 hour, keeping the temperature below 10°C with an ice bath. The solution was removed from the ice bath after 2 hours, and was further stirred for 5 days at room temperature (colour changed from dark green to brown). 700 mL of H_2SO_4 5% aqueous solution were added to the brown suspension dropwise (temp. < 40°C) and the mixture was stirred for 2 hours at room temperature. Then, 20 mL of H_2O_2 (30%) were added dropwise to destroy the excess of permanganate, and stirred for 2h. The solution was diluted to 2 L with 5% H_2SO_4 and, after one day of sedimentation, single layer supernatant was removed and replaced with water (1 L) and H_2O_2 (10 mL). After vigorous shaking, the suspension was allowed to sediment overnight. The supernatant solution was then removed and the suspension washed with an aqueous mixture of 5 wt% H_2SO_4 and 0.3% H_2O_2 (12 times), then HCl 4% (3 times), milliQ water (10 times) and centrifuged after each step. Elemental analysis did not show significant presence of manganese (c < 0.005%) or other metallic contaminants. The lateral size of the GO flakes could then be tuned by sonicating the starting solutions for different times, from 0-100 h) in milliQ water (for a systematic study of GO size vs. sonication time see [118]). Sonication was performed using an Elmasonic S10H bath sonicator (frequency: 37 kHz, effective power: 30 W). Stock suspensions of the as prepared GO samples (1 mg mL^{-1}) were prepared by diluting the initial dispersion (2.5 mg mL^{-1}) into sterile water to the appropriate concentrations for cellular treatment.

It is still not clear which are the most relevant factors regulating the interactions between GO and biological molecules, tissue structures and organisms. Numerous studies [277-279, 284] have shown that GO chemical purity, chemo-physical parameters and morphological properties can play a crucial role on cells viability and functionalities [284].

Taking advantage of the size tunability and high solubility of GO, the effect of the lateral size of GO in different biological systems was investigated for human and murine phagocytic cells [279], human intestinal cells [277], human lung and colon carcinoma cells [285], different enzymes of human [278] or bacterial [286] origin, gelatine membranes and fibres of animal origin [287].

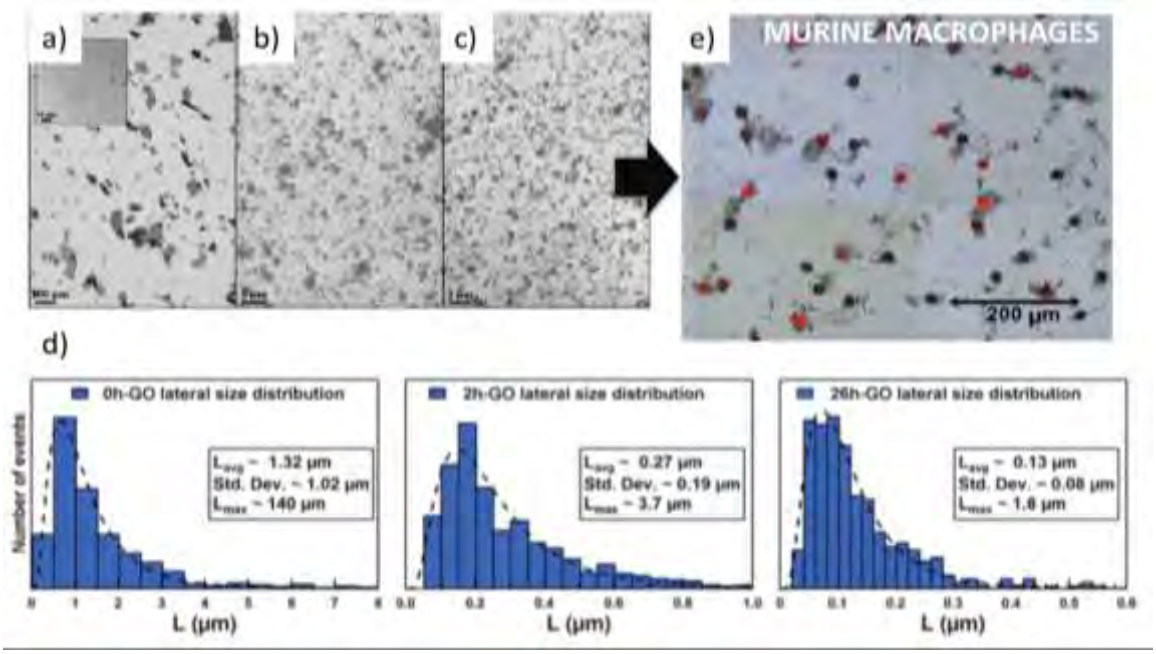

Fig. II.13: a,b,c) SEM image of GO solutions sonicated for different times, then spin coated on 300 nm SiO_2 /Si(100): 0 h-GO (a), 2 h-GO (b), and 26 h-GO (c). d) Flake size distribution of the 0 h-GO, 2 h-GO and 26 h-GO samples from SEM statistics. e) Optical map of mIPM cells incubated with GO. Red dots indicate where Raman spectra was taken to detect internalization of GO into the cell. Adapted from Ref. [279].

In Ref. [279] three GO solutions, sonicated for 0, 2 and 26 hous (with average lateral size~1.3, 0.27 and 0.13 µm) were mixed with human monocyte macrophages (hMDM) and murine intraperitoneal macrophages (mIPM), revealing that the flake size has significant impact on different cellular parameters (i.e. cells viability, reactive oxygen species (ROS) generation and cellular activation, Fig. II.13). Ref. [279] reported observed a strong interaction (>90% internalization) with the cellular membrane, leading to the sliding of flakes under the membrane layer. GO samples could be internalized by both human and murine macrophages in a size-dependent manner : the more the lateral dimensions of GO were reduced, the higher were the cellular internalization and the effects on cellular functionality [279]. Flakes with the smallest lateral dimensions (<300 nm) were better internalized by primary macrophages. A “mask effect” was observed due to the 2-dimensional shape of GO, with a preferential parallel orientation of the GO sheets onto to the cellular surface.

Reduction of Graphene Oxide (GO) is scalable and cost-efficient method for graphene synthesis.

Reduction of GO

There is a growing and active investigation into the preparation and use of RGO due to its excellent electrical conductivity properties (from 10-5 S/cm to 1000 S/cm , [288]) increase in the mechanical reinforcement of polymeric matrixes [289]. For example 0,2% can improve from 25-50% the mechanical properties of epoxy matrix composites, and energy applications [290]. Whereas

thermal, chemical and thermochemical reduction of graphene and GO are customizable and versatile methods for preparing different types of RGO, they show several problems that hamper the synthesis of defect free graphene flakes. Among them, there are difficulties in complete removal of functional groups and the restitution of morphological characteristics of the material prior to the oxidation and sonication processes. RGO has high polydispersion [288] in the lateral size, from less than 1 μm to more than 100 μm, due to the distribution of crystal size in the starting natural or even synthetic graphites , as seen in previous epigraphs, and also due to the scissor effect that break the graphenic planes during the oxidation and/or the sonication processes [291]. However, the RGO thickness is controlled by the exfoliation of GO [292] and, depending on the preparation method and conditions, monolayers can be obtained [293]. Actually, the first isolation of graphene was realized by reduction of GO by hydrazine [265].

There are several key characteristics of RGO that should be considered and evaluated to obtain optimum performance for a particular application: average lateral size, thickness, C/O ratio, the quantification of other heteroatoms, and surface area.

Lateral sizes > 5-10 μm are not suitable for fiber reinforced composites by vacuum assisted liquid resin infusion, LRI, or resin transfer moulding (RTM), due to the difficult filtration of the RGO flakes by the fabrics during the processing [294]. However, lateral sizes [>30 μm produce low percolation threshold composites as compared with medium (<20 μm] and small (< 5 μm)] ones, due to size of overlapped areas and the higher number of contacts between particles [295].

Thickness is also a key factor for the performance of RGO in applications. In photocatalytic applications of RGO-TiO2 it is demonstrated that the highest photocatalytic activity was observed with the single layer graphene composite, and it decreased with the number of graphene layers; this effect is attributed to higher charge carrier mobility and improved prevention of electron-hole pairs recombination [296]. In some composites this effect is also observed [125], however, in most of the applications in composites, SLG is not needed.

The C/O ratio and the quantification of other heteroatoms are important factors to determine the range of applications suitable for RGO. RGO with high (10%) to medium or low (1%) content of oxygen is not suitable for thermal conductive properties and a decrease to the oxygen content to lower than 0.5%w and distances between defects > 15 nm are needed [123]. Also, the sp^2/sp^3 ratio is a relevant for energy applications [297], catalysis [298] and gas absorption [299]. In many applications ,such as mechanical reinforcement of polymers, increase dispersion in composites or fire retardancy [300] and for further covalent functionalization, GO with 15-2,5% of oxygen concentration is needed and levels ~ 8-4% of oxygen are recomended.

Surface area is other of the key characteristics. The Brunauer–Emmett–Teller (BET) theory serves as the basis for an important analysis technique for the measurement of the specific surface area of materials. We will refer to those experimental methods as BET specific surface area, S_{BET}, measurements. The specific surface area of a material, S_{BET}, is related to the number of layers N and is a key factor enabling a material for energy applications. N can be estimated by dividing the maximum surface area of graphene, 2630 $m^2 g^{-1}$ by the specific surface determined experimentally

by BET methods N_G =2630/S_{BET}, [301]. According to [302], RGO with S_{BET} around 600-700 m^2/g are mostly SLG .

The apparent density of RGO, defined as the mass divided by the volume occupied by the material, is another key parameter. GRMs with high S_{BET} values produced by thermochemical reduction exhibit low densities, even lower than 4g/L [292] . For some applications a compaction of the RGO for further processing is needed [303].

Many strategies exist for the chemical, thermal and thermochemical reduction of GO, which strongly depend on the process and conditions selected for the reduction process, and the final performance required. Toxic hydrazine, sodium borohydride, hydroquinone have been used for this [304], as well as "green reducers" such as organic acids [305], alcohols [306]. Also, biochemical molecules [307], amino acids [307] , natural extracts [307] or metals [308], and several mechanisms have been proposed [309].

Based on reproducibility, post-processability and ease up-scaling, alcohols are ideally suited for the chemical reduction [306]. GO is first dispersed in the selected alcohol. Concentrations of GO ~5-20 g/L should be used because, before the reflux of GO in alcohol, ultrasonication (of a batch or in a continuous system) is needed for the exfoliation from graphite oxide to graphene oxide exfoliation of GO and an increase of viscosity should be avoided. The higher the GO lateral size, the lower GO concentration should to be used, due to the lower stability of the GO in the suspension. The main disadvantage of this process is the high volume of alcohols needed. For example, to process 100 grams of GO, a 20 litres vessel is needed. However, alcohols can be recycled by column distillation with recycling yields > 95%. Critical parameters are the selection of the alcohol and the time under reflux. By using X ray diffraction, the reduction can be monitored based in the decrease of the intensity of (001) peak of GO and the presence of (002) peak of RGO [310].

The electrical conductivity of RGO is also dependent on the chemical reduction process [288]. Longer reflux time in isopropylalcohol (IPA) produces higher conductivity. However, after 15 hours no significant improvements are observed, see Fig. II.14).

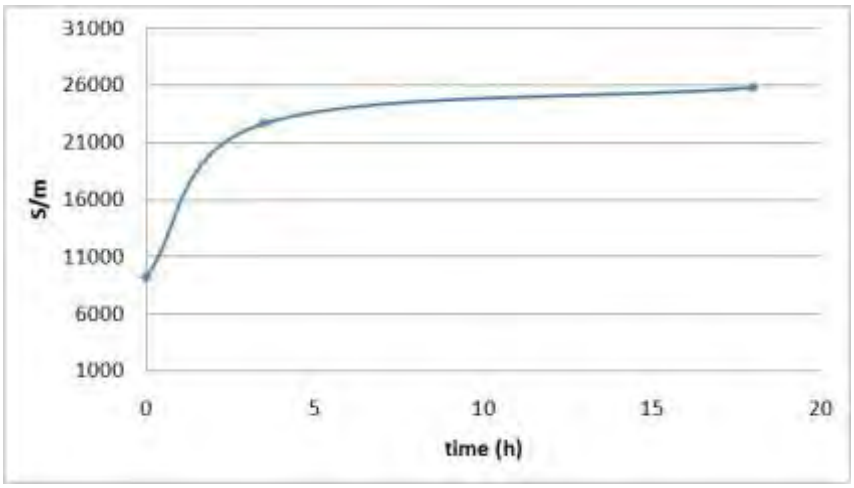

Fig. II.14. Conductivity of RGO reduced in IPA reflux vs. reduction time .

After this reduction step, filtration of RGO at RT is required. This is easy to perform due to the powdery aspect of the material and it can be air-dried or oven dried at less than 100ºC for 12 hours. It is important to control the drying process to prevent contaminations, avoid thermal expansion and decrease apparent density for further processing. High pressure and hydrothermal methods are more complex [311, 312], but very efficient reduction of the GO can be achieved, obtaining lower oxygen concentration of oxygen compare with the traditional chemical redactors such as hydrazine [312].

The products obtained from chemical reduction of exfoliated GO [288] have usually poo, <100 S/cm^{-1}, electrical properties due to the high (>10%) oxygen concentration and the presence of structural defects [140, 141, 313].

RGO can be prepared by thermochemical methods as an alternative route for reduction of GO [292], where restoring the sp^2 graphene structure is additionally achieved by thermal annealing [268]. Besides oxygen removal by reduction of GO, enhancing the graphitization by repairing the C-C sp^2 π-bond network at defect regions during the reduction process [292], can further improve the electrical properties of exfoliated RGO for high electrical and thermal conductivity, and self-sensing applications.

For the preparation of RGO with < 1% oxygen content, several strategies can be used, such as over 1800ºC annealing T, long processing times (> 60 min at 1500ºC), reducing atmospheres such as H_2, alcohols, hydrocarbons, etc. Thermochemical reduction can be done at medium 800ºC or high T (> 1200ºC), depending on the final requirements. The choice of the working atmosphere has an impact on the final RGO characteristic, particularly on its oxygen content. Thermal reduction can be done in vacuum [314] or inert atmosphere [292] in a reducing H_2 environment [315] and using carbon donor molecules. Alcohols are very effective in the reduction of GO and the partial restoration of the graphitic structure due to their carbon donor characteristics. Other carbon donor molecules or a combination of hydrocarbons [316] are alternatives for the production RGO with O content < 2% O at moderate T<800ºC.

In thermochemical reduction, the working atmosphere comprises a gas carrier, which in most cases is an inert gas such as N_2 or Ar, and the carbon donor/source molecule or combination of molecules. Ar is preferred as gas carrier over N_2, giving a more efficient due to the doping of N to RGO during the reduction process. For the restoration atmosphere, it is crucial to control the carbon donor and also the kinetics of the pyrolytic decomposition of the active gas. Carbon molecules results in the decomposition and formation of other non-graphene species and non-desired aromatic molecules [317]. Thus a low concentration, usually less than 5% is recommended. Significant improvement of the reduction process when compared to the material obtained in H_2 was reported [318].The use of carbon donor atmospheres is the most cost-efficient to obtain highly reduced GO, with oxygen concentration from 0,25-1%.

The reduction T determines the kinetics of the thermal decomposition (from 300 to 2000 ºC) but a low cost- efficient reduction must be pursued in an industrial enviroment and the time and T of the process should be the lowest possible. However, efficient processes at low temperatures have

been reported in [319], obtaining high quality graphene for lithium batteries at a low T ~ 300 °C in only 5 min.

Aerogels based on RGO

Graphene flakes can serve as building blocks for the preparation of three-dimensional low density structures, such as sponges, foams, hydro- or aerogels [320, 321]. These materials exhibit a highly opened structure, with interconnected hierarchical pores that enhance the accessibility to the whole surface of the material and improves ion diffusion. The assembly of the graphene sheets into macrostructures can also improve the mechanical properties while retaining other outstanding properties associated to the individual graphene layers [320, 321]. GO can be used for the preparation of composites with tailored macroporous structure through the assembly of GO sheets with different templates. After template removal complex GO-based materials with hierechiral porosities can be prepared [322]. The combination of the processing at RT and a subsequent treatment at moderate T will allow the preparation of highly conductive bare carbonaceous three dimensional electrodes [323] and its composites, which may serve as self standing electrodes for lithium ion batteries [322].

The ice templating approach [324] is a useful technique for the preparation of macroporous reduced graphene oxide-based aerogels (ARGO). Ice templating involve the freezing a GO suspension, which is then subsequently freeze-dryied to sublime the ice crystal formed within the structure. This process is useful for the preparation of a large variety of a homogeneous nanostructured composites with application in energy storage, catalysis, sensing or separation [325], but it can also offer certain control on the porosity of the resultant materials. The modification of different parameters such as temperature or immersion rate, impact the textural properties of the resultant material. Moreover, the ice-templating approach allows obtaining structures with hierarchical porosity, which can favour the transport and diffusion of molecules to the whole surface of the material, highly desired in adsorption processes for separation and purification purposes and catalytic applications, not only of soluble pollutants in waste waters, but also for immiscible substances in biphasic systems. In energy storage applications ARGO has been also proposed as electrodes for supercapacitors, Li-ion, Na-ion or metal-air batteries [321].

Ice-templated ARGO can serve as self-standing electrodes for energy storage devices [326]. They can be directly assembled into the electrochemical cells avoiding the use of binders, which do not contribute to the capacity of the electrode, in contrast, they can decrease its conductivity and block the access of the electrolyte to the surface of the active materials. In the case of anodes for lithium ion batteries (LIBs), sp^2 graphene nature not only help to improve the electrodes conductivity, thus enhancing the power of the device, but it can also buffer the volume changes undergone by some active species that has been pointed out as high energy anodes for LIBs during its alloying with lithium [327] .

The preparation of self-standing composites provides an additional value to these electrodes since they can be assembled into flexible energy storage devices to be mounted into flexible portable electronics [328] .

Si-RGO and SnO_2-RGO Aerogels

Reduced graphene oxide-based aerogels (ARGO) composites can be prepared following the route schemetized in Fig. II.15. First, an homogeneous suspension of GO is produced, alone or in the presence of a certain precursor of the desired particles. Second, the suspension is immediately frozen by inmersion in liquid nitrogen. Then it is freeze-dried to remove the ice-crystals formed upon freezing and leaving the macroporous structured in the GO-based monoliths. Finally, samples are partially reduced by a thermal treatment conducted under inert atmosphere which yield the macroporous carbonaceous structure or the composite in which RGO is decorated with the crystalline phase of the particles.

The microstructure and porosity of the resultant aerogels can be tuned by changing the rate and temperature of freezing. It should be highlighted that fast freezing does not allow graphene layers to self-arrange with the ice crystals front giving rise to materials containing macropores randomly distributed within the structure [329].

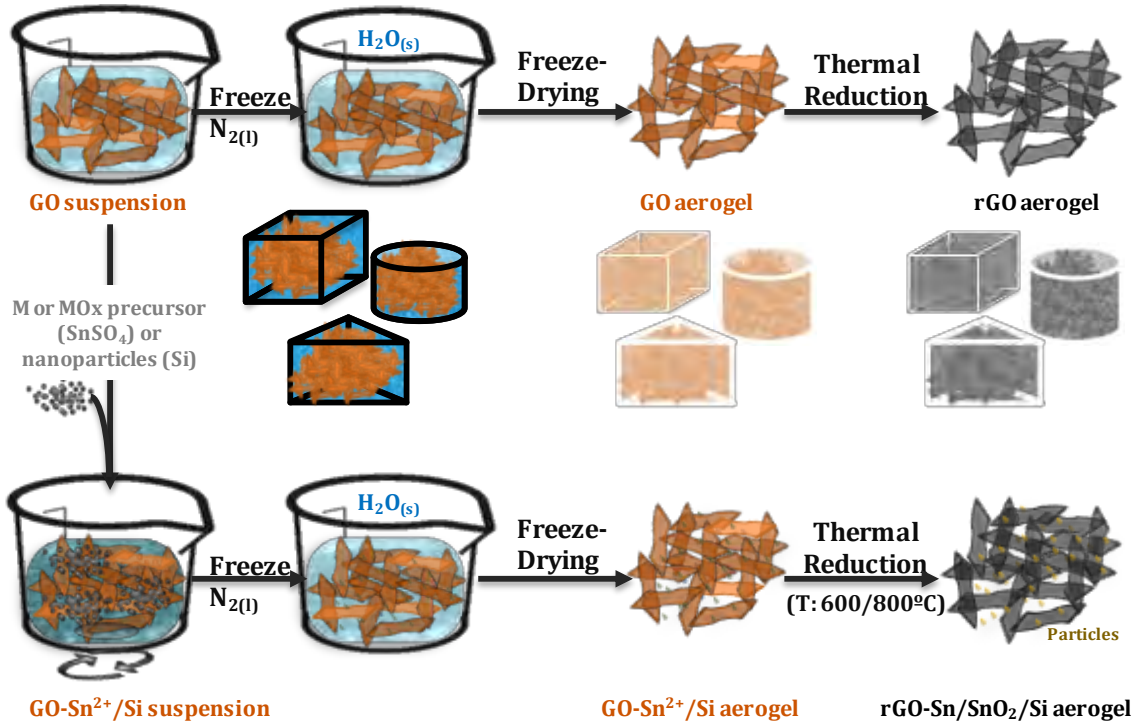

Fig II.15: Schematic representation of the route followed for the preparation of RGO composite aerogels.

Figure II.16 shows photographs of different aerogels obtained by the ice templating approach. In this case, GO suspensions obtained by the sonication of graphite oxide by the Hummer's

method were used [102]. For the synthesis of tin-based ARGO composites an aqueous suspension was used. While in the case of Silicon-ARGO, the GO and the Silicon nanoparticles were initially dispersed in ethanol, a homogeneous suspension of GO is produced that could contain the precursor compounds of the desired particles [327, 330]. Then, the suspension is frozen in liquid nitrogen, and subsequently freeze-dried to sublime the ice-crystals leaving the macroporous structured monoliths. Finally, the samples are submitted to thermal treatment under inert atmosphere to reduce GO and obtain the desired crystalline phase of the particles.

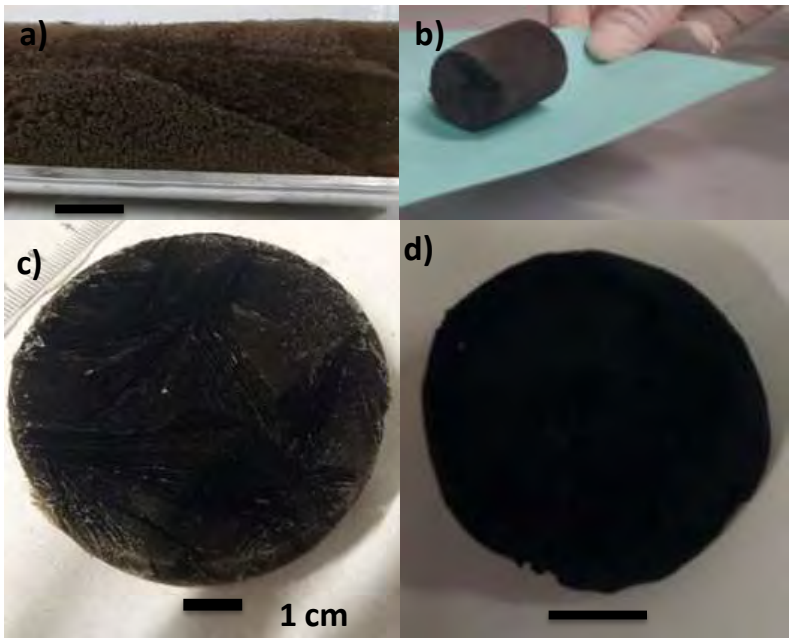

Fig. II.16. Digital photographs of GO aerogels prepared form different suspensions: a) GO (2 mg mL^{-1}), b) GO (6 mg mL^{-1}), c) Sn-GO and b) RGO composite aerogel, obtained after thermal reduction of GO aerogel at 800 C.

For the preparation of the GO suspension in ethanol ~ 5 mg mL^{-1} , an aqueous suspension of GO was washed several times with dry ethanol. The suspension was then sonicated for 1 hour and centrifuged at 3500 rpm during 30 min. After this period the precipitated g solid was discarded. The concentration was ~ 5 mg mL^{-1} by adding the necessary amount of ethanol.

When mixing Si nanoparticles and GO, the use of ethanol is justified, since Si-RGO composites generally need pre-oxidation of the Si nanoparticles or ultrasonication in order to improve their dispersibility in polar media, to be homogeneously mixed with GO [331, 332]. A highly homogeneous, see Fig. II.17, and stable dispersion of Si nanoparticles, avoiding their oxidation was achieved [330].

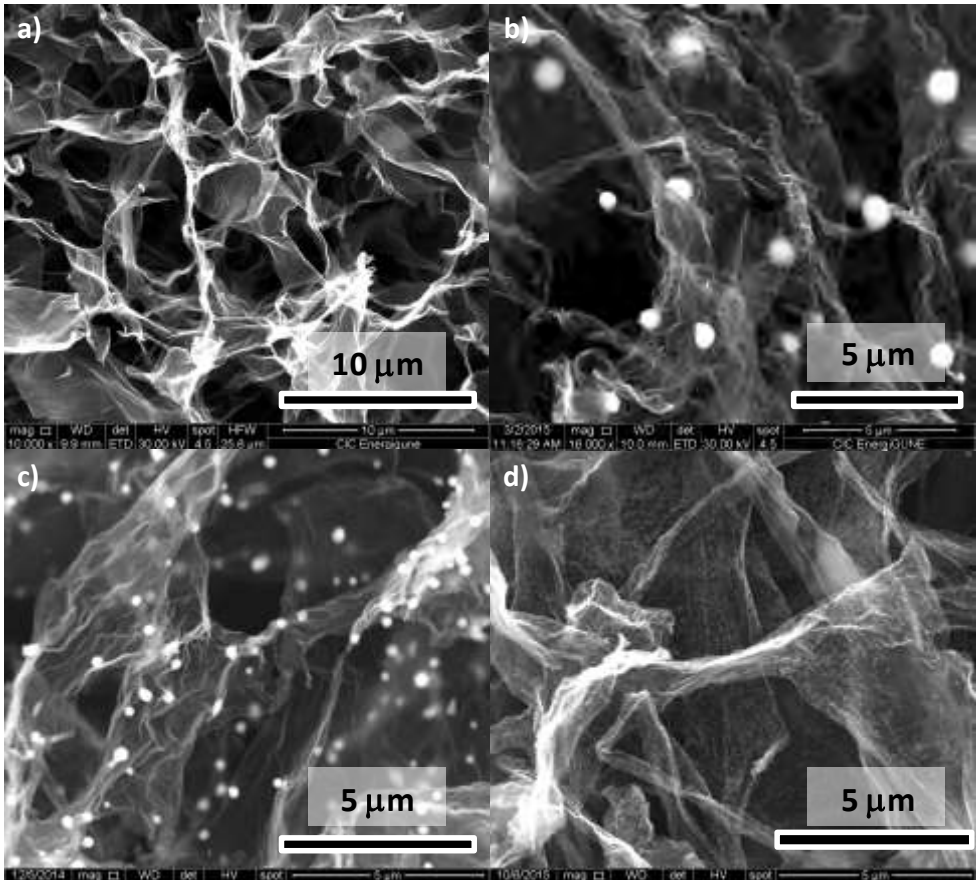

Fig. II.17 .Representative SEM images of a) A-RGO, b) A-Sn-RGO, c) A-SnO_2-RGO and d) A-Si-RGO.

Si-GO composites were prepared by mixing 25 mg Si nanoparticles (Alfa Aesar) with a 20 mL of the GO suspension in ethanol (4.5 mg mL^{-1}) in an Ar atmosphere. The mixture was stirred for 2 h, then evaporated at 30 ºC in a rotary evaporator until the volume was reduced to 10% of the initial volume. Before freezing, the amount of ethanol evaporated was replaced by similar amount of distilled water was added to recover the starting volume and the mixture stirred for 1 hour more. After this, the suspension was sink in liquid nitrogen and fast frozen at -196 ºC . It was freeze-dried in a Telstar LyoQuest freeze-drier. Thermal reduction was accomplished heating in a tubular furnace at 1 ºC min^{-1} up to 200 ºC, to avoid the thermal blasting of GO, and then to 1000 ºC at 2 ºC min^{-1} under dynamic Ar/H_2 (95:5) atmosphere (100 mL ºC min^{-1}), and maintained at this temperature for 1 h. The resulting material exhibits large macropores in a highly open macroporous structure formed by graphitic flakes homogeneously decorated with Si nanoparticles (~50 nm diameter), Fig. II.17d.

This procedure also allows to *in-situ* deposit the particles on the graphene flakes [333]. Tin and SnO_2-ArGO, were prepared by dissolving 100 mg of $SnSO_4$ in 100 mL of the GO suspension (1 mg mL^{-1}), then the pH was increased to 9 by the addition of some drops of a 1 M NH_3 solution and the mixture was heated at 60 ºC for 5 h. At this point, a partial reduction of the GO happens and the colour of the suspension changes to grey. Finally, the suspension is freeze/freeze dried to obtain macroporous above 1 μm in size $Sn(OH)_4$–GO composites [333].

GO-based aerogel was reduced by thermal treatment at 650 or 800ºC. This T range allows crystallizing tin precursors into SnO_2 and Tin, respectively while removing most of the functional

groups, thus increasing the electrical conductivity of the composites. Samples were heated in a horizontal tube furnace at 1 ºC min^{-1} to 200 ºC to avoid the thermal blasting of GO and then to 650 or 800 ºC at 2 ºC min^{-1} under a dynamic argon atmosphere (100 mL min^{-1}), and maintained at this T for 1 hour. By this procedure, two samples, Sn-ARGO (Fig. II.17b) at 800ºC and SnO_2-ARGO (Fig. II.17c) at 650 ºC were obtained [333]. Fig. II.17 shows a highly porous material formed by RGO flakes which contain large macroporous randomly distributed along the surface. In both samples, the Sn sub-micrometer particles show a good homogeneous distribution on the graphene sheets and exhibit a quite narrow particle size distribution, being higher in the case of the metallic Sn particles (ca. 750 nm in diameter) than the SnO_2 particles (ca. 250 nm in diameter), which has to be ascribed to the carbothermal reduction, melting and re-crystallization of the Sn particles [334] undergone over 650ºC.

Aerogels can be used for binder-free electrodes in LIBs with using neither binder nor metallic support, showing very promising results [322]. In the case of the SnO_2-ARGO composites, reversible capacity of 1010 mAh $g_{electrode}^{-1}$ was measured at 0.05 A g^{-1} and 470 mAh $g_{electrode}^{-1}$ at 2 A g^{-1}, and showing good Coulombic efficiencies (>98%) and good stability after 150 charge-discharge cycles [330].The Si-ARGO electrodes showed reversible specific capacities~700 mAh $g_{electrode}^{-1}$ with associated Coulombic efficiencies>99% within the 2-0.05 V range. These electrodes also showed a good stability during 100 charge-discharge cycles[330]. This indicates that ARGO can accommodate volume changes of silicon particles and, at the same time, improve the conductivity of the electrode without additives (nor conductive, nor binder). Due to their high electronic conductivities and light weight, graphene aerogels are good candidates to be used as support in the preparation of advanced electrodes for next-generation lithium batteries such as Metal-air batteries or Lithium sulphur batteries [335] or Lithium Ion Capacitors [336].

II.4 Chemical intercalation and reductive exfoliation

Graphene from graphite intercalation compounds

The intercalation of graphite with sulfuric can be exploited for the production of GO. Graphite can also be intercalated by a number of other species to yield graphite intercalation compounds (GIC) [143]. The fabrication of acceptor-GIC after intercalation with, e.g., alkali metals has gained increasing importance. Refs [337-340] and [341-343] reported that such acceptor-GICs are very suitable precursors for covalent functionalization of graphene.

In typical covalent functionalization sequences, the negatively charged graphene layers first act as reductants for electrophiles (for example alkylhalide) [337], which are subsequently attacked by the intermediately generated organic radicals or H-atoms, yielding covalently modified graphene architectures. This wet-chemical functionalization is facilitated by the fact that, due to Coulomb repulsion, the negatively charged graphenide [344] layers within the solid GICs can be dispersed in suitable organic solvents (see [344] for more details).

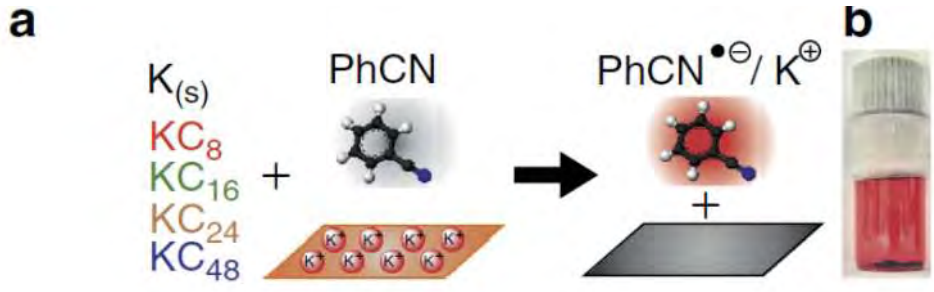

Fig. II.18:(a) Reaction scheme for the quantitative electron transfer from various GICs to PhCN leading to dissolved K^+ ions and the red coloured radical anion $PhCN^{\bullet-}$. (b) Photograph of a sealed vial containing KC_8 in a concentration of $5.0x10^{-4}$ M in $PhCN^{\bullet-}$, adapted from Ref.[345]

One fundamental issue is if all negative charges of the graphenide intermediates can be controlled or even completely removed in such redox reactions [346]. Only complete oxidation is expected to avoid reactions with moisture and oxygen during workup [347], leading to side products with undesired and additional oxygen- and hydrogen functionalities. More importantly, the controlled removal of all negative charges from the solvent exfoliated graphenide intermediates with a suitable oxidation reagent allows for the bulk production of defect-free graphene. Ref.[345] reported that the treatment of K intercalated graphite with benzonitrile (PhCN), leads to a discharging, i.e. taking away of the electrons from charged layers, of the individual graphenide sheets upon the formation of the colored radical anion $PhCN^{\bullet-}$, Fig. II.18, which can be used to monitor the accompanying exhaustive and Coulomb force-driven migration of K counterions from GICs into the surrounding benzonitrile phase. The suppression of reactions of dispersed graphenides with moisture and air takes place when no treatment with benzonitrile is provided, resulting in graphene. This represents a rather mild, scalable, and inexpensive method for wet-chemical graphene production. This reductive graphite exfoliation approach can be extended to water as solvent [348].

Chemical exfoliation of transition metal dichalcogenides

LMs, such as TMDs, can be reductively exfoliated via intercalation compounds [142]. Typically, MoS_2 is intercalated with n-Butyllithium (*n*-BuLi) in an inert solvent such as hexane [349]. In contrast to graphite, intercalated MoS_2 does not react with water[349] so that this can be used for work-up and subsequent exfoliation.

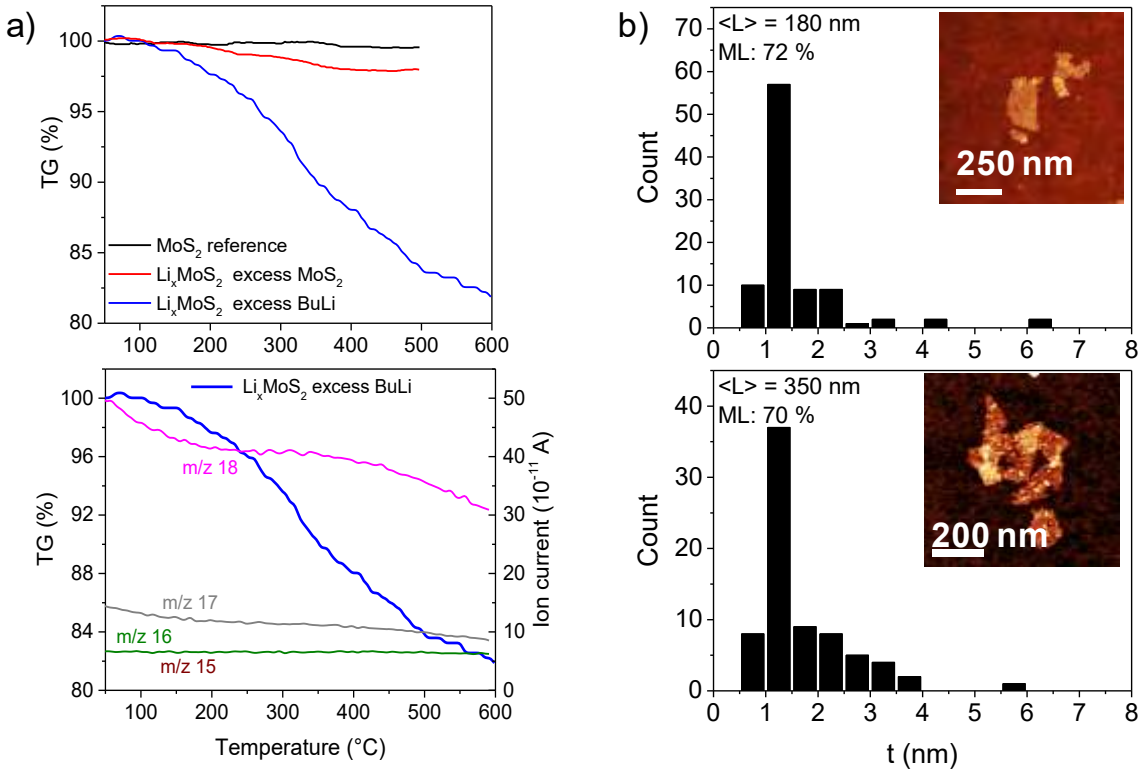

Fig. II.19: Characterisation of chemically exfoliated MoS_2 with different intercalation conditions. A) TGA weight loss of MoS_2 [reference] and MoS_2 chemically intercalated with excess of BuLi and MoS_2, respectively. Bottom: mass profiles for m/z=15-18 which constitute main weight loss in chemically exfoliated MoS_2 using excess BuLi. B) AFM thickness histograms of MoS_2 intercalated using excess MoS_2 (top) and BuLi (bottom). Inset: representative images. Adapted from Ref.[350].

Water is added to the reaction mixture to destroy excess BuLi. At the same time, gas formation occurs which acts as driving force to expand the MoS_2 and individualise the layers. After further washing and centrifugation-based purification, a colloidally stable MoS_2 dispersion in water can be obtained with negatively charged, predominantly single layer nanosheets (70-90%). As a result of the negative charges, a phase transformation from the semiconducting 2H-MoS_2 polytype to the metallic 1T polytype is observed. Such negatively charged MoS_2 can be used as precursor for subsequent covalent functionalisation using electrophiles as reported in [350, 351]. It is worth mentioning that another approach, based on chlorosulfonic acid assisted exfoliation method, has been developed allowing the retaining of the original (semiconducting) electronic properties of 2H-TMD (as MoS_2 and WS_2) [352].

This intercalation chemistry was explored in the 80s [142], but the interest was not in producing exfoliated flakes in a liquid dispersion. Thus, this chemistry needs to be revisited. Ref. [350] studied the impact of the intercalation conditions on the final product of chemically exfoliated MoS_2. In a typical exfoliation of MoS_2 with *n*-BuLi, the *n*-BuLi is used in ~10-fold access. These reaction conditions can lead to the introduction of defects, as exemplified by a significant mass loss in thermogravimetric analysis under inert conditions (Fig. II.19a). No specific mass fragments can be assigned to this weight loss suggesting it is not the result of a well-defined surface derivatisation

[350]. The major mass fragment observed has a mass over charge (m/z) of 18 and was assigned to -OH groups, Fig. II.19a. This disruption of the structure is not observed when MoS_2 is used in excess over n-BuLi. The work-up is more tedious with less material being obtained as individualised flakes, but after centrifugation, flakes with similar lateral dimensions and thickness distribution are obtained (Fig. II.19b) suggesting that there is scope to optimise the chemical exfoliation with respect to the yield of structurally perfect single layer MoS_2.

MoS_2/polyaniline aerogels can be prepared as follows. First, MoS_2 flakes were produced by Li intercalation and further ultrasonication exfoliation. Then, 0.4 g ammonium persulfate is dissolved in 50 mL 1 M HCl, mixed with 50 mL MoS_2 dispersion (0.40 mg/mL), followed by ultrasonication for 15 min to form a homogeneous suspension. Subsequently, 200 µl aniline was injected and the mixture stirred overnight. The resulting green suspension was centrifuged and washed with DI water for 3 times to create a MoS_2/polyaniline hybrid. A MoS_2/polyaniline aerogel, was made by dissolved 50 mL in DI water, after sonication for 1 h, then added into a 50 mL Teflon-lined autoclave. The mixture was heated at 180 °C for 24 h and cooled to room temperature. Then, the obtained material was washed by DI water and dried by freeze-drying.

II.5 Electrochemical exfoliation

Graphite can be exfoliated in SLG and FLG by applying a bias in ionic aqueous (or organic) electrolytes [119, 353]. Electrochemical exfoliation (EE) requires one graphite electrode and a metallic counter electrode in conductive media, which is not equipment-intensive. The exfoliation completes in minutes to hours, producing gram-scale quantities of flakes with high yield (up to 80 %)(defined as as the mass of exfoliated-(dispersible- flakes vs. the mass of the initial graphite raw material). The graphene quality is tunable : sheet size, C/O ratio, solubility and electrical conductivity can be tuned depending on the types of graphite precursors, electrolytes and operating potentials [354].

Aqueous media

H_2SO_4 can be used to prepare GICs as the ionic diameter of sulfate ion (0.46 nm) is close to the interlayer spacing of graphite (0.33 nm), which is the prerequisite for efficient intercalation.Efficiency here relates to the degree of exfoliation, a higher ratio of MLG is considered more efficient than thicker flakes. In this way efficiency is related to the average thickness of the exfoliated platelets, the lower the thickness the higher the efficiency. DiluteH_2SO_4 aqueous solutions were used [355, 356] to encourage graphite exfoliation because it is less corrosive. Ref. [356] immersed a graphite anode together with a counter electrode (Pt foil) into 0.1 M H_2SO_4, the exfoliation started when a potential of 10 V was applied. This gave 80 % one to three FLG with high exfoliation yield (60 %) and high C/O ratio (12.3). Under the electric current, the oxidation effect on graphene is strong owing to the interplay between proton (H^+) and sulfate ion at low pH. The oxidation effect is defined here as the oxygen content in the exfoliated materials, which usually results from the attack of oxygen-

containing radicals by water splitting [357]. Water electrolysis generates a oxidative radicals (HO· and O·), which contains a collection of sulfate salts (e.g. sodium sulfate, ammonium sulfate, etc) instead of H_2SO_4 [358]. By Doing so, Ref. [358] reported>85 % of single to three layer graphene with dimensions up to 40 µm and C/O~17.2, implying a low level of oxygen functionalization. Another strategy to suppress is to remove radicals from water splitting [359]. A series of scavengers have been investigated. Ref. [359] reported that 2,2,6,6-Tetramethyl-1-piperidinyloxy (TEMPO) to be the most effective, reaching C/O~25.3, average sizes~5–10µm and hole mobility up to 405 $cm^2/(V.s)$.

There are still several challenges: 1) the exfoliation only occurs at a single electrode (anode or cathode), indicating limited production rate; 2) the insufficient intercalation results in polydisperse flakes (with various number of layers), which requires additional separate procedures; 3) the graphene flakes trend to restack in solution due to strong in-plane interaction when the stabilizers are absent, which needs careful selection of suitable electrolytes.

Molten Salts

Another strategy to minimise the oxygen content is to use cathodic intercalation and oxygen-free electrolytes [360]. The intercalation of small cations with graphite from organic solvents is the principle of many energy storage devices [360-364]. Graphene can be prepared by electrochemical intercalation of Li^+ within the graphite interlayer space followed by dissociation of the resultant intercalating compound using prolonged sonication. Zhong et al. Ref. [365] tried to reduce the sonication time by intercalating graphite with Li, followed by a second intercalation of large tetra-n-butylammonium ions. In both cases, the strong decomposition reaction of the solvent cations hindered the formation of LiC_6 and/or ammonia graphite intercalation compounds. Therefore, another sonication step was need to completely detach the graphene flakes. Graphite can be fully exfoliated via an electrochemical process in organic solvents without the need of sonication or an inert atmosphere, by using DMSO saturated with lithium and small alkylammonium ions (triethylammonium, Et_3NH^+)[366]. An electrochemical program is used to apply a controlled cathodic potential on the graphite electrode, enabling the formation of exfoliated powder [258].In a three-electrode system, a chronoamperometric step of -1.7 V versus Ag/AgCl is applied for 5 min followed by linear sweep voltammetry at a rate of 10 mV/s. The potential is then kept at -5 V for 5 min to allow intercalation of the electrolyte cations, and finally it is swept linearly back to the open-circuit potential to decompose the resultant complex compound. During the first chronoamperometric and the second linear sweep voltammetry step, solvated carbanion complexes are formed according to reactions 1-5. The second chronoamperometric step at -5V is important to complete the intercalation process. This intercalated compound could decompose cathodically if the potential is held at negative values according to reaction (6) or on the oxidation cycle according to reaction (7). In both cases, dissociation of the intercalated compound is associated with Et_3N gas formation, more likely taking place between the graphene layers, which which applies more stress on the graphene layers and separate them further apart.

$$2Et_3NH^+ + 2e^- = H_2 + 2Et_3N \qquad \text{(II.1)}$$

$nEt_3N + e^- + C = (Et_3N)_n C^-$ (II.2)

$Li^+ + e^- = Li$ (II.3)

$mLi + e^- + C = Li_mC^-$ (II.4)

$nEt_3N + mLi + e^- + C = Li_m(Et_3N)_n C$ (II.5)

$Li_m(Et_3N)_n C^- + e^- + 2Et_3NH^+ = C + mLi + (n+2)\ Et_3N + H_2$ (II.6)

$Li_m(Et_3N)_n C^- = C + mLi + n\ Et_3N + e^-$ (II.7)

The intercalation from RT electrolytes is a slow process (diffusion coefficient is less than 1.2 x 10^{-10} cm^2/s) [367] and limited to few μm from the edge of the graphite grain [368]. The attempts of increasing the chemical activities of the Li ions or the other cations by using pure ionic liquids or deep eutectic solvents did not overcome the kinetic barriers [369]. Hence it was important to repeat the exfoliation process for more than one cycle to obtain a yield higher than 70% of the big flakes [360]. Another alternative is to use molten salts at a temperature higher than 500 ^{0}C as the electrolyte [370-372] developed a process for the exfoliation of graphite based on Li intercalation from molten LiCl electrolyte contains water. In a typical experiment, anhydrous lithium chloride powder (Sigma-Aldrich), 250 g, is charged in a graphite crucible (60 mm diameter and 150 mm height), which also serves as an anode. The cathode is a graphite rod with a diameter of 15 mm and a length of 120 mm. The cell can be heated to~800 °C, above the melting point of LiCl, by a ramp of 5 °C min^{-1}, under an argon flow of 20 cm^3 min^{-1}. At this temperature, a stream of water is bubbled into the molten bath at a flow of 100 cm^3 min^{-1} .Then a constant direct current of 33.0 A can be applied between the cathode and the anode for~30 min. After electrolysis, the cell is allowed to cool to RT under a flow of Ar gas. Graphene powder can then recovered from the solidified salt by washing with hot distilled water and vacuum filtering. Finally, the black powder is heated at 1300 °C at a heating rate of 15 °C min^{-1} under the atmosphere of an inert gas containing hydrogen. The process demonstrates commercial viability and a molten salt volume of 10 L should can produce 4.5 kg flakes in a day [371, 373].

Combination of electrochemical and microwave expansion

Microwave (MW) irradiation is currently employed in many sub-fields of organic synthesis to shorten reaction times, to enhance both reaction yields and product purity, and eventually to provide eco-sustainable synthetic methodologies, by replacing or reducing the use of polluting reagents [204]. Graphite can interact strongly with the oscillating electrical field of the microwave radiation, giving high T gradients and increased reaction rates (e.g. for fast functionalization of GO)[204] as compared to conventional procedures such as conventional chemical functionalization at room temperature in solution. Therefore, the high temperatures attainable using MW (>80°C) can be applied to exfoliate graphite [204].

Electrochemistry can be used for a fast (<30 min) and massive (>70%w/w intercalated molecules/graphite) intercalation of suitable molecules , such as perchlorate ions , into graphite [204]. Degradation of these molecules in GICs could is then triggered by MW irradiation, creating a gas pressure surge in graphite and yielding exfoliation [204].

Charged perchlorate ions could act as “Trojan horses”, to favour the intercalation of uncharged acetonitrile molecules [323]. These work as nanoscopic foaming agents, and decompose with MW irradiation to generate a pressure surge within graphite, resulting in exfoliation. The process yielded highly soluble, monoatomic (52% SLG), large (72 % of the sheets extending beyond 1 μm) that were characterized and then tested as transparent electrodes [323] and capacitors[323]. These electrodes can also be functionalized with nanoporous layers of inorganic oxides after the pre-intercalation of certain electrolyte species (e.g. $FeCl_3$–nitromethane electrolytes), to obtain, e.g. composite electrodes for LIB [322].

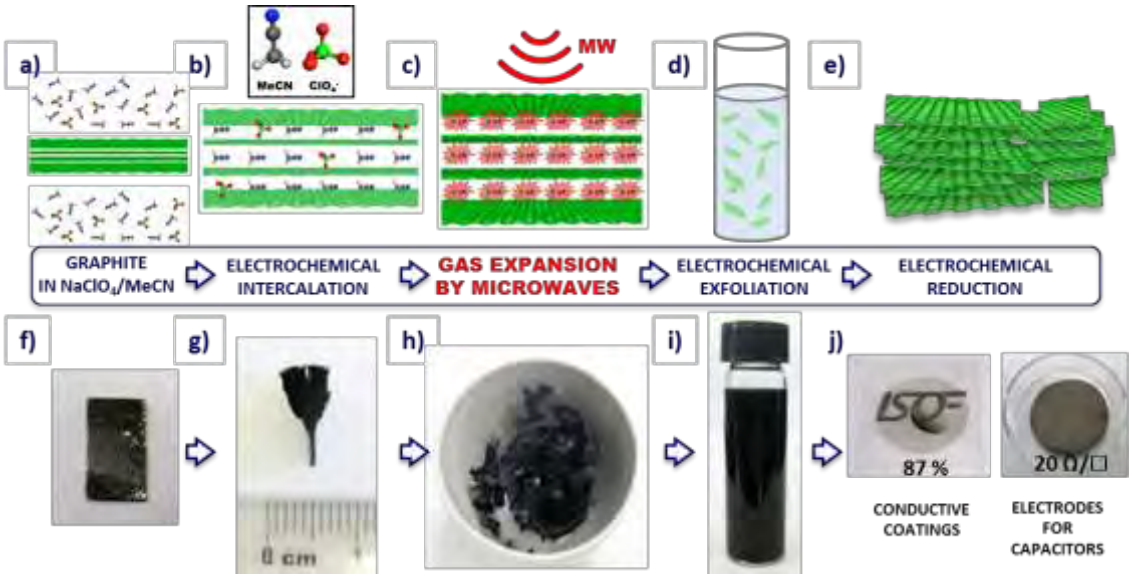

Fig. II.20: Photographs and schematic illustrations of graphite after intercalation, expansion, electrochemical exfoliation and reduction steps (from left to right).Adapted from ref [323].

Electrochemical treatment can be performed starting from highly oriented pyrolytic graphite (HOPG) as a working electrode and a Pt wire as a reference electrode. Ions such as sulfates and perchlorates can be efficiently intercalate into graphite, whereas intercalating uncharged molecules is more difficult [113], and can usually be achieved only by several hours sonication, with a lower yield (few %) of both exfoliated material and single sheets. The exfoliation process works only if the surface energy of the intercalated organic liquid is similar to that of graphene [113]. The process is limited to high-boiling solvents (T>100°C), such as NMP or DMF. To overcome this challenge, Ref. [323] used perchlorate ions to promote the intercalation of an organic, uncharged molecule (acetonitrile), which was present in high excess, as a solvent. Graphite was intercalated and partially expanded by electrochemical insertion of ClO_4^- in acetonitrile by applying a + 5V for 0.5 h. In this way, negatively charged ClO_4^- ions intercalated through grain boundaries or defect sites and favoured the penetration of the smaller, uncharged acetonitrile molecules. The fundamental role of ClO_4^- was demonstrated in a comparison experiment by using acetonitrile alone, for which no intercalation was observed [323]. The amount of molecules successfully intercalated into graphite was quite high (70% w/w), as estimated from TGA of the intercalated graphite electrode [323].

After the electrochemical intercalation step, MW irradiation expanded the graphite interlayers through decomposition and gas evolution of acetonitrile to yield a foam-like, multilayered powder. The expansion was extremely fast (~10 s)and yielded an increase in volume of the initial graphite of ~600%. The role of acetonitrile in the expansion was demonstrated in a comparison experiment, in which no expansion was observed for graphite treated only in aqueous solutions of $HClO_4$ or $NaClO_4$ without acetonitrile. Fig. II.20 shows a schematic of the process, and photographs of the material at the different processing stages.

II.6 Sonication-assisted vs. chemical vs. electrochemical exfoliation

Graphite can be exfoliated by different chemical methods in liquid phase. One of the simplest approaches is ultrasonic treatment in organic solvents (see epigraph II.2). Some dipolar aprotic solvents (e.g. DMF, NMP) or surfactants in aqueous solutions are effective to stabilize graphene in solution without re-aggregation [113].

A more effective but disruptive approach to solubilize graphene is by covalent modification, in particular by the formation of GO (see epigraph II.3). In presence of strong oxidants, the aromatic carbon network is oxidized with the creation of hydroxyl, carboxyl and epoxy moieties. The hydrophilic nature of these moieties on GO facilitates solution processing of highly concentrated single sheets on different substrates substrates (>60% monolayers, for statistics see [267]). The GO flakes can be then reduced to give electrically conductive RGO. However, numerous defects on GO are not fully restored after reduction and the electronic properties of RGO are poorer compared to those of the pristine graphene.

Another more controllable, slightly less disruptive approach to exfoliate graphite takes advantage of electrochemistry (see epigraph II.4). By adjusting the applied potential in suitable electrolytes, graphite electrodes can be either negatively or positively intercalated to obtain GICs, and then exfoliated by solvent decomposition directly during electrochemical treatment or by further thermal treatment.

We compared the most common LPE methods: sonication in solvent, chemical oxidation, and electrochemical oxidation. By using a graphite crystal as starting material, it was possible to study the structure of both the exfoliated and the non-exfoliated fractions on nanometric and mesoscopic scale [374].

Fig. II.21 shows the AFM images of graphite basal surfaces that are left behind after different exfoliation processes. Exfoliation by sonication in DMF proceeds on a layer-by-layer basis; only the upper part of the Highly Oriented Pyrolytic Graphite (HOPG) is interested, and the process is slow, requiring several hours to alter the substrate roughness. CE is the most damaging treatment for HOPG, destroying significantly the crystalline layer through deformation and intercalation; the obtained sheets are mostly monolayers, highly soluble, which tend to re-stack in a very uniform, layered material. Electrochemical exfoliation proceeds by mechanical expansion due to gas formation. Whole areas of the substrate rise up due to gas formation, tearing apart the superficial layers and removing large amounts of material. Electrochemical Exfoliation (EE) works on a larger scale, oxidizing the upper layers of the HOPG with more cracking and swelling on macroscopic scale.

Damage to HOPG is relevant and proportional to the applied bias, with disruption of crystalline stacking. Exfoliation is fast and more efficient than exfoliation in solvent, yielding many (>50%) single layer and bilayer sheets graphene oxide, with tunable oxidation grade.

The differences between the three methods highlight the trade-off between speed and efficiency of exfoliation on one side, and preservation of the material quality on the other.

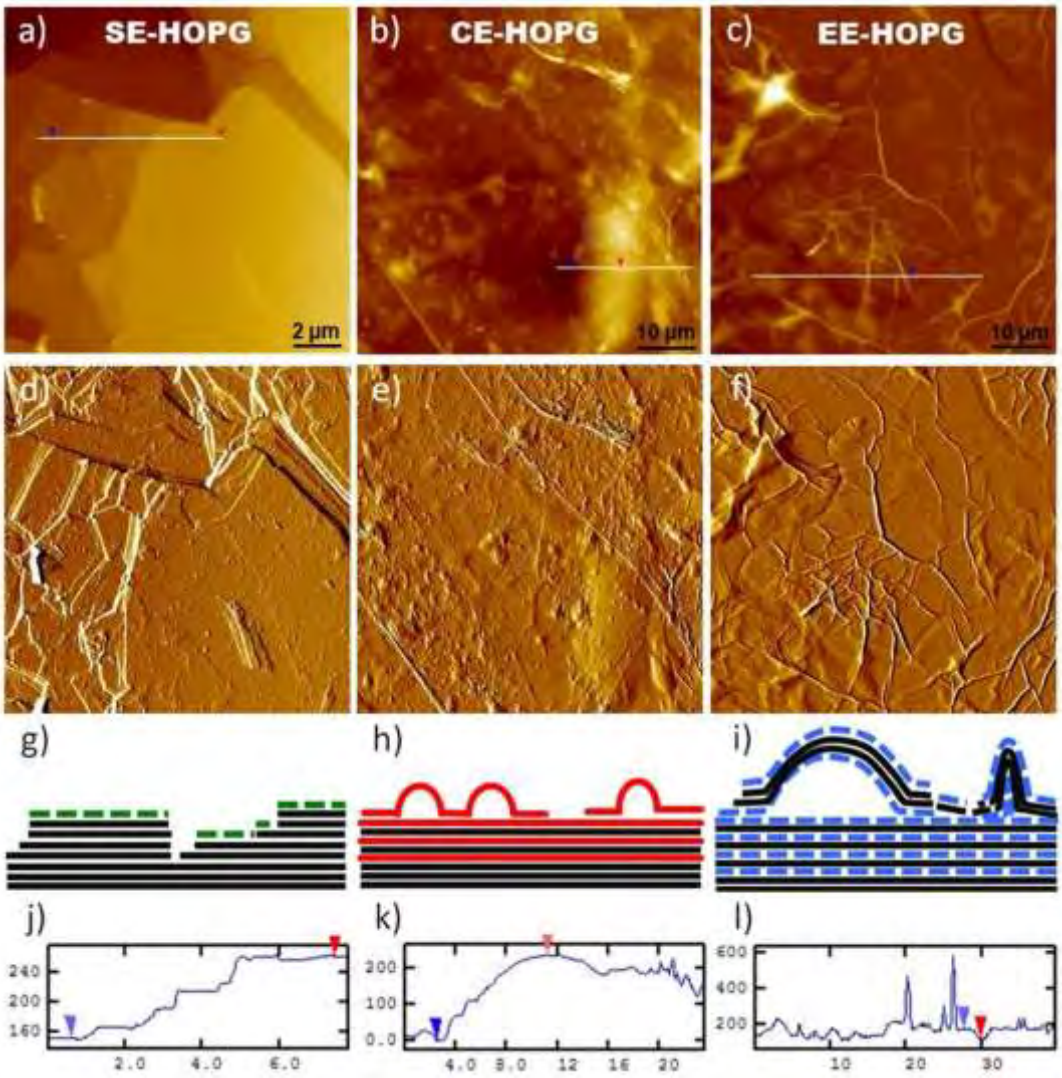

Fig. II.21: AFM images of HOPG basal surface after treatment by a) sonication-assisted, b) chemical exfoliation, c) electrochemical exfoliation. Z-range: a) 400 nm, b) 600 nm, c) 1µm. d,e,f) gradient-filtered version of each image. g,h,j) Schematic representation of the structure of the HOPG substrate after exfoliation procedures. j,k,l) height profiles taken along the lines shown in a,b,c. From ref. [374].

II.7 Computational modelling of exfoliation of 2D materials

The rush towards innovative applications has stimulated the synthesis and exfoliation of novel 2D materials with exceptional properties. Graphene, boron nitride, transition metal dichalcogenides, and black phosphorous are nothing but the tip of the iceberg of a rapidly increasing family of 2D materials. Nonetheless, to keep up with this experimental thrust it is of uttermost

importance to expand the portfolio of potential realistic 2D materials. In this respect, first-principles simulations offer unprecedented opportunities to predict and design novel 2D materials and prototypes [375, 376] providing new directions for experimental explorations. To achieve this computational synthesis of novel 2D materials two main strategies have been put forward, that mirror the bottom-up or top-down techniques of experiments.

Top-down approaches consist in systematically exploring databases of known experimental compounds, looking for layered materials that can be exfoliated into monolayers. This requires first to recognize if a parent 3D crystal structure results from the stacking of chemically disconnected components. Geometrical algorithms based on the comparison between interatomic distances and van der Waals or covalent radii are typically adopted to assess the chemical connectivity between units. The dimensionality of each unit can then be easily estimated, leading in particular to the identification of 2D layers. The first pioneering attempt in this direction has been carried out by Lebègue and coauthors [377]. By data-mining a subset of structures with low packing ratio from the Inorganic Crystal Structure Database (ICSD) they identified 92 layered materials, nearly half of which had never been discussed before. More recently, this portfolio has been significantly enriched by Ashton et al. and Mounet et al. [378, 379] who not only extended the investigation to other databases (including the Materials Project database and the Crystallographic Open Database) but also validated their results against accurate van-der-Waals density-functional-theory calculations of the binding energy. This led to the discovery of respectively 681 [378] and 1844 [379] exfoliable monolayers that will provide a rich portfolio of candidates to explore for optimal electronic, optical, catalytic, topological, and magnetic properties. For instance, a new magnetic 2D material, Fe_3GeTe_2, has been already found [380] among these new exfoliable structures [378] but many more promising candidates await discovery. Finally, we mention that this approach has been adopted not only to collate these extensive databases but also as a one-shot effort to find novel 2D materials from layered compounds; this has been the case e.g. for arsenene and antimonene [381] or monolayer Hittorf's phosphorus [382].

Novel 2d materials have also been "synthesised" computationally through bottom-up approaches, starting directly with some chemical intuition. In this regard, a first possibility is to consider structural prototypes of known 2d materials and create hypothetical new structures by substituting elements with chemically similar species [375]. This led for instance to the theoretical prediction of germanene and silicone [383] by looking for stable Ge- and Si-based analogues of graphene. More recently, a list of 171 transition-metal dichalcogenides and oxides with favorable formation energies has been obtained by decorating the so-called H and T structural phases with 27 different transition metals [384, 385]. Miró et al. [386] extended this approach to other classes of materials including halides, semimetal monochalcogenides and atomically thin monolayers, identifying 146 hypothetical 2d compounds for which the electronic and magnetic properties have been computed. Another promising way to theoretically synthesise new 2d materials from bottom up relies on global optimization techniques. Starting from a given set of elements, the ground-state structure is obtained by searching for the most stable atomic configuration and (possibly) stoichiometry using either evolutionary [387-389] or particle swarm optimization [390, 391] algorithms. These methods

have been adopted for instance to predict 2d materials with no 3d layered counterpart like SiS [392] novel phases of InP [389] and several 2d allotropes of boron [393], [388] , known as borophenes. In the latter case statistical methods based on cluster expansion have been also put forward and predicted the correct structure of borophene on metallic substrates in agreement with experiments [394]. Fig.II.22 provides a classification of layered materials as easily exfoliable, potentially exfoliable, or with high binding energy.

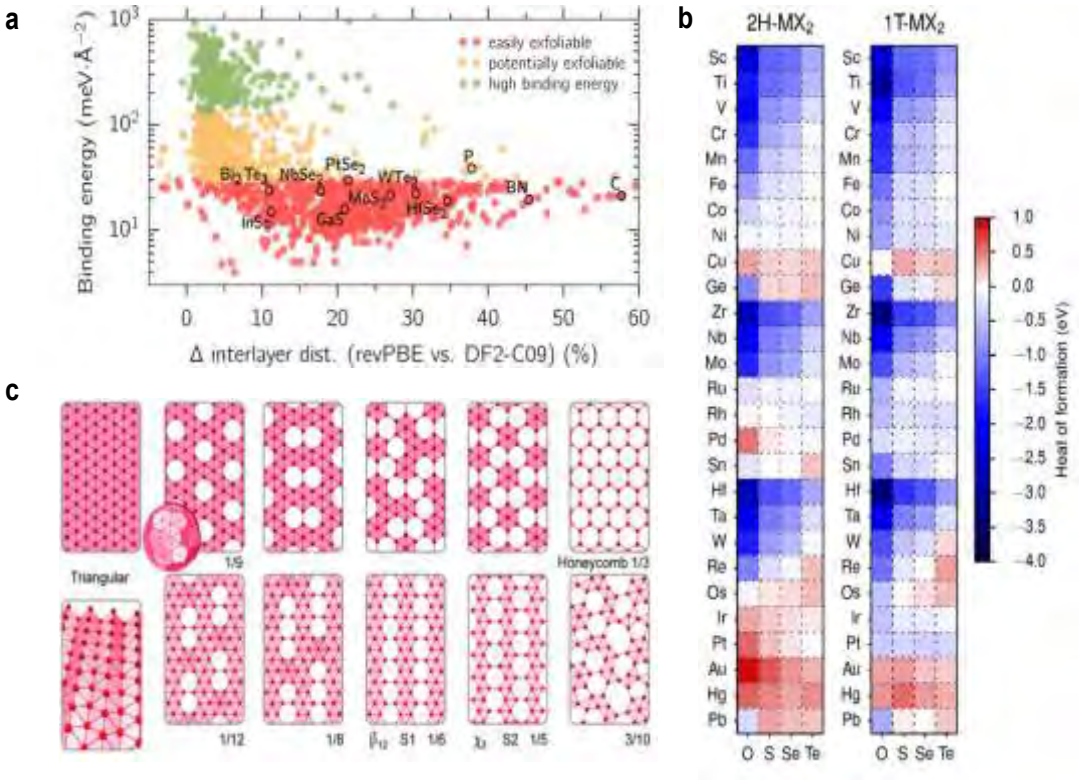

Fig. II. 22: a Binding energy versus relative difference in interlayer distance predicted by vdW (DF2-C09) or non-vdW (revPBE) functionals. Materials classified as easily exfoliable, potentially exfoliable, or with high binding energy are colored differently. Well-known 2D materials are highlighted in the plot. Adapted from Ref. [379] b Calculated heat of formation for 216 transition-metal-dichalcogenide monolayers in the 2H and 1T phases. In general, the oxides have the highest stability followed by the sulfides, selenides, and tellurides, in that order. Furthermore, the stability decreases as the metal ion goes through the transition-metal series. Adapted from Ref. [384] . c Examples of patterns predicted for free-standing boron monolayer polymorphs, from the close-packed triangular, to the familiar honeycomb. The numbers at the bottom right of each model mark the hole density, S1 and S2 are the observed phases. Adapted from Ref. [395].

III. PROCESSING OF DISPERSIONS

III.1 Size selection

Sedimentation-based separation (SBS)

The exfoliation of LMs usually results in a heterogeneous dispersion of flakes having different morphology, i.e., lateral size and thickness [396]. There are many methods for the selection and processing of flakes [96, 113, 168-170, 397, 398] by means of ultrasonication [96, 113, 158, 168-170, 191, 397-400], shear mixing [161, 162, 233, 401-403], ball milling [164, 404-409], microfluidization [163], and wet-jet milling [410-412].Centrifugation based size selection methods can be classified into sedimentation based-separation (SBS) and density gradient ultracentrifugation (DGU) [181]. Nanomaterials subjected to SBS are sorted on the basis of different sedimentation rates in response to a centrifugal force. Owing to its ease in handling, SBS is the most commonly applied size selection technique for GRMs. Typically, small and thin nanosheets are efficiently separated from larger, thicker counterparts. However, achievable size distributions are still rather broad except for the smallest and thinnest nanosheets. To tackle this, a number of improved variations to traditional single step SBS have been developed over the past few years such as band sedimentation [170] and liquid cascade centrifugation [171]. Different to SBS, DGU exploits the movement of the dispersed object to the point in the centrifuge tube where the buoyant density of the material matches that of the surrounding liquid. The addition of density gradient media to the mixture is typically required to adjust the density of the liquid to the higher density nanomaterial [152]. As such, DGU has the potential to separate nanosheets by thickness, but is more challenging to perform than SBS. In the following sections we will discuss these different strategies, highlighting pros and cons.

Single Step Sedimentation

The SBS process is widely used to separate nanomaterials of different nature and morphology ranging from zero-dimensional metallic nanoparticles (MNPs) [413], to one dimensional carbon nanotubes (CNTs) [414-417], to GRM flakes [96, 113, 158, 162, 168-170, 191, 233, 397-401, 403]. A theoretical description of the sedimentation process can be found in ref [181]. In brief, three forces act on the objects during the centrifugation, which determine their sedimentation rate (see Fig. III. 1 left): (I) the centrifugal force $F_c=m_{2D}\,\omega^2 r$, which is proportional to the mass of the GRM flake itself (m_{GRM}), to the square of the angular velocity (ω), and to the distance from the rotational axes (r), (II) the buoyant force $F_b=-m_S\,\omega^2 r$, which is linked with the Archimedes' principle, being proportional to the mass of the displaced solvent (m_S) times the centrifugal acceleration, and (III) the frictional force $F_f=-fv$, i.e., the force acting on the GRM flakes moving with a sedimentation velocity (v) in the solvent.

F_f is proportional to the friction coefficient (f) between the solvent and the GRM flake. f depends on both physical parameters of the dispersed flakes, i.e., lateral size and thickness, and physico-chemical properties of the solvent they are dispersed in, i.e., the viscosity (η). Both parameters have a strong influence on the value of f.

Overall, the sedimentation of GRM flakes depends on their mass and frictional coefficient, which is shape dependent [96, 396, 397]. In first approximation, thick and large GRM flakes, having larger mass with respect to small and thin flakes, sediment faster with respect to the latter, since these have smaller mass. This allows to separate GRM flakes in dispersion with different morphology [396, 397], see Fig. III.1. However, it is challenging to isolate large and thin flakes. The definition of large/thick and small/thin depends on the material that is used in combination with the centrifugal acceleration and the medium. This will be detailed further down below for a few examples.

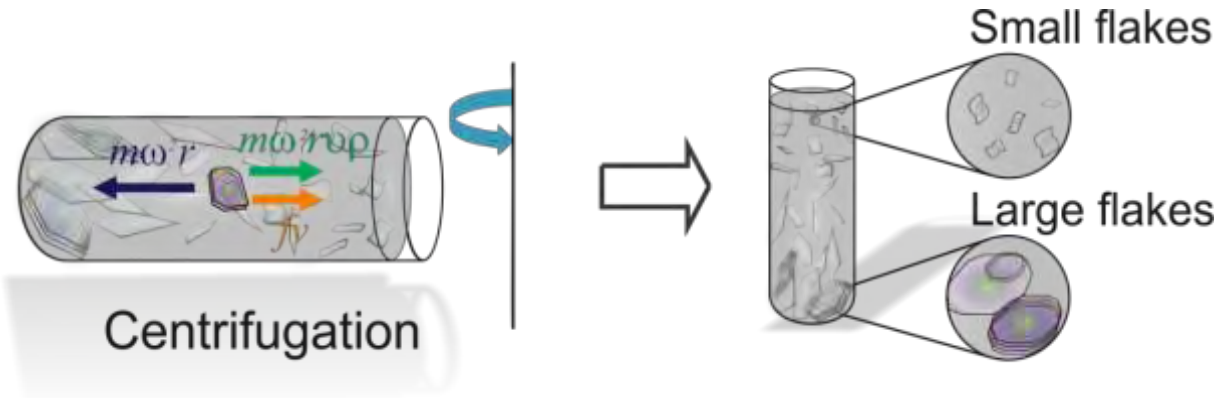

Fig. III.1: Sorting of GRM flakes by ultracentrifugation. The SBS approach allows separating thin and small lateral sized flakes (supernatant) from thicker and larger ones, which precipitate at the bottom of the ultracentrifuge tube as pellet. The actual nanosheet dimensions (lateral size, layer number) depend on the centrifugal acceleration, material and medium.

Thus, taking into account the dependence of the physical dimensions of the flakes on the centrifugal acceleration centrifugal acceleration (expressed as relative centrifugal field, RCF, in units of the earth's gravitational field, g), it is possible to exploit SBS to prepare GRM flakes of different morphology. In a typical experiment, a dispersion is centrifuged at a fixed g-force for a given time. Supernatant and sediment are then separated. The sediment contains larger and thicker flakes than the supernatant. By changing the centrifugal acceleration and centrifugation time, the flake sizes can be adjusted. E.g., the flakes in the supernatant will be smaller after centrifugation at higher accelerations or longer times. Any centrifuge (benchtop or ultracentrifuge) with either fixed angle rotor or swinging bucket rotors can be used.

Even though it is not required that the centrifugation is run for several hours until an equilibrium is reached, i.e. all flakes that will sediment at a given centrifugal acceleration have reached the bottom of the vial, we recommend not to use centrifugation times shorter than 30 min. When centrifugation times are short, a steeper size/thickness gradient is formed in the vial. As a result, the obtained size and thickness distributions in supernatant and sediment will strongly depend on how the sample is decanted, leading to poor reproducibility. Centrifugation times of 1-3

hours are recommended and lead to reproducible results. Note that this depends on the rotor and vial size, hence the distance the flakes need to travel to reach the bottom [237]. Often sediments are then discarded and supernatants collected for analysis and/or further processing. However this makes it a wasteful process.

With SBS, it has been possible to prepare samples having lateral sizes ranging from few nm to a few μ, both for SLG [113, 161, 169, 397-400, 418, 419] and other LMs [158, 170, 235, 398, 420, 421]. E.g., dispersion with high SLG content up to~60% was demonstrated in an sodium deoxycholate-based aqueous dispersion,[418] while~33% SLG was reported for dispersion in NMP [419]. However, it is important to note that such monolayer-rich dispersions from SBS also contain predominantly laterally very small (< 50 nm) flakes [418] [419]. Apart from the difference in percentage of SLG and thus in thickness, the flakes processed in water-surfactant dispersions are, on average, also smaller (~200 nm) [169, 400, 418] with respect to NMP (~1 μm) [113, 419]. This difference is related to the difference in the viscosity of the solvents. When comparing the most widely used solvents (NMP and pure water where, with the addition of surfactant, the viscosity decreases) the viscosity of NMP (1.7 mPas) [422] is significantly higher than water (~1 mPas) [423]. A higher solvent viscosity increases the frictional force [181], reducing the sedimentation velocity [181]. Therefore, when using similar centrifugation conditions (centrifugation time and centrifugal acceleration), the flakes retained in the supernatant will be larger/thicker in higher viscosity solvents.

In addition to the limitation that it is difficult to extract laterally larger (μm), yet thin (1-3 layers) flakes, SBS suffers from the further disadvantage that all nanosheets (also small < 50 nm) remain in the supernatant when operating at low centrifugal acceleration (< 1,000 *g*) used to isolate large (μm) nanosheets. Hence, dispersions containing larger flakes on average are significantly more polydisperse and show broad size (20-few μm) and thickness (1-20 layers) distributions. This can be partially overcome by a band sedimentation approach, where the flakes dispersion is layered on top of a solvent race layer (without flakes) prior to centrifugation [170]. E.g., a dispersion containing flakes in an aqueous surfactant can be layered onto a race layer of deuterated water containing the same surfactant [170]. During centrifugation, the flakes spread throughout the vial according to their sedimentation rate, related to their size. The centrifugation is stopped before the dispersion constituents have reached the bottom of the vial allowing for a collection of various fractions in one run. Importantly, smaller/thinner flakes remain closer to the top and are thus efficiently isolated from larger/thicker one closer to the bottom in a single step. This was demonstrated for MoS_2 [170]. In this case, centrifugation at 1500 *g* for 10 min yielded various fractions ranging from arithmetic mean lateral sizes of 350 nm and arithmetic mean layer number of 15 in fractions close to the bottom to 40 nm and 2 layers in fractions extracted from the top of the vial. Compared to traditional homogeneous SBS, the distribution histograms were narrower, i.e. the standard distribution was reduced by approximately a factor of 2 [170].

Even though this approach can be advantageous when various fractions with narrower thickness distributions than SBS are required, it suffers from a few disadvantages. First, the material quantity that can be processed in a single step is inherently lower because it is beneficial to keep the sample layer thin, so that most of the volume in the centrifuge tube is taken up by the race layer.

Second, the final size-selected sample is diluted during the process, making high concentrations virtually inaccessible. Third, a swinging-bucket rotor is required, as a fixed-angle rotor will not lead to such a defined flake movement through the race layer. Therefore, liquid cascade centrifugation has been suggested as versatile alternative to the above mentioned single step SBS.

Liquid Cascade Centrifugation

Liquid cascade centrifugation (LCC) is versatile and can be carried out using benchtop centrifuges originally described in [171]. This is a multi-step procedure, whereby various cascades can be designed according to the desired outcome. To demonstrate this process, a general cascade is portrayed in Fig. III.2. It involves multiple centrifugation steps, each with a higher centrifugal acceleration [171]. After each step the sediment is retained and the supernatant is then used in the proceeding stage. As a result, each sediment contains flakes in a given size range, "trapped" between two centrifugation stages with different speeds. Similar to band sedimentation, small/thin flakes are removed from dispersions with predominantly larger/thicker flakes. As with traditional SBS, the lateral dimensions and layer numbers obtained will depend on the design of the cascade (centrifugal accelerations), the starting material and solvent. A few examples of achieved lateral sizes and thicknesses are summarised in table III.1.

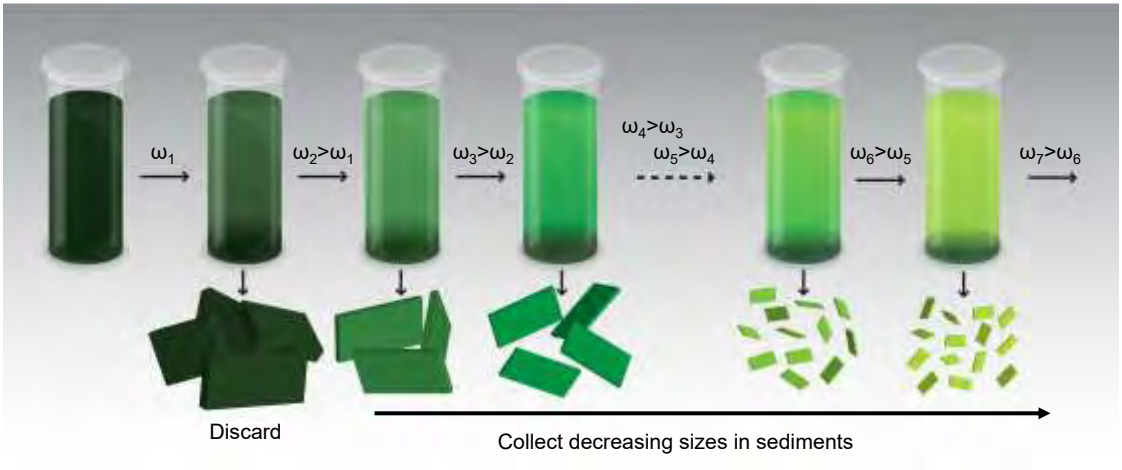

Fig. III.2: Schematic representation of liquid cascade centrifugation. Adapted from Ref.[171]

Critical to LCC, the resulting sediment can be redispersed by mild agitation (shaking, or < 5 min bath sonication) in the respective medium, enabling one to reach any desired flake concentration as well as modification of the concentration of any additives (such as polymers or surfactants). Importantly, virtually no material is wasted in LCC, resulting in the collection of larger masses of size-selected flakes from a single dispersion compared to traditional homogeneous SBS, where the sediments are discarded. The procedure was thus found to be ideal to study size effects in applications [424]. It was already applied to a number of liquid-exfoliated flakes, including WS_2 and MoS_2 [171, 236, 424, 425] as well as $Ni(OH)_2$ [230], GaS [173], black phosphorus (BP) [175] and FLG [161, 227] in solvents [161, 173, 175] as well as aqueous surfactant [162, 171, 227, 230, 424] or

polymer systems [425]. Due to its versatility and the large accessible quantities, other reports adopted the procedure [426, 427]. Typical arithmetic mean lateral sizes and layer numbers are given in table III.1 for a range of materials.

Table III.1: Overview of achievable arithmetic mean lateral sizes (<L>) and layer numbers <N> using liquid cascade centrifugation. For each material, the "large/thick" and "small/thin" fractions are indicated which is defined by the midpoint of the centrifugation boundaries (given as central g). Data includes centrifugation in solvents (NMP, IPA) and aqueous sodium cholate solution (SC).

	FLG SC [227]		FLG NMP [161]		WS_2 SC [236]		MoS_2 SC [236]		BP NMP [175]		GaS IPA [173]	
Central *g*	550	21000	80	1800	0.33	7500	0.33	9900	690	17500	170	850
<L> (nm)	360	90	1000	160	170	35	270	55	615	150	450	100
<N>	8.1	3.3	Not determined		7.5	2.1	7.4	2.4	Not determined		29.5	11

From this table it is clear, that the outcome of the size selection depends on the centrifugal accelerations, the density of the material and medium. A deeper understanding and systematic analysis will enable the prediction of the outcome of the size selection in the future. In any case, to achieve efficient size selection, it is critical to remove the supernatant from the sediment as completely as possible. This also means that for this procedure to work, the centrifugation time has to be long enough to allow the majority of the flakes to sediment to the bottom of the vial. This does not require centrifugation to equilibrium (unlike DGU). One can obtain a good separation of supernatant and pellet-like sediment after 2h of centrifugation, when the filling height of the dispersion in the vial is < 10 cm. Centrifugation times should be extended if greater filling heights are used [237].

The chosen size-selection cascade can be modified readily to suit a desired outcome. While this specific procedure yields flakes sizes and thicknesses over a broad size range in the different fractions, if only specific sizes are targeted the centrifugation steps can be skipped. E.g., if medium-sized flakes are desired, the sample can be centrifuged at only two different centrifugal accelerations and the sediment redispersed. In first approximation, flake size selection occurs by mass in such a standard cascade, still making it difficult to select large (µm), thin (1-3 layers) flakes like in traditional homogeneous SBS. However, a design of secondary cascades [171] involving a combination of long (14 h), low-speed centrifugations (~ $1/5^{th}$ of the lower *g*-force boundary of the initial trapping) to remove thicker material and short (60 min) , high-speed centrifugations (above the higher *g*-force boundary of the initial trapping) to remove very small (10-20 nm) flakes has shown potential to

overcome this limitation yielding a monolayer volume fraction~75% (mean layer number ~ 1.3) with an average lateral size ~ 40 nm in the case of WS_2 [171].

Density gradient centrifugation (DGU)

The key disadvantage of the SBS process, not allowing one to get a high percentage (> 10 %) of 1L-GRM flakes of reasonable lateral size (> 100 nm), can be overcome with the exploitation of DGU. This enables control on N, when flakes are subjected to ultracentrifugation in a preformed density gradient medium.

Two approaches can be exploited for the separation of GRM flakes, and nanomaterials in general: isopycnic [428] and rate zonal separation [428]. The isopycnic separation allows spatial separation inside the ultracentrifuge tube of GRM flakes depending only on their buoyant density. This is defined as the density of the medium at the corresponding isopycnic point and is measured in g/cm^3. GRM flakes, during isopycnic separation, move along the ultracentrifuge tube, until they reach the corresponding isopycnic point, *i.e.,* the point where their buoyant density matches that of the surrounding DGM [429]. Hence, in principle, flakes should be sorted according to N. However, it is nonetheless difficult to obtain dispersions of exclusively large (micron-sized) 1L-GRMs. This likely related to the fact that micron-sized SLG is a minority fraction in LPE samples. Hence, even if all SLG nanosheets are isolated from the dispersion, the average lateral size will still be in the range of only 100s of nm maximum.

For isopycnic separation, the choice of DGM is fundamental. Salts (e.g., sodium chloride, cesium chloride, and lithium chloride), sucrose, and iodixanol are the most widely used DGMs [430, 431]. The use of salts has some issues. First, they induce aggregation on the hydrophobic solutes [432, 433] which may negatively affect the sorting process. Second, density gradients produced with salts are less stable with respect to those using sucrose and Iodixanol due to the lower viscosity of these DGM [434]. Sucrose suffers the opposite problem: it has high viscosity, which further increases exponentially at high concentrations [435]. Iodixanol seems to be better suited, due to density tuneability, with respect to sucrose, and higher viscosity compared to salts.

The effectiveness of the isopycnic separation is also strongly determined by the type of density profile of the DGM and its variation. During centrifugation the density profile redistributes as the DGM responds to the centrifugal force, resulting in a steeper gradient over time [436]. The density profile of the DGM can be: linear, nonlinear, or step [437, 438]. Linear gradients are usually used when the materials to be sorted have small (<0.05 g/cm^{-3}) buoyant density differences. For this reason, linear gradients can sort surfactant-micelle encapsulated CNTs with very small buoyant density difference, such as (6,5) (1.06 g/cm^{-3}) and (7,5) (1.08g/cm^{-3}) dispersed in sodium cholate [439-441]. In nonlinear gradients, the DGM density changes nonlinearly along the ultracentrifuge tube, and the density gradient is established during the ultracentrifugation process [437]. Nonlinear gradients are particularly suited to sediment particles over the entire length of the ultracentrifuge tube [437]. By exploiting nonlinear gradients, a variety of depth-density profiles can be produced

according to the density variation. This allows the trapping of particles of different densities along the ultracentrifuge tube length. Step gradients, formed by stacking layers of different density, are usually employed when the (nano)materials/molecules to be separated have larger difference in density (>0.1 g/cm^{-3}) [442]. The sharp variation in density at the interface of two different layers stops (nano)materials/molecules with a density smaller than the denser layer, letting the larger density ones pass through [442].

In GRM flakes the problem is that the materials have high densities with no intrinsically different density between layer number (e.g., MoS_2, ρ=5.06g/cm^3, WS_2, ρ=7.5g/cm^3, WSe_2, ρ=9.32g/cm^3) - except for the surfactant shell, making this an important aspect of the DGU. This fact practically renders the sorting of inorganic GRM flakes very challenging in common DGM, such as Iodixanol, which has ρ=1.32g/cm [96, 441]. Therefore, in order to separate flakes by thickness, i.e. N, it is important to ensure that the flakes have uniform surfactant/polymer coverage [168, 443]. This requirement is crucial because the surfactant/polymer layer also contributes to the buoyant density of the entire system, thus resulting in slight variations of the buoyant densities of 1L- and FL- flakes which can lead to isopycnic separation. This results in a spatial separation inside an ultracentrifuge tube, overcoming the limitations of conventional ultracentrifugation in a density constant medium.

A successful GRM flakes sorting by isopycnic separation mainly depends on the following: (I1) a large as possible amount of 1L-and FL- flakes in the starting dispersions. Differences in buoyant density can be correlated to specific thickness (1L, 2L, 3L) only if individualized GRM flakes are encapsulated by the surfactant micelles or polymer molecules. This also implies the folding and wrinkling of the nanosheets will be problematic. (2) Uniform flakes coverage. This is ruled by the adsorption of surfactant or polymer molecules, and their aggregation, which can lead to clusters formation (i.e., aggregates of several molecules around the flakes basal plane). The effectiveness of the isopycnic separation is demonstrated by the yield of SLG achieved up to date,~80% [168], which was reported by using isopycnic separation with sodium cholate. Isopycnic separation was also used for GO flakes of different thickness [444].

Isopycnic separation was also used to sort inorganic LMs by thickness [152]. One of the main issues when sorting inorganic LMs by thickness is due to their high density and the use of surfactant molecules, such as sodium cholate [441], which cannot reduce their buoyant density sufficiently enough to match the density of the gradient. By using Pluronic F68, a greater hydration shell than sodium cholate is formed. This procedure allows to reduce the buoyant density of the encapsulated LMs [445, 446]. Moreover, the use of Pluronic F68 allows to reduce the buoyant density of BN [446] as well as TMDs such as WS_2, WSe_2, MoS_2, and $MoSe_2$ [445], within the limit of the used DGM, obtaining a spatial separation along the ultracentrifuge tube.

Another approach to sort inorganic LMs via isopycnic separation relies on the mixing of two DGMs [447]. The addition of cesium chloride to iodixanol, determined an increase of the maximum buoyant density supported by the DGM (i.e., 1.56 g/cm^3) to the point where even the high-density rhenium disulfide can be sorted layer-by-layer [447].

Isopycnic DGU-based separation offers a unique opportunity to sort GRM flakes by thickness and lateral size, rather than mass opposed to SBS, with high. However, DGU separation, although

widely used in biology [181] and successfully applied also to sort GRMs [152], it has the drawback of being a multi-step process involving multiple iterations and, as such, it is time-consuming. Another issue for the further processing of the sorted flakes, i.e., ink formulation, is linked with the presence of DGM in the dispersion, that may be problematic for processing and/or its removal.

Another methodology to sort GRMs in a centrifugal field is the rate zonal separation (RZS) [429, 448]. In RZS, the ultracentrifugation is stopped during the transient centrifugal regime, i.e., before the materials under ultracentrifugation reach their isopycnic points [448]. RZS exploits differences in the sedimentation coefficient of nanoparticles under ultracentrifugation. Therefore, nanoparticles with different sedimentation coefficients will move along the ultracentrifuge tube at different sedimentation velocities [429, 448], determining their spatial separation [413, 448]. RZS was carried out to separate GO flakes with different lateral size [449], exploiting the fact that the larger is the flake lateral size, the larger is the sedimentation coefficient. RZS was also used for the lateral size selection of black phosphorous flakes [398]. Similar to DGU, a downside of RZS is that usually, an ultracentrifuge is used (rather than a benchtop centrifuge) and that a DGM is added to slow down the sedimentation and lead to a more gradual distribution along the vial which has to be removed prior to further processing. Note that this in contrast to the band sedimentation approach [170] discussed above.

III.2 Inks formulation

The production of GRM flakes in dispersion following the exfoliation and sorting strategies aforementioned finds a direct use of the as-produced material only for few applications, such as the realization of polymer composites. In many other cases, the as-prepared dispersion cannot be used directly. For applications requiring coating and printing, the dispersion needs a formulation process to obtain an ink. The composition of functional inks is strongly linked with the target deposition/printing process [150], see table III.2. There are deposition/coating approaches where the ink formulation is not stringent, such depending on the nature of the used solvent for exfoliation and sorting, the deposition can be carried out directly with the obtained dispersion. This is the case for vacuum filtration and transfer, spray and drop casting, where the most critical parameter is the morphology control of the dispersed GMR flakes, in view of the final application. For other printing processes, such as flexographic, gravure, slot-die and ink-jet printing, the formulation of the ink is more complex, requiring the addition of many components in pre-defined steps. In the following, a few examples of producing such inks are given.

Table III.2: Specifications to consider for different printing methods.

Printing method	Viscosity	Layer thickness	Feature size	Registration	Throughput
	[Pas]	[µm]	[µm]	[µm]	[m2/s]
Gravure printing	0.05-0.2[450]	0.8-8 [450] <0.1 [451-453]	75 [454]	>10 [454]	60 [454] , 3-30 [455]
Flexography printing	0.05-0.5 [450]	0.8-2.5 [450]	80 [454]	<200 [454]	10 [454] 3-30 [455]
Offset printing	30-100 [450] 5-50 [456]	0.5-2 [450]	10-50 [454]	>10 [454]	5-30 [454] 3-30 [455]
Screen printing	0.5-50 [450]	3-15 [450] 0.015 [457] , 30-100 [454]	20-100 [454]	>25 [454]	2-3 [454]

Table source: VTT, Finland

Tuning of rheological properties

The control of the ink rheology is key to ensure consistency and reproducibility of the results. This is usually achieved by studying flow and deformation of the materials under external perturbation [458]. The complex structure of the ink determines a rheological behavior which is typical of non-Newtonian flow [459]. Thus, there is a non-linear relation between shear rate ($\dot{\gamma}$), shear stress (τ), and apparent viscosity η ($\eta_{app}= \sigma/\dot{\gamma}$) which depend on $\dot{\gamma}$ (or τ). This behavior is different from Newtonian liquids, where $\eta= \sigma/\dot{\gamma}$ [460]. The shear rate determines the η behavior of inks and, thus, their range of application. Depending on their flow behavior, there are different classifications for non-Newtonian inks [461]: dilatant where η_{app} increases with increasing $\dot{\gamma}$ [461], pseudoplastic, where η_{app} decreases with increasing $\dot{\gamma}$ [461], and thixotropic, where η_{app} decreases with time under a constant deformation and will start to rebuild once the shear force η_{app} is removed [461], Fig. III.3. Moreover, the rheology of the inks is strongly influenced by the GRM volume fraction, ϕ, with their shape and spatial arrangement [462], GRM flakes dispersed in a liquid affect its flow field resulting in an increase in energy dissipation due to fluid-flake and/or flake-flake interactions [462, 463]. These interactions increase with ϕ, restricting the flakes diffusion into small “domains”, formed by the nearest neighbors and η diverges. However, a theoretical model to predict η of fluids

with dispersed GRMs does not exist yet. Such model is not even available for nanoparticles in general, although a significant research effort has been carried out in this direction [464-466].

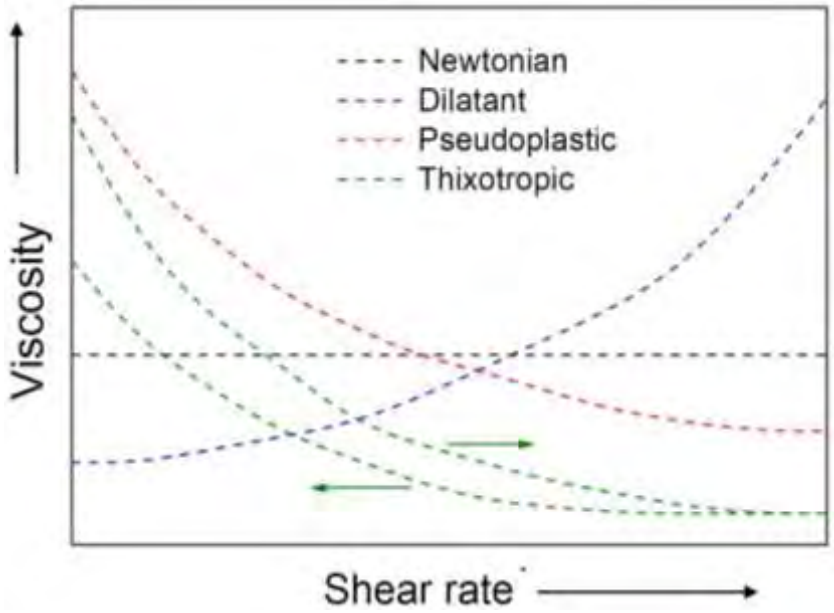

Fig. III.3: Newtonian and non-Newtonian flow behavior of functional inks. If not original refer to publication Adapted from [150]

We now discuss the main ink requirements and the state of the art of the formulation for the deposition/printing of GRM-based inks for the main deposition/printing techniques that are currently more developed/used.

Coating approaches, such as drop and spin coating, do not require a structured ink formulation, and, usually, the as-prepared dispersion can be directly deposited onto the target substrates. On the contrary, although the ink for spray coating deposition does not require a high viscosity value, the aerosol formation and the subsequent drying process need the control of several processing parameters [467] such as viscosity [468], flow rate [469], and the distance substrate/spray-nozzle (*d*) [470]. The nature of the solvent, which determines its evaporation rate at the substrate surface [469], is also a critical point for a uniform deposition. The solvent vapor pressure is crucial. Solvents having low vapor pressure, such as NMP (0.5mm Hg @25°C), one of the most common for LPE of graphite [147], promote long crystal formation time [469]. This allows a consistent structural arrangement prior to the transition to the solid phase of the deposited feature [469]. On the contrary, high vapor pressure solvents, such as, e.g., isopropyl alcohol (IPA, 33mm Hg @25°C) and toluene (24mm Hg @25°C), promote faster solvent evaporation. This subsequently reduces the ability of the functional flakes to organize in a highly ordered mode. The consequence will be a decrease of the final devices performance, such as, e.g., a reduction of the charge carriers mobility in field effect transistors [469]. Moreover, other sources of instability for the coating are linked with the geometry of the spray coating system, i.e. small nozzle size, or the jetting pressure, i.e., low pressure reduce the flow rate, which produce scattered droplets on the substrate and eventually a non-uniform coating [469]. Contrarily, a continuous coating is obtained by high

deposition rates [127, 469]. The uniformity of the coating is also determined by the appropriate substrate/nozzle distance *d* [470]. If *d* is too short, the ink previously deposited onto the substrate can be blown away by the incoming flow. If *d* has a high value, the solvent can evaporate during the flight time, i.e. before the droplets reach the substrate.

The formulation of the ink for an inkjet process requires the control and tuning of various liquid properties such as ρ, η, and surface tension (γ) [471], which are then summarized in the following dimensionless figures of merit (FoM): the Reynolds (N_{Re}) and Weber (N_{We}) [472, 473] and the inverse of the Ohnesorge number, Z ($1/N_{Oh}$) [473]. The Z number is independent on the drop velocity ($m \cdot s^{-1}$) and it is the most used FoM for inkjet printing [474-480]. Different Z values have been proposed, ranging from 1 to 91 with different functional materials [refs].

Other parameters for the ink formulation have to be considered, such as, e.g., the physical dimensions of the flakes dispersed in the ink, that can agglomerate clogging the print-head, determining printing instabilities. Usually, it is required that flakes have lateral sizes smaller than ~1/50 of the nozzle diameter [481] (typically ~ 100μm [482]). Other parameters to be optimized for the printing/deposition process are wetting and adhesion [483] to the substrate, as well as the distance between nozzle and substrate (typically 1-3 mm) [484].

An even more structured ink, with respect to inkjet, is needed for flexography and gravure printing. Although both printing strategies require a high viscosity ink, there are several differences between flexography and gravure [150]. In flexography, there is a plate with a raised surface that spreads the ink onto the target substrate. Gravure is an intaglio process, where the ink is first transferred onto an image carrier and then printed on the target substrate. As summarised in table III.2 and [150], gravure printing is usually faster (~1000 m/min) than flexo (~500 m/min), with printed stripes thicker (~1 μm in gravure) than in flexography (<1 μm). The viscosity is also different: in flexography this is in the 50-500 mPa·s range, while in gravure it is higher 100-1000 mPa·s.

The formulation GRM-based inks for flexography and gravure is at an early stage of development [485, 486]. Ref. [485] formulated a flexography ink by using Carboxymethylcellulose as a binder for FLG flakes in a water/isopropanol solution, obtaining a viscosity, η, of ~20 mPa·s. The as-formulated ink was printed onto a flexible indium tin oxide substrate at a speed of 0.4 m s^{-1}, and used as counter electrode for the realization of a flexible dye-sensitized solar cell (DSSC) [485]. A FLG/terpineol ink (η in the 0.2-3 Pa·s range), obtained from the homogeneous dispersion of FLG-ethyl cellulose powder (5-10 wt%) in a mixture of ethanol/terpineol (2.5:1 volume %) was reported in [486]. For the formulation of high viscosity GRM-based inks, there are several issues to be still solved. First, the solvents used in LPE (e.g., NMP) are toxic and have very low η (< 2 mPa·s). The use of alternatives such as volatile alcohols, *e.g.* ethanol [486] and isopropanol [485], is against the current environmental regulations, requiring the minimization of volatile organic compounds [487]. Second, the GRM concentration in these solvents is low (< 1 g L^{-1}), thus, in order to produce a functional (e.g. conductive) film, many print passes are required. Furthermore, the increase of GRM fillers could determine a problem with the solvent evaporation and in-series printability. In this context, the use of high boiling point solvents requires post-processing annealing for solvent removal [488], thus posing also limitations on the target substrate to be used.

Increasing the η of the ink it is possible to obtain a paste, needed for screen printing. FLG-based conductive-pastes (*i.e.*, FLG [489], RGO [490-492] and flakes [493, 494] used as active material) are emerging as possible alternatives to those based on metal nanoparticles.

A paste based on FLG powder dispersed in terpineol, with ethylcellulose as a binder was prepared in ref. [489]. The paste contained flakes at a concentration of ~80 g L^{-1}, having a η up to ~10 Pa·s at a shear rate of 10 s^{-1}. The as-deposited paste required a thermal treatment at a temperature of 300 °C for 30 min to remove the ethylcellulose. Another FLG-based paste, having shear thinning behaviour, was discussed in Ref. [495], which demonstrated a gelation approach starting from the dispersion of expanded graphite in methyl ether dipropylene glycol in the presence of polyvinyl acetate and polyvinylpyrrolidone acting as binders. However, many parameters still need to be optimized for the development of GRM-based inks/pastes for screen printing the required processing conditions.

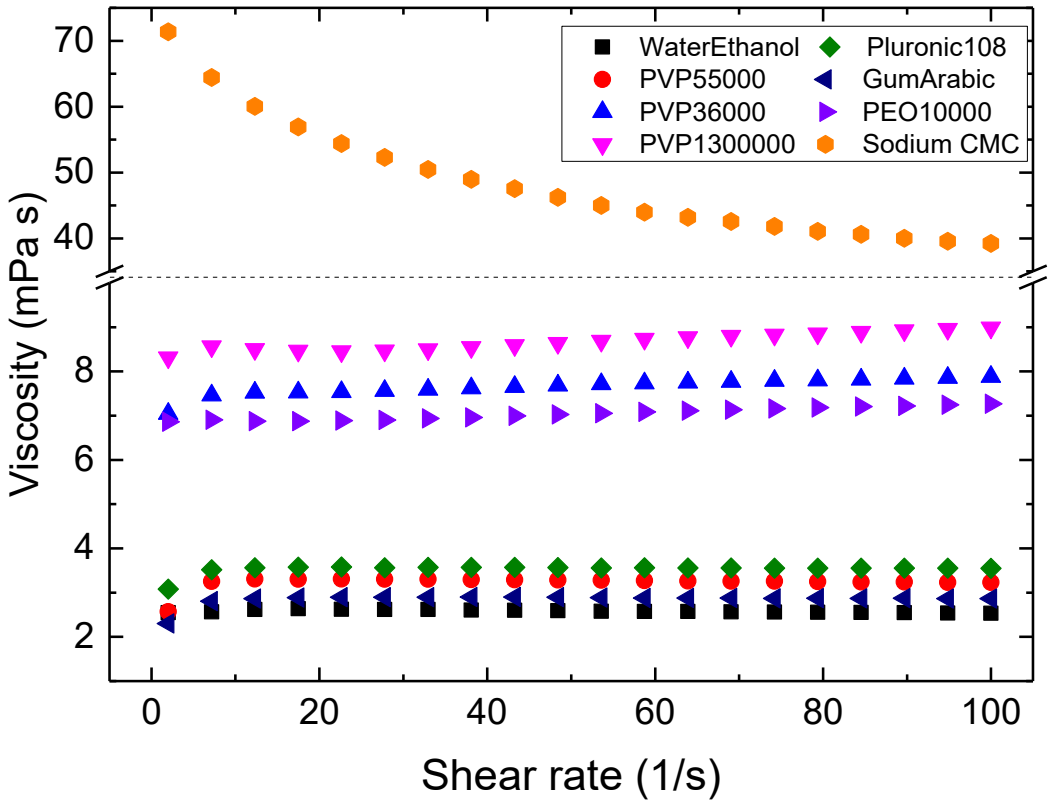

Fig. III.4: Rheology modifiers in 50:50 water/ethanol solution at 1 wt.% loading.

Fig. III.4 shows a selection of polymers at 1 wt.% loading that can be added to water or 50:50 water/ethanol solutions to modify the rheology. Polymers such as polyvinylpyrrolidone (PVP) can be added, with increased viscosity with increasing molecular weight (M_W). Celluloses which are commonly used, provide high viscosity at low loadings, and impart thixotropic behaviour. The

aqueous FLG-based inks produced by microfluidization [163] have FLG loading up to 100 g/L and are formulated using 1 wt.% sodium carboxymethylcellulose (NaCMC) to provide η up to 1800 mPa.s.

NaCMC is not easily dissolved and its preparation can be affected by factors including the NaCMC particle size, rotational speed of the mixer, the rate at which solutes are introduced, and the temperature of the solution [496]. Heating of the FLG dispersion should be avoided as this may promote flocculation. NaCMC is water-absorbent and has very high water retention, therefore it clumps easily. To prevent this, NaCMC is added subsequently until dissolved completely. The solution is stirred at slow speeds (~300 rpm) and is left overnight. Vigorous stirring can cause air bubbles, especially as viscosity builds. These must be removed prior to printing. If clumps of NaCMC do form, it may be necessary to use a spatula to grind them by hand so that they can dissolve.

The rheological properties were investigated using a Discovery HR-1 rheometer from TA Instruments utilizing a parallel-plate (40mm diameter) setup [497]. The elastic modulus G'[J/m^3=Pa] [498] is monitored, representing the elastic behavior of the material and a measure of the energy density stored under a shear process [498], and the loss modulus G''[J/m^3=Pa] [498], representing the viscous behavior and a measure of the energy density lost during a shear process due to friction and internal motions [498]. Flow curves are measured by increasing $\dot{\gamma}$ from 1 to 1000 s^{-1} at a gap of 0.5 mm, because this $\dot{\gamma}$ range is applied during screen printing. Fig. III.5a plots the steady state viscosity of an ink containing 73 wt.% flakes (100 cycles) as a function of $\dot{\gamma}$. NaCMC imparts a drop in viscosity under shearing, from 570 mPa.s at 100 s^{-1} to 140 mPa.s at 1000 s^{-1}. This is thixotropic behaviour [499], since the viscosity reduces with $\dot{\gamma}$.

This behavior is shown by some non-Newtonian fluids, such as polymer solutions [500] and biological fluids [501]. It is caused by the disentanglement of polymer coils or increased orientation of polymer coils in the direction of the flow. On the other hand, in Newtonian liquids the viscosity does not change with $\dot{\gamma}$ [501]. Refs. [502, 503] reported that thixotropy in NaCMC solutions arises from the presence of unsubstituted (free) OH groups. Thixotropy decreases as the number of OH groups increases [502, 503]. Fig. III.5b plots the viscosity at 100s^{-1} as a function of wt.% FLG flakes (70 microfluidic process cycles). The NaCMC polymer (10 g/L in water) has a μ ~0.56Pa.s at 100s^{-1}, and drops to 0.43 Pa.s with the addition of 5 wt.% flakes. The loading wt.% of flakes affects $\dot{\gamma}$, which increases at 51 wt.% and reaches 0.6 Pa.s at 80 wt.%.

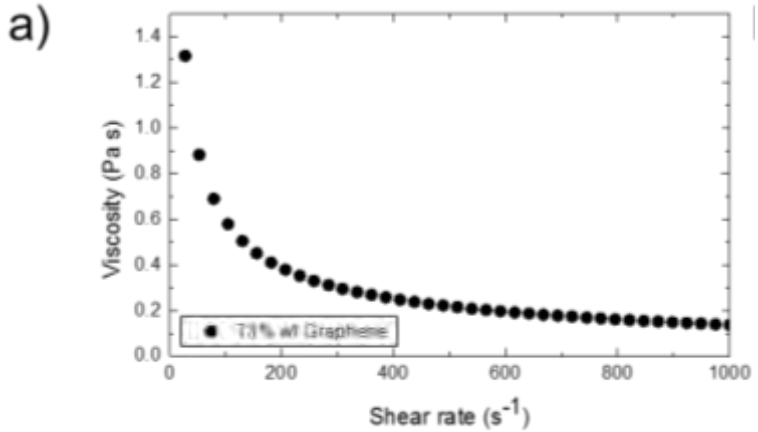

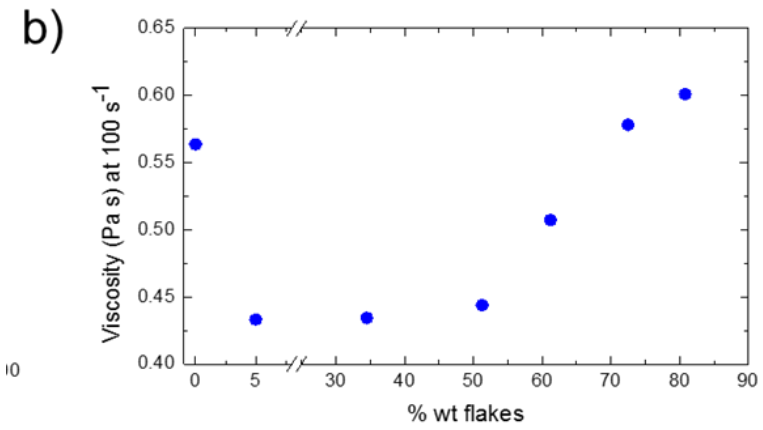

Fig. III.5: a) Viscosity as a function of shear rate for an ink with 73wt% flakes, b) viscosity at 100 s^{-1} for different wt.% of FLG flakes. Reproduced from ref. [163]

2d Hybrid inks

Graphene/polymer blends

This section describes the formulation of a FLG-polymer-fullerene ink that can be conveniently processed by spin-coating to fabricate bulk heterojunction (BHJ) solar cells. The goal is to improve BHJ solar cells performance in terms of hole mobility, photocurrent efficiency and photoresponsivity [504]. Spin coating is commonly used to fabricate BHJ solar cells, allowing rapid deposition of thin films (~100s nm thickness) of different materials. In contrast to other printing techniques, it does not have any requirements in term of surface tension, viscosity, solute concentration and particle size for the ink to be deposited. Viscosity, volatility and concentration will affect the morphology and the thickness of the final film, which can be adjusted by tuning the angular velocity and the time of processing. The main advantages of spin coating are also the low amount of material required (μL) and the reproducibility of the film features for fixed working parameters.

Ref. [504] produced a FLG dispersion in 1,2-dichlorobenzene (ODCB) due to its compatibility with P3HT:PCBM. 100 mg graphite flakes (Sigma Aldrich) are sonicated in 10 mL ODCB for 10 hours followed by ultracentrifugation. After ultracentrifugation, the supernatant is extracted by pipetting. For the P3HT:PCBM dispersion , 10 mg/mL P3HT (Rieke) and 8 mg/mL PCBM (Solenne B.V.) are dissolved in ODCB. The P3HT:PCBM-FLG dispersion is prepared by using the identical P3HT:PCBM dispersion in the ODCB-FLG supernatant, obtained by centrifugation, and stirred under nitrogen atmosphere for 24 h at 50 °C. The BHJ solar cell is fabricated as follows: PEDOT:PSS is deposited by spin-coating at 3000 rpm for 40 s on cleaned glass substrates with a 100 nm ITO coating. The layers are annealed for 20 minutes at 120 °C. After cooling, a 100 nm layer of P3HT:PCBM:FLG is deposited

on the PEDOT-PSS by spin-coating in N_2. A counter electrode of 20 nm Calcium and 60 nm Al is deposited by evaporation.

The critical step of the process is the mixing of the P3HT:PCBM to the ODCB-FLG supernatant, since the addition of the P3HT:PCBM could cause the destabilisation and flocculation of the ink. To prevent this destabilisation, the P3HT:PCBM should be added gradually and the dispersion immediately stirred after mixing. It is also important to not add an excess amount of FLG. In Ref [504], only 2 wt.% FLG is added; further increases cause aggregation of the FLG sheets, having a deleterious effect on exciton generation and charge separation/transport in the active layer.

Graphene/CNT hybrid films

Transparent conductive films (TCFs) on flexible substrates require homogeneity, optical transparency and stability under mechanical stress. In this framework the deposition of films by rod coating [505] fulfils the above-mentioned requirements. The use of the so-called Meyer bar allows deposition at room temperature and is fully scalable over large areas. The diameter of the wound wire of the bar determines the size of the grooves and controls the thickness of the liquid film, as well as giving alignment to the material improving the percolation. The key parameters of the ink to ensure a homogenous coating are viscosity ~1 mPa.s and a small contact angle ~20-30° [506] . The speed of the deposition can affect the homogeneity creating aggregates. Aggregates can also arise from a fast drying of the liquid film.

A water-based FLG dispersion is prepared by mixing 6 mg of natural graphite flakes with 0.6 mg of Triton X-100 in 60 mL of DI water. The dispersion is sonicated for 9 h in a bath sonicator. The dispersion is then ultracentrifuged (1 h, 10000 rpm) to remove the unexfoliated flakes. A CNT dispersion is prepared using P3-SWCNT powder (Carbon Solutions, Inc.). These CNTs have been purified with nitric acid by the manufacturer, and left in highly functionalized form containing 1.0-3.0 atomic% carboxylic acid moieties which can be derivatized with a variety of functional groups. 8 mg CNTs and 35 mg Triton X-100 in 20 mL DI water are tip sonicated for 2 h, followed by ultracentrifugation at 25k rpm, 30 min.

TCFs are fabricated on various flexible substrates such as PET, PEN etc. by rod coating. Typically, for a 10x10 cm^2 substrate, 80 µL of CNTs ink are deposited and spread uniformly on the substrate using the Meyer bar. The wet film is allowed to dry in air before coating another layer. To remove the surfactant, after 2-3 coatings the substrate is soaked in 200 mL water-ethanol (50:50 in volume) solution, kept at 60°C on a hot plate for 3 minutes and then dried with a nitrogen gun. The washing steps help to improve the final TCF conductivity. The same procedure is applied for the deposition of the ink on top of the CNT film. Generally, for a 10x10 cm^2 PET film, 40 repetitions of both inks are required to get to tens of KΩ/□ at 80% transparency.

These coatings can be applied in the fabrication of CNTs/FLG films as pixel electrodes directly on the backplane of an electrophoretic display. The CNT/FLG ratio is 40:60% in mass, assuring the uniformity of the film avoiding any aggregation. After every 3 coatings the film is washed to remove

surfactants. For a 4x4 inch^2 backplane, 150 mL of the water-ethanol solution (50:50 in volume) are used and heated to 40-50°C for 4 minutes before drying with nitrogen.

Inks with conductive polymers

In order to overcome the obstacles of efficient micro-supercapacitors (MSCs) manufacturing, such as scalability, high cost, and flexibility, new strategies based on facile processing of FLG nanocomposite inks are highly appealing. Direct printing/transfer techniques, including spray deposition, inkjet printing, and filtration, offer a promising protocol for future production of MSC arrays, which can be rapidly processed onto both plastic and paper substrates at low temperature and over large areas. As a key component for these techniques, the selected ink should be stable, low cost, and easily printable on appropriate substrates; it should display excellent electrical properties without the need for aggressive post-treatments. High quality FLG obtained from electrochemical exfoliation could meet the above requirements.

Two inks were developed based on electrochemically exfoliated FLG (EEG) and conductive polymers [507, 508]. In one the conducting polymers, such as PEDOT:PSS, are mechanically mixed with EEG in the solvent [507]. In a typical experimental procedure, 5 mL EEG dispersion in isopropanol (1 g L^{-1}) was mixed with 0.5 mL of PEDOT:PSS aqueous solution (1–1.3 wt%), followed by a mild sonication (~ 5 min in bath sonicator) and gentle stirring, to get a homogenous hybrid ink. The other is a EEG/polyaniline (PANI) composite ink [508], based on in-situ polymerization of aniline in the presence of EEG. First, EEG is prepared and dispersed in dimethylformamide (DMF) at the concentration of 2 g L^{-1}, followed by noncovalent functionalization with 1-pyrenesulfonic acid sodium salt to obtain water dispersion of EEG. Then 5 ml of EEG/DMF dispersion is mixed with 20 ml deionized water and 150 mg aniline hydrochloride and gently stirred or sonicated. Afterwards, 300 mg ammonium persulfate is added, followed by a vigorous stirring at 10,000 rpm for 6 hours to form uniform green dispersion of the EEG/PANI composition. After being washed through ultra-centrifugation with water and ethanol for 3 times, the composite is dispersed in 40 ml ethylene glycol to get a stable EEG/PANI ink.

III.3 Printing and deposition of inks

To develop applications that make use of LPE GRMs, it is necessary to convert the dispersed material into structures suitable for further studies. In general, flakes may either be deposited on a supporting substrate (such as glass, metal foil, silicon, or plastic film) or act as a filler within some host material (such as polymers, metals or other nanomaterials) to produce free-standing composites. To this end, numerous liquid-phase processing techniques have been established for the deposition of GRM dispersions in combination with other dispersed nanomaterials or polymers. Here, we outline some approaches used to produce a range of GRM-containing structures and devices such as vacuum filtration, spray coating, ink-jet and screen printing.

Vacuum filtration

Vacuum filtration is a simple technique whereby a GRM dispersion can be filtered through an underlying porous membrane to obtain nanometre-to-several micron thick films [509, 510]. These can be removed from the underlying support to produce a freestanding film, or transferred to rigid and flexible substrates and the porous membrane removed e.g. by chemical dissolution [510]. Although this technique is probably unsuitable for the production of GRM-containing structures for commercial purposes, its low cost and its simplicity makes it ideal for many research purposes. The main advantage is the possibility to wash away surfactants and solvent residues that usually affect the performance (e.g. conductivity) of the final films. Films with different thicknesses and composition can be produced by tuning the amount of dispersion filtered, the pore size of the membrane and the vacuum pressure. GRM dispersions can be filtered on to various membranes, selected based on their pore size and chemical compatibility. Membrane types include cellulose, polycarbonate, anodized alumina, PVDF or PTFE. We would like to emphasise the ease of producing composites such as layered oxides combined with single wall carbon nanotubes (SWCNTs) for supercapacitor electrodes [229, 511], and TMDs/SWCNT composites for electrocatalysis [424, 512].

A wide range of filtration membranes are available with different surface chemistries and pore-sizes, the choice of which depends on the nature of the dispersion media, the size of the dispersed nanomaterials to be filtered and the desired approach to carry out film transfer. As the flakes produced by LPE often have lateral dimensions in 10s-100s nm range, it is often necessary to use filtration membranes with the smallest possible pore diameters. Mixed cellulose membranes with 25 nm pore size are compatible with aqueous/surfactant dispersion media and can be subsequently dissolved using acetone to achieve transfer of the filtered film.

FLG films with thickness ~150 nm, transmittance ~50%, roughness ~8nm and Rs~1-2 kΩ/sq were prepared as conductive electrodes for biological applications [405]. These films have also been exploited in photonic applications, demonstrating sub-50 fs compressed pulses from a FLG-mode locked fiber laser [513], power scaling lasers [514], and monolithic waveguide lasers [515]. To produce these, a 25 mm diameter membrane filtration setup was used. 500 µL of dispersion with concentration~0.1 g L^{-1} is diluted in 1 mL DI water. The dilution is necessary when the amount of the filtered dispersion is less than 1 mL to ensure uniform coverage of the membrane. If the dispersion has a high surfactant concentration, the presence of foam on the liquid surface has to be avoided before vacuum filtration. FLG is filtered through a 100nm pore-size nitrocellulose (NC) filter membranes (Millipore). In order to remove the residual surfactant, the film on the membrane can be rinsed by filtration of 20 mL DI water. The filtering process requires ~2 hours, which will increase with the film thickness prepared.

These films can be transferred on to glass coverslips (25 mm diameter) using the following procedure: 1. the FLG/NC membrane is cut to the size required and soaked in deionized water. 2. The FLG/NC is placed on the glass substrate with the FLG side face down. 3. A sheet of cleanroom paper is

pressed by hand on the back of the NC to remove the excess water and trapped air between the film and glass. This is a critical step, as trapped air can leave some FLG non-transferred and, therefore, holes or fractures in the final film. The substrate is then clamped with two bulldog clips between two glass slides (30 x 30 mm). 4. The sample is left to dry in an oven for ~2 hours at 90°C. 5. The glass slides are removed and the coverslip left to soak in a covered beaker of acetone (50 mL) to dissolve the NC (at least 24 hours) then soaked in isopropyl alcohol (1 hour) and in deionized water (1 hour). 6. The final FLG/glass sample is then dried in oven for 2 hours at 90°C.

Transfer on flexible substrates can be done with the same procedure. However, for improved transfer it is possible to use a hydraulic press in step 3, such as a Specac® Atlas 15T manual hydraulic press with a 40 mm die at 5 ton pressure for 5 minutes.

To prepare free-standing membranes, FLG dispersions in NMP are produced by sonicating graphite (e.g. Graphexel grade 2369) for 24 hours. The suspension is then allowed to settle overnight and then centrifuged at 8000 rpm for 1 hour. ~100 mL of the supernatant is then filtered on an Anodisc membrane (47 mm diameter, 0.2 μm pore size; Whatman). The free-standing paper is then peeled off after drying at 80^{o}C for 12 h under vacuum.

To prepare free-standing GO, 3 mg mL^{-1} GO is dispersed in water by sonication (2 h). Vacuum filtration through an Anodisc membrane filter (47 mm in diameter, 0.2 μm pore size; Whatman), is followed by air drying and peeling of the GO membrane. The thickness of each GO paper sample can be controlled by adjusting the volume of the colloidal suspension.

Another method to make large free-standing membranes is electrophoretic deposition [516]. A suspension of GO with a concentration of 3 mg mL^{-1} is prepared as described above and used as the electrolyte. Two identical pieces of well-polished Cu sheets (30 x 50 x 2 mm) are used as anode and cathode. A constant current of 2 mA is applied between the two electrodes for 2 minutes. The anode coated with GO is then dried under vacuum overnight, and then the free-standing GO membrane can be peeled off.

Inkjet printing

The printing of FLG inks is an attractive approach for developing electronic applications, such as transparent conductive films, printed electrodes and sensors. Inkjet printing is the ideal tool to produce prototype electronic devices at the lab scale. Indeed, it enables high resolution (~25μm) of the pattern associated with the possibility of easily changing the pattern and the printed material. Several examples of inkjet printing of nanomaterials have been demonstrated in literature [419, 517-519]. In order to have a good jettability an ink has to satisfy particular requirements on Z, γ ρ, η and nozzle diameter. If Z, the reciprocal of the Ohnersorge, is in the 4-14 range, satellite droplets recombine before reaching the substrate, but Ref. [419] demonstrated the possibility of having good printing also outside this range. Most lab-scale inkjet printers equipped with disposable cartridges, (e.g. Fujilm Dimatix 2800, Ceradrop X, LP50) mount cartridges with 50μm diameter, so the flakes dispersed in the ink have to be at least 1/20 of the nozzle diameter to avoid printing instability and

nozzle clogging. Dispersions produced by LPE followed by centrifugation are particularly suitable for inkjet printing, since they contain flakes with lateral sizes < 2-3 μm [147]. Inks made by electrochemical exfoliation contain larger flakes even after centrifugation. These should be filtered before printing.

Inkjet printing can be performed on a variety of rigid (glass, Si/SiO_2) and flexible (PET, PEN, PI) substrates. However, the wettability of ink droplets, defined by the contact angle, varies significantly. The most common procedures for changing the surface properties is to reduce the contact angle (improve wettability) by treating substrates. To increase contact angles the substrate can be silanized by spin coating hexamethyldisilazane (HMDS) (40 s at 1000 rpm, followed by annealing at 80°C for 2 min) [419]. Silanization requires surface hydroxyl groups to bind to. For flexible substrates, a preliminary UV ozone or oxygen plasma treatment will help to generate surface oxides. This results in more confined droplets, less spreading of the ink and higher resolution [419].

Flexible substrates already optimized for inkjet can be found on the market i.e. glossy papers, Novele (PET/SiO_2/PVA) [520], etc. which allow the quick wicking away of solvent, reducing the coffee ring effect thanks to their porosity.

Different examples of inkjet-printed FLG based strain sensors on flexible substrates have been already demonstrated. A flexible integrated platform, with 4 linear strain gauges 3mm x20mm and a central Wheastone bridge strain gauge of 1.5cm x1.5cm was printed on Novele substrate. A FLG-NMP ink with a concentration~1 g L^{-1} and FLG flakes lateral size up to 600nm was printed for 50 printing passes with an interdrop distance~27μm, inter-layer delay time~120s, and printer platform temperature at 60°C. Annealing was performed at 80°C in vacuum overnight. The strain gauges with a resistance~100kΩ show a gauge factor~20 at 25 mm bending radius with a change in resistance~5% after 1000 bending cycles. FLG-based strain gauges with similar properties are inkjet were printed on planarized PEN using a FLG-ethanol ink (2 g L^{-1}) to make fully flexible wearable devices. The sensors are aligned with the proximal inter-phalangeal joints of the first and second digit of the hand, allowing the extension-flexion movements of these digits to be monitored. 20 printing passes, 22 μm inter drop distance and RT were used with an additional annealing at 80°C in vacuum for 2 h.

With aqueous-surfactant based inks, one problem is the formation of foam bubbles following agitation of the print-head. This is observed at surfactant concentrations >6 g L^{-1}. Also, the presence of non-conductive species (surfactants, polymers) in the resulting printed films will reduce FLG network connectivity and, thus, conductivity. The ability for microfluidic processing to stabilise FLG at low surfactant concentrations (0.5 g L^{-1}) meant foaming does not occur. The suitability of 0.5 g L^{-1} SDC stabilized FLG inks after 20 process cycles and centrifuged at 10 krpm, 1 h can be tested for inkjet printing (Fig. III.6). Serpentine-type FLG resistors are printed on to photo quality paper (HP Advanced) at room temperature using an interdrop distance of 18 μm, with 20, 40 and 80 printing passes (Fig. III.6b). Prints are left to dry at room temperature for 60 s between passes. Although minimum optimization is required, prints with over 20 layers suffer bleeding, due to insufficient drying time, and nozzles could become partially clogged. During printing, the head is cleaned by an automated Spit-Purge-Spit cycle every 180 seconds. Patterns are printed for 20 passes at a time and

the nozzles wiped by hand with IPA prior to printing more layers. After 20, 40 and 80 passes the resistance of the patterns decreases 220, 31, 3.7 MΩ, respectively, over~40 mm (track width ~0.9 mm) as shown in Fig. III.6b. The resistance response of these devices is tested with strain (3-point bending) and in different gas environments.

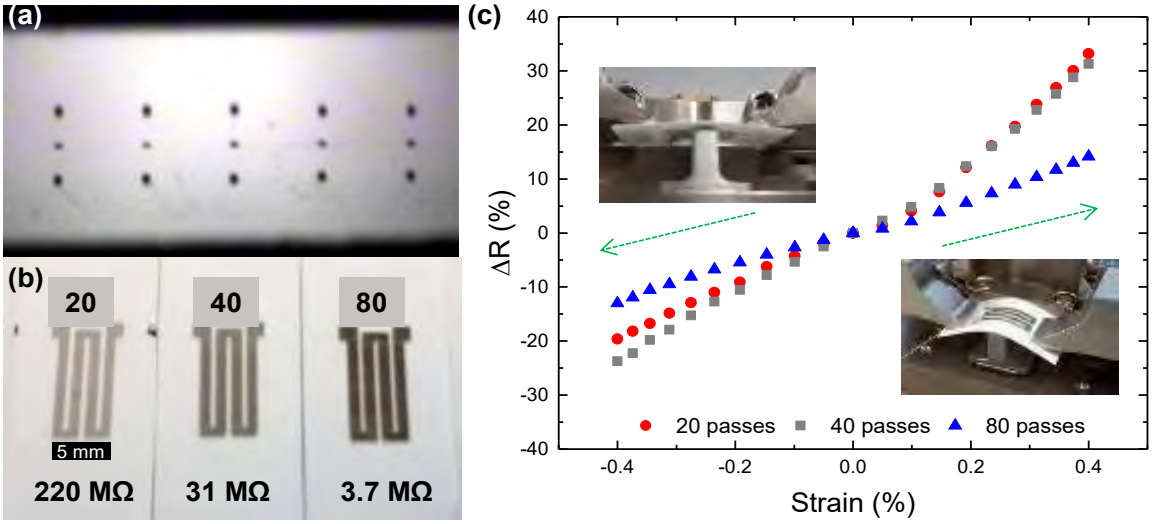

Fig. III.6: Inkjet printing of microfluidized ink after 20 process cycles. (a) Typical jetting behaviour showing good droplet formation and the presence of no satellite droplets. (b) Printed serpentine-type resistors after 20, 40 and 80 passes. (c) Resistance change whilst 3-point bending of three devices under tensile and compressive strain.

3-point bending is performed with a 300 N/2 kN Deben vertical three point bending tensile stage. The samples are bent with an extension rate of 0.5 mm min^{-1} and measured under tension (positive strain) and compression (negative strain), to a maximum of 5 mm displacement. The electrical resistance of the printed strain gauge varies depending on the amount of axial bending strain in the device. Printed structures at 20 and 40 passes show very similar resistance vs. strain curves (Fig. III.6c) with significant response to +0.4% strain (ΔR~+35%) and -0.4\% strain ΔR~-25%). The 80 printed pass sample show significantly lower response (ΔR~±10%) in line with the higher sample thickness. These changes are a result of conductivity variations, due to changes in length and cross-sectional are, as well as the distance between flakes. The relative change in electrical resistance ($\Delta R/R_0$) is related to the mechanical strain (ε) by the gauge factor (GFactor== $(\Delta R/R_0)/\varepsilon$,). These are 93, 85 and 39 for the 20, 40 and 80 print pass samples, respectively and thus comparable to other multi-layer FLG devices produced by drop-casting or spray coating (GFactor: 75-150 at 0.2% strain) [521]. These gauge factors are higher than graphite-based ink strain sensors (GF: 19.3±1.4) [522], and considerably higher than conventional strain gauges [523] or inkjet-printed metal strain gauges [524] in which GFactor~2.

Inkjet printing can also be used to print heterostructure devices by placing one material on top of the other. Inkjet printed MoS_2/FLG photodetectors (PDs) using LPE inks was demonstrated on PET.

The devices were fabricated using a Dimatix 2800. A 40μm MoS_2 channel contacted by two inkjet printed FLG electrodes on top. 100 passes of both FLG and MoS_2/NMP based inks were printed at 60°C using 25 μm interdrop distance and 300s interdelay time. MoS_2 was annealed at 90°C in vacuum for 9 hours before printing FLG. Finally the entire device is annealed overnight at the same conditions. The good performance of the PD showed that the MoS_2 properties could be retained after printing. Similar results have been demonstrated by [188, 525] , confirming that inkjet-printing can become an efficient method to produce functional devices for a variety of applications including photonics, optoelectronics and energy storage.

Screen printing

For flexible electronic devices, e.g. organic photovoltaics (OPVs), sheet resistance (Rs) <10 Ω/☐ is required [247], while for printed radio-frequency identification (RF-ID) antennas one needs a few Ω/☐ [249]. To minimize Rs, μm range films are deposited using screen printing [526-529]. Screen printing is a commonly used industrial technique for fast, inexpensive deposition of films over large areas. It also allows patterning to define which areas of the substrate receive deposition. The screen is typically a polyester mesh with a cured lacquer stencil on top that provides the desired pattern. Mesh grades vary from~10 up to 180 threads/cm. The film or emulsion stencils range from a minimum of 12μm to >300 μm. The ink must have high viscosity (>500mPas) [530, 531], because lower viscosity inks run through the mesh rather than dispensing out of it [530]. To achieve this, typical formulations of screen inks contain a conductive filler, such as Ag particles,[532] and insulating additives [533].at a total concentration higher than 100 g L^{-1} [533]. Of this,> 60 g L^{-1} consist of the conductive filler needed to achieve high σ~10^7 S/m [532, 534]. A squeegee is used to fill the mesh with ink before a high pressure is applied with the squeegee to force the ink through the mesh onto the substrate of choice [533]. Fig.III.7 shows a schematic of the screen printing process. Ref. [535] is a good introduction to screen printing.

The printability of inks with ~80 wt.% FLG flakes after 70 microfluidic processing cycles formulated with 1 wt.% NaCMC was tested using a semi-automatic flatbed screen printer (Kippax-2012-BU) and a Natgraph screen printer (Fig III.8a), both equipped with screens with 120 mesh count per inch. Trials were made onto (PET) (125 μm thickness, PMX729 HiFi Industrial Film Ltd) and paper substrates. Fig. III.8b shows a 29 cm x 29 cm print on paper with a line resolution ~100 μm (Fig. III.8c). The printed pattern (Fig. III.8b) can be used as a capacitive touch pad in a sound platform that translates touch into audio [536] .

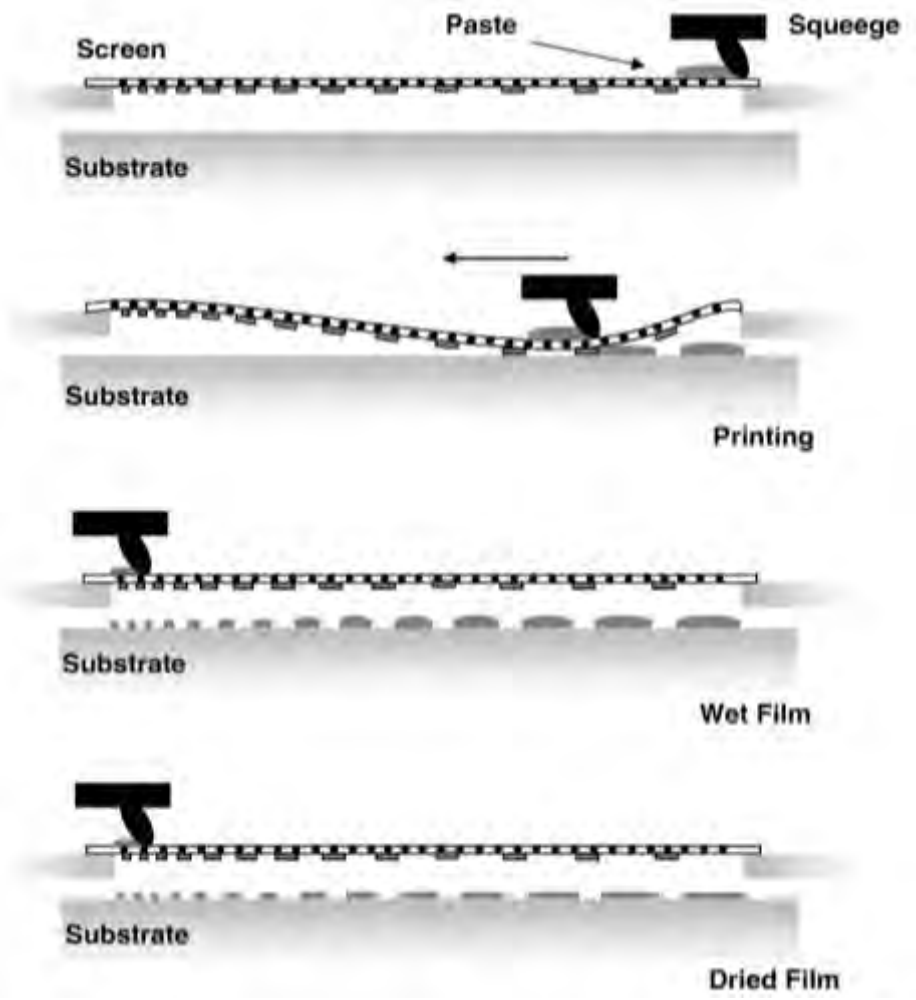

Fig. III.7: Schematic of the screen printing process. FLG ink is applied to the screen and the squeegee is lightly passed over the screen to fill the mesh. The squeegee is then passed over the screen at a higher pressure such that the ink is pushed through the mesh onto the substrate. The wet film is then left to dry to produce the final design. Reproduced from ref. [528].

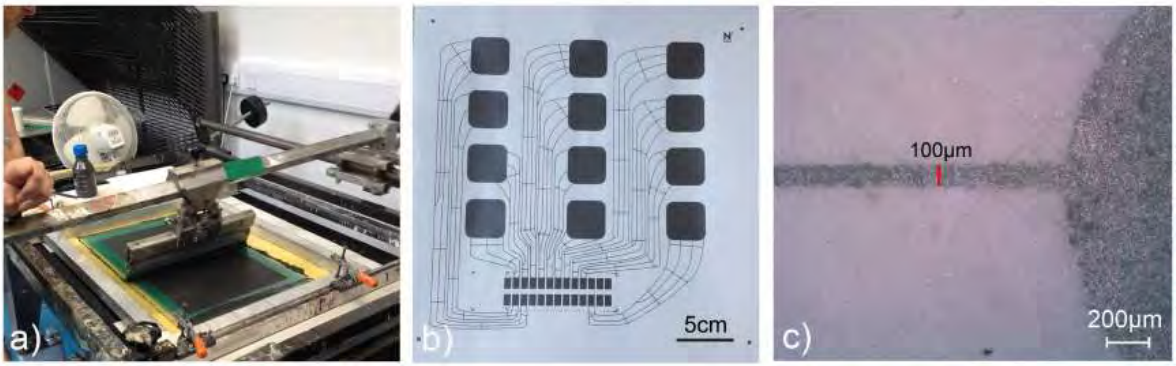

Fig. III.8 a) Demonstration of screen printing, b) capacitive touchpad design (29cmx29cm) printed on paper, c) the line resolution is 100µm. Reproduced[m1] from ref [26].

IV. GROWTH ON SiC

IV.1 Sublimation

The most commonly used SiC structures for growing epitaxial graphene are the hexagonal 4H-SiC and 6H-SiC polytypes [188, 537]. Both of these SiC polytypes are widely commercially available as single crystal wafer of up to 150 mm in diameter. Their (0001) and (000-1)-faces are polar [537], i.e. they are Si- or C-terminated surfaces, respectively. The name epitaxial graphene (or epigraphene - EG) was coined [538] to reflect the idea that graphene has a quasi-epitaxial match with hexagonal SiC lattices, and an exact orientation relation with 4H/6H-SiC(0001)-face. The (hetero)epitaxial orientation of EG on the Si-face relative to 4H-SiC is shown in Fig. IV.1. (For a review, see [539] and ref. therein).

The decomposition of SiC doesn't require an external source of C to produce a layer of graphene. C is provided by the SiC crystal itself when its surface decomposes at high T [540] (T>1000°C in vacuum [540]). The SiC sublimation method is intrinsically a wafer scale method for large-area production of graphene [538, 541-543]. Since Si has the highest partial vapour pressure as shown in Fig. IV.2, Si leaves the surface, resulting in a C rich surface that forms a graphene layer on the SiC substrate. For this reason, the second graphene layer that forms grows under the first one; that is the top graphene layer is always the first one to form on the SiC surface. Because SiC is stoichiometric, the amount of graphene formed is directly related to the amount of silicon that leaves the surface by sublimation, and for the common SiC polytypes used, about 3 Si-C bilayers are required to provide enough C atoms to form a graphene layer. A schematic illustration of the graphene formation steps is shown in Fig. IV.2 (b).

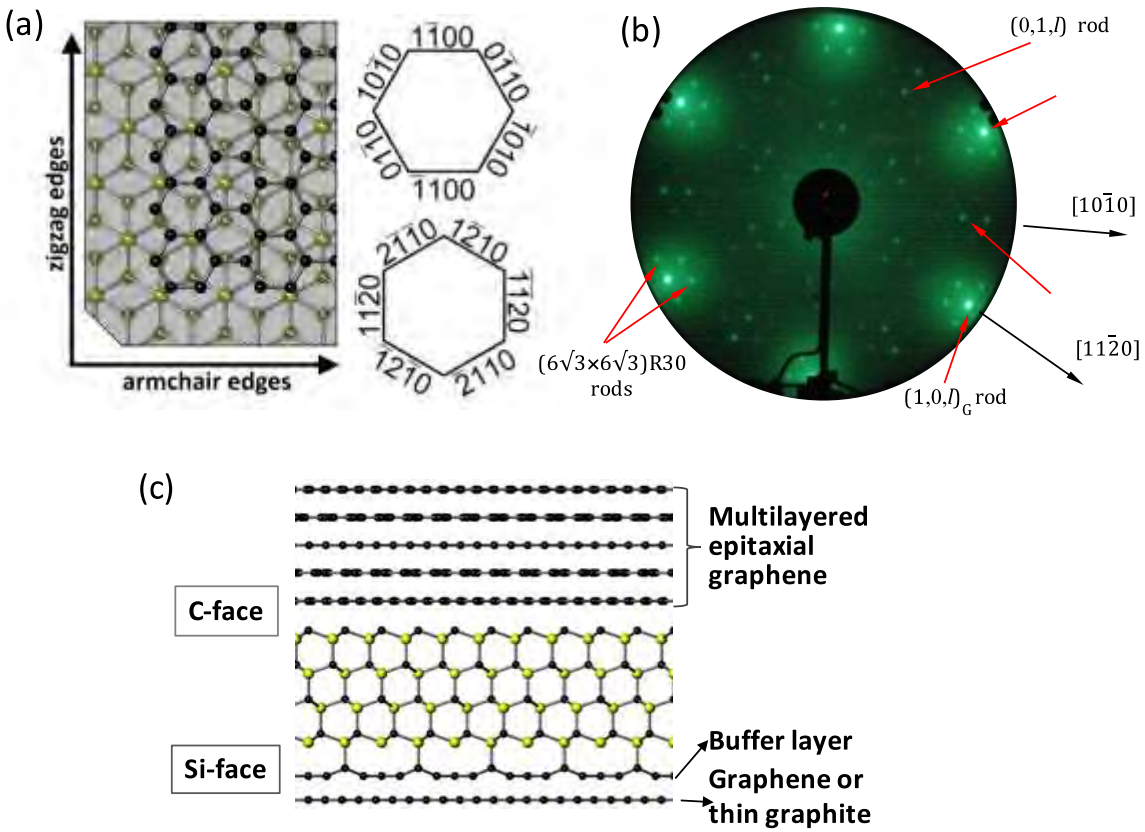

Fig. IV.1 (a) Epitaxial orientation of EG on the Si-face relative to 4H-SiC. (b) LEED diffraction of a multilayer graphene MLG on 4H-SiC, showing the diffraction spots of SiC, graphene and the buffer layer (6√3x6√3)R30). Schematics of the graphene layer growth on the top 6H/4H- SiC(000-1) and bottom (0001) surfaces .Adapted from [539].

Graphene growth is driven by the same Si sublimation process on both the Si face and the C face. However, the surface reconstruction and growth kinetics for the Si terminated and C terminated faces are different, resulting in different graphene orientation relative to the substrate, different growth rates, morphologies and electronic properties, as schematically show in Fig. IV.1(c) (see also for instance review [539] and ref. therein). The first C layer grown on the Si face of SiC polytypes is known as the buffer layer [544] (sometimes called the zeroth layer). It has the graphene atomic structure but it is in interaction with the SiC substrate and doesn't have the electronic dispersion of graphene [544]. Instead the buffer layer is a semiconductor with an energy gap larger than 0.5 eV, as shown by Scanning tunnelling Spectroscopy (STS) and photoemission spectroscopy (See section IX for an introduction to the technique) [545-547]. When the next graphene layer grows, under the buffer layer, the previously grown buffer layer is no longer in interaction with the SiC substrate and turns into a graphene layer (with a linear electronic dispersion), as the newly grown graphene layer becomes the new buffer layer. Therefore, on the Si-face a graphene monolayer always rest on a buffer layer. Graphene on the Si-face has a defined orientation relative to the SiC crystal (see Fig. IV.1(a-b)).

For the $(000\bar{1})$ -face (C-face) no buffer layer has been observed [548]. The graphene layers grow much faster than on the Si-face with 5-10 graphene layers growing on the C-face compared to

one the Si-face in standard Confinement Controlled Sublimation [549] (CCS) conditions (see below). Contrary to the Si-face where they are arranged in a graphite stacking (Bernal ABA, or sometimes rhombohedral ABC [550]), the layers on the C-face are stacked rotationally, that is alternating azimuthally rotated layers with 0° and 30° within +/- few degrees [539, 551, 552]. The stacking explicitly is not turbostratic (random stacking of small grains). Graphite (AB) stacking in this case corresponds to stacking faults that have an occurrence of less than 15-19% [548] .

In the Si sublimation process, Si desorbs through steps [553-555] or from defects [556, 557] and terraces [558] and graphene growth results of a fine kinetic balance of different step evaporation rate, Si sublimation from and re- absorption onto the surface, and C diffusion [549, 553, 559]. When the SiC surface is in equilibrium with the Si vapour, the formation of graphene is arrested. The key to grow high quality graphene is a slow growth at high T, where the kinetic energy and the mobility of C and Si atoms are high. It is therefore necessary to slow down the Si escape rate that depends on the partial pressure of Si (P_{Si}) in equilibrium with SiC at temperature T.

Following Fig. IV.2, P_{Si} increases by more than three orders of magnitude in the range 1200-1600°C, which is a typical temperature range for epitaxial graphene growth.

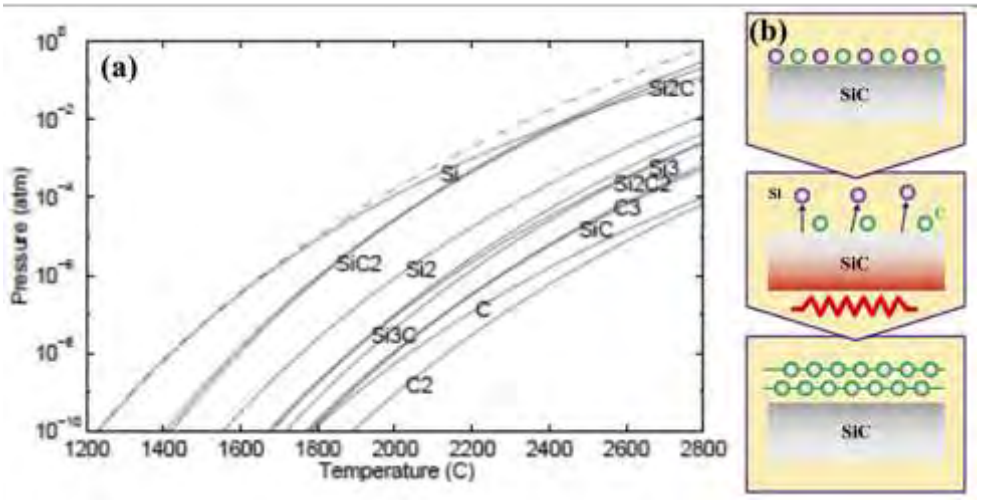

Fig. IV.2. (a) Partial pressure of different vapour spices vs. temperature in equilibrium with a crystal on SiC. (b) Schematics of graphene formation by Si sublimation[560].

Note that the partial pressure of C is less than 10^{-10} atm., at least five orders of magnitude lower than the Si vapour pressure (or that of the residual gasses in the vacuum chamber), so that the role of gas phase C is most certainly negligible in the graphitization process. It is reasonable to assume that each Si atom that escapes from the surface leaves a C atom on it to form graphene. Maintaining a background gas (either Ar [543] or Si [549] for instance) reduces the diffusion out of Si and increases the return probability to the surface, thereby reducing the Si escape rate and consequently the graphene growth (see [549] and [543] for details).

In order to better control the growth rate several methods have been employed, either by providing an external source of silicon (by adding a flux of silane [561], a Si flux [562] or by sublimating a Si piece nearby for instance), or by slowing down the Si escape by diffusion through a neutral gas (Ar atmosphere) [543] or keeping the SiC as close as possible to equilibrium with its own vapour by

confinement [549]. Alternatively CVD methods have been employed, where C species are brought externally [563, 564]. The last three methods are reviewed below.

Growth under Argon

The vertical induction heated furnace shown in Fig. IV.3 consists of a coil to produce a uniform electro-magnetic field in the semi-close graphite platform called crucible on which the T is measured with an optical pyrometer, a quartz tube with a diameter of 100-200 mm depending on the size of the crucible, porous graphite insulation which is slightly smaller than the quartz tube [559]. The role of the radiofrequency (RF) field is to produce Eddy current in the crucible and that heat up the crucible (Fig. IV.3(b)). The long RF coil in the reactor provides a uniform electro-magnetic field distribution in order to ensure a uniform T on the substrate. This design allows treatment of SiC wafers up to 50mm in diameter. Other furnace designs with fully automated temperature controls can be found elsewhere [565].

As the T distribution in the crucible influences the graphene thickness uniformity, a symmetric crucible was designed for good temperature uniformity, with optimization by numerical modelling of the temperature distribution (Fig. IV.3(c)).Also the SiC substrate position should be in the centre of the RF coil. Prior to growth, the substrates are cleaned in organic solvents, then in solutions based on sequential oxidative desorption and complexing with H_2O_2-NH_4OH-H_2O (RCA1) followed by H_2O_2-NCl-H_2O (RCA-2) to remove organic contaminations and dipping in diluted HF. The substrates are then placed in the middle of the graphite crucible followed by the placement in the porous graphite insulation. After that, the whole assembly is loaded in the growth chamber (quartz tube), locked and pumped down. The chamber is ready for heating when the pressure reaches 5×10^{-7}mbar .

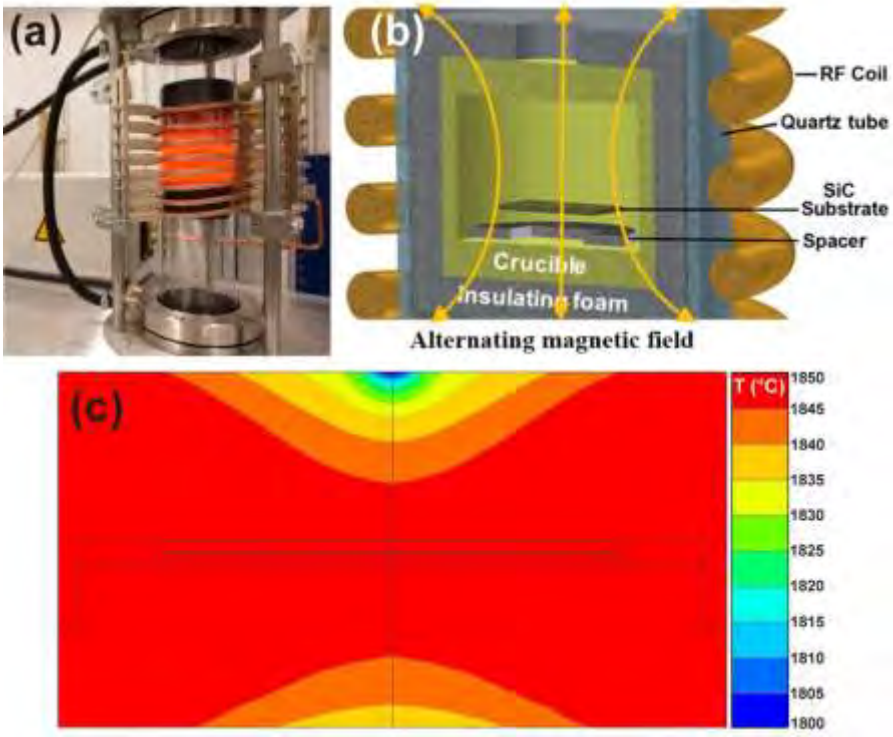

Fig. IV.3. Sublimation reactor (a) Picture. (b) Sketch of the vertical RF-heated furnace in cross-section [559]. (c) Temperature distribution in the crucible. The diameter of the crucible in (c) is 50 mm and the height of the growth cavity (marked by black lines) is 5 mm. (Adapted from [559]).

To slow down the Si sublimation while being close to equilibrium conditions, growth was performed under 1 atm of Argon (Ar) [542, 543, 566]. At 2000°C Si sublimation in 1 atm of Ar yields a SLG on a large area and thickness uniformity [566]. Fig. IV.4 (b) and (c) show LEEM images of graphene layers (small domains of 1-2 micrometer size and thickness more than 5 layers) grown in Ar atmosphere with a better thickness uniformity and quality for graphene grown in Ar [542]. Details about T-time profile can roughly be described as setting temperature ramps (~20 degrees per minute) up to at least 1150°C and once the desired graphitization temperature (usually higher than 1150 °C) has been achieved, keeping this T during the growth time for, finally, decreasing the temperature again down to RT with a slow ramping (70 degrees/min).

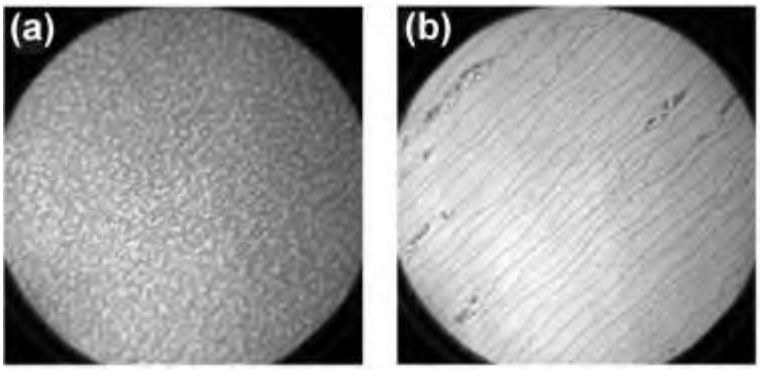

Fig. IV.4. Epitaxial graphene layers grown on the Si-face (a) in vacuum, (b) under Ar [542]; the lines are identified as bilayer graphene [543]. Adapted from [542] and [543].

Near equilibrium confinement controlled growth

The Confinement Controlled Sublimation (CCS) method [549] relies on the SiC being in near equilibrium conditions with the Si vapour. Graphene growth is controlled by encapsulating the SiC crystals in graphite enclosures so as to sequester the evaporated Si (see Fig. IV.5). A SiC crystal is placed in a closed graphite box (called crucible) provided with a very small calibrated hole of typical diameter 1mm. As the T of the furnace is increased above 1200°C and Si sublimates from SiC, the built-up Si vapour remains confined inside the crucible and escapes slowly through the hole (Fig. IV.5(b)). The SiC chip is therefore in a uniform Si vapour as defined by the Psi versus T of Fig. IV. 2, ensuring uniform graphene growth. Because the Si vapour is confined, the graphene growth T is substantially increased (by an estimated 300 K for the CCS method discussed in Ref.[549]) compared to vacuum growth. Details about the full furnace design and operating conditions can be found in Ref. [549, 567]. The Si escape rate that ultimately determines the graphene growth rate, is defined by the geometry of the hole (diameter 0.5 to 2 mm) [549, 567]. The rate of graphene formation by the CCS method can be reduced by a factor of more than 1000 compared to the UHV sublimation method where roughly a graphene monolayer grows on the C-face in about 1 min at T=1.200**°**C [549]. The graphene formation rates can be reduced by an additional factor of up to 10^3 by introducing 1atm of Ar into the enclosed crucible [549]. The system is compact for fast pumping speed and small thermal inertia, allowing fast heating and cooling rate up 150˚C/s in the T range from RT to 2100˚C. The T profile is computer automated [567, 568]. The whole process can be performed in less than two hours, being scalable in principle to full wafer sizes.

An alternative method to CCS is to cover the SiC substrate with a piece of graphite, which provides some Si vapour confinement. The Si escapes on the side providing a non uniform Si vapour gradient that produces narrow tapered stripes of graphene [569].

To grow EG on hexagonal 4H- or 6H-SiC wafers by the CCS method [567] the key step after pumping out the cell to below 10^{-6} mbar, is the Si sublimation at high T (1400-1650˚C). The exact T profile depends the geometry of the graphite crucible and geometry of the hole [567], and on the background pressure (with or without additional Ar backpressure). Optimum T and growth times are specific for each crucible adapted to each type of grown graphene. Typically, a monolayer graphene grows in 20 min at 1520 °C [545] on the Si-face, a graphene buffer layer at a temperature 160°C lower than the Si monolayer in the same crucible [545]. On the C-face, the number of layers is determined by both temperature (1450–1525°C) and time (1 minute to several hours for very thick films), see refs [549, 567] for details and also ref [558] (see. Section IV 1.3. and Fig. IV.5). Templated epitaxial graphene growth of epitaxial graphene nanostructures (for instance SiC sidewalls [570-572]) on non-polar facets (i.e. other that (0001) and $(000\bar{1})$) is finely tuned closed to the buffer layer growth conditions.

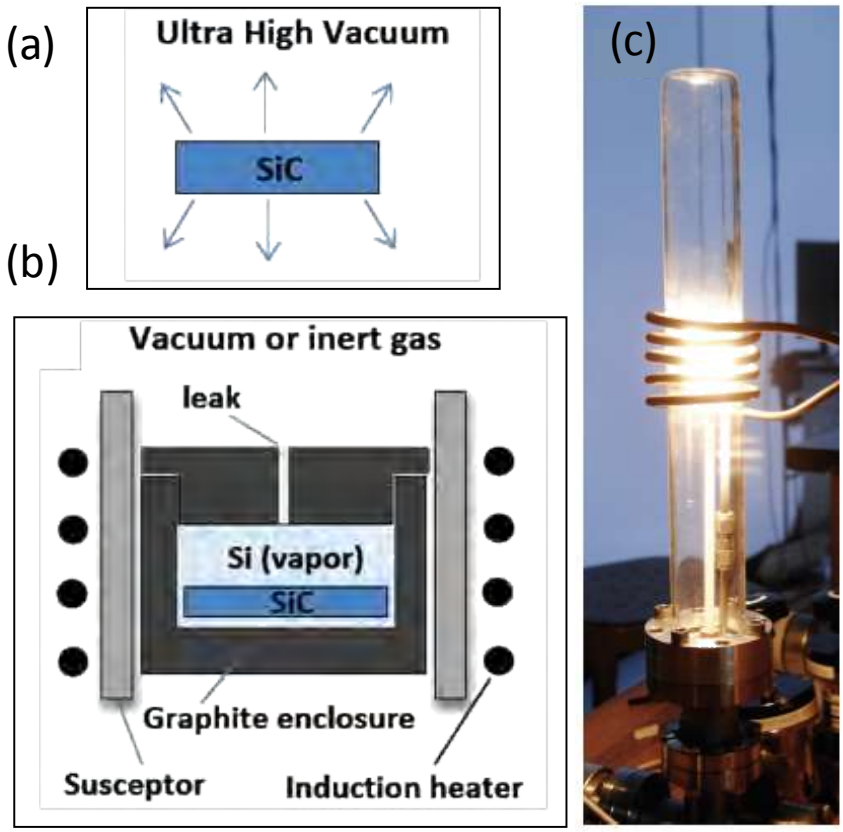

Fig. IV.5. Confinement controlled sublimation. (a) in UHV Si that is sublimated for the SIC surface at high temperature escapes. (b) in the CCS method SiC is in quasi-equilibrium with its own vapour (c) picture of the CCS furnace. Adapted from [549].

Carbon-face

The surface state of the substrate prior to growth is essential, because rough surfaces have multiple disordered nano-steps acting as nucleation centres for graphene growth. The first step is therefore SiC surface flattening. For SiC surfaces polished to optical quality, the deep polishing scratches can be removed by SiC etching at high T in a hydrogen environment [573]. Successful flattening is obtained at 1500°C for 15 min in a flow rate of 200 sccm in 1 atm of a mixture of 5% H_2 in Ar [573], which produces a surface with no observable scratches in AFM and with a step-terrace structure with atomically flat terraces. However, it is observed that on the 6H(0001) face, the average width and step height of terraces after treatment do not have a clear correlation with hydrogen etching, T and time, but are related to the local miscut angle (the local angle θ of the surface relative to the on-axis orientation, generally θ<0.2° for commercial wafers) of on-axis wafer [573]. Commercial SiC wafers (provided by, for instance, ii-vi, CREE-Wolfspeed, SiCrystals) can be purchased with so-called 'epiready surfaces' that have been treated by a chemical mechanical process. These provide excellent starting surfaces, with rms<0.2-0.3nm.

On the 4H- or 6H-SiC carbon face, continuous multilayer EG (MEG) films containing 5-10 layer [574] are grown by annealing for 15 minutes at T in the range 1450–1525˚C. Repeated cycles produce

much thicker films up to 50 layers [575, 576]. Shorter times and lower T are required to produce monolayers. They appear in patches on the SiC substrate (see inset of Fig. IV.7(a)) because of the rapid growth rates on the C-face and the multiple nucleation sites [556, 558, 567, 577].

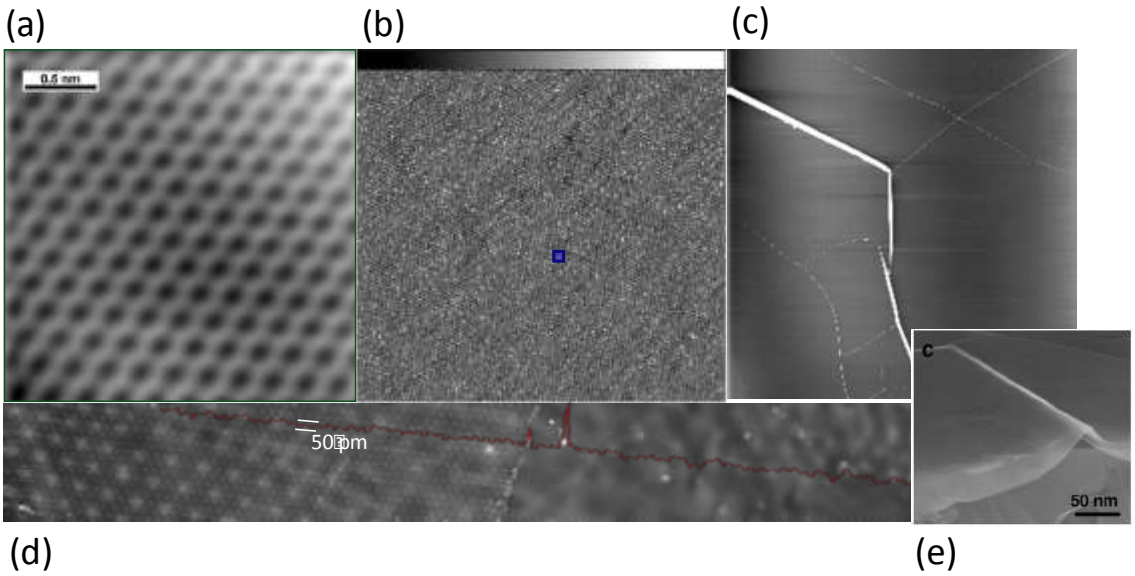

Fig. IV.6. Multilayer epitaxial graphene on the C-face topography images. (a) 4x4nm STM image (From [578]). (b) 400x400nm STM image. The blue square represents the size of the STM scan in (a) (From [578]). (c) 40μmx40μm AFM scan. The white lines are graphene pleats. (d) 400nm long STEM image across areas of different moiré pattern, showing that the top layer is flat (rms<50pm) and continuous (From Ref. [579]) (e) Scanning Electron Microscopy image of a graphene pleat (From ref. [580]).

Sample quality is revealed in AFM and STM images, in multiple spectroscopy techniques (Raman, magneto-optical, photoemission, ultrafast optics) and electronic transport (see Section IX for characterization methods). Specifically Raman spectroscopy shows a vanishing D peak attesting the very low defect density (see Fig. IV.7). The Lorenzian 2D peak of the MEG sample shown in Fig. IV.7(b) is not that of graphite. All spectroscopy studies performed on MEG [574, 576, 579, 581, 582] confirm that the multiple graphene layers of MEG behave as electronically decoupled, that is as a stack of graphene layers with a non gapped linear dispersion down to a few meV from the Dirac point, not like graphite (hence the terminology 'multilayer graphene') and exhibit the quantum Hall effect [556, 577, 583] and high mobility (up to μ = 39,800 cm^2/Vs at charge density n = $0.19\times10^{12} cm^{-2}$ [556]). The MEG layers are continuous over the entire SiC sample, drape over SiC steps and are extremely flat with roughness values rms<5pm as measured by x-ray diffraction [548]. STM shows extended moiré regions [552, 579] providing clear evidence that adjacently stacked graphene layers are rotated creating a superstructure. On a larger scale, smooth graphene pleats are observed, as seen as bright lines in Fig. IV.6(c) and (e), which originate from the differential contraction of graphene and SiC upon cooling.

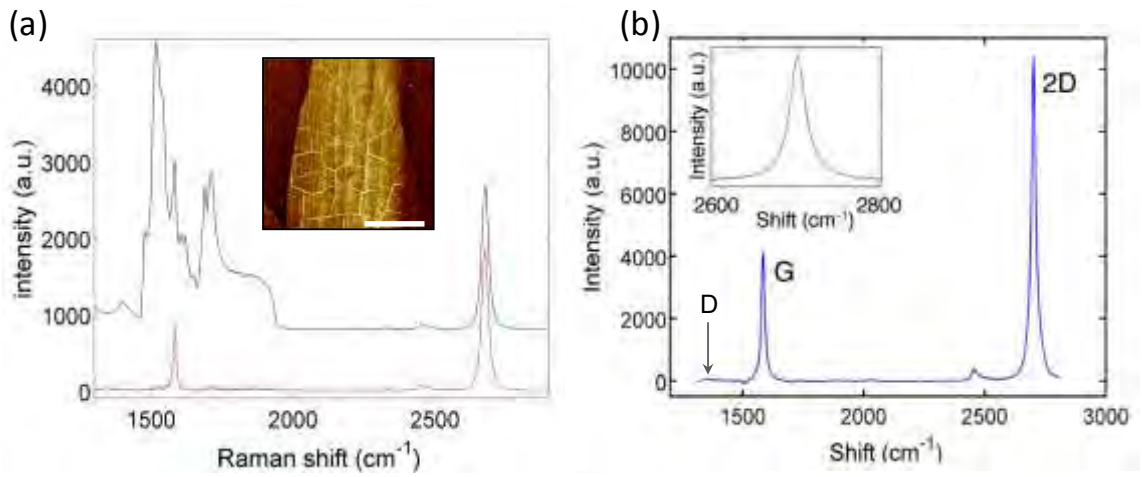

Fig. IV.7. Raman spectroscopy for graphene layers on 4H-SiC C-face (a) monolayer graphene, (b) multilayer graphene, with the Raman contribution for SiC removed. Note the absence of the D peak. In (a) the black trace is the raw data, the red trace is the graphene spectrum once the SiC Raman peaks have been subtracted by the Non-negative Matrix Factorization method [584]. In (b) the inset shows a Lorenzian 2D peak for this ten layer sample. Figure adapted from Ref [583].

MEG films have been amply used as a model system to study graphene properties (see for example review [539]). This stems from a combination of factors: (i) Excellent structural quality (No Raman D peak observed, see Fig.IV.7 and ref. [583]), (ii) Flatness of the layers (rms<5pm as measured by x-ray diffraction [548]) which excludes strain-related gauge field effects [585] and broadening effects in k-resolved spectroscopy measurements (see Fig. S1 in Supp of ref.[572]) , (iii) Extremely small interaction with the substrate and the environment, particularly for the layers in the middle of the stack that are quasi-neutral [582, 586] (charge density $n \sim 5 \times 10^9$ cm^{-2}, that is at most 8 meV away from the Dirac point) with record high mobilities of $10^6 cm^2/Vs$ at RT [581, 586]. (iv) graphene electronic structure for all the layers [587], due to the rotational stacking, providing a large signal intensity very much sought in optical measurements for instance.

Silicon-face

MEG on the Si-face (see Fig. IV.4) is the most studied EG form as it is the realization of quantum resistance standards (as multiples of $R_K=h/e^2=25.812807$ kΩ) at 4.2K in small (<1 Tesla) magnetic fields. EG shows a quantum Hall resistance quantization accuracy of 3×10^{-9} that rivals the best 2D electron gas standards [564, 588]. As growth on the Si-face starts from the SiC steps [553, 555, 589], bilayers (or multiple layers) tend to form at step edges when a monolayer graphene fully covers the terrace (see Fig. IV.4), which makes it difficult to produce extended monolayer sheets. Additionally, the step edges add electronic scattering due to the presence of bilayers/ multilayers, or to the reduction of the carrier concentration on the step (see Ref.[539] and refs therein), which is detrimental for instance to the homogeneity of the quantum Hall effect [590]. Better control of EG growth on the Si-face has been obtained by providing carefully balanced methane and H_2 [591]. Others have produced a MEG that drapes continuously over the steps by graphitization of a polymer

deposited on the bare SiC [592]. Chemical vapour deposition (CVD) on SiC is described in epigraph IV.2.

Step bunching and graphene growth

During annealing above 1200°C, the SiC surface undergoes microscopic restructuring by forming steps and terraces. This process, known as step bunching, is different from atomic surface reconstruction and refers to surface morphology. Step bunching, i e. the bunching of straight steps on vicinal crystal surfaces, which is governed by energy minimization on different terraces is a fundamental phenomenon in SiC. Graphene formation has been analyzed with respect to step bunching of SiC, by studying the influence of the crystal structure at the atomic level for each SiC polytype on the graphene formation [593]. As illustrated in Fig. IV.8 (a), the 4H-SiC polytype has two kinds of decomposition energies, terraces 4H1 (−2.34 meV) and 4H2 (6.56 meV), respectively, and the 6H-SiC (Fig. IV.8(b)) has three distinct terraces, 6H1 (−1.33 meV), 6H2 (6.56 meV) and 6H3 (2.34 meV), while 3C-SiC (Fig. IV.8(c)) has only one kind of terrace, 3C1 (−1.33 meV) [593].

The growth process is schematically shown for 4H-SiC in Fig. IV.8 (d). Since Si and C atoms are bonded more weakly in the vicinity of step edges, Si desorbs from these areas faster in comparison with the terraces [553, 555, 589]. Based on the terrace energies, removing a 4H1 terrace costs less energy and the step decomposition velocity is faster (Fig. IV.8(a)). As shown in Fig. IV.8 (d), from the edge of the 4H1 terrace on the graphene-free surface, C atoms are released onto the terrace as Si atoms leave the surface (stage 1). The C atoms coalesce and nucleate into graphene islands (stages 1 and 2), which act as a sink for subsequently released C atoms. After the 4H1 terrace step catches the 4H2 step, the newly formed two SiC bilayer step provides more C atoms as compared to the one-bilayer step and the first graphene layer extends along the step edge (stage 2). The large percentage of bunched steps with four Si-C bilayers, an increased source of C, will impose the formation of a second layer of graphene (Fig. IV.8(d), stage 3) since some extra C will be released. Therefore, a full coverage of the 4H-SiC substrate surface by just one layer of graphene may be an issue.

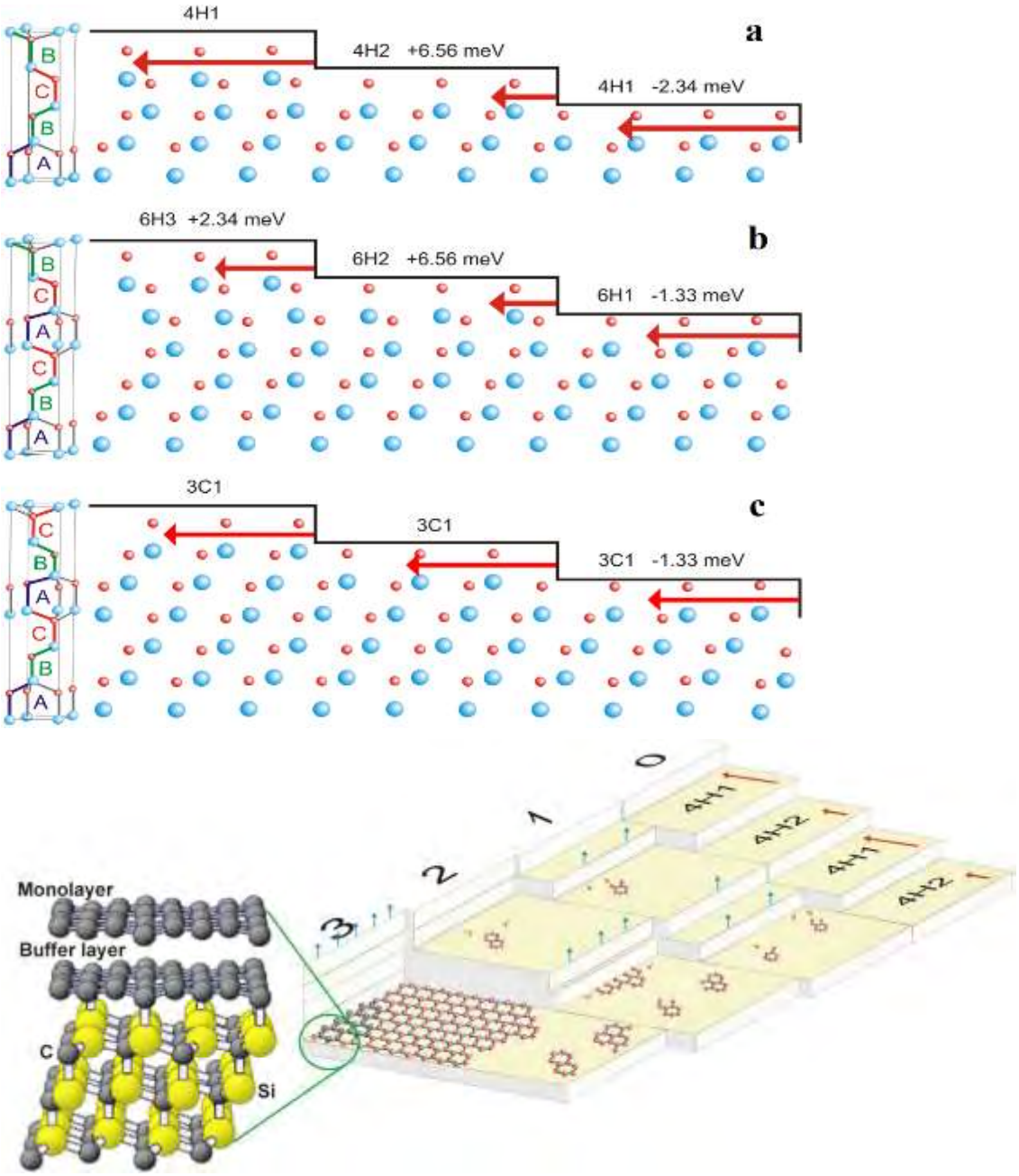

Fig.IV.8. Stacking sequences and possible terraces on (a) 4H-SiC, (b) 6H-SiC, and (c) 3C-SiC surfaces. Large (blue) and small (red) circles represent Si and C atoms, respectively. Length of arrows indicates different step decomposition velocities. (d) Schematic depiction of the formation process of EG via sublimation of Si from the SiC surface. Adapted from [593].

A similar mechanism of energy minimization is expected in the 6H-SiC polytype (Fig IV.8(b)). As a result, first the step 6H1 will catch step 6H2 and forms two Si-C bilayers. Then step 6H3 will advance and merge with the two-bilayer step. The growth process for 6H-SiC is the same as the 4H-SiC [593]. However, on 3C-SiC all terraces have the same decomposition energy [593] (Fig. IV.8(c)) and no energetically driven step bunching should be expected. In this polytype, a non-uniformity of sublimation may be induced by the presence of extended defects such as stacking faults, which are characteristic of this material [594].

A capping technique can be employed to localized the step bunching [595]. It consists in an amorphous grid evaporated on the bare SiC, that pins the SiC steps under it so that upon annealing the steps bunch against one enclosure wall and align along the amorphous C grid, as shown in Fig. IV.9(a). This technique provides large flat terraces of relative large size (Fig. IV.9(c)-bottom) at a predefined location. The amorphous C is removable by plasma etching after annealing, to reveal a SiC step structure ready for graphitization [595].

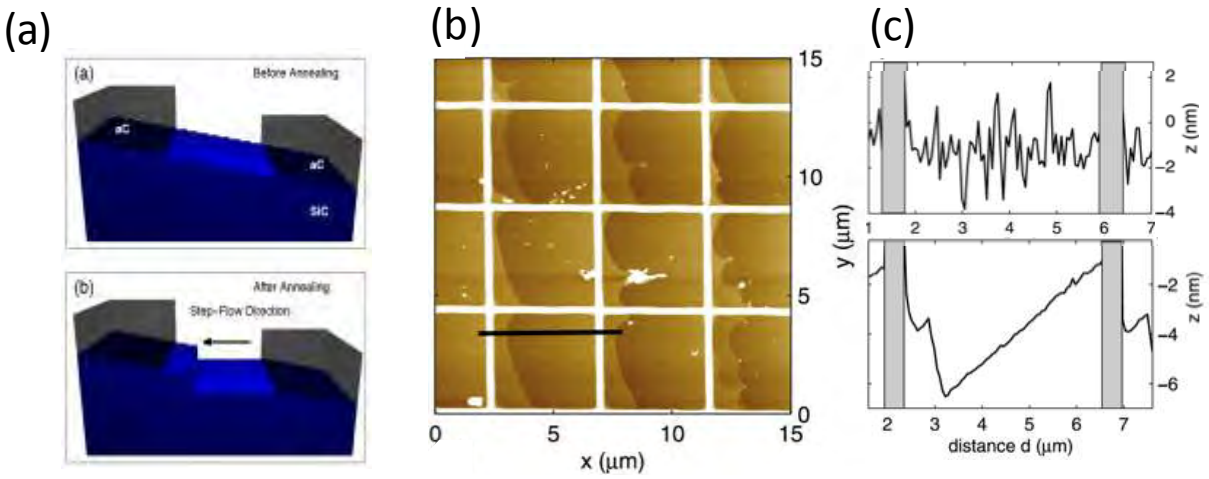

Fig. IV.9. SiC Step pinning under an evaporated amorphous carbon grid. (a) Schematics of step pinning. After annealing at 1350˚C, the steps accumulate at one side of the grid in each enclosure providing large terraces at a locations defined by the grid. (b) AFM image and (c) topographic profile within the grid (top) before and (bottom) after step bunching annealing, showing that a large terrace has developed. Adapted from [595].

Optimization of growth process for scale up

Growth conditions can be developed to increase the size of the SiC substrate to 20×20 mm^2 and ultimately to 100 mm diameter wafers. The furnace is similar to that of Fig. IV.3, but with longer RF-coil with uniform distance between the pipes [596]. The coil can be moved up and down to change the temperature gradient if necessary and it is fully automatic. The key to achieve large area monolayer graphene on SiC is to (a) understand the role of the buffer layer [544, 546, 562] and of the step bunching [559] which takes place during its formation and to monitor the effect of (b) temperature (in the range 1700-1950°C); (c) Ar pressure (in the range 750 - 950 mbar) (d) and growth time (from 0 to 15 min). AFM topography and phase images show that the formation of the buffer layer (at growth T 1850°C and Ar pressure 950 mbar) can start at any place on the substrate, but preferably on the kink of steps as shown in Fig. IV.10 (a). The C atoms coalesce and nucleate into graphene islands on the step kinks (marked with a circle) and these islands act as a sink for other C atoms. As the step edges are the main source of C, the growth rate is two times higher along the step edge compared to that on terraces and for this reason a graphene layer first covers like a ribbon the sidewall of steps (Fig. IV.10(a)) [554, 570, 572, 597] .Then growth continues from the edge of a step to the (0001) terraces, where the graphene layer interacts with the surface and becomes the buffer

layer. Studies show that the graphene layer first covers the steps with larger terrace [596]. A critical issue is to fully cover the substrate surface by a buffer layer before lifting it up as a monolayer by growing another buffer under it. A good quality buffer layer exhibits a particular pattern in LEED, as illustrated in Fig. IV.10 (b) (see also Fig. IV.1(b), and [538, 546, 563, 598-600]. The pattern for a buffer layer grown in the reactor of Fig. IV.3 at 1850°C and 850 mbar is similar over the whole surface.

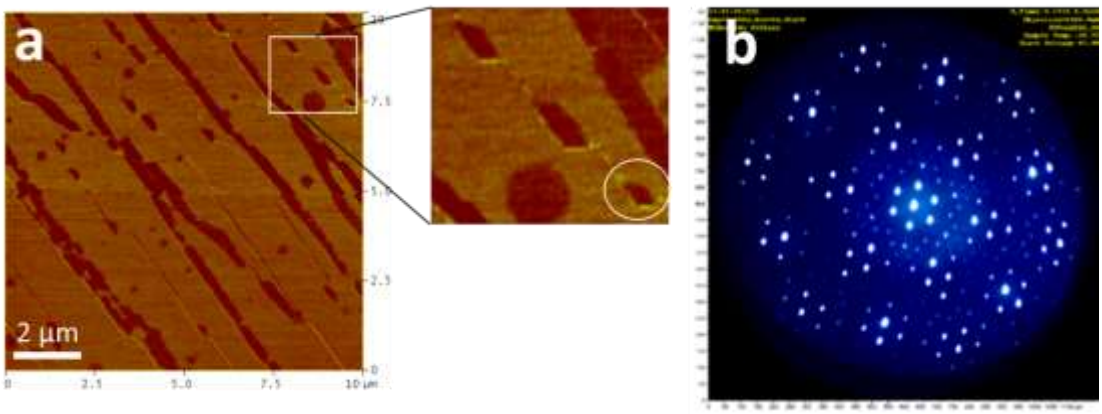

Fig. IV.10. (a) AFM phase images of initial stage of the buffer layer formation, and (b) LEED pattern of the buffer layer (electron energy 60eV) grown under Ar (in the reactor of Fig. IV.3)[596].

Similarly to the amorphous C corral [595], it was shown that the buffer layer can stop the step bunching process (Fig. IV.11(a)) on 4H and 6H-SiC [601]. This means that the surface energy becomes uniform all over the substrate surface after the formation of the buffer layer subsequently resulting in a uniform and continuous monolayer coverage, which doesn't exclude the growth of bilayer at the steps. The T dependence of the buffer layer formation and SLG coverage is sublinear (that is close to linear, not exponential [596]) ,which suggests that the synthesis process is surface kinetics limited on both SiC polytypes (Fig. IV.11(b)) [553, 596]. The results from graphene samples grown under different Ar pressure indicate that there is an optimal Ar pressure yielding a high growth rate of graphene (Fig. IV.11(d)).

The time dependence of SLG and BLG growth under Ar pressure shows that graphene spreads faster on 4H-SiC substrates than on the 6H polytype from the start of the growth, and that monolayer coverage increases approximately linearly with increasing growth time (Fig. IV.11(d)). After the SLG is complete, increasing annealing time does not significantly increase the BLG coverage for both 4H and 6H-SiC polytypes [596].

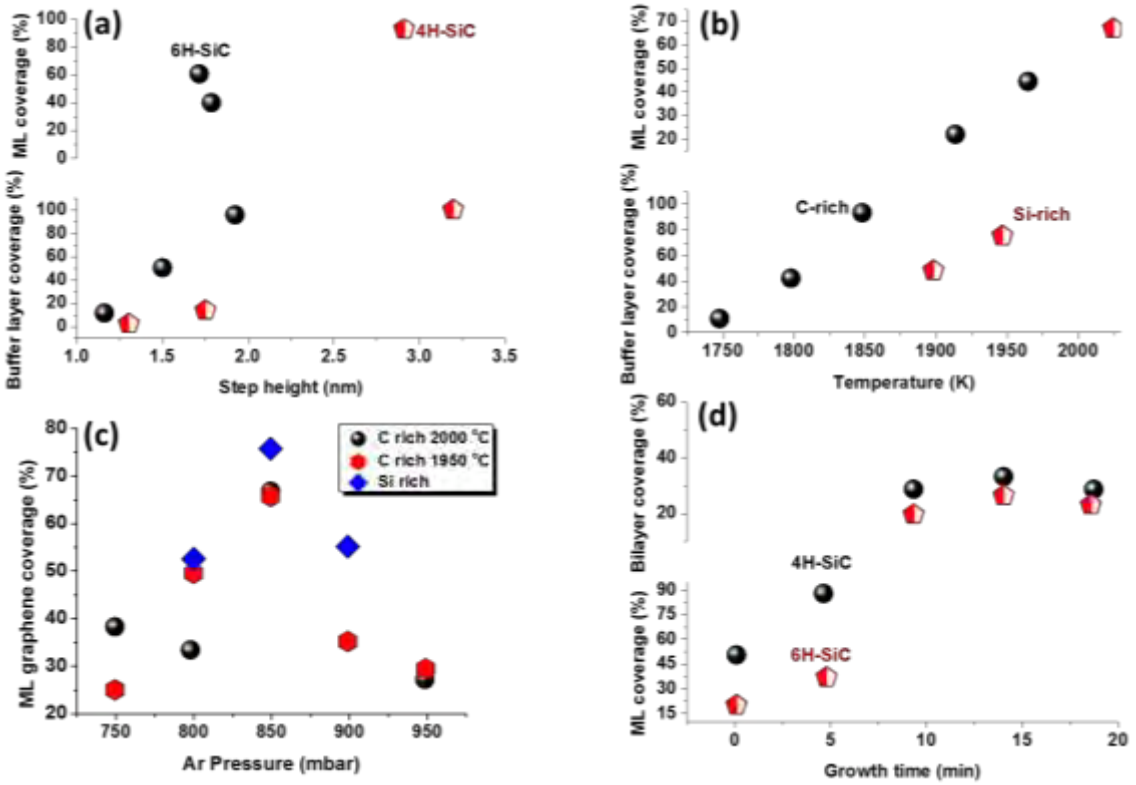

Fig. IV.11. (a)-(b) Buffer layer and monolayer coverage as a function of (a) SiC step height, (b) temperature; (c) monolayer graphene coverage as a function of Ar pressure; (d) monolayer and bilayer coverage as a function of growth time (Figure adapted from ref *[596]).*

Based on the above results, a growth protocol was defined to optimized EG single layer coverage. The result, shown in Fig. IV.12 indicate the growth of ~99% monolayer graphene on 20×20 mm^2 SiC substrates and 99.8 % monolayer for 7×7mm^2 substrate (Fig. IV.12). The EG coverage is determined here by optical reflectance maps [602].

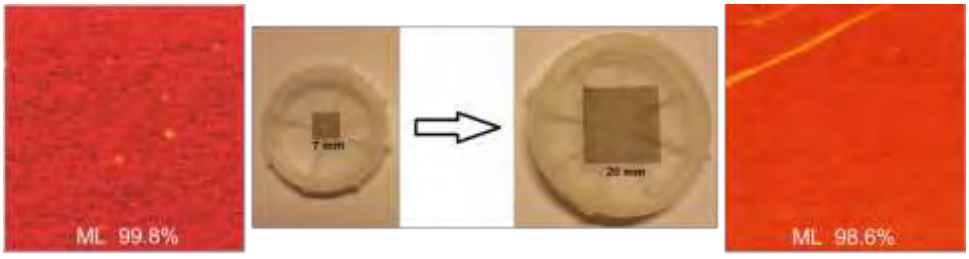

Fig. IV.12. Size increase of monolayer graphene samples from 7×7 mm^2 to 20×20 mm^2. The size of reflectance maps (red scale) are 30µm x 30µm [596].

The preliminary results for graphene on 4-inch SiC wafer showed that the growth rate on the edge of the wafer is higher than in the centre, due a faster Si escape at the wafer edges [549]. Fig. IV.13 shows the recipe for growth of monolayer EG on large area substrates, including on 4 inch SiC wafer. These operation conditions assume different temperature ramps up to 1150°C and to the growth temperature, according to Fig. IV.13.

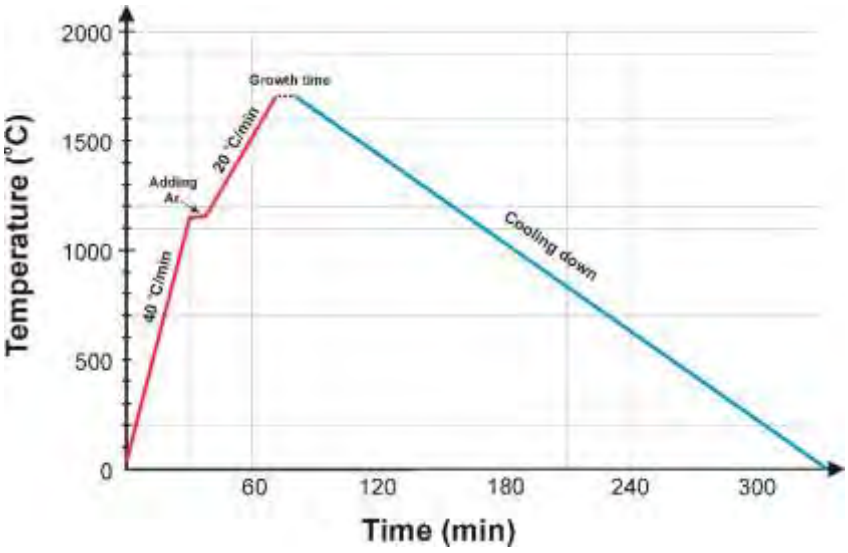

Fig. IV.13. Temperature-time plot for the growth of epitaxial SLG on 4 inch substrates under Ar [596].

Growth on SiC off-axis cut surfaces

Graphene layers are best grown on 4° and 8° off-axis 4H-SiC (0001) substrates to have the right terrace width for performing step flow growth [603, 604]. A general recipe is provided here [605]. Fig. IV.14 shows a side view of the off-axis SiC substrate used for graphene growth, where the off-axis surface is tilted at a specified angle (off-axis angle) from the basal plane surface toward the [11-20] SiC direction. Controlling the tilt angle allows to change step heights, terrace widths and a growth rates.

A direct comparison of graphene formation on an 8°-off axis (0001) 4H-SiC epitaxial layer and on-axis (0001) 6H-SiC [606], [4], performed by uniform graphitization of 1cm×1cm SiC substrates at 2000°C for 30 minutes (with a base pressure in the chamber of 5×10^{-6} mbar and an argon pressure of 1 atm during the growth) shows that the growth of graphene on off-axis SiC starts from the edge and follows the surface of the large terraces (0.5 to 1 µm width), running parallel to the original steps of the off-axis wafer.

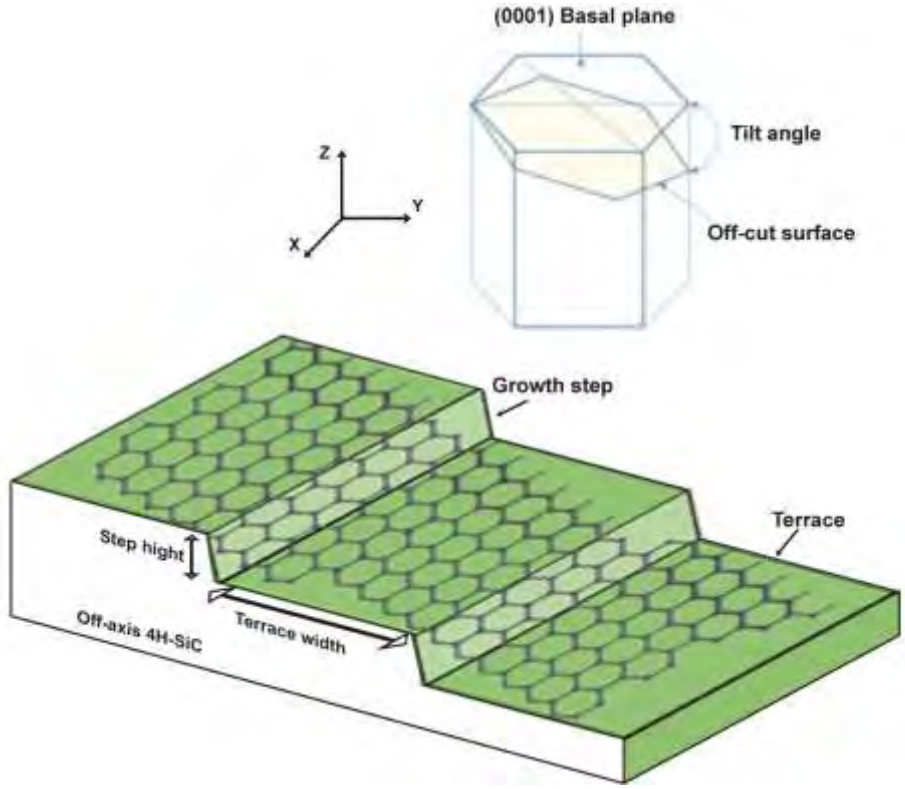

Fig. IV.14. (top panel) A diagram illustrating the off-axis surfaces of 4H-SiC substrate and (bottom panel) a schematic drawing of the off-axis 4H-SiC surface after graphitization [596].

Off-axis samples present significant step bunching after high temperature annealing (RMS roughness =16 nm), while flatter surfaces (RMS=2.4 nm) are obtained on the on-axis sample. A more uniform and homogeneous graphene coverage have been found on on-axis 6H-SiC. The 100 to 200-nm wide terraces of the 4H-SiC (0001) 8° off-axis samples are covered by FLG spreading like a carpet for all growth temperatures in the range 1600 to 2000°C) (growth under Ar) [607], with an increase in the number of layers as a function of temperature (from 0 to 10 layers) (Fig. IV.15).

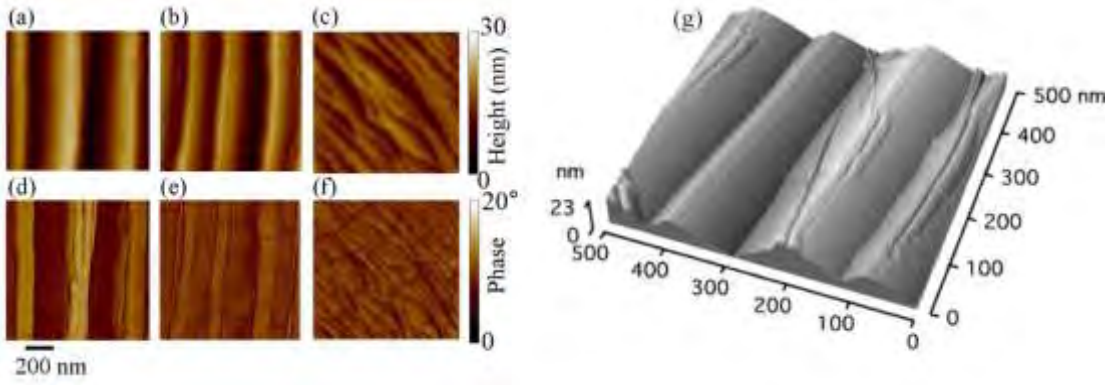

Fig. IV.15. (left panel) AFM images. Effect of graphitization temperature on the surface morphology of the sample 8°-off axis (0001) 4H-SiC: 1600°C (a), 1700°C (b) and 2000°C (c). The phase contrast maps

on the same samples are also demonstrated ((d), (e) and (f), respectively). (right panel) STM image of a sample annealed at 2000°C. (Adapted from Ref [607]).

Similarly to the on –axis surface, the graphitization rate is much higher for the C-face off axis substrates while it is almost an order of magnitude smaller for the Si-face on-axis substrate compared to off axis substrates. AFM analysis showed the presence of the steps with different heights. An approx. 0.35 nm and an approx. 1.1 nm step height can be associated to one and three graphene layers, respectively, over the substrate or stacked over other graphene layers [553]. In fact, like for the (0001) on-axis face, the graphitization starts from the step edges and propagates gradually to the centre of the terrace [553-555, 608]. In this case, the C atoms at terrace kinks and step edges have a lower coordination number, thereby leading to an easier breaking of the bonds at these sites. For this reason, the probability of SiC decomposition and further surface diffusion of C atoms is increased and graphitization of the SiC surface occurs [608]. Regarding the growth kinetics, anisotropy of the Si desorption rate is always present and, thus, different SiC steps have different evaporation rates [553]. In addition, increase in the miscut angle increases the step density, thereby leading to an increase in graphene thickness at this region [553].

Another interesting finding (see Fig. IV.15-right) is that the presence of the atomic steps leads to the formation of pleats similar to the MEG on the 4H/6H on-axis C- face (approx. 1 to 2 nm high and 10 to 20 nm wide) preferentially oriented in the direction perpendicular to the step edges of the SiC terraces (Fig. IV.15(e) and (f)) [607]. Such a parallel orientation of pleats is particular to EG grown on a vicinal SiC surface, while for EG grown on on-axis 4H-SiC it is characterized by a preferentially hexagonal mesh-like network of pleats interconnected into (often) triangular nodes [539] (see Fig. IV.6(c)).

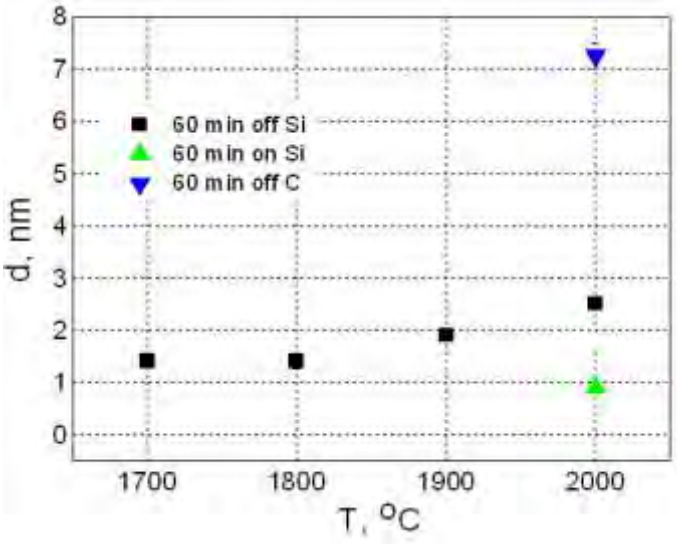

Fig. IV.16. Graphitization thickness vs. T at 60 min for 8 degrees off cut Si- and C-face 4H SiC and for Si-face on axis 4H substrate (Adapted from Ref. [566]).

Growth on non-polar surfaces SiC

The presence of the buffer layer on the Si-face is often argued to degrade the electronic properties of the monolayer above it [609-612]. Quasi -free standing graphene, where the buffer layer is converted into monolayer graphene by intercalation and will be discussed below. An alternative to intercalation is the direct graphitization of non-polar SiC surfaces where there is no buffer layer [613, 614], or to master the delicate graphitization on monolayer on the C-face, where high mobility are measured [556].

According to the crystallography of the hexagonal family of SiC, there are three non-polar planes available for graphene formation: the *m*-plane ($1\bar{1}00$), *a*-plane ($11\bar{2}0$) and *r*-plane ($10\bar{1}2$) (for instance [614]) . Fig. IV.17(a, b) shows the possible polar and non-polar SiC planes for graphene growth. In addition, the growth of graphene can be performed using thermal decomposition of (001)-oriented cubic silicon carbide [614]. However, the commercial production of 3C-SiC substrates is limited, and in contrast to the 4H and 6H- SiC, large single crystals 3C-SiC are not available. Polycrystalline 3C-SiC are often grown as epilayers on SiC or on Si-wafers. Fig. IV.17(c, d) demonstrates the important crystallographic planes in the cubic structure of SiC.

Synthesis of graphene on on-axis (001) cubic SiC substrates can be performed at T above 1800°C for 20 min in a C rich atmosphere [614]. To provide reliable control of graphene formation a low growth rate (about one monolayer per five minutes) should be maintained, which is realized in a close crucible at a Ar gas pressure of 800 mbar.

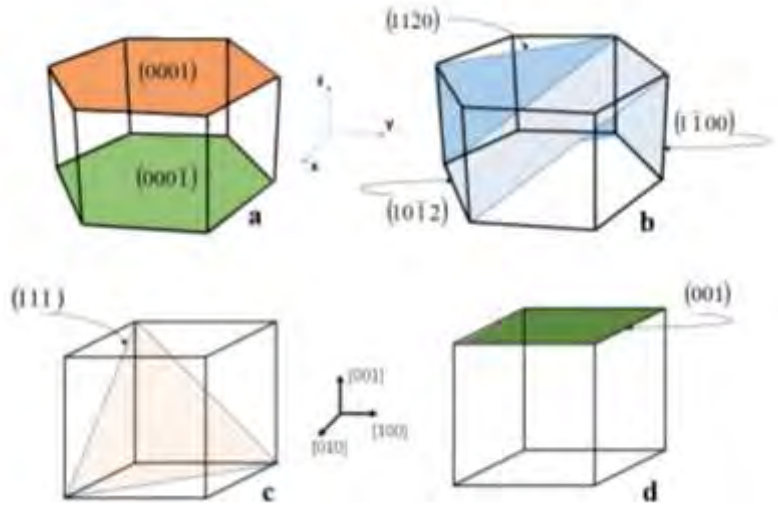

Fig. IV.17. Principal crystallographic planes of the hexagonal (a, b) and cubic (c, d) SiC.

Optimization of parameters (for example, lowering the growth T from 2000°C to 1800°C) can be an effective tool for obtaining EG layers with desired thicknesses (from MEG to FLG) and domain sizes of about of 100 nm. Fig. IV.18 shows the LEEM images of graphene before and after optimization i.e at T = 1800°C in the reactor of Fig. IV.3.

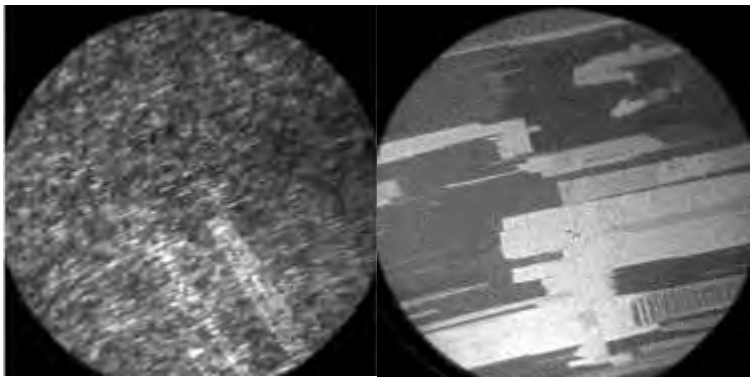

Fig. IV.18. LEEM images of graphene grown on (001) cubic SiC before (left panel) and after optimization (right panel). In the first case, the graphene thickness is 4-5 ML, while optimized growth allows to obtain 1-3 ML graphene with increased domain size up to 10 µm. Adapted from [615].

A (001) cubic SiC substrates with rather flat surface and low surface roughness (rms 2nm) obtained by substrate polishing (rms 0.6 nm) promotes growth of more homogeneous EG with large domain sizes as shown in Fig. IV.18. Growth on (1-100) 6H-SiC resulted in non uniform graphene coverage exhibiting areas of fragmented graphene and some micrometre large areas (Fig. IV.19 - left). Similar results are obtained in [616] for the (11-20) plane (Fig. IV.19 - right).

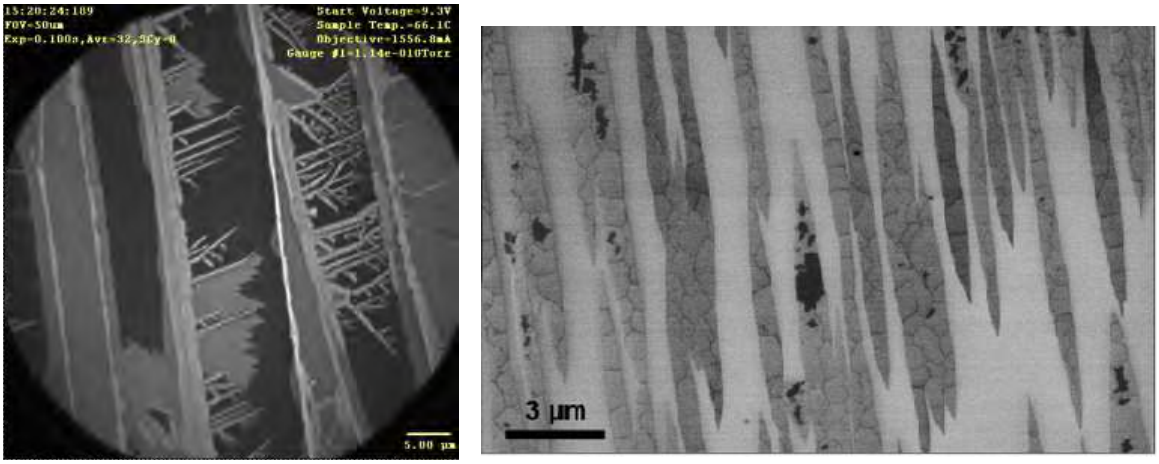

Fig. IV.19. (left) LEEM image of graphene grown by thermal decomposition at 1900°C on (1-100) oriented 6H-SiC substrates, scale bar 5 micron, Adapted from ref [596]. (right) SEM image of graphene grown on 6H-SiC (11-20).

Growth on non-polar SiC surfaces is limited by the vertical growth rate (graphene growth on the polar face proceeds laterally) [594]. Such a complicated vertical growth produces scattered islands of EG on the surface with higher density of grain boundaries (see Fig. IV.20). The latter causes a greater amount of Si out-diffusion from the substrate, leading to a thicker (up to 8 layers) subsequent [559] ML growth on the nonpolar faces in comparison to growth on polar faces [559]. As graphene growth on the low-packed non-polar planes is faster than that on the high densely packed non-polar planes, it is assume that the surface density is a key factor limiting Si desorption and the graphene growth rate.

Surface engineering by intercalation

EG grown on SiC(0001), referred EG to as SLG in the following, by sublimation resides on top of a buffer layer [544, 546], as schematically depicted in Fig. IV.21. As a matter of fact, the buffer layer (denoted also by 6√3) is formed at the early stages of heating of the samples, i.e. before graphene is formed, and it has been observed in several experimental studies of of SiC(0001) surfaces [617-620] and also in an atomistic simulation of graphene formation on SiC(0001) [544, 621]. The buffer layer possesses a (6√3×6√3)R30° periodicity with respect to SiC(0001) substrate surface.

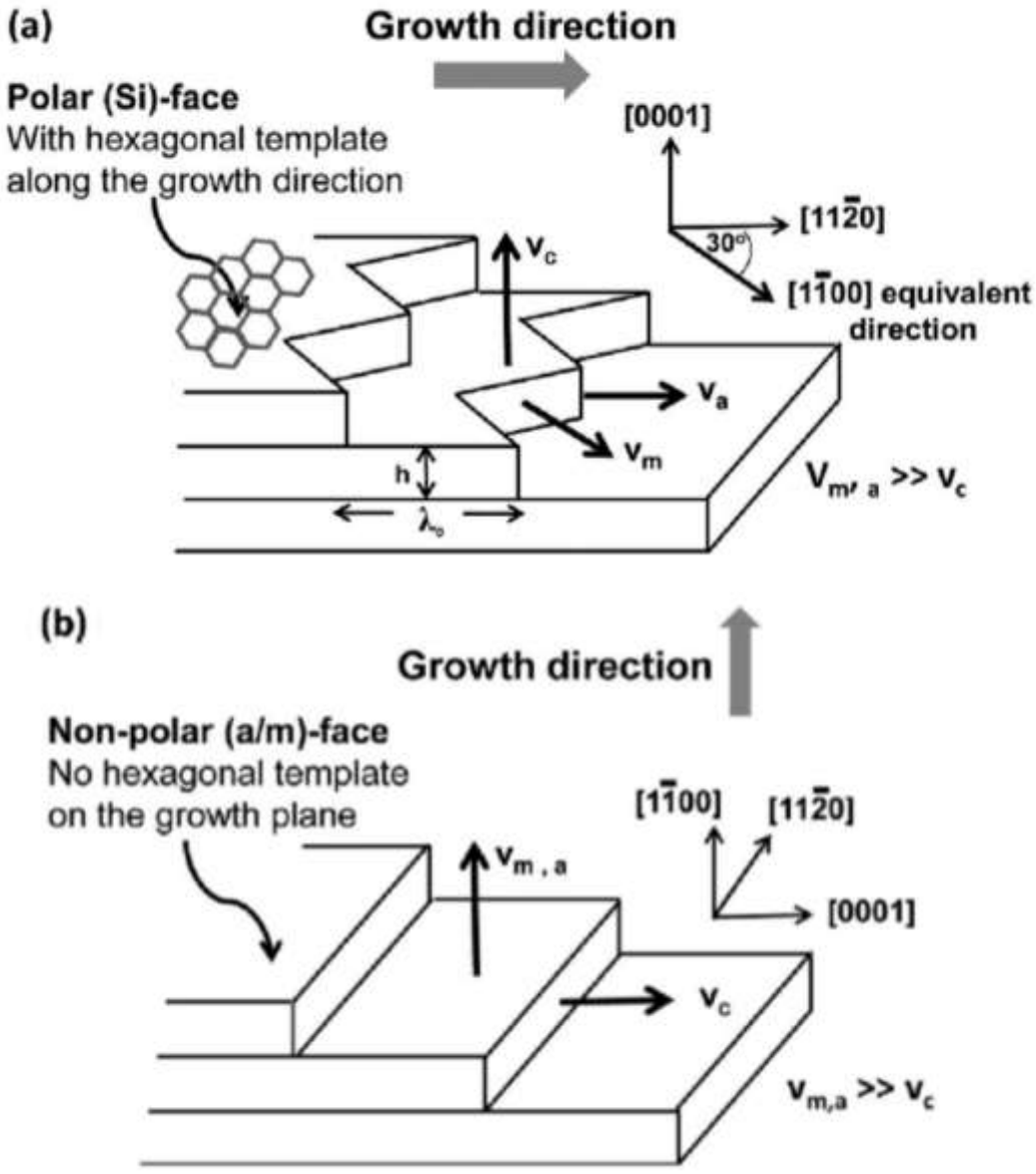

Fig. IV.20. Graphene growth mechanism on (a) the polar (Si) face SiC with offcut toward [11-20] and (b) the nonpolar a/m face with slight offcut along [0001]. The EG growth on the polar face proceeds laterally while the EG growth on the nonpolar face is limited by the vertical growth rate. The zigzag structure shown on the polar face step edge is a consequence of two possible lateral growth directions(.Adapted from Ref. [622])

As already stated, it was demonstrated, that this layer is comprised of C atoms in a graphene arrangement [544, 546, 623]. This means that the structure is made up from C hexagons with a C-C distance like in graphene. The (6√3×6√3)R30° periodicity with respect to the SiC surface corresponds to a (13×13) super cell with respect to graphene. Thus, the super cell contains 169 graphene unit cells. Due to a hybridization of states of the C atoms of the buffer layer with states from the SiC substrate surface, it lacks the typical π-bands of graphene and therefore has no Dirac cone [546]. On the other hand, the σ-bands of the buffer layer are fully developed and indistinguishable from those of graphene [546]. These observations are in agreement with theoretical studies of such a structure [544, 624].

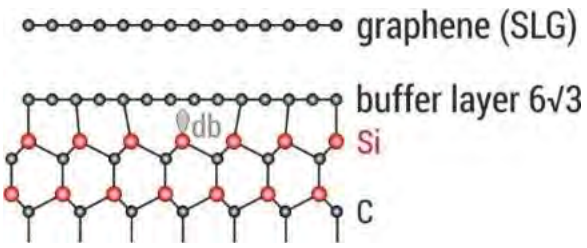

Fig .IV.21. Schematic view of epigraphene on SiC(0001), also referred to as SLG. The graphene layer resides on top of the buffer layer. The buffer layer is structurally equivalent to graphene but strongly bound to the SiC substrate. Dangling bonds (db) may be present due to the lattice mismatch between graphene and SiC. Drawing not to scale (After [598, 625]).

The buffer layer (6√3) induces electron doping in SLG. Typical values for the charge carrier density in SLG are around $n \approx 1\times10^{13}$ cm^{-2} [543, 626-629]. The buffer layer is also partly responsible for the relatively low charge carrier mobility μ and its temperature dependence [611]. Furthermore, the reduction in spin transport in SLG is attributed to the buffer layer [609]. Typical values for the charge carrier mobility are $\mu \approx 1000$ cm^2/Vs at $n \approx 1\times10^{13}$ cm^{-2} and $T = 300$K and $\mu \approx 2000$ cm^2/Vs at $n \approx 1\times10^{13}$ cm^{-2} and $T = 25$K [538, 543, 611, 630, 631]. Note that the mobility in graphene depends on the charge carrier density (see methods of characterization Section IX).

The structural similarities between the buffer layer and graphene suggest that it should be possible to convert the former one into the latter by cutting the bonds between the buffer layer and the substrate through intercalation, as depicted in Fig. IV.22 schematically for the case of hydrogen. Similar procedures have been studied before for graphene (previously called monolayer graphite) on metal surfaces like, e.g., Ni(111). In this case, different metals like Au, Yb, or Cu were intercalated between the metal substrate and graphene [632]. Indeed, several authors showed that different elements can be intercalated between the buffer layer and the SiC substrate. For example, the intercalation of hydrogen [563, 598-600, 611, 633-636], oxygen [637-640], fluorine [641, 642], nitrogen [643], silicon [644, 645], germanium [646, 647], gold [648-651], copper [652], lithium [653, 654], sodium [655] and subsequent transformation of the buffer layer into graphene have been confirmed.

For applications, it is important that the intercalated species does not give rise to electronic states at the Fermi level since these would short-circuit the graphene layer on top of it. This is the case for hydrogen which saturates the SiC(0001) surface with Si-H entities.

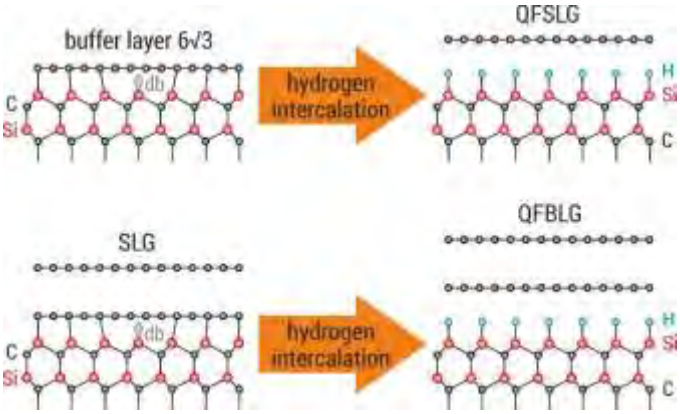

Fig. IV.22. Schematic view of the conversion of the buffer layer into quasi-freestanding graphene (QFSLG) on H-saturated SiC(0001) (also referred to as SiC(0001)-H) and of monolayer graphene on the buffer layer (SLG) into quasi-freestanding bilayer graphene (QFBLG) on SiC(0001)-H. After [598, 625].

The doubly filled bonding and empty anti-bonding Si-H states are located below and above the valence band minimum and valence band maximum, respectively, leaving the surface electronically passivated [656-658]. A similar situation can be expected for oxygen and fluorine passivation of the SiC(0001) surface.

The first study of the intercalation of hydrogen under the buffer layer on SiC(0001) was reported by Riedl et al. [598, 599] who annealed SiC(0001) substrates covered by the buffer layer in one atmosphere of hydrogen at T between 600°C and 1000°C. Similar processes can be employed to intercalate hydrogen under the buffer layer even if an additional graphene layer already exists on top of it [598, 599, 611, 635, 659-661], although the exact conditions may vary. In this case, SLG becomes a quasi-freestanding bilayer graphene (QFBLG) (see Fig. IV.22).

The successful decoupling of the buffer layer and conversion into so-called quasi-freestanding graphene (QFSLG) is confirmed by LEED, ARPES, XPS and LEEM (a description of some of these techniques is given in section IX). Figure IV.23(a) shows typical XPS spectra of the C1s core level of various samples [662]. The spectrum of the buffer layer is comprised of three components. S1 and S2 are caused by the C atoms of the buffer layer [546]. In addition, a component due to C atoms in the SiC substrate is visible. These three components are also seen in the spectra of SLG, BLG and TLG indicating that the buffer layer forms the interface. Upon H-intercalation, the buffer layer is converted to QFSLG which is evident from the disappearance of the components S1 and S2 and the formation of a graphene-related component. This is also the case when SLG/BLG is transformed into QFSLG/QFTLG). The component of the SiC substrate is shifted to lower binding energy due to a change of surface band bending. Fig. IV.23(a) shows examples of the band structure near the K-point of the hexagonal Brillouin zone as measured by ARPES (see Section IX for an introduction) [662] for SLG, BLG, QFSLG and QFBLG.

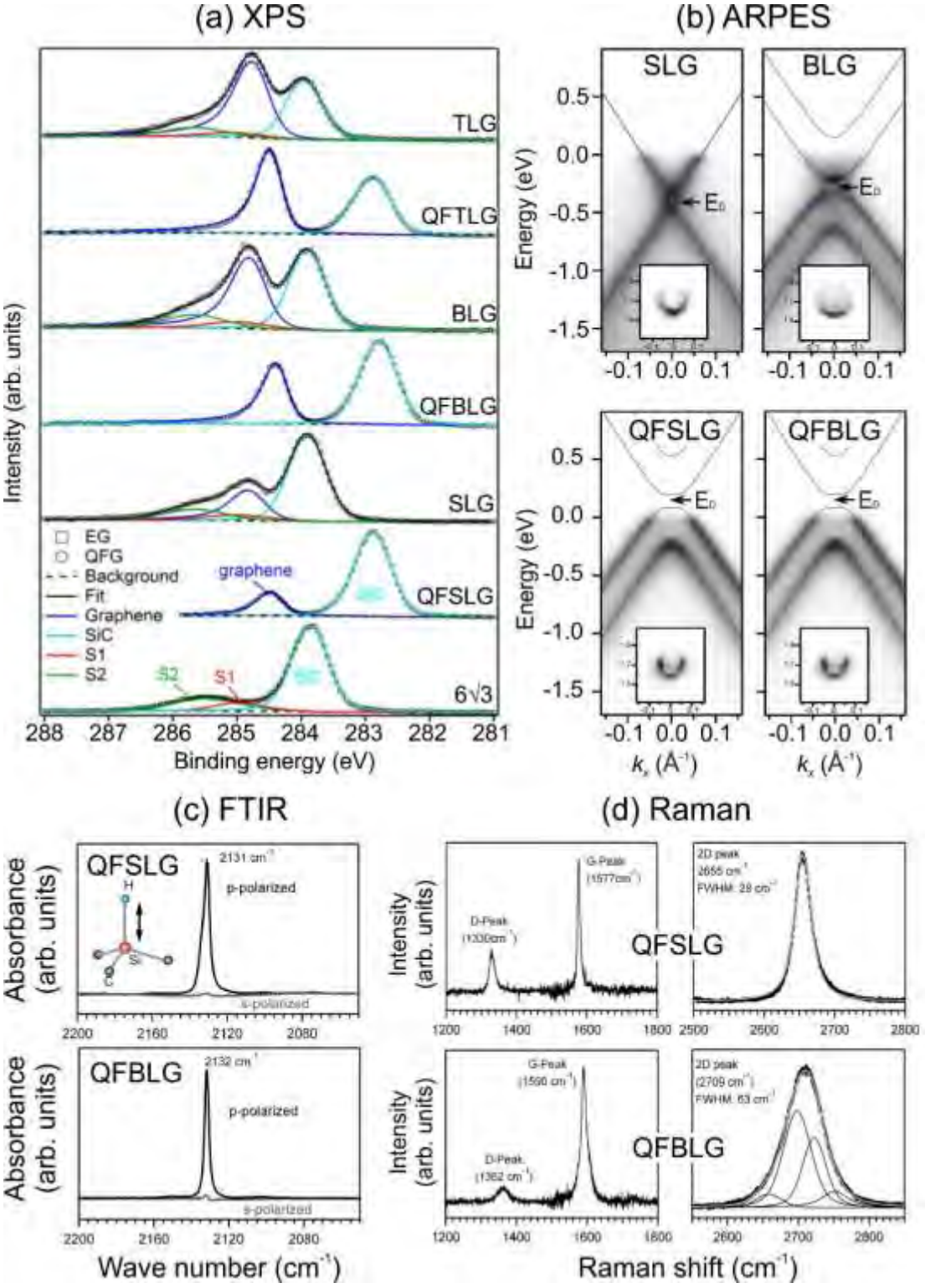

Fig. IV.23. (a) C1s core level spectra of the buffer layer, QFSLG, SLG, QFSLG, QFBLG, QFTLG and TLG. The H-intercalation leads to a disappearance of the buffer layer components (S1, S2) and an increase of the graphene-related component. The signal due to SiC shifts to lower binding energy due to a change of band bending. (b) ARPES intensity maps vs. electron energy and momentum of SLG and BLG on the buffer layer as well as QFSLG and QFBLG on H-terminated 6H-SiC(0001). (c) Si-H stretch mode of the H-saturated SiC(0001) surface below QFSLG and QFBLG. (d) Representative Raman

spectra of QDSLG and QFBLG. (a) Adapted from [662]; (b) adapted from [663]; (c) and (d) adapted from [659].

The charge carrier type is changed from electrons in SLG/BLG on the buffer layer to holes in QFSLG/QFBLG on the H-terminated (0001) surface of hexagonal SiC polytypes [598, 599, 611, 659, 662, 663]. This is due to the spontaneous polarization of hexagonal SiC [663, 664] , which varies with the polytype due to their different ratio of hexagonal to cubic stacking sequences [663-665]. For semi-insulating 6H- and 4H-SiC(0001)-H substrates hole densities of 6.2×10^{12} cm^{-2} and 8.6×10^{12} cm^{-2}, respectively, as determined by ARPES in good agreement with theoretical predictions [663-665]. In the case of QFSLG on n-type doped cubic 3C-SiC(111)-H a slight electron doping is observed, which agrees with the fact that this SiC polytype has no spontaneous polarization. In this case the excess electrons in QFSLG is due to alignment of the Fermi levels as described by the Schottky model for metal-semiconductor interfaces [663]. Speck et al. have provided evidence for the hydrogen at the interface by measuring the Si-H stretch mode vibration using FTIR absorption spectroscopy as shown in Fig. IV.23(c) [611, 659]. This was later confirmed by surface enhanced Raman spectroscopy [666, 667]. Raman spectroscopy also provided evidence for the conversion of the buffer layer to a QFSLG [611, 659, 666, 667]. In the case of QFSLG a narrow 2D line is observed while for QFBLG a broad 2D line indicative for AB stacking is found (see Fig. IV.23(d)). Electronic transport studies on simple Hall bar structures and FET have shown that QFSLG on 4H- of 6H-SiC(0001)-H exhibits a higher charge carrier mobility (typically of the order of 4000 cm^2/Vs) than SLG on the buffer layer and that it has a considerably reduced temperature dependence [611, 659, 660, 668-673].

Decoupling of the buffer layer from the SiC substrate and saturation of the SiC(0001) surface with hydrogen can be carried out in an apparatus depicted in Fig. IV.24 [674], initially designed for the hydrogenation of SiC surfaces [658, 674, 675]. The hydrogen intercalation process occurs inside a quartz glass tube that is held between two stainless steel vessels (R1 and R2). The chamber part R1 is connected to a turbo molecular pump (TMP1) that allows evacuating the apparatus to a base pressure of around 2×10^{-8} mbar. A gate valve (GV1) is placed between the recipient R1 and the turbo pump TMP1. A load lock, which can be evacuated with a second turbo molecular pump (TMP2) is connected to the recipient R1 via another gate valve (GV2). With the help of the load lock, the SiC sample can be placed into the chamber without breaking the vacuum. For this purpose two magnetic transfer rods are used as shown in Fig. IV.24. A single roughing pump is used to provide roughing vacuum for the turbo pumps. The roughing pump is also connected to the recipient R1 via the valve V3. Hydrogen is purified by a palladium purifier and fed through a mass flow controller (MFC) to recipient R2. The latter one also provides support for a graphite block sitting in the centre of the quartz tube. On that, the sample holder with the sample is placed with the help of the transfer rod. The centre of the glass tube is located in the centre of a light oven, which uses five halogen bulbs with a maximum total power of 5kW to heat the graphite block together with the sample holder and sample in a contact-less manner. The T of the graphite block is monitored by a thermocouple. Temperature control is accomplished via an Eurotherm controller, that reads the thermocouple and adjusts the power to the halogen lamps.

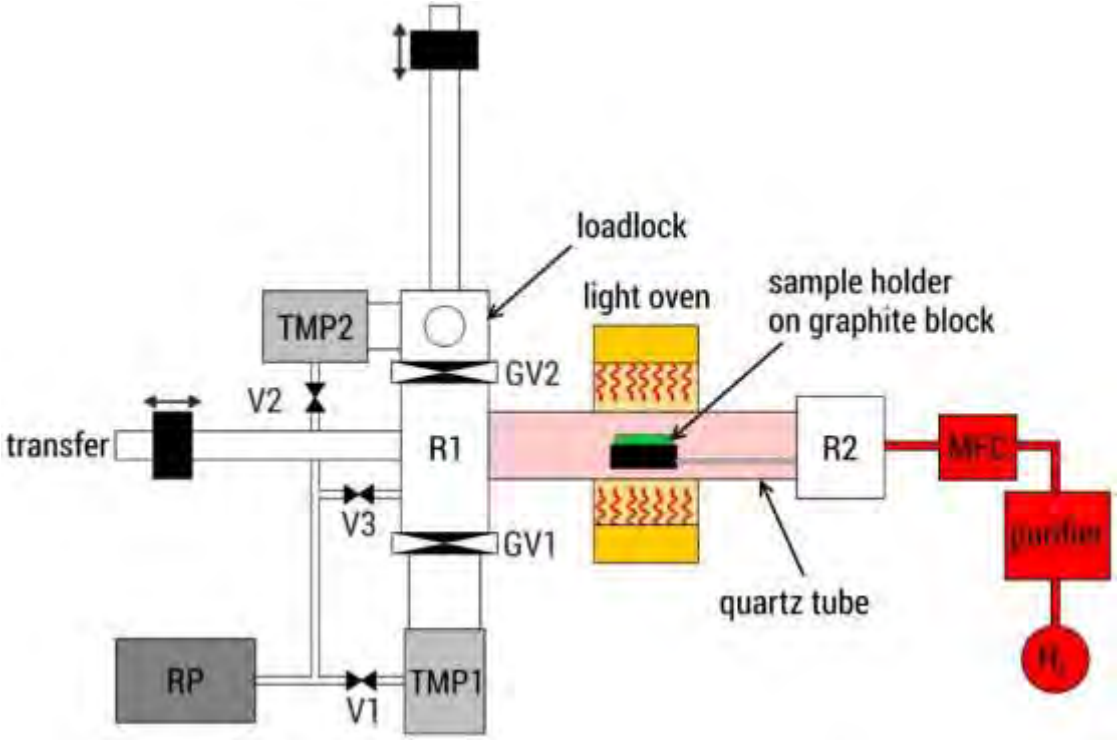

Fig. IV.24. Sketch of the apparatus used for intercalating hydrogen between the buffer layer and the SiC(0001) substrate [611, 659, 663]. After [674].

In order to intercalate hydrogen, the samples with a typical size of 5 mm × 10 mm are clamped on a sample holder which is made from Mo using strips of Mo foils and Mo screws. The sample holder is placed in the load-lock, which is then pumped down using turbo pump TMP2. After the load-lock has reached a vacuum better than ~ 10^{-6} mbar), the sample is inserted into recipient R1 by lowering the vertical transfer rod. The sample holder is grabbed by the horizontal transfer rod and placed on the graphite block. With both gate valves GV1 and GV2 and roughing valves V1 and V2 closed, hydrogen is let into the chamber by adjusting the flow controller to ~ 3 slm. When the target pressure is reached, the flow is reduced to ~ 1 slm and valve V3 is opened in order to adjust the pressure at a constant value of ~ 900 to 960 mbar. Then the light oven is powered up until the desired sample temperature is reached. The sample T and the hydrogen pressure are then kept constant for a certain time. Typical process parameters are compiled in Table IV.1 [611, 659, 663]. After the sample has been annealed in hydrogen, the system is cooled down, the hydrogen flow is turned off and the hydrogen is pumped away by the roughing pump. When the pressure in the chamber has reached a value of a few mbar, valve V3 is closed and GV1 and V1 are opened to further pump down the chamber. Finally, valve V2 is opened and sample is removed first into the load lock and finally out of the load lock.

Table IV.1: Typical parameters for intercalating hydrogen under the buffer layer [611, 659, 663].

Process	Sample temperature in °C	Hydrogen pressure in mbar	Flow rate in slm	Time
$6\sqrt{3}$ to QFSLG	540 – 560	900 – 960	0.9 – 1.0	60 – 90
SLG to QFBLG	840	900 – 960	0.9 – 1.0	60 – 90

Variations of the above procedure have been reported for the synthesis of quasi-freestanding graphene layers on SiC(0001). Ref [598], reported preparation T in the range from 600 to 1000°C at atmospheric pressure without mentioning the annealing time. Ref [668] annealed in molecular hydrogen to convert SLG to QFBLG. They report a H_2 pressure of 800 mbar, T of 600 to 1200°C, and process times between 30 and 120 minutes. Ref [676] carried out the hydrogen annealing directly after the growth of graphene in an Aixtron/Epigress VP508 Hot-Wall CVD reactor. After graphene growth in Ar at 100 mbar at 1650°C, the sample was cooled down to 1050°C. At this T, the gas is exchanged to H_2 and the pressure is increased to 900 mbar. After 30 minutes, the sample is allowed to cool down to 700°C in H_2. Finally the system is evacuated and the sample is allowed to cool down to RT. Ref. [670] annealed their buffer layer samples in H_2 at a pressure of 1013 mbar and temperatures between 600 and 1200°C for 60 minutes. In ref. [661], QFSLG was produced by annealing in a furnace at 800°C and a H_2 flow of 0.2 slm for 1 h at an unspecified pressure. The process time was 60 minutes the highest charge carrier mobility was observed for an annealing temperature of 700°C. Finally, in Ref. [661] QFBLG formed by annealing Hall-bars made from SLEG at 1250°C in H_2 at a pressure of ~ 33 mbar. Finally, ref [635] employed a plasma source as well as an atomic hydrogen source to convert SLEG to QFBLG. They reported that the plasma treatment induces a certain degree of disorder. Kinetic Monte Carlo simulations performed by Deretzis and La Magna [677] have shed light on the atomistic mechanism of H intercalation of the buffer layer which are in good agreement with experimental observations.

Surface analytical tools such as LEED, XPS, ARPES, LEEM and STM along with FTIR and Raman are ideally suited to characterize the quasi-freestanding graphene layers on H-terminated SiC(0001). Table IV.2 lists several methods together with the expected observation and relevant references.

Table IV.2: Relevant experimental characterization techniques and observations to characterize quasi-freestanding monolayer graphene and quasi-freestanding bilayer graphene on H-terminated SiC(0001).

Method	**Observation**	**References**
Process: buffer layer 6√3 to QFSLG		
LEED	Strong weakening of the superlattice diffraction spots caused by the buffer layer	[598-600]
XPS	Disappearance of the C1s signals related to the buffer layer and appearance of an asymmetric C1s signal due to the quasi-freestanding graphene; Shift of the C1s signal related to the SiC bulk to lower binding energy due to a change of surface band bending (see fig. IV.23(a))	[600, 659, 663]
XPS	Shift of the C1s signal related to the SiC bulk to lower binding energy.	[600, 659, 663]
ARPES	Appearance of a graphene π-band at the K-point of the hex. Brillouin zone with the Dirac point located above the Fermi level (see Fig. IV.23(b)).	[598-600, 659, 663]
LEEM	Transition from a flat LEEM-I(V) curve to a spectrum with one dip.	[600]
STM	Topography image without buffer layer moiré structure.	[623, 662, 670]
FTIR	Appearance of a sharp Si-H stretch mode signal (see Fig. IV.23(c)).	[611, 659]
Raman	Disappearance of the broad Raman spectrum of the buffer layer and appearance of sharp G and 2D bands; 2D band symmetric (see Fig. IV.23(d)); appearance of a Raman loss due to Si-H stretch mode vibration.	[611, 659, 668, 672, 678, 679]
Process: SLG to QFBLG		
XPS	Disappearance of the C1s signals related to the buffer layer and increase of the asymmetric C1s signal due to the quasi-freestanding graphene (see Fig. IV.23(a)).	[598, 635, 659, 663, 668, 676]
XPS	Shift of the C1s signal related to the SiC bulk to lower binding energy (see Fig. IV.23(a)).	[598, 635, 659, 663]

ARPES	Disappearance of the linear π-band of graphene with the Dirac point below the Fermi level and appearance of the two parabolic π-bands of bilayer graphene with the Dirac point located above the Fermi level (see Fig. IV.23(b)).	[598, 659, 663]
LEEM	Transition from a LEEM-I(V) curve with one dip to a spectrum with two dips	[598, 599, 635]
STM	Topography image without buffer layer Moiré structure	[662]
FTIR	Appearance of a sharp Si-H stretch mode signal (see fig. IV.23(c)).	[659]
Raman	Disappearance of the broad Raman spectrum of the buffer layer and change of the symmetric 2D band to an asymmetric 2D band considerably broader than that of QFSLG	[659, 668]

Oxygen intercalation has been suggested to be a means for decoupling of the buffer layer from the SiC(0001) surface by annealing the buffer layer samples [637] in one atmosphere of molecular oxygen at 250°C for 5 seconds, using a special oxidation chamber. In the first approach in [640] the buffer layer samples was annealed in-situ, i.e. directly in the UHV chamber used for XPS and ARPES analysis, at 750°C in ~ 10^{-4} mbar of molecular oxygen. The second procedure in [640] was carried out ex-situ in the same oven discussed above by annealing in O_2 with best results at 270°C at 200 mbar. The Raman spectra, however, demonstrated that both processes lead to the formation on numerous defects in the graphene. In ref [638] the oxygen intercalation to transform SLG into a bilayer graphene is carried out on an oxide-covered SiC(0001) surface. They annealed the SLG samples in air at 600°C for 40 minutes. A heat up ramp of 50° per minute was used. They confirmed the decoupling of the buffer layer and the formation of a high quality BLG.

In ref. [639] buffer layer samples as well as SLG were annealed up to 500°C and 650°C, respectively, in a water vapour in order to decouple the buffer layer by oxidation of the SiC(0001) substrate surface. Raman spectroscopy indicated numerous defects in the QFSLG formed by decoupling of the buffer layer. However, like in ref [638], the QFBLG formed by treating SLG showed a negligible D band, indicating also high quality of this material. This was also evident from Hall effect measurements, which indicated a mobility of 790 cm^2/Vs at a rather high hole concentration of 2×10^{13} cm^{-2}. Apparently, while oxidation of the SiC interface by oxygen or water intercalation leads to highly defective QFSLG, this technique appears to be promising for the synthesis of decoupled QFBLG on SiC(0001). One may speculate that the buffer layer, which is highly corrugated and in which C atoms are partially sp^3 hybridized [680], is more prone to be attacked by the oxygen during the

intercalation process. On the other hand, in the case of SLG, the buffer layer is protected by the graphene layer on top of it.

Intercalation with other elements has also been studied; Contrary to Si, that intercalates only at temperature above 800 °C through migration at graphene domain boundaries and other defects, Li [653, 654] was found to penetrate into the C layer already at room temperature through the formation of Li-compounds. Na partial and inhomogeneous intercalation occurs already at room temperature directly after deposition, although most of the Na remained on the surface and formed Na droplets. Na intercalation is promoted both by electron/photon beam exposure and by moderate annealing at about 100 °C. Annealing at higher T results in de-intercalation and Na desorption from the surface [655]. Other elements intercalation would be appealing, such as nitrogen, that is predicted to provide charge neutral QFSLG [681]

Finally, we briefly mention studies regarding Ge [646, 647] and Au [648-651] intercalation between the buffer layer and the SiC(0001) surface. In both cases, the preparation is performed using the following common scheme. First, a thin layer (up to 5 monolayers) of the intercalant (Ge or Au) is deposited on top of the buffer layer using thermal evaporation. Then, the sample is annealed in UHV to induce the intercalation process. The properties of the GFSLG formed by intercalation depend on the amount of material present at the interface. For Au two phases were observed [648]: a highly n-type doped phase with the Dirac point located approx. 0.9 eV below the E_F for 1 monolayer Au at the interface and a weakly p-type doped phase with the Dirac point at 0.1 eV above E_F for one third of a monolayer Au at the interface. Spin-resolved ARPES indicated a Rhasba-type spin-orbit coupling in the π-band of QFSLG at energies where it interacts with Au bands [651]. In the case of Ge [646], an n-type doped QFSLG is obtained when 1 monolayer of Ge resides at the interface while a p-type doped QFSLG is observed when 2 monolayers of Ge are intercalated. Interestingly, the respective hole and electron concentrations in the QFSLG amount to $p = 4.1 \times 10^{12}$ cm^{-2} and n = 4.8×10^{12} cm^{-2}. This means that the shift of the Dirac point with respect to Note that a mixed phase can also be prepared in which n- and p-type regions coexist.

Structured growth

The fact that growth starts at a step edges on the SiC(0001) face (see above), can be used to produce graphene nanostructures for electronics. Masking methods, for selective epigraphene growth using AlN [682], SiN [683] and amorphous C masks [595] with tens of nm precision have been proposed. The template growth method on sidewalls of SiC trenches [556, 567, 570, 571] is described below. It circumvents the detrimental effect of traditional plasma etching methods [684, 685] and resulting sidewall nanoribbons show RT ballistic transport properties [572].

The idea is to tune the EG growth parameters so to stop the graphene growth just as graphene covers the step sidewalls. Steps can be either natural steps obtained by step bunching at the SiC surface or the sidewall of trenches of various shape etched in the SiC substrate. The width of the ribbon is then set by the step height and the angle with the basal (0001) plane (about 27 degrees). Upon heating in the 1400°C -1600°C range for graphitization, the SiC steps flow to produce the equilibrium facets at that particular temperature. For instance for ribbons oriented along the

graphene armchair direction, stable facets are found at (-1 1 0 7), (-1 1 0 6), and symmetrically at (1 -1 0 7), (1 -1 0 6) [686].

For growing graphene on natural steps, SiC surface treatments are used to organize the step-terrace structure prior to graphene growth. These include [567] annealing the chemically and mechanically processed polished SiC substrate in vacuum, in Ar, in a face-to-face SiC configuration or with a refractory capping grid [595]. The key is to obtain a stable step configuration prior to graphene growth. The T for surface structuring are chosen according to the background pressure to prevent graphene growth, that is 1100˚C-1200˚C in vacuum, 1300˚C-1700˚C in Ar or face to face. Step bunching by annealing in these controlled conditions produces arrays of straight steps and terraces with uniform width and height (Fig. IV.25). The step structure depends on the polytype [687] the local miscut of on-axis SiC wafers (see above), which is may vary up to +/- 0.1˚ across the whole wafer, and may be other factors such as the heating method. A complete systematic study is still lacking in the literature. After treatment, the terraces are up to 10-30µm in width and extend over tens of µm in length (Fig. IV.25). Examples of ribbons grown on the sidewall of natural sidewall steps (obtained by step bunching) and on etched trenches are shown in Fig. IV.25.

In a more controllable manner, nano-structured graphene can be grown on structures of various shapes etched in SiC(0001) [688]. Trenches can be etched for instance along the 4H-SiC(-1-120) and 4H-SiC(1-100) directions to produce graphene ribbons along the zigzag or armchair orientation, respectively owing to the epitaxial orientation of graphene on SiC (see Fig IV.1a). For this, an e-beam or a photoresist is patterned on SiC(0001). Plasma etching is used to etch SiC with the resist as a mask for shallow etching; various recipes have been successfully used [567, 570-572], for instance reactive ion etching (RIE) (using SF_6 and O_2 ratio 20:7) with etching rates of around 0.3 nm/sec, or 43%SF6/23% O2/33% Ar RIE operating at 30 mtorr where the radiofrequency power was tuned to give a SiC etch rate of 0.8nm/s [568], allowing fine control of the etch depth. For deeper etching, a Ni mask can be used, that is evaporated on the resist and lifted up. The Ni mask is etched away after the RIE etching by an ultrasonic treatment in nitric acid [570].

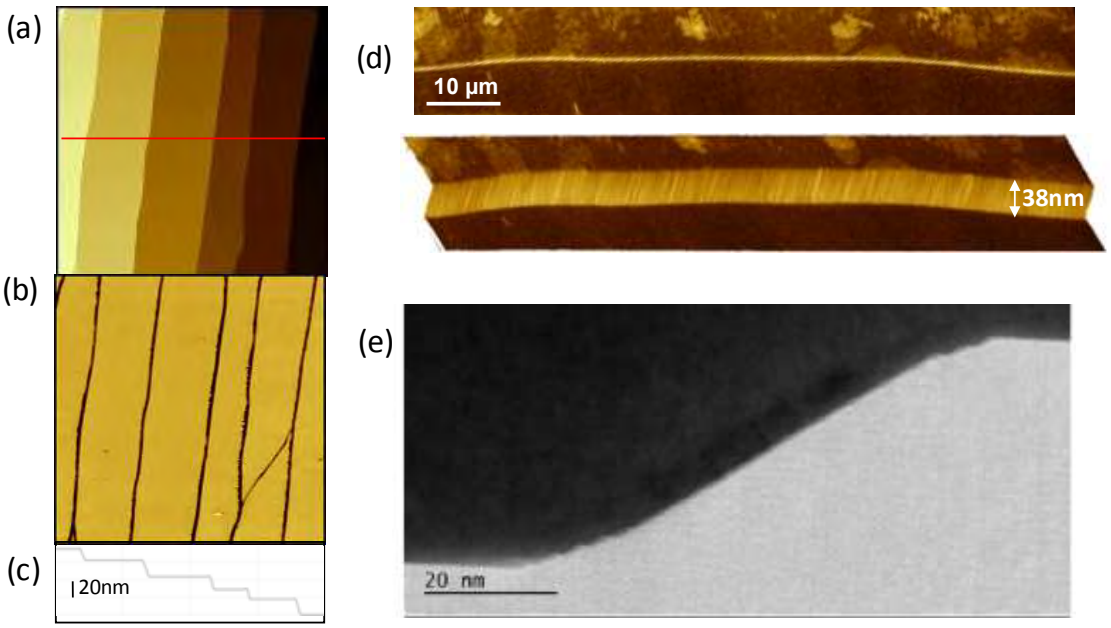

Fig. IV.25 Examples of sidewall ribbons (a-d) on natural steps, 20 nm high. (a) topographic AFM image, (b) lateral force AFM image, revealing graphene (dark) on the sidewall, (c) profile of the steps along the red line in (a)[567]. (d) example of a long isolated natural ribbon more that 80 µm long, 38 nm high (top) lateral force AFM – the ribbon is bright; (bottom) three dimensional rendition by combining topography and lateral force. (e) cross-sectional TEM high resolution image of a sidewall trench etched in SiC, recrystallized at a stable facet angle of ~30°, over which a MEG is draped (Figure adapted from : (a-c) Ref [689], (d)[689]).

The resist pattern is transferred to the SiC as a template for graphene growth, and complex interconnected graphene structures can be designed (see Ref [556, 570, 688] for instance), including pillars to produce nanometric graphene rings [556]. Although trench of any height can be etched, well-formed graphene ribbons are best grown on sidewalls 15-35 nm deep. This is because shallow trenches (≤10nm) tend to get washed out upon annealing in the CCS furnace and deep trenches tend to break into multiple facets revealing multiple parallel ribbons [567].

In the CCS furnace, the structured SiC chip is then heated to 1100˚C to allow the vertical etched sidewalls to crystallize into the equilibrium facets [690] onto which the graphene ribbons grow around 1500-1600˚C [570]. The exact temperature and time depend on the specifics of system, such as the Si escape leak in the furnace CCS method [549, 572]. The sidewall ribbons produced this way are ballistic conductors at RT on micrometre distances [572]. Similar sidewall ballistic ribbons have been produced with the same technique, but by a dc current annealing of conducting SiC wafers (6H-SiC N-doped) in an Ar atmosphere of $4x10^{-5}$ mbar (sample clamped by graphite contacts) [572]. Well-ordered crystal facets are forming around 1150˚C, and further annealing to 1300˚C results in growth of extended graphene nanoribbons on these facets [572, 691].

Because the steps in SiC are etched and annealed prior to graphene growth, the facets onto which graphene grows are smooth and atomically defined. This is demonstrated in cross-sectional transmission electron microscopy (see section IX) [689] (Fig IV.25d), and in ARPES (see section IX) [686] where measurement integrating thousands of parallel ribbons grown on sidewall ribbons show sharp graphene electronic-bands.

Ribbons of any nominal orientation can in principle be produced. By design, tens of thousands of sidewall nano-structures can be produced all at once, following the recipes above [556, 570, 686, 688], in particular long straight parallel ribbons [567]. However, sidewalls may in some cases show restructuring after annealing [556, 572, 688] with rounding and faceting [549, 567]. The effects are sensitive to a number of factors such as the step direction, growth condition (both temperature, time, and also possibly the type of heating), the pinning of steps (for instance under amorphous C pads such as in, Fig. IV.9, or by defects), or the polytype. The most prominent feature of the ribbons, that is RT quantized ballistic transport, is a very sturdy result and was observed for straight as well as curved ribbons [572].

Integration with silicon wafers

As mainstream electronics and very large scale integration is based on Si technology schemes to integrate epigraphene with Si wafers have been devised. Two routes have been investigated. The first proposal is based on the standard industrial silicon-on-insulator technology, where a thin monocrystalline silicon layer ready for CMOS processing is bonded on top of epigraphene on SiC. Fig. IV.26 shows the principle of the design. This three dimensional integration, inspired by the industrial development of three dimensional integration stacking thin-film electronic devices, realizes the interconnection of the SiC supported graphene platform, altogether preserving the integrity of graphene, with a Si wafer enabling in principle the full spectrum of CMOS processing. Full processing details are published in [692].

The main steps consist in the fabrication of graphene structures (either from patterned EG or from template growth on SiC sidewalls), evaporation of an alumina film by atomic layer deposition that serves as a bonding layer between the SiC and the oxidized Si wafer, wafer bonding in a pressure module and finally splitting of the Si wafer by annealing at 400˚C (smartcut) to leave a thin crystalline Si layer on top. The main advantage of the process is that the graphene growth temperature (1400˚C and above) is not limited by the presence of Si (melting point 1414˚C). The Si wafer resides on top of the SiC wafer and is therefore fully accessible. Finally the stacking of the SiC and Si wafers increases the areal density inspired by the three dimensional stacked layers Very Large Scale Integration Technology.

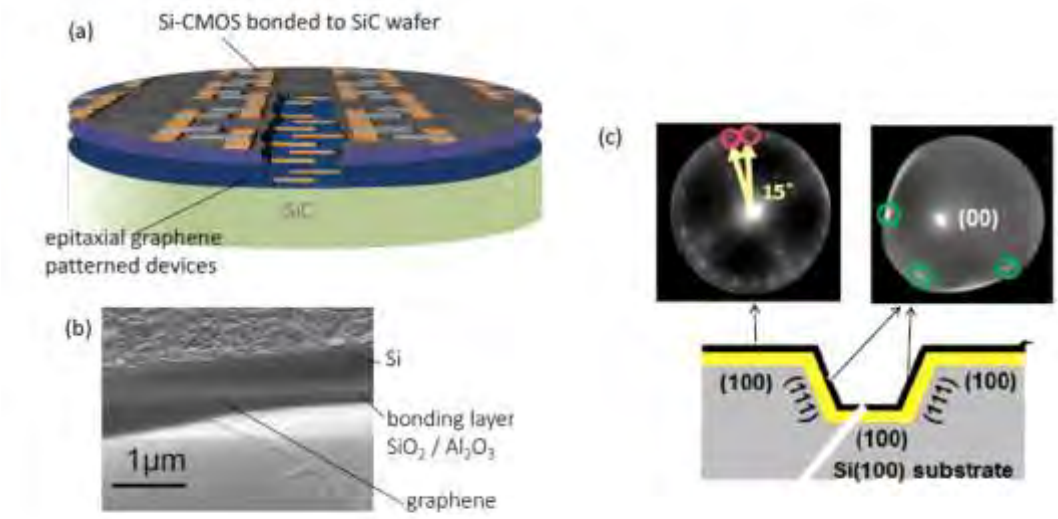

Fig. IV.26. Epigraphene integration with Si wafers. (a) Principle of Si-wafer to graphitized SiC-wafer bonding with the SOI technology, and (b) SEM image of the cross-sectional bonding showing epigraphene at the interface (After [692]). (c) Growth of epigraphene on an epilayer of SiC grown on Si(100), schematics and LEED diffraction, showing rotational order on 3C-SiC(100) compatible with C-termination, and Bernal stacking on 3C-SiC(111) compatible with Si-termination. (From Ref. [693]).

The second strategy, so called Graphene On-Silicon (GOS), takes advantage of the heteroepitaxy growth of 3C-SiC on Si to produce EG on SiC covered Si substrates (3C-SiC is the only SiC polytype known to grow on Si) [693-695] (see Fig. IV.26). The polar Si-terminated 3C-SiC(111)/Si(111) surface grown in UHV shows graphene Bernal stacking with an interfacial buffer layer, similarly to the 4H- or 6H-SiC(0001) surfaces [693]. Conversely, the C-terminated 3C-SiC(111)/Si(110) shows a non-Bernal stacking, with the absence of an interfacial buffer layer, consistent with a C-face termination [693]. The quality of these graphene films is modest as shown by large Raman D peaks. The disorder results from Si diffusion through SiC grain boundary (due to a large ~ 20% lattice mismatch between Si and 3C-SiC) and the lower T allowed for graphene growth (limited by the Si melting point) [696]. Growing an epitaxial AlN layer on Si prior to SiC growth significantly reduces Si out-diffusion and helps grow higher quality EG [693], as well as and interface NiCu layer [697].

IV.2 CVD growth on SiC

High quality EG can be grown by chemical vapour deposition (CVD) on insulating and conductive SiC substrates. In a CVD process, C atoms are provided externally by C gaseous precursors and deposited (with epitaxy) on the SiC substrate, which is different from Si sublimation. The method enables the growth of EG directly on the SiC surface on both Si and C-faces. A CVD process (see section V) typically involves hydrocarbon precursors: methane, propane or acetylene delivered to the reactor by a carrier gas (like Ar). It offers the precision of synthesizing a pre-defined number of C layers [563, 669], including a single layer (buffer layer) on the Si-face of SiC, and is less sensitive to SiC surface defects than the sublimation method [698]. With chemical vapour deposition the nucleation sites for graphene growth are located at the atomic steps, therefore enabling step-flow epitaxy. A CVD process requires high T. However, the lowest T must be higher than the T of thermal decomposition of the gaseous C precursor (around 1000ºC); however, to form graphene of good structural quality requires T ~ 1500ºC to 1800ºC. At that T, SiC substrate decomposition (i.e. silicon sublimation) takes place. Graphene growth by Si sublimation occurs (from about 1300ºC) before the T of CVD growth is achieved. Therefore, the first C layers will be formed by Si evaporation, not by CVD growth. Also, after the CVD growth is finished, uncontrolled sublimation may take place, causing additional carbon layers to grow.

The process presented below [563] is a method for manufacturing graphene by vapour phase epitaxy (VPE/CVD), in which SiC substrates may be used owing to a control of the Si sublimation process. Michon et al. used a combination of hydrogen and propane to balance C supply and etching [591, 695], which provides excellent samples for quantum Hall effect resistance standards [564].

The patented [699] method described below relies critically on the creation of the flow conditions in the reactor that control the Si sublimation rate and enable mass transport of hydrocarbon to the SiC substrate through the argon gas boundary layer. Laminar gas flow over the SiC surface consists of layers moving at different velocities due to the shear stress between adjacent gas layers. Reynolds number (Re) measures the ratio of inertial forces to viscous forces and

consequently quantifies the relative importance of these two forces in a given gas flow [700]. Tuning the value of the Re number ($\mathrm{Re} = \mathrm{Vd}/\nu$), where V is the gas velocity, d is the characteristic dimension of the reactor and ν is the kinematic viscosity, enables the formation of an Ar boundary layer thick enough to confine the Si vapour, and slow down the Si escape that causes graphene to form. The Ar layer however allows the diffusion of hydrocarbon to the SiC surface and, in consequence, the epitaxial CVD growth of graphene on the SiC surface.

When the linear velocity of Ar atoms above the substrate surface is sufficiently high, the flowing gas does not inhibit sublimation, because Si escapes in the Ar carrying gas [699]. If the velocity (that is related to the product of the pressure in the reactor by the flow through the reactor expressed in litre/min) is reduced below a critical value a so-called “stagnant layer” of Ar is created above the surface, while successive gas layers, starting from the substrate, move with increasing velocity [700]. The product of flow rate and pressure to obtain this critical condition depends on the reactor geometry and is adjusted experimentally. In the case of the Aixtron -VP508 reactor, an Ar flow rate of 6 l/min and a pressure of 100 mbar were used in order to completely inhibit sublimation. If the Ar flow is increased to 26 l/min, the stagnant layer thickness decreases, enabling again Si sublimation. Therefore, by adjusting the Arflow rate one can regulate the thickness of the gas layer inhibiting Si escape (the number of atomic gas layers of higher or lower velocity than a typical velocity to start/stop sublimation), thereby regulating the sublimation process efficiency.

Epitaxial graphene was grown by CVD/VPE at 1600^{o}C on both Si-face and C-face of nominally on-axis 4H-SiC or 6H-SiC semi-insulating and conductive chemically mechanically processed substrates. SiC substrate are hydrogen etched prior to the graphene growth to remove a few tens of nm upper SiC, damaged in the polishing procedure. Etching is performed in the same growth conditions as applied for graphene deposition, i.e. T=1600^{0}C, P=100mbar. Hydrogen flow is not as critical as etching time which was adjusted to 5 min.

Best graphene was grown in a pressure of 30 mbar under an argon laminar flow in a hot-wall Aixtron VP508 and an Aixtron G5 reactors, where graphene growth on the 4-inch SiC substrate was also developed. Application of CVD epitaxy to graphene manufacturing enables to obtain thick rotated layers graphene films on a C-face (000-1)SiC. It is also possible to obtain a several graphene layers on a Si-face, which is not easy in the case of Si sublimation, as was described in previous sections.

CVD graphene epitaxy has been studied for both Si-terminated and C-terminated SiC. However, more attention was directed to SiC(0001) since Si-face slower growth kinetics allows a better control of the number of layers. Similarly to the sublimation growth method, the first layer to form on the Si-face is the buffer layer. Hydrogen intercalation decouples the CVD grown buffer layer from the SiC substrate forming a QFSLG . The use of CVD method facilitates the formation of tri-layer epigraphene, however, owing to its high structural quality, hydrogen diffusion through those layers is practically unattainable.

QFSLG exhibits much higher carriers mobility than single layer epigraphene on the Si-face, and temperature independent mobility. This is desirable for high-speed electronics. It is worth noting that the carriers majority changes from electrons for a single layer epigraphene on top of the buffer

layer to holes for QFSLG. The H_2- intercalated mono layer graphene exhibits a few times higher carrier mobility than the un-intercalated one.

QFSLG on the Si-face is also largely resistant to photoresists and solvents applied with standard processing techniques. Importantly, it has been observed that the hydrogen atom presence is maintained up to 700°C, high enough to meet the requirements of high-speed electronics and high-temperature sensing [701]. The intercalation of hydrogen was achieved in-situ in the growth reactor during the sample cool down, by switching Ar to hydrogen at 1100^{o}C at a pressure of 900 mbar. Cooling down in H_2 atmosphere keeps hydrogen atoms trapped between graphene and substrate. Prior to unloading the sample, the process gas was changed back to Ar.

X-ray and TEM experiments show an increase in the interlayer spacing in hydrogenated graphene to 3.6Å-3.8Å, proving that hydrogen actually goes between the C layer and the SiC substrate and increases the separation distance between them, along with decorating Si dangling bonds on the Si face [702].

Raman mapping of the graphene samples are shown in Fig IV.27. The G peak intensity and 2D peak shift Raman maps demonstrate that the SiC surface morphology displaying terraces and step edges, as expected from step bunching at high temperature. The single Lorentzian fitting and the narrow FWHM of 35 cm^{-1} indicate that the areas plotted on the Raman map are indeed monolayer epigraphene. On the steps, the G peak exhibits significant increases in intensity and the 2D peak is blue-shifted and is broader than that of a SLG (FWHM=62 cm^{-1}), indicating bi-layer formation .

The described process leads to the formation of a step-terraces structure. The steps remain within the nm range and are typically limited to 20 nm in height. The step edges follow a general parallel alignment. Regardless of the number of graphene layers on the terraces, there is an additional layer at the step underneath the primary layers. As a consequence, Quasi Free-standing single layer graphene is indeed a bilayer at the step edges, and Quasi Free-standing -bilayer graphene is trilayer [667, 703, 704].

Electrical parameters were measured focusing on large-scale and statistical parameters. The mobility and carrier concentration of multiple as-grown and hydrogen intercalated samples were characterized using Hall effect measurements on 10mm x 10 mm in the van der Pauw geometry in ambient conditions (see section IX). The carrier concentration and electron mobility of SLG were determined as $n_e \approx 1.5\times10^{13}$ cm^{-2} and $\mu_e \approx 1400$-1800 $cm^2\ V^{-1}\ s^{-1}$, respectively. After intercalation with hydrogen: $n_p \approx 8\times10^{12}$ cm^{-2} and on average $\mu_p \approx 6500$ $cm^2V^{-1}s^{-1}$ for 10mm x 10mm ML sample [702].

As expected, the electrical properties differ on the terraces and if there are step edges crossing the device. The step edges prove more resistive and, therefore, introduce a significant anisotropy into graphene electrical [703]. CVD- epigraphene allows the fabrication of a large number of devices (here 320 Hall structures). Excellent performances are achieved, with high mobility exceeding 7000 cm^2/Vs, and a up to 8120 cm^2/Vs in one instance, measured for devices (sizes of 5x5 μm^2 and 10x10 μm^2) located on a single terrace, of widths ranging from 3µm to 15µm. Structures with a single transecting step exhibit mobilities ~4500–6500 cm^2/Vs, and structures with 2-3 transecting steps have mobilities ~3500–5000 cm^2/Vs. Improvements in the large area mobility are likely to be observed in single layer material with large uniform terraces [705].

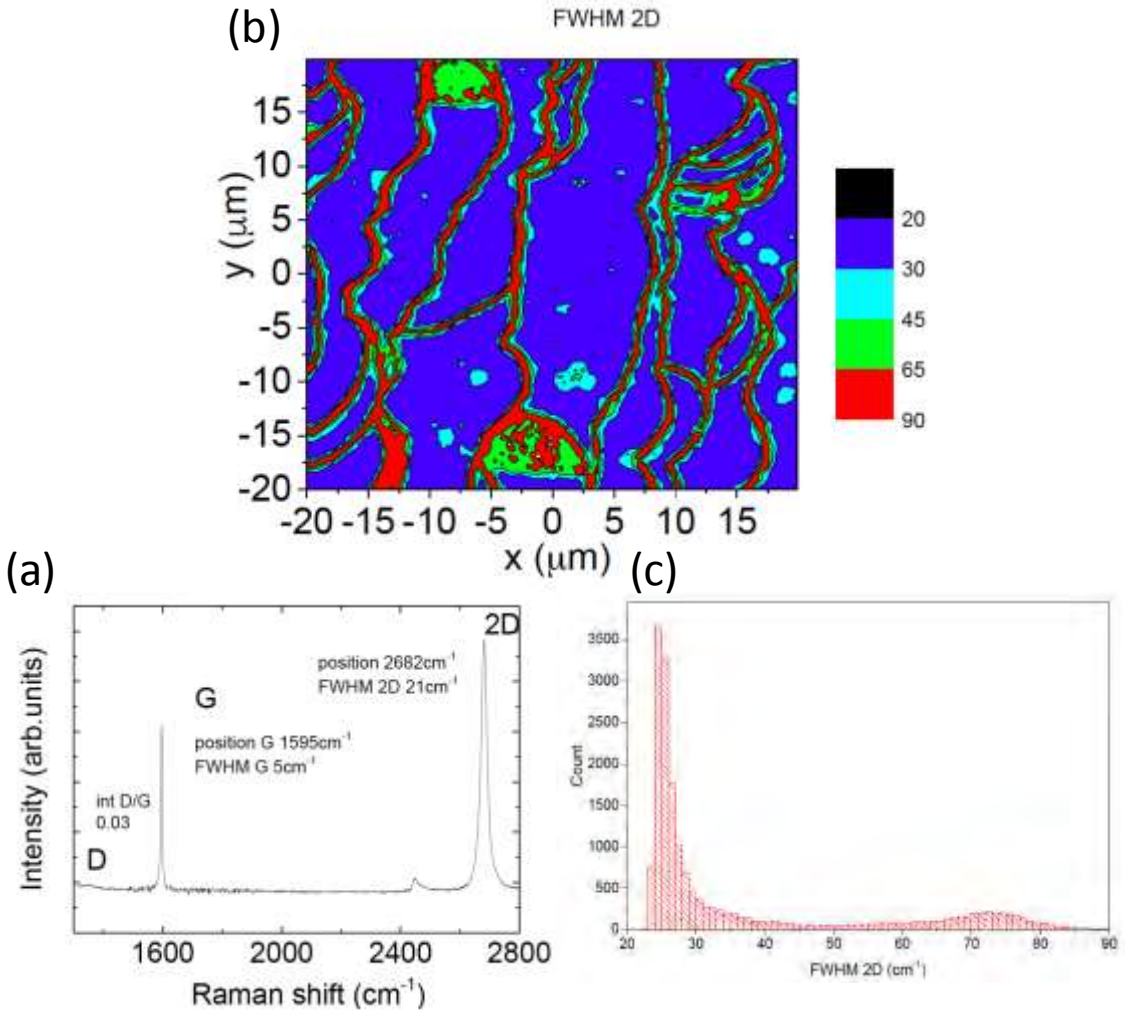

Fig. IV.27. Raman measurements results of epigraphene single layer grown by CVD epitaxy (SiC Raman peak subtracted) (a) spectrum, (b) map 20 mm x 20mm (bilayer graphene on the step edges is depicted with red), (c) histogram of the full-width at half max of the 2D peak FWHM. After [706]

Based on the collected statistical data the QFBLG is also p-type doped, typically in the range between $n = +8 \times 10^{12}$ cm^{-2} and $n = +1 \times 10^{13}$ cm^{-2} for 6H-SiC and between $n = +1.1 \times 10^{13}$cm^{-2} and $n = +2.5 \times 10^{13}$cm^{-2} for 4H-SiC. A strong correlation is observed between charge carrier mobility and charge carrier concentration. The topmost quality processes and record high mobilities are associated with the hole concentration approaching a well-defined substrate-dependent values, which is in agreement with the vision of point defects augmenting the doping level [669]. The scattering at the step is attributed to a lower charge density at the step (sidewall graphene ribbons are known to be charge neutral [572]), and to disorder near the step edge.

Because step edges are believed to result from SiC surface etching in hydrogen prior to graphene growth the anisotropy results call for a etch shortening. However, after a milder H_2 etching, the transport parameters are significantly worse, in the reverse proportion to the steps height. This can be understood by a higher step density (for the same substrate miscut angle) interfering with the

device size. Further development will be to optimize crystal surface with low step height (no higher than SiC bi-layer).

V CVD GROWTH

V.1 Growth on Metals

Chemical vapour deposition

The availability of commercial reactors has made CVD the most extended technique to grow large area SLG [707], [708]. Many studies have been performed on SLG growth on Cu substrates because of their low carbon solubility, which enables self-limiting growth (usually more than 95% monolayer coverage) [708]. Transfer is achieved by etching Cu [708] with various chemicals [709, 710] or by electrochemical delamination allows one to reuse Cu [89] with a significant reduction in cost (see section VI).

Graphene on copper film

The solubility of carbon in Cu is low, even at high temperatures [711]. This eliminates the need for a solution/precipitation mechanism, which is used on Ni substrates. The binary phase diagram for Cu and carbon is shown in Fig. V.1. The solid solubility of carbon in Cu is 0.0076 weight percent at ~1100^{0}C –slightly above the melting point of copper [89, 711, 712]. Mostly on this basis, it is assumed that during the thermal process carbon is liberated from hydrocarbons and attaches to the surface of Cu, creating SLG rather than precipitates, and segregates from the bulk upon cooling down.

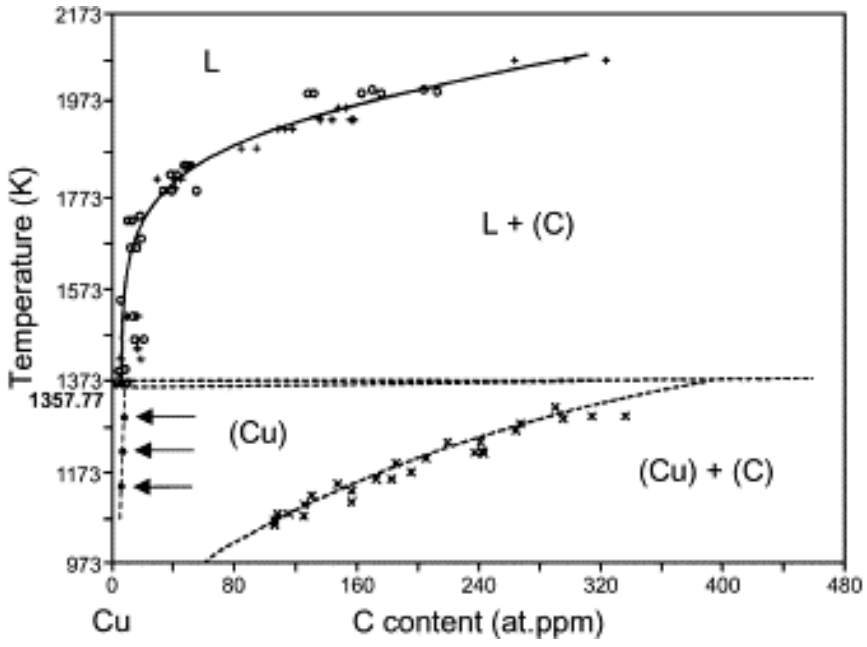

Fig. V.1 Cu-C Equilibrium phase diagram at the Cu rich side, L_ Liquid according to ref .[713]

Carbon adsorbates mobility is higher as the growth T increases , facilitating diffusion across the surface to join the edge of nucleating crystallites. Additionally, these readily desorb from Cu,

resulting in a lower nucleation density for the carbon deposit. Growth on Cu is also limited largely to one monolayer. Cu acts as a catalyst in the reaction, which suggests that the growth is self-limited. However, such an assumption is true only for the simplified version of the process, and especially for low-pressure CVD. It is suspected that the self-limited process is accompanied by other factors such as critical supersaturation and equilibrium concentrations of carbon adspecies [714, 715]. BLG or TLG are observed as 1-2 μm hexagons [716] or dendrites scattered on the surface[155] . These layers are presumed to grow underneath the first layer at the same Cu-active site as the first layer [155, 716].

The CVD graphene process on Cu surfaces in six steps [717-720] :

1.- Adsorption of the hydrocarbon precursor on Cu surface;
2.- Partial dehydrogenation of hydrocarbon, resulting in CH_x species;
3.- Surface diffusion of C adsorbates on Cu surfaces;
4.- Carbon nucleation on the active sites of Cu to form graphene domains;
5.- Growth of graphene domains by adsorbing carbon on their edges; and
6.- Coalescence of adjacent domains to form polycrystalline graphene films

Cu foils [708], single crystals [717] and thin films deposited on dielectric surfaces are used. The most commonly used Cu is high-purity 99.9999%in a variety of thicknesses and sizes. Cu deposited on SiO_2/Si is more controllable in a crystallographic context [721] and more cost-effective because its thickness usually ranges between 200 and 500 nm [722] , see section V.2.2.

Although it is extremely hard to state which factors are most important, it is established that the substrate surface should be free of any defects. Next, growth conditions must be optimized, and the construction of the reactor, i.e. shower head or lateral (laminar or turbulent) gas flow, must be appropriate. Many different methods can be used to grow SLG on copper and other metals at sizes ranging from $1cm^2$ up to m^2. The common technical requirements of the process include ensuring uniform temperature in the growth zone and distributing the precursor precisely. A thermocouple or a pyrometer offer precise temperature control of ovens with resistance, RF or IR heating systems. Hydrocarbon and Ar, N_2, H_2 are commonly applied. The growth processes takes place at pressures ranging between 1 mbar up to 1 bar and at a temperature below copper's melting point of 1084^oC., Some systems are equipped with plasma-enhancing hydrocarbon pyrolysis [www.aixtron.com], enabling growth at lower T, as low as 600 ^oC. Important to the process include also the cooling and heating rates.

The CVD process starts with the cleaning of a 35μm Cu foil substrate of ~ 9 cm x 6 cm is cleaned in acetic acid for 10 minutes and then transferred in deionized water for additional 10 minutes and dried with N_2. Once the Cu foil is introduced in the growth chamber rolled to fit into the diameter quartz tube, it is then inserted in the main tube of the furnace: this is to avoid contaminations of the main tube with residuals deriving from Cu being heated at 1000°C in a subsequent step. Methane (CH_4) and hydrogen (H_2) must be circulated to purge the lines (50:50 sccm) and the base pressure prior to growth is <4mbar. T is then increased from RT to 1000°C in 20

sccm of H_2 in 70mins (see Fig. V.2 upper frame), T is then kept constant at 1000°C for additional 30 mins in order to perform annealing of the Cu foil. This heating can be performed also in Ar gas flow and then in H_2 gas flow at a pressure of less than 100 mbar. The purpose of this step is to improve the quality and enlarge the Cu grain size. A "standard" graphene growth process follows: 5 sccm of CH_4 or C_3H_8 are then added for several minutes (30 in this case) for the growth of graphene to take place. After that, the heater coils are quickly turned away from the Cu foil position for fast cooling down and vacuum is made in the chamber. Four fans also help increasing the cooling speed. The last step is the cooling of the system to RT in an Ar or H_2 atmosphere. The expected size of graphene domains is more than 10 µm. By applying a longer annealing time, higher T, lower pressures, and by maintaining optimal hydrocarbon flow and melting the Cu, the graphene domain size can reach even several mm. Lower frame in Fig. V.2 illustrates domains of 800 µm obtained by systematic process optimization.

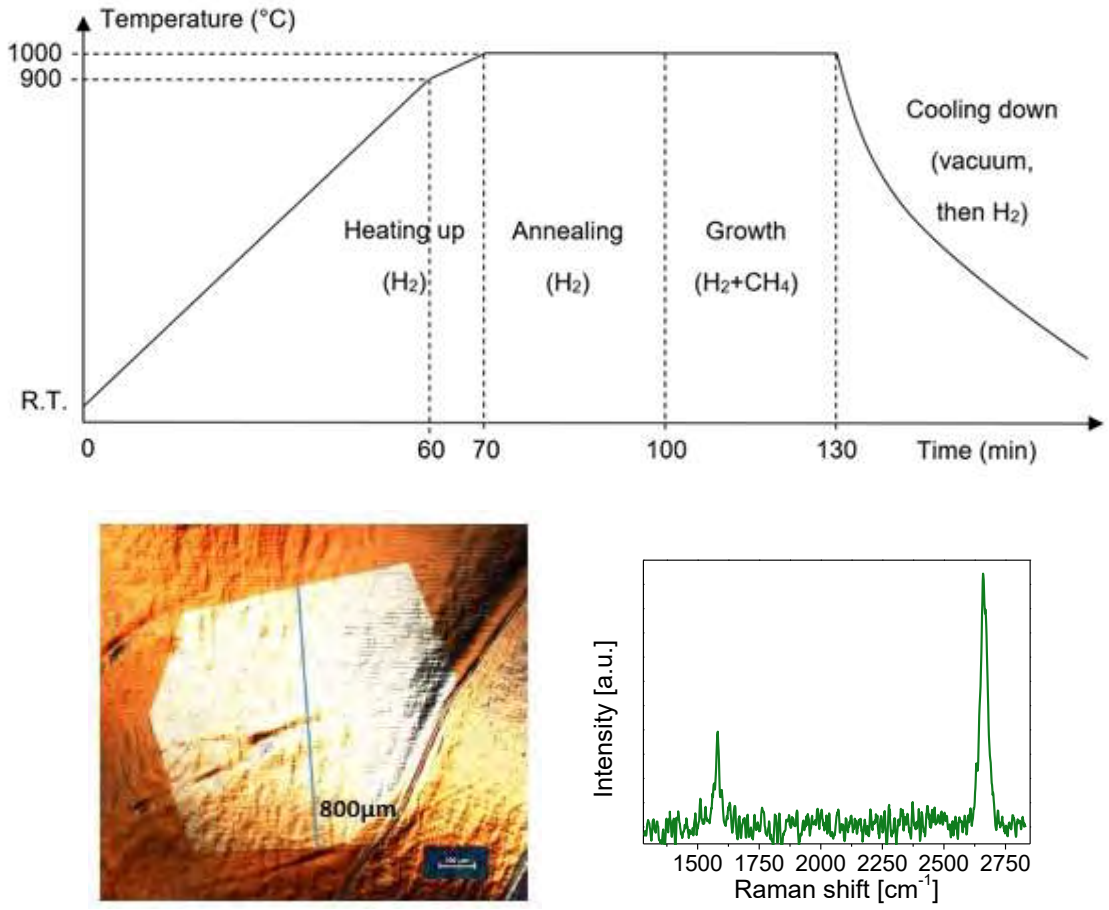

Fig. V.2 Upper – typical schematics of thermal profile during the growth, type of gases used and steps duration in case of growth SLG at 1000 °C, (Lower Left) Optical image of a graphene domain grown on molten Cu (1020 °C) on a molybdenum substrate. Scale bar is 100 µm. (Lower Right) Raman spectrum of a graphene domain grown on molten Cu.

Optical microscopy with Nomarski contrast, i.e. Differential interference contrast (DIC) microscopy, is very useful (see Fig. V.3) to explore the quality of the grown material. This exposes cracks and micro-holes in the graphene layer and allows an analysis of the substrate deformation process, which can affect graphene film quality.

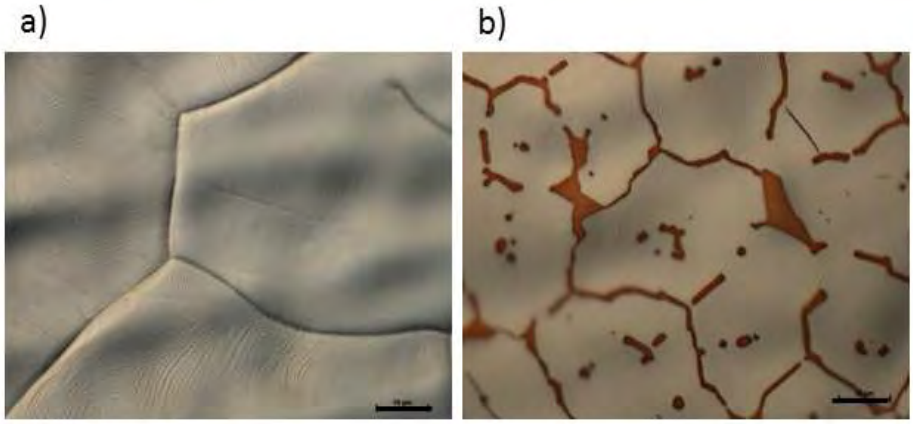

Fig. V.3 Optical images of a) continuous and b) discontinuous graphene films on Cu substrates.

Raman spectroscopy is used to confirm the presence of SLG on the Cu substrates [708]. The technique is introduced in Section IX.2.1, where representative spectra of SLG, BLG , etc are also given.

Measurements done by SEM plotted in Fig. V.4 can identify dark areas interpreted as adlayers of graphene. In addition, wrinkles characteristic of graphene grown on a copper substrate are visible. If Cu of lower quality with [purity 99,9% or 99.999%] is used, e.g. Cu_5N and Cu_3N, the films are heterogeneous mainly in terms of their thickness. In Fig. V.4 bright grey color represents areas with monolayer graphene.

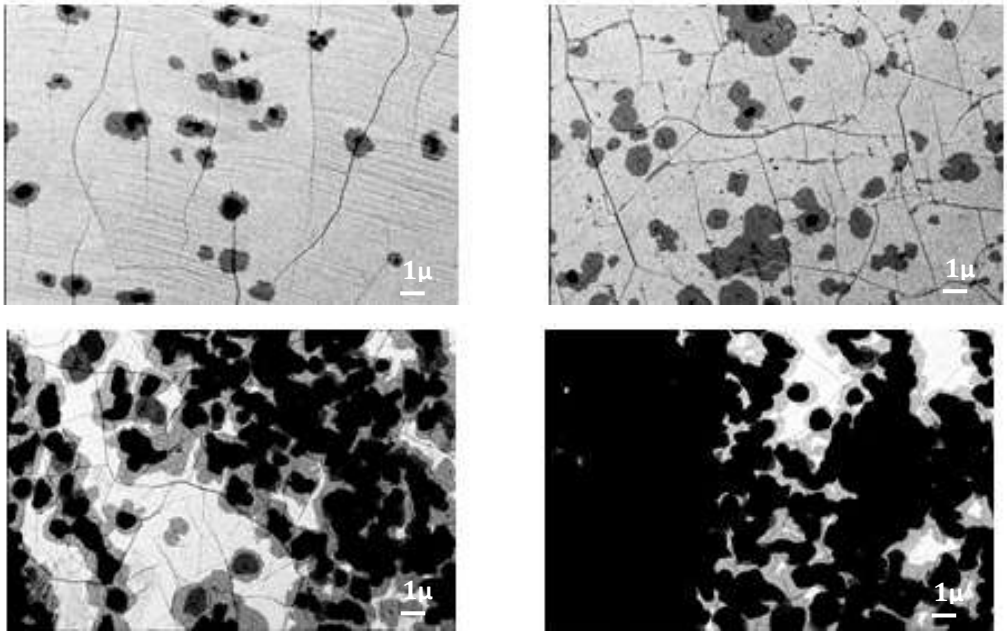

Fig. V.4. SEM images of graphene layers on a) Cu_mono, b) Cu_6N, c) Cu_5N and d) Cu_3N samples. Scale bars are 1 µm

Thus, black spots and areas illustrate a few layer of graphene. The darker the spot is the thicker is the sample.Adlayers of graphene can cover a significant part of the sample surfaces.

STM measurements can confirm that the carbon layer present is graphene [723]. Owing to the high roughness of the Cu foil surfaces (R_q=7.43 nm),it is much easier to characterized samples deposited on thicker and flat Cu monocrystalline substrates. Atomic resolution images presented in Fig. V.5 show the configuration of the carbon atoms in SLG. In the Fourier transform the visible maxima correspond to the pattern formed as a result of the orientation of the SLG in relation to the substrate (lattice mismatch) . The inset of Fig. V.5 shows an area 3x 2.2 nm, on the basis of which the lattice constant was defined as 2.44 Å [723].

The shape, orientation, edge geometry, and thickness of CVD graphene domains can be controlled by the crystallographic orientations of Cu substrates [724].

At the inception of the growth phase, during the nucleation stage, the Cu roughness plays a key role. The Cu-active sites are imperfections on the Cu surface, such as grain boundaries, irregularities or areas of coarseness that are proportional to the number of nuclei of the graphene film. The higher the density of nucleation sites, the smaller the size of the graphene domains and, as a consequence, the larger is the effect of the graphene domain boundaries on the properties of the synthesized graphene.

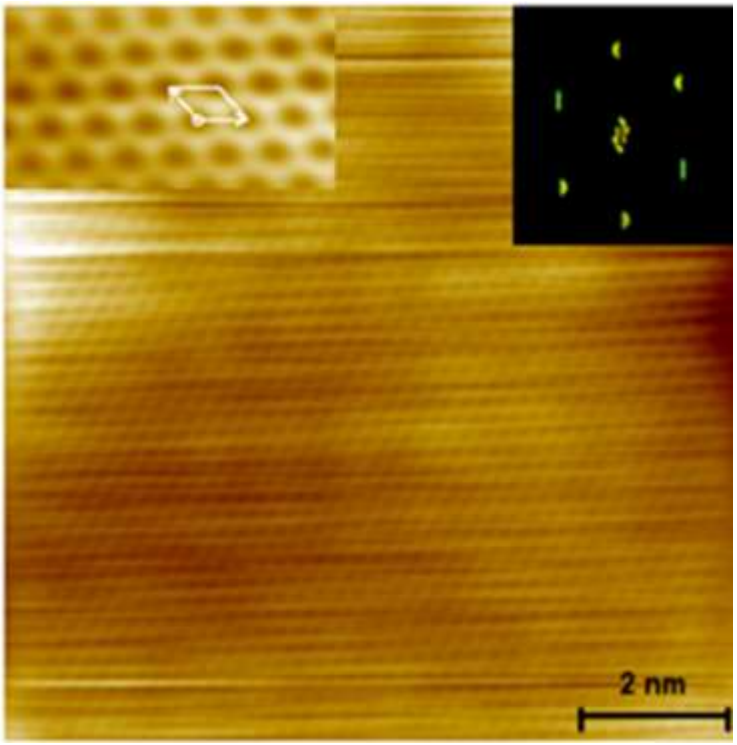

Fig. V.5. Atomic resolution STM of graphene on a Cu mono-crystalline substrate with the Fourier transform (inset). Adapted from [723]

A useful way to improve the properties of polycrystalline graphene on Cu is to minimize the unfavorable influence of the boundaries of graphene domains, as these are an efficient source of charge carriers scattering [725, 726]. Cu surface morphology and crystal quality can be improved by electropolishing [720, 727, 728], more than two hours annealing [729, 730], high-T annealing (even at T above Cu's melting point) [717, 729, 731], Cu surface oxidation [717, 720, 732], and using high purity (99,9999%) Cu with controlled crystal orientation of the substrate [720]. The effect of the H_2/CH_4 ratio on the shape of graphene domains has also been widely reported [720, 731, 732]. Even with a smooth surface(Rs= 0.6 nm), to obtain a graphene domain size of larger than 1mm, less than <1sccm of C precursor flow and time in the range of hours are needed [720] . For this reason, enclosed Cu substrate are used. To achieve their desired effect, thus limiting hydrocarbon access to the surface, pockets or specially designed boxes are deployed [733] to produce domains with sizes measured in millimeters [section V.1.1.3].

For some applications large (m^2) areas of graphene may be needed, as it is the case for the functional coating of large pieces of other materials. This prompted some companies [734] or explore the possibility of synthesizing SLG with Hall mobility above 2000 cm^2/Vs measured after transferring on to SiO_2,by the meter, using specifically designed furnaces. When growing graphene on 500x500mm Cu substrates, temperature distribution on the substrate surface is the main challenge. Because of the polycrystalline nature and its island-like graphene growth, non-uniform T distribution results in inhomogeneous graphene nucleation density. This, in turn, produces a variety of domain sizes and differences in graphene quality over the whole substrate. A high T gradient could even explain why the Cu foil is locally out evaporating T distribution on a 500x500mm Cu substrate, shown in Fig. V.6.

Fig. V.6 Higher temperature near the edges of the substrate caused local melting of copper while the inner part foil was not affected.

In order to examine these large sample sizes properly, detailed measurements should be conducted. A way to do this is to divide the large sample into many small samples (80 mm x125mm) and analyze each individually. By considering the location of these small samples inside the reactor chamber, the uniformity of the large sample can be deduced. Fig. V.7 presents Raman spectroscopy measurements of a 500x500 mm sample divided into 24 smaller sample as described in the Fig. V.7

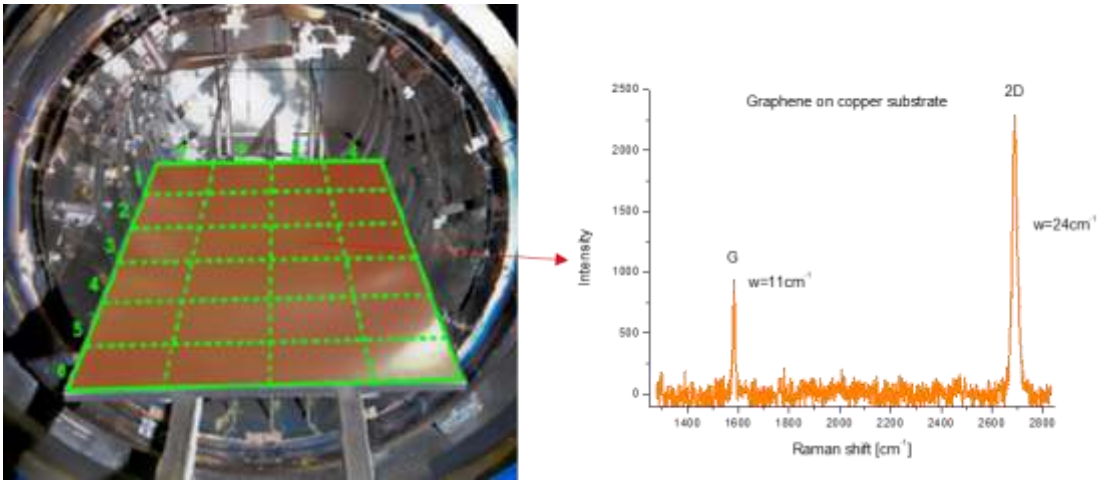

Fig. V.7 Representative micro-Raman spectra of one of the small pieces defined in the text .[735].

Graphene on bronzes

Bronzes are Cu-based substrates that offer antifriction properties [736] and high resistance to heat [737] and corrosion (CDA Publication No 106 Copper Development Association www.copperinfo.co.uk). Coupling graphene and bronze substrates together is expected to enhance these properties. Graphene synthesis processes were attempted on common industrial silicon bronze substrates with a Si content of 3%, on aluminum bronzes with Al content of 7% and on tin bronzes containing 4% Sn . After growth, the Si, Al and Sn bronze substrates were examined, first using optical microscopy and then Raman spectroscopy. Optical microscopy investigations revealed extended and complex surfaces on each of the bronzes (Fig. V.8). Owing to the high surface roughness of bronzes, point measurements were performed instead of linear measurements. Raman spectra taken from the three surfaces showed that for silicon and aluminum bronzes, D and G peaks were dominant, while 2D peaks were very weak (Fig. V.9 a and Fig. V.9b). For these surfaces the spectra could be recognized as amorphous carbon forms created instead of graphene films.

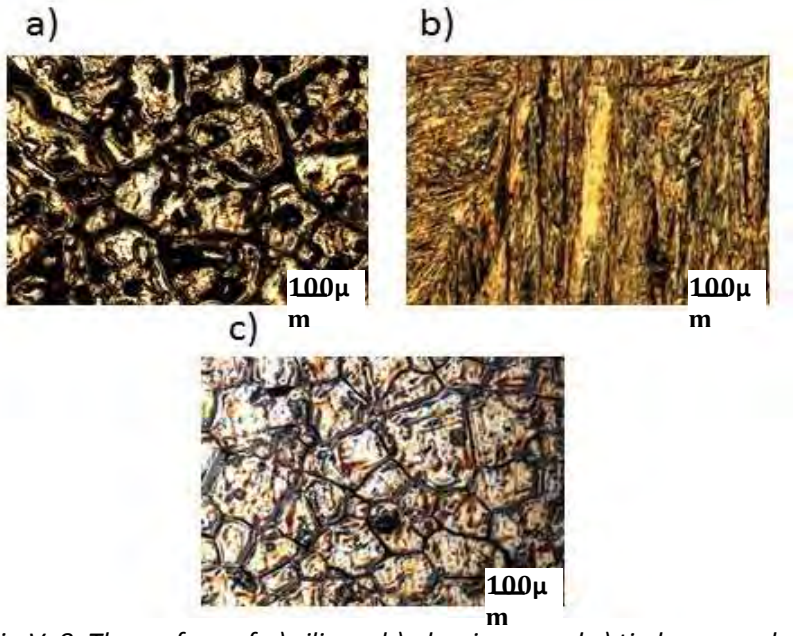

Fig.V. 8. The surface of a) silicon, b) aluminum and c) tin bronze substrates.

For the tin bronze, the 2D peak and the G peak are clearly visible together with a very small defect peak (Fig V.9c). This means that graphene was grown on tin bronze substrates.

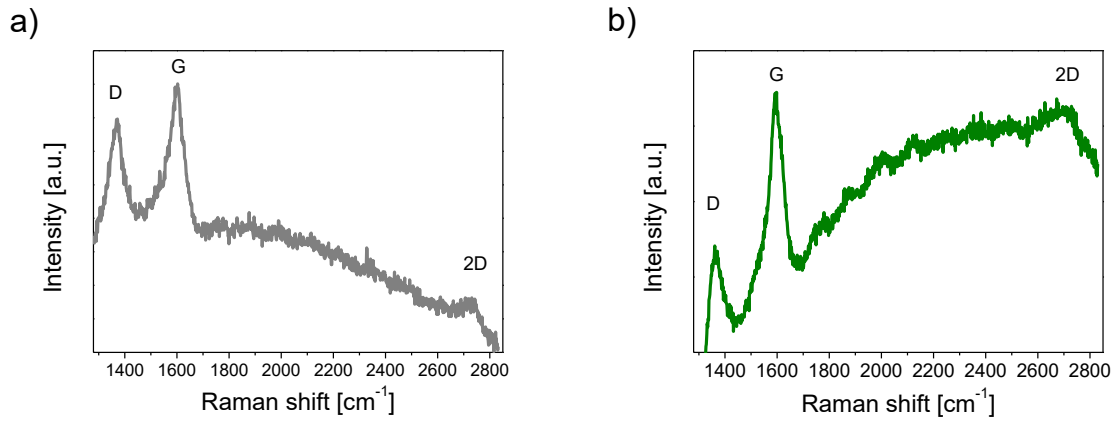

c)

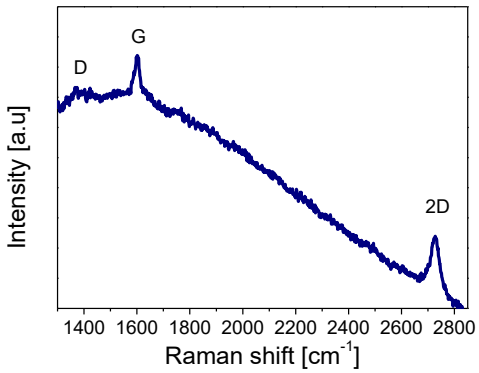

Fig. V.9. Raman spectra for graphene growth process on a) silicon bronze, b) aluminum bronze and c) tin bronze.

Chemically produced carbon-Si and carbon-Al binding explains these phenomena, with the formation of Si and Al carbides likely to have taken place. To overcome the above-mentioned obstacles, Cu coatings were applied to bronze surfaces. As an example, aluminum-iron-manganese bronze BA1032 was used. Its surface was covered with a Cu film and afterwards the production process of graphene was initiated. Fig. V.10 presents the gear wheels used as bronze substrates.

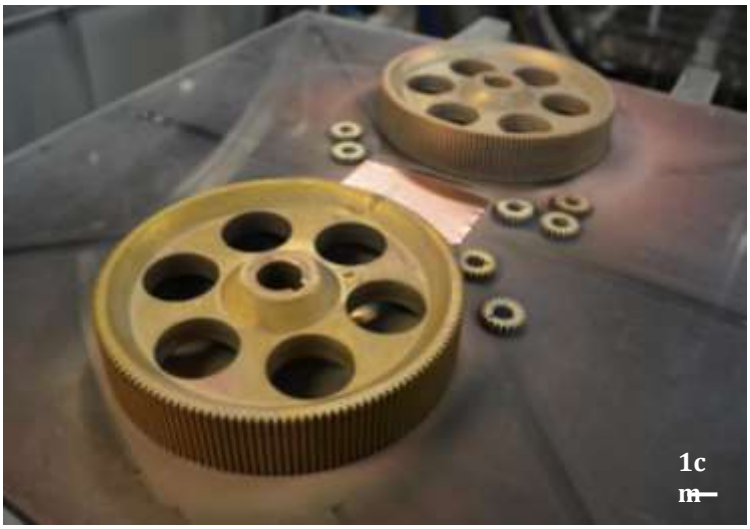

FIG. V.10. Bronze gear wheels after graphene growth process.

Raman spectroscopy results shown in Fig. V.9 indicate that on the surface of the gear wheels a film exhibiting graphene features is observed.

Growth of mm-sized single crystals

The crystal quality of CVD-synthesised graphene can be comparable to that of mechanically-exfoliated flakes [738]. The presence of grain boundaries introduces charge carrier scattering, which ultimately leads to lower mobilities. To mitigate this, one can synthesize large-crystal graphene. Two approaches have been suggested: boundary-free stitching of perfectly-aligned crystals of graphene [735] [537] and growing large crystals of millimetres or even cm size [717, 739, 740]. The first approach requires single-crystalline growth substrates , while the second requires prolonged growth times, reaching up to tens of hours [741], although there has been a lot of focus recently on speeding up the growth of large crystals [717, 740, 742].

The maximum graphene crystal size is typically limited by the merging of neighbouring crystals [717],[740] making the initial nucleation density one of the main factors in the synthesis of large-crystal graphene. There are four conditions relevant to low, highly-controllable nucleation density of graphene on Cu: 1) suitable growth substrate, 2) surface pre-treatment, 3) enclosing the sample to limit precursor flow and 4) non-reducing annealing. Regarding the choice of the growth substrate, it has been demonstrated that the presence of oxygen species in the copper substrates can have multiple benefits for the synthesis of large SLG [717]. Oxygen not only passivates the surface of copper, leading to reduced nucleation density, it also significantly speeds up the growth of graphene crystals by changing the growth regime from diffusion to edge-attachment-limited. Some commercially available Cu foils have a significant pre-determined oxygen content – for example, Alfa-aesar (13382). Alternatively, oxygen-free Cu can be oxidised prior to growth. This can be done either *in-situ* [717], or simply by heating the foil to 200 °C in an ambient atmosphere [743]

While polycrystalline films can typically be grown on bulk-produced commercial Cu foils, substrates intended for the growth of large-crystal SLG require certain surface pre-treatment procedures in order to increase flatness and cleanliness. Many different approaches can be found in literature [537, 744], mild surface etching using acid [717] [745, 746], Electropolishing has provided the most reproducible results [742, 747]. The solution used for electropolishing has a volumetric composition of 45% water, 25% phosphoric acid, 25% ethanol and 5% isopropanol. To increase viscosity, 0.5% (weight) of urea is added. Electropolishing is performed by applying a voltage between the sample (anode) and a Cu plate cathode. A typical electropolishing procedure is 30 seconds at 12V, with a cathode-anode distance of 4 cm. To ensure homogeneous polishing, it is important to keep the electrodes parallel. For this one can employ a Coplin glass staining jar as the electropolishing vessel (Fig. V.11 (a)), which has grooves to keep the foil and the counter electrode in place, Fig V. 11 (b). Following the electropolishing, it is important to rinse the samples under running deionised water to completely expunge the viscous electrolyte, followed by a quick rinse with isopropanol. Finally, the samples are dried with compressed nitrogen.

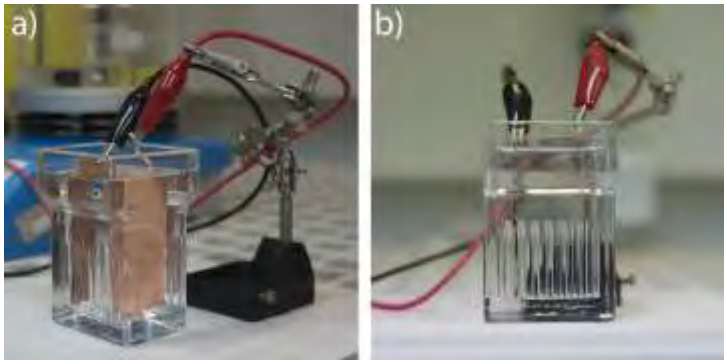

Fig. V.11 Electropolishing set-up. a) Three-quarter view. b) Side view, showing the parallel orientation of the copper foil and the counter-electrode. Adapted from [742]

Owing to the high catalytic activity of the Cu surface, it is important to reduce the carbon precursor flow impinging on the sample. The most commonly-used approach in the literature is to grow large SLG crystals inside "pockets" formed from Cu foil [717, 744, 746]. By folding a piece of copper foil in half and crimping the edges, as shown in Fig. V.12 (a), an enclosed volume is created inside this "pocket", in which the nucleation density is reduced by several orders of magnitude. The disadvantage of copper "pockets" is the deformation of the copper foil, which can lead to the graphene cracking as a result of excessive stress levels. To avoid the deformation one can grow large SLG on a flat foil, enclosing the substrate with a quartz disk place on top of graphite spacer, Fig. V.12(b) [742]. While the nucleation density is not as low as that achievable using a "pocket", crystals ~1mm can be grown. On the other hand, when using the pocket approach it is typically possible to achieve single crystals ~4mm lateral size.

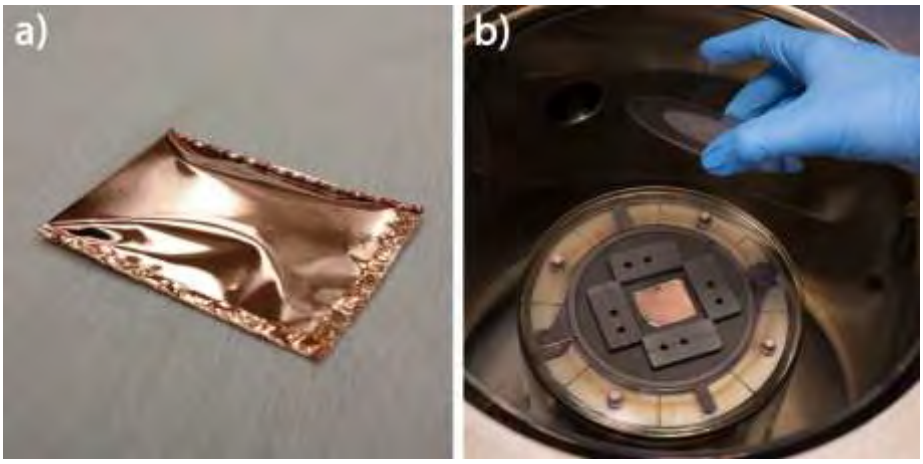

Fig. V.12 a) Cu "pocket" enclosure. b) Graphite/quartz enclosure on top of the bottom heater.Adapted from [742].

Synthesis of large-crystal SLG requires a high mobility of the carbon precursors on the Cu surface and therefore high growth temperatures. A typical growth T is ~ 1060°C, close to the melting point of Cu (1083°C [748]). To avoid melting the samples, it is important to maintain an accurate T reading, which can be highly dependent on the system used. The following applies to Aixtron BM Pro [742]. Although the reactor is equipped with an IR sensor, the reading can be affected by the gas flow above the sample, sometimes giving inconsistent readings during the different stages of synthesis;

the use of a thermocouple reading is advisable. However, since the thermocouple is not in direct contact with the sample, the reading can differ by tens of degrees. A calibration procedure can be performed by intentionally melting a sacrificial sample and using the corresponding thermocouple value as the reference point for 1083 °C. The growth T can then be adjusted accordingly.

Prior to the deposition of graphene, the foil can be annealed to remove contaminations and increase the Cu grain size. Since oxygen has the important role of reducing the nucleation density, it is important to maintain the Cu oxidation during the annealing. One can perform the annealing in a non-reducing argon atmosphere instead of hydrogen [742]. To avoid the risk of a sample melting owing to T fluctuations during the ramp-up, the T is increased quickly to 1000 °C at a rate of 200 °C per minute. In a second step, the final temperature of 1060 °C is reached slowly, at a rate of 6 °C per minute, during which the Cu substrate is annealed, preparing it for graphene deposition. This step causes the domain size of the Cu foil to increase from several microns to several mm.

The nucleation density and growth rates are affected by the growth pressure and gas flow rates. While low pressure can help to radically reduce the nucleation density, it can also lead to extremely slow crystal growth. 25 mbar allows for rapid synthesis of large crystals. With a gas flow comprising 1 sccm CH_4, 900 sccm Ar and 100 sccm H_2, the graphene nucleation density is on the order of several crystals per mm^2 and typical growth rates are ~15 μm/min, allowing the synthesis of 1mm-sized crystals in ~ 1 hour. Following the growth, the samples are cooled down by switching off the heater, under an argon/hydrogen atmosphere. All adopted gases had purities of 99.9999%.

Fig. V.13 illustrates the effect of using a non-reducing atmosphere and sample enclosure on oxidised Cu. When hydrogen annealing is used, the nucleation density is ~ 10,000 cm^{-2} (a). Annealing in an argon atmosphere reduces the nucleation density to ~1000 grains per cm^2. Finally, samples annealed in argon and placed inside an enclosure have a nucleation density ~ 10 grains per mm^2 or lower, enabling the growth of large crystals.

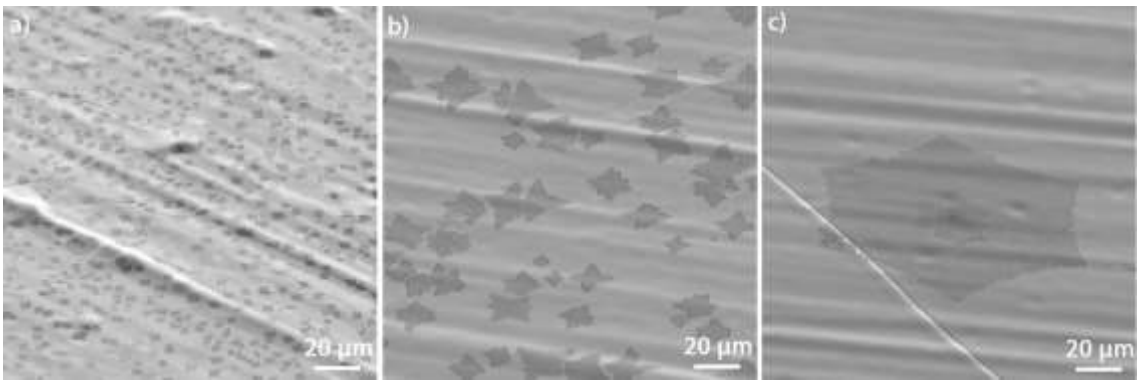

Fig. V.13 Nucleation density of graphene when using a) hydrogen annealing, b) argon annealing c) argon annealing and sample enclosure. Adapted from [742].

Using the steps described here, it is possible to suppress completely the spurious nucleation of graphene on Cu, requiring a surface irregularity or contamination particle to nucleate a graphene crystal. One can take advantage of this by patterning the substrates intentionally with nucleation seeds, as will be discussed in the following epigraph.

Individual SLG crystals on the cm scale can be also be grown using low pressure CVD on Cu foil. Typical growth processes take place at temperatures close to 1050°C and pressures of around 0.1 mbar to 1 mbar using a mixture of H_2 and CH_4. One problem is the enhaced sublimation rate of the Cu, caused by the combination of high T and low pressure [747, 749]. In order to suppress this sublimation, growth can be carried out on the inside of a tightly crimped envelope of copper foil [747, 750]. Inside it, the equilibrium of the Cu partial pressure is established, suppressing sublimation and producing a very flat, smooth surface. This gives rise to very low grain densities, enabling the growth of individual SLG crystals on the order of 10 cm^{-2} or less.

A Cu(111) foil (AlfaAesar 46365) can be prepared in sheets of 8x12 cm and etched in an aqueous solution of ammonium persulfate (30 g/l) for two minutes and subsequently rinsed in DI water and isopropanol and blown dry using nitrogen. Next, the foil is folded over and crimped tightly at the edges (each edge is folded over twice). The resulting Cu enclosures are loaded in a H_2 (15 sccm, p ≈ $8x10^{-2}$ mbar) is turned on. For the growth, the furnace is ramped up to T = 1035°C in 40 minutes and kept at 1035°C under a H_2 atmosphere for 20 more minutes. Next, CH_4 is introduced into the system in order to initiate the graphene growth (5 sccm, CH_4, 45 sccm H_2, p ≈ $5x10^{-1}$ mbar) (See Fig. V.14-a) . After two hours of growth, the furnace is cooled down to room T in 30 minutes by opening the furnace hood.

This process results in individual graphene crystals with a typical size of 200 µm, with the Cu oriented predominantly in (111) direction (See Fig. 14-b). The crystallographic orientation of the copper foil is of utmost importance for a dry transfer method (see section VI), in which graphene is picked up directly from the Cu using a h-BN flake. The interface between SLG and Cu (111) oxidises under ambient conditions within a few days, making SLG visible and decoupled from Cu, required for a reliable dry pick-up using hBN.

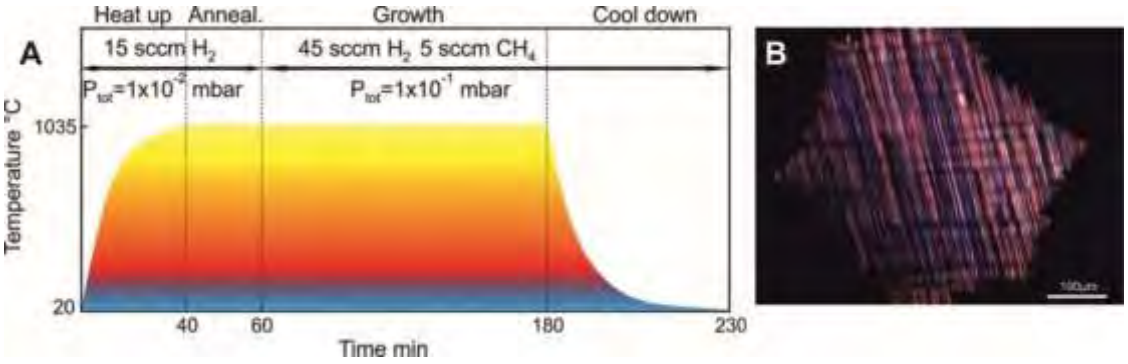

Fig. V.14 a) Typical growth scheme for a low pressure CVD process for SLG on Cu. b) Optical dark field microscopy image of a SLG on Cu foil using the process depicted in a). Panel B is adapted from L. Banszerus et al. Science Advances 1, e1500222 (2015) [749].

Deterministic seeded growth

Ref [733] reported a novel approach that allows for the deterministic synthesis of large crystal SLG on Cu foil by using metallic growth seeds that are removed during the growth process. By growing large single-crystals SLG only at the desired locations, it is possible to design complex devices, and a wafer-scale integration is feasible. This approach has led to the demonstration of large arrays of monocrystalline graphene with crystal sizes measuring hundreds of microns and RT mobilities higher than 20,000 cm^2/Vs .

The nucleation seeds can be patterned by performing optical lithography on electropolished Cu using Shipley S1813 positive photoresist, followed by thermal evaporation of 25 nm of Cr and lift-off in acetone. Cr is chosen because of its high melting point, ensuring that thin films are not evaporated during the annealing of the foil and instead form particles that can act as nucleation points on passivated Cu. Spots with a diameter of 5 µm and a thickness of 25 nm lead to the most reproducible results; smaller seeds or lower film thickness did not ensure reliable seeding, whereas larger spots were sometimes found to initiate the nucleation of several separate crystals. The Cu foil adopted for this approach as well as the process parameters and the experimental set-up are those reported in the paragraph above, where the growth of mm-sized graphene crystals is described. The only difference in this growth approach is in the CH_4:H_2 flow ratio. Indeed, by changing such flow ratio, it is possible to control the presence of residual Cr seeds during the growth by changing the CH_4:H_2 flow ratio. After growing graphene using a H_2:CH_4 ratio of 20:1, particles of Cr are found at the centre of seeded crystals, whereas when using a H_2:CH_4 ratio of 100:1, Cr seeds are removed. Growth was carried out in a 4-inch Aixtron BM Pro. All gases used in the CVD process had purities of 99.9999%. As shown in Fig V.15 (a), arrays with a periodicity of 200 µm show high nucleation control, with less than 10% of non-seeded nucleation. At larger periodicities (see Fig. V.15(b)), sporadic nucleation was slightly higher; however, well-ordered arrays of crystals with a diameter of several hundred microns can be synthesised [733] .

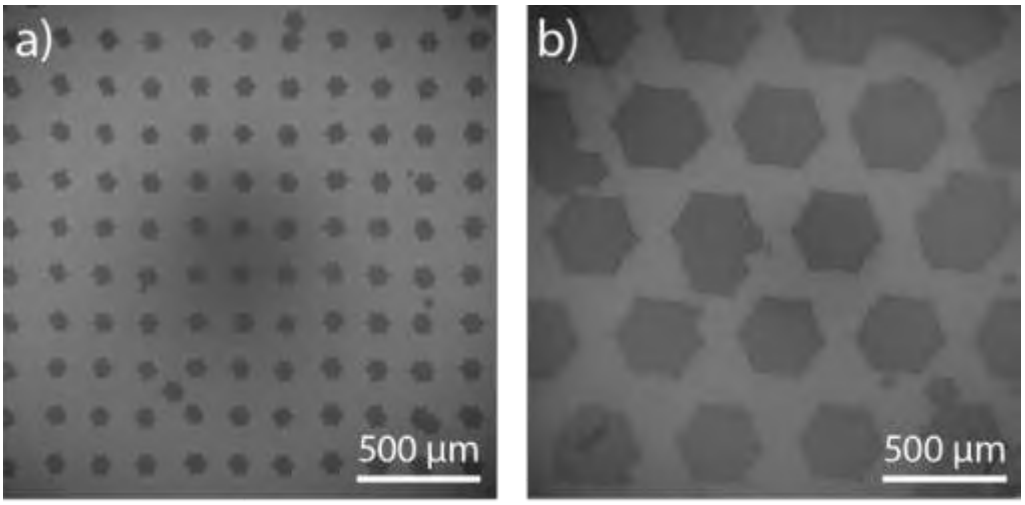

Fig V.15. Seeded arrays of large-crystal graphene. a) Array with 200 µm periodicity and 100 µm crystal size. b) Array with 500 µm periodicity and 350 µm crystal size Adapted from [733]

Low pressure & low T CVD on copper foil

One issue with graphene CVD on Cu from CH_4 is that the growth typically takes place at temperatures just below the melting point of Cu, which occurs at 1084°C. At this elevated T and the low pressure typically employed in CVD systems, Cu atoms readily evaporate from the substrate and condense on all available surfaces upon cooling. This has the effect of reducing the lifetime of the furnace and degrading the quality of the graphene film. Over time, the reproducibility of the graphene growth process is affected. The quartzware used in CVD systems has to be replaced systematically to eliminate drift in the growth parameters and to ensure consistent high quality graphene films. As such, techniques for reducing the growth T are constantly being sought, as even a small reduction in growth T will have a significant impact on the quantity of Cu redeposition on chamber walls. Some groups have turned to the use of liquid precursors such as alcohols [751] or aromatic molecules such as hexane, [750, 752] benzene [753] and toluene, [754] with growth at 650°C for the latter. However, this requires handling of often toxic liquids and the resultant graphene films. Ref [755] reported CVD growth of high-quality, large-area SLG films on Cu foils using ethene gas at 850°C. Spectroscopic and electrical measurements show that these films display high uniformity and crystalline quality with good carrier mobilities [755].

Cu foils were first cleaned in 10% HCl to remove a surface passivation layer and then sonicated in HPLC acetone to clean the surface. The cleaned foils were loaded into an ATV PEO 604 quartz tube furnace and heated to 850°C under an H_2 flow (1 mbar, 15 sccm) and then annealed for 30 minutes under these conditions. Growth was performed with a gas mixture of H_2 (3 sccm) C_2H_2 (1.5 sccm) and N_2 (300 sccm) and a chamber pressure of 2 mbar for a duration of 10 minutes. Next, the chamber was force-cooled to RT with an atmosphere of a small amount of static H_2 in the chamber (2 mbar). The Cu foils were then gently sonicated in acetone for 5min to remove physisorbed contaminants and transferred to SiO_2 substrates via a well-established polymer-supported method (see section VI). PMMA (950k, A2) was spin-coated onto the Cu foil and this stack was floated on an ammonium persulfate (APS) solution (~1 M) to dissolve the Cu. Once this was complete, the PMMA/graphene film was transferred to a DI water bath and dredged onto the target substrate. After drying under vacuum at RT the sample was heated to 130°C to re-flow the PMMA film and improve the adhesion of the graphene layer to the SiO_2. Finally, the PMMA layer was dissolved in acetone. All electrical measurements were performed by defining a graphene channel by pre-patterning the Cu foil with Al_2O_3 deposited via ALD to passivate regions and then contacting the resultant graphene ribbons with Au contacts deposited by thermal evaporation and defined by shadow masking. These pads were then contacted with a 4-point needle probes and the electrical measurements were performed.

Raman spectroscopy shows a SLG film with small islands of secondary layer growth. Fig. V.16 (a) shows the average Raman spectrum of a~20x20 μm^2 area (red) and a discrete spectrum taken at the centre of a SLG domain. The I(2D)/I(G) is lower for the averaged spectrum as this includes the regions of secondary island growth. Fig V.16(b) plots a I(D)/I(G) map with brighter areas corresponding to regions of higher defect levels; highlighting the low defect levels throughout the film. The defects that are present here are attributed to domain boundaries. Fig. V.16 (c) reports

FWHM(2D) across the same area of the film with brighter regions corresponding to wider FWHM. The majority of the film exhibits a FWHM(2D) ~ 35 cm^{-1}, typical of SLG [77, 86].

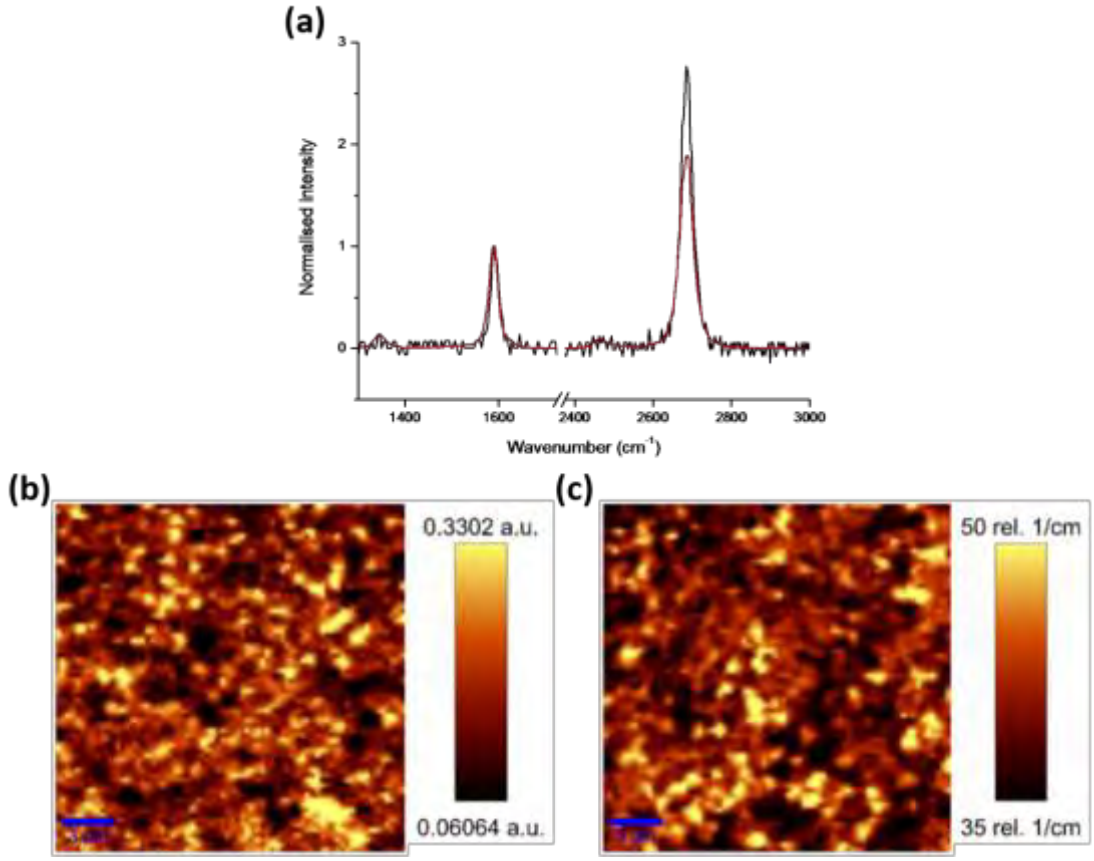

Fig. V.16 (a) Raman spectrum taken at the centre of a monolayer graphene domain (black) and averaged across a 20x20 µm region of the film (red). (b) I_D/I_G map. (c) 2D FWHM map. Adapted from [755]

Further characterisation was carried out by fabricating graphene field effect transistor (GFET) devices. Al_2O_3 pre-patterning of the Cu foil passivates the areas, giving a patterned graphene film on the final substrate. Electrical measurements were performed with source-drain voltage (V_{SD}) maintained at 20mV while the gate voltage was swept to +60 V and -60 V. I_{DS} vs V_{GS} curves are in Fig. V.17 give hole and electron mobilities of 1100 $cm^2V^{-1}s^{-1}$ and 700 $cm^2V^{-1}s^{-1}$ at RT respectively. These values fall short of the best reported values for CVD graphene [756], due to the smaller domains (~1 µm) compared to films grown at higher temperature.

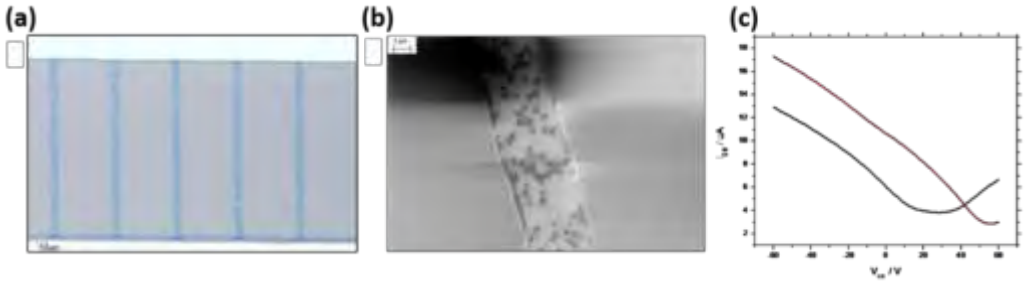

Fig. V.17 (a) Optical micrograph of graphene ribbons on SiO_2 used for GFET devices. (b) SEM image of an individual graphene ribbon with second layer islands visible as darker spots. (c) I_{DS} vs V_{GS} curves for GFETs (red) as-fabricated and (black) after vacuum annealing. Adapted from [755].

Photothermal CVD on Cu

Photothermal CVD (PTCVD) is a fast, usually less than 1 hour and scalable method for graphene production. Refs [757, 758] reported rapid (~ 10 s) growth of graphene films exhibiting (~367 ohm/sq sheet resistance in transparent electrodes. The PT-CVD system is based on a standard halogen lamp-heated rapid thermal processing (RTP) (for up to 300 mm wafers), where gas lines (CH_4, H_2 and Ar) and their mixing manifolds are incorporated. PT-CVD differs from thermal CVD due to its heating mechanism, which both enables ramp rate up to 100 °C/min) during the heating and cooling cycles and keeps the RTP chamber walls cold. This, together with the fast growth process, less than 1 min, helps to reduce the contamination from the walls.

Cu foils (with a typical thickness of 25 μm and 99.8%purity) or thin sputtered Cu films are used as catalytic substrates. The Cu foil is first cleansed of surface oxide by acetic acid. Smoothing of the Cu surface by etching or electropolishing takes place prior to annealing at 800°C for 30 min in ambient H_2 at atmospheric pressure. The pre-treated Cu foil is then placed between two silica plates on a photothermally heated Si- or SiC-coated graphite susceptor. Silica is needed between Cu and Si to prevent reactions between them. The growth process starts by annealing the Cu foil for 5mins at ~ 935°C and pressure ~7-20 mbar). Next, methane at a flow rate of 15 sccm (CH_4/H_2 mixture 4:1) is introduced into the chamber. T is controlled by a pyrometer. Selecting the best growth T is crucial; a too-high T causes detrimental evaporation of Cu, while a too-low T decreases graphene quality. The optimal growth T depends on the type of Cu foil or film and needs to be experimentally determined for each type. A maximum T ~950°C prior to signs of Cu evaporation typically yields the best quality in terms of both highest carrier mobility and the absence of a defect-related D peak in Raman spectroscopy [759].

Continuous SLG film grows on Cu in a few tens of seconds, which is an order of magnitude faster than in thermal CVD using similar growth parameters. The SLG coverage is about 94% in films grown in 60 seconds at 950°C. The SLG contains very small adlayer flakes, and few defects ($\sim 3 \times 10^7$ cm^{-2}) [759]. The light from the RTP lamps enhances the catalytic effect of CH_4 on the Cu surface without generating defects. The grain size is in the μm range. The grain boundaries do not

degrade the graphene's electrical properties with μ as high as 4700cm^2/(Vs) was obtained for a 4 μm channel FET device at a low-bias regime (gate voltage up to 2 V) [760] .

The very fast growth rate (single layer in 10 s) of PT-CVD enables the formation of continuous multilayers on Cu surfaces beyond the self-terminating single-layer limit by extending the growth time from 0.5-1 min to 10-20 min while keeping the process conditions the same [submitted].

Ref. [761] reported a rapid thermal CVD (RT-CVD) suitable for mass-production. In this setup, Cu foils are loaded vertically in the reactor, in which 24 lamps heat vertical graphite receptors around the Cu foil. They obtained a growth rate 7 times higher than thermal CVD using hydrogen-free N_2 carrier gas [761] and reported μ ~ 5000cm^2/Vs and no correlation between grain size and conductivity, when the grain size is > a few micrometers.

Growth on Ir(111)/YSZ/Si(111)

SLG on Ir(111) thin films on YSZ-buffered Si(111) wafers [762] was reported in Ref [763]. The substrate is first cleaned by Ar sputtering (0.8 keV, 5 μA, 15 minutes) and annealing to 900°C followed by an oxygen treatment (p(O2)=5x10^{-8} to 1x10^{-7} mbar, T between 400°C and 550°C) and a final flash annealing (to desorb the oxygen) up to 900 °C.

SLG is grown using ethylene as a precursor CVD at T=850°C, starting from very low ethylene partial pressures (ideally <1x10^{-8}mbar for the first 20-30 minutes), then progressively increasing the pressure up to 2x10^{-7} mbar. This approach prevents the formation of multiple nucleation centers, which would result in the appearance of many rotational domains (mosaicity). The substrate should first be heated to the setpoint T and only then should ethylene be admitted into the chamber. To monitor growth, the photoelectron yield setup is described in [764]. Surface processes such as oxidation and overlayer (including graphene) formation modify the work function of the metal substrate, the photoelectron yield measured while irradiating the sample with a pulsed UV source can be used to track the onset of the surface process under study and to monitor its evolution until saturation is reached.

Growth on Germanium

Graphene grown on Ge is promising in view of SLG integration with CMOS technology [735, 765-767]. As it is not possible to grow SLG directly on Si, owing to carbide formation, germanium substrates, which do not generate carbides [767], provide an alternative [767]. Ge technology is already compatible with CMOS and provides the opportunity to perform selective growth on a predefined device area. SLG transferred from Ge is, in principle, not metal-contaminated.

Because growing graphene on germanium-based substrates is a new process, with only few papers already published, the exact mechanism of growth is still an open question. It is known that germanium does not form stable carbides and that there is no solubility of carbon in solid germanium [767]. SLG growth was reported using LPCVD [735], APCVD [768] and MBE [765] on Ge(110), Ge(100) and Ge(110)/Si(110) and Ge(100)/Si(100) substrates [735, 765, 768]. Ref. [769, 770] reported the CVD growth of graphene on monocrystalline Ge(100) on Si(100) wafers, the preferred wafer

orientation and an easily scaled configuration in CMOS technology. This approach offers cost advantages including the ability to bulk-buy Si(100) wafers and, more importantly, manufacturing compatibilities. The Ge(100) method does not require any special pre-treatment of Ge(100)/Si(100) wafers such as *ex-situ* removal of native oxides and preceding graphene growth with the deposition of fresh Ge layers, which translates in lower costs in the fabrication process. Obtaining high-quality graphene grown on Ge(100)/Si(100) wafers that can then be either transferred using the wafer bonding approach or used directly in the fabrication of, i.e., graphene THz devices could then allow this material to be integrated with Si microelectronics. Ref. [769, 770] reported SLG growth on solid Ge instead of melted substrates which brings additional benefits such as re-usable substrates, easy characterization and smooth surfaces [712].

Ref. [769, 770] uses 6-inch Aixtron Black Magic sysem with a shower head that creates gas turbulence. Ge(110) layers were deposited by the CVD on Si(100). To ensure optimal T conditions, which prevent Si diffusion through Ge layer and Ge melting, T was monitored and set separately and simultaneously in the bottom and top heaters. The growth took place between 900ºC and 930ºC with a ramp-up rate of 1-20 ºC/min at a pressure ~ 700 to 780 and CH_4 flow in the (0.4 - 5 sccm) range. The optimal roughness of the substrate was achieved when the step growth was preceded by annealing at 750ºC-800ºC in a pure H_2 to reduce native oxides *in-situ* [771].

Ref. [769, 770] grew SLG on Ge/Si under laminar conditions with a Aixtron VP508 horizontal CVD hot wall reactor. Ge(100) was deposited by CVD on Si(100). The SLG growth was done at 890-910ºC with a ramp-up rate~1-10ºC/min and a pressure~850-990mbar. CH_4 at flow rate~0.1-0.5sccm was used in an Ar flow~3 l/min. The step growth was preceded by the substrate's annealing at 800ºC-850ºC in H_2. The CH_4 flow was reduced and the growth time XX, longer than in "turbulence conditions". As a result, a uniform graphene film was achieved.

Growth on metalic foams

The integration of graphene into accessible and scalable three-dimensional materials is an issue that is inspiring a growing field of research [772]. Free-standing interconnected porous graphene materials, called graphene foams (GF) attract interest due to their ability to transfer many of the unique properties of graphene to a larger scale, with high surface area > 850 $m^2 g^{-1}$ high electrical conductivity (>10 S cm^{-1}) and good structural, retaining the form of the metallic template on which they were synthesized [773].

Structures such as papers [516] and hydrogels [774] can be prepared starting from chemically exfoliated graphene and/or GO [286]. These often suffer from poor electrical conductivities (e.g. only 5 x 10^{-3} S cm^{-1} [774] thermal properties mainly because of defects and their non-continuous nature. Graphene may be grown on templates of virtually any shape by CVD and continuous structures can be obtained starting from custom porous templates [775]. Ref [773] reported CVD-grown free-standing GFs suited for many different applications such as lithium storage [322], high sensitivity detection of NH_3 (ppm in air at RT and NO_2 gas [773] supercapacitors [776], conductive

scaffolds for the proliferation of neural stem cells [777], superhydrophobic coatings [778] combined with Teflon, or stretchable strain sensors [779] combined with PDMS.

The growth process strongly depends on the metal catalyst. In the case of Cu, the process is self-limited, i.e. growth mostly ceases as soon as the Cu surface is fully covered with graphene principally because of the negligible C solubility and C diffusivity in Cu [780]. In the case of Ni, the carbon atoms diffuse into the bulk of the metal due to the high carbon solubility, ~ 0.9% at 900 °C [780], and graphene is formed both by the isothermal growth on the surface and carbon precipitation from the bulk upon cooling [96]. The shortcoming of graphene growth on Ni is the poor control on the number of layers, which is strongly influenced by the thickness of the Ni, T and exposure time to the hydrocarbon, and the cooling rate, not yielding uniform SLG but rather FLG [780]

In Ref. [781] GF were grown on commercially-available Ni foam templates by CVD in a conventional hot-wall tube furnace (diameter 5 cm) using CH_4.The templates were washed by ultrasonication in dilute hydrochloric acid, then de-ionised water, and finally acetone before being placed inside the furnace and heated to 1000 °C under a H_2 flow of 50 sccm. After annealing under these conditions for 30 min, the flow of H_2 was increased and CH_4 introduced (H_2:CH_4 = 500:50 sccm). Following a 10 min deposition time, the sample was removed from the furnace and allowed to cool in flowing Ar or N_2 for at least 2 h. To remove the sacrificial Ni templates, the samples were immersed overnight either in 17 vol % nitric acid (HNO_3) or in 4.5 vol % iron (III) chloride ($FeCl_3$) followed by 10 % hydrochloric acid (HCl) heated to 80 °C. Finally, they were thoroughly rinsed in deionised (DI) water then allowed to dry completely before further handling.

Fig. V.18 shows the characterization of the synthesized GF. From SEM observations, the wall thickness is estimated to be 10-20 nm, characteristic wrinkles are observed in the foam, arising from the mismatch in thermal expansion coefficients between Ni and graphene [782]; and the interior is hollow, indicating that Ni etching was successful. However, X-Ray Diffraction (XRD) measurements on foams etched with HNO_3 showed residual Ni (Fig. V.18-1g), most likely due to the gas bubbles produced by the reaction of Ni with HNO_3. These gas bubbles could block the infiltration of etchant to some channels of the internal structure. To overcome this, etching was instead performed in $FeCl_3$, which has no gaseous products on reaction with Ni, only soluble salts. These were [781] washed away in hot HCl, which also served to complete the etching process. XRD measurements confirmed that in this way, the resulting GF had few traces of Ni when $FeCl_3$ was used at RT (Fig. V.18-1g), and no traces of Ni when it was at 80 °C. However, in this case there was some residual Fe observed (Fig. V.18-1g).

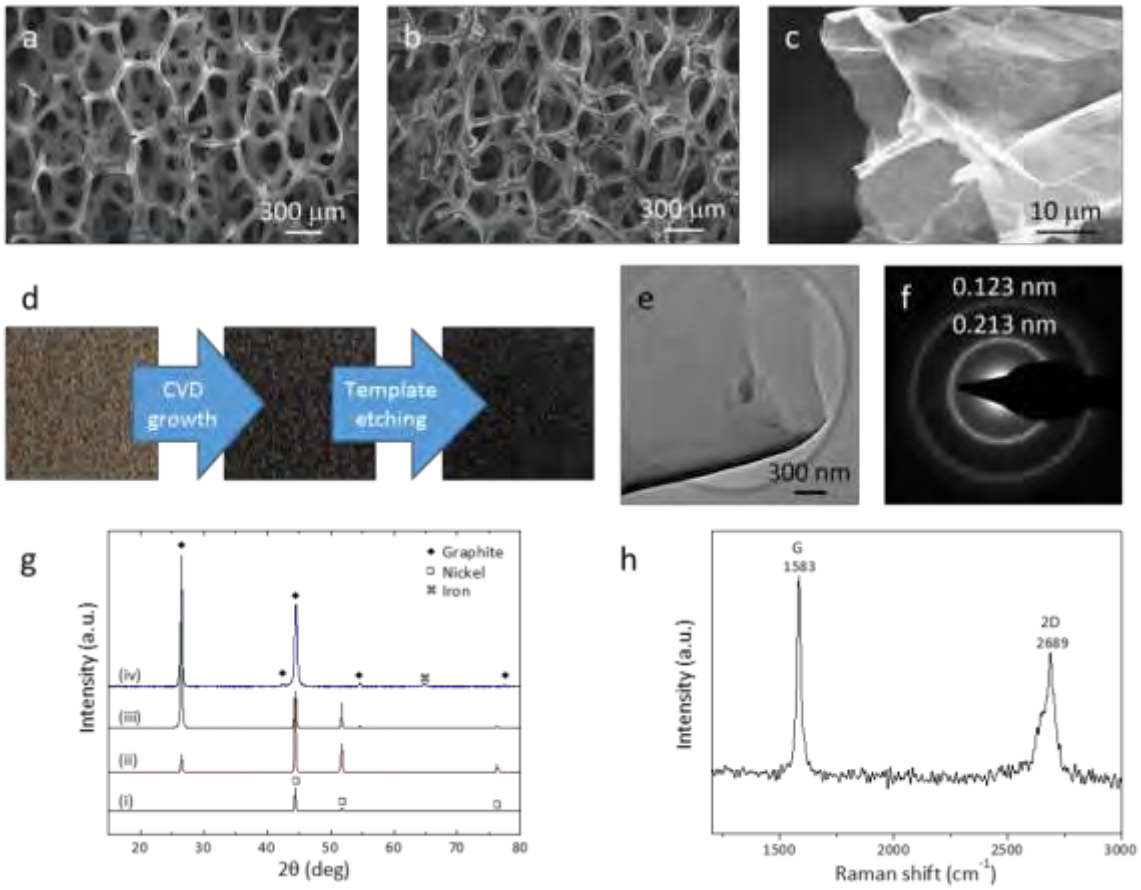

Fig. V.18 Characterisation of GF from Ni foam precursor. SEM images of a) Ni foam as received, b) and c) GF. d) Photographs of foam at different stages of the synthesis process. e) TEM image of GF. f) Electron diffraction pattern from the foam area in e). g) XRD patterns of (i) Ni foam, GF etched with (ii) HNO_3, (iii) $FeCl_3$ followed by hot HCl and (iv) hot $FeCl_3$ followed by hot HCl. h) Raman spectrum of GF, adapted from [781].

TEM diffraction measurements confirmed the polycrystalline graphite nature of the GF, although the thickness of the walls was too large to observe the individual layers of graphene (Fig. V.18 e-f). The quality of the sample was further investigated by Raman spectroscopy (Fig. V.18-h). The lack of a D peak indicates negligible defects. The 2D is consistent with that of FLG. It is worthwhile noting that thinner GF featuring fewer layers of graphene may also be grown by varying parameters such as the amount of CH_4, the growth time and/or T and the cooling rate. However, thinner foams are less robust and require a PMMA support layer during etching process so that they do not collapse [773].

The structures described above, are limited by the commercially-available templates, which typically have pore sizes in the range of 200-400 µm. In this case, most of the volume is occupied by void space rather than graphene, which is a disadvantage in applications such as energy storage, where a high volumetric energy density is required. Thus, a smaller pore size is often desirable.

High density scaffolding have been produced, as described in [783] as follows: Ni and Cu metal powders with typical particle sizes between 0.5 and 150 µm were purchased from Sigma Aldrich (Fig. V.19a). In the case of Cu powder below 1 µm, the powder was additionally mixed with $MgCO_3$ powder to prevent the agglomeration of the metal particles and compressed. The powder was placed into a quartz combustion vessel inserted into a quartz tube in a horizontal tube furnace. An annealing step with a flow of 400 sccm argon and 100 sccm hydrogen at high T for 45 minutes wasused to connect the metal particles (thus forming the metal scaffold, see Fig. V.19b) as well as to remove metal oxides and contamination. The minimum T used for preparing the scaffold was 600°C for Ni and 800°C for Cu. Carbon feedstock was provided by a CH_4 flow of 10 sccm under a constant Ar flow of 400 sccm and a total pressure of 50 mbar and 400 mbar for the case of the growth on Ni and Cu, respectively. These were the minimum pressures yielding closed graphene layers on the metal templates for all the investigated temperatures (Fig. 19c).

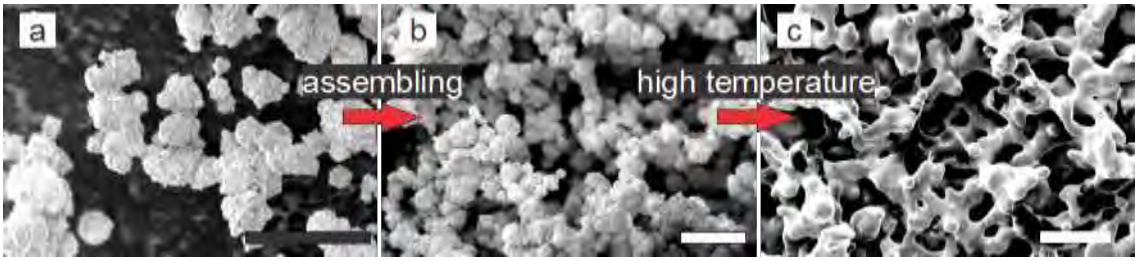

Fig. V.19: Fabrication principle of graphene foams illustrated by scanning electron microscope (SEM) images. (a) Metal particles, in this case Ni, are assembled in a vessel to get (b) a three-dimensional structure. (c) At high temperatures (~600 °C) interconnected metal foams are created; this process is implemented in the CVD annealing step. The scale bars are 20 µm. Adapted from [783]

Fig. V.20a plots a typical Raman spectrum at an excitation wavelength of 532 nm of GFs grown on Cu at 900 °C and Ni at 600 °C. Positions of the 2D peak are ~2695 cm^{-1} and 2699 cm^{-1} for GFs (Cu) and GFs (Ni), respectively, while the FWHM(2D) ~61 cm^{-1} and 80 cm^{-1} for Cu and Ni-grown GFs, respectively, indicating FLG. I(D)/I(G) ~ 0.16 and ~0.25 for Cu- and Ni-grown GFs, respectively, indicating defects.

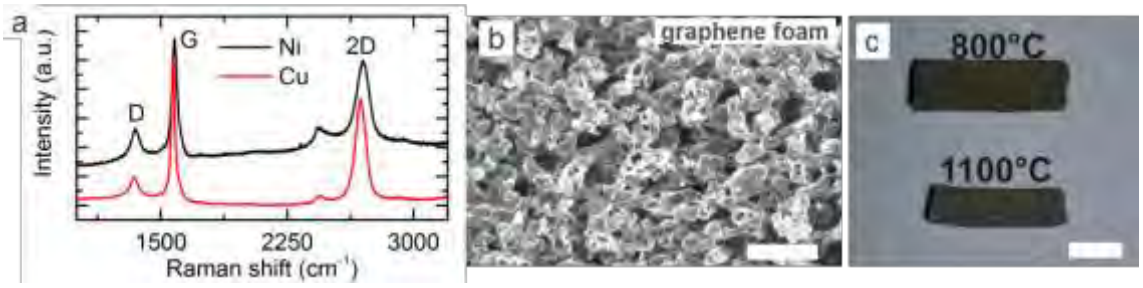

Fig V.20: (a) Raman spectra of GF grown on Cu (red curve) at 900 °C and Ni (black curve) at 600 °C. (b) SEM micrograph of GF grown at 800 °C after metal etch . (c) Optical image of Ni foams fabricated at

800°C and 1100°C using a Ni powder. Scale bar in (b) is 20 µm and in (c) 5 mm. Adapted from ref [781, 783].

For SEM analysis, the GFs were freeze-dried at low pressure in liquid N_2 for several hours in order to prevent the collapse of the foam. A SEM picture of a GF is shown in Fig. V.20b and V.20c depicts an optical image of two Ni foams fabricated at different T.

A similar process was described in ref [781], in which a combination of Ni and NiO nanoparticles compressed into a pellet were used as the template. Despite the presence of NiO, the mechanism for the subsequent growth of graphene did not change, since during the annealing process in a high-T (1000 °C) H_2 atmosphere NiO was reduced to Ni, leading to the same behaviour as for Ni templates. After growth, the sacrificial template was removed. A long period (several days) of immersion in the etching solution was required before no more colour change was observed, indicating that all the Ni had been removed.

Fig. V.21 reports the characterization of the GF produced in this way. The pellet subjected to high pressure (~440 kg cm^{-2}) was too compact (Fig. V.21 a), while the GF synthesized from pellets subjected to low pressure (~50 kg cm^{-2}) shows a well-controlled particle size distribution (Fig. V.21b-c), with a network of interconnected hollow branches of graphene. The pores are in the 1-10 µm range, around 2 orders of magnitude less than the GF grown on commercially-available Ni foam templates. As estimated from the SEM images, the thickness of graphene is less than 10 nm. Indeed, by TEM, 10-30 layers of graphene could be observed (Fig. V.21e-f) and the polycrystalline graphite nature was confirmed as before by diffraction measurements (Fig. V.21g). To analyze the quality of the graphene, Raman spectroscopy was employed using an excitation wavelength of 632.8 nm (Fig. V.21d). The sample was first fragmented slightly to ensure that measurements were taken from the inside of the foam. No D peak was visible in the Raman spectrum, indicating negligible defects and the 2D peak was consistent with that of FLG.

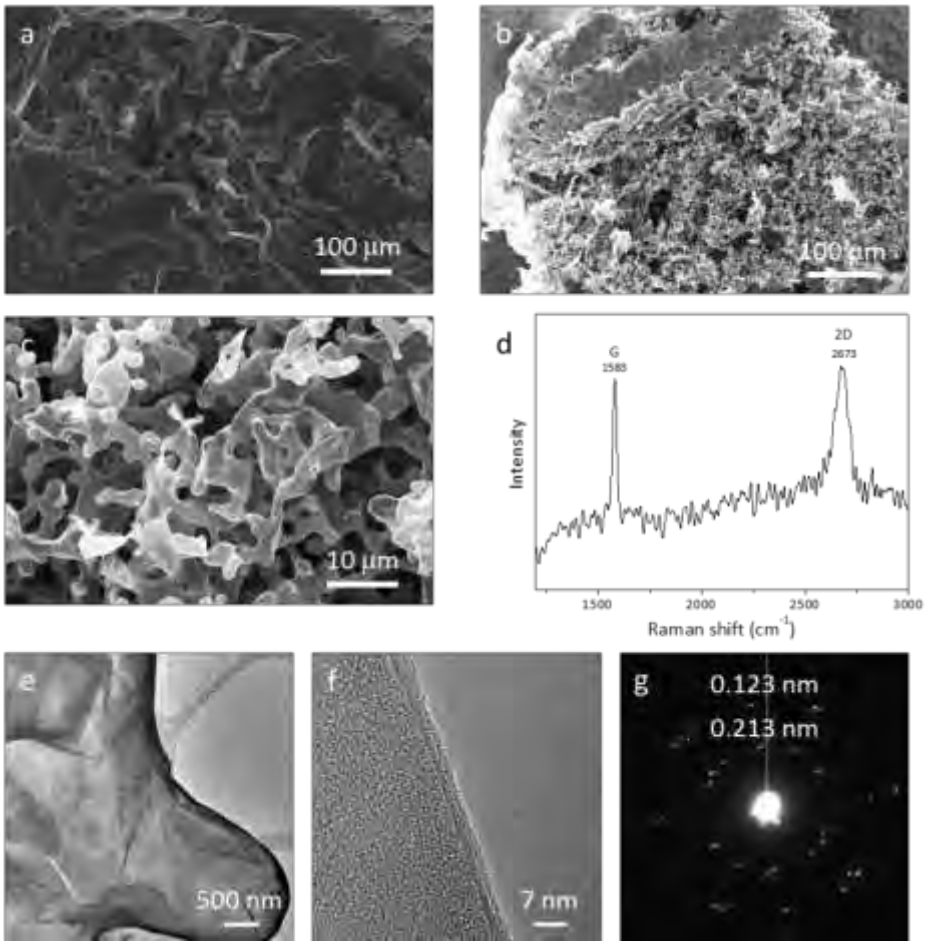

Fig. V.21 a) SEM image of GF from pellet of Ni/NiO nanoparticles pressed under approx. 440 kg/cm^2. The resulting pellets are too compact, with only small areas of porosity where the nanoparticles resist tight packing. b-c) SEM images of the GF from pellet of Ni/NiO nanoparticles pressed under approx. 50 kg/cm^2. d) Raman spectrum from HD-GF sample. e-f) TEM images of the HD-GF foam. g) Electron diffraction pattern from the area in f). Adapted from [781].

UHV-PVD

This method consists in the growth of graphene in a UHV environment, using surface decomposition of organics as C_{60} [784] as a carbon source on polycrystalline Cu foil [785] and Cu, Pt and Ir (111)- single crystals [786-788].

The combination of a UHV environment together with the use of C_{60} molecules provides some advantages with respect to conventional CVD growth [789, 790]. On one hand, this procedure is self-limited, which assures the growth of SLG. On the other hand, the controlled and clean environment (UHV chamber with a base pressure of 10^{-10} mbar) used during the growth results in highly epitaxial graphene samples almost free of defects and impurities with a lower growth T than CVD.

Ref [785] used commercial C_{60} molecules (Sigma, 98% purity) . To control the evaporation rate, a molecular evaporator is needed, that can be either commercial or homemade, as in this case. Fig. V.22 shows a homemade one with a Ta crucible on which a type-K thermocouple has been spot-

welded. The molecules are placed inside the crucible. An electric current is passed through the Cu rods and the molecules are evaporated at 450ºC -500ºC. Molecules are outgassed in UHV conditions prior to growth. To this aim, C_{60} is heated 10ºC above the growth T, until the initial pressure is restored (~10^{-10} mbar) after elimination of the impurities (water, CO, CO_2). Usually the crucible is spot welded to two pieces of steel that are clamped to the copper rods. It is important to have a good electrical contact between the Ta crucible and the rods, otherwise the whole evaporator will be heated and the result will be a rise in the base pressure of the chamber and, therefore, a dirty evaporation.

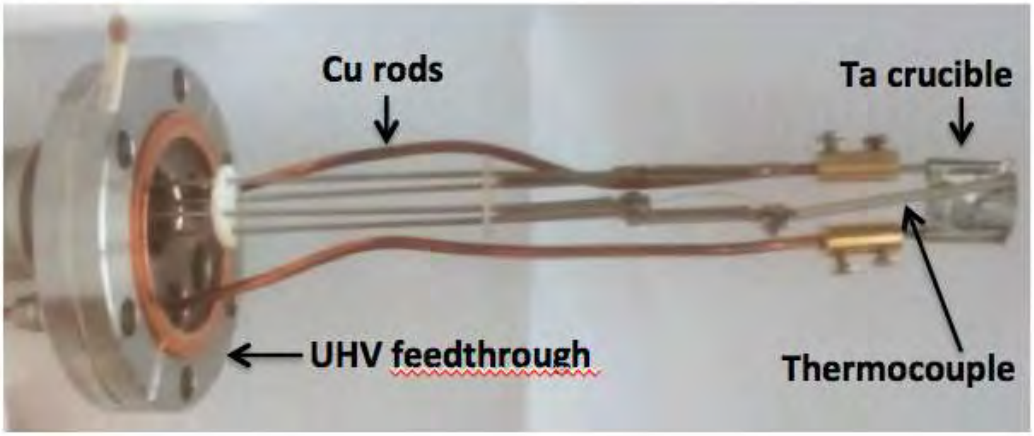

Fig. V.22. Homemade evaporator to evaporate C_{60} in UHV.

Cu, used as a substrate, is cleaned with several sputtering and annealing cycles. A standard preparation consists in five cycles of 10 min Ar sputtering and 10 min annealing by electron bombardment at 800ºC. For the first cycle the sample current is 10 µA. For the last cycle, the sample current is reduced to 5 µA to prevent large surface roughness. With this sample current value a surface roughness of 0.4 nm is obtained. T>800ºC may promote the diffusion of impurities from the bulk to the surface as well as an excessive Cu sublimation, leading to higher roughness.

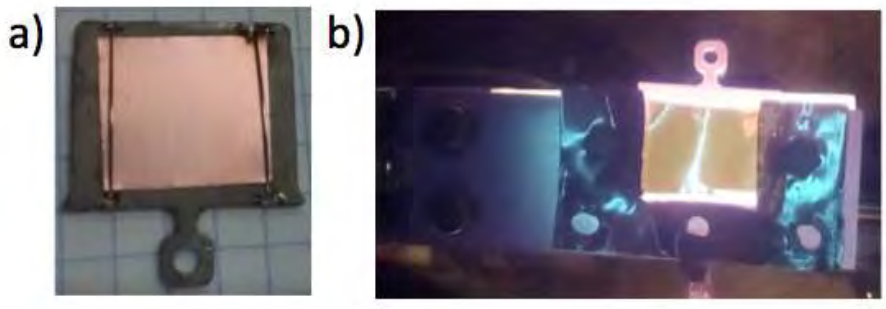

Fig V.23. a) Proper mounting of a Cu foil in a tantalum sample holder. b) Bending of the 25 µm copper foil produced by the thermal expansion of copper.

Fig. V.23a shows a Cu foil mounted on a typical sample holder by using two lateral Ta wires to support it. Other fixing procedures, like the use of glue or carbon tape, are not possible in UHV. The

way the sample is mounted is important because the sample might bend during annealing if the thermal contact with the sample holder is not homogenous (Fig. V.23b). The simplest and more efficient way of improving the thermal contact is the use of thicker Cu substrates.

In-situ surface techniques such as LEED, AES or STM can provide valuable information with no need to expose the sample to the air, thus avoiding surface contamination. Fig. V.24 is a LEED pattern of a Cu foil after cleaning, where multiple spots, corresponding to different grain orientations, are observed.

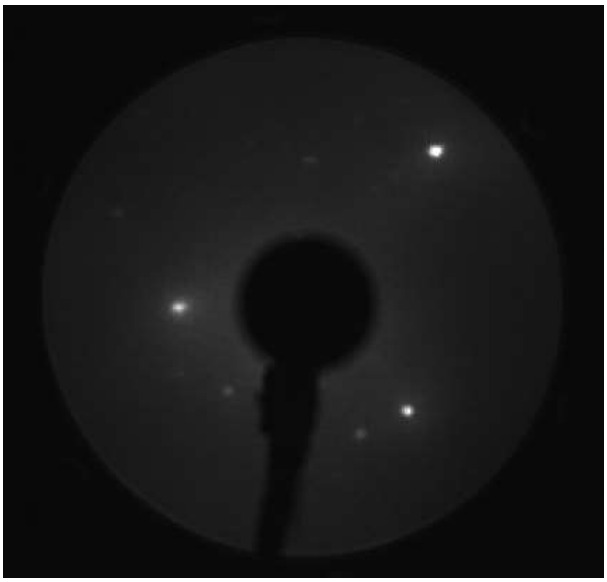

Fig. V.24. LEED pattern at 107 eV of a Cu foil after cleaning and prior to the C_{60} evaporation.

Once the substrate is clean and the molecules purified, the growth consists in exposing the substrate to the molecules at the chosen growth T. Typical parameters are: evaporation T~450ºC, substrate size ~15x20mm^2, 10 cm evaporator/sample distance and growth time ~90min. Coverage can be tuned by changing the exposure time. An important step within the procedure is to have initially the substrate at the growth T before the C_{60} molecules start to sublimate, avoiding that any C_{60} arrives to the sample surface when this is still cold. Different growth trials have been made by first depositing the molecules on the cold surface and making a post-annealing, but this procedure shows less satisfactory results. Once the evaporation is finished, it is important to keep the sample hot until the evaporator gets cold.

This procedure provides polycrystalline SLG on top of the copper foil. The next step involves sample characterization. Fig. V.25a and V.25b exhibit LEED patterns taken at of 50 and 56 eV with a typical ring of a polycrystalline graphene surface. AFM images (Fig. V.25c and V.25d) show very large and flat Cu terraces (hundreds of nanometers) free of contaminants where graphene wrinkles cross all over the area, assuring a complete coverage of a monolayer. Fig. V.25e shows a Raman spectrum

using lambda 532 nm, after background subtraction, taken in the area delimited in the optical image that appears in the inset. The spectrum exhibits a symmetric and narrow 2D peak located at ~2703 cm^{-1} with a FWHM ~28 cm^{-1}, compatible with SLG [86] , with a significant D peak (I_{2D}/I_G ~2.6) that could be due to grain boundaries.

As the solubility of carbon in Cu decreases with decreasing temperature with this method the solubility is reduced four times with respect to the CVD method [715]. For this reason, with this process mainly one layer graphene is growth, without contribution of BLG.

The growth of graphene on single crystals by thermal decomposition of C_{60} does not differ much from the polycrystalline ones. All surfaces must be clean, several sputtering and annealing cycles are mandatory, otherwise defective samples are obtained. Fig. V.26 shows three STM images of graphene on Pt(111), Ir(111) and Cu(111) grown by this method. Some of the typical Moirée patterns that depend on the substrate can be seen. These appear due to the mismatch of the graphene and metal network, meaning that only SLG has grown. More information about STM methods can be found in the section IX. This method leads to a high epitaxial, clean and non-defective graphene not only because it takes place in a UHV environment but also because the precursor contains only C atoms.

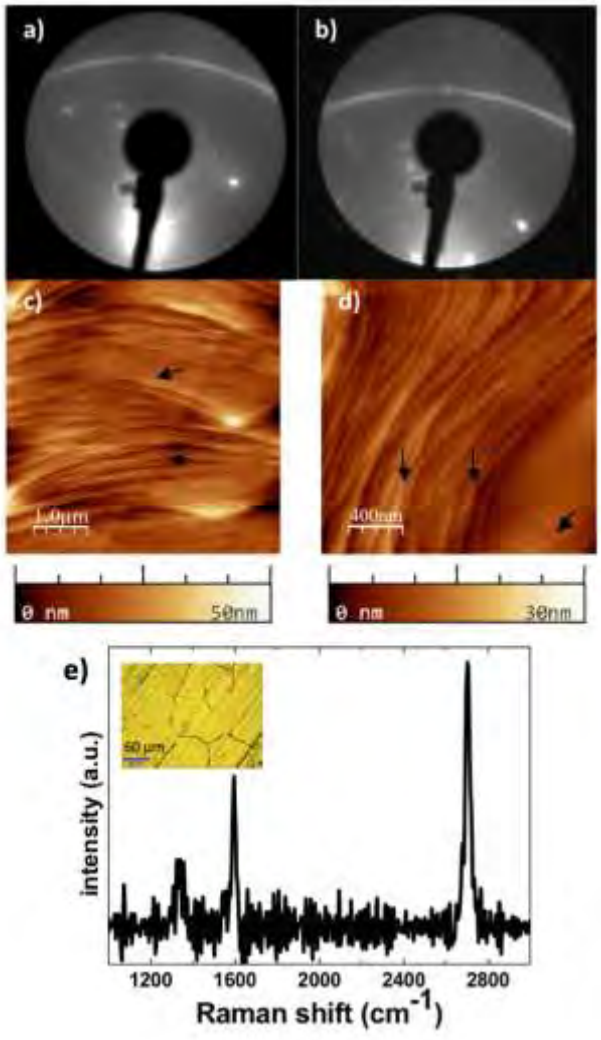

Fig. V.25. LEED patterns with a beam energy of a) 50 eV and b) 56 eV, where the ring of polycrystalline graphene is observed. c) and d) AFM topography images where Cu flat terraces are observed. Wrinkles crossing the terraces (pointed by black arrows). e) Raman spectrum at 532 nm. The inset shows an optical image with Cu grains visible.

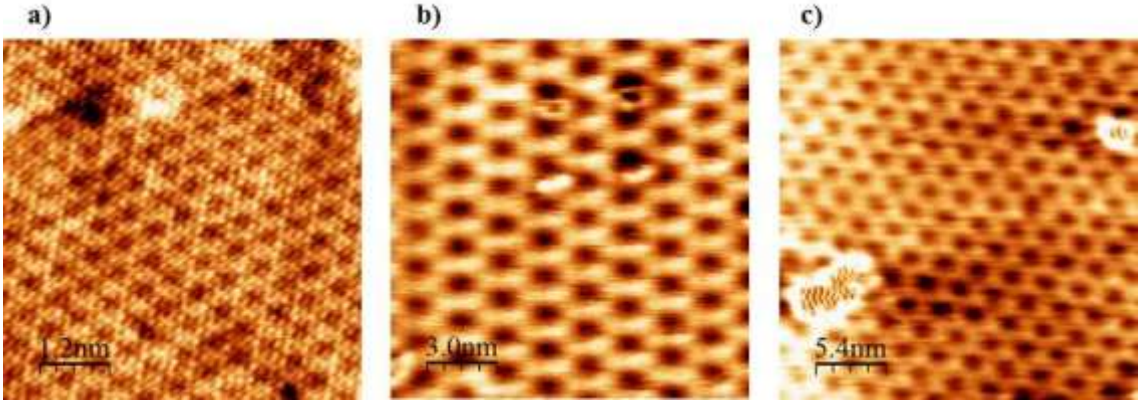

Fig. V.26. STM images of SLG grown from C_{60} on: a) Pt(111), (6x6)nm, 0.11V, 2.3nA. b) Ir(111), (15x15)nm, 1.2V, 2.6 pA and c) Cu(111), (27x27nm), -0.4V, 2.7pA. In every image different Moirée superstructures are shown.

Table V.1 summarizes the main parameters of graphene growth on metals by thermal decomposition of C_{60} for both, Cu foil and single crystals. The key parameter is the substrate T, otherwise C_{60} cage will not break and the result will be a substrate covered with C_{60} molecules.

Table V.1. T and typical evaporation times needed to grow 1ML graphene from thermal decomposition of C_{60} for different substrates (at a sample-evaporator distance of ~10 cm).

Substrate	T sample during evaporation (°C)	Time to have 1ML (min)
Cu foil	800	90'
Cu(111)	900	30'
Pt(111)	850	30'
Ir(111)	900	30'

MBE

Several physical evaporation methods employing sublimation from a carbon source have been used, like electron beam evaporator [791, 792], or a resistively-heated piece of graphite [715,

793] . The growth of single layer graphene (nanometer-sized domains) on hexagonal boron nitride by MBE has been recently demonstrated [794].

Ref [795] used a solid carbon source consisting of a glassy carbon filament connected by two refractory metal bars to a DC current source. Thanks to a 10 times higher resistivity of glassy carbon vs. graphite, it is possible to use moderate electrical current ~ 14-18 A [796] . This fact makes this method simple and easy to install in a UHV system, significantly reducing contamination. Ref [795] showed that for MBE growth of graphene, the substrate can be at lower T than in other methods as hydrocarbon or polycyclic aromatic decomposition [787, 791, 792]. This enables large area growth on dielectric substrates in an inherent transfer free process. Also, in situ surface science analysis techniques (LEED, RHEED, STM, XPS) can be used in a highly controllable growth environment (growth rate, substrate type, substrate temperature, in situ doping).

The evaporation growth rates used are generally very as low as 3×10^{-4}ML/s to avoid a rapid degeneration of the glassy carbon filament. This requires a sample-to-source distance of tens of millimeters. At this distance the sample is radiatively heated.

An evaporation carbon source can be fabricated [797], using as a carbon source a resistively heated piece of glassy carbon [798], with a higher resistivity than graphite, thus makes it an ideal for constructing heating elements [799].

Using a 0.3mm thick glassy carbon plate cut in the desired shape (see Fig V.27) by laser or water-jet cutting, one gets the carbon source as shown in Fig. V.27b. The glassy carbon filament is mounted on a standard UHV feedthrough, terminated with Ta rods, and fixed with Mo screws.

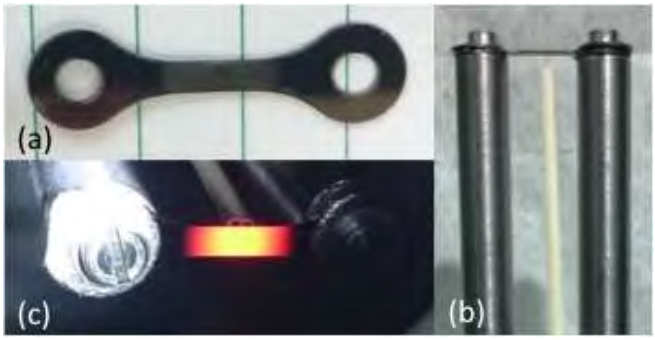

Fig V.27. A glassy carbon filament (a) is mounted on an UHV electrical feedthough (b) and resistively heated (c). T is simultaneously measured with an optical pyrometer and a type-C thermocouple located on the back side.

The C Source is placed in a deposition UHV system, base pressure 1×10^{-10}mbar heated using a DC current. The T calibration of the cell is performed in a separate UHV system with a base pressure 1×10^{-8}mbar. The T in the hottest spot of the filament is measured using a dual-color optical pyrometer through an optical window located in front of the cell. Evaporation of carbon starts for temperatures above 2000ºC. For example, using a DC current of 14A (˜100W) the filament is at 2014ºC. A clear correlation of the increase of the partial pressure of atomic mass unit number 12 (a.m.u.) is observed in a residual gas analyzer (quadrupole) with source temperature. The presence

of amu 12 can be associated to the evaporation of monoatomic carbon. The deposition rate is 3×10^{-4} SLG/s

By exposing a clean Pt(111) substrate to the carbon source the formation of carbon structures is observed [795]. First, the glassy carbon filament at a T> 2000ºC for is degassed for 15 minutes. The pressure is kept< 1×10^{-8} mbar. Before growth, the Pt single crystal is cleaned by cycles of Ar^+ sputtering and annealing at 850ºC. The cycles are repeated until a sharp LEED pattern is observed, an AES spectra where only the platinum peaks appears and/or STM images showing clean and flat extended regions. Then, one places the Pt (111) substrate at ~650ºC in front of the carbon source at 2000º with a distance between them of 20 mm. After 30 minutes a 0.5ML of SLG is attained. During the process the pressure is around 7×10^{-9}mbar. The procedure works equally well if the sample is annealed after growth. The graphene formation is demonstrated by in situ LEED and STM. The LEED diagram as shown in Fig V.28a shows the spots corresponding to the Pt(111) plus a surrounding ring characteristic of the graphene. Brighter spots along the ring are indicative of the preferential orientations of the carbon periodicity with respect to the platinum crystal orientation. Fig V.28b shows an STM image (see section IX.1.4) measured on the graphene areas. The bigger periodicity (bright bumps) of the image corresponds to one of the possible moirés. The smaller periodicity (diagonal lines) is the atomic corrugation of the graphene. Graphene covers extended regions of the surface with a surface morphology similar to growth from decomposition of hydrocarbons or aromatic molecules.

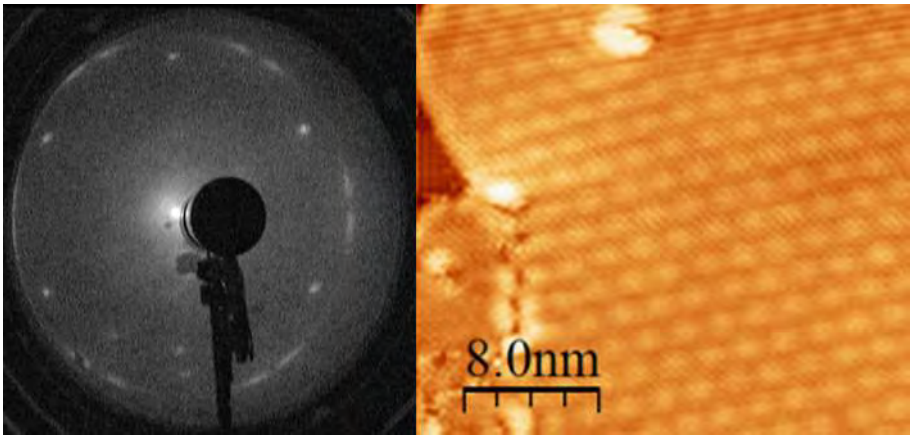

Fig V.28. a) LEED pattern obtained on G/Pt(111). b) STM image showing a moiré and the atomic corrugation of the graphene. Adapted from [795].

The use of gold as a substrate is difficult, since the T neede to obtain graphene is too close to Au melting point [791, 792] . A solid-carbon source can b used to decrease the T needed to obtain graphene on Au.

The Au (111) substrate is kept at 550ºC, with a well degassed Carbon filament. This step can last for days because the freshly new filaments are porous containing many impurities. The degas pressure needs to be <5×10^{-9} mbar when the glassy carbon filament is at~1600°C (12A, 83W) .If this

step is not performed correctly, the samples get covered by an amorphous layer and the substrate has to be cleaned again.

In case of graphene growth by supersonic molecular beam epitaxy (SuMBE) [800, 801], the two major issues to take into account are the substrate type and kinetic energy (KE). The main steps are the following:

- *Surface preparation.* Numerous (up to 40) Ar ion sputtering (0.5 keV) and annealing cycles of the Cu substrate (T>700°C for obtaining optimal LEED diffraction pattern) to avoid the presence of unwanted contaminants, such as oxygen, sulphur or remaining carbons, during the film growth.
- *Carrier gas choice*. He or H_2; in this respect, the use of noble gases prevents strong interactions between the carrier gas and the substrate and does not affect C_{60} internal dynamics, which is frozen unlike ordinary heating that dramatically increases the molecular vibrations.
- *Aerodynamical acceleration* of the highly diluted (less than 1% of the mixture) C_{60} beam by isentropic expansion of the flux out of the injection cell into vacuum through a nozzle. By changing the carrier gas and the seeding parameters (source T, gas inlet pressure), fullerene KE can be tuned, being inversely proportional to the carrier gas mass. KE ~ 10–15 eV using He carrier gas up to 30–40 eV using H_2.
- *Collimation* of the expanded flux and impact of the organic molecules on the Cu reconstructed surface, keeping the substrate at RT.
- *Thermal activated growth* of graphene islands by increasing T to 645 ^{o}C.

Ref [802, 803] showed that substrate temperature must be raised to 645 ºC to synthesize graphene islands as C_{60} high-energy deposition on Cu, even at the highest KE reachable by SuMBE, does not lead to immediate C_{60} cage rupture.

The ultimate evidence of the presence of defected nanometric graphene islands comes both STM and Raman spectroscopy [803]. Finally, this process is expected to be self-limiting and to stop completely as soon as the Cu surface is entirely covered by a monolayer of carbon atoms.

Ref. [803] reported a coating of graphene-like material at 645 ^{o}C using H_2 as carrier gas. These nanoislands also contain pentagons, which come from the original buckyball structures. Thus, at this stage this is just a proof of principle approach. The technique looks could be applied to a wide range of substrates, such as semiconductors and insulators avoiding the transfer from the growth substrate.

V.2 Growth on insulators

Plasma Enhanced CVD

PECVD enables the direct growth, catalyst free, by the activation of molecules in gas phase and reduces the high T in conventional CVD needed on catalysis -or even higher in attempts to use pyrolysis [804-812]. The most important drawback is the resulting small grain size.

Refs [813-815] reported PECVD on non-metallic substrates, resulting in films with small grain sizes -from 2 to 30 nm-, and amorphous carbon . Ref. [816] reported an enlargement of grain size was achieved by a "two-step" growth strategy in a remote electron cyclotron resonance plasma assisted chemical vapor deposition, r-(ECR-CVD), system, Fig. V.29. The entire protocol is shown in Fig. V.30.

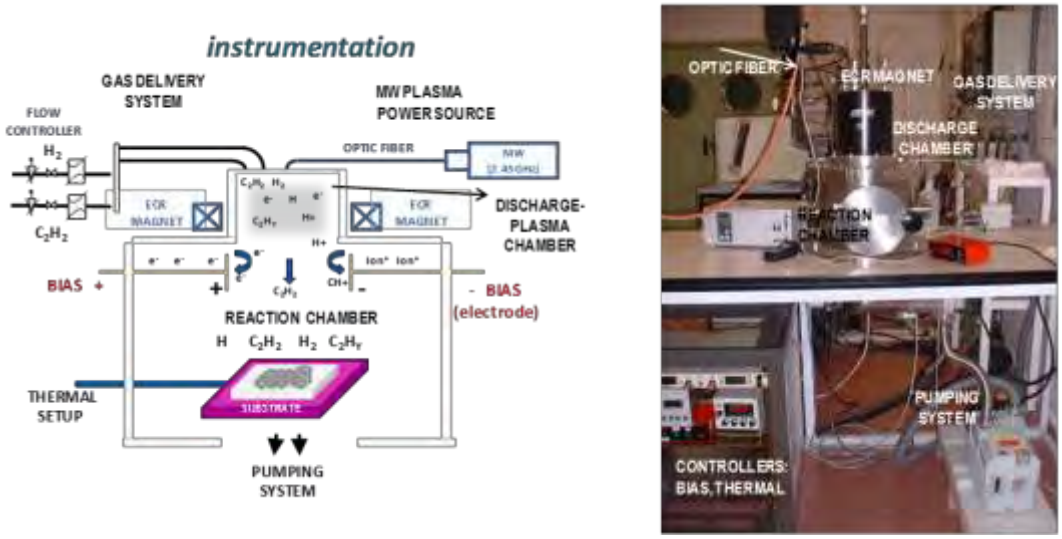

Fig. V.29. Schematic illustration (left) and picture (right) of a r-(ECR-CVD) Plasma system. The instrumentation consists of a gas delivery system with flow controllers, an ASTEX AX 2000 microwave power source with and optic fiber coupling the power to the discharge plasma chamber with an ECR magnet surrounding it. The activated gases are transported by forced convection, with two electrodes attracting electrons and ions. The substrate is independently heated. A two stage pumping system generates the vacuum. Adapted from ref [815].

The various parameters (time (t), T and partial pressures of C_2H_2 and H_2 ,PC_2H_2 and PH_2, respectively) were tuned "in situ" in the nucleation (t_1, T_1, $P_1C_2H_2/P_1H_2$) of high quality graphitic seeds and growth from the seeds edges (t_2, T_2, $P_2C_2H_2/P_2H_2$) stages. A post-growth annealing is applied in UHV, improving the final properties of the film. The detailed procedure is usually as follows :

- Evacuation down to 10^{-5} mbar, introduction molecular H_2 at a $P_1H_{2=}$ 10^{-2} mbar (typical flow of H_2=55 sccm) and increase T up to T_1= 500ºC-700ºC in 40-60 min ($t_{0,}$ Fig. V.30) for stabilization. Subsequently, annealing the substrate for 5 min. In some cases is interesting to bias the substrate with a positive potential (0V- 50V) if the auto polarization due to the plasma is not positive.
- Step 1 (NUCLEATION): Introduction of C_2H_2, at a $P_1C_2H_2$= 10^{-4} mbar, typical flow = 0.25:0.20 sccm and turn on the plasma (100 W) during 5 min (t_1, Fig. V.30).

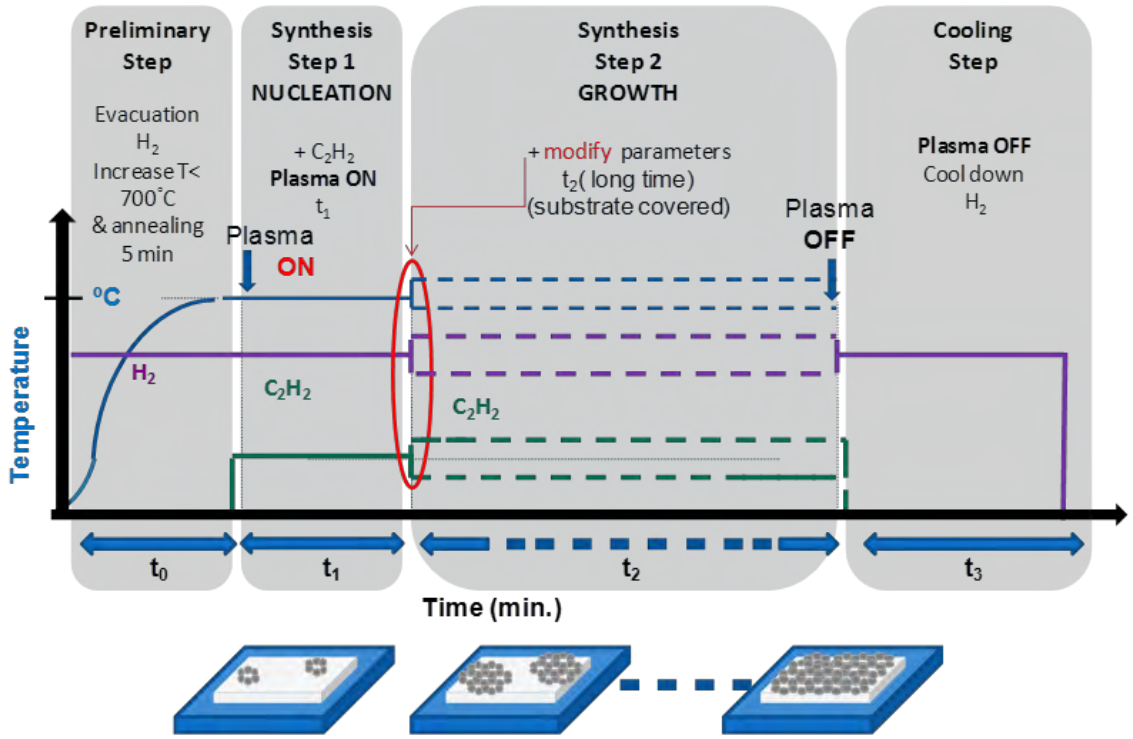

Fig V.30. "Two step" synthesis protocol.

- Step 2 (GROWTH): Modify T_2 in a range of 30-100ºC or $P_2C_2H_2/P_2H_2$ in the 0.1-0.9·10^{-4} mbar range between (10-20 %), maintaining it for few hours (t_2, Fig. V.30), until the substrate is completely covered. As a general rule, ($P_2C_2H_2$ is modified, due to its minimal relevance in the final pressure.
- Turn the plasma and bias off and cut the flow of precursor ($P_2C_2H_2$), cooling down in hydrogen atmosphere (P_2H_2) during 40 min (t_3, Fig V.30) preventing oxidation. Post growth annealing in UHV at 650ºC, to desorb some chemical species attached to grain boundaries and to improve the coalescence among the grains.

AFM images of lateral force contrast are shown in Fig. V.31a-c .Raman analysis strongly indicates in this example the formation of predominantly monolayer graphene at 650°C, FigV.31 a-d).

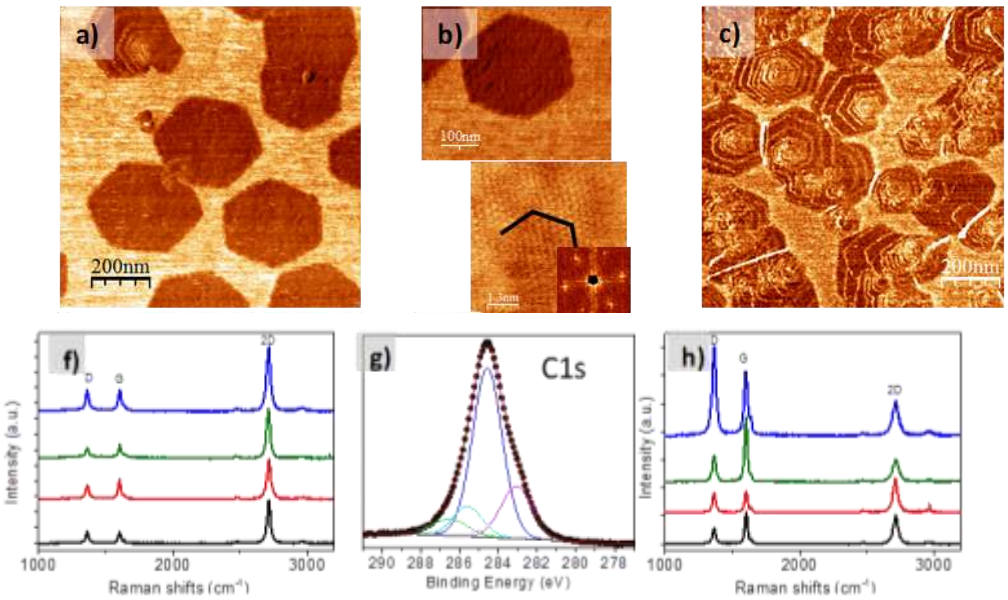

Fig. V.31. Graphene on quartz at H_2 / C_2H_2 = 55/0.25:0.20 (sccm), P_T = 5.4×10^{-2} mbar, P = 100 W for 5 min nucleation time, 9 hour growth. AFM lateral force image of the sample grown at a) T= 650 °C and c) T= 700°C b) High magnification lateral force image of a single flake from sample grown at 650°C. Image below shows the atomic lattice periodicity corresponding to the flake in b). The inset is the Fast-Fourier transform of the periodicity image. d, f) Individual spectra acquired at grain positions, for both samples. e) High resolution XPS C1s core level spectrum (black dots) of the sample grown at 650°C. The C-sp^2 graphitic component (blue, 284.6 eV), C-H (green, 285.6 eV) likely from H-terminated edges, and C-O (cyan, 286.5 eV) species. The component at (magenta, 283 eV) can be ascribed to remainders of the growth process (e.g. C_2H_4Si at 282.5 eV) or to the interaction with substrate (e.g. SiC C(1s) is 282.5-283.5 eV).Adapted from [816].

Fig. V.32 presents an AFM characterization of continuous film, confirmed by four point probe measurements, with a R_S~3.4 kΩ·sq^{-1}. The coalescence of graphene grains follows two different trends (Fig V.32 (a)-(b)). Hexagonal graphene domains of similar orientation often generate a smooth lateral merging, presenting boundaries without linear defects (Fig V.32(b), black arrows) [735, 817-820] [563]. On the other hand, rough lateral merging also takes place at many points, where linear defects occur (Fig. 32(b), pink line). On these defects, carbon species accumulate as in vertical graphene deposition [821] that indicates that the process is not completely self-limiting. From UV-Vis-NIR spectrophotometry transmittance (Fig. V.32c), it is also clear that there is an influence of this accumulation (values around 95%, lower than in typical SLG).

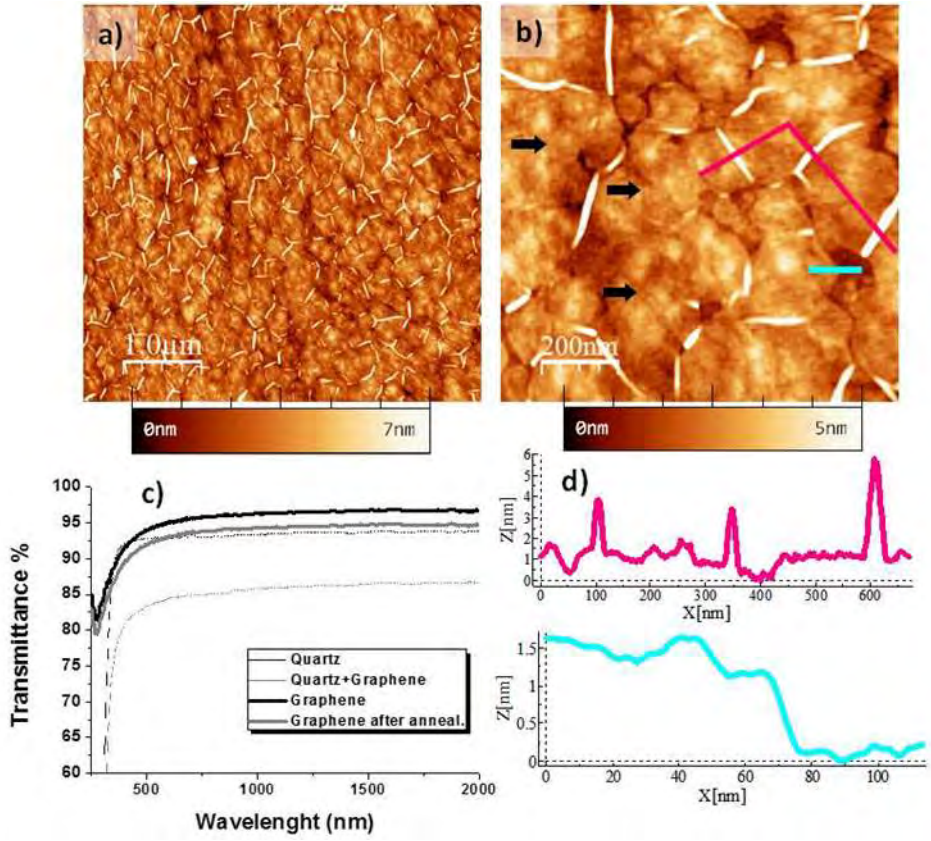

Fig V.32.-.Characterization of continuous film T = 650 °C, H_2/C_2H_2 = 55/0.25:0.20 (sccm), $P_T = 5.4\times10^{-2}$ mbar: P = 100 W. a-b) AFM topographic images of graphene deposition on quartz for 5 min nucleation time and 10 hour growth. c) Transmittance spectra before (95%) and after (92%) post-growth annealing. d) Height profiles taken along the corresponding lines in b) (film thickness, cyan). See main text.

After growth, the sample can be annealed in UHV to improve the final properties of the film. Ref. [816] increased T stepwise up to 600°C. The height and density of the linear defects is lower after annealing. R_S decreased from~3.4 kΩ·sq^{-1} to~900 Ω·sq^{-1}, with transmittance>92%. The protocol is scalable it is likely accelerated by changing plasma power and pressure.

The r-(ECR-CVD) mode activated by microwave (MW) source provides higher efficiency in the dissociation of gases than other plasma sources and it is especially efficient in the dissociation of H_2. It is one order of magnitude more efficient than other DC (continuous polarization) and RF (radiofrequency) plasma sources. Along with the activated species and neutral radicals, ions and electrons coexist, being mostly the highly energetic ions a potential cause of etching of films. From a geometric point of view, a minimum distance between the plasma zone and the substrate (20 cm) should be respected ("remote plasma activation"). Moreover, the inhomogeneous plasma activation (plasma ball) results in different deposition rates on different sites. For this reason, to make de process reproducible the position of the sample in the holder is critical and must be respected. Apart from geometric considerations, one parameter that can minimize the presence of remaining ions reaching the sample is the positive bias of the substrate [822-824]. The activation of the substrate is

also minimized preventing high nucleation density. The last fundamental plasma parameter is the power; the higher the power, the grater is the gas activation. However, as this protocol is a competitive process between etching and growth, assessing the role of power is not so straightforward. The increase of power itself does not reflect a proportional increase of all species.

A T increase keeping the other parameters, results in an increase of the reaction rate but at the expense of an enhanced nucleation density due to the present dangling bonds in freshly activated oxide surfaces. As a minimum T> 400ºC is needed for graphitization. The key is to favor the reaction at the graphene edge instead of reaction with substrate by carefully playing with the local saturation of carbon. In Fig V.31, a deviation in T from the established recipe affects the nucleation density, growth rate, microstructure and number of layers. Fig V.31a shows single layer grains at 650°C. At 700°C, Fig V.31c-f more flakes of few layers are predominant. Moreover, side chemical and topological effects take place, as covalent bonding with substrate or etching, hindering the desired "Van der Waals" interaction. Formation of carbide phases or volatilization of oxide species (CO, H_2O, OH, SiO...) can be produced. There are interdependence between the pressure and T, as the unbalanced pressure has similar effects, as observed in Fig V.33 (variation of 20% of gas flow). If hydrocarbon flow is below the critical value at a given T, there is no deposition in the nucleation step. If it is over, the deposited nuclei suffer from amorphization. In the second step, a similar effect occurs with (T_2) or partial pressures relation ($P_2C_2H_2/P_2H_2$), resulting in secondary nucleation or etching of the deposited material. In Fig V.33a and 33c a deposition of submonolayer graphene can be seen in topography and friction images respectively. In Fig V.33b-d more few layer flakes are deposited increasing pressure.

The precursors and atomic hydrogen (H), also play a critical role. Appropriate H/C_xH_y relation in the atmosphere, is a necessary condition to grow crystalline material [825]. There is a competition between the growth from C_xH_y radicals and the etching of amorphous deposits by atomic H [826] [827]. The etching rate depends on the temperature and number of graphene layers.

Ref. [816] found that C_2H_2 is a suitable precursor for low T, and no relevant differences were found between the films deposited with CH_4 and C_2H_2 diluted in hydrogen, once the appropriate H/CxHy relation and temperature) settings are selected. For C_2H_2 the activation is much higher due to combination of plasma and thermal activation (that does not happen with CH_4) [828]. This enhances the reaction rate because the plasma environment is full of activated carbon dimmers, postulated as the main precursor, or at least the main intermediate product, in the case of the synthesis of graphene, due to their higher mobility [829, 830].

Ref. [816] used fused silica at high temperature, up to 700ºC. However, some kind of modification was detected in the surface and changed to quartz.

Dangling bonds in freshly activated surfaces (oxides or insulators) promote strong chemical interaction between the surface and gases. To overcome this limitation Ref. [816] developed a two step process where the edge growth from seeds is highly favored over the nucleation on substrate. Even so, some limitations continue as the process is slow and not completely self-limiting. High

plasma power in remote systems, confined flow configurations as well as a new revision on precursors and chemical etching agents should be assessed in near future.

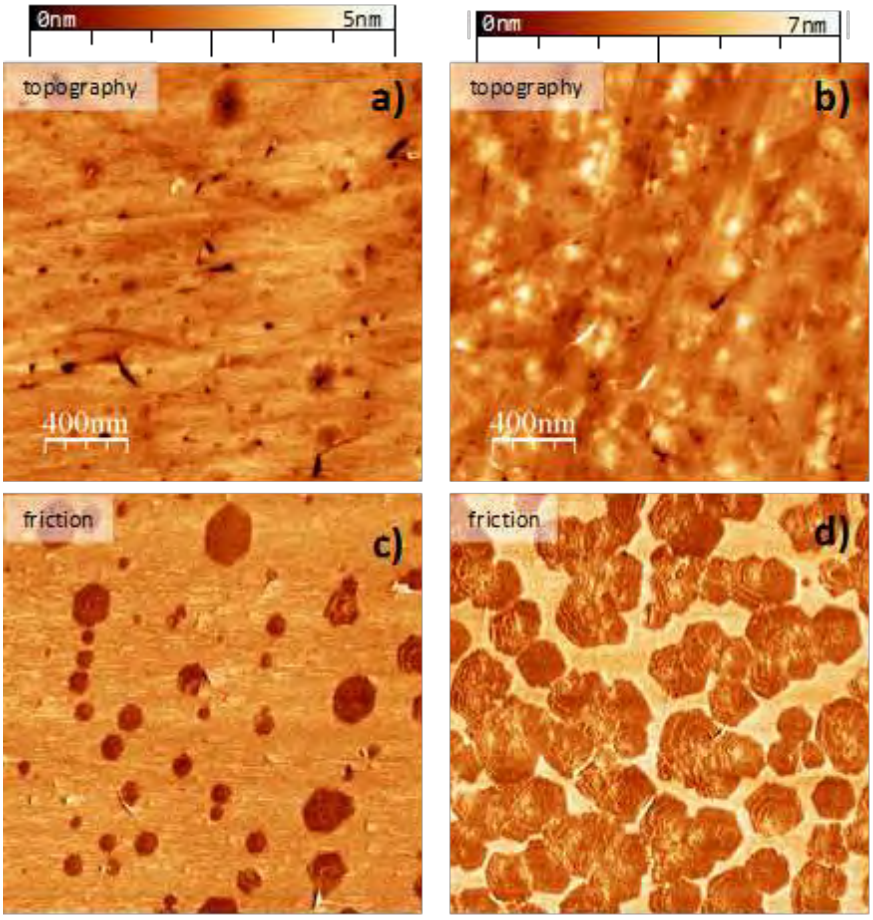

Fig. V.33. Graphene on quartz T= 650ºC, PT = 5.4×10-2 mbar: P = 100 W. t1 =5min. t2= 690min. Topographic (top row) and corresponding lateral force (bottom row) AFM images of samples grown at increasing pressure from a) H_2/C_2H_2 = 55 0.25:0.20 (sccm) to b) H_2 / C_2H_2 = 55 / 0.30:0.25 (sccm). The increase in the number of FLG with increasing pressure is seen.

Growth of vertical structures

PECVD can be used to synthesize graphene directly on insulators. In ref [831-833] a cold wall chamber is pumped by a turbo pump and an RF plasma power of up to 1000W is applied on top of the chamber, through a matching network. H_2 and CH_4 are used as gas precursors (Fig. V.34a). Different growth conditions were investigated and the highest film uniformity was achieved by using a 1000W RF plasma, a T= 750°C and a growth time of 20s. Fig. V.34b shows an AFM image of the grown film directly on Si/SiO_2, highlighting a film roughness of 0.624nm. The film thickness was 3.33 nm (Fig. V.34c), indicating multilayer graphene.

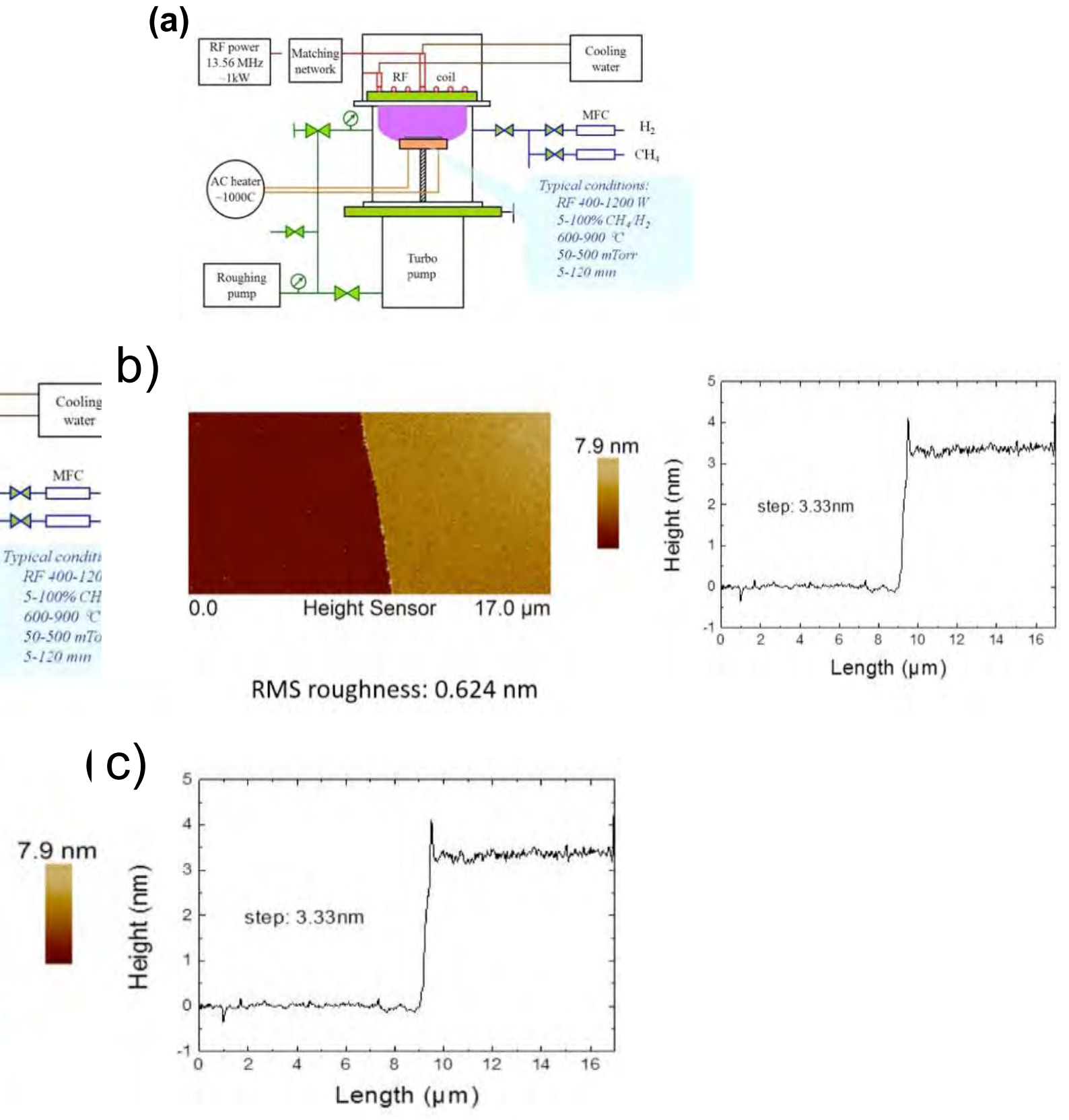

Fig V.34. (a) Schematic PECVD system used to grow graphene films on Si/SiO_2. Figure reproduced from Ref. [833] (b) AFM image of the grown graphene film (c) Height profile.

Using the same PECVD system, vertically oriented graphene nanosheets (VOGNs) on Ni can be prepared [831-833].

Sacrificial metal layers

By replacing Cu foil with a thin sacrificial metallic film one may arrive at an alternative route for the direct graphene deposition on dielectrics. The proposed approach is based on the fact that in the CVD process, graphene grows on copper-substrate interface provided that carbon precursor has access to it [722, 834]. Thus, by removing the graphene from the copper surface and wet etching of the copper remains one obtains graphene deposited directly on a substrate.

Ref. [834] up to 300 nm thick thermally evaporated sacrificial layers of 99.999 % pure Cu on silica or on SiO_2/Si wafer was used. Cu evaporation does not require UHV, although the higher vacuum reduce the oxidation of the deposited copper film. Ref. [834] indicated that a vacuum level~10^{-5} Bar is sufficient. Since the surface of the deposited Cu layer rapidly oxidizes in an ambient atmosphere [835], it is advisable to start the CVD process soon after evaporation to minimize the amount of Cu oxide. Otherwise, the copper oxide can be removed by treatment of the deposited layer in acetic acid [835, 836]. Ref [834] places the substrate into the CVD chamber right immediately after the Cu film deposition and pumped down the chamber for an hour. While pumping injected 5 sccm H_2 is admitted to remove moist and air remains from the chamber. Thereafter, the chamber is heated up to 700 °C in H_2 atmosphere (5 sccm, 0.5 mBar, 20 °C/min). At 700 °C the CVD chamber is vacuumed and CH_4:H_2 (1:1) gas mix injected (8 mBar, static atmosphere). T is risen (10 °C/min) up to 950 °C and kept for 5 minutes and then the chamber is cooled down to 700 °C in one hour. At 700 °C the CH_4-H_2 gas mix is replaced with H_2 (10 mBar) and the chamber is cooled down to RT overnight (see also Ref [834, 837]).

Surface melting is a key process that governs the deposition of graphene. Although the melting T of bulk Cu is 1084 °C, the melting of low dimensional systems takes place in a much lower range [838] . Therefore, although the hydrocarbon catalysis starts at around 800 °C – 900 °C [839, 840], in Ref [834], CH_4 was injected into the chamber at 700 °C. At this temperature, catalytic decomposition of methane involves mobile atoms of molten Cu. Since the carbon solubility in Cu is very low (< 10 ppm at 950 °C) [715] , the migration of the carbon atoms bound to Cu atoms is mainly restricted to the surface [722, 841, 842]. When a few hundred nm thick Cu film melts, melting of each copper grain results in well-defined grain boundaries [722]. Highly mobile Cu atoms carry carbon atoms along the molten grain boundaries allowing them to penetrate into the Cu film and arrive at the substrate surface [722, 834]. This effect eventually results in graphene synthesis on substrate-Cu interface. After reaching the maximum T~950 °C the reactor cools down very slowly, i.e. the carbon precursor (CH_4-H_2 mixture) is available for graphene synthesis at the surface of the melted Cu grains until the Cu solidifies at 700 °C.

The Cu film thickness is an important parameter [834]. When the thickness of an original Cu film < 100 nm the melted Cu film recedes forming mainly round droplets of submicron radii covered

by graphene, with no graphene between those Cu droplets. When the thickness is~300 nm the Cu film remains solid after the process, resulting grainy but continuous graphene film to the Cu-substrate interface [834].

The topmost layer of graphene can be removed from Cu by oxygen plasma (20 sccm/100 W/1 min), while the remaining copper protects the graphene layer at the Cu-substrate interface. The remaining Cu is etched out by ferric chloride solution. If the topmost graphene is not removed, it will usually stay on the substrate surface as small, arbitrary ribbons and fragments.

Raman characterization in Fig. V.35 (c)-(d) shows a small D-peak and the absence of amorphous carbon [843]. The SEM image at Fig. V.35 (b) indicates that the material is grainy and consist of μm and subμm flakes. Ref [722] reported a rather poor μ of about 300 $cm^2V^{-1}s^{-1}$. However, the linear and nonlinear optical properties of directly deposited graphene are somewhat comparable to graphene grown on copper foil [844].

One major part of the process is that of the substrate surface. Similarly to controle the water droplet behaviour by modifying the surface wettability [845], surface modifications can be used to control molten Cu [837]. In Fig. V.36(a)-(c) one can observe a grating structure that has been under the Cu film during CVD. The continuous Cu film has first melted and receded in between grating lines. Under those copper lines, graphene lines are located. When the width of the grating lines is sub-μm, the lines are no more discrete but sometimes merge together [837].

Deposition on thin Cu film does not offer an ideal route for graphene synthesis. An important drawback is the very high, 900 °C – 1000 °C deposition T. This makes graphene deposition impossible on some substrates because (i) substrate melting (e.g. polymer substrates), (ii) recrystallization of a thin film (e.g. amorphous titanium dioxide) or (iii) thin film-substrate thermal expansion mismatch, which may cause thin film material to crack out from the substrate surface. Moreover, high synthesis T may start a chemical reaction between the metal and the substrate (e.g. Si may react with Cu or Ni).

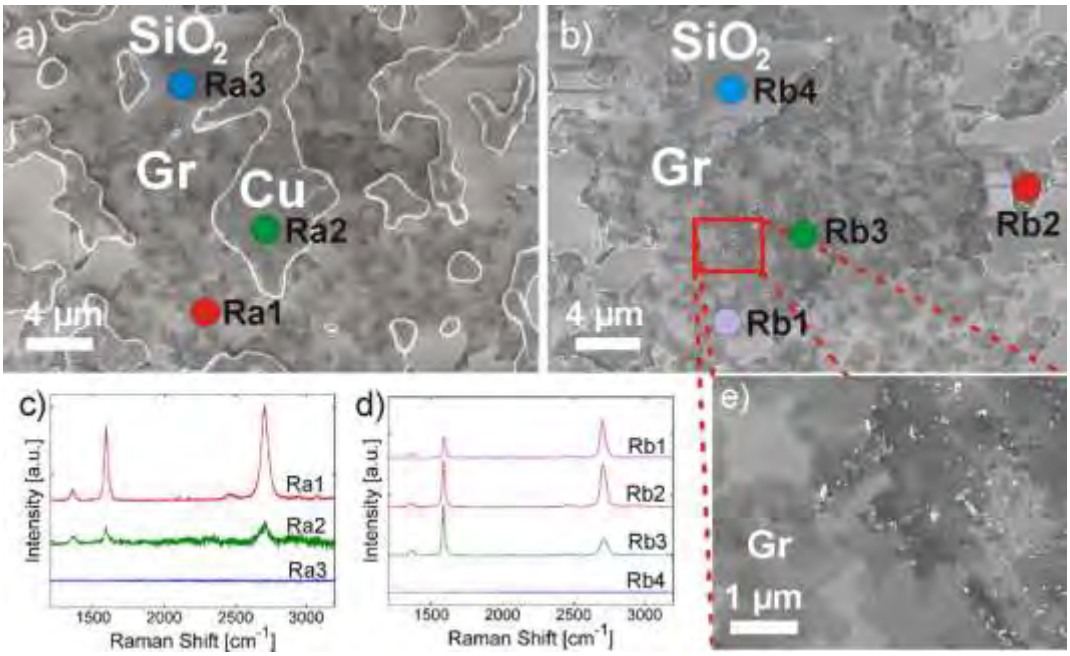

Fig V.35. SEM images of sample with (a) and without (b,c) Cu catalyst remains after CVD. Raman spectra with (c) and without (d) Cu catalyst. (e) High resolution SEM image from border area where Cu remains are removed. Adapted from Ref [834].

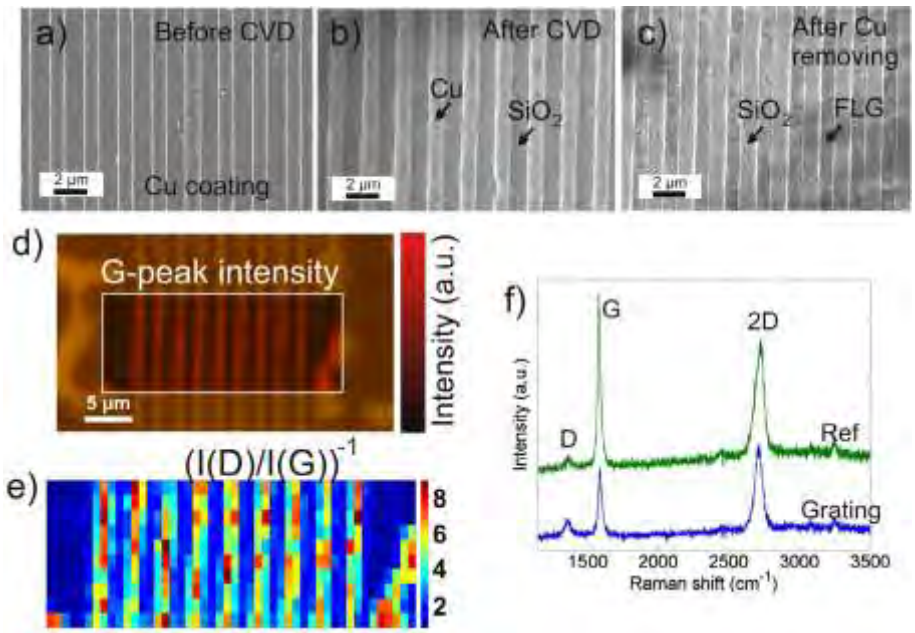

Fig. V.36. (a,b,c) SEM images of sample before CVD, after CVD and after Cu removal in $FeCl_3$. (d,e) Raman mapping reveals graphene on the grating. (f) Raman spectrum of the grating area (Grating) is comparable to that grown outside grating area . Adapted from Ref[837].

Conversion of amorphous carbon and other carbon sources

One can employ liquid and solid carbon precursors for graphene synthesis [753, 846-850]. Regarding the substrate, due to higher carbon solubility and lower reaction T, Ni can be considered a more aggressive catalyst in comparison to Cu. Its use may be advantageous when solid carbon precursors are chosen. Ni-catalysis is activated at a few hundred degrees lower T than Cu [167, 722, 834, 846-850] and may open pathway for direct deposition on bendable substrates [841, 842, 848, 851]. The drawback of Ni is the high C solubility (about 0.6 weight percentage of Ni at 1326 °C [852] that makes difficult to control the deposition process.

Typically, the amount of carbon precursors determines number of carbon atoms available for the catalysis, while the temporal evolution of the process T governs the number of graphene layers [853]. Especially, the cooling rate is important since it defines either the dissolved C will stay inside Ni or they are squeezed on a Ni surface forming SLG or FLG films [853], while the amount C dissolved in the Ni is determined by catalyst amount. Ref [854] minimizes the thickness of Ni to decrease the amount of dissolved carbon because precise T control of the bulky hot wall CVD of was hardly possible. Ref [854] used 10 nm thick Ni film on a silica substrate as a catalyst and the carbon precursor was nLOF photoresist (AZ nLOF 2070, negative tone resist diluted with AZ EBR 70 thinner). The pyrolysis T of the photoresist film in the CVD chamber varied from 600 °C to 900 °C and resulted pyrolyzed photoresist film (PPF) with and without Ni [854]. Since during the CVD process some part of the resist layer is expected to evaporate, the Ni film was deposited under the nLOF layer. Thus the Ni layer did not prevent the evaporation from the resist layer.

Similarly to Cu, Ni will also melt and recede during CVD. Since the thickness of the original Ni film was only 10 nm the particle size is in sub-μm range. Fig V.37 (a) and (b) shows the appearance of the Ni particles on PPF which was pyrolyzed in 800 °C. In Ref [854] the temperature dependency to the PPF graphitization was observed by Raman spectroscopy. Most significant changes in the structure of the PPF with Ni took place when the temperature was 800 °C or above (see Fig. V.37 (c) and (d)) [854]. At this temperature range 2D peak appeared at 2705 cm^{-1}. Moreover, D and G peaks became narrower indicating higher degree of crystallization in to comparison to PPF pyrolyzed in 700 °C and lower T or without Ni catalyst

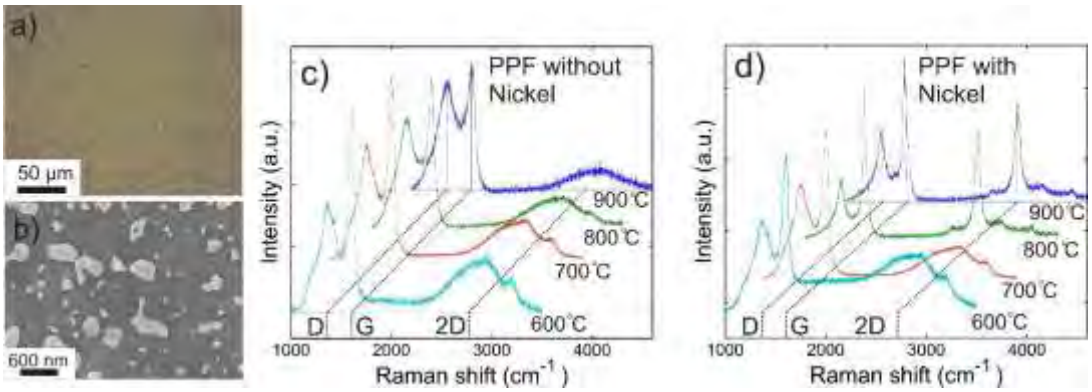

Figure V.37. (a) An optical microscope and (b) a SEM image of PPF with Ni particles fabricated in 800 °C. SEM reveals non-uniform size and shape of Ni particles (bright particles). Raman spectra shows the evolution of the carbon film as a function of temperature (c) without and (d) with nickel in the process. Adapted from Ref [854].

V.3 Brief comparison of all methods based on CVD and MBE techniques

As described along this section, there is a wealth of methods to grow graphene on a variety of methods. More are more suitable to grow on catalytic substrates while others are better suited for the growth on insulators. Most of them allow a variety of precursors. Table V.2 show provides a brief of the methods, substrates, precursors and optimal growth conditions given above.

Method	Substrate	Precursor	Temperature	Pressure
CVD	• Cu Foil • Cu coated Bronze • Partially oxidized Cu foil enclosed	CH_4, C_3H_8	1000°C<T<1084°C	0.5mbar-1 bar
CVD	Cu foil	C_2H_4	850 °C	2 mbar
CVD	Ir(111)/YSZ/Si(111)	C_2H_4	850 °C	$1.10^{-}8$-2.10^{-7} mbar
CVD	Ge(110)on Si(110)	CH_4	900 °C -930 °C	850-990 mbar
CVD	Ni Foam	CH_4	1000 °C	50 mbar
CVD	Cu Foam	CH_4	1000 °C	400 mbar
CVD	Cu film on Silica wafer	CH_4	950 °C	8 mbar
PT-CVD	Cu	CH_4	950 °C	7-20 mbar

MBE	Au(111)	Glassy carbon filament	550 °C	UHV
PVD	Cu (111),Pt(111), Rh(111) single crystal or polycrystalline	C_{60}	800 °C- 900 °C	UHV
PECVD	Glass or Quartz	C_2H_2	600 °C-720 °C	0.1-$0.9 \cdot 10^{-4}$ mbar

Table V.2 Methods, substrates, precursors and optimal growth conditions used in the described synthesis along this section.

VI. GRAPHENE TRANSFER, PLACEMENT AND DECOUPLING FROM SUBSTRATE

VI.1 Wet Transfer

Many advances have been reported in the ways in which such materials are effectively transferred [755, 855-859].The patented (A. Gölzhäuser, C.T. Nottbohm, A. Beyer, Method for transferring a nanolayer, European patent 2144711, US patent 8377243 B2 (priority 11. April 2007)) general wet transfer procedure [860] was originally introduced for all kinds of nanolayers and whatever the synthesis methods. The nanolayer can be a single layer (SLG), bilayer (BLG) or multilayer (MLG) graphene but this aspect is not substantial for the purpose of the description of the transfer process. Even more, it can be understood as a nanolayer of any other stable 2d system, considering that the specific recipe can be adapted changing some details from the delamination procedure here described for graphene. After a nanolayer has been prepared on its native substrate, which can be Au, Cu, Ni etc, a much thicker polymeric layer (typical thickness: 400 nm) is added on top to assure that the nanolayer maintains its shape and integrity during the transfer procedures. The resulting polymer/nanolayer/substrate structure is then dipped into a liquid etchant that dissolves the native substrate or, alternatively, is detached from the substrate by electrochemical methods, leaving an optically visible, several hundred nanometers thick polymer/nanolayer ‘‘hybrid layer’’ on top of the liquid. This “hybrid layer” is then transferred onto a second substrate. Finally, the thick polymeric layer is dissolved or removed and the nanolayer remains on the target substrate only.

Etching of a metallic substrate

Etching of Cu Foil substrate

The wet transfer of CVD graphene, based on the etching of the Cu substrate is a broadly used method. The process is made as follows: the Cu foil on which the nanolayer has been grown is cut according to the final target substrates and taped from the edges on a 125 µm-thick poly-ethylene terephthalate (PET) foil, which acts as a mechanical support. An A4-950K poly-methyl methacrylate (PMMA) resist is spin coated on top of the nanolayer/Cu/PET stack at 4000 rpm for 40 seconds, then the PET support is removed by cutting the edges. Since nanolayer grows on both sides of the Cu foil, that on the side uncoated by PMMA is removed with a Philips reactive ion etcher (RIE) by using a 20W oxygen (O_2) plasma for 20 seconds at 200 mTorr. The PMMA/nanolayer/Cu stack is then dropped at the surface of a solution of ~ 2.0g of ammonium persulfate (APS) in 150 ml DI for Cu etching, as shown in Fig VI.1. When Cu is entirely dissolved, the remaining PMMA/nanolayer stack is lifted with a PET substrate and transferred to a beaker filled with deionized water. The procedure is repeated twice and then the PMMA/nanolayer is lifted with the target substrate and left to dry overnight in slanted position with respect to the worktop. The sample (PMMA/nanolayer/target substrate) is then transferred in a beaker with acetone for PMMA removal for 1 hour, then moved to

a beaker with isopropyl alcohol for 5 min and then dried with nitrogen, leaving the nanolayer film on the target substrate.

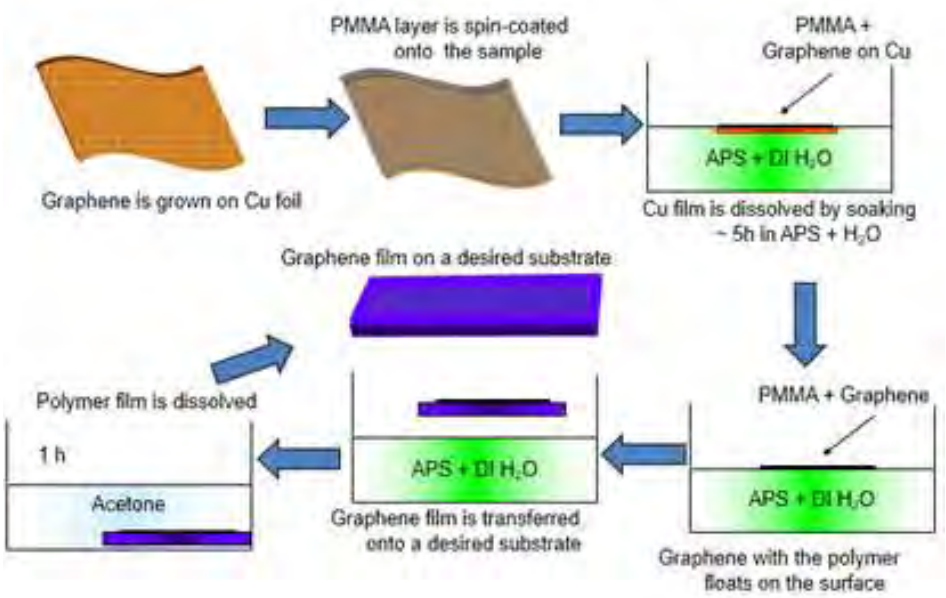

Fig. VI.1 Wet transfer procedure

Etching of gold coated mica substrate

The transfer of a CNM grown on a gold coated mica substrate follows a slightly different path and can be applied also to the transfer (A. Gölzhäuser, C.T. Nottbohm, A. Beyer, Method for transferring a nanolayer, European patent 2144711, US patent 8377243 B2 (priority 11. April 2007)) to many target substrate [55, 56, 58, 861]. The procedure is as follows: PMMA (950K, AR-P 671.04, Allresist) is spincoated at 4000 rpm for 30s, followed by a soft bake at 90°C for 5 min. Optionally, a double layer of PMMA can be applied: (i) a first layer (50K, AR-P 631.09, Allresist) is spun to a thickness of 130 nm at 2000 rpm for 30 s and baked on a hotplate at 90°C for 5 min; (ii) a second layer of PMMA (950K, AR-P 671.04, Allresist) has a higher molecular weight to provide mechanical stability. The latter is spun to a nominal thickness of 310 nm at 4000 rpm for 30 s and also baked at 90°C for 5 min. The advantage of the additional PMMA layer with 50K is that it can be removed more cleanly than PMMA with a higher molecular weight in direct contact with the nanolayer. After the formation of the PMMA transfer medium, the edges of the sample are cut in order to ease the release of the PMMA/nanolayer from the mica substrate. Then, the sample floats on the liquid level of I_2/KI etching bath (I_2:KI:H_2O with ratio of 1g:2g:10ml) for ~ 10 min. Au is slightly etched from its lateral interface with the underlying mica. The separation of polymer/nanolayer/Au from mica is attained by dipping into water. To remove the Au layer, the PMMA/nanolayer/Au floats on the liquid level of I_2/KI etching bath for ~ 20 min. After the gold layer is completely removed, the polymer/nanolayer is transferred to a fresh water bath for rinsing. The hybrid transfer layer can be taken out of solution and placed onto a target substrate following the same protocols used to rinse it in the previous paragraph.

If the new host substrate is not solid and nanolayer is to be free-standing on a grid-like substrate, removing of PMMA can be done by critical point drying [58, 860] (CPD-Tousimis Autosamdri-815B, Series B)) that avoids the damaging effects of surface tension. The mounted sample is carefully immersed into acetone that fills the chamber of CPD. After 60 min, the whole chamber is cooled down with liquid CO_2 and then liquid CO_2 is introduced into the chamber in a very fine way to avoid turbulence. Liquid CO_2 is going to substitute acetone according to a predefined time (15 or 20 min). Finally the dryer heats and pressurizes CO_2 to its critical point, and gas CO_2 bleeds off to leave nanolayer dry.

A scheme of the procedure is shown in Fig. VI.2. A helium ion microscope (HIM) [860] image of a CNM, placed onto a Cu grid with hexagonal pores of 40 µm in diameter, after removing PMMA layer without the use of CPD methods, is show in Fig VI.2. Note the appearance of wrinkles. The effect of critical point drying can be seen in Fig. VI.3a that shows a flat CNM on a grid with 40 µm openings. Fig. VI.3b shows a very large free-standing CNM that has been transferred onto a hexagonal grid with openings of ~ 0.5 mm [860] . In both images, no folds and wrinkles are visible.

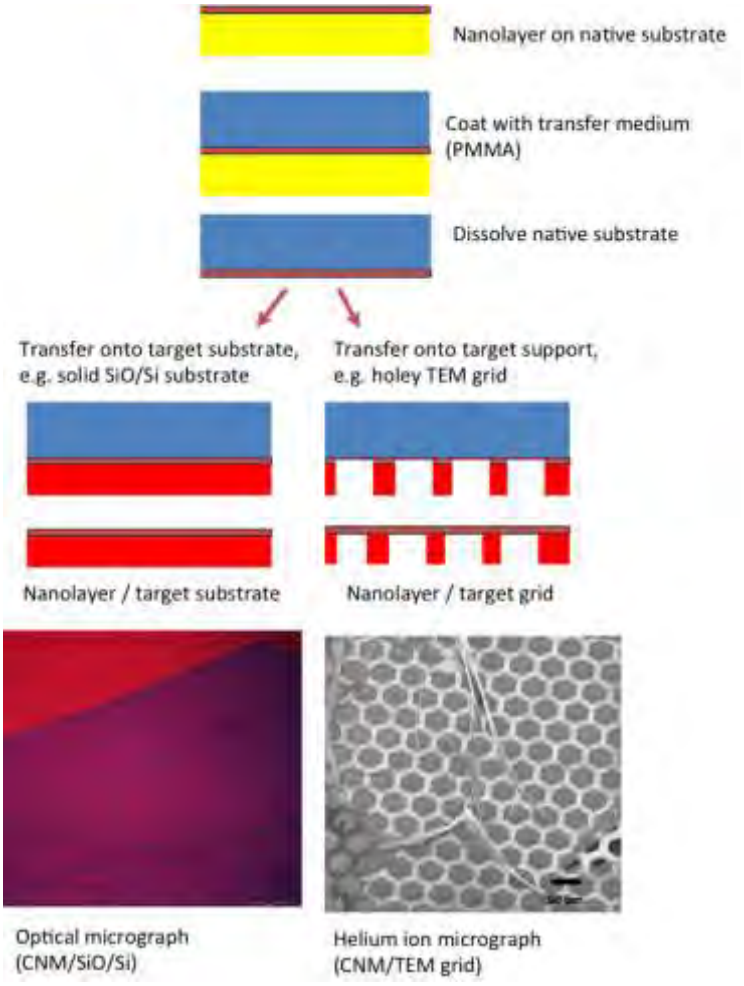

Fig. VI.2: Top: Schematic of nanolayer transfer using polymeric transfer media. Bottom, left: Optical micrograph of CNM transferred onto SiO2/Si showing interference contrast; b*ottom right: Helium ion micrograph of CNM transferred onto a metal grid without critical point drying. Ruptures and faults, as well as large intact areas of the freestanding nanolayer are clearly visible. Adapted from ref [55, 860] and A. Gölzhäuser, C.T. Nottbohm, A. Beyer, Method for transferring a nanolayer, European patent 2144711, US patent 8377243 B2 (priority 11. April 2007).*

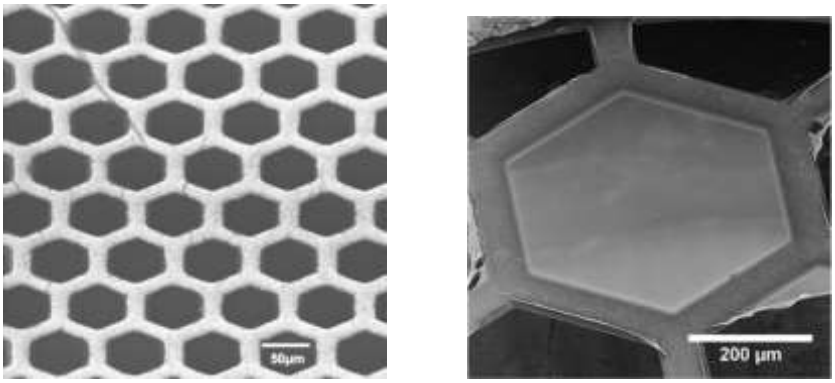

Fig. VI.3: HIM image of large freestanding CNMs that has been transferred onto hexagonal TEM grids. (left) The size of each hexagon is 50 µm and the grid is uniformly covered by the CNM.Scale bar is 50 µm. Right) The size of the hexagon is 500 µm and it is completely covered by the flat 2D nanolayer, no wrinkles or folds are seen.Scale bar is 200 µm. Fig. Adapted from ref. [860]

High Speed Electrochemical Delamination

This technique is nondestructive not only to graphene, but also to the Cu [89, 712]. After the growth process, the Cu foil with graphene on top is spin-coated with a thin layer of poly(methyl methacrylate) (PMMA) (4% in anisole, layer thickness ~350nm) and cut into suitable pieces. The PMMA layer also serves here as a support preventing the graphene film from collapsing during copper removal. Using a custom-made mechanism (Fig. VI. 4) (utility model P.411053) the Cu/Graphene/PMMA is placed in a potassium chloride solution (KCl, 1mol/dm^3) at a rate of 1 mm/s., being the graphene/Cu cathode negatively polarized (from 4 to 10 V). Hydrogen bubbles appear then at the graphene/Cu interface due to the reduction of water molecules and allow graphene to gently detach. The current used depends on the Cu foil size and should be adjusted to maintain the delamination rate of 1mm/s.

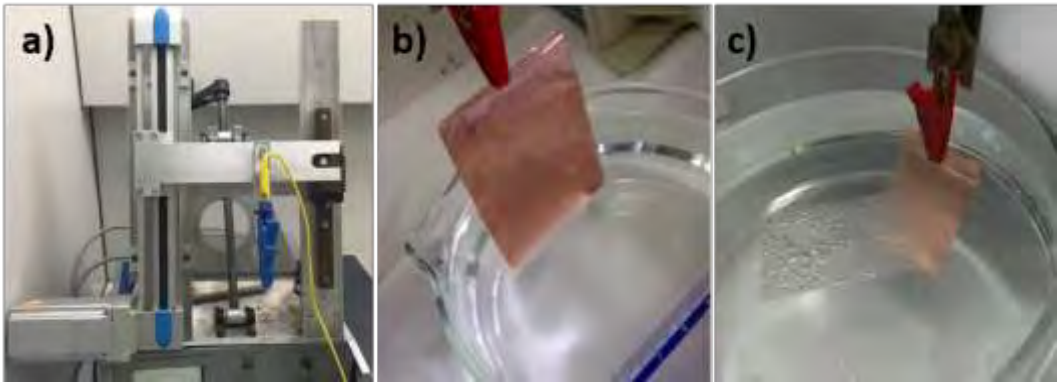

Fig. VI.4 Electrochemical delamination custom-made mechanism (a), starting PMMA/graphene detach (b) and separated PMMA/graphene layer from Cu substrate after high-speed electrochemical delamination (c).

In order to obtain the best results, the samples should be gradually immersed in the electrolyte solution at an angle ~45° as in Fig. VI.5. At this insertion angle graphene is not affected by unnecessary mechanical stress and the Cu foil is targeted towards the bottom of the glass container. After the delamination process, the detached bilayer Graphene/PMMA is rinsed with DI (deionized) water, transferred onto the substrate, heated to 130°C, and treated with acetone to remove PMMA. Next, graphene samples are dried for 1h at 350 °C in a high-vacuum furnace to be sure that the organic residue and impurities are removed. Fig. VI.5 presents the scheme of the graphene transfer process. Fig. VI.6, shows the result of iteration of the transfer process to produce multilayer graphene on PMMA

.

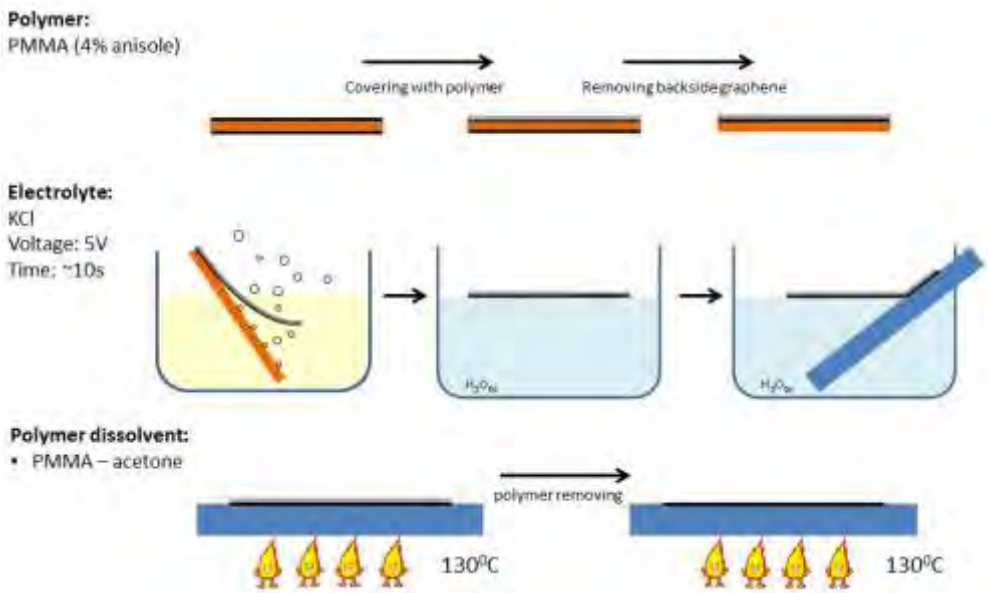

Fig. VI.5 Scheme of high-speed electrochemical delamination graphene transfer method.

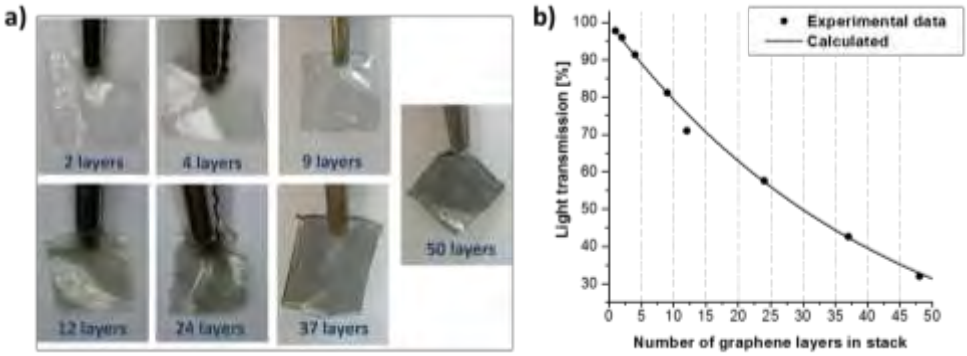

Fig. VI.6 Images of the fabricated stacks of 2, 4, 9, 12, 24, 37, 50 graphene layers on PMMA (a), optical transmittance measurement of graphene layers in multi-layer graphene stack (b).

Note that it is difficult to completely remove all impurities using only the organic solvent and the PMMA residue from the graphene surface. High-temperature treatment in high-vacuum is additionally needed for a more effective and cleaner graphene transfer. To examine the effect of the T during this treatment, X-ray photoelectron spectroscopy was used (see Section IX.2.3) to determine the chemical composition of graphene surface before and after heat treatment. A large O1s [723] peak on the XPS graphene spectrum before the heating is apparent in Fig VI.7. Also an enhancement of the intensity of the characteristic C1s XPS peak located at 288.9eV, which represents the C-C=O and O=C-O groups [723] are signatures of an incomplete PMMA removal. After the heat treatment in 350°C in high-vacuum, the C1s and O1s XPS measured peaks in Fig. VI.7 are the same as those corresponding to graphene samples that had never had been into contact with PMMA, confirming that the removal of the polymers has been completed

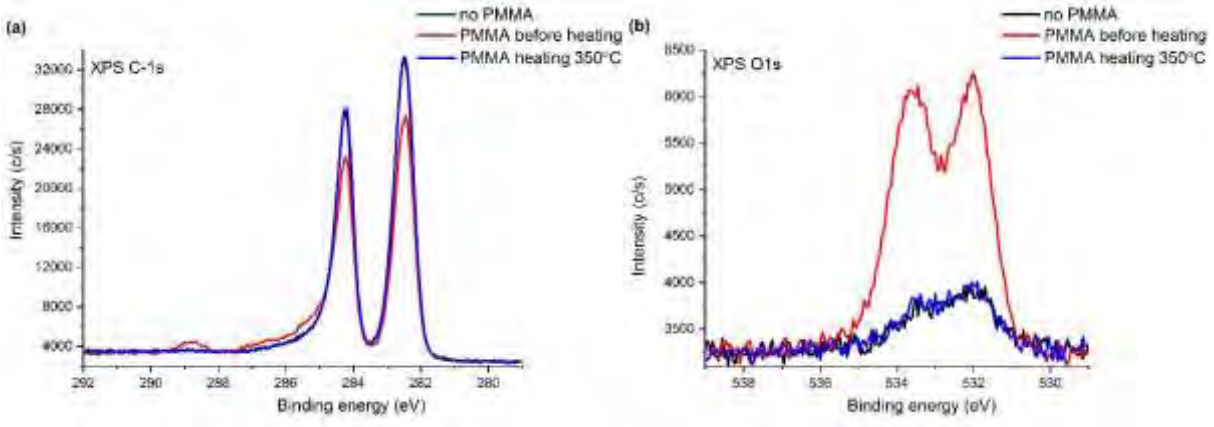

Fig. VI.7 High resolution XPS C1s (a) and O1s (b) spectrum of transferred graphene samples before heating (red line), after heating (blue line) and graphene samples without contact with PMMA (black line).

An additional method for the confirmation of the PMMA residue removal is the scanning near-field optical microscopy (s-SNOM) based AFM [862, 863]. Topography and near-field images recorded on graphene samples on SiO_2/Si before and after heat treatment are shown in Fig VI. 8. After heating the graphene surface looks much cleaner, the wrinkles smoothens and the particles derived probably from PMMA are distinctly rarer.

As the probing depth of s-SNOM is larger compared to the graphene thickness, the recorded optical contrasts show not only the local defects in the graphene layer but also differences in the substrate composition and in the distribution of the PMMA contamination

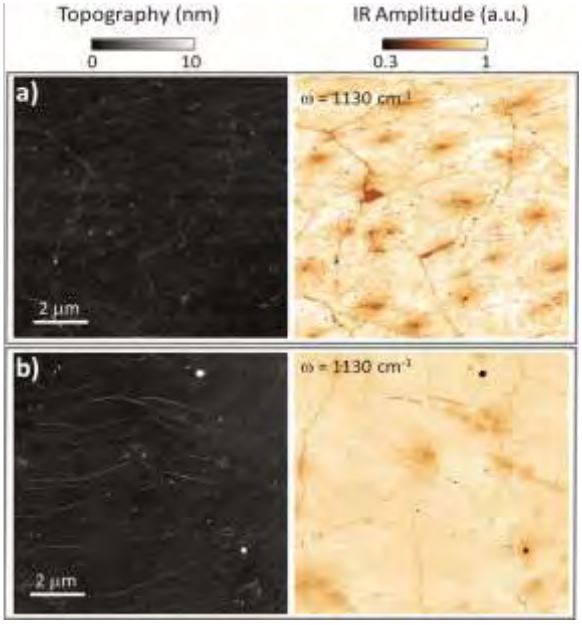

Fig. VI.8 AFM and near-field IR images recorded from samples before (a) and after (b) heat treatment. Scan size for each measurement was 10x10 µm^2. Cortesy of Dr. Adrian Cernescu, Neaspeck GmbH Germany.

A spectroscopic method based on imaging an area at different wavelengths , was used to test whether the contamination particles randomly spread across the graphene samples are indeed PMMA molecules. As the dielectric function depends on the wavelength [864]. the scattering coefficients (amplitude and phase) of the investigated materials varies with the tuning of the laser wavelength [865]. Imaging at 1150 cm^{-1} illumination frequency, which is on resonance with the SiO_2 vibration (asymmetric stretching vibration of the oxygen atoms bridging the Si-O tetrahedral groups) the optical contrast between the graphene/SiO_2 and the PMMA particles are the largest. As expected, the near-field IR images recorded on a PMMA particle in Fig. VI.9 show a stronger phase at 1740 cm^{-1} due to the carbonyl band absorption at this specific wavelength [866] while the optical phase on the graphene and substrate is larger at 1150 cm^{-1}, matching the SiO_2 phonon absorption [867]. For both wavelengths, the optical amplitude (scattering efficiency) is stronger on the inorganic materials compared to PMMA due to the lower reflectivity coefficient on the polymer [868]. These measurement indicate that particles might be PMMA.

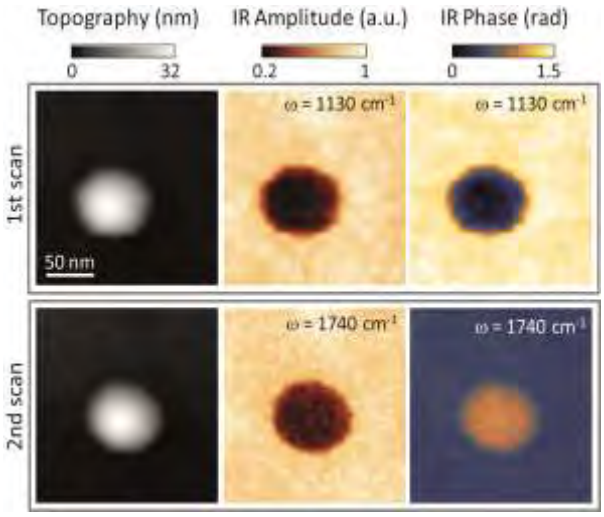

Fig. VI.9 Sequential imaging of a PMMA particle at 1130 cm-1 and 1740 cm-1. Scan size: 200x200 nm. Cortesy of Dr. Adrian Cernescu, Neaspeck GmbH Germany.

TOA-assisted chemical delamination

Tetraalkylammonium (TOA)-assisted electrochemical delamination is a modified electrochemical delamination ('bubbling') method which enables the exfoliation of single and few-layer graphene or h-BN from substrates which are more strongly interacting than Cu [869]. The TOA pretreatment was first introduced in [870] to enable the subsequent delamination of Graphene on Ir.

Tetraalkylammonium compounds are known to weaken the van der Waals interactions of sp^2 materials with the underlying metal [870-872], thus facilitating the subsequent detachment of the layer from the substrate. TOA^+ intercalation is a 3-electrode electrochemical procedure which requires the use of a potentiostate to ensure a fine control on the bias applied between working and reference electrode. In the following, reference will be made to graphene grown on iridium, but the same protocol applies to many other 2D layered materials, including h-BN/Rh and $MoSe_2$).

The experimental set up of the electrochemical cell can be seen in Fig. VI.10. The cell is open to the air or Ar atmosphere. The Working Electrode (WE) is the graphene/Ir sample. It should be fixed on one corner by an alligator clip; The reference electrode (RE) is an Ag wire (alternatively one can use a standard Ag/AgCl or any other reference electrode, in which case one needs to correct the bias between WE and RE to account for the potential offset of the RE); the Counter Electrode (CE) is a Pt wire. The WE and the RE should be placed as close as possible facing each other (avoiding contact, though!); the CE should be facing the WE (with the RE between the two) and should be immersed in such a way to expose a large area. The operation of the vessel follows several steps: Fill the vessel with 10-20mL of TOABr/acetonitrile solution (0.1 M concentration, i.e.5.46 g of TOABr every 100mL of solution). Subsequently, degassing the solution with Ar or N_2 for 15 minutes is required. After degassing, leave the Ar/N_2 capillary tube above the vessel, in order to maintain an Ar or N_2 atmosphere on the electrochemical cell and prevent air from dissolving into the solution. Then, Apply -1.9V between WE and CE for 10 minutes to promote TOA^+ to the graphene/metal interface. A partial

discharge of the sample for 20 s at -0.2 V follows to obtain Ir/TOA/graphene stack. This step is needed to prevent the negatively charged graphene from reacting with the PMMA and facilitate the subsequent PMMA removal.

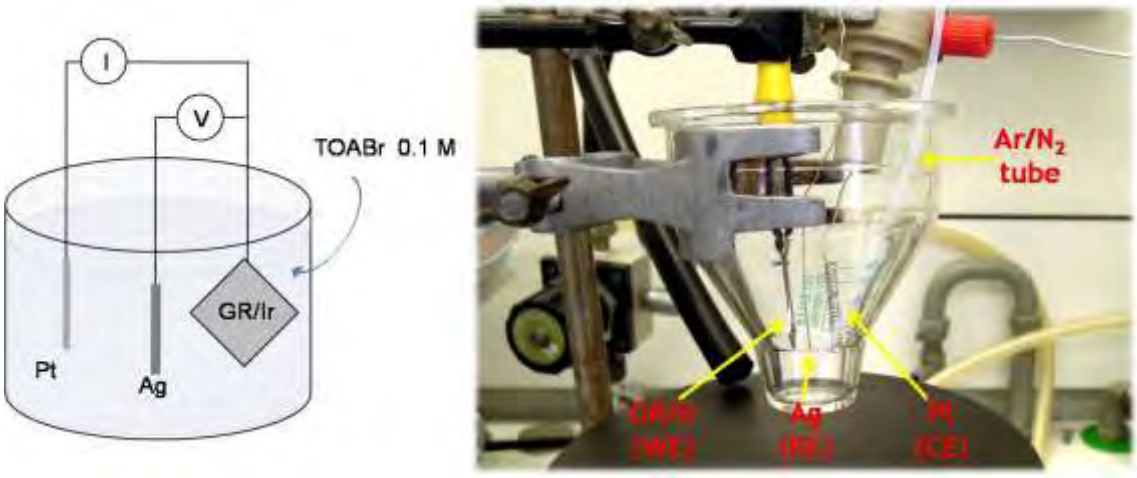

Figure VI.10: 3-electrode setup used in TOA intercalation and voltammetry experiments. Adapted from [872].

After TOA-pretreatment, the samples must be rinsed in acetonitrile, dried in N_2 atmosphere, and spin-coated (or drop-coated) with PMMA. The samples can be then exfoliated according to the electrochemical delamination explained above [873].

Electrochemical oxidation by cyclic voltametry

The electrochemical oxidation process is understood in terms of intercalation of metal-oxide layer at the interface between the graphene and the metal. Any rational optimization of the parameters of this process should follow as the methodology described below. Here we will refer to Pt single crystal as its voltammetric profile in non-adsorbing electrolytes is well known [874] but the conclusions can be extended to other metals. It has been demonstrated [875] that the processes that occur at the very surface of the metal can be described by the reaction

$$H_2O + (*) \leftrightarrow OH_{ads}(*) + H^+ + 1e^-$$

Being * a free Pt adsorpiton site. In a first step, the water molecules interact with the stack graphene/platinum electrode, intercalating through graphene. Then dissociate in the Pt surface taking place the reversible formation of a platinum hydroxide $Pt_2(OH_{ads})$. A charge about 101.5 $\mu C.cm^{-2}$ is transferred, corresponding tothe formation of $Pt_2(OH_{ads})$ with a coverage close to 1 monolayer.

Even though the SLG presents a barrier to direct access to the metal (Pt) surface, the water molecules are able to diffuse onto the metallic substrate via surface defects [876]. This intercalated

water between the graphene sheet and the metal surface is responsible for the oxidation of the outermost Pt atoms when an appropriate potential is applied.

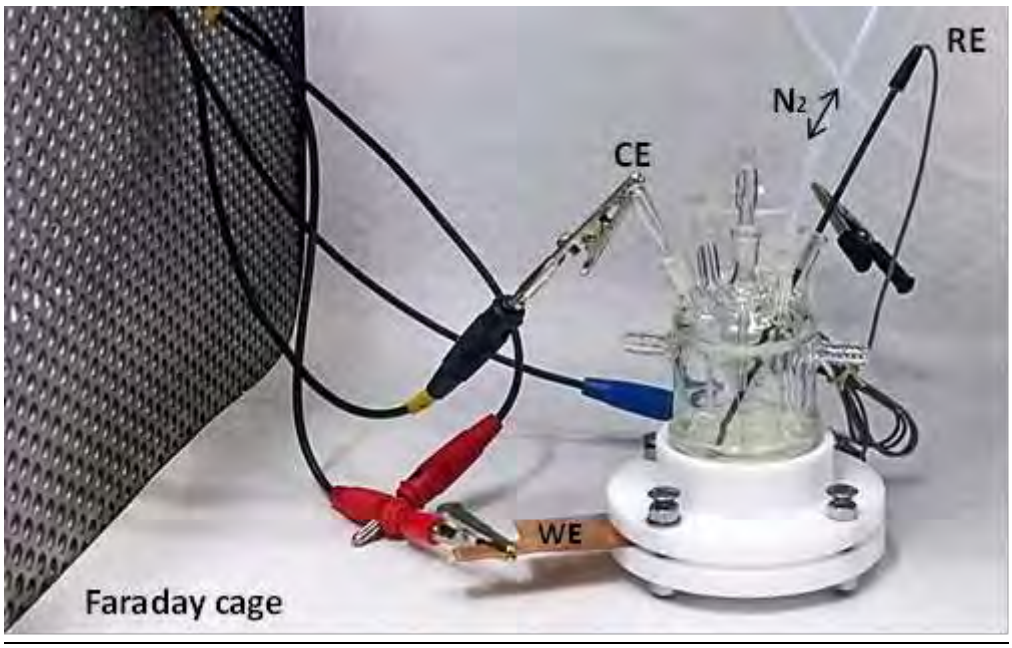

Fig. VI.11. Electrochemical cell used for the electrochemical oxidation of Pt in the Graphene /Pt (111) stack. RE, is the Ag/AgCl reference electrode, CE the Pt counter electrode and WE the working electrode (i.e. stack graphene/ Pt(111). The cell is purged with N_2 and installed inside a Faraday cage.

Voltammetric measurements were performed under N_2 atmosphere in a three-electrode set up (Fig. VI.11) [877]. There is a N_2 gas inlet and outlet to assure an inert environment during the electrochemical oxidation. A platinum wire (99.99% purity) serves as counter electrode (CE) and all the potentials are quoted with respect to the Ag/AgCl reference electrode (RE). The Ag electrode is specific for the cell (Ag/AgCl electrode driref-25H, WPI). The working electrode (WE) is the Pt(111) sample covered with a SLG. The area of the working electrode exposed to the solution is 0.33 cm^2 in all experiments. The electrochemical cell is set into a Faraday cage in order to reduce the signal-noise ratio. Cyclic voltammetry experiments were performed with an Autolab PGSTAT 30 potentiostat from Eco-Chemie. The electrolyte employed is 0.1 M $HClO_4$ and the water is purified with a Millipore Milli-Q purification system. A scan rate of 0.05$V.s^{-1}$ is selected to control the oxidation reaction. The anodic potential is varied to obtain the optimal conditions to decouple graphene from Pt avoiding side reactions such as the evolution of CO_2 and O_2, and the induced creation of defects in the graphene network. The sample is placed on the electrochemical cell and leave it for 1.5 hours soaked into the previously deoxygenated acid solution so water molecules are able to diffuse onto the metallic substrate via surface defects [876].

Fig. VI.12 shows four cyclic voltammograms with different experimental conditions used to decouple an area of 0.33cm^2 of graphene from Pt(111).The first protocol (Method A, Fig. VI.12a) is an anodic potential scan from 0.36 to 1 V followed by a cathodic potential scan between 1 V to 0.7 V. The second protocol (Method B, Fig. VI.12b) is rather similar but with a higher applied potential (1.05 V). In the third cycle (Method C, Fig. VI.12c) the potential is even higher (1.45 V). In the last one (Method D, Fig VI.12d) two cycles are involved; a complete oxidation-reduction cycle in the range 0.45 - 1.1 V and a subsequent oxidation scan up to 1.1 V, followed by reversing the potential finishing at 0.7 V. The applied potential in method A is not high enough to decouple the graphene. Protocol D is the most aggressive one and the sample is decoupled but also damage. Both protocols B and C are the ones accomplishing the perfect decoupling, meaning that every method in between those ranges will be appropriate to decouple graphene from Pt.

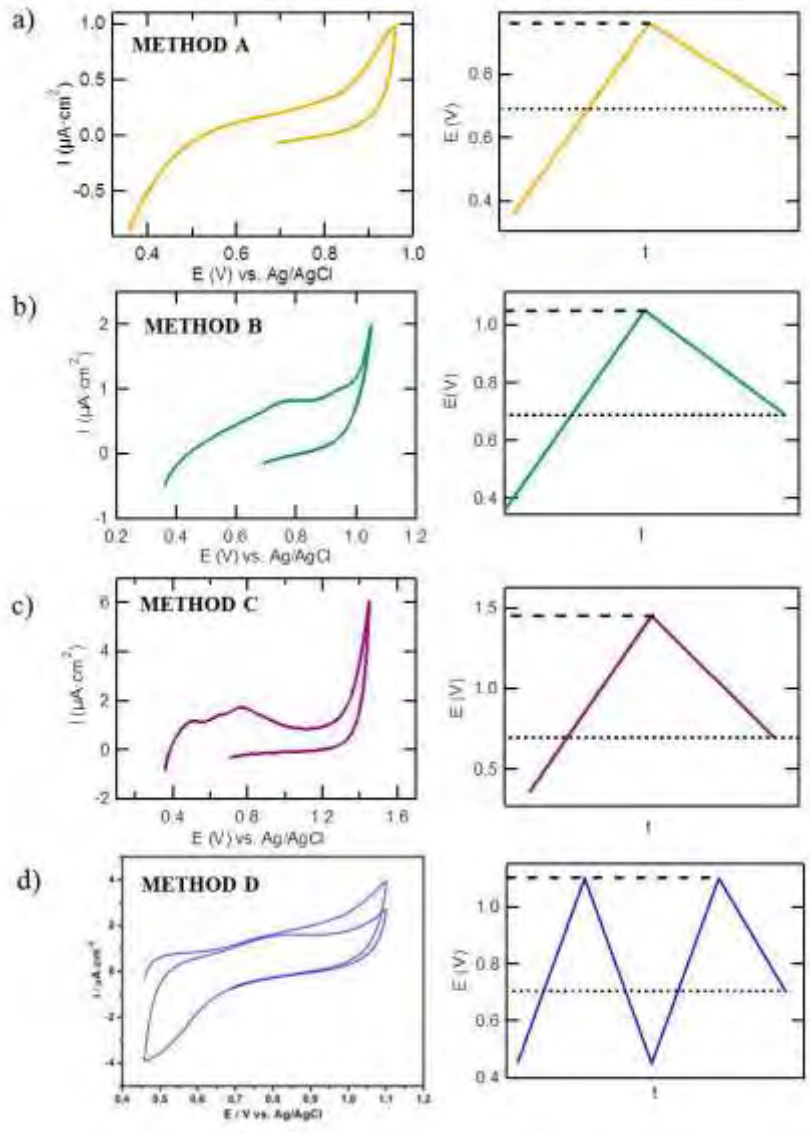

Fig. VI.12 Cyclic voltammetries for graphene on Pt(111) in 0.1M aqueous $HClO_4$ solution. Four different voltammetric treatments have been applied (methods A,B, C and D), being the scan rate 0.05 V.s^{-1} in all the cases. In the right panels a graphical representation of the potential programs

applied to the Gr-Pt electrodes, producing the corresponding cyclic voltammograms of the left panels.

Table VI.1 summarizes the potentials and scan rates for the shown cyclic voltammograms. It also includes the parameters to oxidize clean platinum sample and the charge involve in the oxidation process, as well as the needed charge to get 1 monolayer of Pt_2OH. Clearly, the presence of the monolayer of graphene delays the oxidation process compared with the clean Pt(111) sample, being necessary to apply higher overpotentials to attain a comparable oxidation charge. In fact, the charge obtained by integrating the anodic peaks for the other treatments is lower in comparison with the target. However, it has been demonstrated that the decouple process starts when the oxide coverage is much less than one monolayer (~ 0.25 of monolayer).It is also included the parameters to decouple graphene from Ir(111).

Table VI.1. The table shows the parameters used for the potential-controlled electrochemical oxidation of Pt(111) and Ir(111) with 1ML of graphene on top. E_i stands for the initial potential, E_{sup} for the upper limit of the potential, E_f for the final potential, v for the scan rate and Q for the charge.

		E_i (V)	E_{sup} (V)	E_f(V)	v ($V.s^{-1}$)	Q ($\mu C.cm^{-2}$)
1 ML de Pt_2OH						120
Gr/Pt(111)	Method A	0.36	1	0.7	0.05	10
	Method B	0.36	1.05	0.7	0.05	32
	Method C	0.36	1.45	0.7	0.05	106
	Method D	0.46	1.1	0.7 (cycle and a half)	0.05	24
Clean Pt(111)	Method B	0.36	1.05	0.6	0.05	101.5
Gr/Ir(111)		0.2	1.0	0.9	0.05	140.8

There are many types of wet transfer methods. Two incr

VI.2 Semi-dry transfer: Hot press lamination and UV assisted transfer

Increaseasingly common variants are UV adhesive (UVA) and hot-press lamination (HPL), which can be broadly classified as semi-dry transfer methods. Both methods have proven to be large-area-compatible, all of for facile processing, are scalable, and are capable of producing transferred layers that are optically transparent and electrically conductive whilst retaining high levels of areal uniformity with only a few percent variation. UVA and HPL transfers are extremely stable under bending stress and bend fatigue with an impressive resistance towards micro-crack formation compared to existing ITO and FTO platforms.

Figure VI.13(a) outlines the HPL process. Thermally activated ethylene vinyl acetate (EVA) treated polyethylene terephthalate (PET) substrates (GBC Co.) have been used herein, however other

supports such as thermal release tape (TRT), with different adhesive strengths ranging from 2.5 to 7.0 (N/20mm), can be also used . First, the as-synthesized graphene-on-Cu stack is sandwiched between the polymer and a 125 μm-thick PET substrate, the latter of which acts as a mechanical support. The sandwich structure then it traverses a dual roller laminator, which is, contingent on the laminate used, either cold-rolled or heated to ~ 100°C. Following lamination, the backside laminate, deemed as that side of the defective graphene, namely that side which was in contact with the heated stage during CVD, was mechanically detached. For ensured quality of the transferred graphene, this exposed graphene-coated-Cu face can then be ashed to remove residual organics along with the defective graphene layer. The Cu catalyst is then etched, in this case, using in $(NH_4)_2S_2O_8$ in de-ionised (DI) water (1 M) for 12 h. The transferred films are subsequently rinsed in DI water and dried in high-purity N_2. Up to 0.1 m^2 areas have been successfully transferred using this method, though larger areas and subsequent integration into roll-to-roll process lines are easily accommodated. The EVA technique is also suitable for flexible substrates, which cannot withstand solvents such as acetone and/or isopropyl alcohol. Following the transfer, the resulting polymer/graphene stack remains attached to the target substrate. Repeated lamination, at RT ort elevated temperatures, can be undertaken to further remove absorbates, bubbles, voids and non-conformalities in the transfer. In the case of TRT, the support-coated substrate is finally baked at 120^oc to remove the TRT.

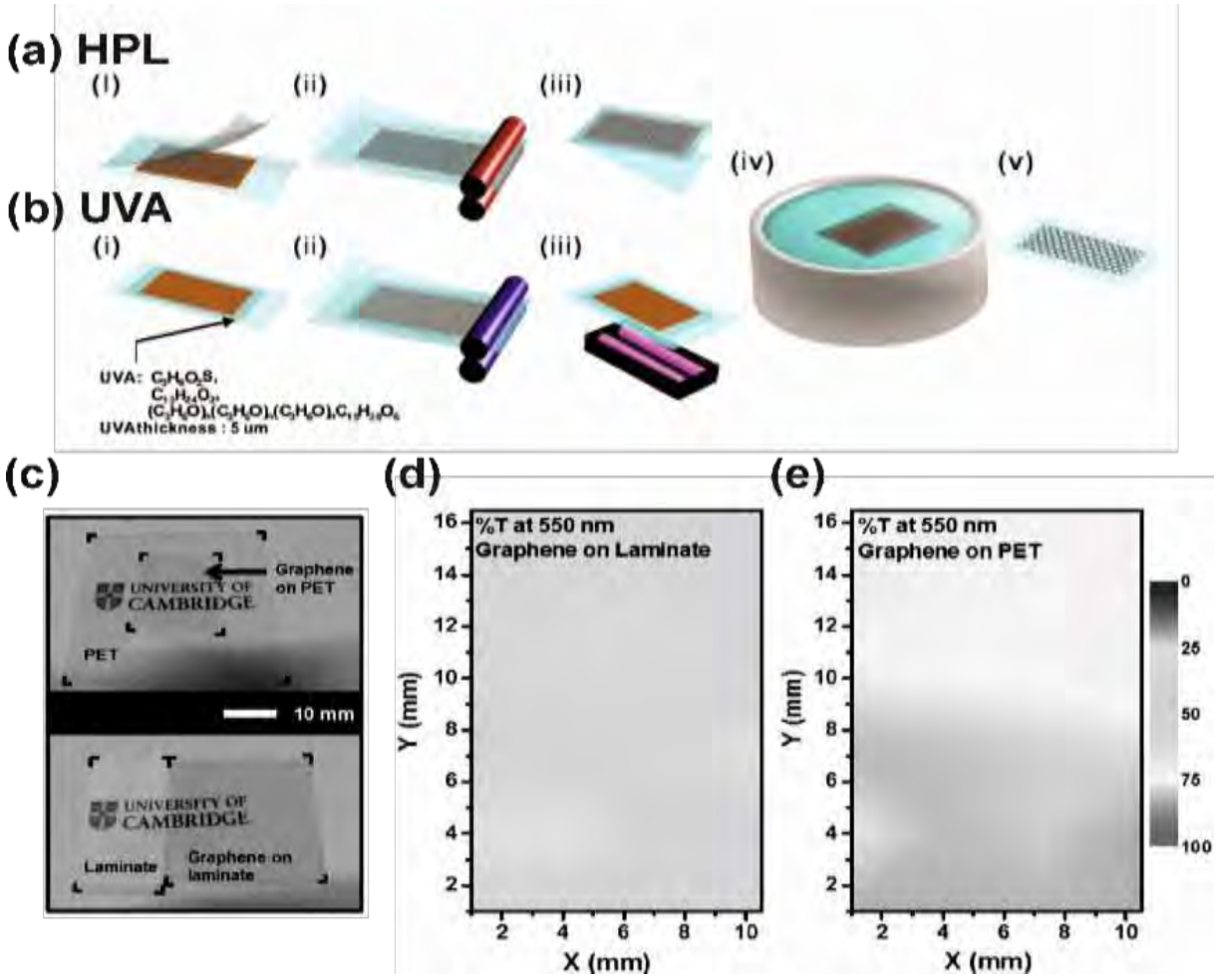

Fig. VI.13 Schematic depicting graphene transfer by (a) HPL and (b) UVA, and (b) corresponding optical images and (c, d) 550 nm optical transmission maps. Adapted from [856, 857, 878]

Fig. VI.13(b) outlines the UV-adhesive (UVA) transfer process. The UV adhesive was first coated onto the selected arbitrary polymer substrate by spin coating at 5000-8000 rpm for 30-60s following a preliminary casting at 500 rpm for 10-20s. This coated substrate was then placed in contact with the as-grown graphene-on-catalyst. This sandwich was then compressed at 0.2 MPa using a cold-roll laminator, ensuring to avoid air pocket formation at the interface. The UVA was subsequently cured by exposing the backside of the PET to an ultra-violet optical source (365 nm, 20-25 mW/m^2) for 10-15 min. The Cu foil was etched in aqueous ammonia persulfate for 12 h, rinsed in DI water and dried in high-purity N_2. All the UVA processing was undertaken at RT, making the approach applicable to a wide range of polymer substrates with the present content focussing on PET for no other reason than popularities sake. Fig. VI.13(c) shows typical optical micrographs of transferred samples that exhibit long-lasting robust adhesion between the substrate and the graphene, as reported elsewhere in work [857].

Benchmarking and ageing effects

When considering the optical transmittance spectra (%T) for HPL and UVA transfers, the UVA and HPL transfers were some 10 and 12% less transparent than the uncoated substrates; collectively associated with the transferred graphene and the augmented optical properties of the interfacial binding layer. The spatially averaged 550 nm transmittance of the HPL and UVA transfers was 58.6 ± 3.6 and 76.5 ± 3.8%, respectively. Both techniques afforded equivalent areal uniformity of < 4.0% variation. The modest increase in absorption between the two samples is likely due to folding and wrinkling of the graphene during the transfer process. Indeed, the root mean square surface roughness of HPL transfer was some 26% higher than the UVA. The evident agglomerates, 5.5 ± 5.6 µm (UVA) and 7.9 ± 3.9 µm (HPL) in diamete, are most likely adhesive residues.

Using PMMA transferred graphene on quartz with Cr/Au Van der Pauw structures on the order of tens of micron in channel size, graphene showed the sheet resistance be 5.47 ± 1.20 kΩ/sq. The sheet resistance for the HPL transfers was 9.9 ± 3.8 kΩ/sq, whereas for the UVA showed markedly lower values 3.5 ± 2.3 kΩ/sq; Elemental analysis by energy dispersive X-ray revealed significant sulphur (S) and oxygen (O) peaks in the UVA transfers, attributed to Cu etchant exposure. Such peaks were absent for HPL transfers. Sulphur is an established, and particularly potent dopant of graphitic carbons. Evidently, significant, albeit unintentional, but nevertheless advantageous, doping occurred during the catalyst etching.

Interestingly, the (550 nm) transmittance of the UVA transfers tended to increase with time (ca. 80%). Conversely, there was no observable change in the transmittance for the HPL transfers, likely due to the absence of notable doping. The metallic component of the Me_xCl_y is certainly central to the doping temporal stability [856].

HPL transfers had a largely time invariant R_s (5.0→5.2 kΩ/sq), whereas the R_s of the UVA transfers tended to increase from an initial 2.2 kΩ/sq to 3.5 kΩ/sq, after 200 h, suggesting the need for an hermetic capping layer. We attribute such deleterious increase in R_s to the time and ambient unstable sulphur doping associated with the necessary Cu-etching. Though the present etch system does indeed beneficially dope the graphene, achieving otherwise low R_s, under the thesis of attaining time-stable conductivity other etchant system could perhaps be considered more appropriate.

To attain a robust mechanical interface, the graphene requires proximal contact to the substrate. In both transfer cases, the as-grown graphene-on-catalyst achieves intimate contact with the EVA melt and to the low-viscosity UVA prior to curing. Graphene transferred with the two proposed methods showed lower surface energy and displayed a higher degree of adhesion (UVA: 4.40 ± 1.09 N/m, HPL: 0.60 ± 0.26 N/m) compared to equivalent conventional PMMA transfers (PMMA: 0.44 ± 0.06 N/m).

To assess the bending fatigue performance transfers were assessed during 10^4 bend cycles with the differential resistance extracted after each (Fig. VI.14(b)). ITO on PET showed a 95-fold increase in differential resistance, with a final differential resistance of 190 kΩ. After such testing, the fatigued ITO showed a significant difference in resistance between its bent and relaxed state. The

differential resistance of the graphene, in both the UVA and HPL cases increased from around 46 kΩ to 74 kΩ. The differential resistance in both UVA and HPL cases showed only less than ±0.5 kΩ difference between their bent and relaxed states, highlighting their impressive robustness in maintaining their electrical continuity even after many thousands of mechanical cycles. The robustness, in terms of maintained electrical performance upon mechanical fatigue, of both the UVA and HPL transfers was around 60 times improved over ITO/PET.

The differential resistance as a function of bend angle and bend radii has also been investigated (Fig. VI.14(b)). All the graphene transfers demonstrated a low (of near 1.0) normalized resistance even at bend angles of 100° (1.05, PMMA; 0.94, UVA; and 1.04, HPL), all of which were almost two orders of magnitude less than that of optoelectronically comparable ITO on PET (79.8). Certainly, the mechanical robustness of transferred graphene is, regardless of the transfer method, much improved over ITO. Amongst the graphene transfers, unlike PMMA transfers, UVA transfer showed consistently lower resistance for all bend angles, though HPL graphene repeatedly showed the lowest for bend angles >40°. Certainly our bend angle experiments strongly suggest that UVA and HPL graphene transfers are somewhat more robust than PMMA transfers in high-bend-angle applications, such as e-paper and wearable sensors. For bend radii R_b = 1−5 mm we find that the ITO normalised resistance increased dramatically; approximately a factor of 20 / 90 at R_b = 5 / 1 mm. Conversely, the change in the normalised resistance of all graphene transfers, including PMMA, were much smaller (PMMA: 0.5−0.9, UVA: 0.5−0.8, and HPL: 0.2−1.2) and showed no measurable dependence on R_b for the bend radii considered. UVA and HPL approaches seem to offer a viable solution to the limited flexibility, with maintained conductivity, of transparent electrodes used in flexible electronics.

Conventional T-peel tests were also conducted to explore the level of adhesin between the graphene and the flexible substrate. A low peel strength represents weak adhesion between the elements of the laminate and substrate, while a high peel strength suggests that the graphene is strongly adhered. As depicted in Fig. VI.14(c), UVA-transfers showed the highest peel strength (4.39 ± 1.09 N/m), followed by the HPL (0.60 ± 0.26 N/m) and then PMMA (0.44 ± 0.06 N/m). These results demonstrate conclusively that UVA transfer allows for significantly enhanced adhesion relative to both HPL and conventional PMMA-based transfer techniques.

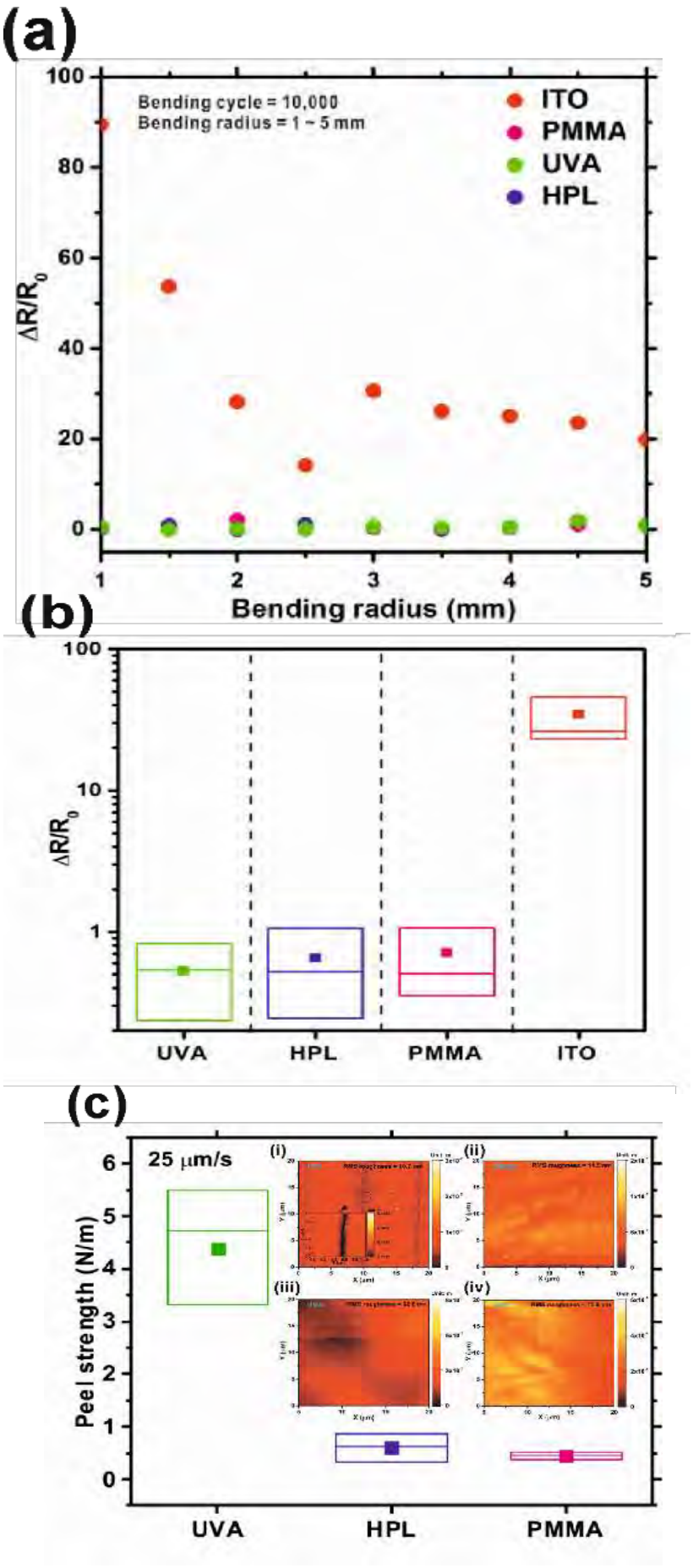
(a)
Bending cycle = 10,000
Bending radius = 1 ~ 5 mm
ITO
PMMA
UVA
HPL
ΔR/R0
Bending radius (mm)
(b)
ΔR/R0
UVA
HPL
PMMA
ITO
(c)
25 μm/s
(i)
(ii)
(iii)
(iv)
Peel strength (N/m)
UVA
HPL
PMMA

Fig. VI.14: (a) Change in normalised resistance ($\Delta R/R_0$) with bend radius. (b) $\langle \Delta R/R_0 \rangle$ for all bending diameters for UVA, HPL, PMMA and ITO. (c) Common peel strengths for the transfer methods considered. Inset: Typical AFM height maps of fatigued transfers. Adapted from [856, 857, 878].

VI.3 Dry transfer using h-BN crystals

Recently, new dry strategies have been proposed preserving the best properties of the grown CVD graphene and allowing a deterministic placement of the graphene sheet in the predetermined spot. This contamination free transfer process utilizes exfoliated flakes of hexagonal boron nitride (h-BN) in order to pick up graphene directly from the Cu substrate that was used for the CVD growth (see section V for details on the growth method) [749, 879]. Fig. VI.15a depicts an optical microscopy image of a graphene crystal on Cu, which has been exposed to ambient conditions for a few days, resulting in the oxidation of the interface between Cu and graphene. The oxidation of the interface does not only make the graphene optically visible, but also decouples the graphene from the substrate.

For the transfer process, a polymer stack consisting of PDMS, PVA and PMMA is prepared: First, a glass slide is covered with scotch tape and drop coated with a 13% aqueous solution of PVA and baked at 95°C for 5 minutes. Subsequently, the slide is spin coated with PMMA (4%, 50k, in ethyl lactate) at 1000 rpm and baked for 10 minutes at 110°C. Now, h-BN is exfoliated on the PVA and large, thin and defect free flakes are selected and cut out in a 5mmx5mm square. The polymer stack can be lifted off the scotch tape using tweezers and placed on a 3mm thick cushion of PDMS, which is resting on a glass slide. As depicted in Fig. VI.15b, the h-BN flake is aligned with a graphene flake using a mask aligner, brought into contact and heated to 125°C. During the cool down (at around 75°C), the polymer and the copper foil are separated again, resulting in an h-BN flake covered with graphene on the polymer stamp. Next, an arbitrary substrate, e.g. an h-BN flake on a Si/SiO_2 substrate is aligned with the h-BN/graphene stack, brought into contact at 125°C and peeled off the PDMS. Subsequently, stack of SiO_2/h-BN/graphene/h-BN/PMMA/PVA is placed in hot water, acetone and isopropanol, in order to dissolve the polymers. Fig. VI.15c depicts such an h-BN/graphene/h-BN sandwich on a SiO_2 substrate.

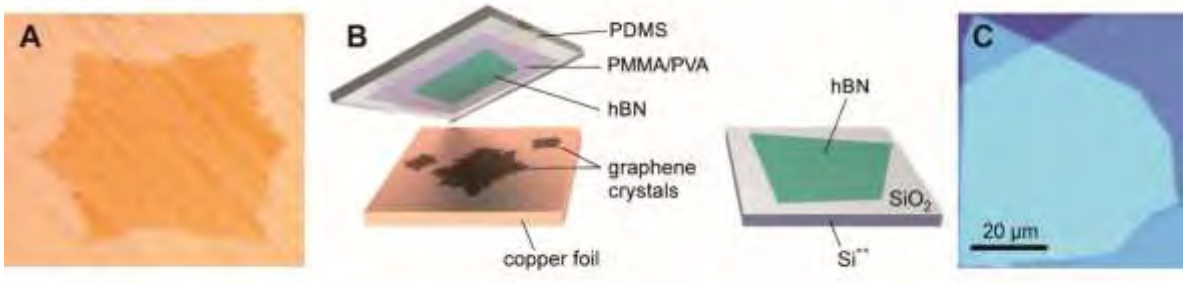

Fig. VI.15: A) Graphene crystal on copper foil grown as described in section 6.1.2. After being exposed to ambient conditions for several days. B) Scheme of the dry transfer process. C) h-BN/Graphene/h-

BN sandwich fabricated using the contamination free dry transfer. Panel B is adapted from [749] . Panel C is adapted from [879].

VI.4 Graphene/PMMA sandwich structures

Removing of the PMMA layer after graphene transfer is not always necessary as there are potential and benefits of building up graphene/PMMA heterostructures. PMMA is a colorless polymer, which is commonly used as a glass replacement (acryl glass). Very thin, transparent PMMA substrate could be proven to be beneficial for e.g. ultrafast optics, where a thick substrate may affect a femtosecond pulse properties. Also, the dielectric constant of PMMA is 2.6 and is thus almost comparable to that of the fused silica (~3.5) [880] which makes the PMMA a decent insulating layer between multiple graphene layers.

High resolution positive tone electron beam resists, ARP-661.08 and ARP-672.08 (by Allresist(tm)), have been used to build PMMA/Graphene heterostructures [881, 882]. ARP-661.08 has the molecular mass of 600 000 g/mol and requires chlorobenzene as a thinner, while ARP-672.08 has the molecular mass of 950 000 g/mol and requires anisole as a thinner. Both thinners consists of a benzene like ring structure and are small size molecule solvents (molecule weight is about 110 g/mol). The higher molecular mass of the ARP-672.08 can increase the durability of the resist film, which can be beneficial if the resist film is wanted to be transferred or made free standing. When the PMMA/Graphene film is deposited on a substrate, long PMMA molecules can be reduced in size by electron beam lithography [880]. This will open up an interesting route for graphene patterning [880].

PMMA layers with thickness of ~ 600-800 nm have been used for this heterostructures [883]. After spin coating the Cu/graphene/PMMA sample was baked at 60 °C for 10 minutes to evaporate the most of the solvents. The transition temperature of PMMA from soft polymer to acryl glass is about 100 °C [880]. Similar recipes can be used to transfer the PMMA/Graphene hybrid or to be used as a free standing one. Moreover, elastic and thin graphene/PMMA films can be stacked as it was done in [881]. Fig. VI.16 shows a free standing 500 nm thick graphene/PMMA sandwich placed on an aluminum plate with 10 mm diameter hole. The sample is prepared by using ARP-672.08 resist (4.5 % diluted with anisole). Similar 1 µm thick free standing films were fabricated using ARP-661.08 (4.5 % diluted with chlorobenzene) were examined more carefully in ref [882].

Fig. VI.16 Free standing 500 nm thick and 10 mm in diameter graphene/PMMA structure. The film is transparent and thus convenient for optical experiments.

Multi-layered structures, where the graphene is sandwiched between two PMMA layers, can be prepared and used as an electromagnetic interference (EMI) shielding layer by absorbing more than 50 % of electromagnetic waves at 30 GHz frequency [881]. Those 600-800 nm thick samples, spin coated with ARP-661.08 resist as a dielectric spacer were prepared. The graphene/PMMA layer was fabricated as earlier described. At the end, when graphene/PMMA film floats on water surface, the film is deposited on a silica substrate. Because of a water layer between graphene/PMMA film and the silica substrate, the sample thus was dried on a hot plate for 20 – 30 minutes with 50 °C temperature. If the temperature exceeds 60 °C the water layer will start boiling causing small bubbles to the graphene/PMMA-silica interface. When the sample is fully dry, another graphene/PMMA film can be deposited on top of the first one. One should be aware that a residual moisture might result in lifting out the graphene/PMMA layer while attempting the deposition another one on the top.

VII GROWTH AND TRANSFER OF OTHER 2d MATERIALS

VII.1 Hexagonal BN

CVD synthesis of h-BN on Rh(111)/YSZ/Si(111)

The h-BN on Rh(111) (h-BN nanomesh) was first reported in 2004 [884]. The h-BN nanomesh is a corrugated honeycomb superstructure and is the product of a high temperature CVD growth using borazine $(HBNH)_3$ as a precursor. The highly regularly corrugated structure with a lateral periodicity of 3.2 nm is determined by the mismatch between the boron nitride and the Rh. The unit cell of the h-BN nanomesh consists of 13×13 BN units on 12×12 Rh atoms. The h-BN nanomesh unit cell has one "pore" with 2 nm diameter, and is surrounded by "wire" regions [884, 885] (Fig. VII.1(c)).The high temperature CVD growth procedure of h-BN nanomesh on Rh(111) single crystal or Rh(111) single crystalline films on YSZ-buffered Si(111) wafers [886] is as follows. The substrate is first cleaned in UHV by Ar^+ sputtering (1.0 keV, 3.5 μA/cm^2 sputter current) for about 30 mins, and annealed to 700 °C. The substrate is kept at 700 °C for 5 mins., and oxygen (P(O2)=5~8 x10^{-7} mbar) is dosed at this temperature for 10 mins. This is followed by a flash-annealing treatment up to 900 °C for 5 mins. The substrate is then cooled down to RT; the whole preparation cycle (sputtering + annealing + O2 dosing + flash-annealing) must be repeated twice to ensure high quality of the h-BN monolayer on Rh(111). At the third treatment cycle, no O_2 dosing step is needed. The substrate is directly flashed to 900 °C for 5 min after the annealing treatment. Then the substrate T is stabilized at 800 °C, and borazine is dosed at P=5x10^{-7} mbar for 5 min. Afterwards the sample is cooled down to RT with an initial cooling rate of 10 °C /min.

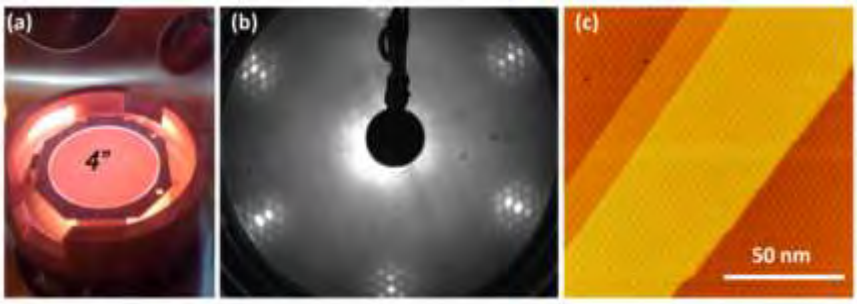

Fig. VII.1: 800 °C hot 4 inch wafer (a). Low energy electron diffraction (LEED) pattern of h-BN/Rh(111) at 60 eV kinetic energy (b). STM image of the same surface with U_t =- 1.2 V and I_t = 0.5 nA.

LPCVD of BN on polycrystalline metals

The growth is carried out in a homemade hot-wall low-pressure ~ 10^{-3} mbar, sketched in Fig. VII.2, consisting of a 7-inch chamber with induction heating. Compared to the standard tubular CVD

reactor, scaling-up can be readily achieved with this system as a result of the free aspect ratio (up to 80 cm^2). The gases flow through the bottom of the reactor, parallel to the substrate. Hydrogen is used as a carrier gas for the BN precursor, borazine $(HBNH)_3$ which has an ideal 1:1 B:N stoichiometry and decompose into BN and hydrogen. It is a volatile liquid with a high vapor pressure (280 mbar at 25 °C), air and moisture sensitive [887]; therefore, its use requires a specific set-up to have an accurate control of the gas flow. To avoid gas flash in the CVD chamber and good control the flow rate, borazine is maintained at 0°C with a chiller to lower the vapor pressure and a system of mass flow controller is used. A cold trap was installed to prevent the damage of the scroll pump with potentially non-decomposed borazine. The process follows the typical cycle of heating, pre-annealing (30 minutes under H_2 at 1000°C) of the metallic substrate, usually polycrystalline Cu or Ni, growth at 1000°C, a regulated pressure of 0.3 mbar, under 50 sccm of H_2, with $P_{borazine} = 10^{-2}$ mbar, for a time between 10 minutes and 2 hours, and slow cooling down under H_2 flow.

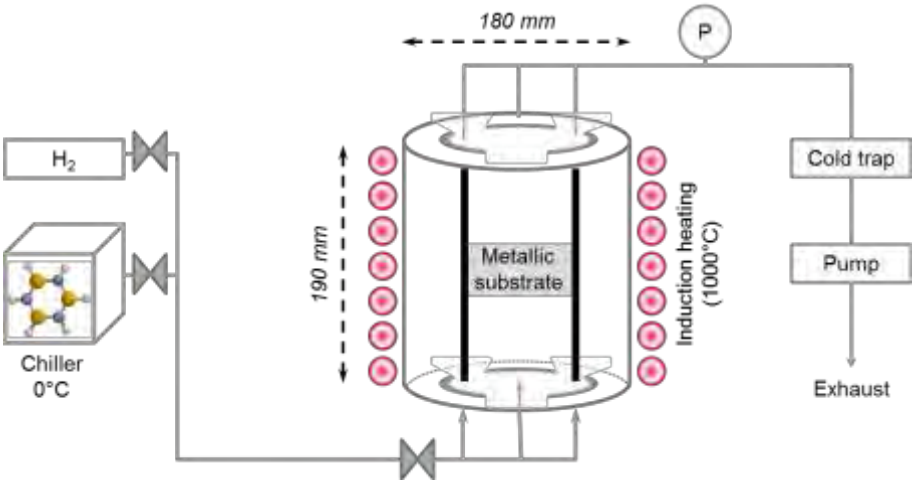

Fig. VII.2: schematic of the vertical CVD set-up for boron nitride film growth on polycrystalline metallic foil.

After the growth, BN films need to be transferred from the growth metallic substrate onto appropriate substrates (SiO_2/Si or TEM grid) for their characterization. The techniques described for graphene transfer in section VI have to be adapted for BN transfer. Both electrochemical delamination process and chemical etching to remove the metallic substrate are used, with or without a temporary support of polymer.

Transfer of h-BN grown on metals

Transfer of multilayer h-BN on Cu

A PMMA layer is first spin coated on BN/Cu system, which will play the role of temporary support during the transfer. For the electrochemical delamination process, an aqueous solution of KCl (1M) is employed as electrolyte, with a glassy platinum anode and the PMMA/BN/Cu cathode is negatively

polarized (5V). The formation of H_2 bubbles at the BN/Cu interface leads to the separation of the stack PMMA/BN and the Cu substrate. The film is then rinsed with DI water, deposited on the target substrate and , at 20°C/ 10 min, heated up to 120°C to remove excess water and to stretch it. After one night, the PMMA film is removed with acetone at RT. An example of BN transfer from Cu substrate onto SiO_2/Si and TEM grid is shown in Figure VII.3a and b, respectively. We can achieve a size of 1 X 1 cm^2.

Transfer of multilayer h-BN on Ni

The previously described electrochemical delamination does not work I this case due to the stronger BN/Ni interaction compared to BN/Cu interaction. The TOA-assisted chemical delamination, described in VI.1.2, has already been tested for this system and new strategies are required in order to remove all the ions residues. In this particular case , the standard chemical etching (see section VI.1.1) is used to remove the Ni substrate, without the use of any polymer [710]. The nickel substrate is etched with a commercial solution (TFB Nickel Etchant, Transene) for one night. The BN film is rinsed with DI water, deposited on the target substrate and slowly heated until 120°C to remove excess water. This polymer-free technique does not create any contamination and, preserve the integrity of the film. An example of BN transfer from Ni substrate onto SiO_2/Si and TEM grid is show in Fig. VII.3c and d, respectively. We can achieve a size of 1 X 1 cm^2, and a full TEM grid coverage.

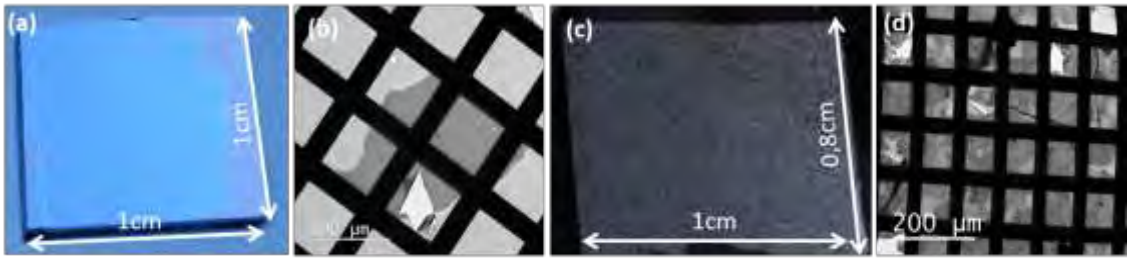

Fig. VII.3: Examples of large areas BN film transferred on 90 nm SiO_2/Si (a and c) and TEM grid (b and d), from copper and nickel growth substrate, respectively.

We have studied the role of the underlying metal nature and crystalline orientation on the multilayer BN film morphology. We first present the analysis of BN growth on polycrystalline copper substrate with a growth time of 90 minutes under the conditions detailed above. Fig. VII.4a shows an optical image of a BN film transferred on 90 nm SiO_2/Si; yellow and pink areas correspond to folded edges of BN film in light green. The thickness of the film determined from the AFM profile is about 70 nm, with a 20 nmroughness (Fig. VII.4b). This behaviour is confirmed by TEM observation of the sample (Fig. VII.4c). On the electron diffraction pattern (Fig. VII.4d), both several six-fold symmetry patterns and diffuse rings are observed, which is characteristic of a weakly crystallized turbostratic structure. This result is in agreement with that already described in the literature in the same range of temperature and borazine partial pressure [888, 889], for which a non self-limited growth, with a turbostratic stacking is expected. Due to its non-flatness and turbostratic structure, such kind of thick

BN films grown on Cu is not suitable to be used as a graphene substrate but could be a good candidate to be used as capping material of a 2D crystal in a device.

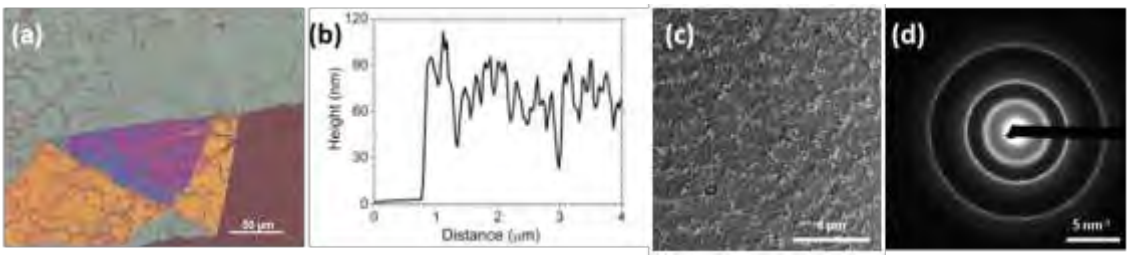

Fig. VII.4: (a) optical image of BN film grown on copper and transfer onto 90 nm SiO_2/Si, scale bar is 50 mm. (b) AFM profile showing the 90 nm thickness and the high roughness of the BN film. (c) TEM image with scale bar 4 mm and (d) electron diffraction pattern showing the rough/turbostratic behavior of the multilayers BN film grown on copper with scale bar 5 mm.

According to the literature, a higher crystallinity is achieved when growing by CVD BN on Ni substrate [890, 891] as compared to the growth on Cu. However, the reported analyses are restricted to few nano- or micrometers scale areas. Few investigations were conducted to elucidate the influence of the underlying Ni grain orientation on the BN growth kinetics and coverage but there is hardly any record in terms of crystallinity, morphology and thickness of the BN film [892, 893]. In order to fully characterize the influence of the grain orientations of the substrate on the BN film structure, combined SEM and TEM imaging (see sections IX.1.4 and IX.1.3 for an introduction to these techniques) and electron diffraction of both the BN film and the underlying Ni substrate are used. Fig. VII.5a shows a SEM image of the as-grown BN film on its substrate showing an area at the intersection of three differently oriented Ni grains. Their respective crystalline orientation is determined by Electron Back Scattering Diffraction (EBSD) as shown in Fig. VII.5b.Two different surface aspects of the film can be identified and are clearly highly dependent on the Ni orientation. In the first situation found for the Ni (111) orientation (blue grain), the film aspect is striated and nearly smooth, while for other orientations (001) orinetations (red grain) its appears to be very rough. Direct transfer on the TEM grid enabled TEM observations of the same area. TEM image of Fig. VII.5c reveals the print of the Ni grain boundaries on the BN film and confirms the presence of different BN morphologies depending on the underlying nickel grain orientation: flat and rough BN [894]. As on Ni (111) hBN lattice displays an almost perfect lattice match, the BN growth is highly oriented resulting in the formation of a flat h-BN as shown in Fig. VII.5c. In particular, by recording electron diffraction patterns in different areas as the example shown in Fig. VII.5d, the single crystalline character of the h-BN film over the whole Ni (111) grain is assessed. For (001) Ni grain orientations, the h-BN growth domains nucleate at different places on the Ni surface and grow independently from each other. This growth process is responsible for the island morphology characterized by important thickness variations from an island to another, discontinuity between the islands (darker and brighter contrast on TEM image Fig. VII.5e) and multiple orientation domains (several rotated electron diffraction patterns, Fig. VII.5f).

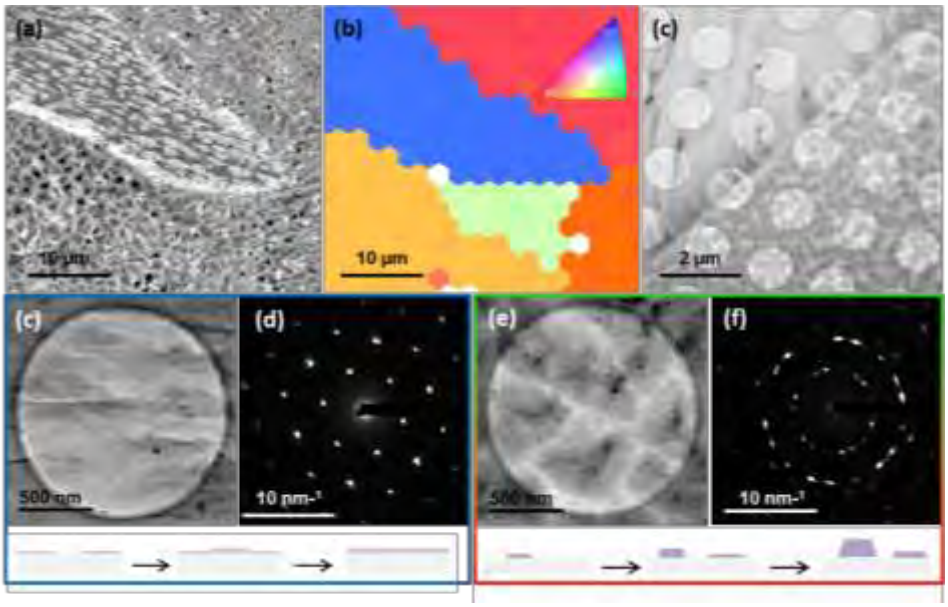

Fig. VII.5: (a) SEM image and (b) the corresponding EBSD mapping of the BN film on nickel substrate. (b) TEM image of the BN film transferred by the polymer-free technique on holey amorphous carbon film TEM grid. High-resolved TEM images and the corresponding electron diffractions of (c) and (d) a flat BN area and (e) and (f) a rough BN area with the schematic of the growth process: Van der Merwe for Ni(111) and Volmer Weber for Ni(110) and Ni(001).

This detailed analysis on the growth of h-BN on polycrystalline Cu and Ni provides insights and guidelines for further optimization of the synthesis conditions to planar and single crystalline layers appropriate for a use as substrates of dielectric layers. Note that a full account on characterization methods developed for h-BN are given in Section IX.

Benchmarking of the transfer of CVD grown BN

CVD BN is usually grown on metallic (transition or noble metals) substrates, or insulating (sapphire) substrates that are not suitable for characterization and device manufacturing. The goal of a transfer process is to get the 2D material on the suited host substrate.

Transfer processes are based on the use of a temporary support, most of the time a polymer. Several methods have been developed during the past years to address this issue that can be sorted in two categories: wet transfer, involving the use of a liquid aqueous solution, and dry transfer, relying on solid adhesive layers. The latter ensures the absence of water between the layers, which can be detrimental for device properties. The Table VII.1 scrutinizes advantages and drawbacks or difficulties inherent to both kinds of transfer processes.

Several parameters can impact the feasibility and quality of transfer, including the roughness and the thickness of the film, its homogeneity, the interaction with the growth substrate , and the roughness and surface termination of the host substrate.

Wet transfer techniques include chemical etching, and electrochemical delamination, preceded or not by ion intercalation. These techniques involve touchy steps for which an experienced operator

may be needed. Dry transfer methods listed here use PVA/PMMA or scotch tape as the adhesive material. Most of the time using an adhesive strong enough to pick up the film is necessary but not sufficient, as the redeposition on the targeted substrate may be hard to achieve. If the adhesive material is transparent, it can be done under a microscope, which permits to target precisely the area to pick up and where to deposit it.

Table VII.1: Comparison of the various procedures developed to date for transferring CVD grown BN

Method		Metals	Potential contamination	Special equipment	Re-use of the substrate	Time	Key parameters	Other
WET	**Chemical etching**	Cu [895, 896] , Ni[891, 893, 897]	etchant, polymer, metal residues, interfacial water		no	several hours	etchant nature and concentration	
	Electrochemical delamination (ECD)	Cu[898], Pt[899], Fe[900]	electrolyte, polymer, metal residues, interfacial water	5V DC generator	yes (smoothed)	A few minutes	voltage, electrolyte nature and concentration	Possible damage due to gas bubbles produced at the interface
	Ion intercalation + ECD	Rh[901], Ni	ions, electrolyte, polymer, metal residues, interfacial water	3 electrodes set-up	yes	~20 minutes	voltage, electrolyte nature and concentration	
	Lift-off transfer	Cu[902]	NaOH residues, polymer, metal residues, interfacial water		yes	2-3hours at 60°C	Interface oxidation	
DRY	**PMMA/PVA** [749]	Potentially any (depends on the interaction BN - substrate)	PMMA	Heating plate	yes (if no BN remaining)	~2 hours	PMMA adhesion	Semi-dry transfer: water at the very end
	Scotch tape		Adhesive residues			a few minutes	scotch tape choice	Difficult release / deposition

VII.2 Layered Semiconductors

CVD Growth

As is the case with graphene, CVD of 2d materials is a synthesis route which offers a compromise between film quality and large area coverage and uses techniques compatible with CMOS processing. CVD of 2d materials other than graphene typically requires two precursor materials which adds to the complexity of depositing uniform, monolayer films. Precursors can be sourced as solids materials which sublime under heating with these vapours then reacting to complete the CVD process, or as gaseous materials in their own right. Gaseous precursors allow much greater control of parameters such as flow rate, but are often toxic or highly flammable materials, such as H_2S and H_2Se [903].

Fig. VII.6 describes the microreactor set-up for CVD of MoS_2 in which flakes of MoO_3 and sulphur powder are used as solid precursors to supply Mo and S, respectively. LPE MoO_3 flakes in IPA were drop-casted on a SiO_2 chip with the target SiO_2 chip placed face-down on top. This assembly was heated to 750 °C in a quartz tube furnace under Ar flow (150 sccm) with sulphur powder heated to 120 °C in a separate heating zone upstream of the microreactor. The samples were exposed to the resulting S vapour for 20 minutes before annealing at 750 °C under just Ar flow (150 sccm) for a further 20 minutes.

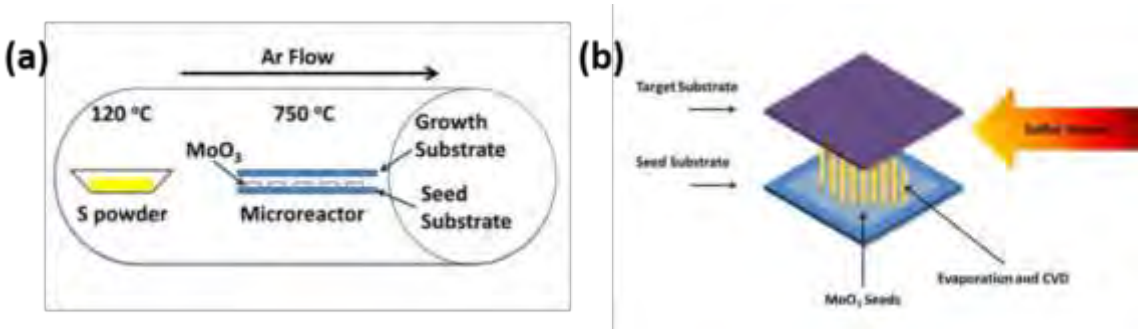

Fig. VII.6: (a) Schematic of the set-up for CVD of MoS_2. (b) Illustration of the mechanism by which MoS_2 is deposited on the target substrate. Adapted from Ref [903].

Imaging of the resultant deposit shows a film consisting of single crystal domains joined together to form a continuous film (Fig. VII.7(a)). Raman spectroscopy shows the A'_1 and E' peaks characteristic of MoS_2 (Fig. VII.7(b)), while the spectral contributions to the Mo 3d region of the XPS spectrum are consistent with that of MoS_2 with a small amount of oxide present [903] (Fig. VII.7(c)). The A'_1 to E' peak separation of 18 cm^{-1} and the strong PL (Fig. VII.7 (d)) are evidence for monolayer MoS_2 [903].

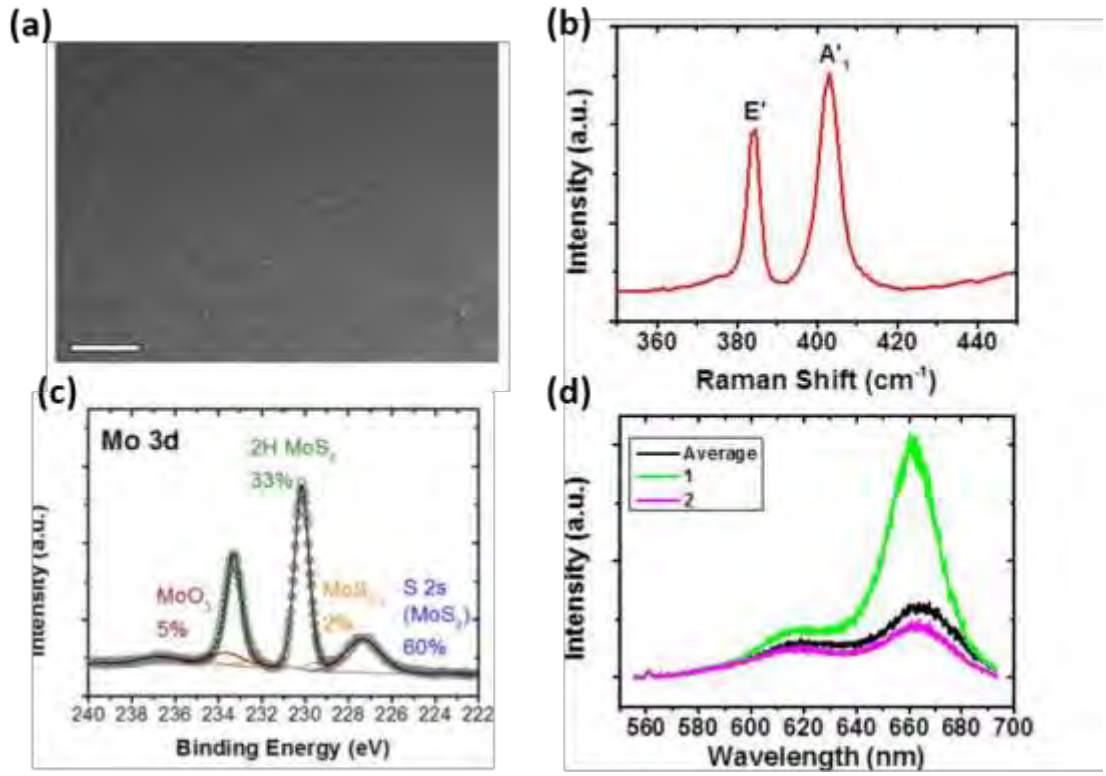

Fig. VII.7: (a) SEM image showing continuous MoS_2 film. Scale bar is 2 µm. (b) Average Raman spectrum measured across a 20x20 µm area of the film. (c) Mo 3d core level showing contributions consistent with MoS_2.(d) PL measured across monolayer region (green) and bilayer island (pink). Adapted from Ref [903].

MOCVD

MOCVD, as an enhanced CVD technique, is a more suitable method for mass-scale production of the 2d dichalcogenides due to a larger degree of control over the precursors.

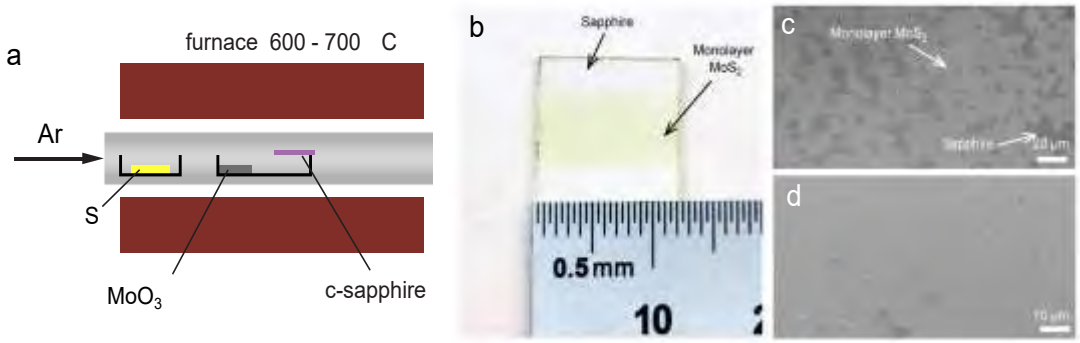

Figure VII.8. a) A CVD setup for deposition of monolayer MoS_2 using conventional solid precursors, MoO_3 and S. b) Photograph of MoS_2 deposited on c-plane sapphire. c) Monolayer MoS_2 covering c-plane sapphire without complete coverage. d) Monolayer MoS_2 with complete coverage Adapted from ref. [904].

CVD of MoS_2 on c-plane sapphire using solid inorganic precursors [904-906] (Fig. VII.8) has enabled an efficient route toward producing high quality monolayer MoS_2 films with lateral dimensions (> cm^2) beyond that of the mechanically exfoliated flakes (less than 100 µm) with electronic properties matching those in mechanically exfoliated samples [907].

However, the solid precursors such as S and Mo oxide exhibit negligible vapor pressure at RT. This leads to requirement of positioning the precursors inside the heated zone of the reaction chamber to reach temperatures usually above 200 °C for S and 500 °C for MoO_3 with fixed distances from the position of the substrates. Since the available composition of the precursors in the atmosphere of the reaction chamber depends on the evaporation from the time-dependent masses and surface areas of the solid precursors, it is challenging to consistently control the flow of the precursor vapours reaching the substrates over the period that affects the uniformity and stoichiometry of the resulting film. There is also a practical issue of over-consumption of the precursor materials that may lead to unwanted deposition of residual by-products on the substrates and walls of the reaction chamber which also hinders the growth uniformity and technological feasibility.

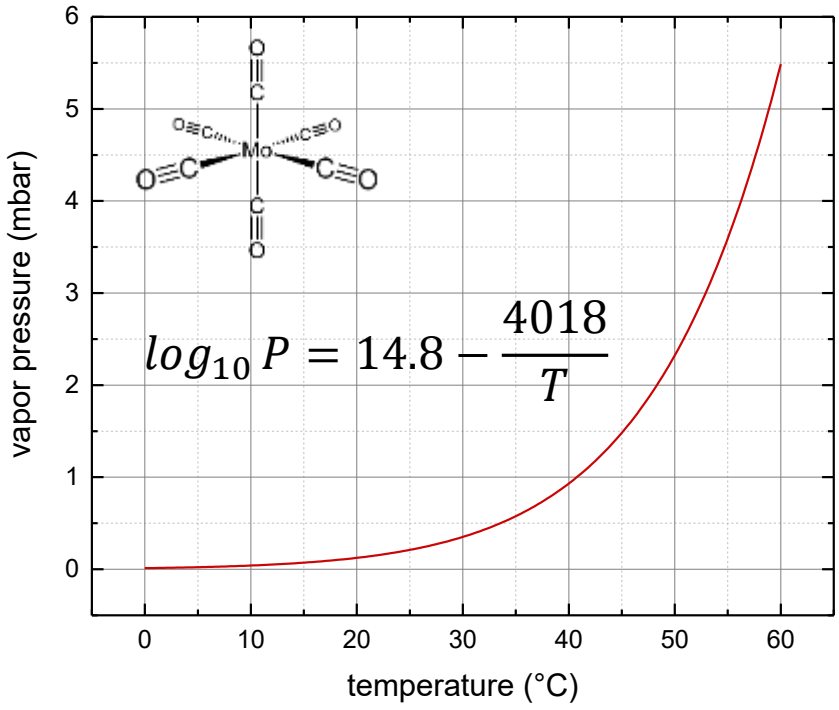

Fig. VII.9 Equilibrium vapor pressure of $Mo(CO)_6$ as a function of temperature. The plot was drawn based on the measured thermodynamic constants by ref.[908]

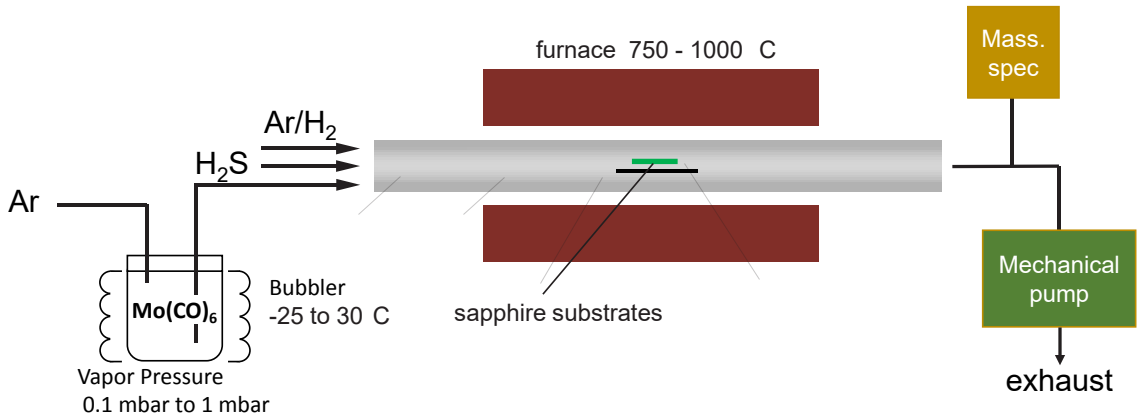

Fig. VII.10. The schematic of our MOCVD setup. Note the reverse bubbler configuration in the $Mo(CO)_6$.

In order to achieve a better control over the gas phase composition of the precursors in the chamber, metalorganic sources with high RT vapor pressures (> 0.1 mbar) can be used, which allow the precursors to be stored in a temperature-and pressure-controlled bubbler, outside the heated zoned of the reaction chamber where the vapour pressure and mass flow rate can be controlled independently, see Fig. VII.9 and VII.10.

Already before the TMDs received the current tremendous attention, a large range of MOCVD precursors containing Mo and S were developed for semiconductor and catalyst industries. They include $Mo(CO)_6$ [909], $MoCl_5$ [910], $(NH_4)_2MoS_4$ [911] for molybdenum and H_2S [910], diethyl sulphide [912] for S.

So far, the growth of atomically thin layers of MoS_2 by MOCVD was demonstrated by a few groups with a varying degree of coverage, crystallinity, thickness uniformity, and scalability. Ref [913] developed a method to grow a wafer scale polycrystalline monolayer MoS_2 thin films on SiO_2/Si wafer substrate with $Mo(CO)_6$ (molybdenum hexa-carbonyl) and $(C_2H_5)_2S$ (Diethyl sulfide; DES) with relatively low growth temperature (~ 550 °C) albeit with a rather long growth time to achieve a continuous film (~ 26 hours) in low vacuum conditions (7.5 Torr). Ref [914] have also developed a method to produce average-thickness controlled MoS_2 mono-to-multilayers on cm scale SiO_2/Si and sapphire substrates after a thermodynamic modelling of vapor phase equilibrium reaction of the precursors $Mo(CO)_6$ and H_2S. The growth pressure (~ 1 atm to 1 Torr) and temperature values (400 - 850 °C) were considered as a main factor in determining the range of growth parameters for the synthesis of high quality MoS_2 films of a good stoichiometry without any carbon residues originating from the carbon-containing Mo precursor.

Additionally, atomic layer deposition (ALD) techniques were presented as a modified CVD technique to produce thin layers of MoS_2 using the precursor pairs - $MoCl_5$ and H_2S [915]; $Mo(CO)_6$ and H_2S [916]; $Mo(CO)_6$, and dimethyl disulphide [917] ; $Mo(NMe_2)_4$ and 1,2-ethanedithiol [918] on various insulating substrates such as SiO_2/Si, sapphire, and mica. However, often the end products produced by these approaches are misaligned nanocrystalline MoS_2 thin films with varying degree of thickness likely resulting from the low growth temperatures (ranging from 300 – 600 °C) employed by

this approach. Moreover, although it is more challenging to prepare and control the stoichiometry of the product, MOCVD of MoS_2 using single-source precursors, tetrakis(diethyl-dithiocarbamato)molybdenum(IV) [919] and $Mo(S\text{-}t\text{-}Bu)_4$ [920] were also investigated.

Here, $Mo(CO)_6$ and H_2S are used [921] as model precursors. The choice was based on the fact that both of the sources are readily available, well-established high purity (> 99.9%) MOCVD sources with thermochemical properties that are relatively well known [914, 922-926].

In designing how the sources are delivered, a solid precursor such as $Mo(CO)_6$ is to be loaded into an inert, stainless-steel bubbler immersed inside a temperature controlled bath. Ideally, the evaporation of $Mo(CO)_6$ is considered to be fast enough to always completely saturate the bubbler with equilibrium vapor pressure (Fig. VII.9) which would determine the concentration of the precursor exiting the bubbler with the carrier gas. However, the common problem with solid precursors is that the actual vapor transported out of the bubbler quickly decreases over multiple growth runs because of increased dead volume of the precursor and decrease in the available precursor surface area for an efficient evaporation (at least ~ 1 μL/min·g). In order to tackle this issue, a reverse bubbler configuration (See Fig. VII.10.) and packing of precursor with an inert silica beads of ~ 2 mm are used to increase effective dwell time of the carrier gas and the precursor surface area [927] by an order of magnitude. These approaches have been previously employed for solid metalorganic precursors to ensure efficient evaporation [927]. The evaporation rate of the $Mo(CO)_6$ precursor should now be fast (at least ~ 1 μL/min·g) enough to assume an instantaneous phase equilibrium between gas and solid phases of $Mo(CO)_6$ within the bubbler while the $Mo(CO)_6$ precursor vapour is carried into the reaction zone of the system by an inert gas (specifically Ar). In this case, the partial pressure of $Mo(CO)_6$ exiting the bubbler can be easily estimated by the vapour pressure of $Mo(CO)_6$ at the T of the bubbler (T_b). T_b is preferably kept below the RT to prevent unwanted condensation of the precursor material upstream, before reaching the heated zone. Typically, a bubbler equipped with a chiller can reach a minimum bubbler temperature of –30 °C.

The actual amount of $Mo(CO)_6$ introduced to the reaction chamber can be monitored by mass spectroscopy that samples a part of the atmosphere inside the chamber. Although calibration of the absolute concentration of the precursor in the reactor chamber is somewhat challenging, the relative concentration can be obtained for every run of the experiment serving as an indicator for the amount of the precursor material remaining in the bubbler. At the outlet of the bubbler, in order to abruptly turn on and off the flow of $Mo(CO)_6$, a solenoid valve was installed, which can be automatically controlled so that the precursor mass flow from the beginning to the end of the MOCVD growth cycle is timed precisely.

As for the S source, mass flow control is more straight-forward as H_2S is in gaseous state at ambient conditions and high purity (99.999 %) gas can be provided readily from commercially available compressed gas cylinders. However, extreme caution should be exercised since the H_2S gas is a highly flammable and toxic gas with an acceptable exposure limit of 20 ppm (set by the Agency for Toxic Substances and Disease Registry, USA). In this regard, H_2S gas level detectors both in the ventilated gas cabinet storing the H_2S gas cylinder and near the CVD furnace are installed. They are connected to a sound alarm and that alert the appropriate emergency services immediately. In addition, we

have as well conducted thorough He leak test (Pfeiffer Adixen ASM 340) of the assembled CVD system before performing the experiments involving H_2S to prevent anyone in the work area from exposure.

The CVD system used, as illustrated in Fig. VII.10 is made of horizontal hot wall filament three-zone, quartz tube system (Carbolite HZS 12/-/600) that is commonly used for laboratory scale CVD synthesis experiments as one of the most economical ways to produce cm scale thin films. The quartz tube is coupled to KF-standard (DIN 28403, ISO 2861) high-vacuum compatible flanges which can be evacuated by a mechanical pump to the ultimate pressure of ~ 10^{-3} mbar. All the gas lines are made of stainless connections that prevents any outgassing and extraneous chemical reactions. The size of the sample produced is limited by the diameter of the tube and length of the heating zone.

In accordance to the CVD method already reported in ref [904], the MOCVD MoS_2 was deposited onto single crystal c-plane sapphire substrates (supplied by MTI Crop., USA), which were pre-annealed in air at 1000 °C for 1 hour to yield atomically flat terraces. This substrate has yielded much better growth morphology than other amorphous substrates such as SiO_2/Si. This presence of atomically flat surface is likely to be one of the prerequisites for the 2-dimensional and aligned layer-by-layer van der Waals epitaxy [904, 928, 929] . Typically, c-plane sapphire substrates were cut into square pieces of 1 by 1 cm by first scratching them with diamond tipped pen and snapping them into separate pieces by hand. Before the pre-annealing procedure at 1000 °C in air, they were subsequently cleaned in the IPA, acetone, and DI bathes inside a bath sonicator for at least 10 min.
Authors of Ref [914] have computed the thermodynamic “map” of all the possible phases resulting from the vapor phase reactions for different compositions of $Mo(CO)_6$:H_2S:H_2, growth T, and growth pressures. They found that a set of growth parameters with a high growth T of ~ 850 °C, presence of H_2(99%), and high growth pressure of ~1 atm lead to a good morphology with a large monolayer domain size bigger than 1 µm and stoichiometry predicted from the equilibrium thermodynamic modelling of the vapor phase. However, it must be noted that vapour phase reactions may not translate very well to what takes place at the substrate surface level, as the non-equilibrium dynamics, mass-transport, presence of boundary layers due to the fluid dynamic condition, and surface reactivity will also play an important role in the final surface mediated growth mechanism [155, 708, 930].

For instance, excessive vapour phase reactions must be avoided as they may lead to a significant formation of MoS_2 particles rather than substrate assisted 2-dimensional epitaxy of atomically thin layers [931-934]. In order to enhance the heterogeneous, surface reaction over the vapour phase reactions, generally speaking, higher temperature (> 800 °C) and pressure (> 850 Torr) are preferred [930].

H_2 during the MOCVD is used as a reducing agent to prevent the oxidation of the MoS_2 layer and deposition of carbon based species. However, H_2 is shown to be detrimental to the grain size of the film where the nucleation concentration could increase by an order of magnitude reported for increasing H_2 concentration [913]. Moreover, we observed that performing the growth at high T, low vacuum environment (~ 800 °C and 10 mbar) in the presence of H_2 would lead to silicon contamination of the substrate hindering the growth.

In turn, the growth conditions based on reference [914] were used for initial growth studies. The saturated vapour of $Mo(CO)_6$ at the bubbler temperature of 30 °C was introduced into the CVD system (a quartz tube three-zone hot-wall furnace) through Ar carrier gas. C-plane (1000) monocrystalline sapphire substrates (MTI Corp.) were placed in the center of the furnace by loading them onto a larger sapphire plate (which serves as a boat) and were heated to the growth temperature (750 – 1000 °C) and annealed for 15 min in Ar (75 sccm) followed by added flow of the S precursor, H_2S (1.5 - 20 sccm), before introducing $Mo(CO)_6$ to initiate the MoS_2 growth in the sulfur rich conditions that prevent the creation of vacancies due to sulfur removal within the as-grown MoS_2. At the end of the growth (typical growth time of 30 min), the $Mo(CO)_6$ flow was shut-off abruptly by a solenoid valve and the sample was cooled naturally to RT with Ar and H_2S gases still flowing through the quartz tube. All the stages of the MOCVD growth were performed under atmospheric pressure.

After each growth run, the inner wall of quartz tube was rinsed with DI water and IPA and blow-dried with N_2. Afterwards, it was annealed at 1100 °C in Ar (100 sccm) for 2 hours and in air for 2 hours order to eliminate all the residual precursor and by-product materials.

In order to optimize the growth morphology toward large lateral size (> 1 um) and crystalline monolayer MoS_2, we explored the growth parameter space. The temperature dependent growth of MoS_2 on sapphire in Fig. VII.11 shows the AFM height images of MoS_2 film morphology with the conditions that yield low overall coverage without merging of individual nuclei. The MoS_2 nuclei form randomly over the surface.

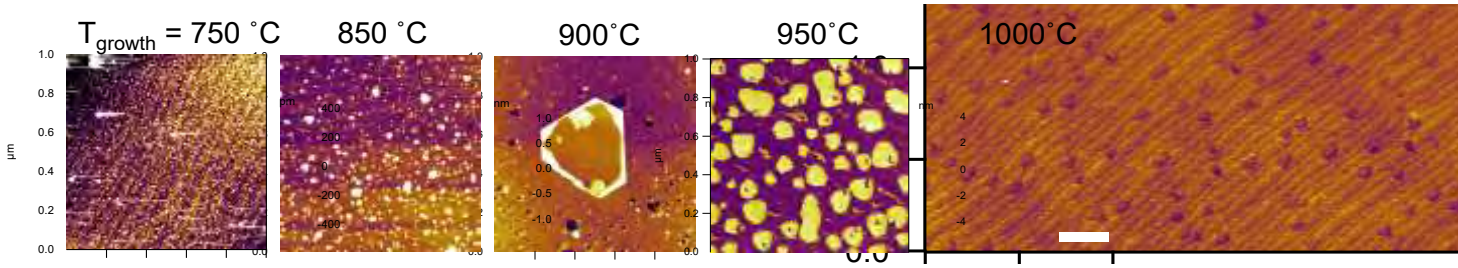

Fig. VII.11. Temperature-dependent growth morphology illustrated by AFM height images of as-grown MoS_2 sapphire samples produced at different growth temperatures. Scale bar, 250 nm. Adapted from ref. [921].

The nucleation concentration exponentially decreases with increasing temperature in an Arrhenius fashion (Fig. VII.12). This is consistent with the surface-mediated process where the apparent activation energy is linked with various activated surface reactions such as adsorption, attachment, and diffusion [935, 936] .

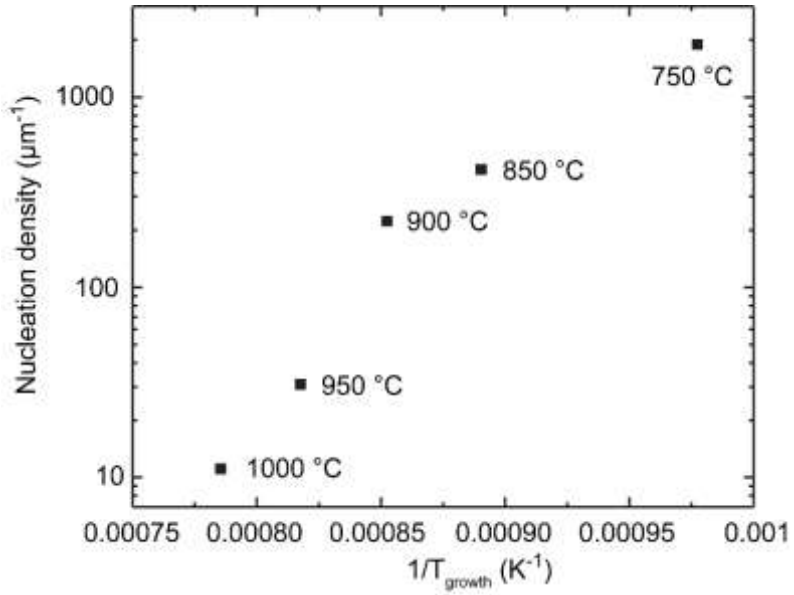

Fig. VII.12. Nucleation density versus 1/T plot for the samples illustrated in Fig VII.11. Adapted from ref. [921].

Raman and absorption spectroscopy techniques (Fig VII.13) demonstrate the high optical quality of the as-grown monolayer MoS_2 that are comparable to the exfoliated and CVD deposited MoS_2 films [904]. For instance, the A, B, C, and D excitonic peaks were clearly visible [904, 921] which is a clear optical signature of the MoS_2. Moreover, the wavenumber difference between the two prominent Raman peaks, relating to E' and A1' modes is 19.7 cm^{-1}, close to the standard value of a MoS_2 monolayer. Nevertheless, the grain sizes of the MOCVD MoS_2 films even for high growth T (1000 °C) are less than hundreds of nm. This makes further characterization of individual flakes difficult and the polycrystallinity of the film may lead to a significant degradation and non-uniformity in electronic quality of the MoS_2 layer for wafer-scale applications.

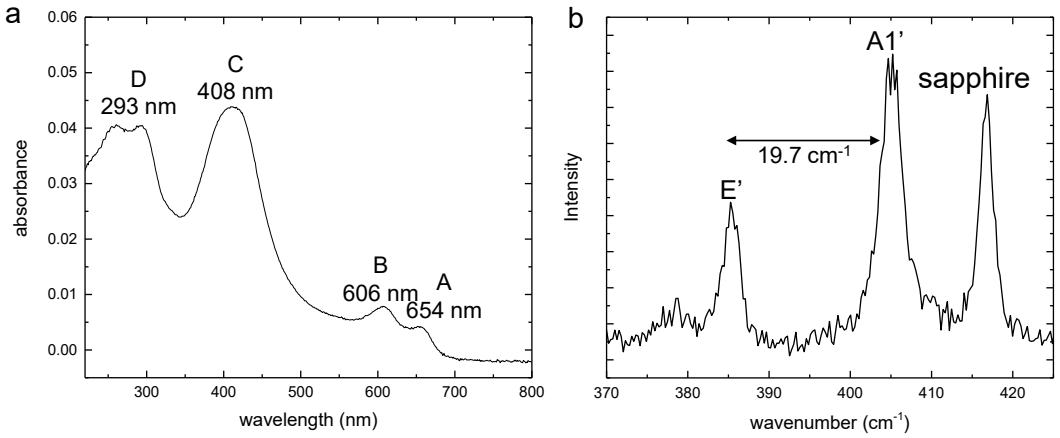

Fig. VII.13. μ-Raman (a) and optical absorption spectra (b) from the MoS_2 monolayer sample grown at 950° C. For Raman spectroscopy, 532 nm laser was used for excitation. Adapted from ref. [921].

The effect of partial and overall pressures of the gas species, $Mo(CO)_6$:H_2S:H_2 on the grain size was investigated. Using X-ray photoelectron spectroscopy (XPS, see epigraph IX.2. for an introduction) analysis, it is found that for low growth pressure conditions (10 mbar or below), the MoS_2 film becomes contaminated with Si (Fig VII.14) likely originating from quartz tube with reducing environment originating from H_2 in the carrier gas and from the decomposition of H_2S of this setup – not ideal for a clean, two-dimensional growth of the monolayer MoS_2. In addition, larger amounts of $Mo(CO)_6$ compared to H_2 tend to yield bulk particles of non-sulfurized, Mo oxides as probed by the XPS (Fig. VII.15). Fig. VII.15 a, b shows the representative optical microscopy images of MoS_2 films grown on sapphire, for two different $Mo(CO)_6$:H_2S ratios, 4:1 and 1:1 respectively. The core-level XPS spectra of Mo 3d, S 2s, and S 2p demonstrate that the low $Mo(CO)_6$:H_2S condition provides a good stoichiometric film of MoS_2 with only small (< 1%) amount Mo in different chemical state (Mo^{5+}) than that of MoS_2 (Mo^{4+}), while the high $Mo(CO)_6$:H_2S condition leads undesired deposition of thick particles of Mo likely oxidized in 5^+ state with a poor Mo:S stoichiometry that is consistent with the thermochemistry of the Mo, O, S, H system [926].

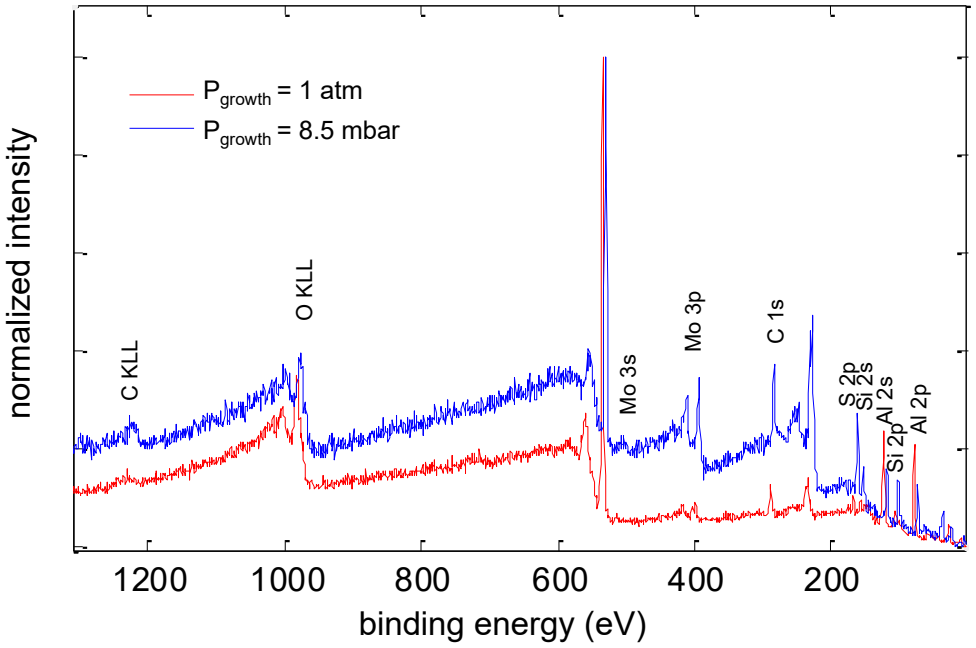

Figure VII.14. XPS survey spectra of MoS_2/sapphire samples from the two growth runs with different chamber pressures (1 atm and 8.5 mbar). XPS measurements were performed with PHI Versaprobe II equipped with *X-ray source, Al Kα; hv = 1486.6 eV.*

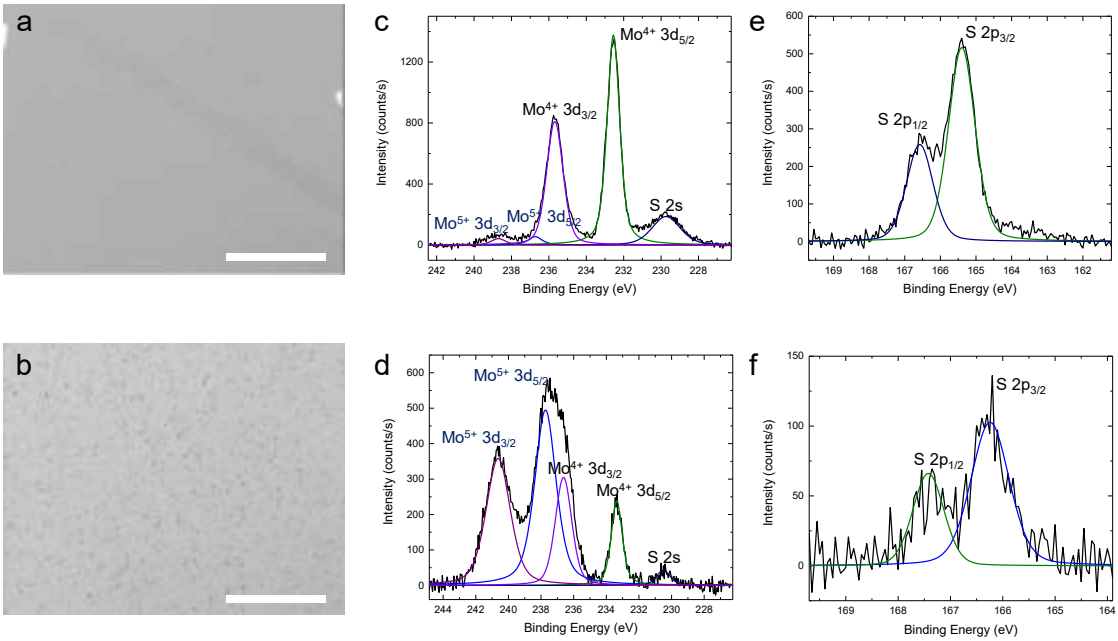

Fig VII.15 Influence of the $Mo(CO)_6$:H_2S flow rate ratio on the MoS_2 film composition. a) and b) optical microscopic images of the two different $Mo(CO)_6$ Ar carrier and H_2S mass flow rates of 15 (actual $Mo(CO)_6$ flow rate of 0.0053 sccm) and 15 sccm (a), and 5 (actual Mo(CO)6 flow rate of 0.0018 sccm) and 20 sccm (b), respectively with growth temperature of 950 °C, bubbler temperature of 30 °C, H_2 of 10 sccm, growth pressure of 1 atm, and growth time of 30 min. Scale bar, 25 µm. c, d) Mo 3d and S 2s core-level XPS spectra for the corresponding growth conditions of a and b, respectively. f) S 2p core-level XPS spectra for the corresponding growth conditions of a and b, respectively. XPS measurements were performed with PHI Versaprobe II equipped with a Al Kα X-ray source; hv = 1486.6 eV.

So far, this MOCVD approach has produced monolayer MoS_2 with average domain size of only less than 1 µm, similar to what had been observed previously [937, 938]. This presents as a challenge towards production of single-crystal MoS_2 monolayers over the length scale of the substrates. In order to improve the domain size, one could employ alkali metal halide salts such as NaCl, KI, and KBr. The use of thes salts has been documented previously in MOCVD experiments to improve the domain sizes that involve precursor combination of $Mo(CO)_6$ and $(C_2H_5)_2S$ [913], $MoCl_5$, and $(CH_3)_2S$, [939] and conventional CVD [940] on SiO_2/Si substrates. Here, a metal halide is placed, specifically, NaCl or KI powders (~ 0.01- 1 mg) in the upstream area of the furnace placing it either in an alumina boat or on a plate of alumina [921]. The $Mo(CO)_6$ was introduced at the temperature of 600 °C for 30 min before introducing H_2S at higher temperatures (750 °C – 1050 °C). As reported in ref. [913], a similar nucleation suppression effect is observed, where maximum monolayer flake sizes bigger than 10 µm can be achieved. Analysis by optical absorption, Raman, PL spectroscopy and XPS in Fig VII.16 have shown that the MoS_2 layer exhibits a direct-band gap without significant defects, strain, impurities and doping comparable to those of MoS_2 monolayers grown by conventional CVD. Furthermore, the crystal facets of MoS_2 grains are highly aligned in one direction demonstrating a successful lattice-orientation matched epitaxial deposition of MoS_2 on single-crystal sapphire.

Moreover, the temperature dependent field-effect transistor characterisation using polymer electrolyte gating has demonstrated a promising n-type mobility close to 100 cm^2/Vs, similar to those of monolayer MoS_2 deposited by conventional chemical vapor deposition [928].

It is currently not clear exactly how the domain enlargement or the suppression of nucleation by the metal halides occurs. The desiccating effect of salt as suggested by ref. [913] is not likely to be the dominant factor since even a very small amount of salt (< 10 ug) could be used, where it would decompose before the growth reaction. Ref. [939] suggested that salt helps to reduce the carbon contaminant, which might hinder 2D crystallization, from organic parts of the MOCVD precursor. Ref. [941, 942] suggested that the presence of alkali metals leads to decrease in the melting point of the oxide-based Mo precursors and even the melting point of a substrate [943], increasing the reactivity. This in turn could lead to the increased diffusion and reduction in the nucleation density. The form of sodium oxides or compounds of sodium and molybdenum oxides ($Na_xMo_yO_z$) [940, 942, 944] may also play a role as they were found at the interface between as-grown monolayer MoS_2 and substrate [944]. It was also found that after the growth, where the salt was initially present, the halogen atoms will evaporate away from the substrate surface while the alkali metals remain [921]. Indeed, having Na_2MoO_4 alone (without any halogens) has shown to be an effective precursor for two-dimensional growth with large domain sizes [945]. Recently, large area MoS2 growth of large domain sizes was acieved on Na doped glass substrates [946, 947] . They report that Na especially impatts the 2d growth of large crystalline domains at a wide range of growth temperatures [720-1050 C).The exact role of the alkali metals remains to be investigated as there are numerous competing atomistic processes such as surface diffusion, nucleation site activation, attachment kinetics that control the nucleation and growth processes, which all can influence the nucleation density and domain size.

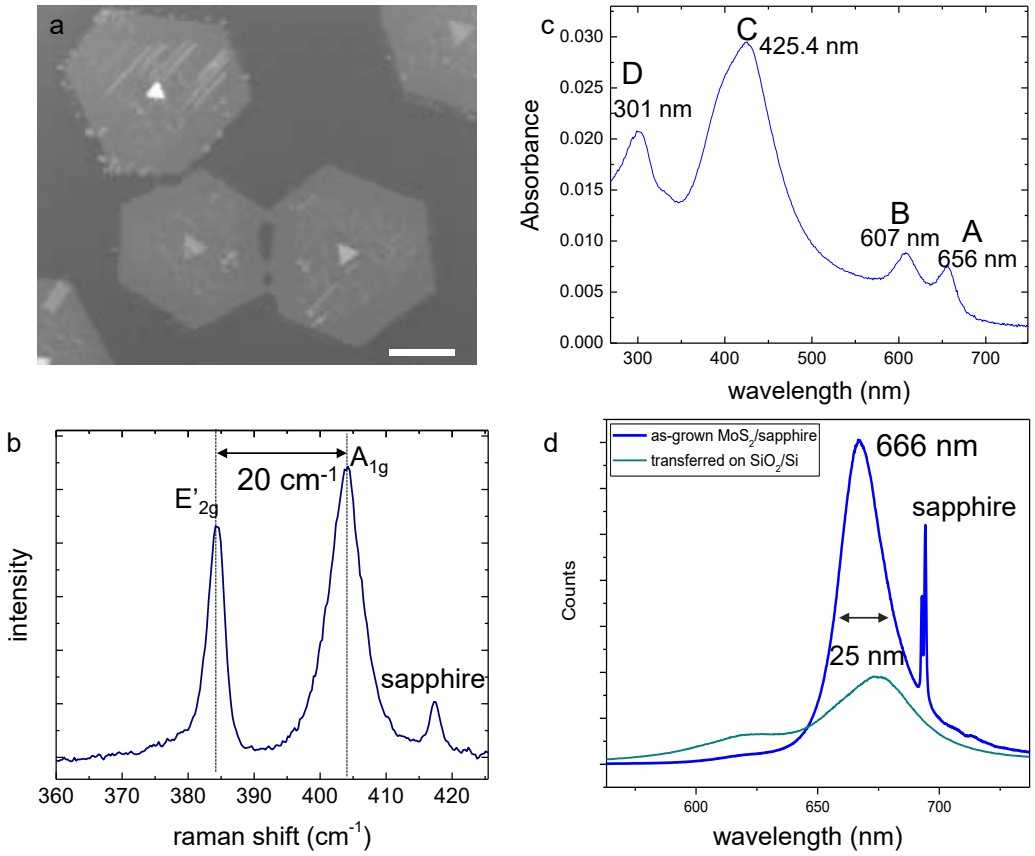

Fig VII.16. a) Optical microscopy image of MoS_2 monolayer with NaCl placed upstream. Scale bar: 25 µm. b) Raman spectroscopy on a single crystalline monolayer MoS_2 area on the sample c) optical absorbance spectra. d) PL spectra from the single crystalline monolayer MoS_2 flake as-grown on sapphire and transferred onto SiO_2/Si substrate. Adapted from ref. [921].

It can be concluded that MOCVD presents a significant progress towards growth of large-area, reproducible, high-quality two-dimensional TMDs. The challenge still remains to obtain a single crystalline continuous film of MoS_2 grown by MOCVD with a reasonable growth time (~ 1 hr). Time-dependent two or multi-step growth studies may determine the limiting factors for the surface coverage and help resolve this issue. More investigation on the growth mechanisms such as in-situ growth observations are required to determine the growth kinetics and rate limiting steps for systematic MOCVD control of the film morphology and micro-nanostructures. Low toxicity, low-cost precursors should also be considered in order to ultimately achieve a safer and more accessible production of MoS_2 and other TMDs. This work can be extended to perform MOCVD of vertical and horizontal heterostructures of TMDs such as $MoWS_2$ and $MoWSe_2$ using currently available metalorganic sources such as $W(CO)_6$, and dimethyl selenide [948]. In addition, intentional doping of the TMDs may also be easily achieved by introducing additional dopant precursors during the MOCVD growth as commonly achieved in MOCVD systems [949, 950].

Thermal assisted conversion

While CVD provides feasible route towards deposition of 2d materials, other approaches offer simpler, but highly scalable methods to grow thin films of these materials, at the expense of crystallinity. Thermally Assisted Conversion (TAC) [951] of metallic transition metals to TMDs is one such technique are employed. Thin films of the appropriate transition metal are typical deposited via sputter coating or electron beam evaporation onto appropriate substrates (often SiO_2 or sapphire) and then exposed to chalcogen vapour at elevated T (400-1000 °C). Controlling the thickness of the initial metal layer allows some control of the thickness of the final [define range] TMD film, but achieving consistent monolayer films remains a problem. Additionally, TAC films are polycrystalline in nature [951, 952].These features limit the practical usage of TAC films in certain applications such as electronic devices, as the abundance of grain boundaries compromises the electrical properties to a certain extent. However, TAC films are suited to other areas, such as gas sensing and electrochemical applications and, as such, have seen extensive research in those fields [903, 951-955]

A variety of TMD films via TAC have been grown and employed across a wide range of applications [903, 951-955].Thin films of Mo or W of varying thickness (typically 0.5-20 nm) were deposited on to SiO_2 and heated to 750 °C in a quartz tube furnace under Ar flow (150 sccm), see Fig VII.18, and annealed under these conditions for 30 minutes. Following this, S powder was heated to 113 °C in a separate heating zone upstream of the samples to generate S vapour. Sulfurisation was carried out for 20 minutes, after which the supply of S vapour was shut off and the samples were annealed for a further 20 minutes. The samples were then cooled to RT by switching off the heating over several hours under Ar flow.

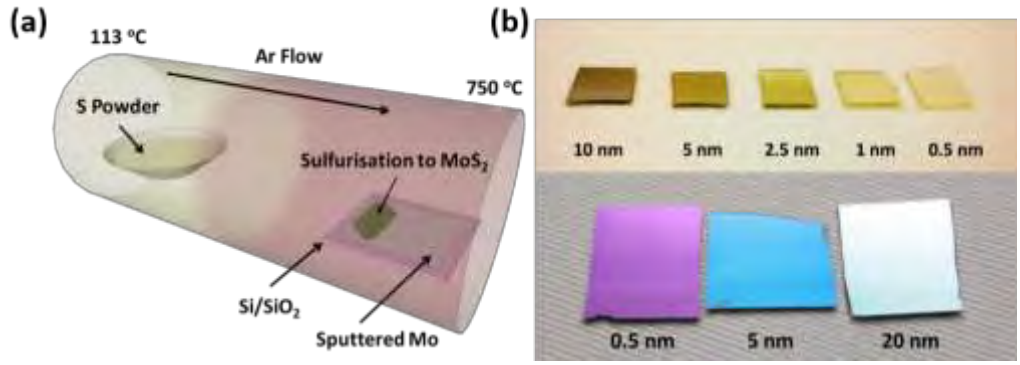

Fig VII.17: (a) Schematic illustrating two zone furnace for TAC of Mo to MoS_2. (b) Photographs showing different thicknesses of resultant MoS_2 films as formed on fused quartz (top) and SiO_2 (bottom) substrates. Adapted from Ref [951].

Raman spectra and PL of MoS_2 films grown via TAC from different initial thicknesses (0.5-20 nm) of Mo are shown in Fig VII.18 (a)-(c). Of note is the decreasing separation between the characteristic A'_1 and E' peaks and increasing PL intensity with decreasing film thickness. This signifies that, although these samples are polycrystalline few layer films, thinner samples exhibit significantly more monolayer character. This is of particular interest if one wishes to tune the characteristics of

such TAC films to suit a particular application. Fig VII.18 (d) and (e) show the Mo 3d and W 4f spectral regions for MoS_2 and WS_2 films, respectively. The Mo 3d core level exhibits spectral features consistent with a M:S stoichiometric ration of 1:1.9; signifying an almost ideal MoS_2 film. A small amount (<5%) of surface oxide was also present in the form of MoO_2 and MoO_3. The W 4f core level is typical of WS_2 with minimal oxides or unreacted sulphur on the film surface.

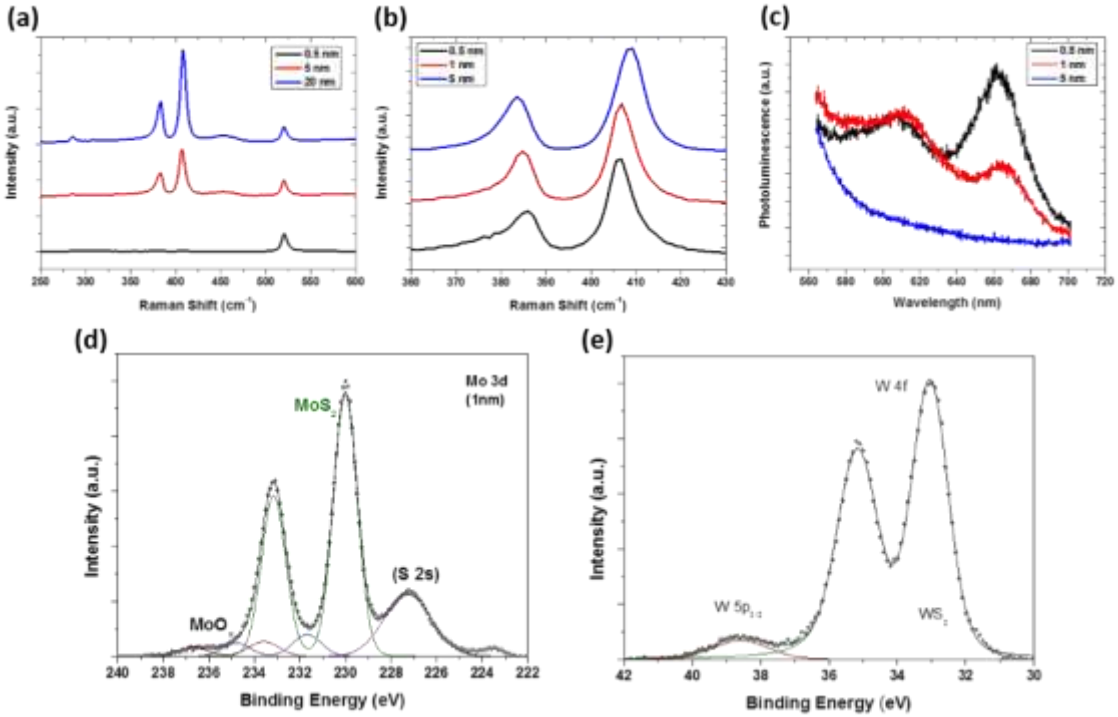

Fig VII.18: (a) and (b) Raman spectra and (c) PL of TAC MoS_2 grown from Mo films of differing thickness. (d) Mo 3d peak for MoS_2 grown from 1 nm Mo. (e) W 4f peak for WS_2 grown from a 20 nm thick W film. Adapted from Ref [951].

One strength of TAC production of TMD films is the ability to pre-pattern the starting metal prior to conversion to the resultant TMD. This eliminates subsequent processing steps which would be necessary if one were to use lithography to pattern a pre-existing TMD film. MoS_2 devices were fabricated by sputter-coating of Mo through a shadow mask, conversion to MoS_2 and then contacting with a second metal deposition with a second shadow mask defining the contacts. A photograph of the resultant device is shown in Fig VII.19 (a). This device was employed as a gas sensor for NH_3 as depicted in Fig VII.19 (b), whereby adsorption of NH_3 molecules onto the MoS_2 film surface causes a change in resistance, as shown in Fig VII.19 (c). This change in electrical properties was successfully used to generate a calibration curve, demonstrating the sensor response of the device in Fig VII.19 (d).

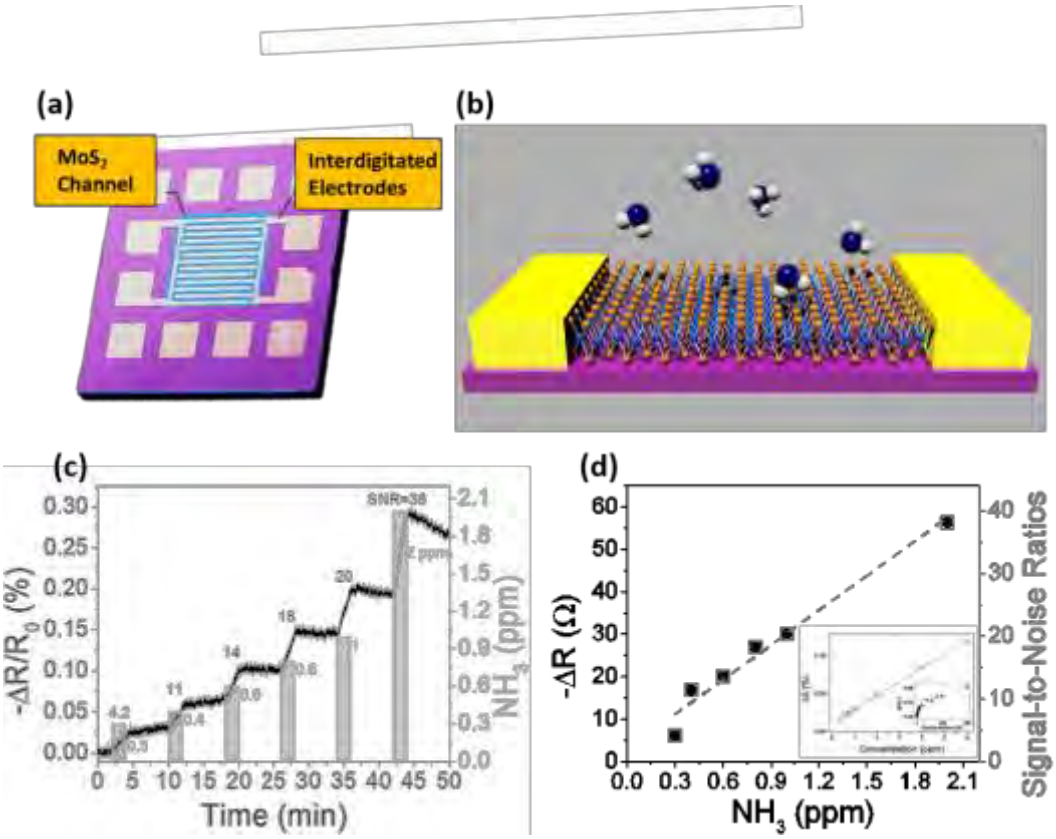

Fig VII.19 (a) photograph showing MoS_2 device with Ti/Au contacts. (b) Illustration of NH_3 gas sensing device. (c) Sensor response plot showing percentile resistance change versus time for the MoS_2 film with a bias voltage of 0.5 V. NH_3 exposures range from 300 ppb to 2 ppm. (d) Resistance change (black solid circles) and signal-to-noise ratios (gray open boxes) as a function of NH_3 concentration. Inset: full calibration curve ranging from 300 ppb to 200 ppm. Adapted from Ref [953].

Physical vapour transport

Among the large family of vdW crystals, the two-dimensional (2d) layered compound InSe is attracting increasing interest for its desirable electronic and optical properties [956]. More generally, indium selenide compounds with different stoichiometry, In_xSe_y, and their different polytype phases, *e.g.* α, β, γ, possess physical properties relevant for several applications in electronics, thermoelectrics and optoelectronics [957-960]. In particular, they have band gaps in the near infrared to visible range of the electromagnetic spectrum, 1.25 – 2 eV, high electron mobility at RT (> 0.1 m^2/Vs) and an interesting "Mexican hat" valence band energy dispersion [961-965], which is very sensitive to the layer thickness [962, 963, 965] and/or an externally applied electric field [961].

Several methods have been employed for the synthesis of In-Se compounds with different stoichiometric ratios, such as InSe, In_2Se_3, and In_4Se_3, and their polytype phases [966], but the synthesis of 2d nanosheets has been demonstrated only recently for the α-phase [967, 968] and β-phase [969, 970] of In_2Se_3, and for γ-InSe [971]

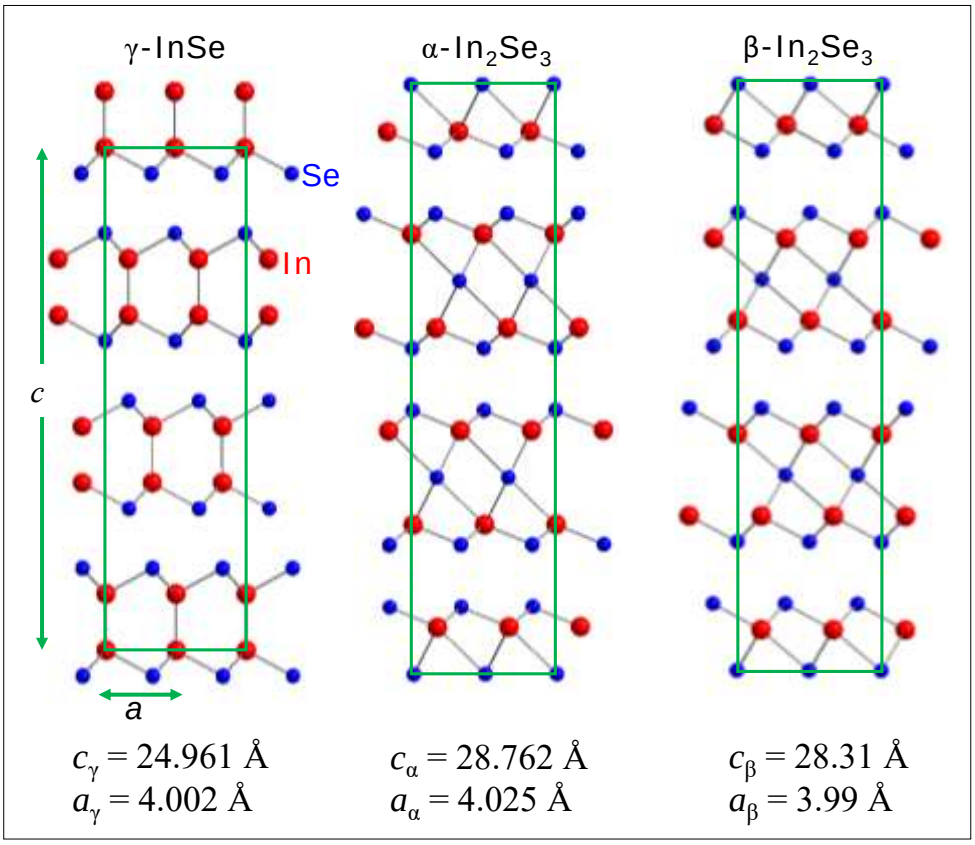

Fig VII.20: Side view of the crystal lattice and unit cell of γ-InSe (left), α-In_2Se_3 (middle) and β-In_2Se_3 (right). Blue and red spheres correspond to Se- and In-atoms, respectively. The primitive unit cell of γ-InSe contains three layers, each consisting of four closely-packed, covalently bonded, atomic sheets in the sequence Se-In-In-Se. For both α- and β-In_2Se_3 phases, the primitive unit cell contains three layers, each consisting of five closely-packed, covalently bonded, atomic sheets in the sequence Se-In-Se-In-Se. In α-In_2Se_3 the outer Se-atoms in each layer are aligned, whereas in β-In_2Se_3 they are located into the interstitial sites of the Se-atoms in the neighboring layers, thus leading to a smaller volume in β-In_2Se_3.

Fig VII.20 shows the crystal structures of α- and β-In_2Se_3 and γ-InSe. Thus electronic, thermal and optical properties of these nanosheets are still largely unknown [970, 972], although crucial to the implementation of the layers in several technologies, including molecular sensing [958], high-performance thermoelectric devices with low thermal conductivity [964], phase-change memories [973], and high-gain photodetectors [974].

β-In_2Se_3 nanosheets grown by physical vapor transport are optically active with a RT PL emission that is blue-shifted relative to that of exfoliated layers of α-In_2Se_3 and γ-InSe [969, 975]. Also, the grown layers have distinct Raman lines. More importantly, the RT PL peak energy of β-In_2Se_3 is strongly sensitive to the thickness of the nanosheets due to quantum confinement of carriers by the boundary of the layers and light electron mass [969].

The synthesis of the In_2Se_3 layers by physical vapor transport involves three separate steps as described below:

For the growth of β-In_2Se_3 layers by PVT, we used ground powder of Bridgman-grown [976] γ-polytype InSe as source material, see Fig VII.21a. Bulk Bridgman-grown γ-InSe crystals were ground into fine-grained powder using a pestle and a porcelain mortar. Then the powder was loaded into a quartz beaker and mixed with ethanol (96% purity) in a 1:4 weight ratio of InSe:ethanol, which acted as a dispersing liquid environment. The obtained suspension was sonicated for 18 hours at RT (f = 21.2 kHz and P = 100 dB). The resulting solution was dried in a porcelain beaker at RT. The dried powder was rinsed with DI water five times and finally dried in a drying chamber at 50 ^{o}C for 24 h. Then the powder was ground again using a pestle and a porcelain mortar. Finally, the InSe powder was sieved (200 x 200 μm^2).

The β-In_2Se_3 layers can be grown on different substrates such as Si/SiO_2, mica and graphite (HOPG). Prior to growth, the Si/SiO_2 substrate (7 mm wide and 3 cm long) was cleaned in hot acetone (T = 60 ^{o}C) and ultrasonicated in methanol and isopropanol (10 mins in each solvent) and then cleaned by oxygen plasma at T = 100 ^{o}C for t = 10 mins to remove ambient adsorbates from its surface. The cleaned substrate was immediately loaded into the tube furnace for the growth. Mica and graphite were cleaved prior to the growth and the fresh surface was used as substrate.

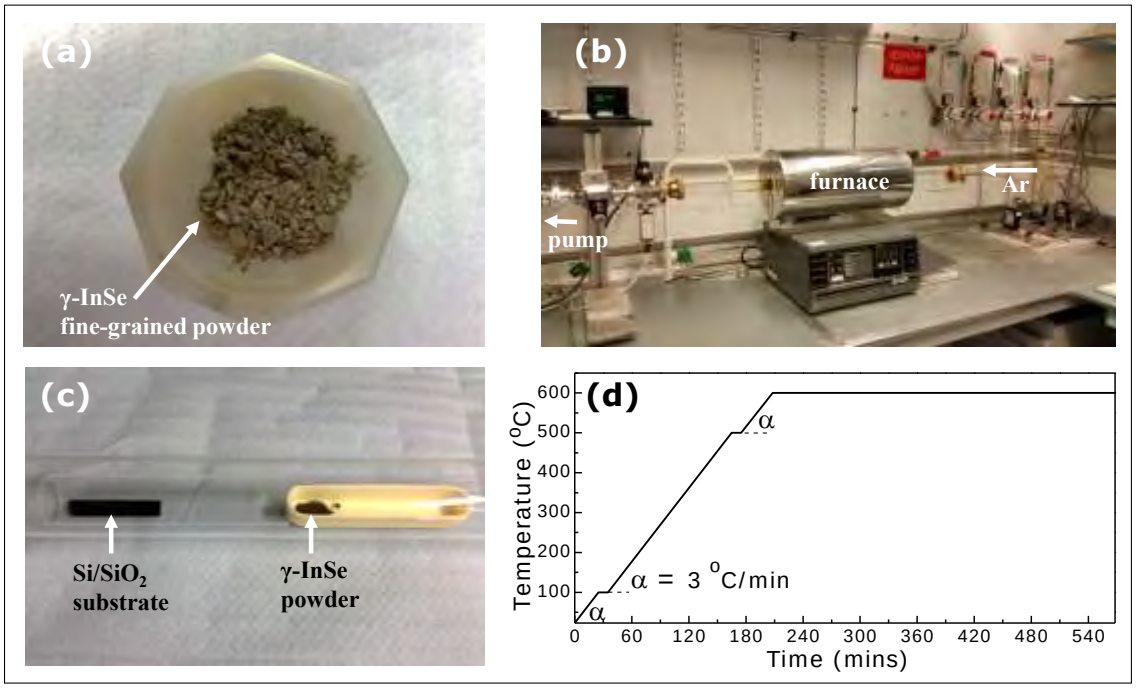

Fig. VII.21: (a) Optical image of fine-grained powder of γ-InSe. (b) The tube furnace system used for the growth of In_2Se_3. (c) The source material and the substrate in the quartz tube. (d) Program profile of the furnace heater for the growth.

A tube furnace system was used to grow the In_2Se_3 layers (Fig VII.21b). The system comprised a Carbolite furnace, a 1 m long quartz tube, a rotary pump and an Ar flow controller (Hastings mass

flow controller). The γ-InSe powder (~ 300 mg) was loaded into a ceramic boat and placed at the center of the tube furnace. The substrate was placed in the downstream side at 6-10 cm away from the source material, see Figure VII.21c. The pressure was lowered down to $P \sim 6 \times 10^{-3}$ mbar using the rotary pump. Then an Ar gas was flow at a rate of 150 sccm for 2 hrs provided a pressure of P = 1.6 mbar. Thereafter, the system was heated from T = 22 °C to 600 °C at a rate of 3 °C per minute and kept at 600 °C for 6 hours or longer (up to 9 hrs), see Figure VII.21d. The vaporized In- and Se-atoms were carried by the Ar gas and deposited on the substrate. The system was then allowed to cool naturally to RT. Typically, the source material can be reused for a second cycle of growth.

Fig. VII.22a-c shows the as-grown β-In_2Se_3 layers on Si/SiO_2, mica and graphite, respectively. The growth on Si/SiO_2 substrates produces near-circular, slightly facetted films with lateral size between 1 and 15 microns (Fig VII.22a), while highly facetted hexagonal films with lateral size ~ 100 micron grew on mica, see Fig. VII.22b. On graphite, films with arbitrary shape grew (Fig.22c) with preferential growth at step edge bunches on the substrate. The thickness, *t,* was measured by atomic force microscopy (AFM). It ranges from 100s of nanometers down to 2.8 nm on Si/SiO2 substrate.

For the same growth conditions (T = 600 °C, t = 9 hrs and Ar flow = 150 sccm) β-In2Se3 layers were grown on mica with layer thickness between 80 nm and 5 nm and on graphite from 100s nanometer down to 10 nm, (see Figure VII.20). Figure VII.23a-c shows some examples of growth obtained at different conditions. 'Hay'-like growth was obtained on mica at T = 620 °C for t = 9 hrs under an Ar flow of 150 sccm, see Fig. VII.23.a. Nano rods were grown on mica and Si/SiO_2, respectively, at 570 °C growth T or under 170 sccm flow rates of Ar gas (Fig. VII.23b-c).

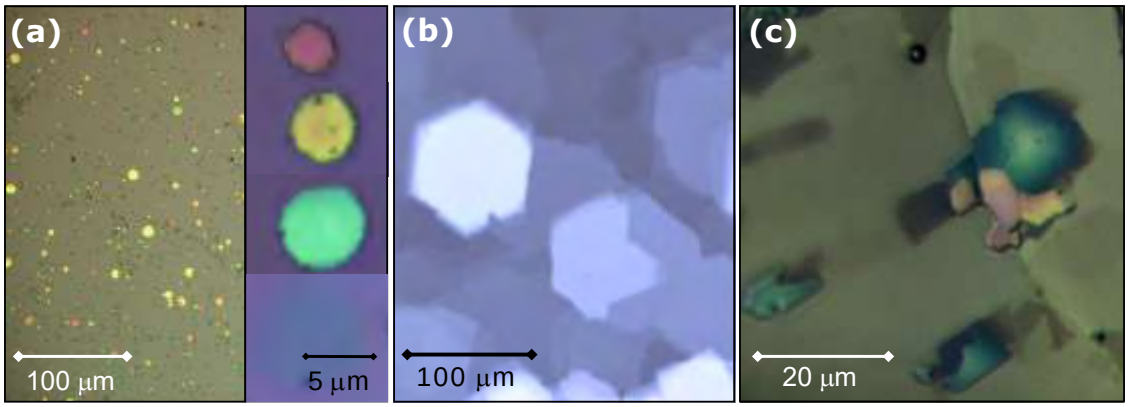

Fig.VII.22 : Optical micrographs of β-In_2Se_3 layers grown on (a) SiO_2/Si, (b) mica, and (c) graphite (T = 600 °C, t = 9 hrs and Ar flow rate of 150 sccm). Different colors correspond to different thicknesses of the layers. The layer thickness ranges from 100s of nanometers down to 2.8 nm. Adapted from [969].

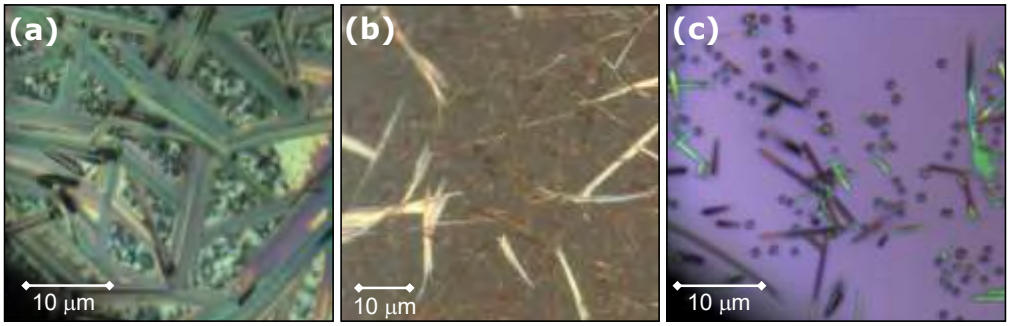

Fig. VII. 23: Optical micrographs of β-In_2Se_3 rods (a) grown on mica at T = 620 °C for t = 9 hrs under an Ar flow rate of 150 sccm, (b) grown on mica at T = 570 °C for t = 6 hrs under an Ar flow rate of 150 sccm, and (c) grown on Si/SiO_2 at T = 600 °C for t = 6 hrs under an Ar flow rate of 170 sccm.

The electronic and vibrational properties of the as-grown films of different thickness *t* and were compared with those of a series of thin α-In_2Se_3 and γ-InSe layers exfoliated with adhesive tape from Bridgman-grown ingots [976, 977]. The α- and β-phases of In_2Se_3 are characterized by distinct Raman modes. For the as-grown β-In_2Se_3 films, the Raman peaks are centered at ~ 110, 175, and 205 cm^{-1} at *T* = 300 K (Fig. VII.23a), corresponding to the intralayer vibrational A_1-modes (110 and 205 cm^{-1}) and the E_g-mode (175 cm^{-1}) of bulk β-In_2Se_3 [970, 978]. For exfoliated flakes of α-In_2Se_3 the Raman modes are narrower and centered at ~104, 181, and 200 cm^{-1} at *T* = 300 K. The β-In_2Se_3 nanosheets exhibit RT PL. RT normalized μPL spectra of as-grown β-In_2Se_3 nanosheets with *t* ~ 50 nm are compared with those for bulk α-In_2Se_3 and γ-InSe in Fig. VII.23b. The PL emission for the β-In_2Se_3 films is peaked at higher energy compared to that for α-In_2Se_3 and γ-InSe, and it blue-shifts with decreasing layer thickness (inset of Fig. VII.24c).

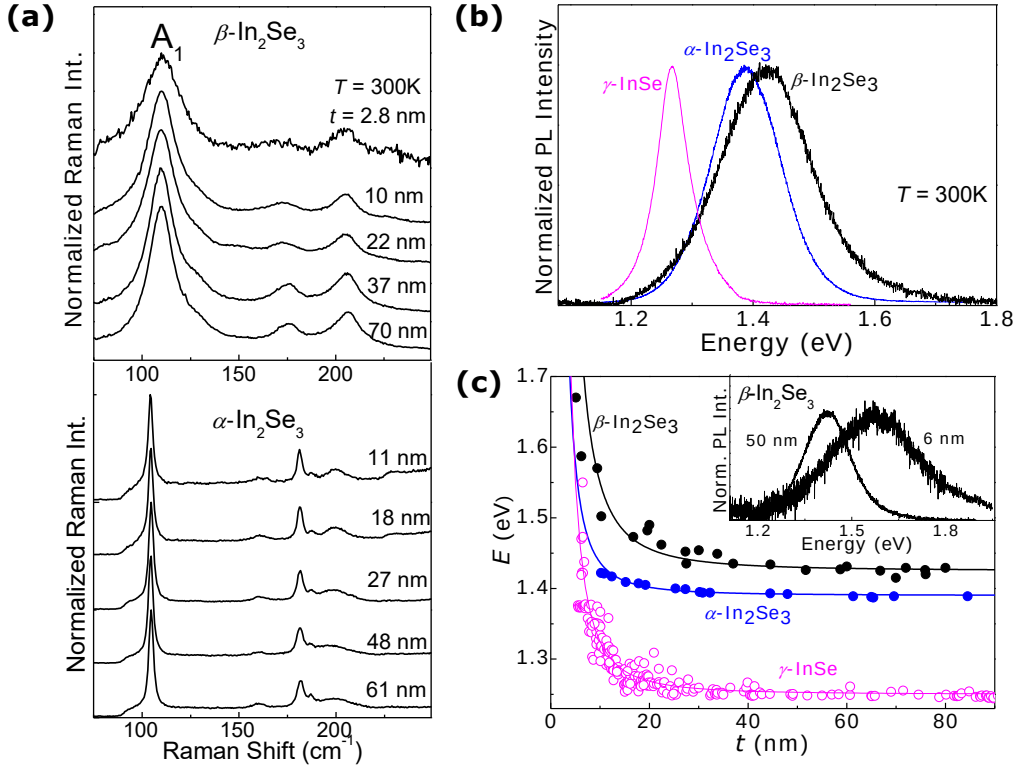

Fig. VII.24 (a) Normalized Raman spectra of as-grown β-In_2Se_3 layers (top) and exfoliated flakes of α-In_2Se_3 (bottom) at T = 300 K (P = 0.1 mW and λ = 633 nm). (b) Normalized μPL spectra of bulk γ-InSe, β-In_2Se_3 and α-In_2Se_3 at T = 300 K (λ = 633 nm and P = 0.1 mW). (c) Measured and calculated dependence of the peak energy, E, of the μPL emission on the layer thickness t of as-grown β-In_2Se_3 layers (black dots) and exfoliated Bridgman-grown α-In_2Se_3 (blue dots) and γ-InSe (magenta dots) flakes. Inset: Normalized μPL spectra of β-In_2Se_3 nanosheets with t ~ 50 nm and 6 nm at T = 300 K. Adapted from [969].

Fig. VII.24c shows the dependence of the PL peak energy, *E*, at RT on the layer thickness *t*, as obtained from several PL and AFM studies of as-grown β-In_2Se_3 layers (black dots) and α-In_2Se_3 and γ-InSe flakes [975] exfoliated from Bridgman-grown crystals [969, 976] (blue and magenta dots). The PL peak energy undergoes a blue-shift to higher photon energies with decreasing layer thickness consistent with the quantum confinement of photo-excited carriers along the *c*-axis. We model this energy shift by a simple quantum well potential of infinite height, *i.e.* $E = E_{3D} + \pi^2\hbar^2/2t^2\mu_{\|c}$, where E_{3D} is the band gap energy for the bulk and $\mu_{\|c}$ is the electron-hole reduced mass for motion along the *c*-axis. For β-In_2Se_3, the best fit to the measured values of *E* versus *t*, gives $\mu_{\|c}$ = 0.04 m_e and E_{3D} = 1.428 eV, where m_e is the electron mass in vacuum. These values differ from those for α-In_2Se_3, *i.e.* $\mu_{\|c}$ = 0.08m_e and E_{3D} = 1.390 eV, and γ-InSe, *i.e.* $\mu_{\|c}$= 0.05m_e and E_{3D} = 1.250 eV.

The comparison of the PL peak energies for our β-In_2Se layers with those for α-In_2Se_3, and γ-InSe nanosheets from this work and the literature [968, 971, 975] indicates distinct spectral ranges for these In-Se compounds and a wider spectral tunability for β-In_2Se_3 and γ-InSe, among the largest within the wide family of 2d crystals. The larger quantum shift and lighter electron-hole reduced mass for the β-phase compared to the α-phase are assigned to the closer spacing of the vdW layers in the β-phase (*Dc/c* ~ - 1.5%) (Fig. VII.20), leading to a stronger inter-layer coupling. On the other hand, the larger value of E_{3D} in β-In_2Se_3 compared to α-In_2Se_3 cannot be accounted for by a simple argument and may involve a redistribution of electronic charge between the Se- and In-atoms in neighboring vdW layers [966] . This may be also affected by the presence of crystal defects, such as In- and Se-vacancies (V_{In} and V_{Se}), which tend to form in In_2Se_3 due to the misvalency between the III- and VI-atoms [966]. Vacancy ordering and bond relaxation due to vacancies are expected to modify atomic orbitals and increase the band gap energy of bulk layers [979], and may play a more important role in 2ds [980].

VII.3 General growth method for binary layered materials

As described in Section V, the success of CVD 2D growth of graphene on Cu, which allows high quality mono-layers, is in part due to the efficient phase separation of the carbon source and the catalyst. Solubility of carbon is low in Cu, which confines crystal growth to the surface. Also,

copper does not react with carbon. These features contribute to facilitate robust growth of high quality monolayers.

By creating an situation analogous to the graphene-Cu system, a general growth scheme for binary layered materials of general formula $MX_{n,}$ M being a metal and X a chalcogenide (S, Se..) or N, was designed. The method is described in more detail in Shivayogiumath *et al* [Arxiv, reference will follow shortly], with additional TEM, AFM, SAED, EBSD, PL and XRD data.

As was shown recently for hBN [981] growth, only one component of a binary compound needs to be insoluble to ensure interface-limited growth. In this general scheme, Au was found to be an excellent choice of catalyst as the diffusion and transport medium for the M atoms to reach the surface. Au alloys with nearly all metals and does not react with any of the relevant X species, while the X species of interest are not soluble in Au. This allows mono- to few layer crystals to be formed at the interface.

An overview of the method used to synthesize binary compounds MX_n such as WS_2, WSe_2, MoS_2 etc, is shown in Fig VII.25. A thin film of metal M is deposited on a <001> sapphire wafer (Fig. VII.25a), and is encapsulated by a 0.5-1 μm thick layer of gold**.** When heated inside a quartz tube furnace (Fig VII.25b), the gold layer forms an alloy with the M layer, where the relative thicknesses can be tuned to adjust the concentration of M in the alloy, and thus the amount of M-component near the surface. The Au/M surface typically obtains {111} orientation on {001} sapphire. Formation of MXn compounds is then achieved on the surface of Au by exposing the substrate to volatile X species in the gas phase, Fig. VII.25(d), which is generated in the case of S, Se, and Te by volatizing solid precursors upstream of the substrate. In Fig. VII.25(e) the growth setup is illustrated, with the X compound (i.e. S, Se or Te) being heated upstream of the Au/M alloy, inside the quartz tube. In the example, Fig VII.25(f), WS_2 is shown to grow epitaxially on the a single-crystalline area of the Au/W alloy surface.

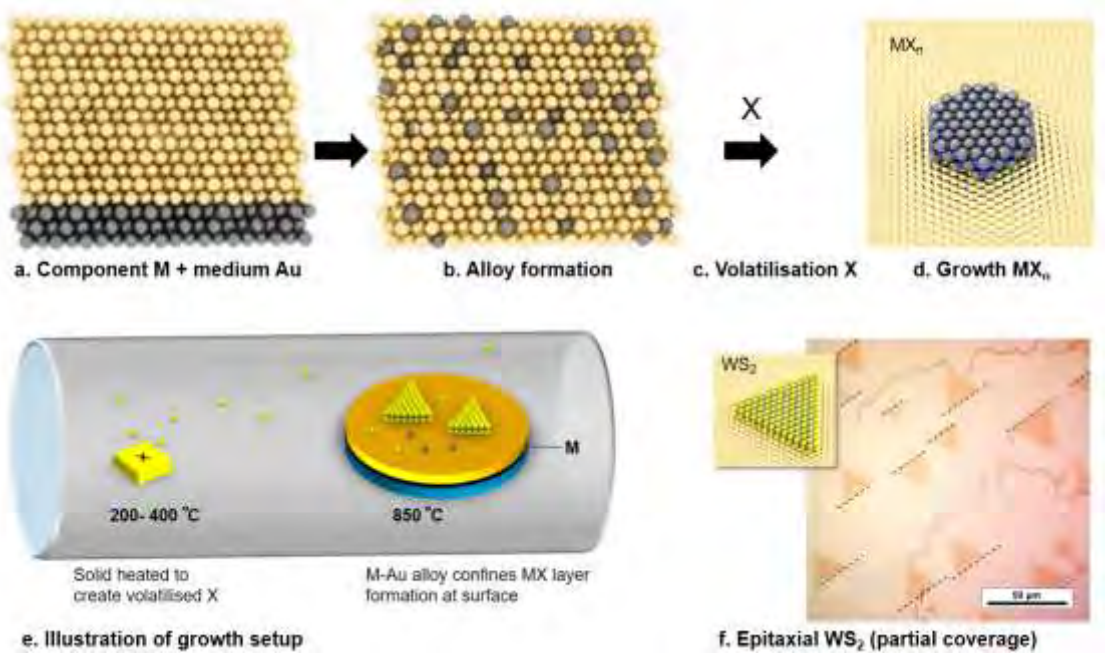

Fig. VII.25. Illustration of the growth process (a-d), the growth setup (e) and an example of epitaxial MX_n growth here WS_2 (optical image). The dashed lines show that the triangular crystals are co-aligned across an area of ca 150 x 150 µm^2

.

A standard tube furnace was used to grow binary combinations of M(Mo, W, Cr, Fe, Hf, Nb, Pd, Pt, V, Ta) and X(S, Se, Te). The materials were transferred by etching of the Au substrate in a standard Au etchants (potassium iodide), after spin-coating PMMA on top as a handle layer. The films were washed in DI water and transferred to SiO_2/Si wafers, followed by PMMA removal in acetone. Transfer to TEM grids and second transfer for electrical devices was done subsequently using wedging transfer [982, 983].

Fig. VII.26 shows magnified SEM images of WS_2 and MoS_2, as well as a selection of binary compounds out of 26 binary growth combinations that were carried out. TEM real-space and diffraction images confirmed that the two examples are indeed single crystals. Since many materials could not be transferred easily to TEM grids, XPS was used to verify that the chemical composition was as expected. All materials formed mono- or few-layer deposits, with exception of the iron-group metals (Fe, Co) where both few-layer and monolithic thin films were observed. While SEM images of many compounds indicated mono-crystallinity, unambiguous confirmation of the crystal structure is inherently difficult for the non-transferrable materials.

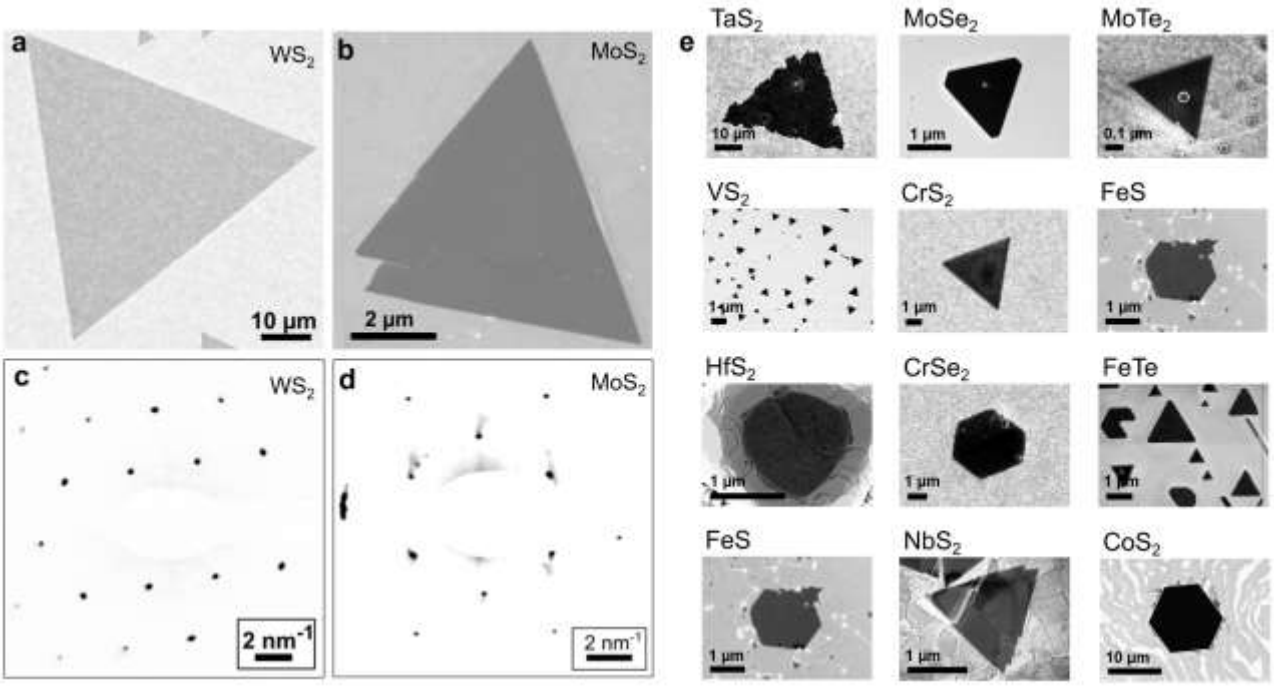

Fig. VII.26. SEM images of (a) WS_2 and (b) MoS_2 . TEM diffraction patterns of WS_2 (c) and MoS_2 (d) crystals after transfer onto TEM chips indicate monocrystallinity. (e) Selection of 12 binary compounds grown with the same method and similar process conditions.

While many materials were difficult to lift off the gold by the etching procedure without damaging or entirely removing the crystals, all Mo and W sulphides and selenides were successfully transferred. This probably points out to the need to tuning the transfer protocols to the requirements of a particular growth method and specific sample, as observed in other systems (see Sec. VI). A continuous layer of MoS_2 was transferred directly onto microelectrodes and measured by van der Pauw technique (see Section IX). Figure VII.27 shows two traces of the conductance vs gate voltage, from which a field effect carrier mobility of order 20-40 cm^2/Vs was extracted. The on-off ratio is of order 10^4 while the gate voltage hysteresis is low considering that the film was simply dropped down on the electrodes and measured without encapsulation, as in Ref [984].

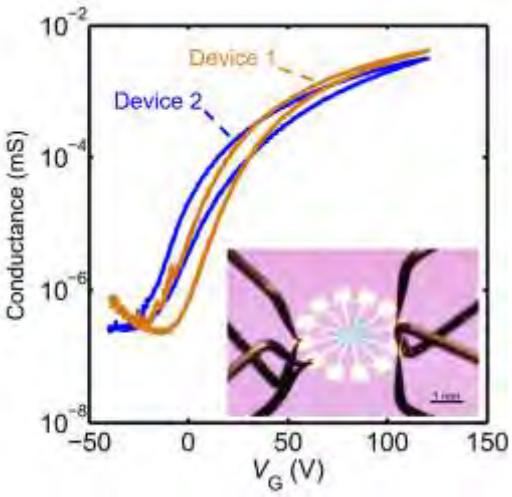

Figure VII.27 4-terminal electrical measurement of 1x1 mm^2 of continuous MoS_2 on 300 nm SiO2/Si substrate, after wedging transfer onto a predefined electrode structure (inset). The samples were annealed for 30 minutes at 225°C in dry N_2 to desorb water. Field effect traces from 2 devices are shown.

Similar processing conditions were achieved with an Aixtron Black Magic system to grow nitrides, using H_2 flow instead of Ar to avoid oxidation. Uniform 5.6 nm thin films of vanadium nitride (VN), which has to our knowledge not been synthesized in uniform thicknesses before, were grown using ammonia as X compound. HRTEM of FIB lamellas and SAED indicated FCC lattice structure with the {111} facet perpendicular to the surface, and XPS showed the expected bonding between vanadium and nitrogen and (1:1) stoichiometry [985] . The sheet resistance of transferred VN thin films was ca. 2 kΩ/□.

The advantage of the proposed method for growth of binary materials is that it allows to synthesize a large range of materials, including some that have never been synthesized before, with relative ease in a single setup. Some of the materials grow epitaxially on the growth substrate into regular, similar sized single crystals, and have promising structural and electrical characteristics. After transfer, the electrical characteristics for continuous MoS_2 films were found to be comparable to high quality encapsulated CVD films reported in literature [986]. The issue related to transfer, however, still needs to be addressed. The difficulty in transferring many materials with KI etching, particularly those which are sensitive to oxygen or water, limits the options for electrical characterisation as well as practical applications. While TMDs on Au could be used for photonic applications [987, 988], it is obviously highly desirable to develop robust transfer protocols that can lift off more of the crystals without damage. We consider intercalation to be an interesting route to provide a more gentle transfer of the crystals off the Au substrate (see Sec VI).

VII.4 Layered materials heterostructures

Graphene/h-BN stacks

Recently, great attention has been given to the possibility of synthetizing graphene directly on h-BN. Indeed, thanks to its atomically flat surface, low interlayer electronic coupling and almost perfect reticular matching, h-BN acts as the ideal substrate to graphene [989]. CVD is presently considered the most scalable approach to grow graphene directly on h-BN. To date, most of the works reporting vdW epitaxy of graphene on h-BN with appreciable growth rates are rather complex as they require either a PECVD [818] approach or growth catalysts [990, 991]. For the catalyst-free approach, poor control over the shape and crystallinity of the graphene grains and low growth rates are typically reported [812, 991, 992]. Here, a catalyst-free CVD approach which allows to synthetize crystalline graphene directly on exfoliated h-BN flakes with noticeable growth rates is reported [993] using single-crystal on-axis SiC dices (either Si- or C-face) as substrates for the exfoliation of h-BN flakes. This choice is due to the high thermal stability of SiC [994], in view of the high growth T typically >1200 ˚C, requested in a classical CVD approach to grow graphene on non catalytic substrates. The use of Si/SiO_2 substrates was also attempted but with poorer results: a significant Si sublimation during graphene growth led to the presence of carbidic particles embedded or on top of the synthesized graphene.

The SiC(0001) samples were diced from commercially available wafers (purchased from SiCrystal if semiconductive and CREE if insulating) and then cleaned via wet chemistry prior to mechanical exfoliation of h-BN. They were immersed in an ultrasonic bath of acetone and then IPA for 3 minutes each, and rinsed in DI water. They were then cleaned in HF (48% solution, Sigma Aldrich) diluted in DI water (1:10 HF: DI-H_2O) for 1 min to remove the native oxide and thoroughly rinsed in DI water. The samples were then subjected to oxygen plasma (O_2 flow, 80W, 5 min, from Diemer Oxygen Ashing) to completely remove the organic or carbonaceous contaminants. In order to make the SiC surfaces (which as purchased present polishing scratches) atomically flat, the dices were hydrogen etched in the same vertical cold-wall reactor (Aixtron, HT-BM) where also growth was performed. Hydrogen etching was carried on for 4 minutes in an atmosphere of 500 sccm of H_2 and 500 sccm of Ar (both gases with purity 99.9999%) at 1230^{o}C and a pressure of 450 mbar. Before that, annealing was performed for 10 min at 900^{o}C in the atmosphere of 1000 sccm Ar and 500 sccm H_2. Successfulness of the hydrogen etching process was confirmed via AFM: only samples presenting atomically flat surfaces where adopted for the subsequent steps.

PDMS stamps were used for carrying on the mechanical exfoliation of h-BN on hydrogen etched SiC. To this end, two PDMS stamps with dimension of 2 x 2 cm^2 were adopted and the mechanical exfoliation process was repeated for more than 40 times. The clean SiC substrate was then pressed on top of the PDMS stamp and kept for 30 min. With this procedure large h-BN flakes with lateral size up to 150 μm were obtained. To remove the residue of PDMS from the h-BN/SiC, the substrates were cleaned for 3 min first in acetone and then in isopropanol while gently shaking the

beakers. Ultra-sonication was not adopted since it causes detachment of the mechanically exfoliated h-BN flakes from the SiC substrate. Finally, the samples were treated with oxygen plasma in the flow of O_2 for 30 sec and with a power of 25W. This last step was found to be crucial for obtaining single-crystal graphene on h-BN as it allows for removal of adventitious carbon contaminations [993].

The h-BN/SiC substrate was placed in the Aixtron HT-BM system and positioned in the central recess of the heater (see Fig. VII.28).

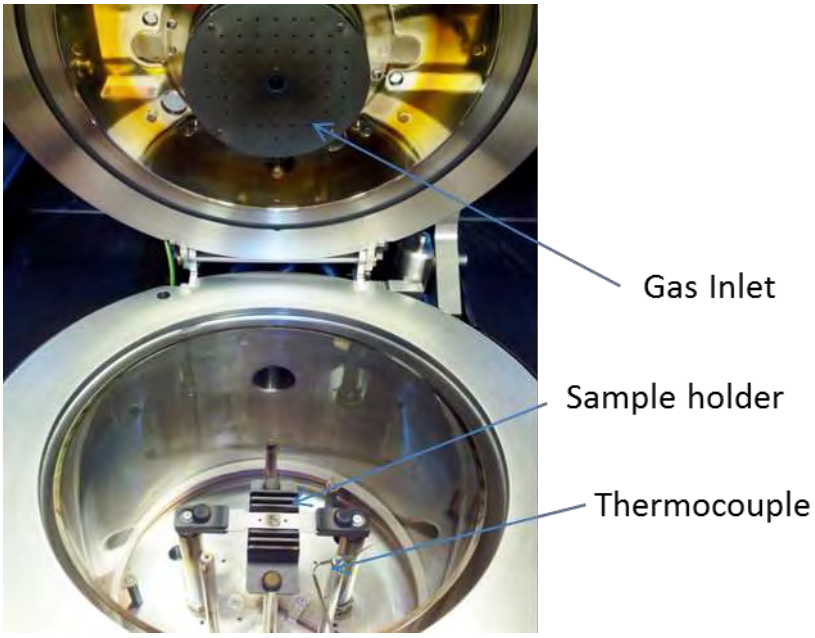

Fig. VII.28. Growth chamber of the Aixtron HT-BM vertical cold-wall reactor used for growth of graphene on h-BN

As a purging step, 1000 sccm of Argon (Ar) were initially flown in the system for one minutes.The annealing step was carried on in hydrogen atmosphere as this was found to be relevant for obtaining single-crystal graphene [993]: H_2 was flown at a rate of 1000 sccm with a system pressure of 8 mbar, at a temperature of 1150^{o}C, for 10 minutes. The best parameters for single-crystal graphene growth were found to be the following: 150 sccm of H_2, 1000 sccm Ar and 5 sccm of the carbon precursor methane (CH_4) for 30 minutes. The H_2:CH_4 ratio was found to be the most important parameter in determining the crystallinity of the grown graphene. While H_2:CH_4 ratios of 1:1 were always found to lead to the synthesis of polycrystalline graphene pads (rounded shaped), increasing the ratio to 1:30 was found to be necessary to obtain hexagonally shaped single-crystal graphene pads. The best T was found to be 1150 °C: growth with lower growth rates is possible also at 1000°C [993] while below this T no growth was observed. Above 1150 °C growth was also achieved but clustering of amorphous carbon was often observed. Growth was achieved at different process pressures ranging between 7 mbar and 150 mbar, which resulted in smaller (< 0.5 µm) and bigger (>

2.0 μm), grain sizes, respectively. Indeed, the highest growth rates, i.e. 100 nm/min were obtained for a process pressure of 150 mbar, although in this case the presence of carbonaceous clusters was occasionally observed. For this reason, if such growth rates are not needed, the growth pressure to be preferred is 25mbar. Lower hydrogen flows (i.e., 100 sccm) and longer growth times can also be used to obtain continuous films (note that with hydrogen flows higher than 150 sccm only partial growth of hexagonal single-crystals could be achieved). As a final step, the system was quickly cooled down (300˚C/min) in the same atmosphere of Ar and H_2 while maintaining the fluxes used during growth. The sample was extracted and exposed to air at T< 120 °C.

WS_2/h-BN and WS_2/ Graphene heterostructures

CVD is the most suitable technique for the scalable synthesis of highly-crystalline 2d heterostacks [878, 993]. However, such an approach is not trivial as weak interlayer interactions favor three-dimensional three dimensional island growth [995]. The formation of multi-layer islands is typically avoided by adopting short reaction times, which lead, however, to the synthesis of isolated crystals [995-999]. To date, the few works on direct growth of WS_2 on other 2d materials have demonstrated isolated micrometer grains [997] or not controllable growth of few-layer thick WS_2 on graphene [998] and isolated grains on h-BN substrates [999]. Recently, a CVD approach which allows one to obtain continuous atomic-thick WS_2 on h-BN and graphene has been reported [1000] .
The chemical strategy adopted is the sulfurization of WO_3 powder (Sigma Aldrich, 99.995%), carried out within a horizontal hot-wall furnace (Lenton PTF). The furnace comprises an inner hot zone, in which WO_3 is placed, and a cooler outer zone where sulfur (Sigma Aldrich, 99.99 %) is put inside a quartz crucible (see Fig. VII.29). The system is connected to a scroll pump, which ensures a vacuum of 5×10^{-2} mbar when no gases are flowing.

The substrates (i.e., h-BN and graphene) need to be prepared before WS_2 growth. For the growth on h-BN, the flakes are exfoliated via conventional scotch tape on either quartz or silicon carbide (SiC) substrates with variable (up to 1 cm^2) surface area. Quartz dice are cleaned with piranha solution (3:1 H_2SO_4:H_2O_2) for 15 minutes and acetone and 2-propanol semiconductor grade for 3 minutes each before flake exfoliation. SiC substrates are also threated with 5% HF solution in water for 1 minute to remove the thin layer of SiO_x on the surface. After the exfoliation of h-BN, the sample (either quartz or SiC) has to be treated with oxygen plasma (5 min, 80 Watt) to remove possible scotch tape residue.

WS_2 can also be grown on polycrystalline or single crystal CVD graphene [733, 742] transferred on a selected substrate such as quartz or SiC cleaned as described above. For WS_2 growth on epitaxial graphene on SiC fresh as-grown graphene samples are used. Both CVD graphene and epitaxial graphene are cleaned for 3 minutes in acetone and for 3 minutes in 2-propanol.

Cleaning the crucibles where the reactants and the powder are placed is also important to obtain a reproducible process. Thus, crucibles are cleaned with 2-propanol wet tissue and subsequently annealed in the furnace used for the growth at 1100 °C for 60 minutes in 200 sccm Ar flow before each growth. This “empty run” process ensures having both a clean reactor and clean

crucibles. Notably, after annealing usually the crucibles turn to be electrostatically charged. This can alter the weighing of the reactants. Moreover, the electric field interacts with the WO_3 powder, which sticks to the crucible and spreads around in a not reproducible way. Hence, the crucible needs to be grounded before weighing.

Another important aspect is how to place the powders and the substrate in the furnace. The substrate and the WO_3 are placed in the same flat 1-inch wide crucible, next to each other but well separated avoiding any accidental deposition of the powder on the substrate. The WO_3 powder has to be spread on the quartz crucible after weighing with a clean spatula in order to maximize the reaction surface. The distance between the substrate and the WO_3 powder is also important to control the coverage. The samples have to be placed around 1 cm away from the WO_3 powder.

Moving the sample further away will affect the total coverage. The sulfur powder is placed outside the hot zone of the oven in the Ar upstream part, approximately 20 cm away from the furnace (see Fig. VII.29). A heating belt is wrapped around the tube region where the sulfur is placed to speed up sulfur evaporation during the process.

It is important that the growth reaction occurs in an over sulfurized environment. To ensure this, two aspects are crucial.

- The S and WO_3 powder have to be in a ration between 50:1 and 100:1 respectively. If not, the reaction typically stops at the intermediate step forming clusters of WO_2. In our case we found optimum weights to be 100 mg of S and 1 mg of WO_3.
- The sulfur has to be delivered just when the WO_3 is at the right temperature. To achieve this, we have found necessary to follow the process steps described below.

Once the crucibles and the target sample are in place within the reactor as shown in Fig. VII.29(b), we proceed with the growth process. The ramp-up phase has two steps: i) ramping up to 350 °C at 10 °C/min with no gas flowing to favor sample outgassing; ii) ramping up to 900 °C (still at 10°C/min) while the Ar flow is set at 500 sccm (tube pressure equals 4 mbar) in order to keep the sulfur powder solid. The purity of the Ar gas used is 99.9999%. Once the hot zone reaches the working temperature at 900°C, Ar flow is reduced to 8 sccm (i.e., tube pressure of 0.5 mbar) to ensure sulfur delivery. The heating belt wrapped around the sulfur zone has to be turned on in order to reach 200°C when the hot zone reaches the working temperature. This ensures sulfur feeding for approx. 30 min. However the total process is about 1hr long to anneal the surface of the sample after the growth reaction. The cooling down occurs naturally and the oven lid is opened when the temperature of the furnace reaches 400 °C to speed up the cooling down without harming the reactor with excessive thermal stress.

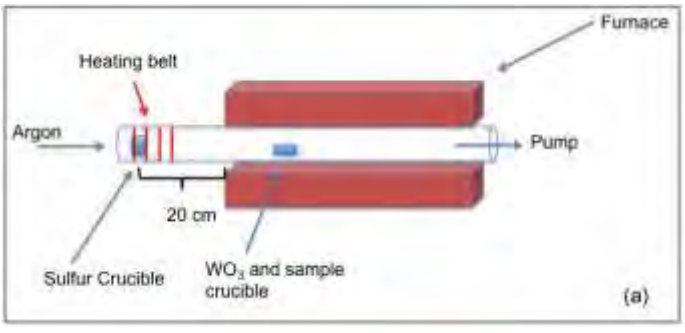

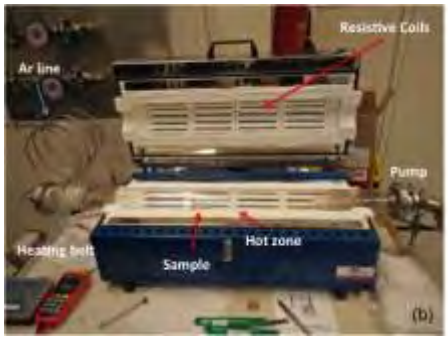

Fig. VII.29: (a)Scheme of the furnace set-up used to grow continuous film of WS_2 on graphene and h-BN; (b) picture of the furnace. Adapted from [1001].

Large scale synthesis of heterostructures Graphene/Si and TMD/Si

Heterojunction devices with large (>1 cm^2) lateral dimensions have been developed for a range of applications [955, 1002, 1003]. In these devices, films of 2d materials (graphene and TMDs) were transferred via polymer support to the final substrates. This process was initially developed in the fabrication of graphene/Si diodes as 2d-semiconductor heterojuntions which [1002] many processing steps to obtain the clean interfaces required for successful device performance, as depicted in Fig VII.30. Initially, HF (3%) was used to remove the native oxide from Si to allow Ti/Au contacts to be deposited directly on to the pristine Si surface. Both n-Si and p-Si were used in this study. A layer of SiO_2 (150 nm) was then deposited on a portion of the sample onto which drain electrodes were deposited. Monolayer graphene was then transferred via PMMA support, described in previous Section VI, onto the resultant assembly in such a way so that it contacted the n-Si and drain electrode, without contacting the source electrodes. This ensures that all current passing form the source to the drain passes through the graphene/n-Si interfacial region.

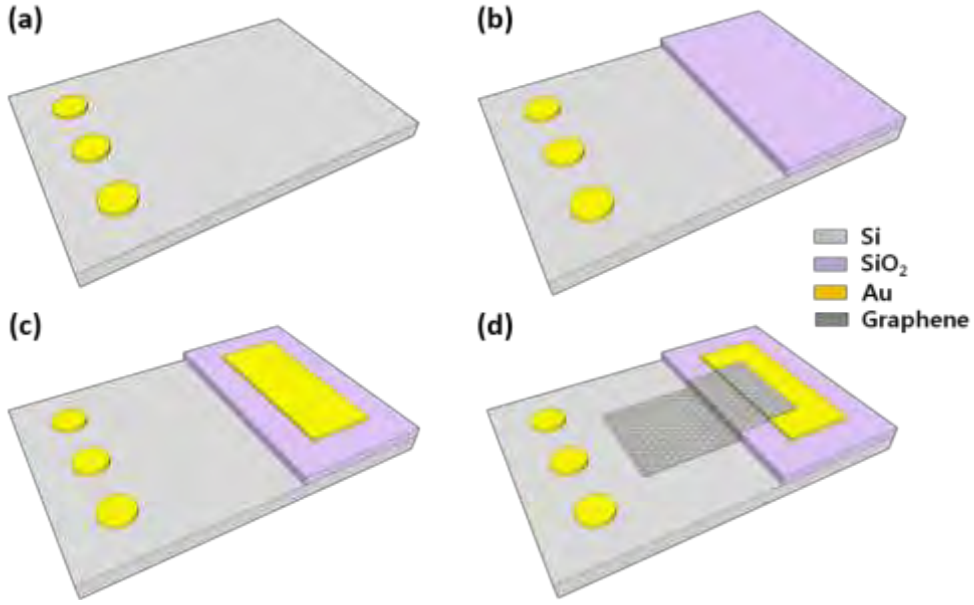

Figure VII.30: Graphene/n-Si diode fabrication process. (a) Deposition of source electrodes on pristine n-Si. (b) 150 nm SiO_2 sputter-coated on one portion of wafer. (c) Drain electrode deposition. (d) Transfer of graphene to complete device. Adapted from Ref [1002].

Characterisation of the resultant device confirms the quality of the graphene film (Fig VII.31 (b)) and displays the rectifying behaviour typical of a Schottky junction (Fig VII.31(c) and (d)). Exposure of the diode assembly to different chemicals modifies the electrical properties of the graphene sheet and, hence, the characteristic behaviour of the Schottky diode (barrier height and ideality factor) on the basis of how strong an electron acceptor the molecule in question is [1002]. Fig VII.31 (e) shows the change in J-V characteristics for a graphene/n-Si diode for exposure to a range of

different organic solvents. Fig VII.31 (f) shows a how the series resistance of the diode changes as a function of concentration of anisole in benzene. The same system was also successfully applied as a gas sensor for NH_3, showing the robustness of this device geometry for a range of sensing applications.

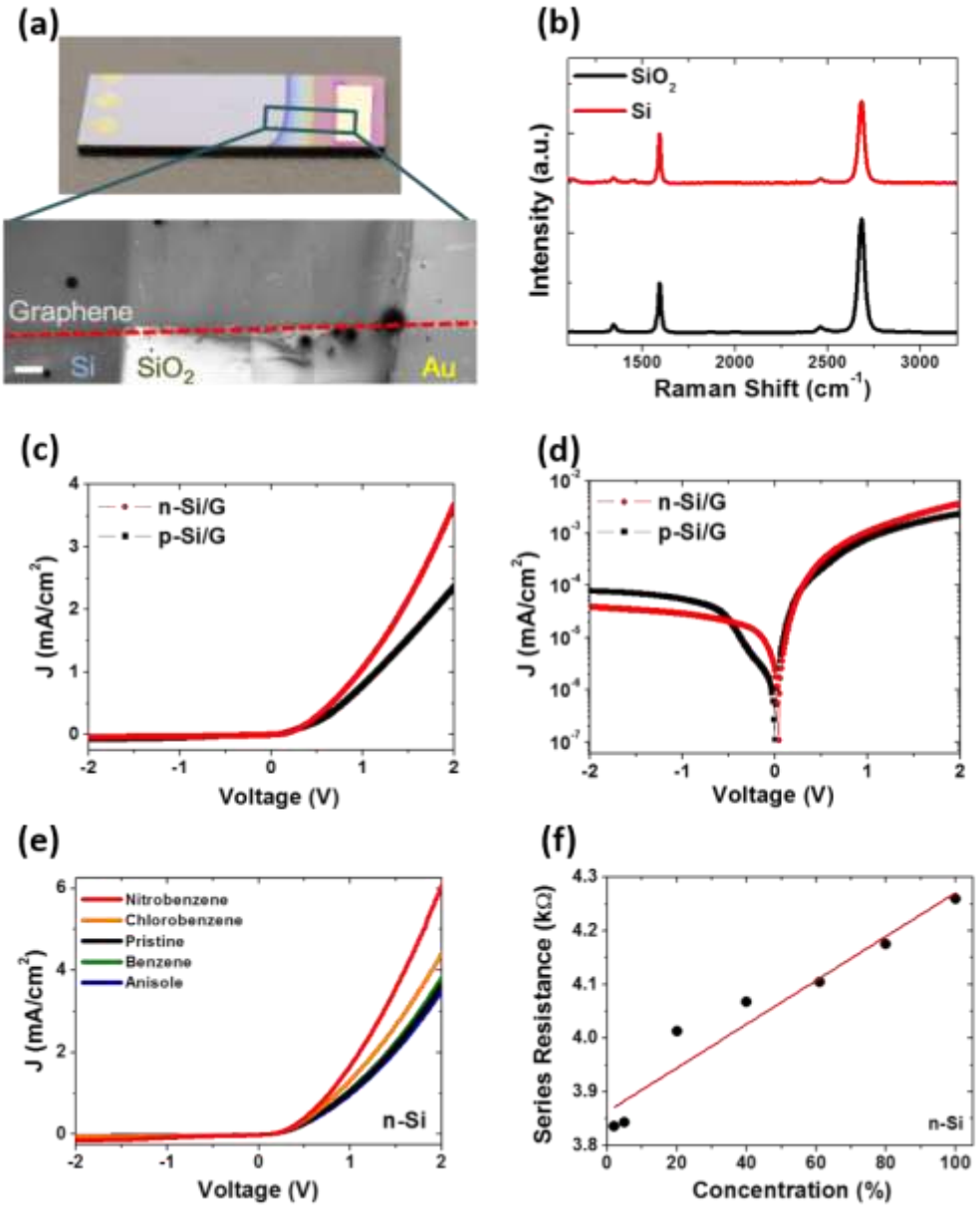

Fig. VII.31: (a) Photograph (top) and SEM image (bottom) of graphene/Si diode. (b) Raman spectra of graphene film on both Si and SiO_2 regions of the device. (c) Linear and (d) semi logarithmic J-V characteristics of graphene/n-Si and p-Si diodes showing rectifying behaviour. (e) J-V characteristics of a graphene/n-Si diode when exposed to different organic solvents. (f) Series resistance of graphene/n-Si as a function of the concentration of anisole in benzene. Adapted from Ref [1002].

The same device geometry was also extended to MoS_2/p-Si devices. MoS_2 formed via TAC behaves as an n-type semiconductor in this scenario which allows the fabrication of a basic p/n junction device. Device fabrication broadly followed the same process as for the graphene/Si diode,

except that TAC MoS_2 was grown on SiO_2, diced to the desired size and the resultant film was transferred to the diode wafer. A range (4.17 ± 0.18, 8.26 ± 0.29, 12.52 ± 0.26 and 15.96 ± 0.16 nm) of MoS_2 thicknesses were investigated for these devices with the thickness measured accurately by spectroscopic ellipsometry [1003]. Electrical characteristics of a device with a 12.52 nm MoS_2 layer are show in Fig VII.32. Of note, is the modification of the device performance under light and dark conditions. It was found that the generated photocurrent was strongly dependent on the MoS_2 thickness, with thicker films displaying greater photocurrent due to the greater volume for optical absorption [1003] .

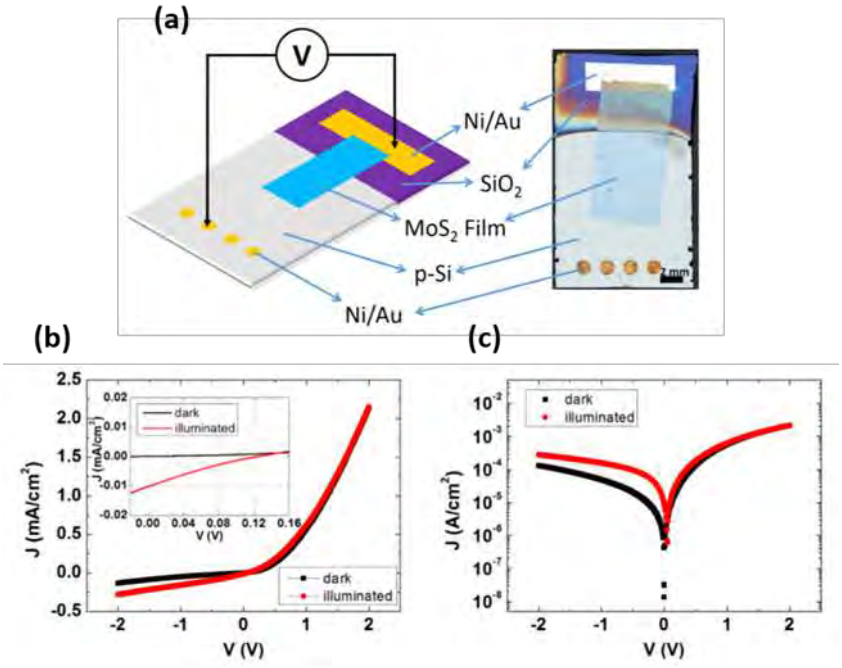

Fig. VII.32: (a) Schematic and photograph of MoS_2/p-Si diode device. (b) linear and (c) semi logarithmic J-V plots of a diode with 12.52 nm thick MoS_2 under dark (black) and illuminated (red) conditions. Adapted from Ref [1003].

VIII FUNCTIONALIZATION OF GRM

VIII.1 Covalent Functionalization of Graphene

Reductive Bulk Functionalization

The covalent functionalization of carbon allotropes – especially graphene – represents a main topic in the growing field of functional nanomaterials. The development of novel architectures built-up from graphene materials requires the availability of a cheap graphene source with low polydispersity. Chemical bulk functionalization of graphene using graphite as starting material has gained significant interest since it allows for (i) the generation of exfoliated graphite sheets in large quantities compared to other exfoliation techniques [345, 348, 1004], (ii) access to solution-processable graphene [342, 343], (iii) access to GRM with modified physical properties compared to pristine graphite [1005, 1006] , and (iv) the investigation of the intrinsic chemical and physical properties of this carbon allotrope [143, 1004]. Graphite can be activated by reductive charging using an alkai metal, which subsequently leads to a Coulomb driven, solvent-based exfoliation as sketched in Fig. VIII.1. The intermediately generated GRM is negatively charged and commonly referred to graphenide [1007]. It can be reoxidized by benzonitrile or other chemical agents [1008], yielding SLG and FLG [345], or trapped by a variety of different electrophiles, yielding covalently functionalized graphene with a variety of functional entities. By this route, hydrogenated [338, 1009, 1010], alkylated [337, 1011-1013] and arylated graphene [339, 1014, 1015] is accessible in a one pot synthesis.

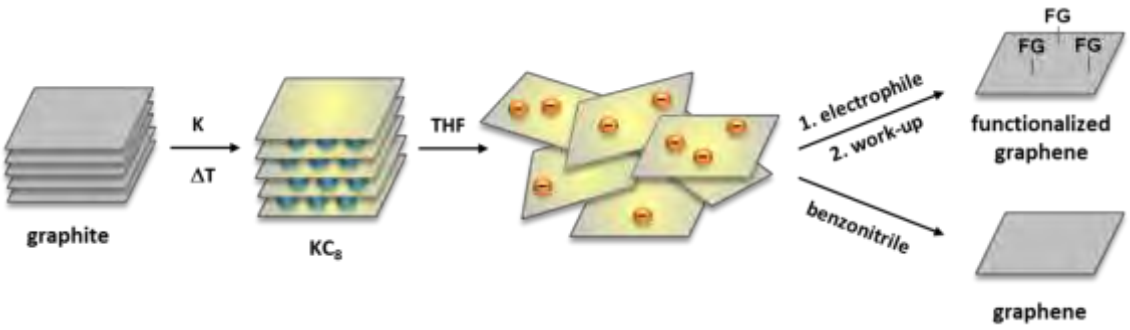

Fig. VIII.1: Reductive exfoliation/functionalization of graphite.

The entire functionalization sequence has to be carried out without oxygen and moisture under inert gas atmosphere in a glove box – otherwise a substantial amount of side products are formed [345, 1008, 1016, 1017]. The reductive graphene functionalization represents a versatile protocol which can be applied to bulk graphene in dispersion as well as to SLG on substrates. The latter approach can be used to elucidate topological and mechanistic details of the reaction [1011, 1018].

A variety of experimental conditions are reported in the literature. From the starting graphite sources, to the composition of the graphite intercalation compounds, the employed solvents and/or the used equivalent number of the organic addends, to name a few. We will overview the different aspects which are of fundamental importance for the successful covalent functionalization of graphene, starting from reductively activated bulk graphite: (a) Type of starting graphite, (b) reductive activation methods and conditions, (c) solvents used for the exfoliation, and (d) type of electrophilic trapping reagent. Covalently functionalized graphene, without initial reductive activation of graphite, can be accessed by a variety of other synthesis approaches, as described in Refs.[1019-1021].

a) *Type of starting graphite*

Bulk Graphite as starting material*:* In the context of the reductive graphite exfoliation/functionalization protocol, almost any type of graphite, can be used in principle. Based on that Hirsch et al. screened a variety of graphite starting materials with different physical and morphological properties [1022], and focused their covalent functionalization studies on 3 types of graphite [1012]: (a) Natural flake graphite (Kropfmühl AG, Passau) with a particle size of 18 mm and a low intrinsic density of defects as expressed by the intensity ratio of the Raman D-mode to G-mode I(D)/I(G)~0.2, with a regular stacking order, (b) PEX 10 (Future Carbon AG) – an expended powder graphite with a small particle size of ~3–5 mm and I(D)/I(G)~0.3 and, (c) SGN18 (Future Carbon AG) – a spherical, defect-rich graphite with I(D)/I(G)~0.4, with a grain size~20 mm.

In general, the chemical reactivity of graphite with respect to a reductive covalent functionalization scenario strongly depends on the nature and in particular the morphology of the starting material. Moreover, it is key that the respective starting material is dry and free of oxygen. Therefore, a thermal annealing step (300 °C, vacuum, 4-5 days), is used to remove any intrinsic oxygen inclusion. For graphite starting materials with intrinsically large graphene basal planes (e.g. natural flake graphites) a reductive charging/exfoliation is very difficult. The intrinsic flake size can be reduced by grinding with sodium chloride, in particular, the graphite is ground with 5 times the amount of sodium chloride in a mortar for 20 minutes. After the elution of the sodium chloride with distilled water and drying in vacuum, smaller and easier dispersible graphite flakes can be obtained.

For the reductive charging/activation of graphite, four different approaches can be pursued: (a) Electron transfer reagents [1013], (b) *Birch*-type based reduction [1023-1026] in liquid ammonia with alkali metals [343], (c) reduction with sodium/potassium alloy [1027], and (d) the generation of alkali metal / graphite intercalation compounds (GICs) [342, 1028], In the latter two cases, the balanced combination of intercalation driven layer expansion in combination with a Coulomb repulsion driven interaction facilitates exfoliation and the wet chemical functionalization of the electronically activated graphene sheets. Moreover, the solid state based graphite intercalation process (d) allows for a fine tuning of the different alkali metal to carbon stoichiometries from KC_4 to KC_{24} [339]. K is used to reduce graphite and to generate the respective graphite intercalation compounds. The metal is directly mixed with graphite in an inert gas atmosphere (glove box <0.1 ppm O_2, <0.1 ppm H_2O) at 150 °C overnight. By changing the alkali metal amount, different intercalation compound stages can be obtained e.g. KC_4, KC_8, KC_{16}, and KC_{24}. The reductive activation

of SLG flakes, deposited on substrates, or single layer CVD graphene can be carried out by the application of a droplet of liquid Na/K alloy (1:3) in 1,2-dimethoxymethane (DME). Here, the deep-blue Na/K alloy solution is prepared inside a glovebox and stirred for 3 days in an argon atmosphere. Prior to the graphene activation, the solution is shortly treated with ultrasounds and after the subsequent addition of the trapping electrophile, the remaining reagents can be rinsed off by dry and degassed DME.

The type of graphite activation used prior to the addition of the trapping electrophile has a significant influence on the outcome of the functionalization sequence and the obtained graphene architectures [1009]. The hydrogenation of graphite *via* the GIC protocol (d) yields polyhydrogenated graphene with the highest hydrogen content when alcohols are used as trapping reagents, whereas for the *Birch*-type reductive activation (b) the highest hydrogen content is obtained for water [338]. This can be explained by the nature of the solvent. In the latter case, ammonia is used at −75 °C and interacts with the trapping water (formation of ammonium hydroxide in an equilibrium reaction). This underlines that the applied reductive activation conditions of graphite have a fundamental influence on the outcome of the reaction.

b) *Solvent preparation*

Water- and oxygen-free solvents are mandatory for the successful exfoliation of the reductively activated graphite starting material and in order to suppress side reactions during the functionalization sequence [345, 1016, 1017]. The solvent has to be stable against the intermediately generated negatively charged graphene sheets (graphenides). Most suitable solvents with respect to these prerequisites are tetrahydrofuran (THF) [1016], 1,2-dimethoxymethane (DME) [1029] and *N*,*N*'-dimethylacetamide (DMAc) [1030]. Although widely used for the dispersion of negatively charged carbon nanotubes and graphene, dimethyl sulfoxide (DMSO) is thought to partially quench the respective negatively charged carbon allotrope, yielding methylated side products [1016, 1030].

Regardless of the solvent used, the most crucial step for the wet-chemical reductive functionalization of graphite is the initial solvent purification. Stabilizers, water and/or oxygen traces can influence the reaction outcome and may lead to undesired and uncontrollable side reactions [1016]. Ref. [1031] established a multistep solvent purification protocol, as follows: 300 g molecular sieves (3 or 4 Å) (suitable amount for 1 L solvent) are dried under vacuum (approx. 10^{-2} mbar) at 300 °C for 3 days. The water molecules are trapped in the pore cavities and thus the water content is lowered in the solvent. The freshly distilled solvent is added to the activated molecular sieve at RT under an argon atmosphere and stored for another 3 days. Ethers (THF, DME) must be stored under light exclusion in order to suppress any auto oxidation processes. The water content of the solvent can be determined by a Karl-Fischer titration. A sufficiently low water content value – THF: < 2 ppm, DME: < 0.5 ppm – allows to proceed with the next solvent treatment step – the removal of oxygen traces by a freeze-pump-thaw degassing. For this purpose, the solvent is transferred into a Schlenk flask and frozen by the aid of liquid nitrogen. The flask is connected to a vacuum line in order to remove the gas phase. Afterwards, the solvent is allowed to warm to RT (gas bubble evolution from the solution). Subsequently, the solvent is frozen again and the gas phase is removed *in vacuo* (approx. 10^{-2} mbar). This procedure is iteratively repeated several times (4-6 cycles) until no gas

evolution is detected during the thawing process. In order to remove any residual water traces, a distillation over Na/K alloy is carried out. Here, a Na/K alloy (1:3) is freshly prepared and added dropwisely to the solvent. A water separator connected to the distillation apparatus and filled with dried molecular sieves allows additional drying of the solvent. Preferably, the solvent is stored in an argon filled glove box in order to prevent any further contamination. The purity of the solvent can be checked upon addition of GIC. Here, the bronze color of the GIC must be preserved.

c) Type of trapping electrophile – functionalization protocols

Several electrophiles have been utilized in solid support and in homogeneous dispersion functionalization of graphenides, like the diazo coupling [1027], iodonium coupling [1014, 1032], alkylation [337, 1011-1013], arylation [339, 1015], hydrogenation [338, 1009, 1010], halogenation [1033], and silylation [1029]. In addition, by a iterative repetition of the charging/functionalization step mixed functionalized graphene derivatives are accessible[1018]. However, there is a huge dispersion of the experimental conditions in the respective reports. In this sense, a complete study surveying all the reaction parameters and determining the most effective synthetic routes is highly desired. Even more important, a deeper understanding of the correlation between bulk approaches, aiming at functionalized SLG and direct functionalization is of uttermost interest [337, 339, 340, 1012, 1014, 1027]. Ref. [340] compared 3 reductive functionalization pathways (phenyldiazonium- and bis-(phenyl)-iodonium salts as well as aryliodide) and the reductive alkylation route using hexyl- and dodecyliodide. The use of iodide derivatives with spherical graphite as starting materials is the most efficient with respect to highly functionalized GRM. A single-electron transfer (SET) process from the charged graphenides towards the electrophilic trapping reagent can be expected as the primary reaction step. This leads to the generation of radicals in the proximity of the graphene sheet, with subsequent covalent bond formation [1034, 1035]. In this line, the diazonium/iodonium coupling reactions are more expedite than the alkylation, because the generated phenyl radicals are significantly less stable than the alkyl ones due to the much higher bond strength of aromatic C–H bonds [1036]. This higher stability as well as improved solubility of the resulting functionalized graphene in DME, plays the major role during the functionalization process, favoring the reaction of hexyliodide with new graphenide activated surfaces, leading to higher degrees of functionalization and explaining the narrow Raman I(D)/I(G) distributions. In contrast, faster reactions (i.e. diazonium) lead to broader distributions, probably related with a clustering of the functionalities. The open question regarding the role of remaining negative charges after the initial electrophile addition step was also addressed [1016]. According to Ref. [340] the role of the remaining negative charges can be neglected. This is in contrast to unfunctionalized graphenides. The exposure of these air-sensitive intermediates towards air, leads to a covalent framework modification with an attachment of OH- and H- groups [345, 1017].

d) GICs as starting materials for production of graphene

Refs [337-340] and refs [341-343] demonstrated that GICs are suitable for the covalent functionalization of graphene. In typical covalent functionalization sequences, the negatively charged graphene layers first act as reductants for electrophiles, subsequently attacked by the intermediately generated organic radicals or H-atoms yielding the covalently modified graphene architectures. This wet-chemical functionalization concept is facilitated by the fact that, due to Coulomb repulsion, the negatively charged graphenide layers within the solid GICs can be dispersed in suitable organic solvents [342]. One fundamental question is whether all negative charges of the graphenide intermediates can be controlled or completely removed in such redox reactions [346]. Only the complete oxidation is expected to avoid reactions with moisture and oxygen during workup leading to side products with undesired and additional oxygen- and hydrogen functionalities. More importantly, the controlled removal of all negative charges from the solvent-exfoliated graphenide intermediates with a suitable oxidation reagent allows for the bulk production of defect-free graphene. Ref [345] reported that the treatment of K intercalated graphite with benzonitrile (PhCN), leads to a quantitative discharging of the individual graphenide sheets upon the formation of the colored radical anion $PhCN^{\cdot-}$ (Fig.II.18), which can be monitored by the accompanying exhaustive and Coulomb force-driven migration of the interlayer potassium counterions (K^+) from GICs into the surrounding benzonitrile phase, the suppression of any reactions of dispersed graphenides with moisture and air that is shown to take place when no treatment with benzonitrile is provided, and the successful generation of defect-free SLG. This could be confirmed by Raman spectroscopy and Atomic Force Microscopy of exfoliated charged material on a Si/SiO_2 substrate, treated with benzonitrile leading to graphene flakes bearing defect-free single-layer nature over a lateral grain size of 10-18 nm. This represents a rather mild and inexpensive method for the wet-chemical graphene production on a small scale. This exfoliation approach was also extended to water as solvent [348].

Electrochemical Functionalization

As outlined above, the high chemical stability of the SLG basal plane surface requires highly reactive conditions for its covalent modification. While reductive functionalization shall be achieved after intercalation/activation of graphite commonly via GICs, thermal or photo-induced cycloadditions of SLG with nitrene and carbene intermediates are commonly employed (see. Ref. [1037] and references therein). However their long (≈3 h) reaction time and/ or low yield (<10% surface functionalization) hinders a facile and useful covalent functionalization.

Functionalization can be enhanced using electrochemistry [1037]. The electrochemical potential applied can shift the Fermi level of graphene, graphite, glassy carbon or any conductive substrate, increasing their reactivity as compared to a direct attack of the covalent sp^2 bonds with aggressive chemicals. Ref. [1037] demonstrated that electrochemistry can also be used to functionalize SLG with organic molecules, and that the functionalization can be controlled on the nm scale. A two-steps process was used that allows the independent control over the adsorption of the

molecules on graphene as ruled by supramolecular interactions, and their successive covalent grafting (Fig. VIII.2). The molecule used is 4-docosyloxy-benzenediazonium tetrafluoroborate (DBT), an aryl diazonium salt comprising a long (C12) aliphatic chain and a diazonium grafting unit. The alkoxy chains promote the physisorption of DBT forming ordered patterns. Meanwhile, the highly reactive diazonium salt head group allows the covalent attachment of DBT onto graphene, disrupting its sp^2 lattice, modifying its optical and electronic properties [1037].

In Ref. [1037], DBT was first physisorbed from solution onto SLG, allowing the molecules to self-assemble on the surface into ordered monolayers. The maximal amount of molecules deposited on the SLG surface depends on the packing density of the DBT monolayer, and could be as low as few ng/cm^2. After drying in air, a polydimethylsiloxane (PDMS) circular mask was fixed on the top of SLG along with an electrochemical setup composed of a three-electrode cell: a Pt wire as counter electrode, Ag/AgCl as reference electrode, and the target substrate used as working electrode. The substrate was high-quality SLG obtained by CVD on silicon, or on polymeric substrates. The PDMS mask confined laterally the electrolytic solution giving a fixed reaction area of ≈0.1 cm^2 on the CVD graphene, making it possible to perform electrochemical treatments with very small amounts of solution (10 μL). An acidic solution (0.1 M H_2SO_4) was then deposited inside the mask as the electrolyte, and DBT molecules were not soluble in this acidic aqueous solution. The grafting process was done by ramping the voltage from +0.2 to −0.7 V at 100 mV/s. After the electrochemical reaction, functionalized SLG sample was sequentially washed by DI water and dried under a gentle flow of nitrogen gas.

The versatility of this approach was demonstrated by using it on different carbon-based materials, graphite, glassy carbon and SLG on SiO_2, PET, or quartz [1037]. Utilizing a homemade electrochemical setup (Fig.VIII.2d). Besides the easy packing of aliphatic chains, the two-step approach could be used in principle also with more complex patterns, e.g. based on arrays formed by adsorption of alternating complementary building blocks, or 2d nanoporous organic frameworks, paving the way to a versatile, ordered and simple route to functionalize such a technologically important, yet poorly reactive material. The maximal amount of molecules deposited on the graphene surface depends on the packing density of the DBT monolayer and can be tuned using molecules of different packing density [178]. Combining the DBT surface density (as measured by STM) and the DBT molecular weight of 401 g/ mol (with no diazonium group), a DBT coating of ≈35 ng/cm^2 could be estimated for a uniform, perfect coverage, although the defects observed in the grafted layer will significantly modify this theoretical value.

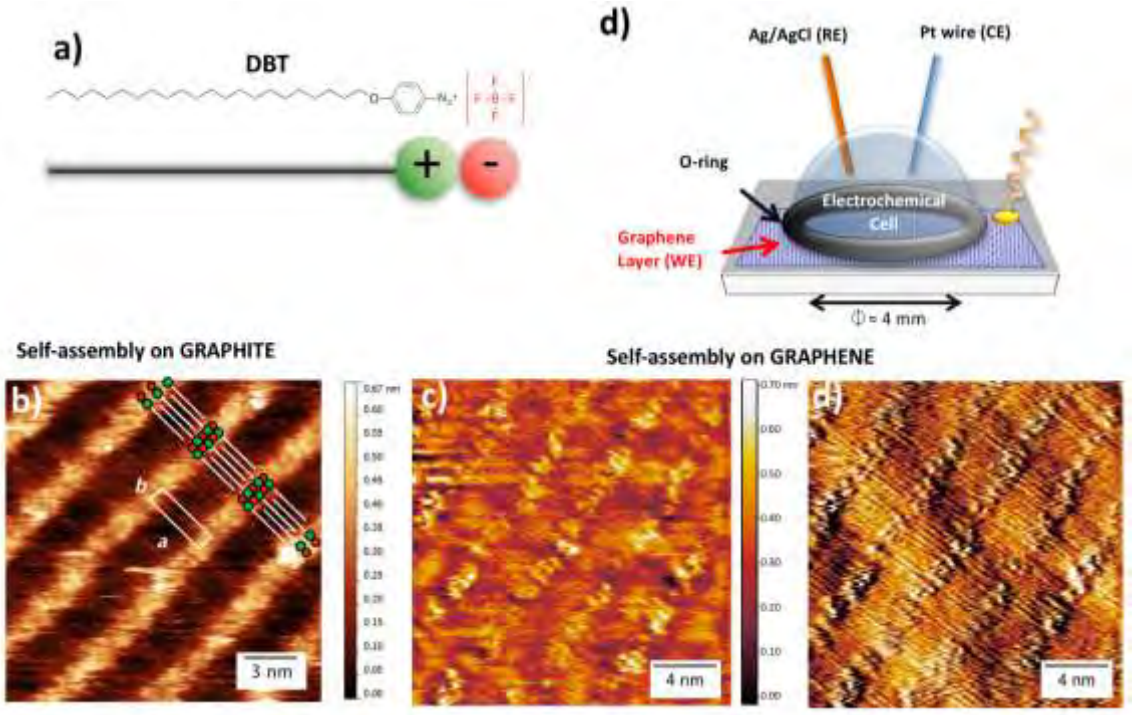

Fig. VIII.2: a) Molecular structure of DBT. b) STM image of DBT assembly on graphite, showing also the unit cell; the possible molecular packing is also schematized. The position of BF_4^- counterions is indicative. Lattice parameters: a=3.9±0.1 nm: b=1.0±0.1 nm: a=89°±2°: A=3.9±0.1 nm^2. c,d) STM height (c) and current (d) images of DBT self-assembled on SLG. The quality of the image is not as good as on graphite, as a result of the few Å roughness of the underlying SiO_x, causing a blurring effect. e) Schematic representation of the electrochemical setup used for grafting. WE (working electrode)= graphene; CE (counter electrode)= Pt; RE (reference electrode)= Ag/AgCl (3 M KCl). Adapted from ref [1037].

VIII.2 Functionalization of GO

Covalent Derivatization

GO is rich in polar oxygen-containing functional groups that make it highly soluble in a wide range of solvents [203]. The different functional groups (i.e. hydroxyl, epoxy, carboxylic, lactones, phenols, etc.) can be exploited to prepare chemically functionalized GO for a wide range of applications [143, 1038]. Due to the presence of the different oxygenated functional groups and their high chemical reactivity, simultaneous reactions of these functions may occur leading to uncontrolled GO derivatives. Most of the reactions reported in literature concern the functionalization of the carboxylic functions *via* amidation, using a variety of amine derivatives [1039, 1040]. Most of the protocols performed in the conditions to form amide bonds lack of appropriate controls. Indeed, other functional groups can participate. For example, epoxy ring opening can take place in the conditions of amidation, as epoxides are highly reactive towards nucleophiles like amines [1041-1047]. To clarify the chemical reactivity of carboxylic acids and epoxides, Ref. [1048] elucidated the

structure of GO in the presence of amines and the reactivity of the functional groups towards amines [1048]. In particular, magic angle spinning solid state NMR allowed to prove the absence of reactive COOH groups. As a consequence, the amidation reaction of carboxylic groups with amine derivatives did in fact occur to a negligible extent, while the main reaction consists in epoxide ring opening. This is also the case in the presence of coupling reagents necessary to form the amide bonds. Therefore, the reaction between GO and amine functions involves mostly the epoxy groups, and not the carboxylic acids that are present in a small amount. This situation cannot be generalized to all types of GO. Ref. [1048] underlines the importance to well characterize the starting material and use the appropriate controls (see for examples the conditions for the amidation versus the epoxide ring opening reaction) to prove the reactivity of the different oxygenated functions on the surface of GO. A better understanding of the reactivity of GO is essential for controlled derivatization.

Although polymerization on the GO surface in polar solvents, e.g. water, has been widely studied, it remains a great challenge to achieve polymerization reactions on RGO in organic solvents due to the limited functional groups for dispersing RGO in organic solvents. RGO was produced from the reduction of GO by hydrazine hydrate [1049]. Then, RGO was functionalized using *p*-bromobenzene diazonium salt under aqueous conditions to produce *p*-bromobenzene functionalized RGO (RGO-Br). This was dispersible in DMF for further reaction. Afterwards, two-dimensional conjugated microporous polymers (CMPs) were prepared through the Sonogashira-Hagihara coupling reaction [1050] of ,3,5-triethynylbenzene and halogenated aromatic monomers by using RGO-Br as structural-directing template. 1,3,5-tri-ethynylbenzene was selected as key monomer, mixed with another monomer of aryl halides (such as 2,5-dibromothiophene, 2,5-dibromo- 1,3-thiazole, and 2,6-dibromopyridine) or Halogenated BODIPY (2,6-diiodo-1,3,5,7-tetramethyl-8-phenyl-4,4-difluoroboradiazaindacene) in the RGO-Br dispersion. The above mixture polymerized at 80 °C for 72h catalyzed by tetrakis-(triphenylphosphine) palladium ($[Pd(PPh_3)_4]$), copper iodide (CuI), and triethylamin (Et_3N), forming a series of CMPs on graphene-based template (RGO@CMPs). The as-prepared insoluble precipitated polymer networks were filtered and washed several times with chloroform, water, and acetone to remove any unreacted monomers or catalyst residues. Further purification of the polymer networks was carried out by Soxhlet extraction with acetone for 48 h. The powder was dried in vacuum (0.1 mbar) for 24 h at 60 °C to obtain the final product.

This method not only offers a new way to polymerize on RGO surface through the Sonogashira-Hagihara coupling reaction, but also paves the way for versatile reactions on the RGO surface in organic solvent.

GRMs are ideal materials for energy applications because of their large accessible specific surface areas and high electrical conductivity [1051].The SLG theoretical specific surface area is~2600 $m^2\ g^{-1}$ [1052]. However, a common problem is the restacking of SLG sheets, i.e., the aggregation during the wet-processing, resulting in a decrease of accessible specific surface area [1053]. E.g. the reduction of unmodified GO typically leads to the irreversible aggregation of RGO sheets [1054]. In order to overcome this issue, the bridging of GO layers into macroscopic porous structures is a key step to modify SLG-based multifunctional materials, which could preserve many of the unique properties of the individual SLGs [1055]. In particular, the high specific surface area and porous

structures can provide space for hosting electrolyte ions, therefore increasing the capacitance performance in supercapacitors [1056]. In this context, graphene-based networks through covalent linkage between individual SLGs is one among the greatest challenges, with the aim to achieve a high control over the structures with a nanoscale precision and consequently tuning of the material's physical properties [1057-1059].

Ref [1060] reported a method for the facile preparation of graphene-based covalent networks (G3DCNs) with adjustable interlayer distance upon covalent functionalization of GO. This method relies on the condensation and ring-opening reactionsof the carbonyl and epoxy groups on GO with benzidine (BZ) at different temperatures. In Ref. [1060] the controlled polymerization of BZ with GO, to obtain the G3DCNs, was performed under catalyst- and template-free conditions. By varying the reaction temperature, BZ monomers or polymerized BZ (PBZ) units can bridge GO sheets to form covalent networks with tunable interlayer spacing. The reduced form of the G3DCNs (RG3DCNs) was used to develop high-performance supercapacitors (see below), taking advantage of the high specific surface areas (280 m^2 g^{-1}) combined with N doping obtained through chemical functionalization. While in the three-electrode configuration it resulted in 460 F g^{-1} at a current density of 0.5 A g^{-1}, in the two-electrode configuration it amounted to 156 F g^{-1} at a current density of 1 A g^{-1} in combination with a cycling stability over 5000 cycles. This combination of physicochemical stability and high supercapacitor performance demonstrates that integration of GO sheets into covalent nanostructures with tuneable structures and properties is an ideal route to obtain multifunctional G-based hybrids.

Most of previous reported methods towards porous carbons mainly focused on hard template and activation approaches, which long suffer from poor rational design micropores and heteroatom components. Most importantly, preparation of 2D porous carbon remains great challenge. In references [1061, 1062] the as-prepared 2D porous polymers (RGO@CMPs) were directly pyrolyzed at X °C (X=700, 800, 900 and 1000) for 2 h under inert atmosphere, affording 2D heteroatom-doped (boron, nitrogen or sulfur) porous carbon materials. This method not only provides a new way for the direct preparation of 2D porous carbons without using any inorganic templates, but also offers a rational approach to control the heteroatom in porous carbons by choosing different heteroatom-contained monomers.

The electrochemical experiments were conducted in O_2-saturated 0.1 M KOH electrolyte for the oxygen reduction reaction (ORR). A catalyst ink was prepared, which was loaded onto a glassy carbon electrode. It was prepared by dispersing 10 mg of catalyst in 500 µL of Nafion/ethanol solution(1 wt%). The dispersion was stirred overnight and sonicated for at least 30 min. After that, 6 µL catalyst ink was pipetted onto the disk surface of glassy carbon electrode. The concentration of the catalyst was~0.5 mg cm^{-2}. Cyclic voltammetry (CV), rotating disk electrode (RDE), and rotating ring-disk electrode (RRDE) investigations were performed to evaluate the electrochemical properties by using a basic bipotentiostat (Pine Research Instrumentation, USA) with a three-electrode cell system. The working electrode was rotating glassy carbon disk and Pt ring electrode (Pine Research Instrumentation, USA). An Ag/AgCl (KCl, 3 M) electrode was used as reference, while a Pt wire was served as the counter electrode.

Refs. [1061] tested primary and rechargeable Zn-Air batteries in electrochemical cells. For the primary cells, a polished Zn plate was used as anode and gas diffusion layer (Hesen Electric Inc. (Shanghai), carbon paper HCP-120) coated with catalyst ink was used as cathode. A microporous membrane (25 μm polypropylene membrane, Celgard 5550) was selected as the separator, and stainless steel mesh was applied as the current collector. The electrolyte used in the Zn-air battery was 6 M KOH aqueous solution. Based on the battery design, the area of the gas diffusion layer exposed to the electrolyte was 3.14 cm^2. All the catalysts were coated onto the gas diffusion layer using an airbrush to achieve a loading~3 mg cm^{-2}. The catalyst ink was prepared by dispersing 10 mg of catalyst in 0.9 mL of isopropanol and sonicated for 30 min, followed by 100 μL of Nafion solution (5 wt%) and sonicated for 30 min. Measurements were carried out on the above laboratory-constructed cell at RT with a CHI 760E (CH Instrument, USA) electrochemical workstation.

Chemical functionalization of GO is a key step to prepare covalent conjugates that can be exploited not only energy applications or in the biomedical field, but also in the studies related to the impact of such material on health (i.e. biodistribution and biodegradation). In the context of pharmacokinetic studies, GO needs to be labelled with molecules that can be traced once the conjugates are injected into a body. For this purpose, radiolabelling is extremely powerful, as the material can be followed using different imaging techniques and many radionuclei can be exploited. GO has been modified with the chelating agent DOTA (1,4,7,10-tetraazacyclododecane-1,4,7,10-tetraacetic acid) for complexation of the radionuclide [^{111}]In to assess the *in vivo* biodistribution in mice [1063]. GO was initially functionalized with triethylene glycol diamine to open the epoxy rings and introduce amino functions on its surface. Then, the amino groups were derivatized with an isothiocyanate DOTA reagent. Structural characterization of both GO and GO-DOTA revealed that the thickness of the GO sheets was increased from single to few layers after functionalization. GO-DOTA was subsequently radiolabelled with [^{111}]In and injected into mice to follow its organ distribution, accumulation and elimination. An appropriate functionalization of GO can also be useful to modulate its biodegradability. Covalent functionalization was conceived by designing surface-functionalized GO with the capacity to be degraded more effectively compared to unmodified GO [475] The surface of GO was tailored with different ligands able to enhance the catalytic activity of the horseradish peroxidase (HRP). GO was functionalized with two reducing substrates of HRP: coumarin (7-hydroxy azido coumarin) and catechol (3,4-dihydroxy benzoic acid) derivatives. The kinetic of the biodegradation process was enhanced in comparison to unmodified GO.

Noncovalent Derivatization of GO for Thermoplastics

When GRMs are incorporated into a polymer matrix, one of the most important problems is the lack of affinity between them due to differences in polarity [1064]. Just a few polymers, such as polyaniline and Kevlar, contain aromatic rings in their structure. π-π interactions between these chains and SLG/GO can take place [1065], however most of the polymers do not have not these moieties that facilitate interaction with SLG/GO.

Re-agglomeration or bad interaction between them and polymer chains lead to creation of defects and discontinuity regions, and finally loss of mechanical performance such as a decrease of the elastic modulus at break. Besides, this affects the properties of the SLG/GO and the composite does not show the desired performance, i.e. electrical conductivity, thermal management, gas barrier properties, flame retardance or other due to the creation of these agglomerates.

To solve these problems, functionalization is needed to change the surface chemistry and improve the compatibility with the polymeric matrix. Another effect of the functionalization is the reduction of agglomeration during the preparation of the composite due to the electrostatic repulsion that can be produced [1066, 1067]. Non-covalent functionalization can enhance dispersability, compatibility and binding capacity with the matrices, with less impact in the structural properties of the graphitic sheets than covalent functionalization, as this one creates sp^3 carbon centers (see above). Non-covalent functionalization helps in networking or connecting the molecules without forming chemical bonds. This process requires physical adsorption of suitable molecules by forming van der Waals bonds between functional groups and SLG, such as π–π interactions, electrostatic attraction, adsorption of surfactants and polymer wrapping [1068].

When organic molecules or hydrophobic character polymers are the functionalities, van der Waal forces are created between them and SLG/GO. When the functional groups are molecules with an extended π-system, the predominant interactions are π-π based. Besides, hydrogen bonds and ionic interactions can be involved due to the presence of oxygen groups, especially in the case of GO, and in minimum percentage in the case of *R*GO or SLG [273].

For the design of the non-covalent functionalization strategies, an important decision regards the polymer matrix and the processing method. In the case of thermosets, most of the processes consist on liquid phase polymerization. For thermoplastic matrixes, most of the polymers are processed by melt mixing, and just in a few cases *in situ* polymerization can be an alternative. The polarity of the matrix, from very nonpolar such as the polyolephines, to polar such as polycarbonate needs to be taken into account. Besides, the groups on the surface of the GO or *R*GO will be of crucial importance of the strategy for functionalization. In this regards, X-ray photoelectron spectroscopy (XPS) is a tool to understand the distribution and binding of the moieties and functional groups over the surface of the GRM.

Many different organic molecules were used in literature [179, 205, 273, 1040, 1069-1072]. The selection is based on availability on the market or ease to synthetize them and scale up. For the preparation of thermoplastics and thermoset composites, even at lab-scale, at least hundreds g are needed. For scale-up at lab or pilot level, few kgs are needed.

A typical amphiphilic non-ionic surfactant, commercially available as Triton X-100 (polyoxyethylene octyl phenyl ether, POPE) can be used to increase the compatibility of GRMs and polymer matrix [1064].

Aqueous surfactant solutions of *R*GO above the critical micelle concentration (CMC) are enough to ensure physical adsorption and non-covalent adsorption. Aqueous dispersions of functionalized materials remain stable during long (more than one month) periods, while pristine graphene suspensions may sediment in less than one day [1073], due to low viscous and

agglomeration problems. For laterally large (more than 20 μm) *R*GO, sonication is needed, in bath or tip or even a combination of both processes. For *R*GO of lateral dimension > 50 mm, 2 cycles of 10 min of tip and 10 min in bath is the recommended process to achieve dispersion without significant decrease in lateral size. After filtration and drying of the non-covalently functionalized *R*GO, the GRM can be dispersed in the polymeric matrix.

Polyvinylpyrrolidone, SDS, SBDS, CTAB and other surfactants can be added to water suspensions of GRMs to stabilize them thanks to the electrostatic repulsions created [1064, 1074]. In most cases, interaction occurs in the absence of ultrasound, which is required to increase the accessible surface area of the GRM and it is especially helpful when lateral size of GRM is medium or large (more than 20μm). The same strategy has been used to improve the dispersion of *R*GO in plasticized polymers and in epoxy resins before curing [1067, 1075]. The results of the dispersion have a strong influence on the final properties of the composites. Epoxy composites prepared with this functionalized graphene materials have shown better interaction to the matrix in SEM micrographs and improved mechanical behavior at very low loadings [1064, 1070, 1076, 1077].

Covalent silanization is a common strategy for the functionalization of GRMs for their use in polymers [1078].

For this, the GRMs selected need a high number of hydroxyl groups for the functionalization. This functionalization usually is done at RT or under reflux conditions in organic solvents such as toluene, ethanol [1079]. Silanization of OH groups shall also be accelerated using microwaves; it is well known that coupling microwaves (energy source) with graphite (support) is responsible for a high temperature gradient leading to increased reaction rates as compared to conventional procedures; this approach shall be used with graphene or GO as well. Conventional silanization generally require reaction times of 1–7 days. The procedure reported in Ref. [204] uses microwaves to reduce the functionalization time down to 40 min. Besides OH functionalization, also the COOH groups of GO shall be used to attach a wide range of commercial molecules, using as example amines [204].

Silanes can also be used for non-covalent functionalization of GO. This usually involves mild conditions [i.e. ethanol dispersions of the GO and the selected silane are mixed under bath sonication for 15 to 30 minutes at RT, and filtered in air or oven dried at lower than 80ºC] to avoid covalent reactions with graphene oxide between the alkoxy groups of silane molecules and the hydroxyl groups of the graphene surface. Then, it is also important to select the adequate graphene material with lower number of hydroxyl moieties. Several silanes can be used, e.g. 3-(aminopropyl)triethoxysilane, 3-glycidoxypropyltrimethoxy silane, tris[3-(trimethoxysilyl)propyl]isocyanurate.

π-π functionalizations/interaction of GRMs have been discussed in several reviews and books [1080, 1081]. Some organic molecules can be used for the non-covalent functionalization to improve the dispersion in polymers; i.e., melamine [1082], chitosan [1083], glycidyl 2-methylphenyl ether, anisole, 4-ethynylanisole among others [273]. These were dissolved in organic solvents of slightly acidic solutions in the presence of the GRMs and agitated under bath sonication for 15-30 min, then filtered and dried [273].

To establish the success of the functionalization in the dispersion of GRMs in thermoset composites, a fast method is vertical casting (Fig. VIII.3). This employs two polished surfaces (e.g. glass) treated with release agent or covered with peel ply. Few silicone double tapes of 1 mm are glued at the same distance (e.g. 2 cm) to the polished surface. Another silicone tape is glued perpendicular to the other tapes to the bottom surfaces. This system is used as the mould, and the epoxy-graphene dispersions are introduced.

In the case of thermoplastics, a polymer adapted microtome which allows to obtain flat and smooth slices or ultrathin slices of the composite is needed [1082] and cryo-microtomography, working at temperatures between -15º to -185ºC, to avoid disturbing the positions or relocating nanoparticles along the sample [1084, 1085]. The analysis of the graphene composites' mechanical and electrical properties is key to understand if the functionalization works properly, to improve the dispersion and interface.

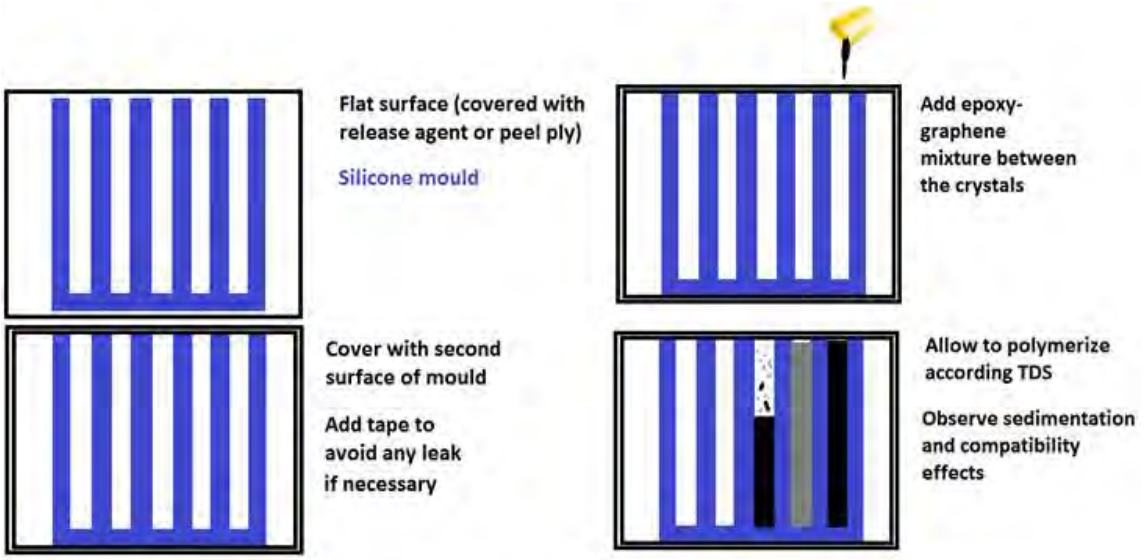

Fig. VIII.3. Preparation of a vertical casting system for the evaluation of a graphene dispersion.

By optical microscopy, even at low resolution, it is possible to characterize the effectiveness of the functionalization, understanding this point as the homogeneity on the dispersion of graphene oxide in an epoxy composite, and decreasing the large size aggregates rate.

VIII.3 Noncovalent Functionalization of Graphene

In Dispersion

Besides the use of organic solvents such as DMF or NMP, graphene can be exfoliated also in water with the help of amphiphilic surfactants [167, 169]; most published works use "conventional" aliphatic surfactants (i.e. soaps) [167, 169]. However, stable dispersions of graphene in water can also be obtained using small polyaromatic dyes as surfactants. [179, 201, 202] Thanks to their aromatic core, these molecules can adsorb strongly on the graphene surface, forming also ordered layers [178], noncovalently functionalizing SLG/FLG. They have also a strong and unique absorption

(molar absorption coefficient ε>15000 L $g^{-1}m^{-1}$) and emission spectrum in the visible range, which allows to monitor their interaction with graphene in solution and in solid. [203, 204] Many of these molecules are also low cost dyes, already widely used in large-scale compounding of polymers, e.g. as industrial additives and colorants dyes [205]. These molecules can exfoliate not only graphene but also a wide range of LMs, such as BN, WS_2 , MoS_2, selenides and tellurides with concentrations up to 0.54 mg/mL. [206].

Several pyrene derivatives with a varying number of polar functionalities could be used as exfoliation agents [179]. A significant part of the solubilized material was composed of single graphene sheets (up to 22%), with most of the remaining material composed of a few-layer graphene (50% to 60% of fakes having less than 7 layers). The total concentration depends on the polar functionalization present on the pyrene core. Molecular dynamics calculations revealed that a critical factor is a on molecule thick solvent layer present between the dye and SLG. The amphiphilic molecule changes its orientation when approaching the surface to slide into this layer, and the asymmetric shape of the dyes facilitates this step. In these graphene organic hybrid systems, colloidal stabilization is achieved through electrostatic repulsion between charges introduced by the surfactant, and can be overcome by changing pH or adding salts [179].

Exfoliation in organic solvents

The use of small organic molecules acting as stabilizing agents is expected to promote the LPE of graphite when the molecules have a stronger affinity to graphite/graphene than the solvent/graphene interactions. A good starting point in terms of molecular design relies on the use of alkanes which exhibit a high affinity (ca. 2kcal mol^{-1} per each methylene unit) for the basal plane of graphite/graphene [1086]. Ref. [218] reported that arachidic acid (C19CA) can promote the exfoliation of graphene in NMP. The addition of C19CA does not affect the quality and structure of obtained graphene, as compared to NMP alone, highlighting the non-invasive nature of the process, but alkyl chain based stabilizers led to an increase of the percentage of SLG (25%) and FLG (70% for 2-6 layers) [218].

The use of α-functionalized alkanes as stabilizers during LPE allows one to increase the yield of exfoliation by weight (Y_W) of graphite in liquid media. To understand the role of the functional group in α-substituted alkanes, Ref. [223] used the $C_{21}H_{43}$ alkyl chain as a scaffold and decorated it with simple, yet chemically distinctive groups, methyl, alcohol, amine, and carboxylic acid. The most effective exfoliation was obtained with docosanoic acid, with Y_W~1.6%, with a~100% increase when compared to control samples (0.8%). Y_W of LPE in docosane is~1.35%, while docosanol and docosan-1-amine have lower performance (1 and 1.1%, respectively). The thermodynamic analysis in Ref. [223] suggests that aliphatic chains functionalized with carboxylic acid groups promote the stabilization of the exfoliated SLG and FLG in NMP due to synergistic interactions between DSAs, the surface, and the polar solvent.

Ref. [219] also reported that the performance of linear alkanes exposing a carboxylic acid head group as stabilizers directly depends on the length of the linear alkane chain. Five linear modules were explored, i.e., hexanoic acid (C6CA), lauric acid (C12CA), stearic acid (C18CA),

lignoceric acid (C24CA) and melissic acid (C30CA), whose different adsorption energies on graphene and tendency to form tightly packed self-assembled monolayers on such a surface affect their performances as stabilizers. The analysis of the carboxylic acid assisted LPE revealed that the concentration of graphene dispersions prepared in NMP, *O*DCB and TCB increases linearly with the length of the aliphatic chain. The observed dependence Y_W with the length of the aliphatic chain was interpreted by means of a thermodynamic model of molecular self-assembly on graphene. This showed that the shorter the aliphatic chain, the larger is the (rotational and translational) entropic cost of forming a 2d structure. These results suggest that a model based on molecular mechanics for the energetics and a statistical mechanic treatment of entropy, could be used to predict the efficiency of supramolecular building blocks as stabilizers and guide the chemical design of the next generation of stabilizers. Nevertheless a role of kinetics cannot be fully ruled out.

Ref [222] reported that alkoxy-substituted photochromic molecules can act as photo-addressable stabilizers to enhance Y_W in an upscalable molecule-assisted LPE-based method. It was demonstrated that the large conformational change associated with the *trans–cis* photochemical isomerization of alkyl-substituted azobenzenes can be used to improve Y_W. The simultaneous use of UV light, promoting the *trans*-to-*cis* isomerization, as well as thermal annealing at 40°C and mechanical forces generated by sonication, both favoring *cis*-to-*trans* isomerization of 4-(decyloxy)azobenzenes, promotes the exfoliation of graphite in liquid media. The most effective exfoliation is obtained with azobenzene molecules irradiated with UV light in NMP at 40°C, with a concentration of exfoliated graphene of 110 mg ml^{-1}. This corresponds to an ~80% increase in Y_W when compared with pure NMP (63 mg ml^{-1}). By depositing the hybrid film onto Au pre-patterned SiO_2 substrates, light- responsive thin hybrid films, formed in a one-step co-deposition process, can be realized, whose conductivity can be reversibly modulated by the *trans*-to–*cis* photoisomerization of the azobenzenes. By combining this approach with cost-effective techniques, such as ink-jet printing, more complex responsive device designs and architectures may be realized.

Exfoliation with aromatic dyes in chloroform and THF, and further processing in polymers

Graphene can be exfoliated in water, using surfactants, or in high-boiling solvents such as DMF or NMP. For an effective, technologically competitive application of GRMs as additives in (nano)composites for electronics or structural applications it may be preferable to solubilize graphene in low-boiling volatile solvents, like $CHCl_3$ or THF. However, the use of amphiphilic surfactants is not suitable to solubilize graphene in organic solvents whose polarity is low [178].

Ref. [178] used perylene diimide (PDI) molecules soluble in organic solvents as “apolar surfactant” for exfoliation and successive processing in polymeric commercial films of poly(vinyl chloride) (PVC), to render them conductive. The PDI has an extended polyaromatic core (which can interact via π-π stacking with the GRM) and flexible side groups, with low, but tunable polarity that make these molecules soluble in a range of organic solvents (Fig. VIII. 4).

The experimental procedure was as follow: mixtures of graphite (3 mg/mL) and PDI (0.1 mg/mL) were added to the selected solvent. The solutions were sonicated for 4.5 hours (Elmasonic P70H, frequency = 37 KHz, power = 110 W) at a constant T=50°C. After sonication, the macroscopic, non-exfoliated graphite particles were eliminated from the dispersions by mild centrifugation at 2200 rpm for 45 min (Omnifuge 2 RS).

Transparent sheets of PVC (thickness 182±4 μm) were dipped into chloroform dispersions of FLG and PDI at RT, a procedure already used for rubber [1087]. They were then dried in air, to let the chloroform evaporate. The swelling process was completed in less than 3 minutes, and gave an increase of ≈80% in volume. No further change of the swollen area/size was observed when the polymer films were left in the dispersions for more than 3 min. After the swelling treatment, the PVC samples showed a dark color due to the presence of the FLG as well as a bright fluorescence due to the PDI.

SEM images showed a dense coating of rectangular and polygonal shapes covering the surface. The sheets were not just deposited on the surface, but embedded into it, in some case reaching some microns (< 10 μm). Control experiments conducting by swelling in PDI only gave surface covered by PDI crystals, and no improvement of electrical conductivity. Typically, when deposited by conventional solution processing, 2d sheets tend to lay flat on a substrate [264, 267]. Due to the swelling, the sheets penetrate into the polymer in an isotropic way, in some cases protruding out of the surface [178]. A strong improvement of material hydrophobicity by ≈40% was observed in all cases, with measurements of water contact angle increasing from 72° (blank PVC) to >100°. The sheet resistance, R_s decreased significantly, going from completely insulating to $\approx 10^5$ Ω/sq, a value useful, e.g. for applications in antistatic coatings.

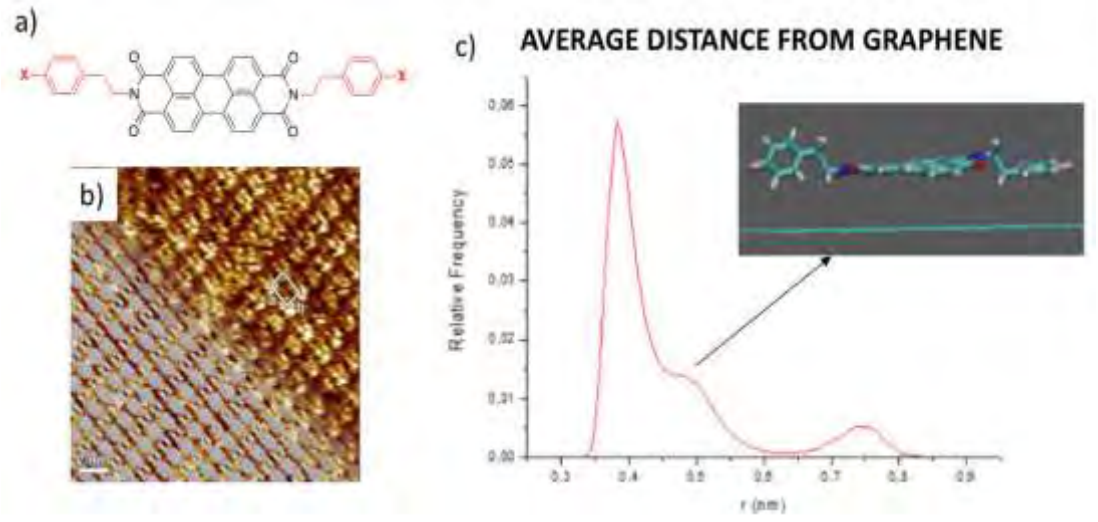

Fig. VIII.4 a) General formula of the PDI used for exfoliation. b) STM image of the typical packing of PDI adsorbed on graphite. c) Average distance of the side groups of the PDI from SLG, from molecular modeling. In the inset, a typical snapshot of the simulation. Adapted from [178] .

On Substrate

Doping of CVD Graphene

Halogenation or doping of graphene with halogens is a process in which halogens, such as fluorine, chlorine, bromine and iodine, are either used to replace one of the carbon atoms or are attached to the graphene surface [1088-1092]. As for all doping or chemical modification processes stability is of importance. Here we focus on chlorination, as this has proven to be a reliable, stable way of halogenation allowing SLG doping without losing transparency [1088].

Ref. [1088] achieved R_s ~30 Ω/sq using up to 5LG, while keeping a high transparency of ≥85%. Depending on whether the doping agent is an electron acceptor or donor, p- or n-type doping can be attained. To achieve a high doping level in the range 10^{13} cm^{-2}, thionyl chloride ($SOCl_2$) is recommended. $SOCl_2$ induces p-type doping due to the higher electronegativity of Cl compared to C.

CVD-grown graphene is first transferred on glass. Ref. [1088] used thermal release tape for the transfer process. Different approaches for doping with thionyl chloride have been tested: last layer doping, where the last or top layer of 1 to 5 layers of GRM has been doped after all layers have been transferred in a staggered fashion, or interlayer doping, where the top layer after each transfer of SLG/FLG is doped creating a doped surface in between the layers. The doping is achieved as follows [1088]: $SOCl_2$ treatments are performed in a dry chamber by placing graphene/glass substrate and 1 mL of liquid $SOCl_2$ (avoiding direct contact) at 105 °C for 60 min. Doping of multilayer samples was performed by repeating $SOCl_2$ treatment after transferring and stacking each SLG/FLG.

R_s is then measured in a van der Pauw configuration. Ref. [1088] suggested to use a large sample area of 4x4mm^2 to obtain a representative R_s. Fig. VIII.5a plots R_s as function of N for interlayer doped and undoped samples. $R_s = 1/ne\mu$, where n is the doping level, e the elementary charge and μ the mobility. The mobility is affected by defects, therefore $\mu \sim 1/n_D$, where n_D is the defect concentration. It is thus important to know doping and defect concentration. $SOCl_2$ allows a nucleophilic substitution by chlorine atoms, which selectively occurs on defective sites, without affecting the existing sp^2 carbon bonds, therefore, without introducing any new defects [1088]. In order to verify this doping mechanism a controlled amount of defects (see below) was introduced in graphene by H plasma.

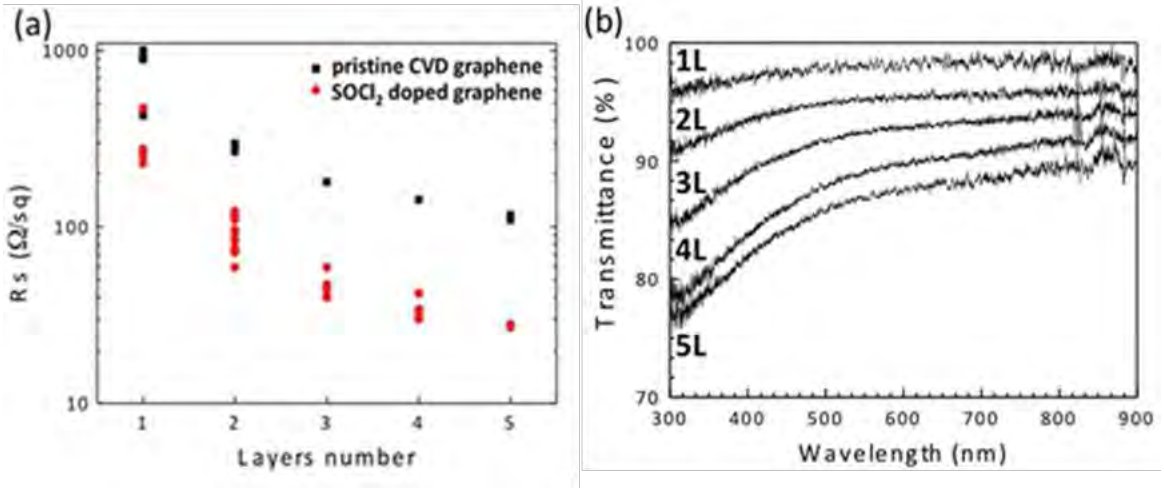

Fig. VIII.5: a) Comparison of R_s *of chlorinated and non-chlorinated CVD graphene as function of number of layers. b) Transmittance for 1 to 5L of graphene. Adapted from ref [1088]*

The quality of graphene after doping can be assessed by Raman spectroscopy. It is important to follow the correct procedure to extract the correct doping level and defect density [1093, 1094]. Graphene with controlled amount of defects induced by mild H plasma showed a higher doping level compared to a pristine, reference sample doped with $SOCl_2$ under the same conditions, but without being subjected to H plasma. This shows that $SOCl_2$ molecules selectively chlorinate defective sites in graphene. However, defects are always counter-productive for achieving low R_s and high mobility. Thus, a compromise between doping level and R_s has to be made. It is therefore more favorable to abstain from the introduction of defects by mild H plasma in order to achieve lower R_s instead of inducing structural defects to which Cl will attach and increase the doping level.

The most critical point is the doping stability with time. Fig. VIII.6 shows the Raman spectra of pristine, chlorinated and defective graphene (induced by H plasma) measured directly after chlorination and after 3 months. Pristine graphene shows a Pos(G) and FWHM(G) of 1583 cm^{-1} and 14 cm^{-1}, while FWHM(2D)=31 cm^{-1}. No D peak is present, i.e. I(D)/I(G)< 0.1. Therefore, the doping level is estimated ~100meV. Hydrogenated graphene on the other hand shows D, D' and D+D' peaks as result of defect introduction *via* H plasma treatment with I(D)/I(G)~1.65. Following the flowchart diagram the doping is estimated~107 meV. This gives $n_D = 4*10^{11} cm^{-2}$. This confirms the presence of defects introduced by the plasma treatment with no change in doping. After chlorination of the plasma treated sample the doping is~380 meV. This is higher compared to that achieved by doping pristine SLG, suggesting that $SOCl_2$ molecules selectively chlorinate defective sites. The Raman spectrum of chlorinated graphene after plasma treatment shows a reduction in D peak intensity. This can be explained by the doping dependence of the D peak [1093]. This gives a defect density $n_D = 3*10^{11} cm^{-2}$ consistent with that of the hydrogenated sample before chlorination. Therefore, although the chlorination process is able to increase doping, the defect density remains unchanged, in agreement with the chemistry of the $SOCl_2$ doping process.

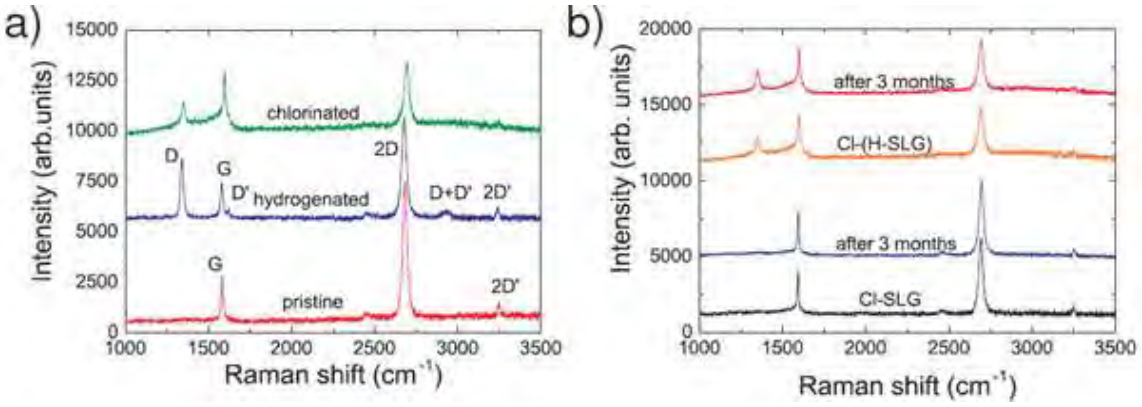

Fig. VIII.6: a) Raman spectra of pristine, hydrogenated and chlorinated graphene after hydrogenation. b) Raman spectra of chlorinated, Cl-SLG, and hydrogenated and chlorinated graphene (Cl-(H-SLG))

measured directly after doping and after doping and after three months left in ambient conditions. Excitation wavelength of 514.5 nm.

Considering that after chlorination, one chlorine atom is attached to each defect and taking a charge transfer of 0.57 electrons [1089], i.e. each Cl takes 0.57 electrons from graphene to induce p-doping, the doping can be estimated from the defect concentration. As a result, the estimated defect density evaluated in hydrogenated graphene corresponds to a doping~65meV. This is the doping level introduced *via* additional defects introduced by plasma etching. The doping of a chlorinated pristine graphene sample was ~304 meV. This is the doping introduced directly *via* chlorination. Adding these two contributions to the doping coming from only chlorination, the final doping level is ~370meV, in agreement with the~380 meV of the hydrogenated and chlorinated sample that was estimated from the Raman spectra measured directly after plasma treatment and doping with $SOCl_2$.

To check stability, Fig. VIII.6b compares the spectra of chlorinated (Cl-SLG) and chlorinated hydrogenated graphene (Cl-(H-SLG)) recorded after three months. The initial doping levels are ~304 meV for doped pristine graphene and ~380 meV for doped hydrogenated graphene. After three months these are~250 meV and ~350 meV. This shows that doping is stable over time.

UV-Vis spectroscopy can be used to assess the optical properties of the chlorinated samples. Fig. VIII.6b) reports the transmittance of 1L to 5L interlayer doped graphene using thionyl chloride. The transmittance is still ~85% even for the 5L interlayer doped sample, making this attractive for applications where low R_s and high transparency are needed.

Solution based processes for halogenation of graphene were also proposed (see e.g. refs. [1090, 1091]), Ref. [1092] studied the approach of using CVD grown FLG on Ni and transferred it on a glass substrate to induce doping by bromine vapor at RT in inert atmosphere: a glovebox with <0.1ppm of O_2 and H_2O and nitrogen filled glovebag with 2000 ppm of O_2 and 2500ppm of H_2O. Ref. [1092] reported R_s ~180 Ω/sq with a reduction in transmittance of 2-3% with respect to pristine SLG. A drop of R_s from 1548 Ω/sq to 602 Ω/sq after exposure to Br for 60 min was reported [1092] .

Functionalization with Polycyclic Aromatic Hydrocarbons

Non-covalent functionalization of CVD graphene films transferred to SiO_2 was achieved *via* drop-casting of an aqueous solution (1 mM in phosphate buffer solution, pH 7) of the perylene bisimide **1** (structure see Fig. VIII.7a) onto the SLG surface [1095]. The packing density of the perylene self-assembled monolayer (SAM) was related to the cleanliness of the SLG surface. Vacuum annealing prior to functionalization removes polymer and leads to a much higher denser perylene packing density than on untreated SLG. This is illustrated when the Raman spectrum and water contact angle measurements are considered (Fig. VIII.7). The increased relative intensity of the perylene Raman peaks (pale shading) when compared to the SLG peaks (dark shading) for the pre-annealed SLG *versus* the as-transferred one is indicative of a greater quantity of perylene on the surface of the former sample. Likewise, the high density packed perylene on graphene has the smallest water contact angle (58 **°**) compared to the as-transferred graphene sample (89 **°**) and low density

perlylene sample (67 °). Again, this increased hydrophilicity indicates a greater number of molecules on the SLG surface for the pre-annealed film.

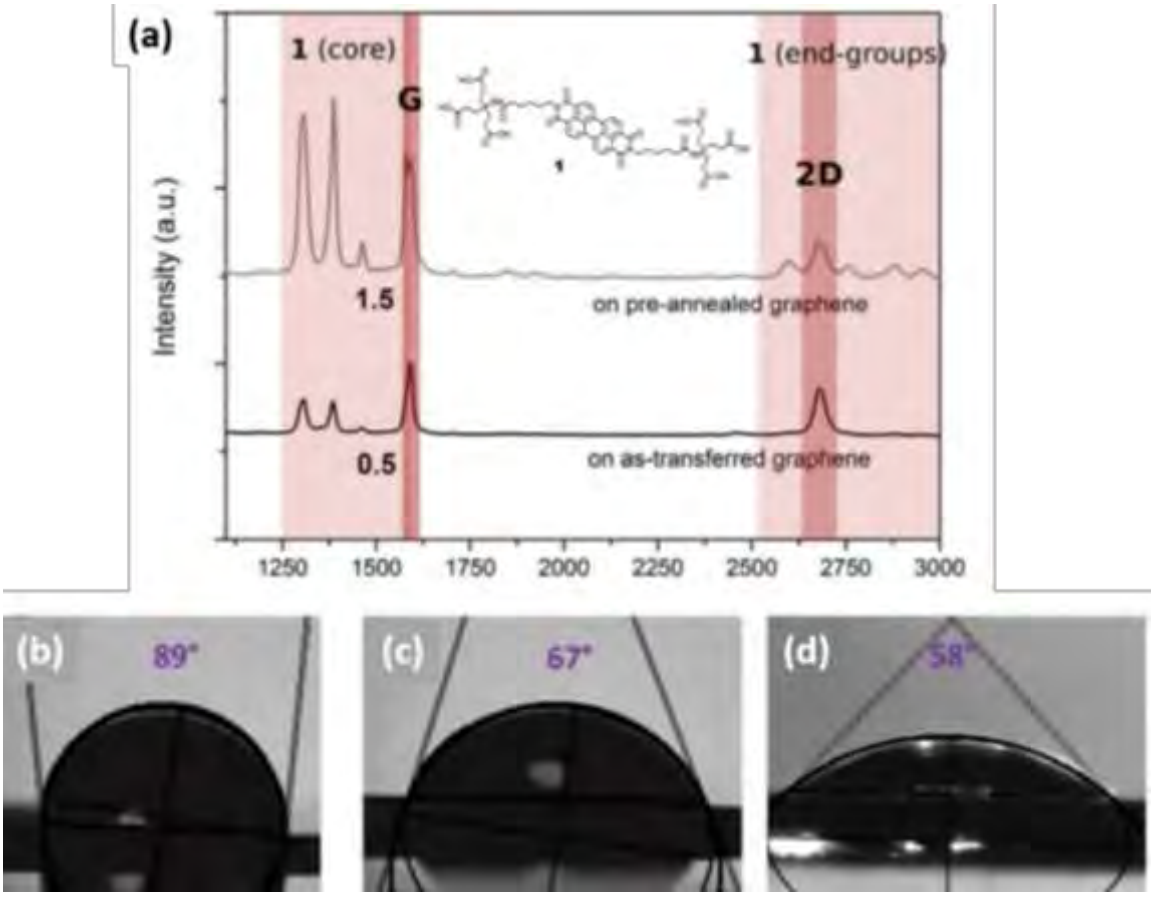

Fig. VIII.7: (a) Raman spectra for high and low packing density perylene1 SAMs on as-transferred and pre-annealed SLG. Inset: Structure of perylene1. Water contact angles on (b) bare SLG, (c) low and (d) high packing density of perylene1 on SLG. Adapted from [1095]

STM can be used to estimate the SLG cleanliness before and after annealing, Fig. VIII.8. An image of the resultant high packing density perylene SAM is shown in Fig. VIII.8b. Analysis of the periodicity of the line profiles indicates that the perylene molecules pack together with the perylene cores perpendicular to the SLG surface, Fig. VIII.8. This is at odds with the observed common believe [1096-1098] that organic molecules with large conjugates systems will adsorb via π- π interactions between the conjugates core and SLG/FLG. This suggests that the method of deposition has a large bearing on the adsorption mechanism, as the liquid deposition process discussed here results in significantly more neighboring molecule-molecule interactions [1095] than if another techniques, such as thermal evaporation, were used.

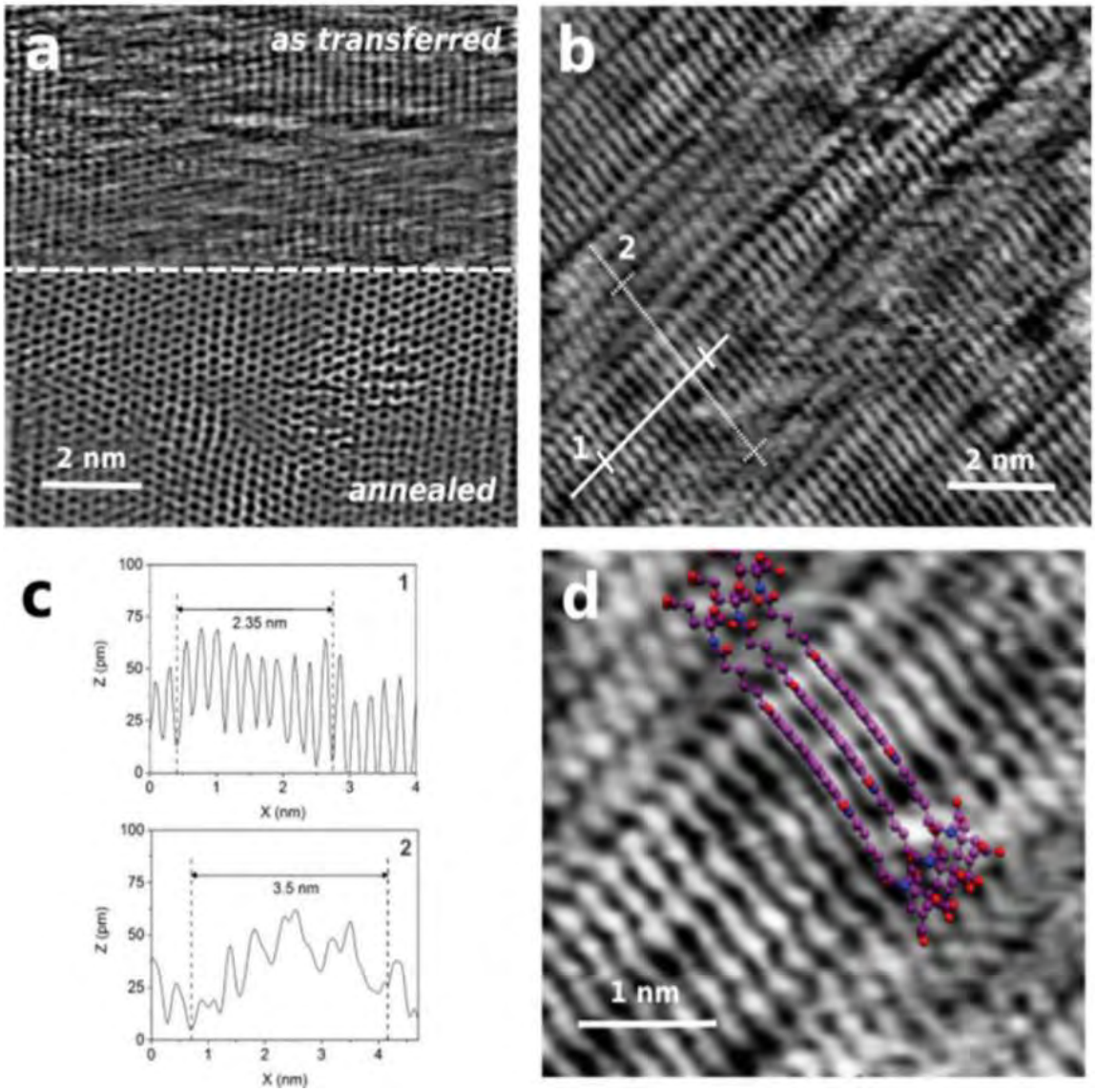

Fig. VIII.8: STM images of (a) as-transferred (top) and subsequently annealed (bottom) CVD-SLG on SiO_2 and (b) after wet-chemical deposition of perylene1 on the same annealed substrate. (c) line profiles from (b) and (d) zoomed in area with molecular structure overlay. Adapted from [1095]

This non-covalent functionalization was taken a step further by chemically modifying the functional end groups, as well as showing that perylene functionalization can successfully be carried out prior to polymer transfer to arbitrary substrates, effectively creating a functional layer transfer (FLaT) [1099]. The latter finding is important, as it allows perylene SAMs of very high packing density to assemble on pristine SLG without having to anneal the as-transferred SLG to remove any polymer residues as depicted in Fig. VIII.9a. Reacting ethylene-diamine (EDA) with the carboxylic acid groups of the perylene1 SAM using O-(7-azabenzotriazole-1-yl)-N,N,N,N'-tetramethyluronium hexafluorophosphate (HATU) was carried out to investigate the possibility of converting the carboxylic acid groups to amines [1099]. This would allow the use of perylene1 as anchor in SLG-based biosensing.

Figs. VIII.9b-d show that after reacting the perylene molecules with HATU and EDA new contributions can be seen in the N1s core level XPS spectra of the material. The relative intensity of the peak component arising due to the presence of amine groups has increased (pink), along with other contributions likely due to HATU residues (grey). Annealing the derivitized sample at 220 °C was found to reduce the relative intensity of these peaks, indicating that the any unreacted physisorbed surface contaminants are removed [1099]. These results show that it is possible to use perylene functionalized graphene films as the basis for further chemical modification with a view towards biosensing applications.

The non-covalent functionalization, shall then be, if needed, transformed also in covalent functionalization, triggering the covalent grafting of molecules self-assembled on graphene using, as example, an electrochemical pulse (see section VIII.1.2 Electrochemical Functionalization) [1037].

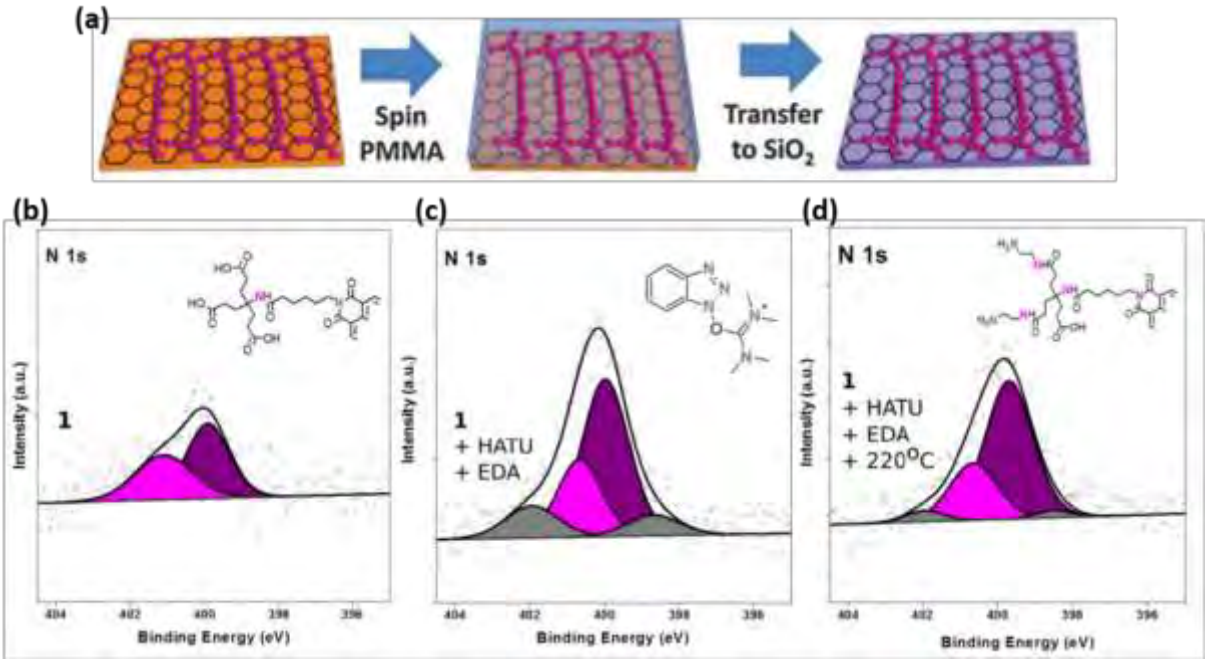

Fig. VIII.9: a) Schematic of the functional layer transfer (FLaT) in which perylene fucntionalised graphene is transferred b-d) XPS spectra of perylene on CVD-SLG for each derivitization step. (b) As-transferred perylene1 on SLG. Inset: Partial structure of perylene1 with corresponding nitrogen contributions. (c) Perylene1 on SLG after reaction with HATU and EDA. The two new contributions are from HATU residue. Inset: Chemical structure of HATU.(d) After annealing of derivatized sample at 220 °C. The HATU contributions reduce, but the amine signal increases. Inset: Partial structure of perylene1 after reaction, depicting corresponding nitrogen contributions. Adapted from [1099]

Non-destructive Functionalization with Carbon Nanomembranes

Non-covalent functionalization (via van der Waals forces) can be used to fabricate heterostructures of graphene and carbon nanomembranes (CNMs) [1100].Fig. VIII.10a shows a route to non-destructive chemical functionalization *via* assembly of all-carbon vertical heterostructures consisting of amino-terminated CNMs (NH_2-CNM) on SLG produced by CVD on copper foils [1100].

The chemically active amino groups of NH_2-CNMs are located in these heterostructures in close vicinity to the SLG plane, as they are separated from it only by the ~1 nm dielectric CNM [61]. As shown by complementary spectroscopy, microscopy and electric transport measurements, the pristine SLG properties in these heterostructures remain unaffected [1100], which opens avenues for implementations in graphene-based electronic devices. In Fig. VIII.10b, an optical microscope image of an NH_2-CNM/graphene FET in the Hall bar geometry is presented. The structural quality of the device characterized by Raman mapping (Fig. VIII.10c) shows homogeneity. Fig. VIII.10d presents RT electric-field effect measurements as a function of back-gate voltage, V_{BG}, at 4 side contacts, Fig. VIII.10b, P1-P4. The electrical characteristics are homogeneous on the scale of ~3500 μm^2. μ is nearly a factor of two higher (~3000cm^2/Vs) in the heterostructure devices in comparison to the starting SLG (~1500 cm^2/Vs), Fig. VIII.10. This may results from a reduction of charge impurities at the SLG/SiO_2 and SLG/ambient interfaces. Shubnikov – de Haas oscillations accompanied with resistivity plateaus of the quantum Hall effect at low T, Fig. VIII.10f, demonstrate the high electronic quality in the engineered NH_2-CNM/graphene heterostructures [1100, 1101].

The NH_2-CNM/graphene FETs are promising for biosensors. As amino groups can further be functionalized with respective receptors, one could use NH_2-CNM/SLG FETs as analyte-specific electrochemical sensors. GFET biosensors have a very high sensitivity up to the fM level [1102]. However, this is difficult to achieve in combination with high selectivity and specificity of the biomolecular binding events. While any covalent SLG functionalization may affect the electronic quality, a functionalization *via* physisorption typically involves larger distances leading to the reduced sensitivity. Ref. [1100] used 1 nm dielectric and specifically functionalized CNMs to overcome these problems. It is also promising to use them in graphene-based electronics as a complementary dielectric, similar to hBN, for engineering top-gate electrodes, for field-effect tunneling transistors or in flexible electronic applications.

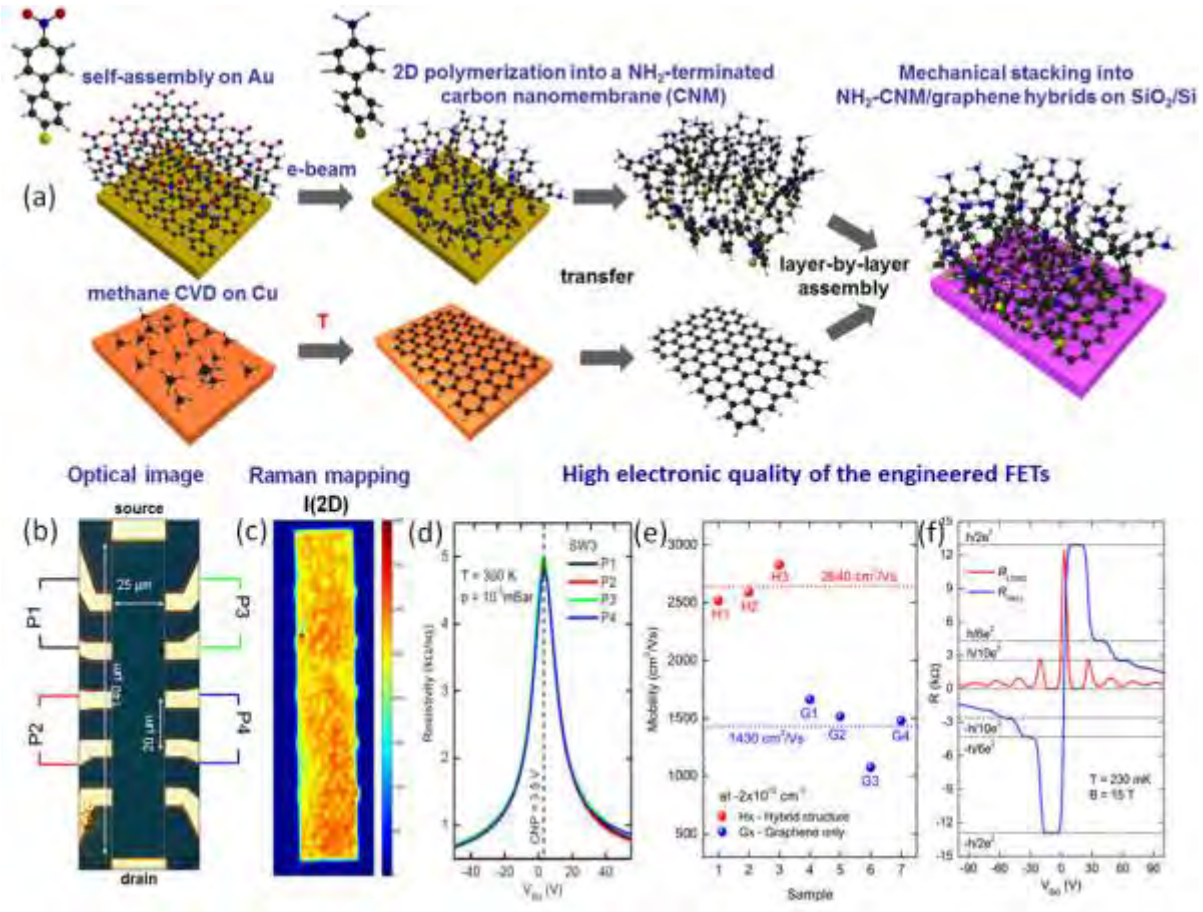

Fig. VIII. 10: Non-destructive chemical functionalization of SLG. a) Schematic of the fabrication of NH_2-CNM/SLG heterostructures via mechanical stacking of the individual sheets. b) Microscope image of the fabricated FET with Au contacts in the Hall bar geometry. c) Mapping of the Raman 2D peak on the active device area. d) RT homogeneous electrical field effect at different side contacts of the FET as a function of V_G. e) Mobility of heterostructure and reference devices. f) Quantum oscillations in a magnetic field at low T confirming high electronic quality of SLG in the fabricated heterostructures. Adapted from ref [1100]

VIII.4 Defect Functionalization of Graphene

In Dispersion

Edge selective functionalization would be of particular interest to obtain engineered samples able to further react or assemble in a controlled way. Edge functionalization is in principle driven by the reactivity of the carbon atoms localized at the peripheral edges, which differs from the inertness of the C atoms on the basal plane due to the stability of the extended delocalized π-system. In fact, edges may be regarded as defects in the graphene structure, which can exploited for its functionalization without severely disrupting the π-conjugated network [1103, 1104]. Edge functionalization may also be carried out on GRMs [1020, 1105].

The diazonium chemistry of carbon nanostructures is one of the most convenient methods to covalently functionalize the edges of graphitic materials [1106-1109]. This reaction proceeds through a free-radical mechanism as a result of transfer of a delocalized electron from a graphitic substrate to the aryl diazonium cation to form an aryl radical after the release of nitrogen [1020] (Fig. VIII.11).

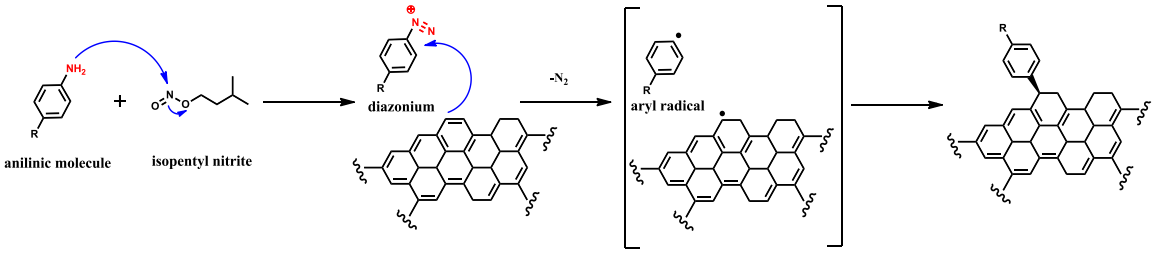

Fig. VIII.11: Free-radical mechanism for edge-selective functionalization using diazonium species. Adapted from Ref. [1110]

The standard protocol [1104], which generates the reactive diazonium species *in situ* from a stable anilinic compound in the presence of an alkyl nitrite (radical initiator), was followed by performing the reaction in DMF with different equivalents of the aniline derivative per carbon atom. In Ref. [1111], graphite flakes (G2Nan grade from Nanesa) with lateral size ~ 10-50 μm and thickness ~ 10nm, were first dispersed in DMF at a concentration of 1 mg mL^{-1} and sonicated in an ultrasonic bath in mild conditions (maximum operating power 320 W) for 30 min while N_2 is bubbled in the suspension to avoid the full exfoliation into graphene sheets. Then, 4-aminophenol was added to the dispersion and the mixture was sonicated for further 15 min under N_2 to achieve a homogeneous suspension which was heated to 80 °C. After that, isopentyl nitrite (6 equiv. per carbon atom) was slowly added to the dispersion and the reaction mixture was kept at 80 °C for two different reaction times, 24 and 48h. After cooling to RT, the reaction was quenched by pouring the mixture into distilled water and filtration of the GRM dispersion through a PTFE membrane (0.2 μm, Whatman). The filtered cake was redispersed in DMF by ultrasonication in a bath for 10 min and filtered through a PTFE membrane (0.2 μm). This sequence was repeated twice with DMF, distilled water, methanol and diethyl ether. The resulting solids were dried at 80 ºC for 24 h (Fig. VIII.12) [1112].

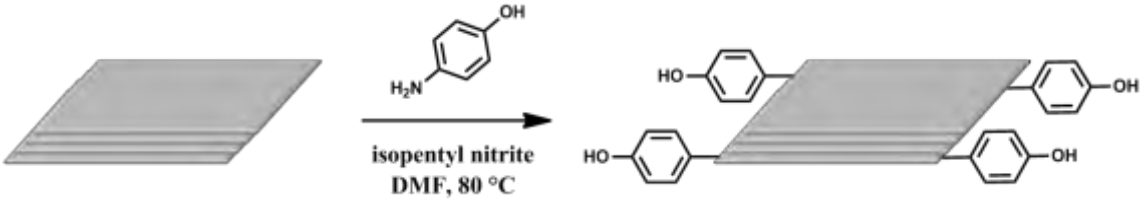

Fig. VIII. 12. Edge-selective functionalization with 4-aminophenol.

Functionalization of the flakes was confirmed by a dispersibility test in an organic solvent, where the functional groups present good solubility: Pristine and functionalized flakes were dispersed in IPA at a concentration of 0.1 mg mL^{-1} and sonicated for 30 min. After 2 days, chemically modified flakes with 2 and 4 equiv. of 4-aminophenol during 24 and 48 hours, respectively, precipitated from the dispersion. The functionalized sample prepared with 4 equiv. of the anilinic

compound using a reaction time of 24 hours displayed better dispersibility and was the only sample that did not precipitate after a few days in IPA, which suggests the presence of a higher concentration of hydroxyl groups on graphene nanoplatelets (GnP).

The chemical composition of pristine and chemically modified flakes was investigated by XPS. Upon functionalization, both the C-C sp^2 content and the π-π^* shake-up band decrease due to the disruption of the delocalized π conjugation in the graphitic structure, while the content of C-OH/C-N and >C=O/C=N increase. The O/C ratio increases from 1.7% to 8.2%, while the N concentration is ~3-5%, ascribed to adsorbed molecules or residual solvents [1106, 1113].

The degree and selectivity of the edge functionalization is influenced by the number of layers, edge states, degree of exposure of the interior basal planes and defects [1104, 1106]. In Ref. [1111], the edge selective functionalization was maximized for 4-aminophenol while it is confirmed that these conditions can be extended to *para*-substituted aniline derivatives. This opens new possibilities to modulate their physical and electronic properties for diverse applications such as catalysis and opto-electronics [1109, 1114]. Similar functionalization can be used to obtain building blocks for the design and manufacturing of functional materials.

On Substrate

Ref. [1115] functionalized graphene on SiC with organic molecules forming covalent bonds. This is alternative to wet-chemistry protocols that reported covalent modification methodologies incompatible with some functional groups due to harsh conditions (such as high thermodynamic force, generally exceeding 20 kcal mol^{-1}, or long reaction times, even more than 12 hours)) used e.g. diazonium salt, click chemistry or surface reactions [1006, 1018, 1081, 1116-1120].

Ref. [1115] reported the controlled atom-molecule substitution in ultra high vacuum (UHV, $P<2x10^{-10}$ mbar) by using p-aminophenol molecules, consisting of an aromatic ring with an amino and a hydroxyl group, linking the amino group to the graphene network and leaving free the hydroxyl group. This method was also successfully carried out on graphene grown on Ir.

The substrate was degassed in UHV annealing it at 200-400°C (depending on the type of sample, SLG was degassed at 350ºC and quasy free standing monolayer graphene QFSLG at 200°C during 10-15 minutes, in order to remove physisorbed contaminations. This thermal treatment was performed by electron irradiation in a heating stage placed at the manipulator, while the annealing temperature was monitored with an infrared pyrometer (emissivity of 0.9). After the degassing procedure, the cleanness of the sample was confirmed by STM.

The next step consists in creating single atom vacancies (SAV) by bombarding SLG with low energy ions (Ar^+). For this procedure, the sample needs to be placed close to the ion gun (10 cm maximum) at a 0°-15° angle incidence. The acceleration of the electrons inside the Specs IQE 11/35 ion gun should be 100-140 eV, 10 mA, having a controlled Ar pressure 1×10^{-7} mbar. The most important parameter is the exposure time, that varies between 30s-2min for producing the desired density of mono-vacancies [1121-1124].

After irradiation, the sample is subjected to a thermal flash to remove the physisorbed Ar. This flash should not be longer than 5 min, reaching different T for each type of sample: 550ºC for the SLG and 250ºC for QFSLG. It is important to check the mono-vacancies that have been created by STM as soon as possible. Defects are very reactive and they could get passivated with air contamination [1125, 1126].

After modifying the graphene network, we proceed to evaporate organic molecules (P-aminophenol). They need to be purified by turbo pumping for at least 6h to remove impurities. Following this strategy, Ref. [1115] tested by STM that the organic molecules filled most of the SAV defects, as it is apparent in Fig VIII.13.

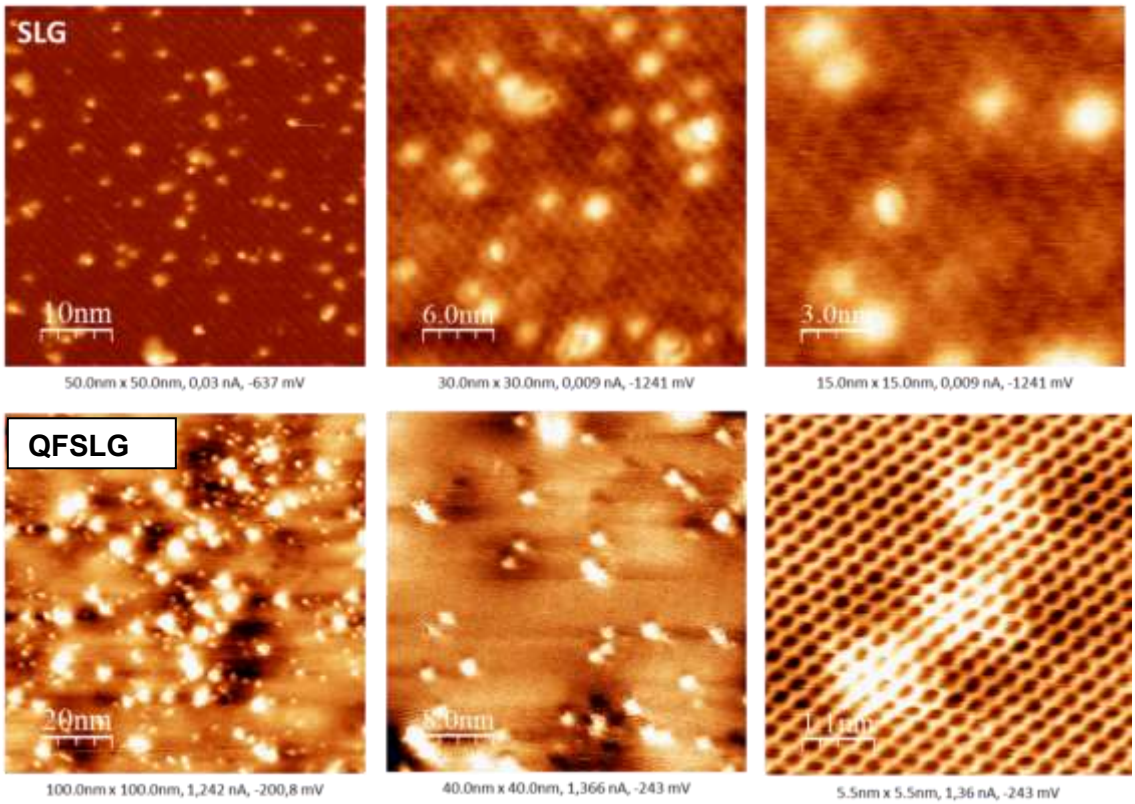

Fig. VIII.13: STM images of the p-aminophenol molecules covalently anchored to the monovacancies created by the soft irradiation of the surface with argon ions in both types of samples: SLG (upper panel) and QFSLG (lower panel). The graphene in the SiC samples was grown according to the reference [563]. *Note that in the images of the SLG sample appears reconstruction (6√3 x 6√3)R30° that comes from the buffer layer of SiC, whereas in the QFSLG sample we only see the graphene network due to the intercalated hydrogen has decoupled buffer layer. The molecules appear as protuberances inserted into the graphene network.*

VIII.5 Decoration with Nanoparticles

The large surface area, electrical conductivity and mechanical strength make SLG a promising substrate to be coupled with nanoparticles (NPs) for synergistic benefits in applications such as catalysis, energy storage, plasmonics and optoelectronics or solid state hydrogen storage [1127].

Depending on the Fermi level/work function of SLG and metal NPs, interfacial charge transfer can be from SLG to NPs or *vice versa*. Hence, decorating with nanoparticles is an efficient method for graphene doping with electrons or holes. To enhance interfacial charge transfer, a strong interaction between graphene and NPs is required [1127]. SLG can be decorated with NPs either by growing NPs directly on its surface, by mixing it with NPs or by depositing NPs produced in the gas phase in UHV conditions.

Graphene-metal NPs

Graphene and other surfaces can be decorated with NPs *via* electroless plating [1128]. Nanotubes/SLG act as reducing agents towards metal salts; the Fermi level of nanocarbons allows them to spontaneously reduce Au^{3+} and Pt^{2+} salt solutions to form their respective $M^0_{(metal)}$ NPs on the nanocarbon surface [1128]. To extend this to other metal NPs, reductive charging protocols can be used to increase the reducing strength of the nanocarbons. Fulleride, nanotubide and graphenide and can be generated following reduction using alkali metal/liquid NH_3 [1007, 1129, 1130] alkali metal naphthalide/THF [1131, 1132], or electrochemically in non-aqueous electrolytes [1133]. All reductive charging techniques insert electrons into the carbon π* orbitals, shifting the Fermi energy, resulting in increased reactivity. Subsequent chemical reaction may take place *via* redox or electrophilic addition reactions that are believed to involve SET (*i.e.* radical based reactions) [1035, 1134-1138]. Due to the high reactivity of reduced nanocarbons towards oxygen and moisture in the atmosphere, these materials should be handled using inert gas filled glove boxes or Schlenk techniques [1139].

Ref. [1140] used graphenides to reduce a series of Cu, Zn and Mg salts/complexes, to generate metal NPs on the SLG surface. KC_8 and KC_{24} potassium-graphite intercalation compounds (K-GICs) were produced *via* the vapor transport [1139] from natural graphite, giving the corresponding characteristic bronze stage 1 KC_8 and steel blue stage 2 KC_{24} compounds. For each experiment, 20 mL, NMP (anhydrous grade, 99.5%, further dried by 4 Å molecular sieves, Sigma-Aldrich, UK), was added to 10 mg K-GIC in a 100 mL Young's tap Schlenk tube. The sample was removed from the glove box, mildly sonicated for 30 min and returned to the glove box for subsequent reactions.

MX_2 (M = Mn, Zn and Cu) salts and Cu mesitylene (CuMes) were dissolved in NMP to yield 0.1 M stock solutions. Aliquots were added to the KC_x dispersion to give the desired stoichiometry of metal to K. Typically, reactions are performed using the exact stoichiometry as number of charges that are available for the reduction, *e.g.* for M^{2+} salts, M^{2+}:K = 0.5:1, M^+ salts, M^+:K = 1:1, *etc.* It should be noted that the reduction potential of the metal salt/complex is shifted dependent on its concentration as defined by the Nernst equation [1141], $E_{M^{n+}/M} = E^0_{M^{n+}/M} + ((RT/nF) \ln [M^{n+}])$, where E^0 is the standard reduction potential, and n is the number of electrons involved. The reaction was left to stir for 72 h before being removed from the glove box, washed and filtered under vacuum with 100 mL each of NMP, water, chloroform and ethanol, and left to dry in air.

Another approach for NP decoration is anchoring them to a polymer matrix surrounding SLG/FLG [1142]. Electrochemical exfoliated graphene (EEG) was prepared in Ref. [1142] with a sodium methanesulfonate aqueous solution as electrolyte. The EEG was then dispersed in DMF and mixed with polyaniline (PANi, emeraldine base). The strong π-π interaction between PANi and EEG facilitated anchoring of PANi on EEG, achieving controlled surface functionalization. Subsequently, various colloidal NPs (Si, Fe_3O_4 and Pt) were added into the above PANi-functionalized EEG dispersion. During this process, NPs were bound to the amine/imine groups of PANi and assembled into EEG-PANi *via* electrostatic interaction and hydrogen bonding. Protonic acid doping of PANi with HCl generated EEG-NPs with sandwich-like nanostructures.

Plasmonic coupling of AuNP creates intense hot spots with large electromagnetic field-enhancements within the cavity formed by the two metallic surfaces. However, this localized field is extremely sensitive to morphological fluctuations and subtle changes in the dielectric properties of the cavity contents. SLG was used as an ultrathin spacer between AuNPs and a Au substrate to create plasmonic field enhancements. By gating, the possibility to produce plasmon tuning was demonstrated .

NPs can also be grown on SLG by gas phase synthesis [1143]. This approach was used to grow clusters (hence the name Ion Cluster Source or ICS [1144]. It has evolved for the growth of NPs. The ability to control the mean NP size (from 1 nm to few tens nm) with a quite narrow size distribution while keeping a high chemical composition has converted the ICS in a versatile tool for the fabrication of NPs [1143]. The replacement of the single magnetron of the ICS by multiple magnetrons (Multiple Ion Cluster Source or MICS), offers the advantage of the synthesis of complex highly crystalline NPs with core-shell and core-shell-shell structures [1145-1147], hence providing multiple functionalities to the decorated material [1148, 1149].

One of the important issues in this fabrication method is the vacuum quality in terms of base pressure and purity of the injected gases. A good base pressure is needed (below $5.\ 10^{-9}$ mbar – $5.\ 10^{-7}$ Pa) in order to avoid contaminations as much as possible. Ref. [1150] showed that small amounts of oxygen could modify the atomic structure of Au clusters. One can assume that other contaminants, such as C, N, He, etc. could also affect the growth and properties of the NPs. Therefore, it is crucial to obtain the best base pressure in the vacuum vessel. For the fabrication of the nanoparticles depicted in Fig. VIII.14, a base pressure below 5.10^{-10} in the MICS set-up was measured [1145-1147]. To ensure a minimum contamination, all gas pipes used to inject Ar and He are made of stainless steel and vacuum sealed. The purity of Ar and He was~99.5% and >99.5% respectively. Additionally, the purity of Au was ensured by 99.99% and a systematic pre-sputtering of the targets was performed during 4 min to remove possible contaminants adsorbed on the target surfaces. The samples were handled following basic precautions like using plastic tools (in order to avoid metallic contamination) [1151] flushing the fresh Si substrates with nitrogen to remove possible dust and depositing less than 4% of a monolayer of NPs to avoid NPs interactions [1152] .

The structure and properties of NPs grown by gas phase synthesis is dependent on the parameters that have been used in the cluster sources. Ref. [1153] reported that the power applied to the magnetron and the positioning of the magnetron inside the cluster source that defines the

residence time of the NPs in the cluster source (and hence their size) can be used to tune the proportion of icosahedral (Ih), decahedral (Dh) and face-centered cubic (fcc) isomer structures. Therefore, a detailed description of the used parameters is mandatory for any attempt to reproduce the growth of NPs by using the gas phase synthesis route.

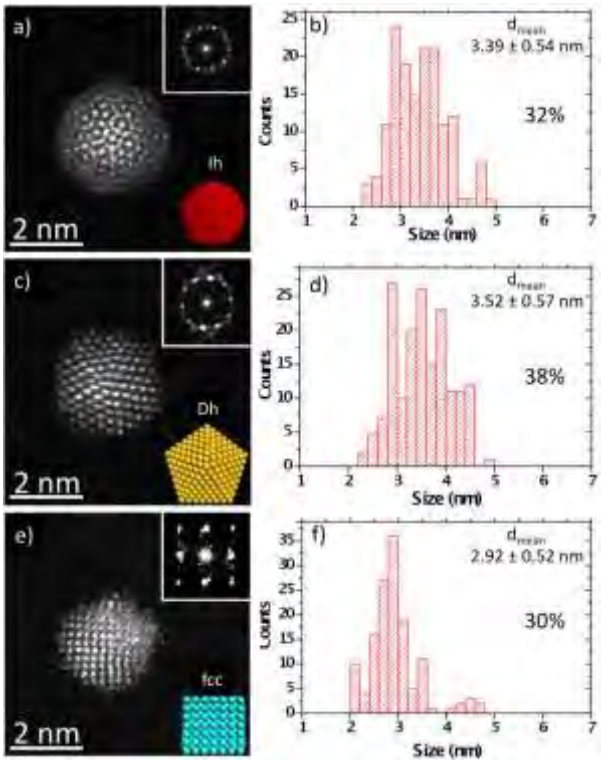

Fig VIII.14. Representative C_s-corrected STEM-HAADF images of Ih a), Dh c) and fcc e) nanoparticles and their corresponding size distributions b), d) and f) for Ih, Dh and fcc respectively for Au NPs grown by the MICS. The FFT and the model of each structure are shown as insets in each image. The mean diameters d_{mean} are also given.

The next step is the deposition of the NPs on SLG. a series of samples with different coverages are needed to evaluate the evolution of the SLG properties with increasing amounts of NPs. When using gas aggregation sources, the NP density is controlled by the deposition time. Once the number of NPs per time unit is known, one can calculate the time needed for a given coverage. However, if the calibrations are made on a different substrate, the different sticking coefficient will modify this value. The sticking coefficient of metallic NPs on SLG is 3 times SiO_x (i.e.: the sticking coefficient of metallic NP)s on SLG is 3 times higher than SiO_x as depicted in Fig. VIII.15).

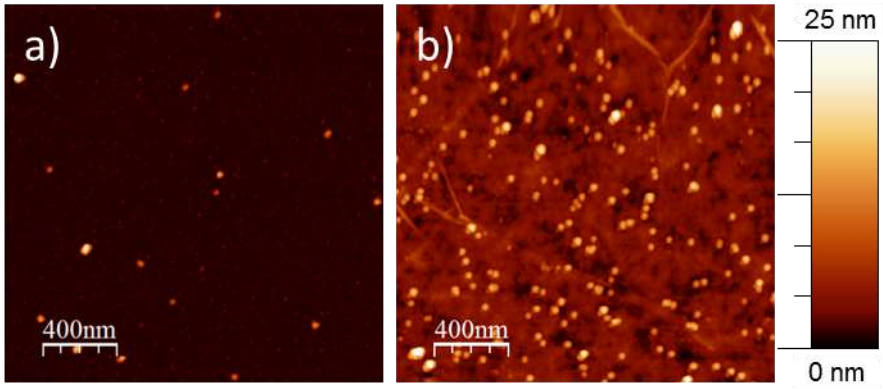

Fig VIII.15. AFM of Au nanoparticles a) on SiOx and b) on SLG after a deposition time of 4 s and 3 s, respectively to illustrate the importance of the sticking coefficient.

GRM as Support to Grow Mg Nanoparticles

For the synthesis of MgH_2 nanoparticles (MgH_2NP) a support is needed to better control the NP dimensions. GRM are a possible alternative to other substrates such as porous carbon, carbon nanotubes or other carbon nanostructures [271, 1154-1161]. Ref. [1162] used graphite flakes as support and anhydrous tetrahydrofuran (>99%) and *n*-dibutyl-Mg from Sigma-Aldrich. High purity hydrogen gas (99.999%) was used throughout the experiment. Graphite flakes (Graphene Supermarket, 4603 Middle Country Rd Unit 125, Calverton, NY, 11933, USA) with 12 nm, 6 nm and 1.6 nm thicknesses and tens of microns in lateral size were used. All the samples were annealed at 800°C overnight to remove organic residuals and oxygen, in hydrogen atmosphere to hydrogenate dangling bonds. Successively, the material processing was performed in a glove box filled with high purity argon (O_2 and H_2O <1 ppm) to avoid oxygen contamination of the reactants preventing the formation of the Mg hydride.

MgH_2 was synthesized by decomposition of *n*-dibutyl-Mg leading to the direct formation of MgH_2 and under an inert atmosphere [1026] at 110 °C. A rapid formation of MgH_2 is expected for higher temperatures following the reaction [1163]:

$$(C_4H_9)_2Mg \rightarrow 2C_4H_8 + MgH_2 \qquad \text{(VIII.1)}$$

In a typical synthesis protocol, *n*-dibutyl-Mg was mixed to THF or C_6H_{12} in different proportions. The mixture was placed in a stainless steel reactor vessel and porous carbon, MWNTs or FLGs added. THF is slightly polar (0.207), while C_6H_{12} non-polar (0.0006). For this reason, we expect different solubility in relation to the solvent used. In addition, MgH_2 is highly reactive toward organic molecules [1164]. Then the process of thermal degradation of *n*-dibutyl-Mg reagent is expected to be susceptible to the synthetic solvent utilized. Hence the use of different solvents in principle should lead to different MgH_2 structures and hydrogen performances [1165] .

Hydrogen was introduced in the reactor at a pressure of 10 bar or 20 bar, respectively. and the solution heated at 170 °C and stirred at 50 rpm overnight [1166]. After 12 h, a black/gray precipitate was obtained from the decomposition of *n*-dibutyl-Mg. The suspension was then transferred in appropriate vessels under inert atmosphere and the main part of the solvent was removed by using a

centrifuge at 5000 rpm (~2000 *g*). To further dry the material and remove the remaining organic residuals, the material was exposed under dynamic vacuum of ~10^{-2} mbar for about 5 hours. The exsiccated material was placed in sealed vials to avoid Mg oxidation for the characterization [1162, 1167].

Stabilization of the MgH_2NP depends on the interaction between the NP and the support surface [1168-1170]. Defects and functional groups in this respect, play an important role and a description of synthesis recipes should always be accompanied by a detailed description of the material. The TEM analysis showed crumpled surfaces (Fig. VIII.16). Curvature leads to higher reactivity of FLG towards chemical elements such as hydrogen or magnesium [1169, 1171, 1172]. Wrinkles may then play an active role in limiting the formation of MgH_2NP in the solvent and enhancing the decoration of the graphene surface.

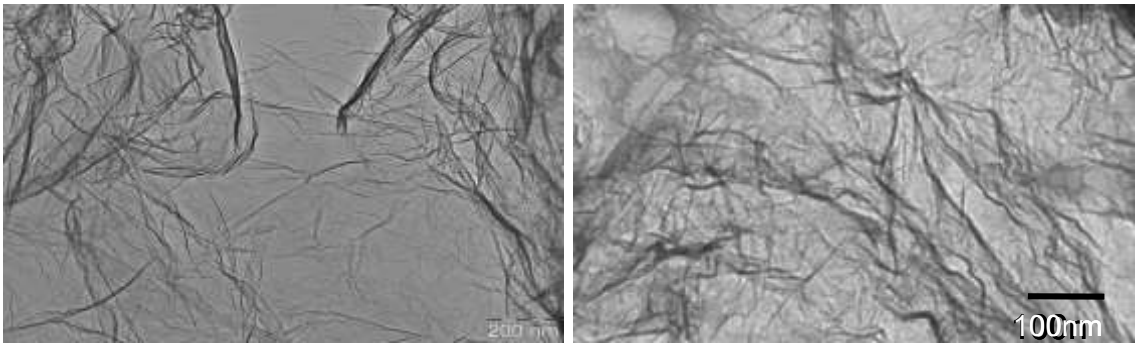

Fig. VIII.16: TEM images showing wrinkles and crumpling.

In this synthesis 20 mg of flakes were mixed to 100 ml of THF or C_6H_{12}. 2ml of *n*-dibutyl-Mg were then added to the solution [1162, 1167]. Extended sonication was applied to improve the dispersion: Tip and bath sonicators were utilized for 10 min to apply ultrasounds, while the increase in temperature was avoided using ice cooling. THF leads to more dispersed FLG with respect to cyclohexane. An amount of 10-30 mg of FLG were dispersed in a solvent volume ranging between 50 and 100mL while the amount of *n*-dibutyl-Mg was between 2 and 4 mL. Better graphene dispersion could affect the size of the Mg NP since cyclohexane produced bigger MgH_2 NP than THF.

The XPS analysis showed that Mg in a completely oxidized form because it is almost impossible to introduce the sample in the XPS instrument avoiding exposure to atmosphere. The oxygen is~34%. However, if oxygen is considered as exogenous due to atmosphere exposure, the quantification can be limited to C and Mg core lines. The Mg concentration corresponds to ~27%.

Normally lower reactant concentrations lead to better results in terms of NP size. MgH_2 NP with size lower than 5 nm were obtained using 10 mg of GNP in 100 ml of THF and adding 2ml of n-dibutyl-Mg. Nowadays the use of hydrogen is limited by the difficulties of synthesizing efficient storage materials. Magnesium offers a good compromise between good hydrogen storage (7.6 wt%) and reasonable desorption temperature if compared to other materials. In addition, Mg is an interesting material because it is low cost and non-toxic. For Mg/MgH_2 the enthalpy of reaction is 75 kJ/mol H_2 corresponding to a H desorption temperature of ~350 ºC [1173, 1174]. However the thermodynamic properties of this material can be improved lowering the Mg-H bond formation

enthalpy. For practical application in automotive, the metal-hydrogen formation enthalpy should be around 30 kJ/mol H_2 [1175, 1176]. It has been demonstrated both theoretically and experimentally that the reduction of the Mg particles affects the bond energy with hydrogen [271, 1177], although it is not easy to confine the Mg nanoparticle size to the nanometer scale. The possibility to synthesize Mg nanoparticles with size on the nanometer size is then of great interest for both automotive and stationary applications. Materials on these size scale exhibit hydrogen desorption temperatures of about 160 ºC , 140 ºC [1162].

VIII.6 Functionalization of other LMs

Covalent Functionalization of MoS_2

Reductive Covalent Functionalization

Functionalization of MoS_2 can be achieved by ligand conjugation of thiols at sulfur vacancy sites either introduced by ion irradiation [1178] or naturally occurring after chemical exfoliation [1179, 1180]. Such methods are interesting but limited in their utility. Ref. [351] reported the first step toward a general route to functionalize TMDs by grafting functional groups to the exposed sulfur atoms, with a functionalization sequence based on intercalation, chemical exfoliation and subsequent quenching of the negative charges on the MoS_2 by organic halides or other strong electrophiles [350, 351]. In this functionalization sequence intercalated, chemically exfoliated MoS_2 is reacted with electrophiles such as halides and diazonium salts (Fig. VIII.17). The use of chemically exfoliated MoS_2 is beneficial due to the good exfoliation in water making both sides of the LM accessible. Chemically exfoliated MoS_2 can be obtained by reacting it with *n*-butyllithium (*n*-BuLi). This leads to the formation of a Li intercalation compound associated with a widening of the interlayer distance between the individual MoS_2 layers and a charge transfer from n-BuLi to the MoS_2. In contrast to negatively charged graphenides, the resultant material is reasonably stable under ambient conditions and can be dispersed in water. Due to that fact, the preparation of the solvents used for the initial intercalation process is easier in this case. Solvents only have to be dried and not necessarily freed from oxygen. For this purpose, it is recommended to distil and reflux the solvents (e.g. *n*-hexane and cyclohexane) two times over a Na wire under Ar atmosphere prior to the use of the intercalation reagent. Since MoS_2 has long been considered to be unreactive and almost inert even after intercalation [142], Ref. [350] used very aggressive electrophiles: diazonium salts to quench the negative charges on the MoS_2 and functionalize the material. After the final sonication step of the purified intercalate 4-methoxyphenyldiazonium tetrafluoroborate was dissolved in distilled water and added to the dilute yellowish/brownish MoS_2 dispersion dropwise under exposure to light. After addition of only a few drops of reagent, a black precipitate formed. The reaction mixture was stirred overnight and filtered through a 0.2 µm reinforced cellulose membrane filter (Sartorius). Material which passed through the membrane in the first step was collected and filtered again.

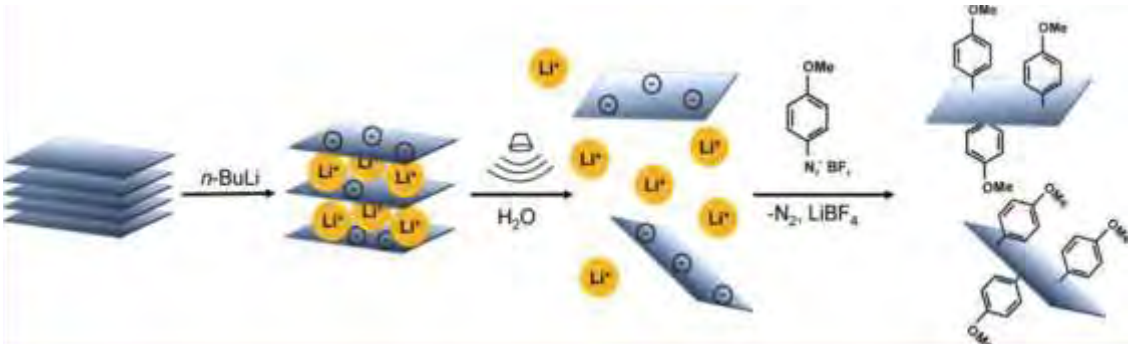

Fig. VIII.17: Schematic of the basal-plane functionalization of MoS_2. After intercalation with n-butyllithium, the negatively charged MoS_2 is dispersed in water by mild bath-type sonication leading to an efficient exfoliation into individual sheets. The charges on the MoS_2 are quenched by the addition of 4-methoxyphenyldiazonium tetrafluoroborate obtaining the functionalized product . Adapted from Ref [350]

Washing with ~100 mL isopropanol to remove organic side-products such as the correspondent biphenyl and washing with distilled water yielded the functionalized MoS_2 product after drying under vacuum (approx. 10^{-2} mbar) at room temperature. By this approach, typically 10-20 atom % of the sulfur bear a functionality [350, 351].

This strategy can be used for the fabrication of MoS_2-templated conjugated microporous polymers (M-CMPs) by growing nitrogen-rich CMPs shells on both sides of 4-iodophenyl-functionalized MoS_2 templates [1181].The synthesis strategy for M-CMPs is illustrated in Fig. VIII.18. First, chemically-exfoliated MoS_2 (CE-MoS_2) was achieved by reacting bulk MoS_2 with *n*-butyllithium (*n*-BuLi) [350, 351, 1181]. Then, CE-MoS_2 was functionalized with 4-iodophenyl diazonium salt under aqueous conditions [350, 351, 1181]. The obtained 4-iodophenyl-functionalized MoS_2 (MoS_2-I) can be well-dispersed in various organic solvents, such as toluene and dimethylformamide. Next, the arylacetylene building block 1,3,5-triethynylbenzene mixed with an aryl di- or trihalide was reacted with MoS_2-I in anhydrous dimethylformamide in the presence of Pd(PPh3)4, CuI and Et_3N under inert atmosphere. This Sonogashira-Hagihara cross-coupling reaction was carried out at 100 ^{o}C for 3 days under vigorous stirring and yielded an insoluble, crude product that was collected by filtration and purified by Soxhlet extraction with THF for two days. Finally, the unique sandwich-like M-CMPs with high specific surface areas and hierarchically porous structure were obtained after vacuum drying. As-prepared porous polymer-MoS_2 sandwiches can be converted into the corresponding hierarchically porous MoS_2/nitrogen-doped porous carbon hybrids by direct pyrolysis the M-CMPs flakes. The hybrids are characterized by high specific surface areas and aspect ratios and showed a promising oxygen reduction reaction (ORR) and supercapacitor performance due to the maximized interfacial interaction between nitrogen-doped porous carbon and MoS_2 layers.

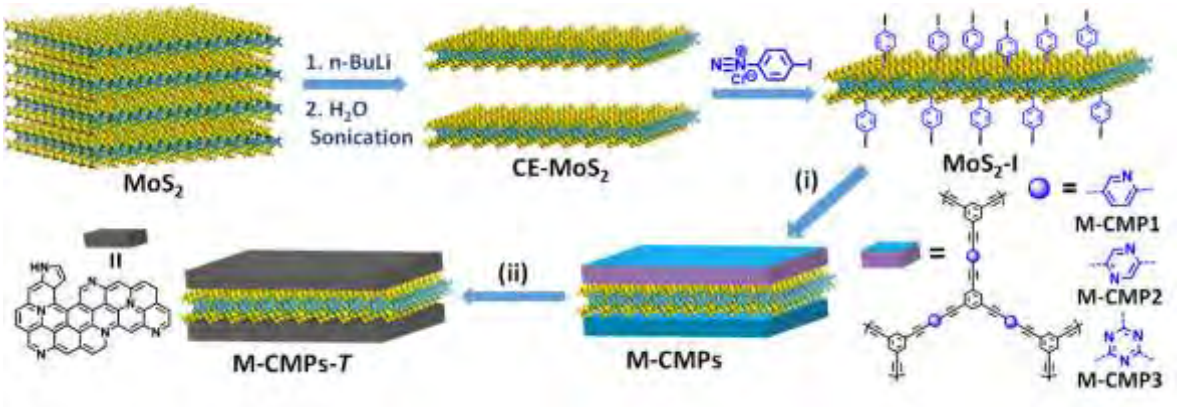

Fig. VIII.18: Idealized formula scheme depicting the chemical exfoliation of bulk MoS_2 and subsequent functionalization with 4-iodophenyl substituents under formation of MoS_2-I as well as the preparation of MoS_2-templated conjugated microporous polymers (M-CMPs) and the corresponding MoS_2/nitrogen-doped porous carbon (M-CMPs-T) hybrids. (i) monomers: 1,3,5-triethynylbenzene and 2,5-dibromopyridine, 2,5-dibromopyrazine, or 2,4,6-trichloro-1,3,5-triazine, argon, Pd(PPh3)4, CuI, Et_3N, DMF, 100 ^oC, 3 days; (ii) argon, heating rate: 10 ^oC min^{-1}, pyrolysis temperature: 700, 800, or 900 ^oC, 2 h.

A pathway towards covalent functionalization of TMDs has been established through the reaction between liquid-exfoliated MoS_2 and various metal acetate salts [1182]. This process is notable as it involves functionalization of the semiconducting 2HMoS_2 polytype. Most literature report functionalization of the metallic 1Tpolytype [1183, 1184]. Generating it requires treatment of the 2H material with *n*-butyllithium, necessitating safety steps when handling this harsh substance. Direct functionalization of 2H TMDs negates the requirement to use this treatment. Furthermore, acetate functionalization of LPE MoS_2 was shown to stabilize the exfoliated flakes in IPA and acetone, rather than having to use toxic solvents such as NMP and CHP [1182]. Dispersions of exfoliated 2H-MoS_2 in IPA (10ml, 0.2 mM) were mixed with a given metal acetate dissolved in IPA ($M(OAc)_2$, 10 ml, 10 mM). This mixture was then sonicated for 30 minutes and the functionalized 2H-MoS_2 was separated and collected by centrifugation and washing [1182].

XPS analysis was performed on the thin films of material formed via vacuum filtration [1182]. The Mo 3d and S 2p spectral regions shown in Fig. VIII.19 demonstrate functionalization of the flakes after treatment with $Cu(OAc)_2$. The Mo 3d core level displays a new doublet associated with MoS_2 shifted to higher binding energies than the unfunctionalized 2H-MoS_2, which arises due to functionalization. The S2p core level exhibits a new spectral feature for the same reasons. Re-dispersing dried functionalized 2H-MoS_2 flakes in NMP totally removed the functional groups from the flakes [1182]. Fig.VIII.19c,f show that the material returns to its original state without any permanent changes in the spectral features; indicating no permanent structural or chemical modification during functionalization with $M(OAc)_2$.

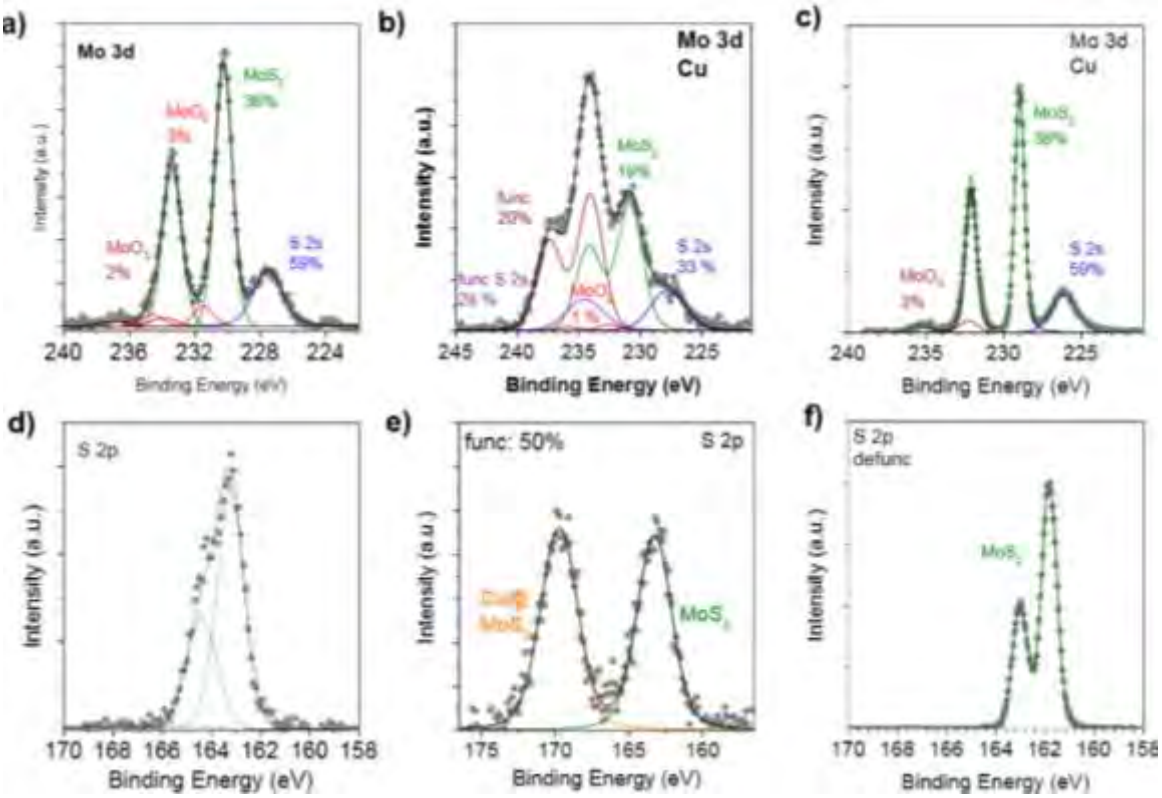

Fig. VIII.19: Fitted XPS Mo 3d and S 2p core level peaks for 2H-MoS_2 reference (a and d), 2H-MoS_2-$Cu(OAc)_2$ (b and e), and defunctionalized 2H-MoS_2-$Cu(OAc)_2$ (c and f). Adapted from Ref. [1182]

The most critical step in the protocol is to provide sufficient energy in the functionalization step, where the liquid exfoliated MoS_2 in IPA is mixed with the acetate salts. This was achieved by additional sonication using a tapered microtip with high local energy input [234]. When using a larger diameter tip (required to produce larger quantities), the degree of functionalization (i.e. the number of S atoms on the surface decorated by the functional group) drops to < 20%. Furthermore, depending on the purity of starting MoS_2 and water content in the IPA, the initial MoS_2 dispersion is sometimes not colloidally stable and the MoS_2 precipitates from the dispersion while leaving a deep blue colored supernatant. This is currently not understood, but likely related to MoO_x impurities in the powder that form complexes with the IPA/H_2O solvent. A stable dispersion can be obtained by again sonication this precipitated MoS_2 in a second sonication step. However, in such cases, the degree of functionalization was again lower than reported.

Noncovalent Functionalization of MoS_2

Perylene functionalization of CVD-grown MoS_2 and WS_2 layers was carried out in a similar manner as for SLG [1095, 1099]. MoS_2 and WS_2 grown on SiO_2 were coated with aqueous perylene solutions creating a non-covalent functionalization. It further was reported that the resulting perylene layer was suited to seed ALD growth of Al_2O_3 on 1L TMD flakes (Fig. VIII. 20) [1185]. The ALD growth directly on TMD flakes, while successful for N>2L, was unsuccessful on 1L. This was attributed

to the selective growth to the electronic structure of 1L-TMDs, and their cleaniness. After functionalization with perylene1 the ALD growth of Al_2O_3 takes place uniformly across the sample. Thus the non-covalent functionalization provides a robust mechanism to seed thin films of dielectric materials on 1L-TMDs, a requirement for many proposed TMD device applications and for further functionalization.

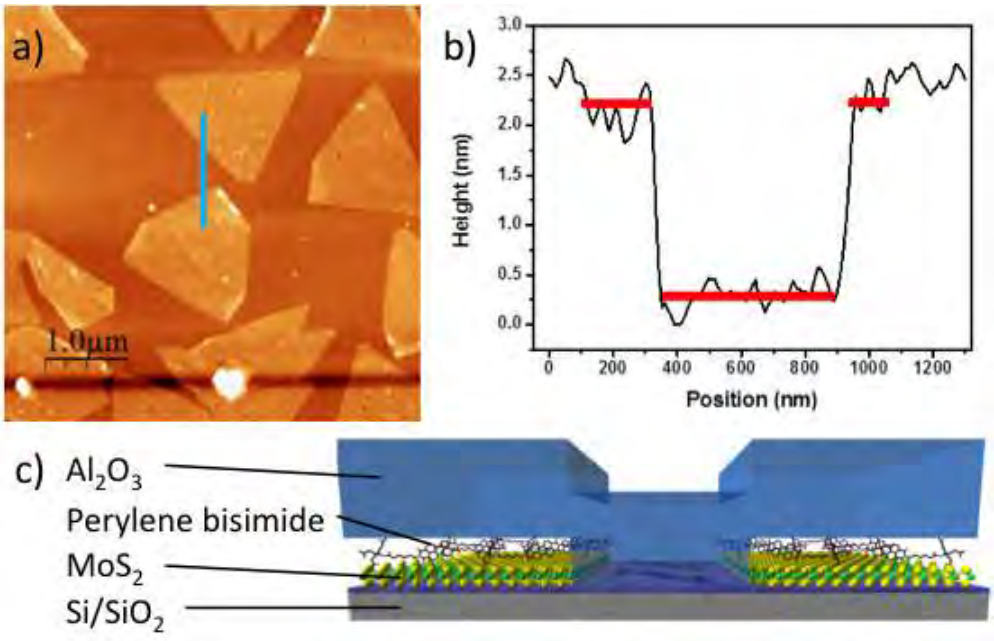

Fig. VIII.20(a) Topography of MoS_2 triangles after 27 cycles of ALD after seeding with a perylene bisimide derivative. The flakes are higher than the surrounding substrate. (b) Line profile along the line marked in (a). The step height is 1.9 nm. (c) Schematic representation of the structure of (a) as indicated by the scan. Adapted from Ref [1185].

IX CHARACTERIZATION METHODS

IX.1 Microscopies

Optical microscopy

Quantitative analysis of the optical microscopy images

Many optical characterization methods rely on the quantitative analysis of the optical microscopy images [1, 1186-1188] [1186-1189]. One can extract the contrast difference between GRM and substrate by analysing the red, green and blue channels of the digital images. For each camera channel the reflected intensity at the substrate and GRM can be measured and the contrast difference can be directly calculated.

Fig. IX.1 (a-l) shows an example of a collection of epi-illumination (the illumination light is reflected by the surface of the sample and then detected) mode optical microscopy images of MoS_2 flakes with different number of layers (previously determined by AFM) where the thickness dependent colour is evident. The contrast difference in the optical images for the red, green and blue channels, extracted for flakes with different thicknesses requires an initial calibration, using an alternative thickness determination method, and it might slightly depend from one experimental setup to another one as it depends on the spectral response of the employed digital camera, the microscope lamp emission spectrum, and the numerical aperture of the microscope objective.

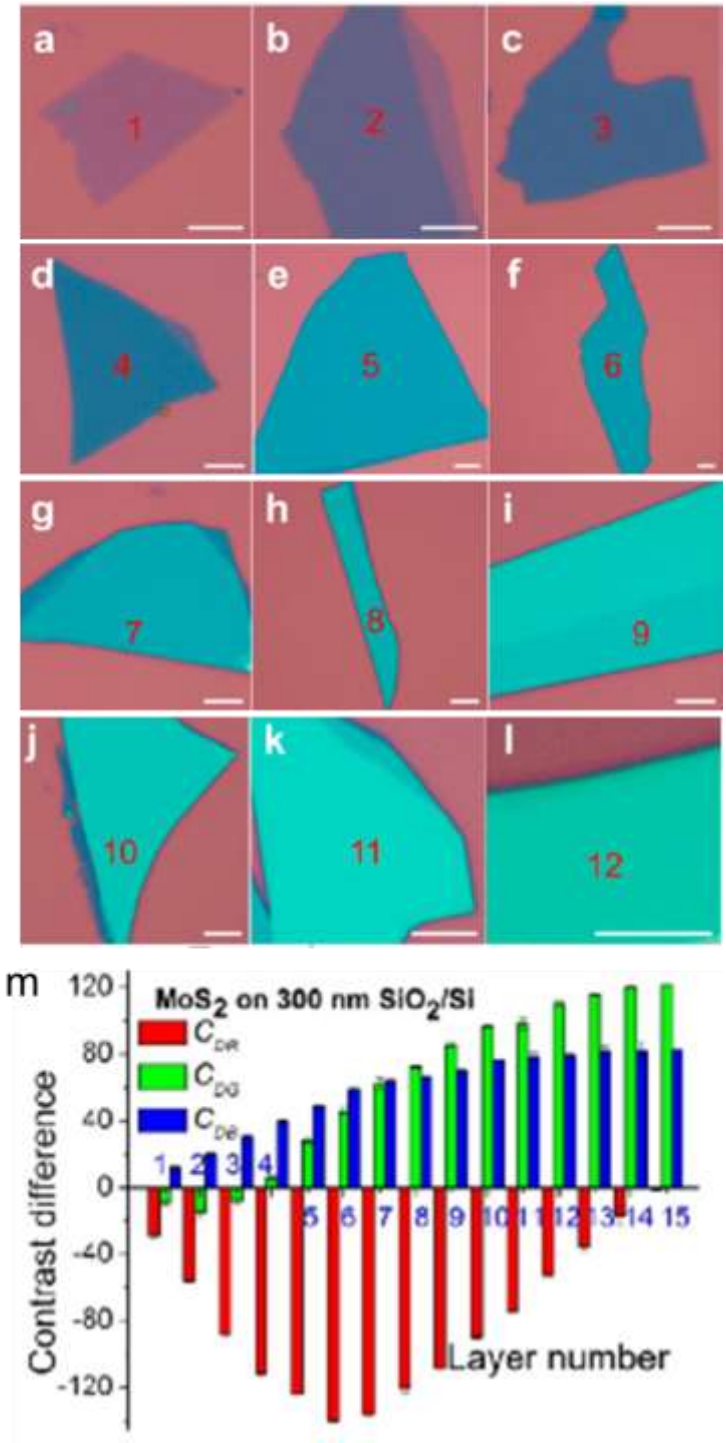

Fig. IX.1. (a-l) Color optical images in epi-illumination mode of MoS_2 flakes with different number of layers (1 layer to 12 layers) deposited on a 300 nm SiO_2/Si substrate. The scale bar is 5 µm. (m) Thickness dependent contrast difference extracted from the red, green and blue channels. Fig. reproduced from Ref. [1187] .

Multispectral imaging

Multi-spectral imaging characterization of GRMs was originally introduced by Blake et al. [1190] Casiraghi et al. [1191] and Roddaro et al. [1192] to identify N for graphene flakes deposited on SiO_2/Si substrates and it has been rapidly adapted to characterize and identify other GRMs [1187, 1193-1197]. The method involves the acquisition of optical images using narrow bandpass filters to select the illumination wavelength. The optical contrast, *C*, is typically extracted from these images in order to obtain a quantity that does not depend on the illumination intensity. *C* is typically defined as:

$$C = \frac{I_{2D} - I_{substrate}}{I_{2D} + I_{substrate}} \quad \text{(IX.1)}$$

where I_{GRM} and $I_{substrate}$ are the reflected intensities from GRM and substrate respectively. A quantitative analysis of the optical contrast can be done in the basis of a Fresnel law based model, where the system is modelled as a stack of different optical media under monochromatic illumination in a normal incidence configuration [1190, 1191, 1198]. Hereafter the subscripts 0, 1, 2 and 3 will be used to refer the media air, GRM, SiO_2 and Si. First we focus on the case where only air, SiO_2 and Si media are considered. The Si layer is modelled as a semi-infinite slab whose optical properties are determined by its complex refractive index $\tilde{n}_3(\lambda)$ that strongly depends on the wavelength (λ) [1190, 1191, 1198]. The SiO_2 layer, with a thickness d_2, is modelled with its refractive index $n_2(\lambda)$ that also depends on the wavelength [1190, 1191, 1198].

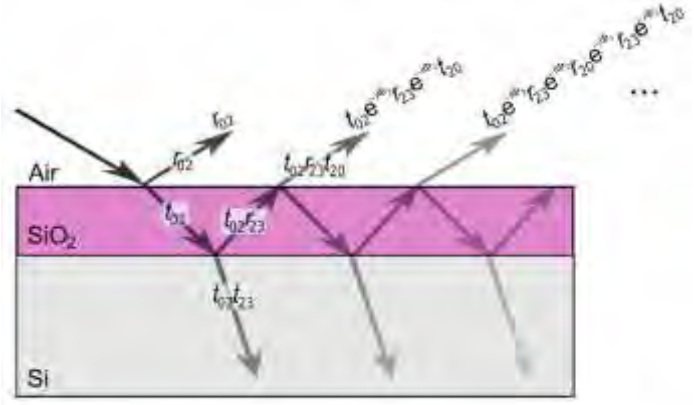

Fig. IX.2: Sketch of the optical beam path transmitted and reflected at the different interfaces in a multilayer structure air/SiO_2/Si to understand the role of the different optical paths on the optical contrast. Adapted from Ref. [1199]

The total amplitude of the light beam reflected by the SiO_2/Si substrate (*r*) can be obtained from the infinite sum of light beams coming from the multiple reflections in the central SiO_2 layer (see Fig. IX.2). Anytime that a light beam reaches an interface the Fresnel equations are applied, considering both the real and the imaginary part of the refractive index and accounting for the phase shift between the different light beams. E.g. the phase shift between the reflected beams at the air/SiO_2 and those transmitted through the air/SiO_2 (going across the SiO_2 then getting reflected at

the SiO_2/Si interface then going across the SiO_2 and finally being transmitted at the SiO_2/air interface) is $2\Phi_2$ (see the sketch in Fig. IX.2) with $\Phi_2 = 2\pi n_2 d_2 \cdot \cos(\vartheta_2)/\lambda$. All this being considered, the total amplitude of the reflected light by the SiO_2/Si substrate (r) is:

$$r = r_{02} + t_{02} e^{-2i\Phi_2} r_{23} t_{20} \left[1 + \sum_{m=1}^{\infty} \left(r_{23} r_{20} e^{-2i\Phi_2} \right)^m \right] \tag{IX.2}$$

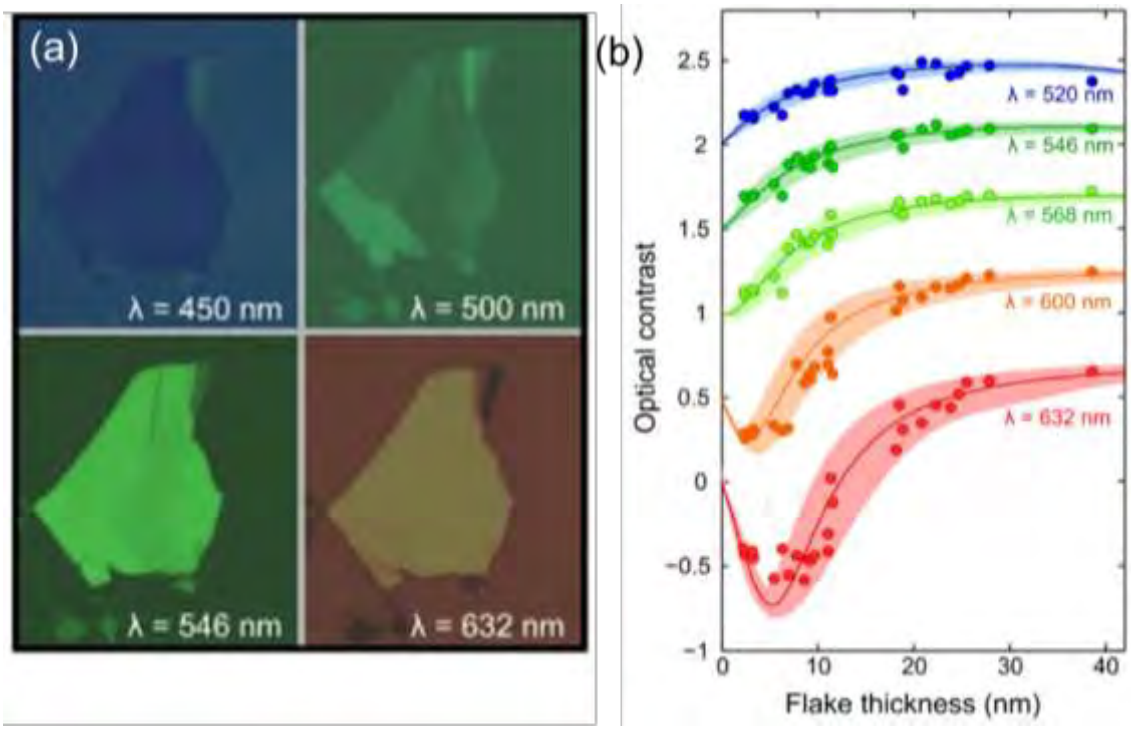

Fig. IX.3: (a) Optical images of a $TaSe_2$ flakes with regions with different thicknesses, acquired at different wavelengths. (b) Optical contrast as a function of thickness for different wavelengths. The experimental data (circles) can be reproduced by the Fresnel law based model by using the refractive index for bulk $TaSe_2$ (solid lines). Reproduced from Ref. [1187].

where r_{ij} and t_{ij} are the amplitude of the beam reflected and transmitted at the interface between the media i and j. These coefficients r_{ij} and t_{ij} can be obtained directly from the Fresnel law. Considering that $r_{ij} = -r_{ji}$ and $t_{ij}t_{ji} - r_{ij}r_{ji} = 1$ and summing the geometrical series

$$r = \frac{r_{02} + r_{23} e^{-2i\Phi_2}}{1 + r_{02} r_{23} e^{-2i\Phi_2}} \tag{IX.3}$$

Then the intensity of the light reflected by the SiO_2/Si is $I_{substrate} = |r|^2$.

$$I_{substrate} = \left| \frac{r_{02} + r_{23} e^{-2i\Phi_2}}{1 + r_{02} r_{23} e^{-2i\Phi_2}} \right|^2 \tag{IX.4}$$

Under normal incidence assumption this expression is simplified because $r_{ij} = (\tilde{n}_i - \tilde{n}_j)/(\tilde{n}_i + \tilde{n}_j)$ and $\Phi_2 = 2\pi n_2 d_2/\lambda$. When a GRM is placed on the SiO_2/Si substrate, the intensity of the light reflected by the stack can be calculated in a similar way as $I_{substrate}$:

$$I_{2D} = \left| \frac{r_{01}e^{i(\Phi_1+\Phi_2)} + r_{12}e^{-i(\Phi_1-\Phi_2)} + r_{23}e^{-i(\Phi_1+\Phi_2)} + r_{01}r_{12}r_{23}e^{i(\Phi_1-\Phi_2)}}{e^{i(\Phi_1+\Phi_2)} + r_{01}r_{12}e^{-i(\Phi_1-\Phi_2)} + r_{01}r_{23}e^{-i(\Phi_1+\Phi_2)} + r_{12}r_{23}e^{i(\Phi_1-\Phi_2)}} \right|^2 \quad \text{(IX.5)}$$

Although the previous approach is general and it can be applied to stacks with an arbitrary number of media, it might become cumbersome to calculate the intensity of the light reflected by stacks with more than 3 media. The transfer matrix formalism is the most appropriate approach to analyse the light propagation in systems formed by a stack of many different media. From the previous expressions one can deduce that if one determines the GRM thickness (e.g. with AFM) it is possible to use the optical contrast measured at different illumination wavelengths to determine the GRM refractive $\tilde{n} = n - i\kappa$ [1193, 1196, 1200-1202]. On the other hand, if the GRM refractive index is well-known one could determine its thickness directly from the measurement of the optical contrast acquired at different wavelengths with no need of AFM (Fig. IX.3).

Hyper-spectral imaging

In this technique the illumination wavelength is selected with a tuneable light source, based on a halogen lamp and a monochromator, instead of using narrow band pass filters [1203]. Fig. IX.4 shows a schematic experimental setup for transmission mode hyperspectral imaging. Epi-illumination hyperspectral imaging (or reflection mode hyperspectral imaging) can be also done with minimum modifications of the setup [1204].

Hyperspectral imaging is carried out by sweeping the excitation wavelength in steps and acquiring a microscope image of the sample for each wavelength. The acquired images are then arranged forming a Three dimensional matrix, being the first two matrix indexes the *X* and *Y* spatial coordinates and the third index (λ) the wavelength (Fig. IX.4b). Spectral information of a certain sample region can be directly obtained by plotting all the elements of the matrix along the wavelength dimension λ for fixed *X* and *Y* coordinates (Fig. IX.4b). Fig. IX.4c shows two spectra extracted from two regions in the sample: substrate (red) and GRM (blue). The GRM transmittance (*T*) can be obtained by dividing both spectra: $T = I_{GRM}/I_{subs}$ (inset in Fig. IX.4c), where I_{GRM} is the intensity acquired on the GRM and I_{subs} that of the substrate. The absorbance *A* can be obtained from the transmittance *T* as: $A = -\log_{10}(T)$.

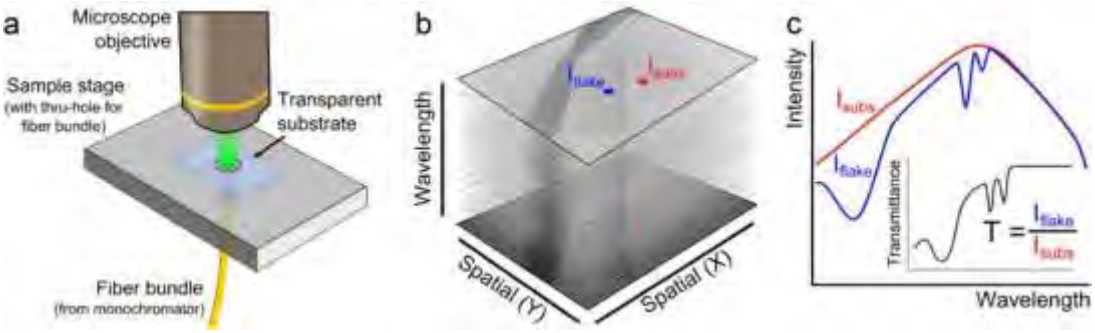

Fig. IX.4. (a) Schematic setup for transmission mode hyperspectral imaging. (b) Data acquisition process: optical images are acquired while the wavelength is varied. The resulting dataset is arranged in a 3d matrix. (c) Spectral information extracted from the dataset. The inset shows a transmittance spectrum obtained by normalizing the GRM spectrum to that of the substrate. Adapted from Ref. [1203]

Fig. IX.5 shows an example of characterization of GRM by means of hyperspectral imaging. The panels (a) to (f) show transmission mode optical images of a MoS_2 flake for different wavelengths. From the collection of hundreds of images from 400 to 1000 nm one can extract the absorbance, Fig IX.5g.

Micro reflectance/transmittance spectroscopy

In this method one illuminates the sample with white light and the reflected/transmitted light is analysed with a spectrometer (see Fig. IX.6) [1200, 1201, 1205-1208]. The acquired reflection/transmission spectra can be analysed with the Fresnel law to extract information on the GRM optical properties. In Fig.IX-7 the refractive index of 1L-MoS_2 is determined by fitting the measured optical contrast on different SiO_2/Si substrates to the Fresnel law based model, using the refractive index of 1L-MoS_2 as a fitting parameter (panel a) [1200]. The resulting values of the real and imaginary part of the refractive index are displayed in Fig. IX.7b and compared with bulk MoS_2.

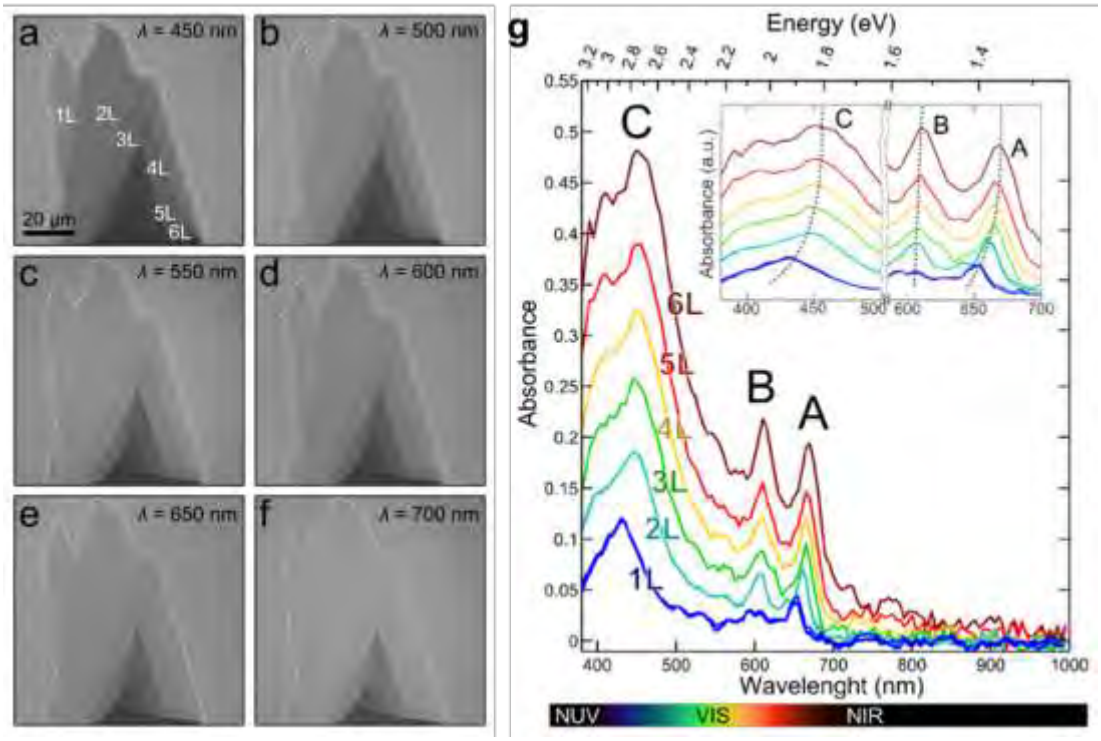

Fig. IX.5. (a)-(f) Transmission mode images of a MoS_2 flake acquired at different wavelengths, selected with a tuneable monochromatic light source. (g) Absorbance vs. wavelength, extracted from the sequence of MoS_2 images on a flake with regions of different thicknesses (N=1-6), for different wavelengths. Adapted from Ref. [1203]

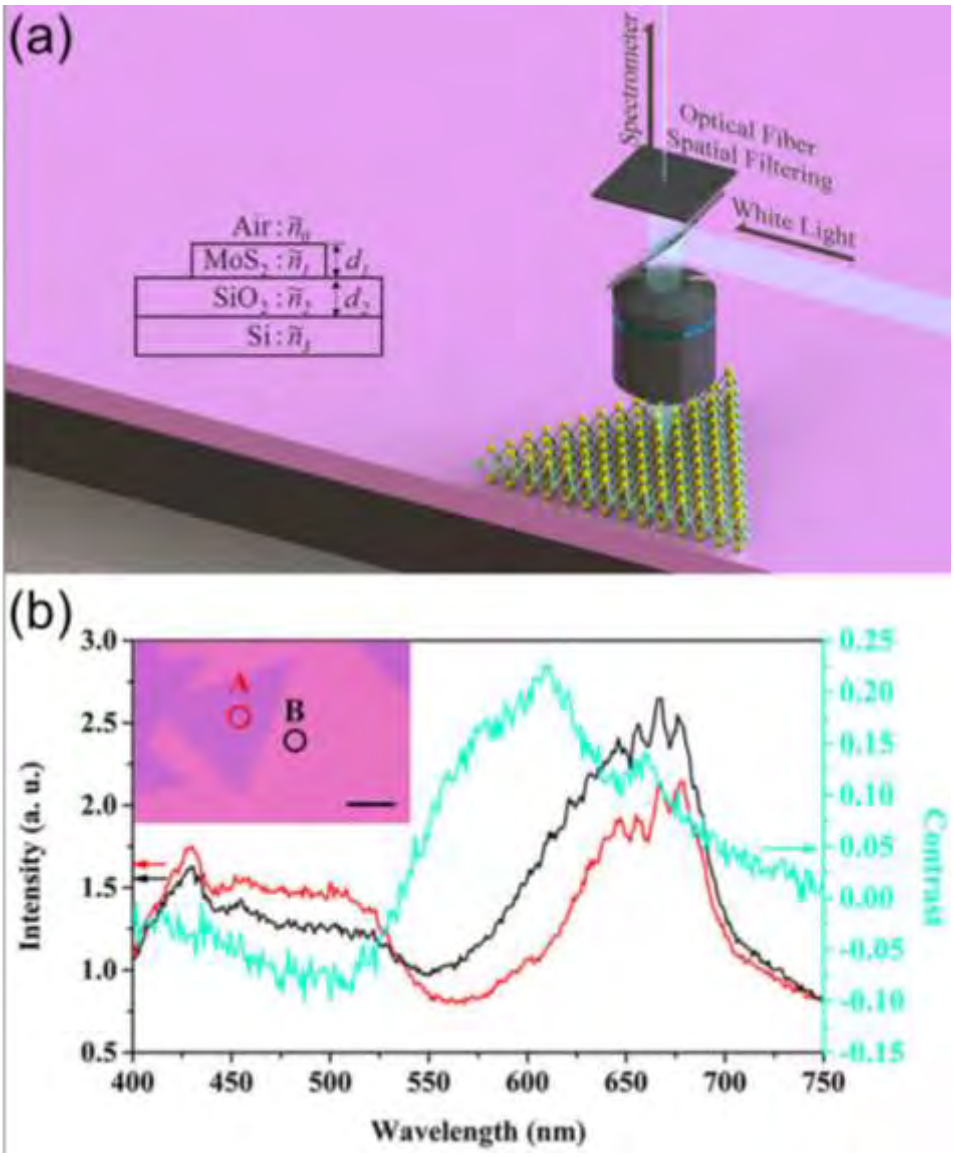

Fig. IX.6. (a) Setup to characterize GRMs with micro-reflectance. (b) CVD grown MoS_2 studied by micro-reflectance. Two spectra are acquired on MoS_2 (A) and on the SiO_2/Si substrate (B) and the optical contrast is extracted from them. Adapted from Ref. [1200].

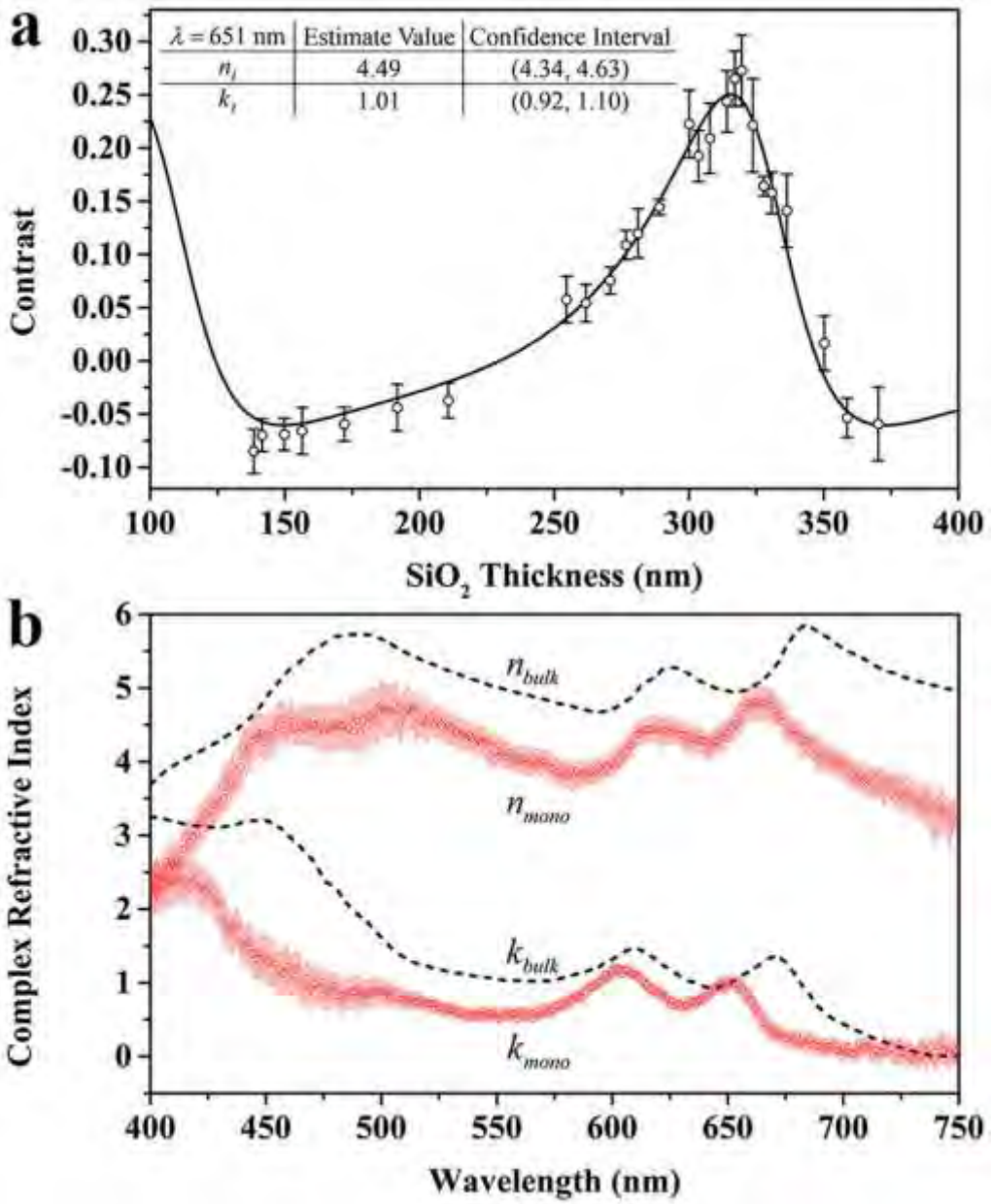

Fig. IX.7. (a) Optical contrast for 1L-MoS_2 on SiO_2/Si substrates with different SiO_2 thicknesses. The datapoints are fitted to a Fresnel law using the refractive index of 1L-MoS_2 as fitting parameter. (b) The obtained refractive index of 1L-MoS_2, compared with the bulk value. Adapted from Ref. [1200]

One can also obtain the dielectric functions from the measured reflectance spectra by means of a Kramers-Kronig constrained analysis of the spectra of GRMs on transparent substrates [1207]. From the resulting dielectric function, the refractive index can be calculated [1207]. Fig. IX.8 shows an example of determination of the dielectric function from the reflectance spectra of 1L of four TMDs. From the resulting dielectric function, the absorption spectra refractive index can be calculated [1207]. Fig. IX.8 shows an example of determination of the dielectric function from the reflectance spectra of 1L of four TMDs.

Another feature of the micro-reflectance/transmittance measurements is their speed, each spectrum can be acquired in ~1s, allows one to characterize large scale samples (e.g. films grown by

CVD, centimetre square in area) at hundreds of different locations to get an insight about uniformity [1201]. Fig. IX.9 shows a differential reflectance spectrum acquired at one position on a 1L-MoS_2 epitaxially grown on sapphire. It also plots the histograms of the energy and FWHM of the A and B excitons measured at 550 different locations to characterize the sample homogeneity.

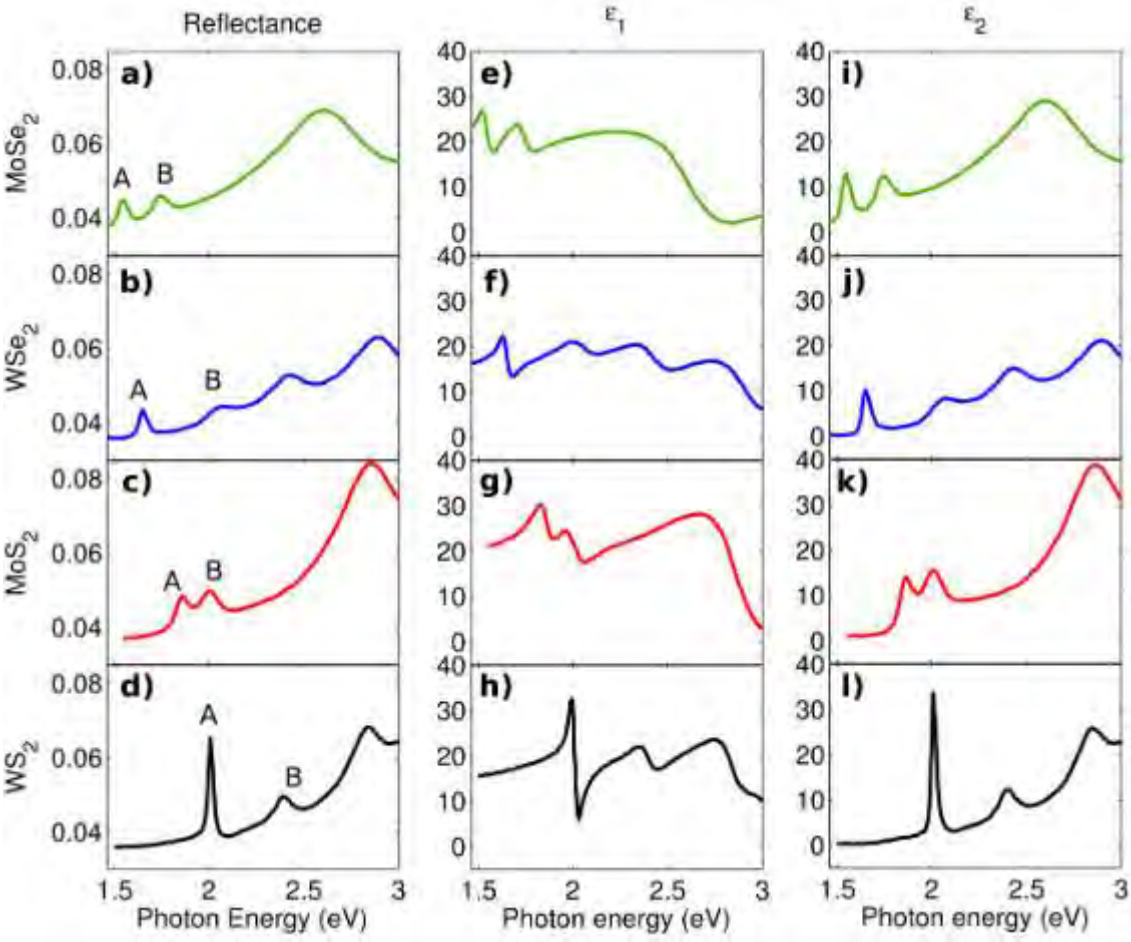

Fig. IX.8. (a-d) Reflectance spectra for 1L-$MoSe_2$, WSe_2, MoS_2, WS_2. (e-h) Real part and (i-l) Imaginary part of the dielectric function. Adapted from Ref. [1207].

Comparison between multispectral, hyperspectral and micro-transmittance

Fig. IX.10 compares different optical microscopy characterization methods, studying the same system: multi-spectral, hyper-spectral and micro transmittance of 1L-, 2L- and 3L-MoS_2 [1193, 1203, 1208]. Table I compares the area characterized, the spectral resolution, and the time to carry out one measurement. This shows that micro transmittance/reflectance is a powerful tool to perform fast measurements in one spot of the sample, due to its high spectral resolution and low measurement time. Moreover, as discussed in section IX.1.1.4 the short measurement time of micro transmittance/reflectance allows one to perform point measurements at hundreds of different locations in the sample [1201]. Multi-spectral and hyperspectral imaging are very interesting to study large areas as in one shot a portion of ~10000 μm^2 of the sample can be measured at once allowing for the acquisition of spatially resolved maps with diffraction limited spatial resolution [1209].

Table IX.1. Comparison between different methods to measure the GRM optical properties.

Method	**Area**	**Spectral resolution**	**Measurement time**
Multi-spectral	~10000 μm^2	~20-100 nm	10-30 min
Hyper-spectral	~10000 μm^2	~1-5 nm	30-60 min
Micro transmittance	~1-4 μm^2	~1 nm	~0.1-5 s

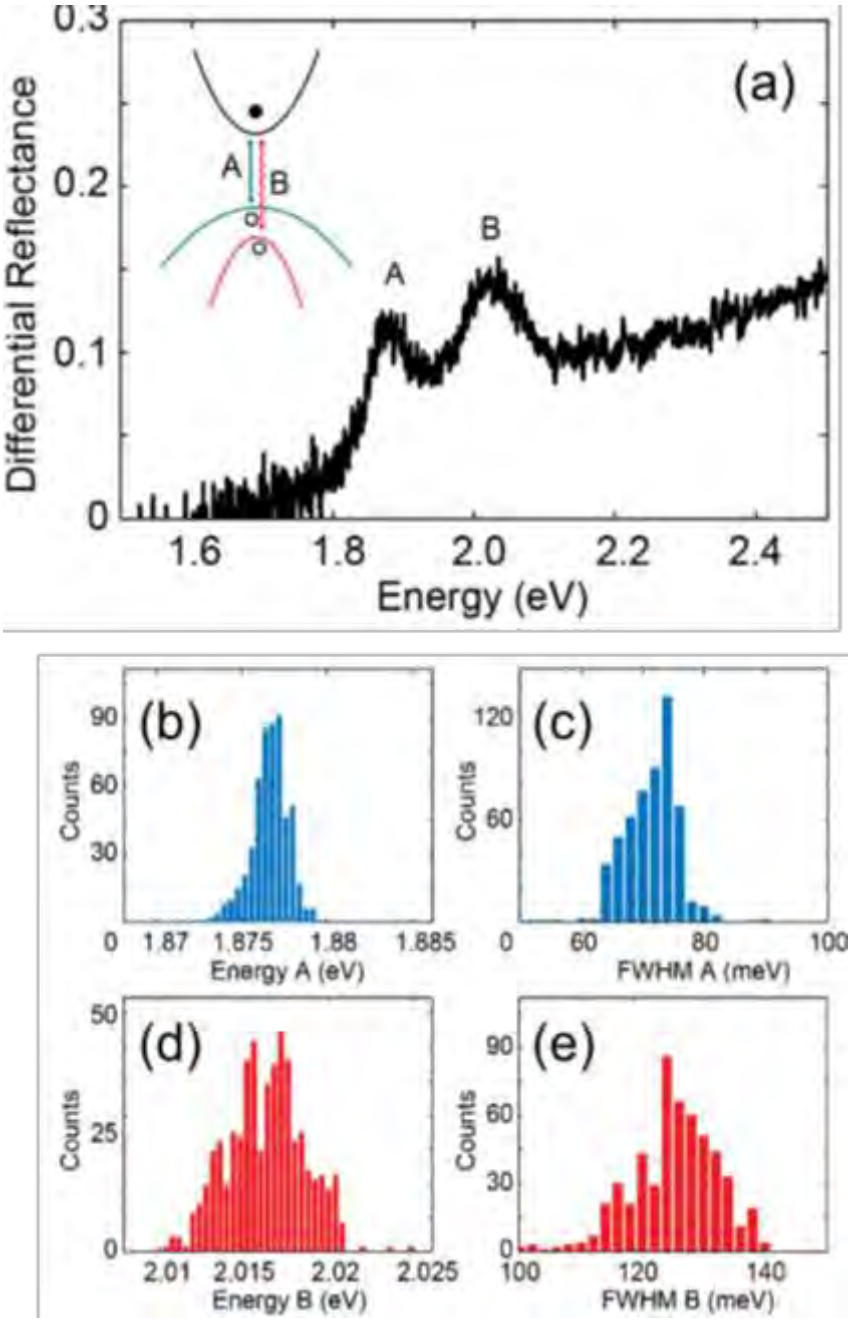

Fig. IX.9. *(a) Differential reflectance of 1L-MoS_2 grown on Sa. (b,c) Histograms of A and B exciton energy for 550 flakes. (d,e) Histograms of FWHM of A and B excitons. Adapted from Ref.* [1201]

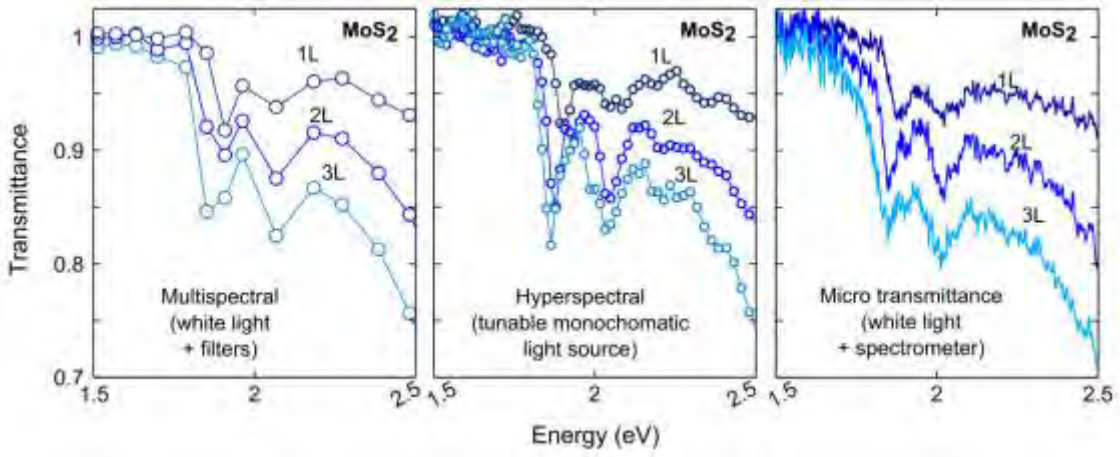

Fig. IX.10. Comparison between different methods to measure the optical properties of 1L, 2L,3L-MoS_2). In multispectral imaging narrow bandwidth filters (10 nm FWHM) are used to select the wavelength (the wavelength resolution is limited by the number of filters employed). In hyperspectral, the illumination is carried out through a white light source connected to a monochromator (2-3 nm of wavelength resolution). In micro-transmittance, white light is collected through an optical fiber (as a confocal pinhole) and sent to a CCD spectrometer (~1 nm of wavelength resolution). Adapted from Ref. [1210].

Atomic force microsocopy

LPE GRMs

AFM provides fast (<10 min/measurement) and reliable characterization of the lateral size and thickness distribution of flakes deposited on different substrates, allowing one to investigate large areas (hundreds of μm^2) and to collect data from hundreds of flakes (Fig. IX.11-c). The size distribution of the sheets can be roughly modelled using a log-normal distribution, as observed experimentally for a range of GRM exfoliated in the liquid including graphene [163], boron nitride[1211], MoS_2 [170], WS_2 [171], GaS [173] and black phosphorus [175]. More extensive statistical studies, performed on GO nanosheets using AFM, SEM and fluorescent microscopy measurements, demonstrated that the fragmentation process can be described by a series of rupture-like breakup events, yielding two different populations of sheets featuring different size distributions [118].

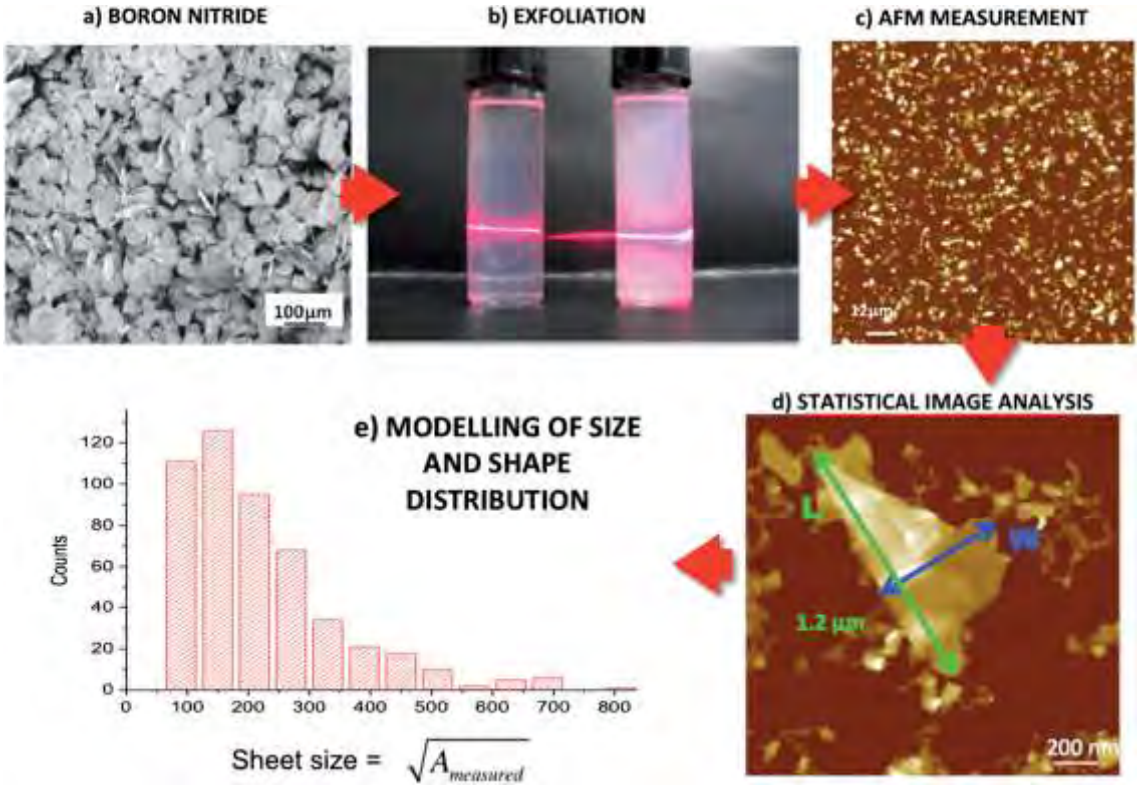

Fig. IX.11 (a) SEM micrograph of bulk BN flakes. (b) Solutions of exfoliated BN in isopropanol. (c) AFM image of BN flakes on SiO_2. (d) Individual BN flake. (e) Histogram distribution of flake sizes. From ref. [1211]

When working with LPE samples for AFM analysis, it is critical to avoid re-aggregation of flakes during solvent evaporation. For this, drop-casting the dispersion on pre-heated wafers (10 µL per 0.5×0.5 cm^2 wafer) is often used. The solvent evaporates and bubbles are formed, resulting in more uniform deposition compared to drop casting at lower T. The wafer should be heated to ~ 50-70°C above the boiling point of the solvent.

In the case of surfactant-based dispersions, it is recommended to dilute the sample with water (rather than surfactant) prior to deposition and wash the wafer thoroughly with water and isopropanol (~ 5 mL each) to remove residual surfactant. Residual surfactant can make the thickness measurements very tedious especially for very small flakes that are more difficult to distinguish from surfactant. In this case, phase images can provide a guide as they usually give a good contrast between different materials. If problems with residual surfactant persist, the substrates can be soaked in water overnight without significant loss of flakes. Deposition from high boiling point solvents such as NMP may be challenging, and re-aggregation and residual solvent or polymerized NMP covering flakes are observed. In order to overcome this problem, it is advisable transferring the material exfoliated in NMP to isopropanol by centrifugation prior to AFM [175].

Si substrates with a 200-300nm SiO_2 enable flakes to be seen with an optical microscope/optical (see previous epigraphs) [1191]. This is a useful guide to identify regions of interest for imaging. Measured, apparent AFM heights of LPE GRMs are overestimated compared to theoretical values due to the presence of residual solvent. In general, accurate height measurements

on inhomogeneous surfaces (such as nanosheets deposited on a substrate) are challenging due to contributions from capillary forces and adhesion, which depend on the material and measurement parameters [1212, 1213]. In addition, crosstalk between electrostatic and topographic signals [1229, 1230] can occur leading to a bias of the height.To overcome these problems and obtain layer numbers from the apparent height values, a step height analysis procedure has been developed in references [171, 175, 224, 1214]. Incompletely exfoliated flakes showing clear terraces are first examined and the height of a various of steps are recorded. These terrace step heights will always be a multiple of the apparent 1L thickness. Depending on the material, the apparent measured SLG height to be 1-2 nm, much greater than the theoretical thickness [173, 175, 224, 230, 1214, 1215]. That the thinnest objects do indeed correspond to SLG can be confirmed by Raman or PL analysis [224, 1214]. The apparent SLG height can then be used to convert the apparent measured AFM thickness to N. For statistical analysis, it is recommended to record the height of at least 100-150 individually deposited flakes. If the thickness varies across the flake, the mean value should be taken. From such statistical analysis, population histograms can be constructed. These are typically log-normal [170, 171, 173, 175, 1211] (also in the case of flake length). If this is not the case, the counting and/or imaging may be biased. For example, if reaggregated rather than individually deposited nanosheets are included in the counting, this will lead to a deviation from the log-normal shape at the thicker end of the thickness distribution histogram. On the contrary, if surfactant and solvent residues are included in the counting, a deviation is obtained on the smaller end of the length distribution histograms. From these histograms and the statistical analysis, the arithmetic number mean for length and thickness is obtained.

Since AFM can be used to measure both nanosheet thickness and lateral dimensions, for each nanosheet of a given thickness, the volume can be estimated as thickness (N)×length(L)×width(w). This allows for the calculation of the volume-fraction-weighted mean layer number, $\langle N \rangle_{Vf} = \sum N^2 LW / \sum NLW$, where the summations are over all nanosheets. This is an alternative measure of nanosheet thickness which reflects the fact that mass tends to be concentrated in thicker nanosheets (the difference between arithmetic and volume fraction weighted mean is akin to the difference between number-average-molecular-weight and weight-average-molecular-weight in polymer physics [1216]). Arithmetic and volume fraction weighted mean values are typically related linearly, therefore both are an adequate measure of thickness [227].

Conductive SPM, like Kelvin probe microscopy (KPM), beside imaging capabilities, can be used to investigate charge transfer in exfoliated GRM films [267] , while conductive AFM, providing localized current injections, can be used to locally modify the GRM chemistry, e.g. directly drawing conducive paths in GO films on SiO2 [1217].This can also be used to probe other electronic properties of GRM, such as piezo-electric effects [1218].

Grown and transferred GRMs

When referring to growth materials (see section IV for Graphene grown on SiC) or Section V (Graphene grown by CVD techniques), measured heights in SLG can be affected also by artefacts (i.e. crosstalk between electrostatic and topographic signals [1219, 1220] or can be overestimated due to the presence of adsorbates between the substrate and the monolayer [1221]. By combining two of the most employed measuring modes (contact and dynamic modes), these can be minimized and more accurate height values obtained. Recording secondary signal channels such as phase (in dynamic mode) or lateral force (in contact mode) is useful in revealing information such as different local mechanical and/or electrical properties [1222] or different polymorphic structures [1223] sometimes difficult to detect, or even hidden, in topographic images [1219-1221, 1223]. Dynamic and contact modes measurements can be performed at RT, purging the sample chamber with N_2 to decrease the relative humidity and minimize capillary forces between tip and sample surface. Details about measuring modes in AFM can be found in Refs. [1224, 1225].

Fig. IX.12 shows representative images of graphene layers grown on different substrates acquired in dynamic mode. In this mode, which employs the oscillation amplitude as feedback parameter [1224], the durability of the AFM probes (i.e. tip sharpness) is usually larger than in contact mode, since the tip gently [1226] taps the surface during the scanning [1222, 1227]. Probes with nominal force constant values~3nN/nm and resonance frequencies~75kHz are used. The most characteristic features in these topographic images are the pleats, commonly referred to as wrinkles, Fig. IX.12. These correspond to pleated/folded SLG due to released stress caused by the differences in the thermal expansion coefficients between SLG and the substrate, during cooling after growth [1228, 1229], or to local accumulation of carbon material at defects between coalescing grains of different orientation [583]. The maximum scanned areas are limited by the morphology of the substrate. In Cu foils this is usually<5×5μm^2, due to the high overall roughness that can exceed several hundreds of nm for those areas . For epigraphene on SiC, the scanned area is only limited by the piezo range thanks to the flatness of the SiC wafer [579, 583] (for chemical mechanical polished on-axis wafers).

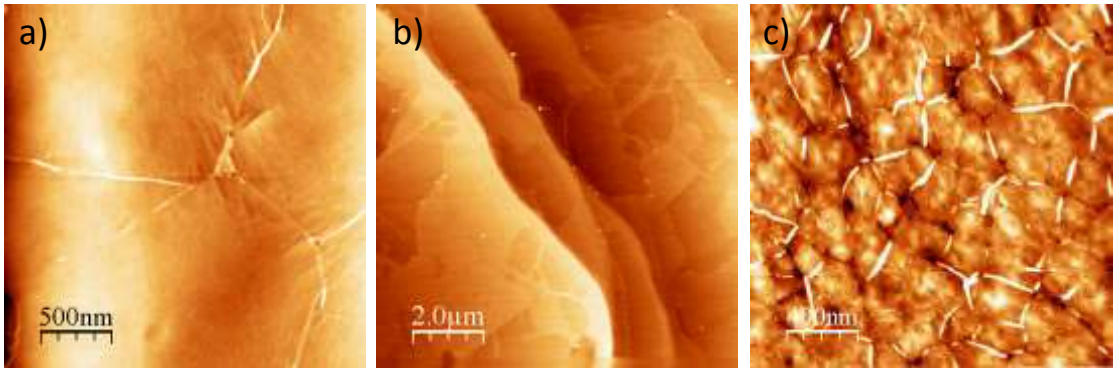

Fig. IX.12: AFM topographic images measured in dynamic mode of SLG grown on a) Cu foil by PDV, b) SiC(0001 by CVD, c) quartz by remote electron cyclotron resonance plasma assisted chemical vapour deposition r-(ECR-CVD) [816] z-scale: 0-12nm.

In dynamic mode, phase images can be acquired simultaneously with topography. Phase contrast is generally ascribed to differences in local energy dissipation and can reveal local mechanical and/or electrical properties [1222, 1227]. As shown in Fig.IX.13, this signal can be very useful to identify areas of different thickness. Top and bottom images in Fig. IX.13a illustrate this case, where circular brighter patches corresponding to BLG areas are distinguished in phase imaging due to their different dissipative properties arising from mechanical and electrostatic difference as a function of N [1230]. Damaged areas in transferred layers (Fig. IX.13b) or covered areas in sub-SLG growth (Fig. IX.13c) can be identified in phase images. However, phase images can also be misleading since the contrast measured is very sensitive to the measuring parameters (oscillation amplitude and control setpoint [1231, 1232]). This is shown in Fig. IX.14, where phase contrast can be turned on and off at will, and even reversed, by changing the measured amplitude. There is no fixed recipe that ensures a good phase contrast, and tuning of the measuring parameters is necessary. Small amplitudes and amplitude set-points>50% of the cantilever free amplitude usually enhance the phase contrast [1232]. The main disadvantage of using dynamic mode stems from the possible crosstalk arising between tip and sample surface. This is particularly critical in heterogeneous surfaces, with areas presenting different mechanical, electrostatic and/or hydrophobic/hydrophilic nature, and can lead to wrong N determination [1219, 1233]. This is illustrated in Fig. IX.15 graphene on quartz at submonolayer coverage. The thickness of the flakes measured in dynamic mode is~3nm, almost twice that in contact mode. This is due to the influence of uncompensated electrostatic forces, particularly affecting samples grown on insulating substrates. Ref. [1219] suggested to use KPM to avoid this problem [1230]. However, when dealing with insulating substrates, like in Fig. IX.15, it is not so straightforward, and the alternative is switching to contact mode (Fig. IX.15b). In contact mode, the lifetime of the probes is usually shortened compared to dynamic mode [1224] (tip radius increases after successive scans and resolution worsens), but height artefacts as those shown in Fig. IX.15 are seldom encountered. Commercial probes of low force constant (0.05-1nN/nm) are used to minimize damage to the sample. Similar to the dynamic mode, secondary signals can be recorded when measuring in contact [1234]. Lateral force imaging can reveal differences in friction between tip and surface [1234]. This is particularly interesting GRMs since they usually present a low (below 0.1) friction coefficient [1235], which yields images like Fig. IX.16.

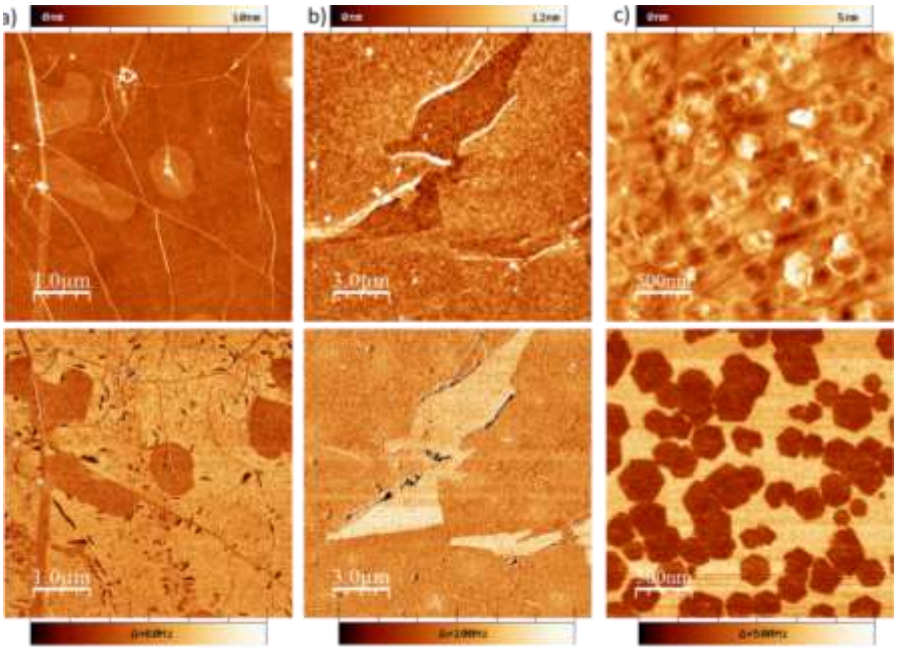

Fig. IX.13: Simultaneous topographic (top row) and phase (bottom row) AFM images in dynamic mode of a), b) CVD-graphene transferred to SiO_2. c) flakes grown by r-(ECR-CVD) on quartz at submonolayer coverage.

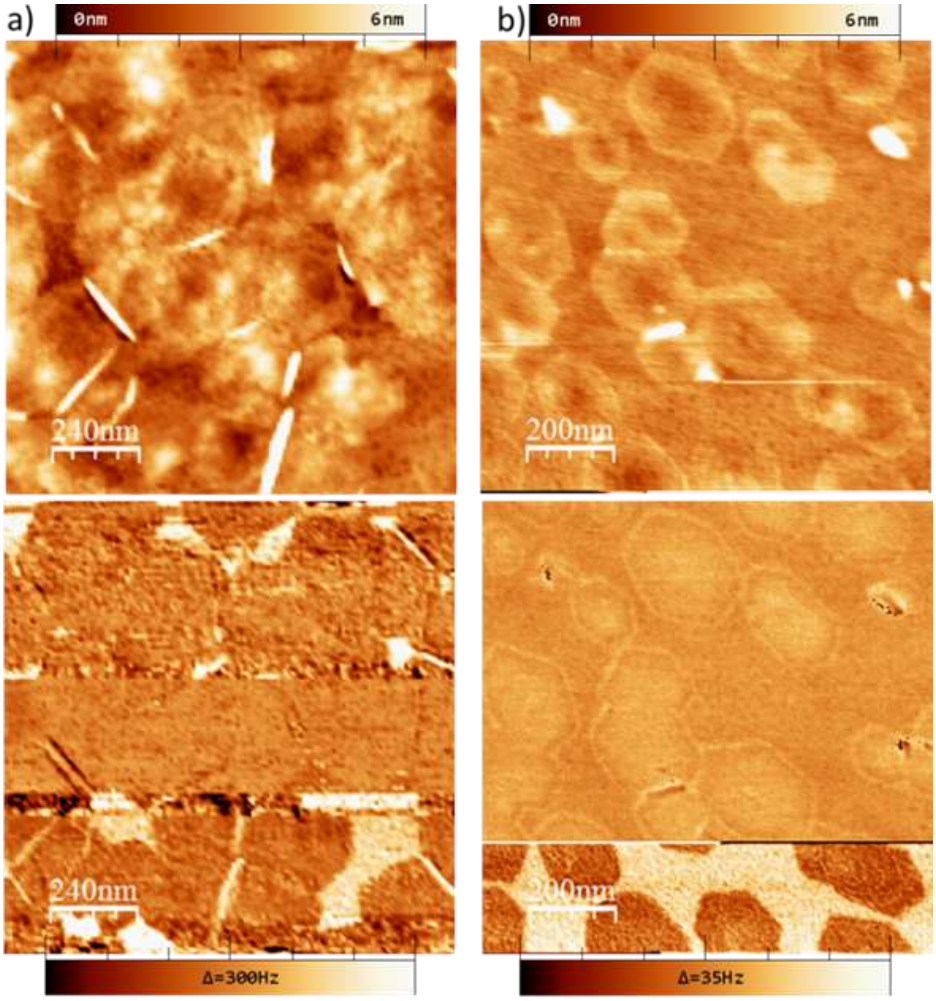

Fig. IX.14: Simultaneous topographic (top row) and phase (bottom row) AFM images measured in dynamic mode of graphene flakes grown by r-(ECR-CVD) on quartz at submonolayer coverage. a) Phase contrast between graphene and substrate disappears in the center of the image after changing the amplitude setpoint. b) Phase contrast between graphene and substrate is reversed at the bottom of the image by increasing the amplitude setpoint.

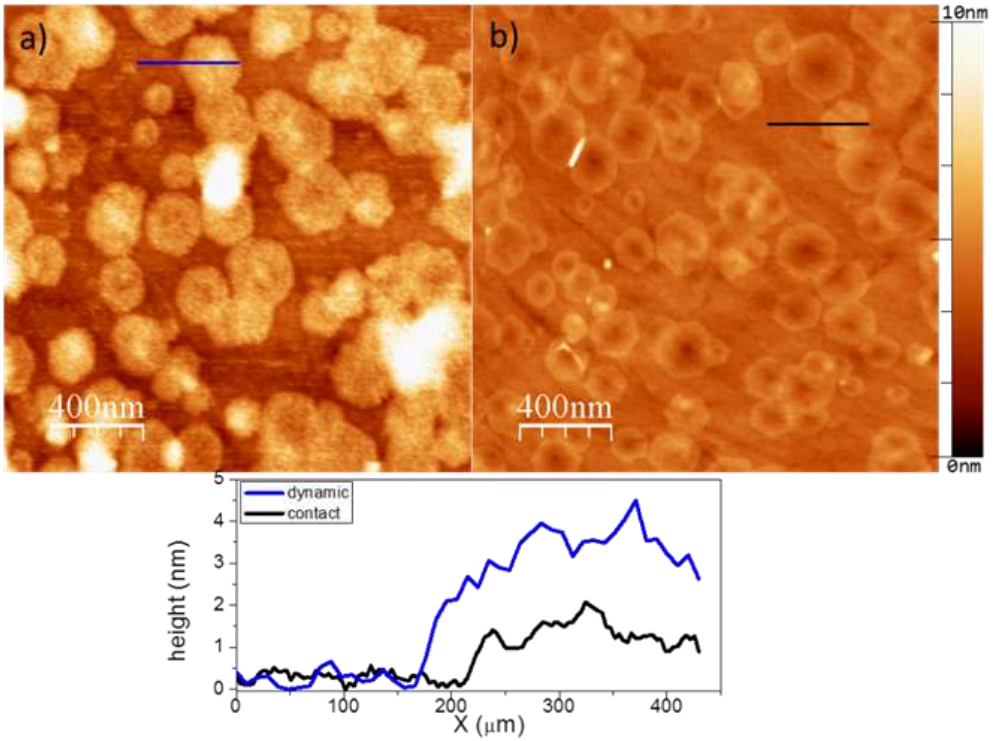

Fig. IX.15: Topographic images of graphene flakes on quartz measured in (a) dynamic and (b) contact mode. Bottom: height profiles from the corresponding lines marked in the above images. The thickness measured on the same sample is different, depending on the mode used.

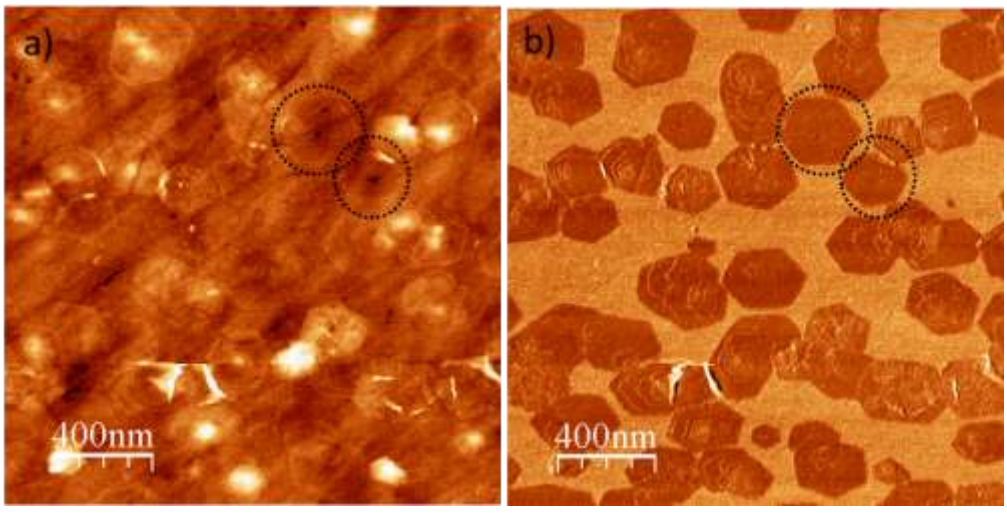

Fig. IX.16: Simultaneous a) topographic and b) lateral force images of graphene flakes on quartz substrate measured in contact mode. Dotted circles marked flakes location, hardly distinguishable in topography but clearly resolved in lateral force images.

The SLG areas are distinguished in lateral force images, facilitating flakes location, coverage quantification and size analysis. With lateral force images it is also possible to visualize the internal structure of SLG grains, masked in topographic images due to surface roughness. In Fig. IX.16, lateral force images reveal the multilayer structure of some flakes.

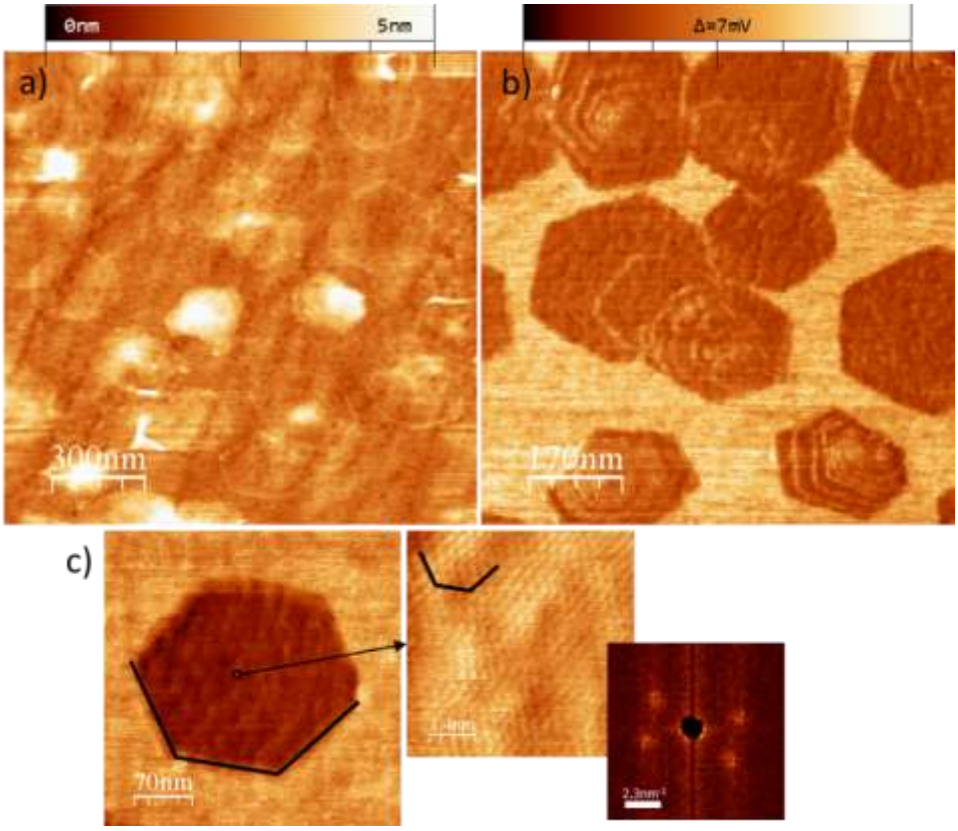

Fig.IX.17: Simultaneous a) topographic and b) lateral force images of graphene flakes on quartz in contact mode. The multilayer structure of some flakes can be distinguished in lateral force images. c) High resolution lateral force image. Right: high resolution image acquired at the marked area. Inset: Fas-fourier transform (FFT) of the high-resolution image to better observe the lattice periodicity.

To better visualize these internal features in graphene flakes, soft tips (0.05nN/nm) and forces between 5nN and 10nN are recommended to avoid graphene wear [1231]. Lattice-resolved lateral force imagescan also reveal the lattice periodicity, Fig. IX.17. To acquire these images, small scans are performed (5-20nm lateral sizes), at frequencies~2-3Hz, with low feedback parameters. Applied forces are~5-15nN. These images do not correspond to true atomic resolution like routinely measured in STM, but lattice orientation and average lattice parameters can be determined.

The AFM tip can also be used to displace the samples. Ref. [816] swept the tip to determine N in fully covered samples. This should be used as last resort, after morphological characterization,

since the tip can be irreversibly damaged due to the high (above 100nN) forces needed to remove the material. This damage can be visualized by recording force-distance curves prior and after sweeping. Fig. IX.18a compares these two curves, and shows that adhesion is one order of magnitude larger after the experiment. This is mainly due to the increase in tip radius, which translates in a worsening of the resolution [1236, 1237]. Taking this into account, sweeping experiments should performed as follows. 1) an area is scanned either in dynamic or contact mode to check the morphology prior to sweeping. 2) contact mode is selected, and the same area (2-5µm lateral size) is repeatedly scanned while increasing the scan rate (5-10Hz), decreasing the number of points (256/128) and increasing gradually the applied force. By controlling the topography and lateral force signals, one can detect the onset of the removal of the material. Once the critical applied force is reached, the scanning is repeated during several images to ensure the complete displacement of the material. 3) To visualize the swept area it is recommended to switch to dynamic mode, to avoid spreading the accumulated material at the edges of the scanned area. To acquire final image is better if the scan is performed at 90°, since debris are accumulated at the lateral edges (fast scan direction). Fig. IX.18b summarizes the results of this procedure.

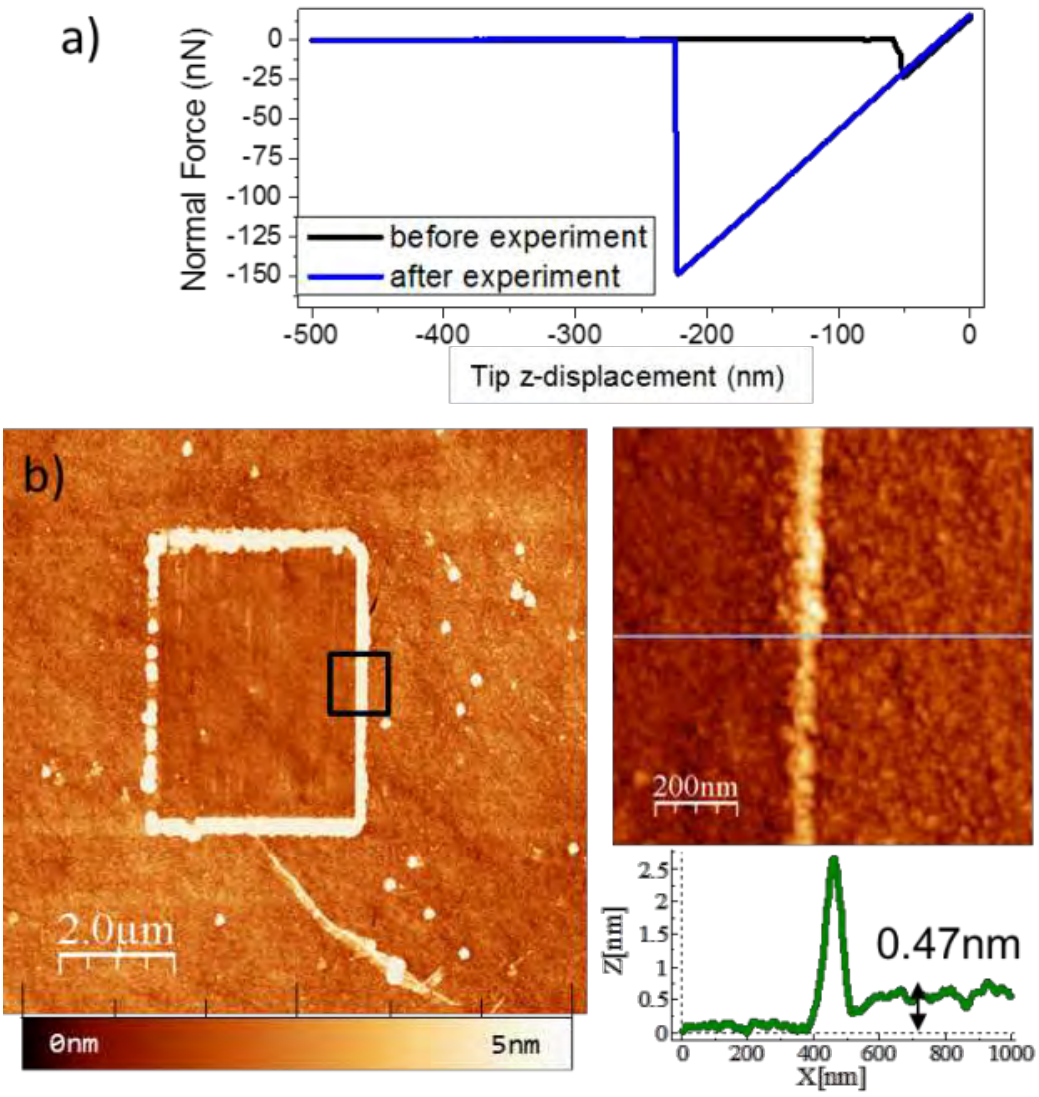

Fig. IX.18: a) Force versus distance curves acquired before (black) and after (blue) sweeping. Only the retract branch is plotted to better visualize the increase in the adhesion force. b) Topographic image showing the rectangular area where SLG was removed. From line profiles taken across the edge, the thickness can be obtained as in as pointed out scanning the inset in b)

Depending on the applied force, the material swept by the tip can be either the contaminant layer adsorbed on SLG exposed to air, if forces are restricted to few nN, or the complete layer for forces up to hundreds nN.

KPM can give information on thickness, layer-dependent distribution of charges, electrical potential and work function [1238]. Measurements are performed in dynamic mode, using the amplitude as feedback channel for topographic determination, and the retrace mode for surface potential acquisition, at a lift distance between 15-20nm. NT-KP tips from Next-Tip S.L. provide very good resolution for KPM [1239].

Surface potential maps can be used to discriminate between N, Fig. IX.19, for graphene grown on SiC. While the topography image (Fig IX.19a top) is dominated by SiC terraces, a contrast is observed at the step bunches in surface potential images (Fig. IX.19a bottom), a fingerprint of the presence of BLG [1238, 1240]. The dark contrast corresponds to SLG and the brighter contrast areas, at the step bunches, indicate BLG. Small islands (300-500nm in diameter) decorating the terraces are assigned to BLG from their contrast. This contrast observed in surface potential as a function of N is ascribed to different work function values for different N, due to different substrate induced doping and different energy dispersions of SLG and BLG [704, 1241, 1242].

When measuring in ambient conditions, aging of the sample can affect the contrast in surface potential. This is shown in Fig. IX.19b, where the same sample is measured after growth and several days later. In addition to the presence of small clusters (2-5nm high) in the topographic image, due to adsorbates, the corresponding surface potential image shows negligible contrast between terraces and steps bunches. This is due to the passivation layer that screens any electrostatic difference between 1SLG and BLG areas. Annealing in controlled atmosphere above 150°C is enough in this case to recover the original KPM signal.

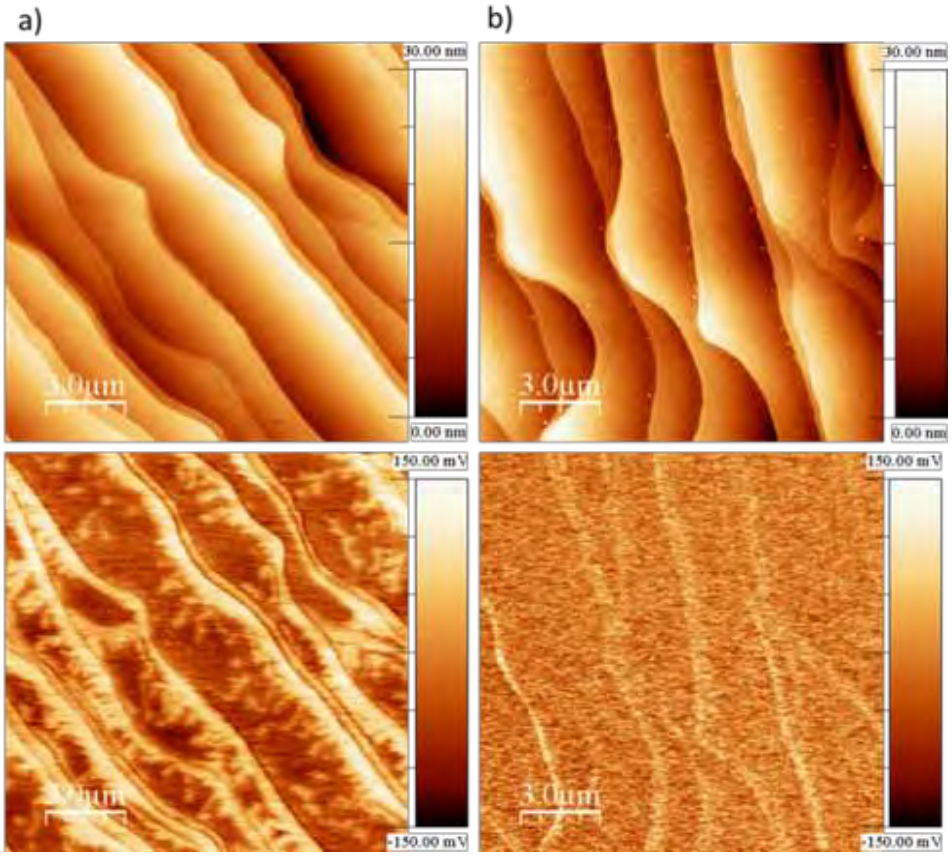

Fig. IX.19: Simultaneous topographic (top) and surface potential (bottom) images acquired on graphene on SiC. a) Measurements performed after sample growth. b) After several days, with the sample kept in ambient conditions

KPM was also employed to investigate the changes in work function upon controlled doping [1243]. By definition, the measured surface potential (V_{SP}) is related to the work function (Φ_S) [1244] as :

$$eV_{SP} = \Phi_T - \Phi_S \qquad \text{(IX.6)}$$

where Φ_T is the work function of the tip, and e is the electron charge. Therefore, changes in the surface potential for differently doped samples reflect changes in Φ_S. The critical point in these studies is ensuring that the tip conditions (particularly, Φ_T) do not change. To monitor this, a reference sample of known Φ_S (i.e. HOPG, Au) is measured between samples.

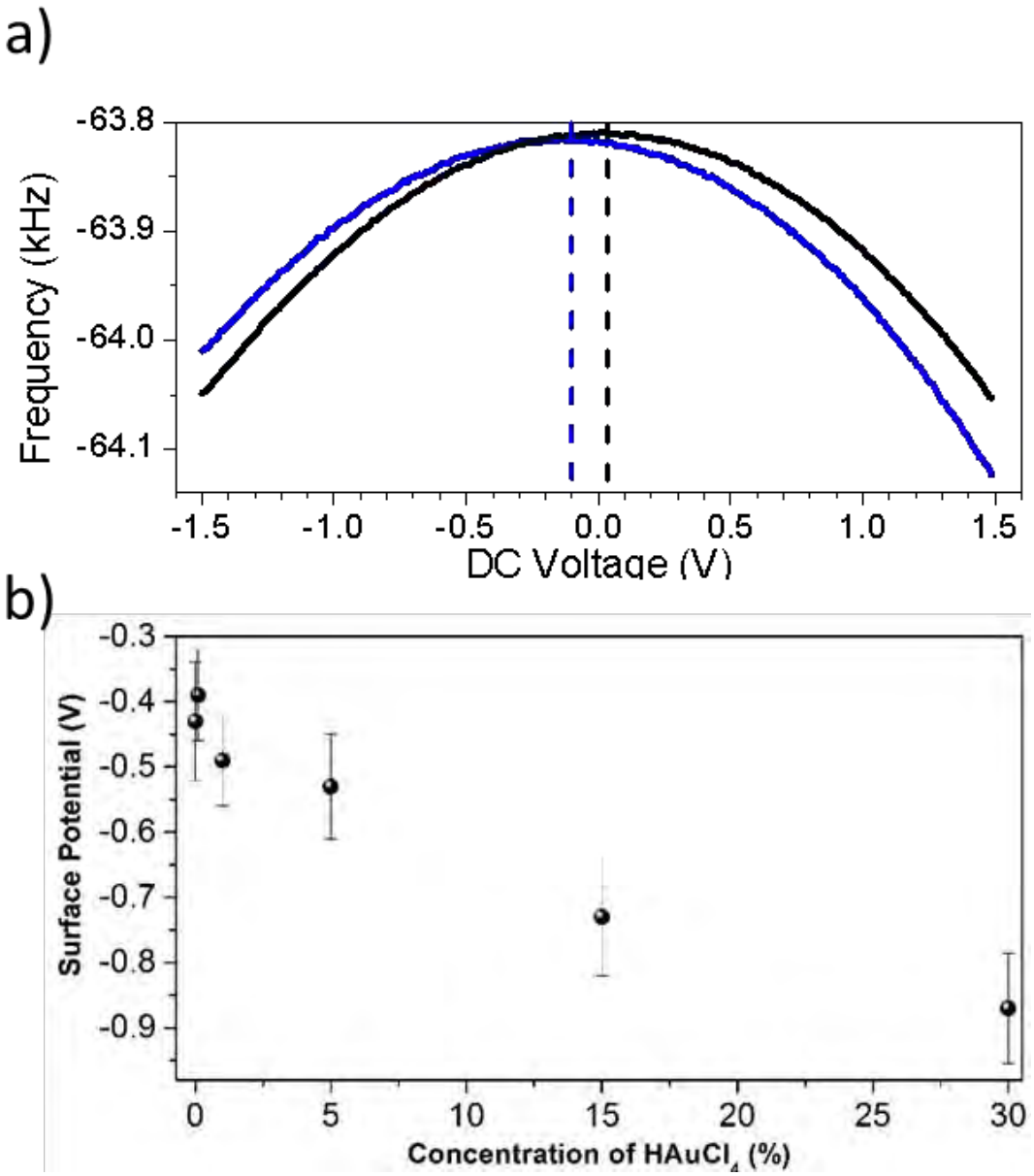

Fig. IX.20 a) Frequency versus voltage curves acquired on SLG on SiO_2 doped with $HAuCl_4$ for two concentrations [1243]. *V_{SP} corresponds to the maximum of the parabolas, marked with dashed vertical lines. b) The variation of the measured V_{SP} reflects the tuning of the Fermi level upon doping with Au nanoparticles* [1243].

To preserve tip conditions, these comparative studies can be done using Kelvin probe force spectroscopy (KPFS) instead imaging acquisition [1245, 1246]. KPFS consists of applying a varying DC bias, to the tip, located above a single spatial location, while monitoring the dynamic response of the cantilever using heterodyne detection [1246]. The force-voltage or frequency-voltage (depending on the detection mode used [1233]) curves obtained have parabolic voltage dependence, and the position of the maximum of the fitted parabola yields the V_{SP} value. Two representative curves are shown in Fig. IX.20a, for SLG doped with Au NPs, for different NP concentration [1243]. The difference in the maximum position of the curves corresponds to a difference in the Fermi level [1243]. For sample comparison, several curves are acquired on different locations, and

measurements are repeated altering the sample order, to ensure reproducibility of the measured differences in surface potential. Similar curves are measured in the reference sample after each round. Fig. IX.20b compares the results of the gradual doping with Au NPs, reflected in a gradual variation of the surface potential measured by KPM [1243].

Transmission electron microscopy

TEM techniques can be used to investigate individual flakes from solutions, measuring their lateral size and thickness, the characterization of their crystal structure and chemical composition. Since TEM provides a higher resolution compared with SEM and higher throughput compared with AFM, low resolution TEM is frequently used to analyse the shape and lateral size of liquid exfoliated nanosheets statistically [113, 161, 162, 169-171, 173, 175, 180, 229-232, 235, 1247]. To perform this measurement the dispersion is drop-cast onto a TEM grid. Here, it is important to use dilute dispersions (*i.e.* optically transparent if the material absorbs in Vis region) to avoid reaggregation. For statistical length analysis, the longest dimension is measured and denoted as length and the direction perpendicular is denoted as width [113, 161, 162, 169-171, 173, 175, 180, 229-232, 235, 1247]. Depending on the expected nanosheet size, continuous film grids can be beneficial to avoid small flakes falling through the holes. When drop-casting, the best results are obtained when the grid is placed on a filter paper to wick away access solvent [113, 161, 162, 169-171, 173, 175, 180, 229-232, 235, 1247]. During image acquisition, it is important to adjust the field of view according to the flake size. Without size selection, samples can be very polydisperse with lateral sizes often ranging from 20 nm-a few µm. This is extremely challenging and requires recording higher magnification images as to not bias the statistics towards larger, more easily discernible flakes in wide-view images. Similar to the AFM statistics, the log-normal shape of the histogram can be used as a guide whether counting/imaging are biased [171, 173, 175]. In such cases, a comparison of the statistically determined mean nanosheet length from AFM and TEM [171, 173, 175] suggests that ~ 150 counts are sufficient to obtain robust mean values.

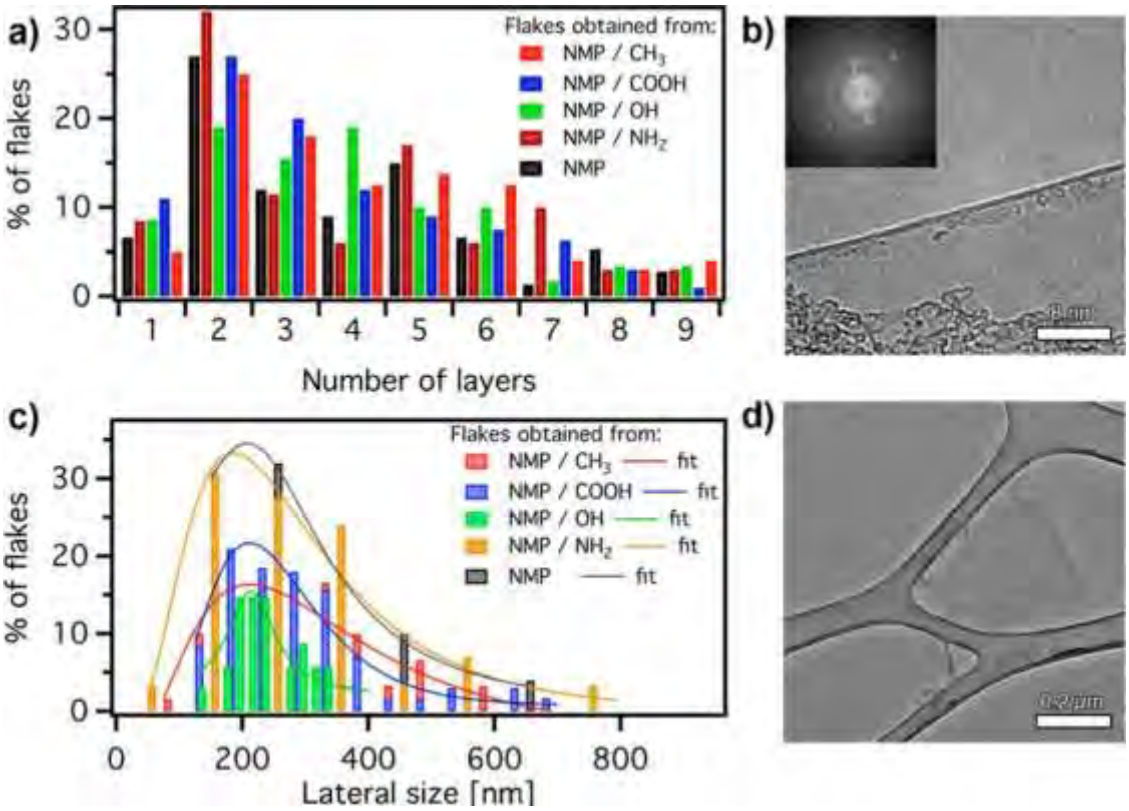

Fig.IX.21 TEM analysis of graphene flakes exfoliated in NMP and different Alkanes. (a) Histogram of N. (b) HREM of folded edge. (c) Flake size distribution; data fitted with a log normal function. (d) TEM micrograph of graphene flake. From ref. [279]

In addition, thickness determination of FLG and SLG can be achieved from high-resolution electron microscopy (HREM) images This is done by counting the number of (0,0,2) lattice fringes (see Fig. IX.21-b) exposed in folded flakes [279] or by analyzing the electron diffraction pattern intensities from individual crystal [279], providing statistical qualification of the exfoliation process [279]. Additional functional properties can be engineered by decoration with either organic moieties or NPs. In this case, STEM imaging and elemental mapping can provide nanoscale characterization of the decoration and of the interface between NPs and GRMs [279]. Electron beam damage can be limited by reducing the accelerating voltage, making it possible to use TEM for the characterization of blends between GRMs and organic complexes [279].

Low energy HRTEM

For structural characterization on the atomic level, aberration-corrected high-resolution transmission electron microscopy (HRTEM) is the method of choice, however, for very thin samples, such as two-dimensional materials, the interactions of energetic electrons with the material during imaging may result in permanent changes in the structure, also referred to as radiation damage, which can be both an obstacle for imaging as well as a useful tool for manipulating matter at the atomic scales [1248-1251]. The best investigated damage mechanism is the so-called knock-on damage [1252], where the impact of fast electrons gradually removes atoms from the sample. From

kinematic considerations [1253], it follows that these alterations can be prevented if a certain threshold energy is undercut [1254]. Depending on the two-dimensional material, acceleration voltages of 80kV and less are required [1255]. At such voltages, in conventional TEMs without aberration correction, atomic resolution is not achievable as the resolution is worse than 0.35nm already at 80kV; however also nowadays, high-end TEMs equipped with a spherical aberration corrector (C_S), usually operating at acceleration voltages between 300kV to 80kV, are strongly limited at low accelerating voltages. The resolution is ~0.8A at 300kV and ~1.9A at 80kV, which allows to resolve single atomic columns of many bulk crystalline samples. For two-dimensional materials such as SLG, the pristine lattice withstands 80kV for a sufficiently high electron dose for HRTEM imaging with good signal-to-noise ratio (SNR), however edges and pores will be more quickly altered and much lower voltages are required [1255]. The resolving power of C_S-corrected microscopes is however not sufficient as it is limited by the chromatic aberration C_C of the objective lens. In recent years this limitation has been tackled by two approaches: Either the effect of the chromatic aberration is reduced due to a reduced energy width of the primary electron beam by a cold field emission gun [1256] or by a monochromator (e.g. [1257, 1258]) or most efficiently by a chromatic aberration corrector [1259]. The Ref. [1259] reports a microscope, the so-called Sub-Angstroem Low-Voltage Electron microscope (SALVE), which is equipped with a C_C/C_S corrector optimized for voltages between 80 and 20 kV. Even at 20kV, this microscope can resolve individual carbon atoms with a resolution better than 0.14 nm [1259] over a wide field of view of 4000x4000 pixel. With the SALVE microscopey, sub-Å resolution resolution is achieved for voltages between 40kV (0.92A) and 80kV (0.76A) and the achievable contrast for the same electron dose is increased [1250, 1259].

Example low-voltage HRTEM images of GRMs are shown in Fig. IX.22. The diffractograms of SLG and MoS_2 (30kV images) feature reflections up to the third and fourth order. A good agreement between image calculation and experiments can be seen (see linescans A6/B6).

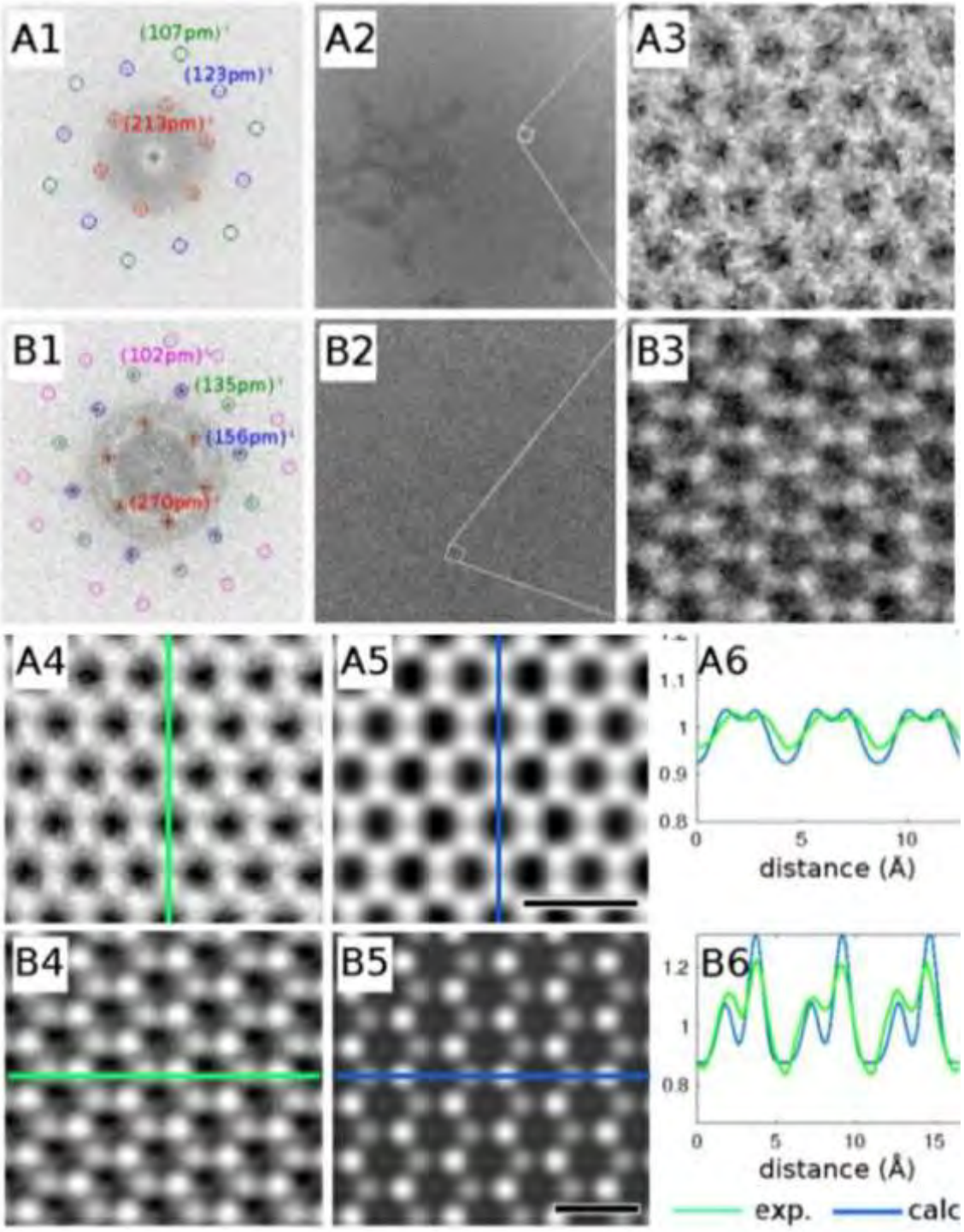

Fig. IX.22 Experimental and calculated Cc/Cs-corrected HRTEM images of (A) SLG[1259]*] and (B) MoS_2 at 30 kV. (A1, B1): Fourier transforms of A2, B2. The outmost reflections demonstrate a resolution~1 Å. (A3, B3) show atomic resolution with magnified areas. The signal-to-noise ratio can be improved by averaging the experimental images (A4, B4). The results are in good agreement with simulated HRTEM images (A5, B5)* [1260]. *The line scans (A6, B6) show the intensity profiles along the marked lines in the experimental and simulated images. If figure not original , pleaser refer to publication: Adapted from Ref. [1259].*

The tuneable low acceleration voltage allows for its optimal choice for each sample. The chosen one is a compromise between the resolving power (which is higher at higher voltages) and knock-on damage. In addition materials, especially non-conducting ones, suffer from ionization effects, which usually increase at lower voltages [1250, 1261]. Sophisticated sample preparation methods are then needed to reduce these effects. The following techniques provide good results: the production of clean surfaces [1262], sandwiching the radiation-sensitive material between two SLGs [1263] and isotope substitution [1264]. To summarize, the choice of the acceleration voltage depends on the trade-off between resolution, knock-on damage and ionization. Appropriate sample preparation is crucial for reaching the voltage-dependent resolution limits. The Cc/Cs-corrected technology for TEM is regarded a major improvement of the current technology which can be judged from the single shoot images of SLG in Fig. IV.23, at 80 and 30kV from the new (Cc/Cs) technology compared with the old (Cs) technology (all single-soot images). Reliable information from HRTEM images about pore sizes distributions in GRMs, or edge structures can now be obtained at lower voltages with higher resolution and higher contrast [1259]. In addition, due to the wide field of view of 4000x4000 pixels, this microscope is also very useful for dynamic studies and manipulations at the atomic scale.

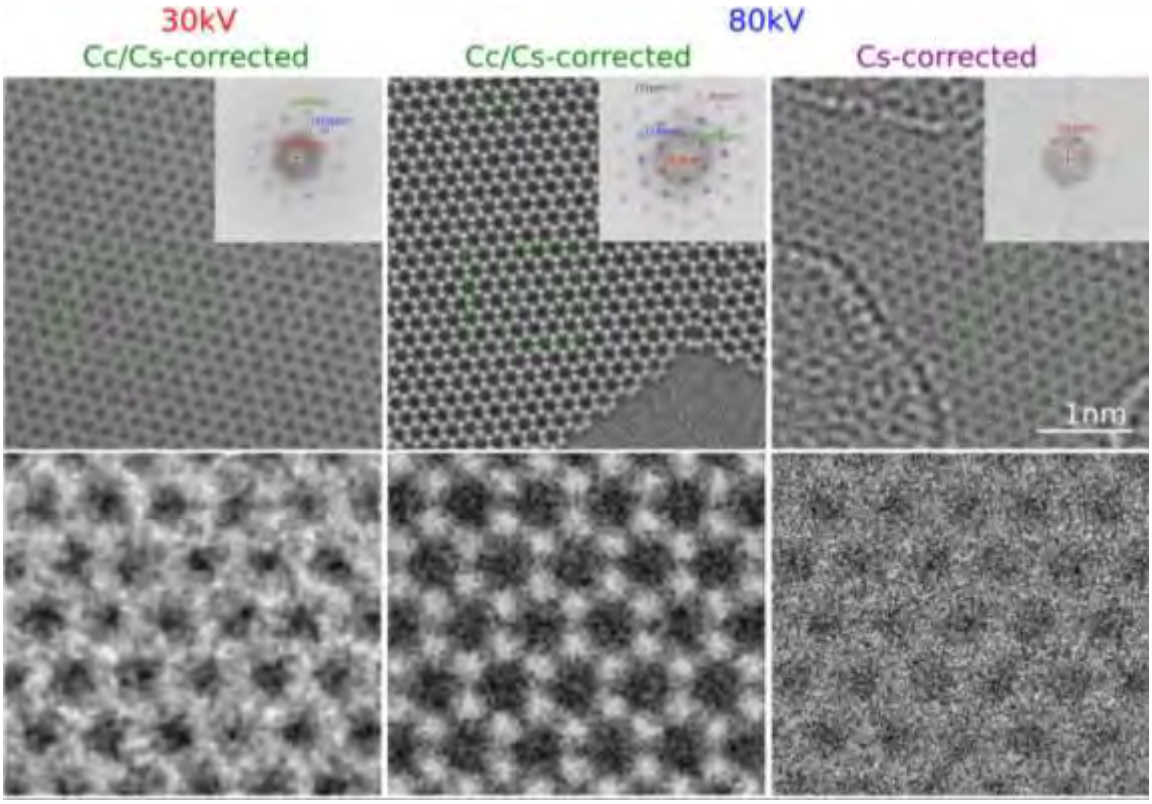

Fig. IX.23. SLG HRTEM images obtained at 30kV (left) and 80kV (middle) in the Cc/Cs-corrected SALVE microscope and at 80kV (right) in the Cs-corrected TITAN-microscope. The inserts show the corresponding Fourier Transform patterns. The {0-110}, {-1-120}, {0-220} and {1-320} reflection are encirled in red, blue, green, and purple, respectively. Adapted from Ref. [1259].

Scanning tunnelling microscopy

Scanning tunnelling microscopy (STM) is a powerful tool for epitaxial graphene characterization. It is generally used inside UHV chambers for in-situ structural and electronic studies at the atomic level. When the graphene samples are measured in ambient conditions or after ex-situ manipulations, AFM is a preferred tool as force maps are more directly interpreted in terms of topographic features of the sample. STM images, in contrast, are proportional to the tunnel current which is sensitive to the electronic structure of the tip and surface [1265, 1266]. When samples are characterized in ambient conditions, data acquisition can be quite difficult as atmospheric contaminants may intrude between the tip and the surface as they diffuse, thus provoking current instabilities and hindering high-quality data acquisition. After graphene exposure to ambient conditions, annealing in-vacuum for a short period of time at about 250 °C before measurement is strongly recommended in order to remove possible involuntary adsorbates. With respect to the acquisition mode, topography images at constant current are preferred as they are typically more stable and avoid tip crashes during measurements. Nevertheless, the use of constant-height or current-error images can also be useful in some cases for obtaining atomically-resolved images of local features [1267, 1268].

The atomic lattice of graphene can routinely be resolved with STM. A hexagonal lattice with a periodicity of 2.44 Å is normally observed for epitaxial graphene and graphite samples. When imaging graphene, the smaller periodicity (1.42 Å) of the honeycomb lattice can sometimes also be resolved. Low voltages and high currents (short tip-sample distances) are recommended for obtaining atomic resolution images, with typical values ranging between 50-200 mV and 1-4 nA, respectively. Graphene superlattices of larger scale (1-2nm) can also be resolved with STM images (see below). In addition, STM is the ideal tool for local measurements needing ultrahigh spatial resolution. STM has demonstrated its capabilities for resolving low-dimensional (0-D and 1-D) structural defects with unmatched atomic resolution. There are several defective structures that have been described by STM images. The most important 1-D defective structures are graphene wrinkles and graphene edges between different (rotational) domains. Fig. IX.24 shows a representative STM image of a graphene on Pt(111) sample together with a representative LEED pattern of the same system [875]. In the constant-current topographic image, a graphene wrinkle/pleat and some graphene nanobubbles can be seen. Profiles along this wrinkle/pleat show an apparent height of 2-2.5nm. The origin of these structures is the difference between thermal expansion coefficients of graphene and Pt, which result in compressive strain during the cooling process. Graphene nanoscale dome-like structures, also known as nanobubbles, can also be resolved with STM images. In Fig. IX.24 a one is encircled in red and in Fig. IX.24 b one nanobubble is shown with atomic resolution. Structures submitted to compressive strain, like graphene pleats and nanobubbles, have been proposed to induce high pseudo-magnetic fields, which lead to Landau quantization of the electrons in graphene when measured with STM at cryogenic temperatures [585].

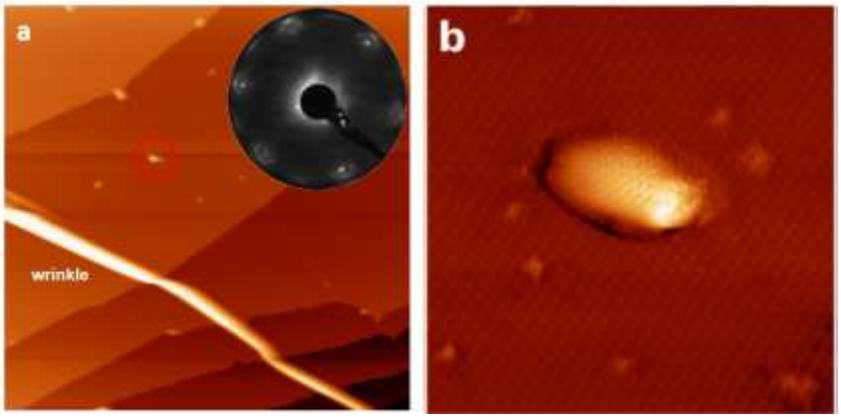

Fig. IX.24 .a) STM image of a 200 x 200nm^2 area of graphene epitaxially grown on Pt(111), I=0.15nA, V=750mV. A single graphene layer covers the whole surface. In the image a wrinkle/pleat and several nanobubbles one of them is encircled in red, can be seen. The inset shows the characteristic LEED pattern of Gr on Pt(111). b) High resolution STM image of a graphene nanobubble (20x20nm^2, I=0.6nA, V=310mV) and few point-like atomic defects with atomic resolution. Figure a is adapted from reference [875] *.*

In Fig. IX.25 different 0-D point defects of a G/Pt(111) system are depicted. Fig. IX.25a shows a single atom defect which can be explained in terms of an in-lattice heteroatom inclusion–most likely a nitrogen impurity coming from the residual gas in the chamber [1269] Fig. IX.25 b displays a multiatomic vacancy which induced a reconstruction of a region of 1-2nm. Although a dome-like local configuration can be expected one must take with caution the fact that this region appears brighter – and thus higher- in the STM images as electronic effects are normally occurring in the defective regions of graphene. Fig. IX.25 c shows a strain-induced lattice dislocation involving at least two unit cells of graphene.

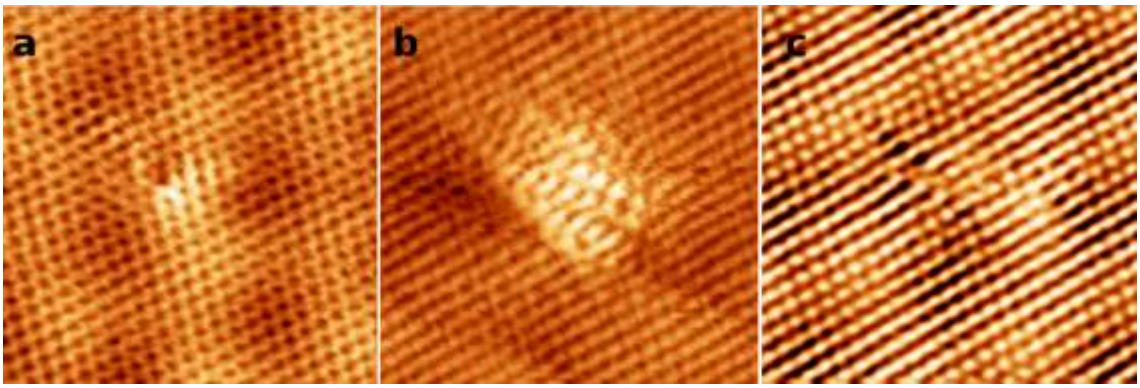

Fig. IX.25: Three 5x5nm^2 images showing 0-D graphene point defects on Pt(111). a.10 mV, 3.9nA . b. 10 mV, 2nA. c. 10 mV, 3.9nA. See main text for detailed description.

Graphene on metals.

The formation of graphene has been mostly studied by STM on hexagonal metal surfaces, like the (0001) for the HCP crystallographic structures –Ru, Co, Re - and the (111) for the FCC metals – Ni, Cu, Rh,Pd, Ir, Pt and Au- but it has also been observed to grow on non-hexagonal crystallographic surfaces such as Pt(100) [869].

Moiré superstructures [1270], arise from the electronic interference between two periodicities with a difference in lattice parameter and/or angle. In the present case Moirés are originated by the interference between the graphene lattice and the metal surface beneath it. Fig. IX.26 shows a ball and stick model of a Moiré pattern for describing the different distances and angles occurring in Moiré superstructures. With these structural parameters, simple models minimizing lattice mismatch can be used for describing the structure of graphene with respect to the metal substrate. In Fig. IX.27 we present STM images of four Moiré superstructures found on the G/Pt(111) system and that can be described with these structural parameters (see blue hexagons overlaid onto it). In every STM image, two periodicities can be seen: the short one corresponding to atomic resolution, and the long one corresponding to the Moiré superstructure.

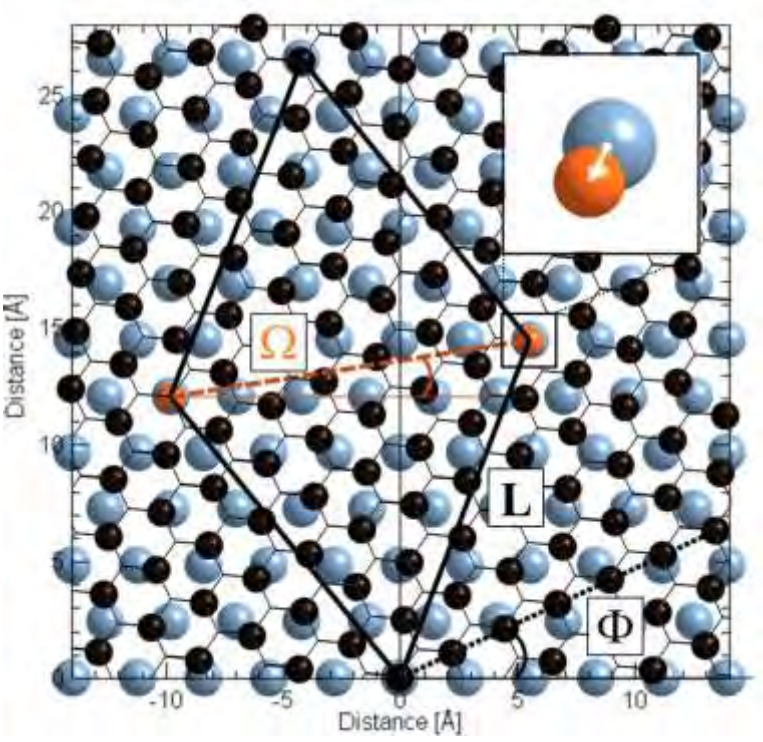

Fig. IX.26: left side. Diagram of the model represented for a moiré superstructure. Pt atoms are represented by blue spheres, whereas the hexagonal lattice of graphene is represented by black spheres. The angle between the black dotted line and the Pt [1$\bar{1}$0] surface direction (x axis) represents the crystallographic angle, Φ, which is equal to 25.1° for this particular case. The orange spheres are the carbon atoms with the lowest mismatch for a given Φ, which define the Moiré unit cell indicated by the black rhombus. The angle between the orange dashed line and the Pt [1$\bar{1}$0] direction is the Moiré apparent angle (Ω). The white arrow in the inset represents the mismatch. Adapted from ref [1270].

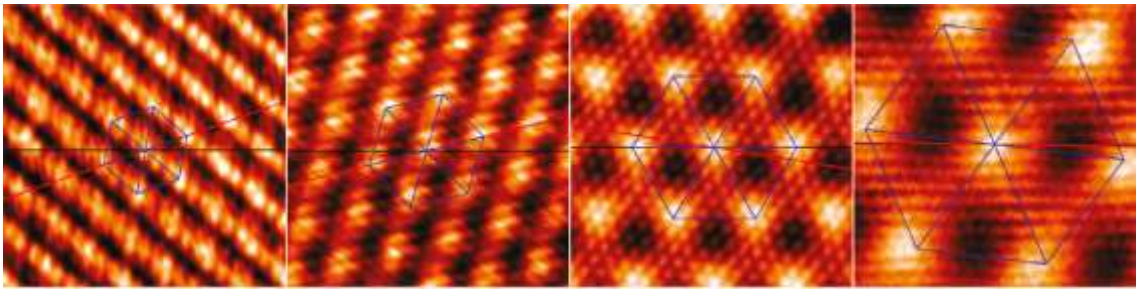

Fig. IX.27: High resolution atomically resolved STM images of some of the periodically modulated graphene structures. The red line indicates the graphene orientation with respect to the black line, which indicates the Pt [110] surface direction. The blue hexagon denotes the resulting Moiré structure. All images are 5x5 nm^2. V ≈-250,+250 mV; I≈ 1,3 nA. Adapted from ref [1270].

Depending on the reactivity of the metal, the interaction between graphene and the metal substrate can range from van der Waals physisorption to strong bonded chemisorption. The interaction between the substrate and the graphene overlayer drives the measured STM corrugation of graphene and the mean distance from the substrate [788]. Typical corrugations of Moiré supperlattices range between 0.2-1.2 Å for graphene epitaxially grown on metal surfaces, and typical corrugations for the atomic lattice range between 0.1-0.3 Å [788] .

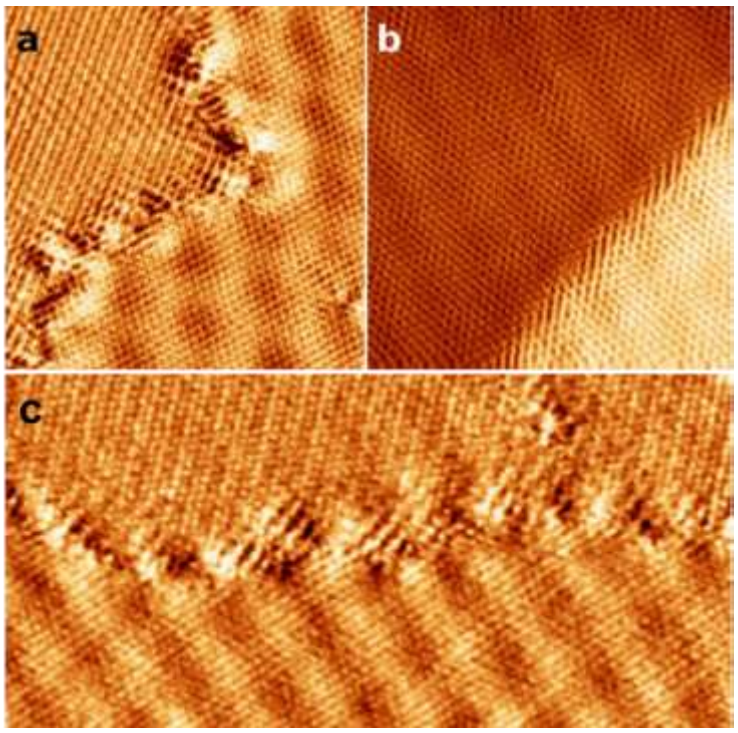

Fig. IX.28. Examples of 1-D defective structures of graphene. a) G-G edge between two rotational domains (Moirés) 10x10 nm^2 1.9nA, 10mV. b) Graphene running through a Pt step in a carpetlike fashion 7.5x7.5 nm^2, 8nA, 2mV. c) Pseudo periodic G-G edge, the grain boundary follows the periodicity of the Moiré appearing in the lower part of the image. 18.4 x 9 nm^2, 2nA, 10mV.

In Fig. IX.28 we present a series of 1-D defective structures appearing on the G/Pt(111) system. This figure shows how graphene adjusts itself to the lowest energy conformation when epitaxially grown on surfaces, thus deforming its atomic structure to fit to the substrate and other graphene grains in the vicinities. In Fig. IX.28a we show two Moiré domains lying in the same Pt(111) terrace and connected by an amorphous grain boundary. The strain accumulated between the two domains induces the appearance of this G-G edge. In Fig. IX.28b we show that graphene can, in some cases, run across an atomic step without forming a grain boundary in a "carpet-like" fashion (covering unperturbed the higher and lower part of the step while running through it), in this case the only effect appearing on graphene is an out-of-plane bending of the layer. In Fig. IX.28c a pseudo-periodic graphene grain boundary is presented. The structure involves several, unresolved, vacancies and lattice deformations. Interestingly, in cases like this, the G-G grain boundary can be pseudocrystalline (contrary to Fig. IX.28a) and adopt the periodicity of one of the two Moirés that reaches the interface.

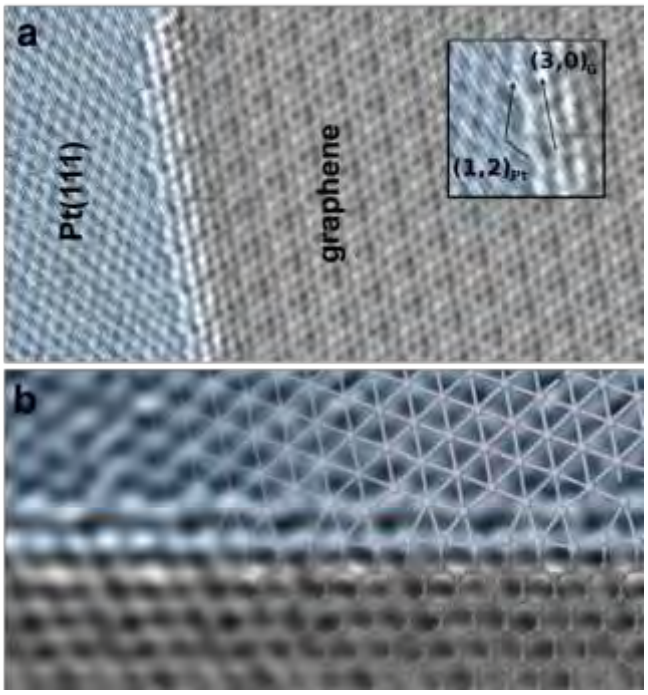

Fig. IX.29. Example of a graphene-metal interface. a) High resolution, atomically resolved, STM imags of the G/Pt(111)-Pt(111) interface. These crystalline edges are energetically favoured have the same orientation as the graphene Moiré superstructures. 12.6 x 6.8 nm^2, V=40.2mV, I=5.2 nA. The inset shows the chiral vectors of this particular edge. b) Ball and stick model of the DFT relaxed structure (right-hand part of the image) compared with the STM image of the graphene-Pt(111) edge boundary. The atomic positions of the calculations reproduce with great accuracy the protrusions in the STM images. Adapted from reference [1267].

Fig. IX.29 we present a different 1-D structure occurring on graphene on metals: the interface between graphene and a metal step (in particular a Pt(111) surface). In this case a crystalline

structure emerges permitting to perform a combined experimental-theoretical approach to study the he contact region formed along the interface at the atomic scale. Fig. IX.26 a shows a high-resolution STM image of atomically resolved border-like edge of (√7x√7)R19° graphene with a Pt(111) step. Combining STM experimental images with DFT simulations, the atomic and electronic structure of the Pt-graphene edges can be fully characterized (see Fig. IX.26 b). This approach reveals the presence of 1D electronic highly localized state in one of the graphene sublattices, and thus the brighter aspect in the STM images of the contact region. Theory predicts, and STM images confirm, that this state is mainly confined on the first carbon atomic lines of the edge [1267].

Silicon carbide.

Graphene grown on SiC(0001) shows very interesting electronic properties at the nanoscale. When inspected with STM, graphene can appear transparent depending on the bias voltage used: the honeycomb graphene structure is "visible" only within a small range of scanning conditions which typically involve voltages bias near the Fermi level (see Fig. IX.30) [612] . G/SiC(0001) presents quantum interferences between electrons of different sublattices which result in a √3x√3R30^{o} lattice appearance of graphene lattice near defective structures. All these characteristics makes G/SiC(0001) an ideal system to test the fundamental electronic properties of this pure sp^2 compound with STM, although typically cryogenic temperatures and low temperature STM are needed to decrease electronic broadening effects. The, so called, C-terminated SiC face or SiC(000-1) develops multilayer graphene. These layers are very weakly bound and stacked in different orientations forming graphene-graphene Moirés with different orientations and periodicities [552, 612].

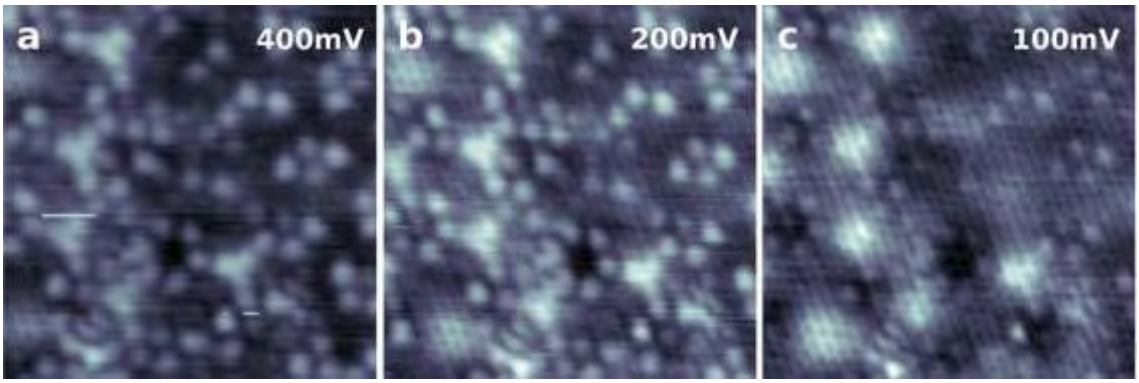

Fig. IX.30.- Series of STM images of the same region showing the bias dependence of the SLG/SiC(0001). When scanned at bias near the Fermi edge (100mV) the main feature is the graphene lattice, while scanned at higher bias (400mV) the subsurface buffer layer structure is revealed. 7x7 nm^2

Graphene grown on the Si terminated surface -SiC(0001)- can show different surface reconstructions (see Section IV). There are three main surface terminations that can be distinguished by STM and will be discussed below. First, (6√3x6√3)R30^{o}/SiC(0001) or buffer layer (Fig. IX.31 a) is a carbon rich termination which is usually described as sp^2 carbon lattice covalently bound to the

uppermost SiC slab. Second, Single layer graphene (SLG), Fig. IX.31 b, is characterized by a (6√3x6√3)R30° superperiodicity overlaid with an atomic scale graphene lattice. As we have described before, when measuring SLG at high voltage bias one can normally measure the atomic features of the SiC beneath graphene [1271]. Third, bilayer and more generally multilayer graphene. When SiC samples are annealed at very high temperatures Si depletion can be very high and promote the apparition of graphene multilayers. STM measurements of graphene multilayers (Fig. IX.31 c) have lower corrugation and, in some cases, the underlying superperiodicity disappears and graphene-grephene Moiré superlattice dominate. Similar multilayers are also found in the SiC(000-1) surface [1272]. At last, graphene can be decouple from the SiC substrate by H intercalation. Fig. IX.31 d shows a STM image of hydrogen intercalated graphene, also known as quasi-free standing graphene. In this case, the underlying (6√3x6√3)R30° superperiodicity is not appearing in the STM images and only the graphene lattice can be resolved. The low surface corrugation measured with STM on the hydrogen intercalated samples might be related to the high charge carrier mobility reported for these samples.

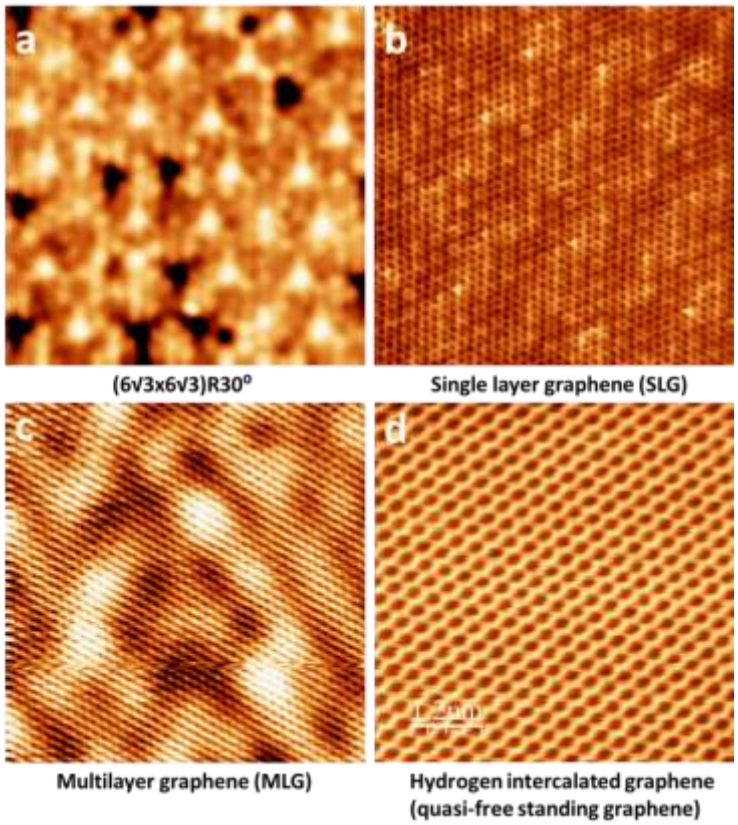

Fig. IX.31. Atomically resolved STM images of the SiC surface with different terminations. a. 6√3x6√3)R30°1000mV, 200pA.b. Single layer graphene, -100mV, 200 pA. c. Multilayer graphene, -100 mV, 100 pA. d. Hydrogen intercalated epitaxial graphene. V= 243 mv; I= 1.33 nA. I*mages a-c are 10x10 nm^2. d is 6x6 nm^2.*

Scanning thermal microscopy

Heat transfer properties of graphene have been a topic of high interest [1273-1276] based on calculations and measurements of its thermal conductivity in the range of a few thousands W/mK, *i.e.* about one order of magnitude higher than conventional graphite [1277]. Due to the strong covalent sp^2 bonding, heat transport in carbon materials is usually dominated by phonons [1276]. However, lattice defects, impurities, interfaces as well as the presence of sp^3 bonds can limit heat conduction [1276]. Several techniques have been proposed for characterizing the GRM thermal properties [1278], however accurate and reliable measurements remain challenging. Electrical methods and the Raman optothermal measurements were used to determine the thermal conductivity of both suspended and supported SLG [1276, 1279, 1280].The main limitations are in the rather complex setup and limited spatial resolution: indeed, optical techniques are limited to a few hundreds nm by the diffraction limit of the incident light, while electrical measurements provide a result representing the average of the conductivity on the whole specimen.

Scanning Thermal Microscopy (SThM) [1281] [1282] represents an interesting technique to measure heat transfer in GRMs, which requires limited sample preparation and with lateral resolution of some tens nm or less. Although a quantitative determination of the thermal conductivity of GRMs by SThM [314, 1282]is very challenging, it was demonstrated to be possible in at least some specific cases and with particular probes, *e.g.* by electrically heating a suspended SLG film and by using the so called null point scanning thermal microscopy technique adopting probes integrated with a thermocouple junction [1283]

SThM can be performed by using resistive probes where a Pd film acts both as the heater and the temperature sensor (the so-called Pd probes) [1282]. The 40 nm-thin [1284] Pd film, deposited near the apex of the Si_3N_4 tip, acts as the element of a Wheatstone bridge. The resistor is heated by the Joule effect and, when the tip is in contact with more thermally conducting regions of the sample, its T (and therefore resistance) decreases, while it increases when scanning on less conductive areas, since less heat is carried away by the material under investigation. The change in the sensor resistance is monitored by measuring the bridge voltage which is sent to the controller in order to display the thermal maps, that are subsequently converted into temperature by using the Wheatstone bridge formula and the temperature coefficient of the probe that we determined to be about $8.92 \times 10^{-4}\ K^{-1}$.

RGO flakes produced by the thermal expansion were studied by SThM in Ref. [314]. These nanoflakes were measured both “as-received” (RGO) or after a high temperature annealing at 1700 °C in vacuum for 1h (referred to as RGO_1700) to gain insight into the evolution of the heat dissipation properties due to the simultaneous reduction of disorder and defectiveness upon annealing [314]. SEM and AFM analyses did not evidence significant changes in the morphology of the nanoplates upon annealing. XPS showed a strong reduction of oxygen content, by the elimination of carboxylic and carbonyl groups. A considerable reduction of defects was observed by Raman spectroscopy which also indicated an increase of the graphitic stacking order in the structure. This

result was further confirmed by X-ray diffraction experiments which revealed an increased ordering both along and perpendicular to the planes.Fig. IX.32 shows the SThM maps for (a) RGO and (b) RGO_1700 on Si/SiO_2. Topography artefacts are observable owing to the dependence of the tip-sample contact on the steep edges and on the wrinkles and bulges present on the surface [314, 1285].

The tip heater T reported in panel (a) shows that on the flat areas of the sample (see for example the masked region), the temperature is basically the same as when the tip is scanning the substrate ($T_{sub} - T_{Gr} = \Delta T = (8 \pm 14) \times 10^{-3} K$). This does not mean that the two materials have the same thermal conductivity but only that their apparent thermal conductance is the same. On the other hand, if we observe panel (b) we can see that for the annealed flakes T is now *lower* when the tip is on the flake than when it is on the substrate, $\Delta T = (42 \pm 15) \times 10^{-3} K$. Thus, by comparing (a) and (b), Ref. [314] concluded that the annealed flake features a *higher* thermal conductivity than the as-received ones, due to the reduced disorder and defectiveness upon annealing. Panel (c) and (d) show an analogous result but with the flakes supported by the less (one order of magnitude) thermally conducting PET. In this case, the heater temperature on the RGO flake is now lower than that of the substrate ($\Delta T = (103 \pm 18) \times 10^{-3} K$) and also in this case ΔTincreases when looking at the RGO_1700 sample, where it goes to $\Delta T = (143 \pm 13) \times 10^{-3} K$. The results on PET confirm that RGO_1700 flakes are more thermally conducting and also show that the use of a less conducting substrate enhances the sensitivity of the measurement. This is due to the fact that the absolute decrease of the spreading resistance [1286] of the substrate that occurs when enlarging the heat flow area, is larger when the thermal conductivity of the substrate is smaller [314] Thus, the T difference substrate-flake is also expected to be higher.

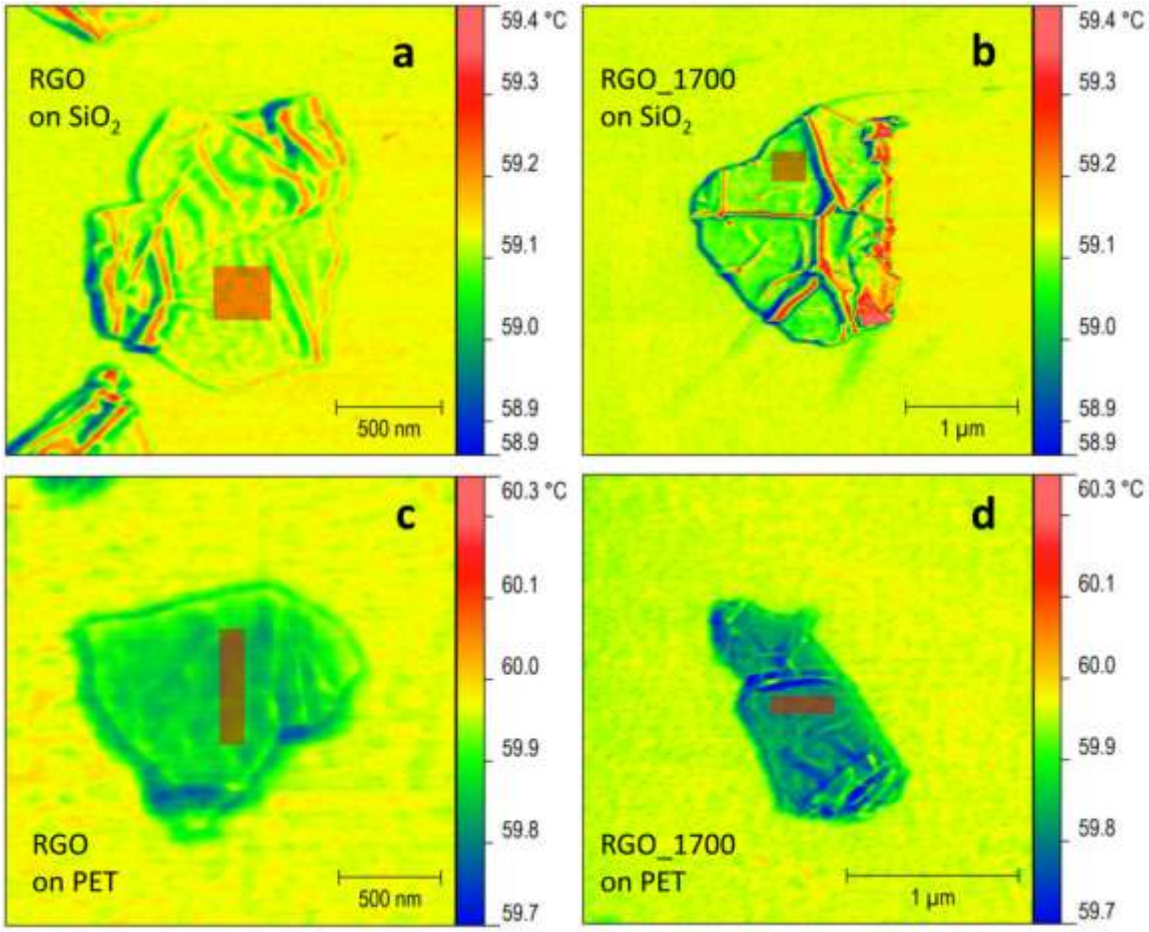

Fig. IX.32 SThM maps of (a)RGO and (b) RGO_1700 on Si/SiO_2 and (c) RGO and (d) RGO_1700 on PET. Adapted from ref [314]

Fig. IX.33 reports a summary of the SThM results obtained in terms of T differences between substrate and flakes for several samples on both substrates. Although these are small and the error bars rather large, the result is reproducible on both substrates, showing that the annealing process improves the thermal conduction of flakes. No particular dependence on the thickness of the flakes has been observed, likely due to the fact that the in-plane component of the thermal conductivity is at least two orders of magnitude higher than the out-of-plane one and a considerable amount of heat could be spread along the planes.

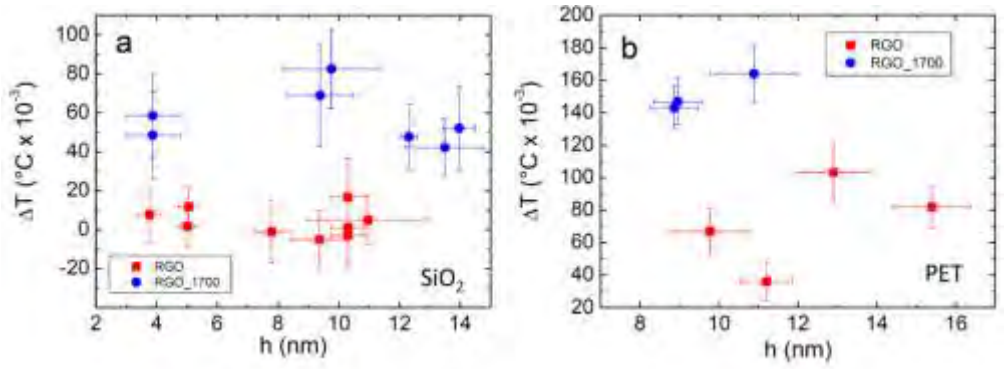

Fig. IX.33 (a) Summary of T difference between Si/SiO_2 and the RGO (red) or RGO_1700 (blue). (b) The same as in (a) but for PET substrate. Adapted from ref [314].

SThM was also applied on CVD 4LG, 2LG and 1LG supported by SiO_2/Si, Fig.IX.34.

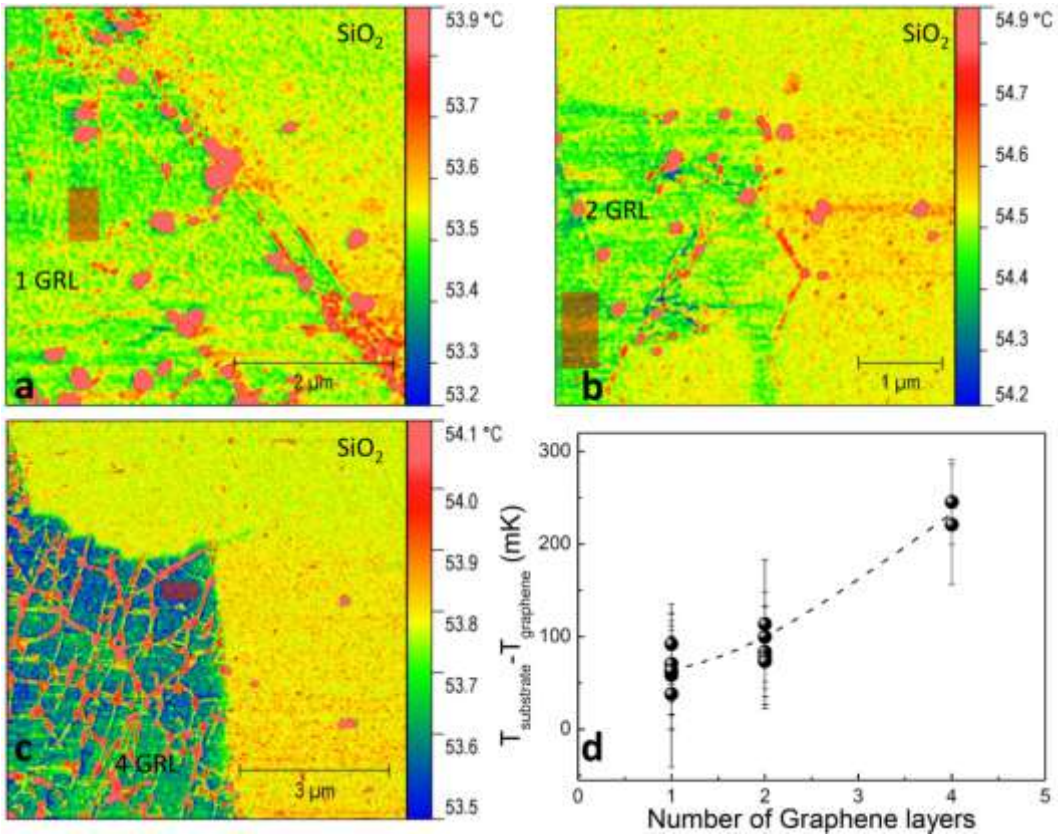

Fig. IX.34 SThM maps of (a) 1LG, (b) 2LG and (c) 4LG on Si/SiO_2. (d) Sensor T difference as a function of N. The dashed line is a guide for the eye

Fig. IX.34a shows a thermal map SLG on SiO_2/Si. The high-T spots are due to impurities and the corresponding T value is due to a topography artefact [1285]. When averaging over the flat areas (with no topography artefacts) the measured tip T is lower than on the substrate. By averaging the red masked area on 1LG and on a similar area on the substrate (not shown), the T difference between substrate and sample was found to be $\Delta T = (71 \pm 42) \times 10^{-3} K$. Fig. IX.34(b) reports a

similar image for 2LG. Apart from topological features giving rise to high-temperature spots, the flat areas of the surface feature on average a lower T than the substrate, with a T difference (averaged on the red masked area) increased to $\Delta T = (100 \pm 48) \times 10^{-3} K$, suggesting that 2LG has a higher thermal conductance than SLG. Fig IX.34(c) shows the 4LG case, in which both impurities and grain boundaries are visible due to the topography-related T readings. The representative T on the sample flat areas is much lower than on the substrate. The T difference between substrate and 4LG is now higher than for the two previous samples. $\Delta T = (245 \pm 46) \times 10^{-3} K$, indicating that the thermal conductance of 4LG is further increased with respect to the 1L and 2LG. Fig IX.34(d) summarizes the results obtained by performing several SThM measurements as a function of N. Even though the error bars for SLG and BLG overlap, the thermal conductance increases with N.

A similar trend was reported for mechanically exfoliated flakes using either the resistive Si [1287] or Pd probes [1284]. The topography of CVD graphene, with grain boundaries and crystallites, is considerably different from mechanically exfoliated flakes, that are much flatter and more regular. This affects also the heat dissipation properties and the thermal response of the SThM probe.

IX.2 Spectroscopies

Raman

Raman spectroscopy is an integral part of graphene research. It may be used to determine the number and orientation of layers, the quality and types of edge, and the effects of perturbations, such as electric and magnetic fields, strain, doping, disorder an functional groups.

This, in turn, provides insight into all sp2-bonded carbon allotropes, because graphene is their fundamental building block. Ref. [77] reviewed the state of the art, future directions and open questions in Raman spectroscopy of graphene. It described the key physical processes, such as the various types of resonances at play, and the role of quantum interference. It outlined the basic concepts and notations, and a terminology able to describe any result in literature for graphene and other 2d materials. Here we briefly describe some of the key concepts, referring the reader to Ref. [77] for a more complete overview.

An ideal characterization tool should be fast and non-destructive, offer high resolution, give structural and electronic information, and be applicable at both laboratory and mass-production scales. Raman spectroscopy fulfils all these requirements. The Raman spectrum of graphite was first recorded more than 40 years ago [1288] and, by the time the Raman spectrum of graphene was first measured in [86] Raman spectroscopy had become one of the most popular techniques for the characterization of disordered and amorphous carbons, fullerenes, nanotubes, diamonds, carbon chains and polyconjugated molecules [1289]. Raman techniques are particularly useful for graphene, because the absence of a bandgap makes all wavelengths of incident radiation resonant, thus the Raman spectrum contains information about both atomic structure and electronic properties. Resonance could also be reached by ultraviolet excitation [1290, 1291] either with the M-point Van Hove singularity or in the case of bandgap opening, such as in fluorinated graphene.

Raman spectroscopy is a tool to measure atomic vibrational energy in materials, phonons in crystals. Raman spectra can fall into two spectrum ranges in terms of energy scale, an ultra-low frequency ULF (<100 cm^{-1}) and a high frequency (>100 cm^{-1}) range. In general, Raman spectra are measured in the high frequency range because of the cut-off limit of Raman filters (edge or notch filters) used in the Raman spectrometer. From the Raman spectra in the high frequency range, various properties of materials can be obtained such as, structural, number of layers, defects, doping and strain information. In the ULF Raman spectra, interlayer interaction can be estimated by the shear (C) and layer breathing modes (LBMs), which can also be used to determine N [1292, 1293]. Traditionally, a triple stage spectrometer is used to measure ULF Raman spectra, but its low throughput and complexity for operation restricted its utilization. A new method was developed to get ULF Raman spectra easily, using volume Bragg grating filters to reject a strong laser line down to 5 cm^{-1} [1294]. When measuring GRMs, the damage threshold for the laser power should be considered. Typically, the power should be kept below 1 mW for SLG, and few hundreds μW for TMDs depending on the material. Specially, some of materials should be isolated from air with a protection layer or vacuum to avoid photo induced oxidation [174].

Graphene

A typical Raman spectrum of defect-free SLG consists of two main peaks, the G peak located at ~1580 cm^{-1} and the 2D peak at ~2700 cm^{-1} [77], Fig. IX.35. In defective graphene, additional peaks such as the D, D' and their combination D+D' appear [77, 1295] and [1093], Fig. IX.35 bottom spectrum. The 2D and 2D' peak are second order peaks involving two phonons and are thus always present even in the absence of defects. The fitting parameters, such as peak position Pos, FWHM, height (I) and area (A) are important to interpret Raman data. I (intensity) is used to denote the peak height, A to denote peak area, Pos for peak position and FWHM for peak full-width at half-maximum. E.g.: I(G) for G peak height, A(G) for G peak area, Pos(G) for G peak position and FWHM(G) for G peak full-width at half-maximum.

The lineshape of the 2D peak can be used to distinguish between different N. For SLG it can be fitted with a single Lorentzian, while in BLG it splits into four components as result of the evolution of the band structure [86]. For N>5 the 2D peak shape is similar to that of graphite. Therefore, ULF Raman measurements should be performed. The C and LBMs can be observed for GRMs. Their positions change with N. They can also be used to calculate coupling constants related to in-plane and out-of-plane Young's moduli [1292]. Fig. IX.36b) shows the ULF Raman spectra of different graphene layers. While the G peak position is nearly constant, Pos(C) changes and can be used to determine N Fig. IX.36c).

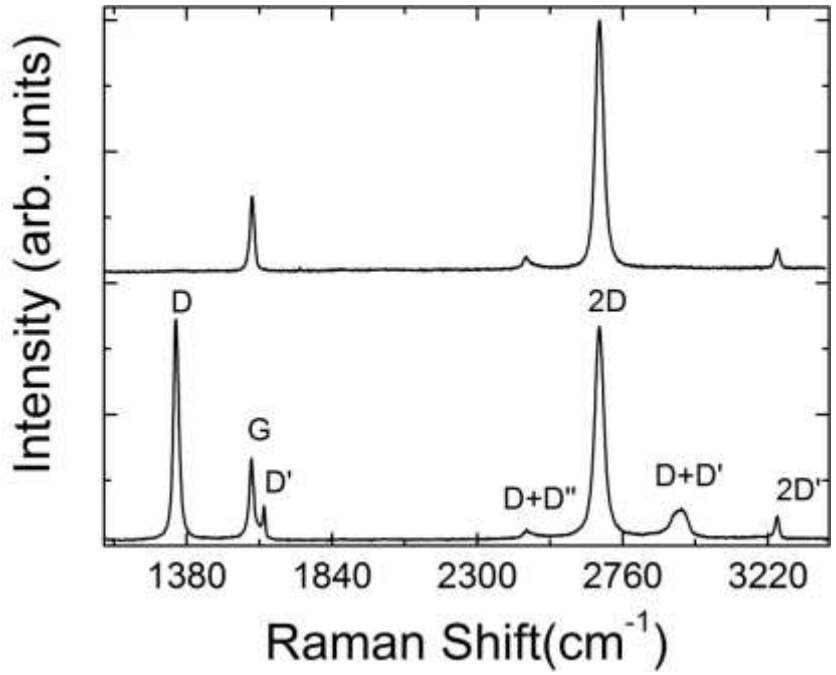

Fig. IX.35: Typical Raman spectra of defect free (top) and defective (bottom) graphene. Figure. taken from ref [77]

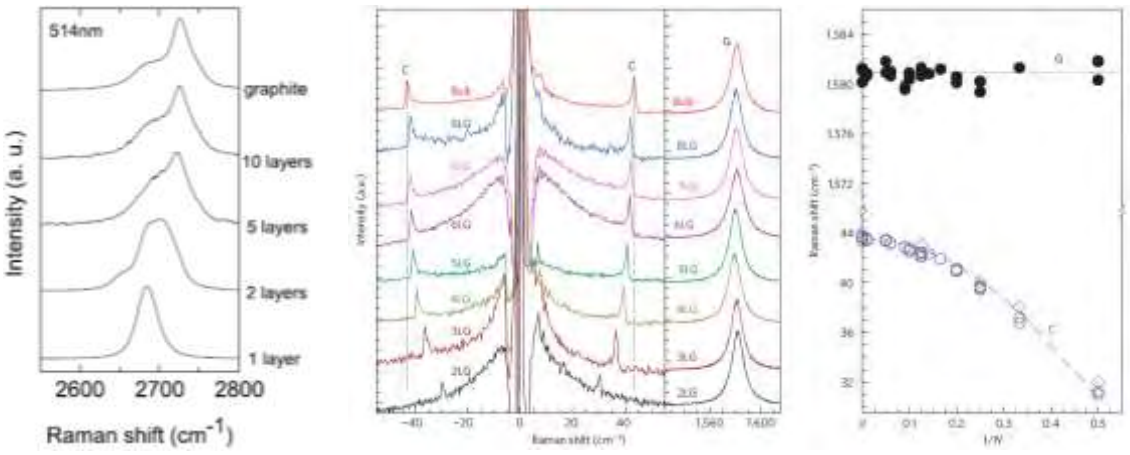

Fig. IX.36a) Raman spectrum of 2D peak as function of N [78]. b) C peak as function of N. c) Pos(C) and Pos(G) as a function of 1/N [1292].

Raman spectroscopy can also be used to determine the doping level [1093, 1296, 1297]. There are two major effects: (i) a change of the equilibrium lattice parameter with a consequent stiffening/softening of the phonons, and (ii) the onset of effects beyond the adiabatic Born-Oppenheimer approximation that modify the phonon dispersion close to the Kohn anomalies (KA) [1296, 1298].

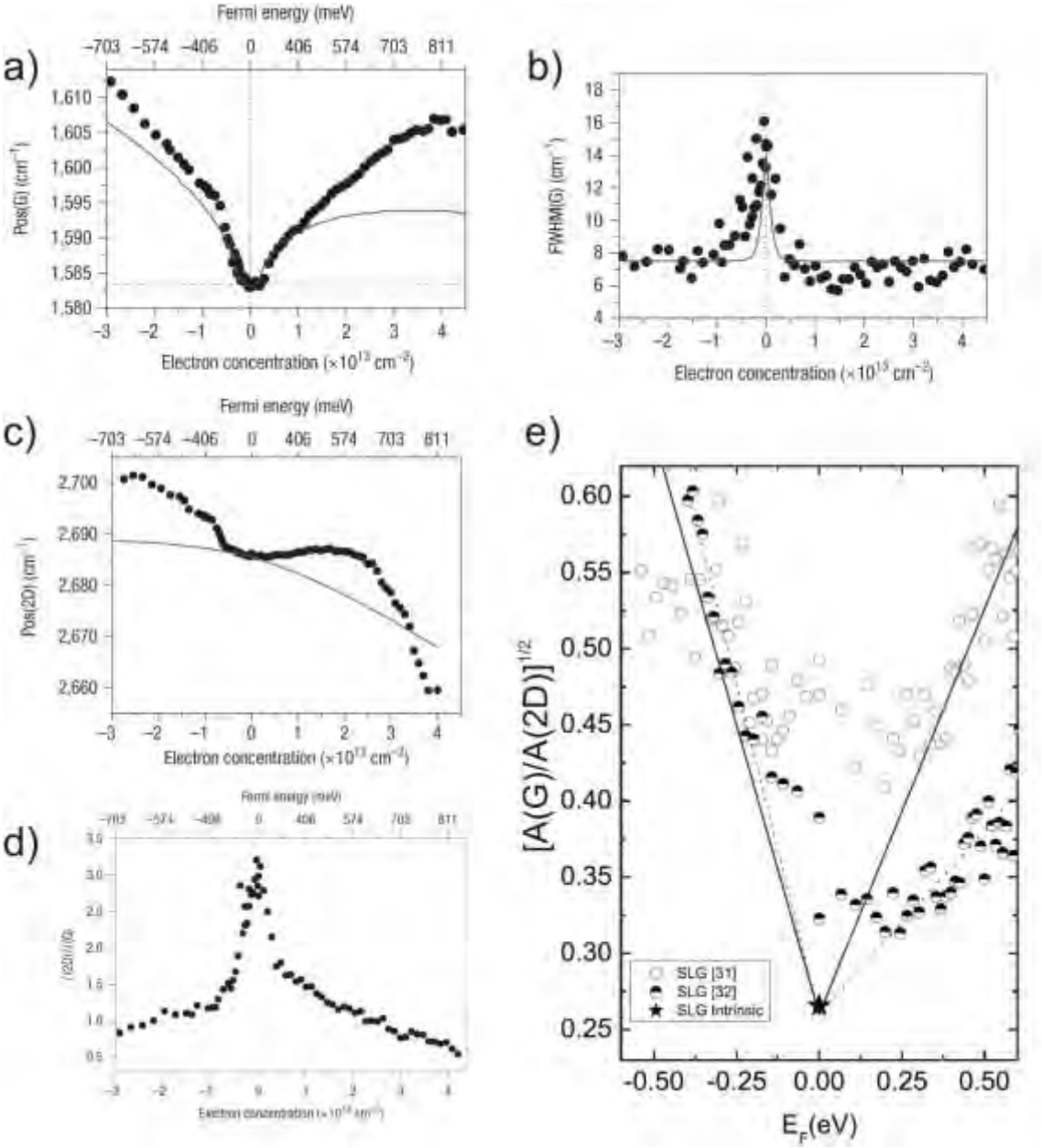

Fig. IX.36: Doping dependence of Raman fitting parameters a) Pos(G), b) FWHM(G), c) Pos(2D), d) I(2D)/I(G) and e) $[A(2D)/A(G)]^{1/2}$. Adapted from [1296] [1297]

In doped samples Pos(G) increases, while FWHM(G) decreases independently from the type of doping, e.g. electron or hole doping [1296, 1299-1301]. The increase in Pos(G) is due to the non-adiabatic KA removal, while the decrease in FWHM(G) is due to Pauli blocking of the phonon decay channel into e-h pair due to the increase in E_F [1300]. The 2D peak instead shifts up for hole doping and down for electron doping due to the change of the equilibrium lattice parameter. Therefore, Pos(2D) can be used to determine the type of doping. Doping also has an effect on I(2D)/I(G) and A(2D)/A(G). Both, I(2D)/I(G) and A(2D)/A(G) are maximum for zero doping and decrease for increasing doping [1300]. Fig. IX.36 summarizes the doping dependence of all the fitting parameters. Using Pos(2D) one can distinguish between electron and hole doping, and then use all the remaining fitting parameters and Pos(2D) to estimate the amount of doping. This is usually given in either

charge carrier concentration n with units 10^{13} cm^{-2} or Fermi level in units of meV. The charge carrier concentration is related to the Fermi level by [1296]: $E_F(n)=\hbar|v_F|\sqrt{(\pi\ n)}$, where $\hbar=h/2\ \pi$ is the reduced Planck constant, $v_F=1.1*10^6$m/s is the SLG Fermi velocity

Ref.[1302] introduced a three-stage classification of disorder, leading from graphite to amorphous carbons, that allows to simply assess all the Raman spectra of carbons:

- Stage 1: graphene to nanocrystalline graphene.
- Stage 2: nanocrystalline graphene to low-sp^3 amorphous carbon.
- Stage 3: low-sp^3 amorphous carbon to high-sp^3 amorphous carbon.

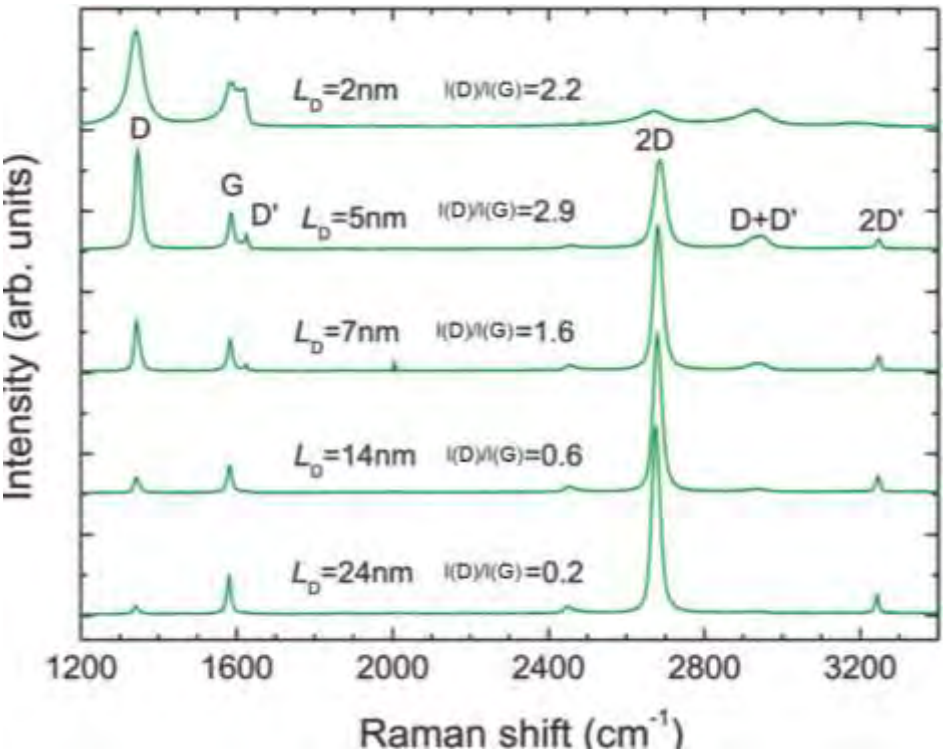

Fig.IX.37. Representative Raman spectra of ion bombarded SLG measured at E_L=2.41 eV [1295].

Here we focus on stage 1, the most relevant when considering the vast majority of publications dealing with graphene production, processing and applications. As shown in Fig. IX.37, in stage 1 the Raman spectrum evolves as follows: (a) the D peak appears and the ratio of D and G peak intensities, I(D)/I(G), increases; (b) the D' peak appears; (c) all peaks broaden; (d) the D +D' peak appears; (e) at the end of stage 1, the G and D' peaks are so wide that it is sometimes more convenient to consider them as a single, up-shifted, wide G band at ~1600 cm^{-1}[1295, 1302].

For a sample with rare defects I(D) is proportional to the total number of point defects probed by the laser spot, giving rise to I(D)/I(G)~$1/L_D^2$, where L_D is the average inter-defect distance. Taking into account the excitation energy dependence of the peak areas and intensities the inter-defect distance can be expressed by [1295]:

$$L_D^2\left[\mathrm{nm}^2\right]=\frac{4.3\times10^3}{E_L^4(\mathrm{eV})}\left[\frac{I(D)}{I(G)}\right]^{-1} \quad \text{(IX.7)}$$

E_L is the laser excitation energy in eV. This relation is valid for $L_D \geq 10$ nm (stage 1). By considering point-like defects, separated from each other by L_D, eq. (7) can be restated in terms of defect density, n_D, given by $n_D(cm^{-2}) = 10^{14}/\pi L_D^2$, as [1295] :

$$n_D\left[\mathrm{cm}^{-2}\right]=7.3\times10^9\,E_L^4(\mathrm{eV})\frac{I(D)}{I(G)} \quad \text{(IX.8)}$$

Eqs. (IX.7,IX.8) are limited to Raman-active defects. Perfect zig-zag edges [1303], [1304], charged impurities [1296, 1305], intercalants [1306], uniaxial and biaxial strain [1044, 1093, 1307-1314] do not generate a D peak.

Eqs.(IX.7,IX.8) are derived assuming negligible E_F shift. However, most samples in literature show doping levels of ~200meV up to 500meV. I(D) depends on the doping level [1292]: I(D) decreases for increasing doping. This needs to be taken into account when estimating the defect density. Eq (IX.7, IX.8) can be modified for samples with non-negligible doping [1292]

$$L_D^2\left[\mathrm{nm}^2\right]=\frac{(1.2\pm0.3)\times10^3}{E_L^4[\mathrm{eV}]}\left[\frac{I(D)}{I(G)}\right]^{-1}\{E_F[\mathrm{eV}]\}^{-(0.54\pm0.04)} \quad \text{Eq. (IX.9)}$$

$$n_D\left[\mathrm{cm}^{-2}\right]=(2.7\pm0.8)\times10^{10}\,E_L^4[\mathrm{eV}]\frac{I(D)}{I(G)}\{E_F[\mathrm{eV}]\}^{(0.54\pm0.04)} \quad \text{Eq (IX.10)}$$

Eqs (IX.9, IX.10) are valid for samples with a defect concentration corresponding to stage 1, and for $E_F<E_L/2$, which is by far the most relevant for graphene production and applications [1292].

In order to extract the defect density of the sample correctly the flowchart presented in Fig. IX.38 should be followed.

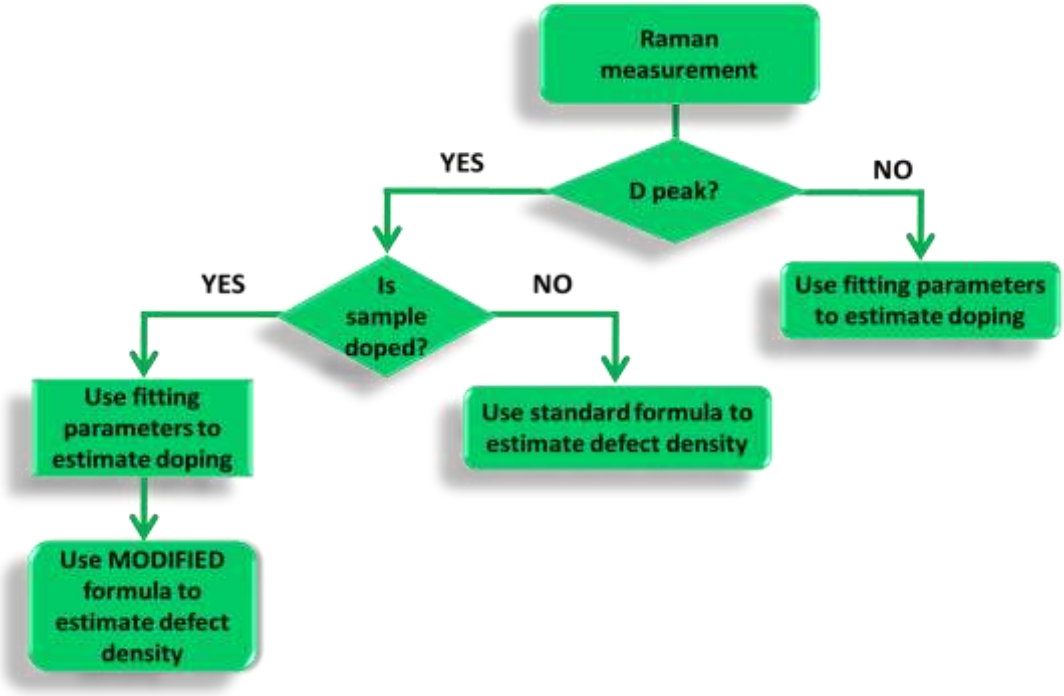

Fig. IX.38. Flowchart to estimate defect density in doped and undoped samples.

After recording a Raman spectrum, one first has to check whether a D peak is present. In case no D peak is present, the standard procedure of estimating doping from the Raman fitting parameters, such as Pos(G), FWHM(G), Pos(2D), I(2D)/I(G) and A(2D)/A(G), can be used. The presence of a D peak, leads to the next step, where one needs to check if the sample is doped or not, e.g. by looking at the relevant Raman peak fitting parameters. If the sample has doping≤100meV, Eq. (IX.8), can be used to estimate the defect density. If however the sample has non-negligible doping, the modified equation, Eq. (IX.10) has to be used. E.g. Fig. IX.39 shows spectra of a defective SLG at low, E_F=100meV, and high, E_F~500meV, doping. By analysing the spectra of doped and defected SLG (black line in Fig. IX.39) we get Pos(G)=1599cm^{-1}, FWHM(G)=12cm^{-1} and I(2D)/I(G)=0.94. This allows us to estimate ~500meV for the doping level of the sample using the graphs from ref. [1296]. The 2D peak is upshifted with Pos(2D)=2651cm^{-1} suggesting a hole doping. A decrease of the I(D) with doping is seen. The red spectrum for the undoped case gives I(D)/I(G)=2.8. Using Eqs. (IX.7,IX.8) gives n_D~3.1x10^{11}cm^{-2} and inter-defect distance L_D=10nm. The black line gives I(D)/I(G)~1.24. Taking the doping level~500meV into account we get n_D=3.4x10^{11}cm^{-2} and L_D=10nm, using Eqs. (IX.9,IX.10).

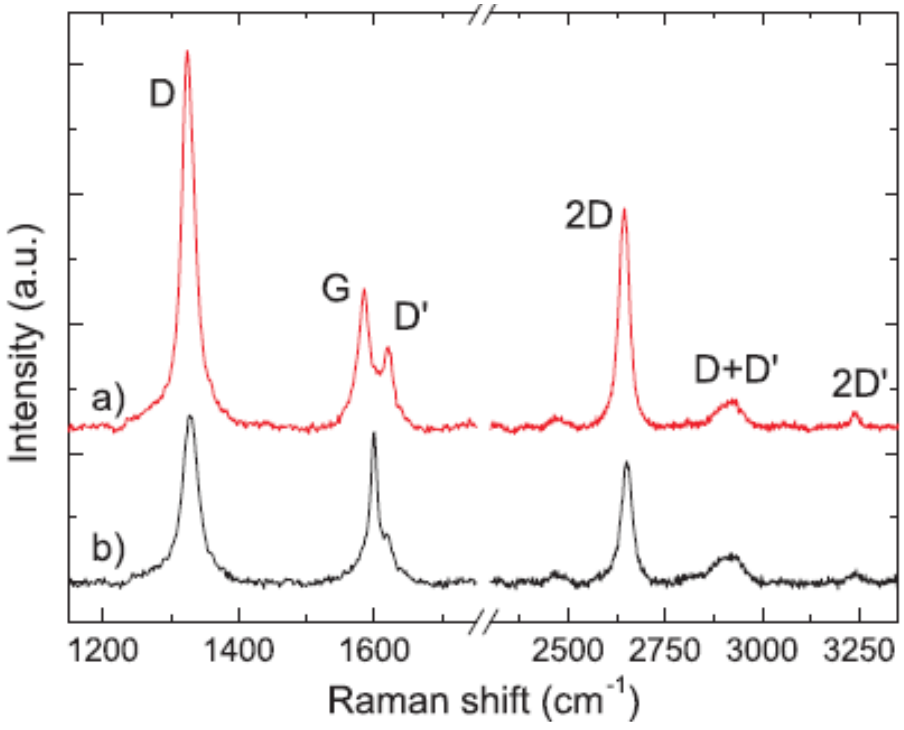

Fig.IX.39. Raman spectra of a defective graphene sample a) E_F≤100meV and b) E_F~500meV. Excitation wavelength: 633nm. If not original, please refer to publication. Adapted from ref [1093]

Strain can be present in a material compressed or stretched out of equilibrium. Strain can be either compressive or tensile. While compressive strain causes an upshift or stiffening of the Raman peaks, tensile strain causes a downshift or softening. Strain can be either isotropic, i.e. biaxial strain, or along a certain axis, i.e. uniaxial. Biaxial strain does not cause any change in peak shape, while uniaxial strain causes splitting of the G peak into two components G^+ and G^- for ε≥0.5% [1307], Fig

IX.40. The G peak is due to a doubly degenerate E_{2g} mode [1288]. By applying uniaxial strain this splits into two components, one along the strain direction and one perpendicular to it. While Pos(2D) changes as $\delta Pos(2D)/\delta\varepsilon \sim -64 cm^{-1}/\%$, the G peak changes as $\delta Pos(G^{+})/\delta\varepsilon \sim -10.8\ cm^{-1}/\%$ and $\delta Pos(G^{-})/\delta\varepsilon \sim -31.7\ cm^{-1}/\%$ [1307] in uniaxial , tensile strain experiments. Ref [1307] reported $\delta Pos(2D)/\delta\varepsilon \sim -144 cm^{-1}/\%$ and $\delta Pos(G)/\delta\varepsilon \sim -58\ cm^{-1}/\%$ for biaxial strain. To estimate the strain, the difference between fitted peak positions and unstrained reference peak positions needs to be derived. Then, by knowing how much the peaks shift with strain, i.e. $\delta Pos(2D)/\delta\varepsilon \sim -64 cm^{-1}/\%$ in case of the 2D peak for uniaxial strain, one can calculate the strain. To distinguish and decouple the combined effects of doping and strain a thorough analysis of all the fitting parameters is necessary [1305].

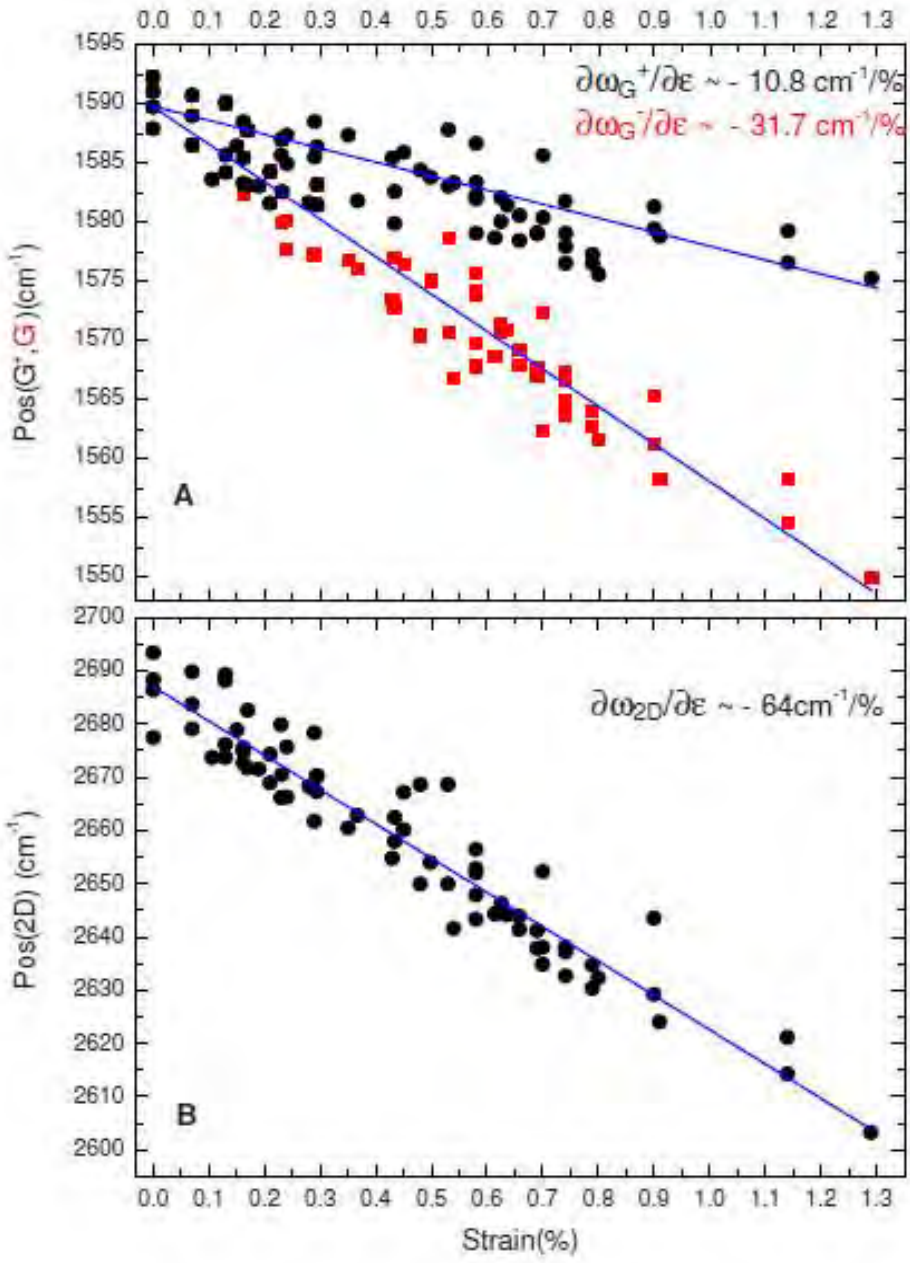

Fig IX.40: Change in Pos(G) and Pos(2D) with increasing amount of tensile, uniaxial strain. Fig. adapted from [1306].

Hexagonal Boron NIitride

Two Raman peaks in hBN are observed with the excitation of visible laser light, the C peak near 50 cm^{-1} and a high frequency E_{2g} mode near 1366 cm^{-1}[1315]. The C peak strongly depends on N so that it can be used to estimate N [1316, 1317]. The high frequency E_{2g} Raman peak weakly depends on N. The peak positions for the mono layer and bulk are ~1368 cm^{-1} and ~1366 cm^{-1} [1317-1320]

Transition metal dichalcogenides

Many TMDs are composed of three atomic layers X-M-X, represented by MX_2, where M is a [1321] ordering, 2H (Hexagonal symmetry), 3R (rhombohedral symmetry) and 1T (tetragonal symmetry).The most common polytype is 2H, for example, MoS_2, $MoSe_2$, WS_2, and WSe_2. For 2H-MX_2, two prominent Raman peaks appear in the high frequency range, A_1` and E` modes. A_1` is an out-of-plane vibrational mode and E` is an in-plane one [1322, 1323]. The peak positions depend on N so that the difference of their positions can be used to estimate N. Typically, the peak position of A_1` decreases with decreasing N, and E`is opposite to A_1`. In the ULF range, C and LBMs are observed and can be used to estimate the coupling strength between layers and N [77]. Defects in MoS_2 broaden the E' and A_1' peaks and E' becomes asymmetric to the low frequency [1324] . A new Raman peak near 200 cm^{-1} appears due to the defect induced longitudinal acoustic (LA) phonon at M point [1324]. As uniaxial strain increases on 1L-MoS_2, the A_1' peak shows no measurable shift while the degenerate E' peak splits into two peaks, E'^{+} and E'^{-}[1325]. The E'^{-} peak shifts by 4.5 cm^{-1}/% strain and E'^{+} peak shifts by 1.0 cm^{-1}/% strain. The A_1' peak is not sensitive to the strain, while is sensitive to the doping. By increasing doping level of 1L-MoS_2, the E' peak shows no change, while A' redshifts and broadens due to electron-phonon interactions [1321].

Absorbance and Fluorescence

Transition metal dichalcogenides

UV/Vis transmission spectroscopy can provide information on the structure of GRM flakes, as especially inorganic LMs have well documented excitonic transitions [1326] characteristic for the material and even its polytype or phase [349, 350, 1215]. Information on concentration can be extracted [171, 227, 1214, 1215, 1327]. However, for this to be performed reliably, it is essential to be aware that when transmittance mode is used, extinction and not absorbance spectra are obtained. Extinction is related to the transmittance, T, via $T= 10^{-Ext}$, where $Ext=\varepsilon C\l$, with ε the extinction coefficient, C the nanosheet concentration and $\l$ as the path length This means that the quantity that is measured contains information related to both the absorbance and the scattering of light [173, 175, 227, 230, 1214, 1328]. Although the scattering component of the extinction coefficients is size dependent [173, 175, 227, 230, 1214, 1328], it is also the case that the absorbance coefficient is dependent on size, due to edge effects [170, 171, 173, 175]. Hence, the overall extinction coefficient is heavily size-dependent and it is required to determine it gravimetrically for

dispersions with a range of nanosheet lateral sizes and thicknesses to achieve an accurate determination of the concentration in unknown samples.

The systematic change in extinction and absorbance spectra with nanosheet lateral size can be used to establish quantitative metrics for lateral size once the nanosheet sizes are determined by statistical microscopy. Such quantitative relationships were established for MoS_2 [170], WS_2 [171], GaS [173] and black phosphors [175].

In addition, changes in the LM band structure as a result of confinement effects are reflected in changes in the peak position of the excitonic transitions. This means that information on nanosheet layer number is encoded in optical extinction spectra [170, 171, 173].

An example of the spectral changes with nanosheet size and thickness for LPE MoS_2 and WS_2 is shown in figure IX.41 [236]. Figure IX.41 A and C plots optical extinction spectra of MoS_2 (A) and WS_2 (C) with different mean nanosheet sizes and thicknesses. In particular due to the power law nonresonant scattering background (> 680 nm for MoS_2, > 650 nm for WS_2), peak positions are best found from the second derivative. Second derivative spectra of a subset of the samples in the region of the A-exciton are shown in figure IX.41 B and D. Peak intensity ratios can be used to express the spectra changes associated with edge effects. Figure IX.41 E, F shows plots of peak intensity ratios as function of mean nanosheet length for MoS_2 and WS_2 with both materials behaving similarly. This means that the nanosheet size for both materials can be quantitatively linked to the nanosheet length via identical equations [236]. Due to the changes in spectral shape, extinction coefficients are also dependent on nanosheet size. This is more or less severe depending on the spectral position. For example, as plotted in Figure IX.41 G, the extinction coefficient of the A-exciton for both materials is strongly length dependent. However, this is not the case at 345 nm for MoS_2 and 235 nm for WS_2 so that the extinction coefficient at these spectral positions can be used as a robust measure for nanosheet concentration over a broad range of sizes. In addition, extinction spectra do not only provide insight in nanosheet lateral size and dispersed concentration, but also in nanosheet thickness. The number of layers can be quantitatively related to the peak position/energy of the A-exciton (obtained from an analysis of the second derivative) as plotted in Figure IX.41 H.

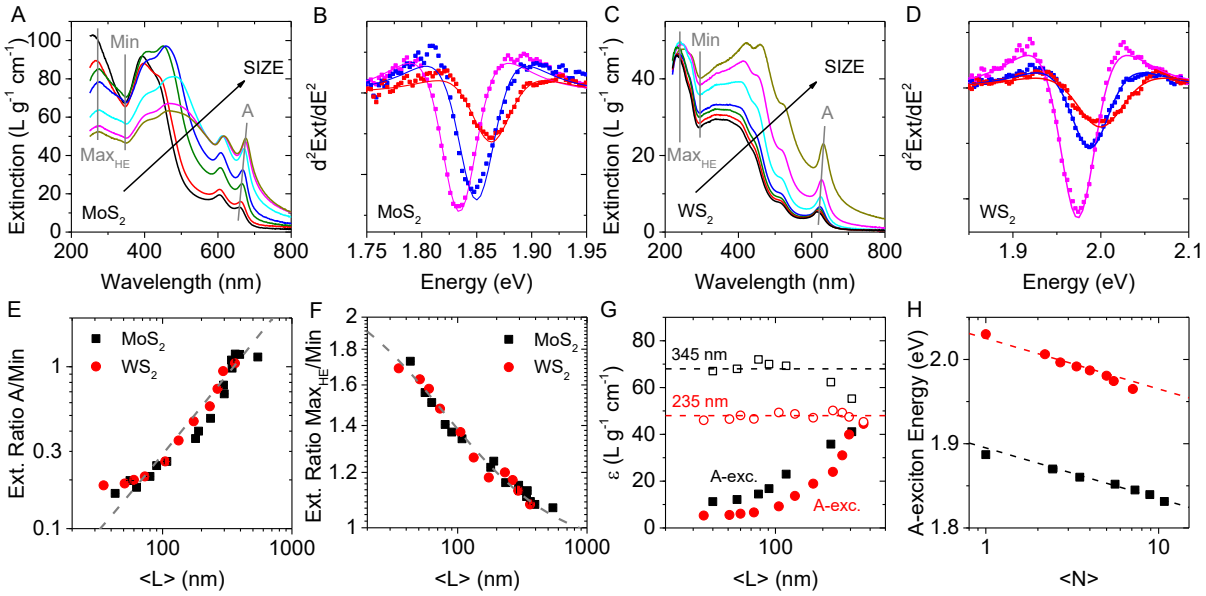

Fig. IX.41: A, C) Optical extinction spectra of LCC separated MoS_2 (A) and WS_2 (C). Peaks relevant for the analysis are indicated. B, D) Second derivatives of the A-exciton plotted versus energy for MoS_2 (B) and WS_2 (D) after smoothing the second derivative with Adjacent Averaging. The solid lines are fits to the second derivative of a Lorentzian to assess peak positions/energies. E, F) Plots of peak intensity ratios as a function of mean nanosheet length <L>. Data for MoS_2 and WS_2 falls on the same curve. Hence the same equations can be used to quantify nanosheet length. E) Plot of the peak intensity ratio at the A-exciton / local minimum. F) Plot of the peak intensity ratio at the high energy maximum / local minimum. G) Extinction coefficient at different spectral positions as function of nanosheet length. At some spectra positions (such as the A-exciton), extinction coefficients are highly size dependent, while at others (345 nm for MoS_2 and 235 nm for WS_2) this is not the case. H) Plot of A-exciton peak energies (from second derivatives) plotted as function of layer number <N>. Adapted from Ref. [236].

PL is also a very powerful tool to study GRMs, as it provides information on the band gap and its direct/indirect nature [1329, 1330]. In PL measurements, the GRM is excited with a laser with higher energy than bandgap to create electron-hole pairs. The emission yield upon radiative recombination is studied with a spectrometer. The excitation laser is notch filtered at the entry of the spectrometer to remove the Rayleigh contribution, which is much larger than the photoluminescence yield and might saturate the detector. Fig. IX.42a compares PL spectra in MoS_2 flakes with different N. The peaks correspond to the recombination of excitons. A and B are related to direct bandgap transitions at the K point of the Brillouin zone and the I corresponds to an indirect bandgap transition along ΓK, that becomes favourable for multilayery. Therefore, PL allows one to observe quantum confinement in MoS_2, resulting in a N dependent bandgap. PL also makes evident the direct-to-indirect transition that occurs due to the interlayer interaction in MoS_2. While 1L-MoS_2 has direct bandgap with a bright PL emission, ML flakes are indirect bandgap with a much lower PL yield.

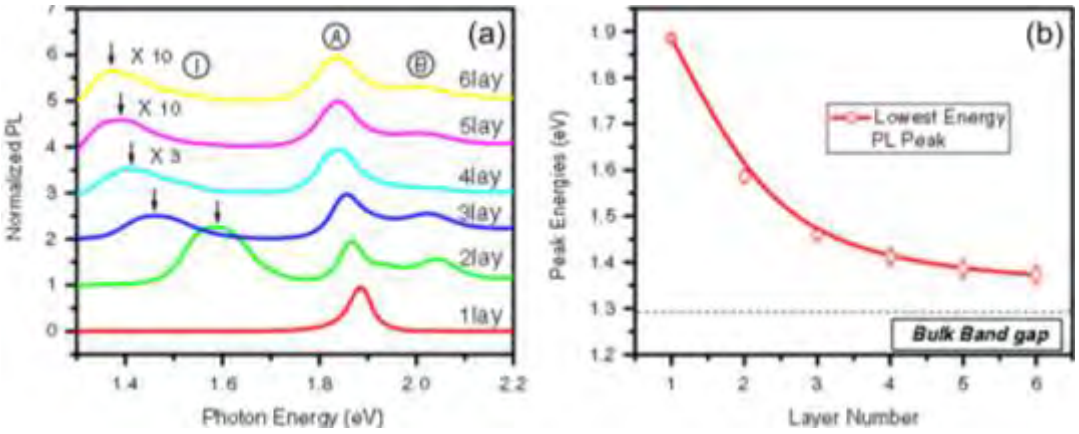

Fig. IX.42. (a) PL spectra on MoS_2 flakes with N=1-6.. The spectra show peaks corresponding to excitonic features, labelled A, B and I. (b) N dependence of the lowest energy PL peak peak. Adapted from Ref. [1329]

Hexagonal Boron Nitride

As detailed in [1317] this spectroscopy has the capability to investigate and to benchmark the optical and structural properties of both bulk and layered hBN samples. To this aim, hyperspectral capabilities of cathodoluminescence set-up dedicated to the study of large band gap materials at 10K are particularly suited [1331, 1332] and are reviewed in Fig. IX.43**.** This Figure shows a typical cathodoluminescence spectrum recorded at 10K on a sample prepared from a reference single crystal [1333] together with monochromatic images recorded at energies related to the different emission bands. It displays emission lines in a broad energy range from almost 6 eV to 3 eV, which are described below.

Luminescence properties of hBN are governed by unusually strong excitonic effects resulting in recombinations at energies below the bandgap energy. It is recalled that according to the most reliable ab initio calculations, hBN is a large band gap material with an indirect band gap around 6 eV and a direct band gap around 6.5 eV. Excitonic recombinations are the so-called near band edge (NBE) recombinations located in the deepest UV region presented in Fig. IX.43. Among them, a series of peaks at the shortest wavelength (210– 215 nm) is referred as the S series which intrinsic origin was proven recently in an investigation of hBN materials obtained from different growth procedures [1317, 1334]. The excitonic nature of these recombinations is supported by theoretical studies [1335, 1336] but their fine structure splitting and their correlation with absorption data are still intensively debated [1334, 1337-1340].

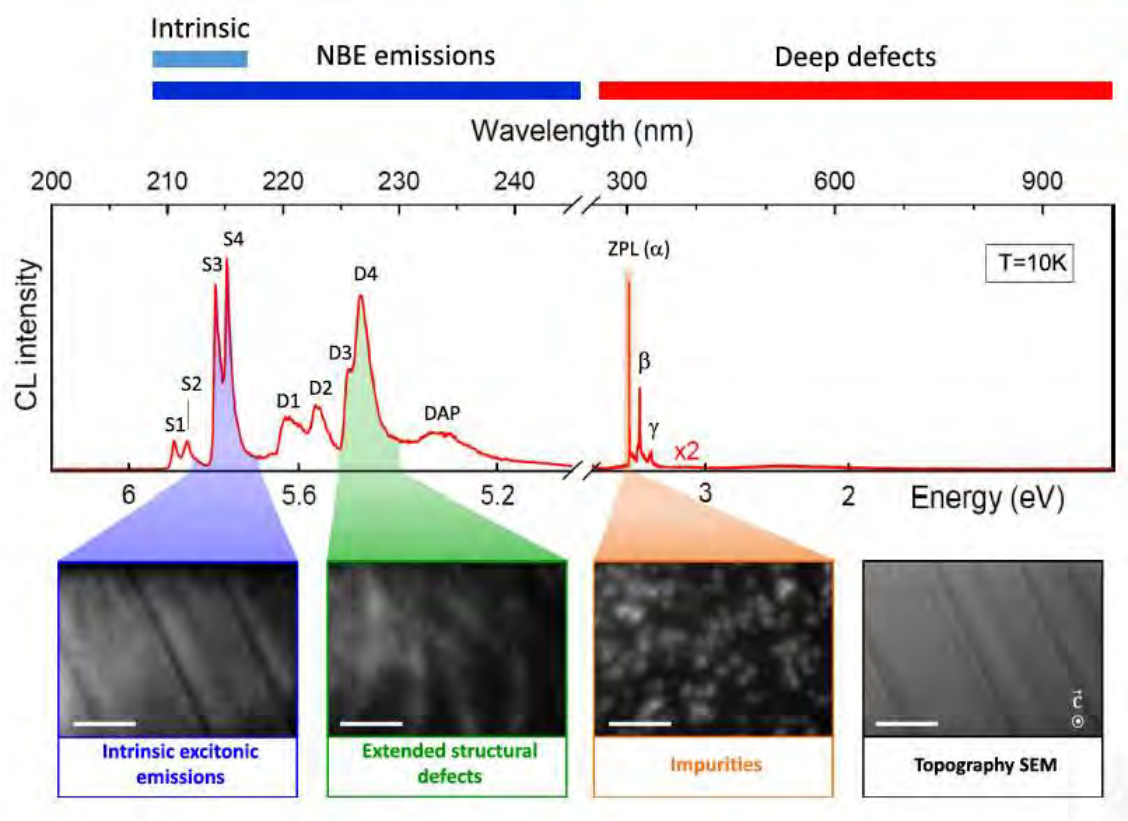

Fig. IX.43 : Upper: typical cathodoluminescence spectrum of hBN in the 200–1000 nm range acquired at 10 K on a sample prepared from a reference single crystal [1333].*Lower: SEM image (black) with the corresponding monochromatic CL images recorded in the same area at ±3 nm around 215 nm(blue), 227 nm(green) and 303 nm(orange). Scale bar: 1 µm. Reproduced from* [1317]

Other luminescence features can be observed in the 210– 250 nm region tentatively assigned here to the NBE region. At larger wavelengths than the S series, the most documented luminescence feature is the so-called D series (220– 227nm) (see Fig. IX.42) related to the presence of extended structural defects. These emissions have been shown to arise from recombinations of excitons trapped at structural defects such as stacking defects, dislocations or grain boundaries [1332, 1341, 1342]. Finally, a weak and broader emission is often observed at 233 nm, such a Fig. IX.43, and has been attributed to donor-acceptor pairs (DAP) recombination processes [1343].

The series of CL monochromatic images recorded from the same zone, Fig IX.43, illustrate the distinct origins of the S and D luminescence features. The image, related to the intrinsic emissions (S series) and recorded by collecting photons emitted at 215± 3 nm, is almost homogeneous except along on parallel black lines due to thickness variations along the sample (see the SEM image of the same area). The CL image taken from the D series (227 ± 3 nm) displays several continuous lines crossing the sample in random directions at the places where structural defects are present in the sample. From these features, it has been proposed to use the ratio of the integrated intensity of the D band relatively to that of the S band, called D/S ratio, as an indicator of the structural defect

concentration [1342]. Typically in defect free areas, the D/S ratio can be as low as 0.3 while it can increase up to two order scales at the location of structural defects. Therefore, as illustrated in Fig IX.44, hyperspectral mapping of the D/S ratio provides the most valuable tool to get, in a non destructive way, the spatial distribution of structural defects in any hBN sample and to assess its crystalline quality, as shown in [1317].

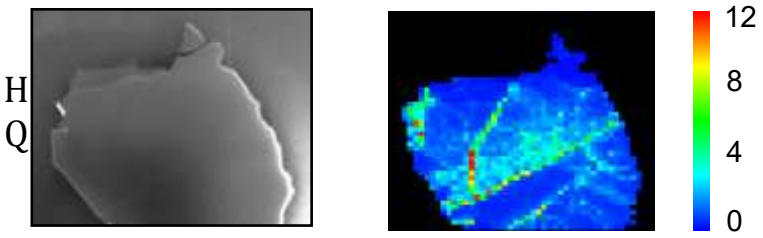

Fig. IX.44: left : SEM image of a hBN crystal flake (commercial source 'HQ Graphene'). Right : Catholuminescence mapping of the D/S ratio of the integrated intensity of the D band relatively to that of the S band. Adapted from [1317]

At larger wavelengths (> 250 nm), the luminescence spectrum of Fig. IX.42 reveals deep defect emissions. A luminescence signal with a maximum at 302.8 nm is regularly detected in various hBN sources. This emission is extremely sharp: its linewidth is lower than 0.075 nm, the spectral resolution of the experiment. It has been identified as the zero-phonon emission line (ZPL), labelled here α, of impurities introduced in the lattice during the synthesis, probably carbon (or possibly oxygen) as revealed by a detailed SIMS analysis [1333]. The β and γ peaks are assigned to phonon replicas, with an energy of 195 meV, involving a local vibrational mode (LVM) [1344] or phonons of the hBN bulk crystal lattice [1345]. In Fig. IX.44, The CL image recorded from the ZPL emission at 302.8 ± 3 nm reveals a spatial distribution which is typical of chemical impurities. The luminescence from the deep defects is distributed as bright spots, which confirms their distinct origin from D and S series. The observed luminescence spots unveil a discrete and random distribution of impurity centers throughout the sample. Similar spots were recently reported and have been identified as single photon emitters, indicating that they correspond to isolated atomic centers randomly diluted in the crystal lattice[1346]. In recent studies, sharp emissions from deep defects have been also been identified as single emitters in the visible and the near-infrared spectral ranges after introducing intentionally defects in the hBN crystal [1347], [1347].

Since the ultimate characterization relies to mono and few BN layers, the dependence of the number of layers on the NBE emission has been investigated on mechanically exfoliated flakes from hBN bulk crystallites [1334]. The samples inspected were free of defects with no detectable D band. Typical thickness evolution of the CL spectra is shown in Fig. IX.45. The S series, characteristic of the bulk hBN luminescence, progressively vanishes in the thinnest layers in favor of a single peak found at 5.909 eV in 6L samples. Such an effect was observed in different kinds of samples, including reference single crystals and commercial sources, which points an intrinsic behaviour and can be

considered as a signature of low dimensionality effects on the intrinsic luminescence of hBN. With the support of combined ab initio and tight binding calculations, the remaining line observed in the thinnest layers is assigned to direct bright excitons, as theoretically expected for the monolayer [1335]

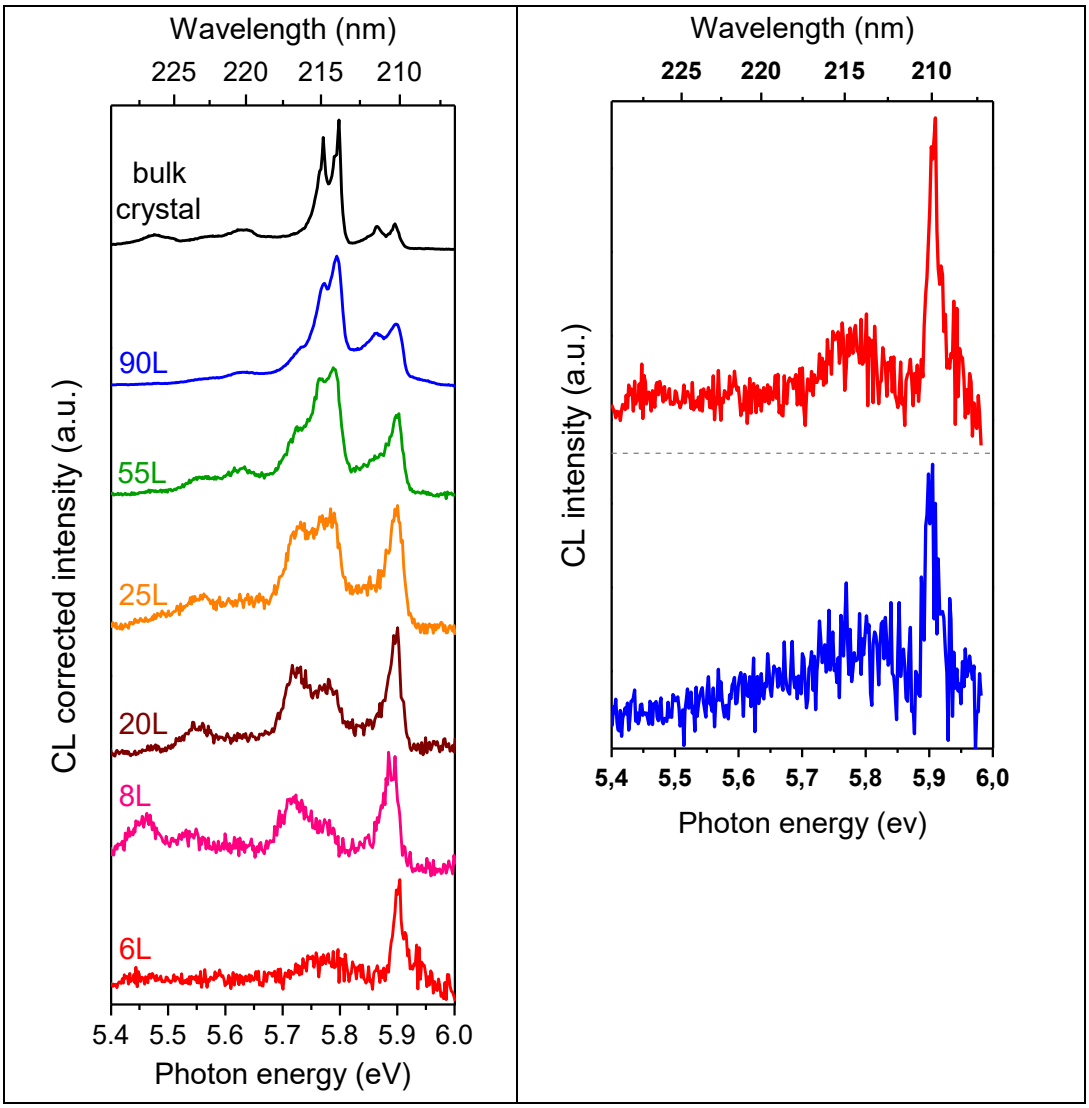

Fig. IX.45 : left : series of CL spectra recorded at 10K on mechanically exfoliated flakes from a commercial source (St Gobain Tres BN source) with different thicknesses from bulk to 6L and transferred on to Si/SiO2 substrates by a wet technique. The number of layers is determined from both optical and AFM measurements. Right : CL spectra recorded on 6L exfoliated flakes from the St Gobain crystallite (upper spectrum) and from a single crystal grown at NIMS [1333] (bottom spectrum). Adapted from [1334].

XPS

XPS measures the kinetic energy of photoelectrons emitted from a sample irradiated with X-rays, which transfer their energy to a core-level electron. This electron is emitted out of the sample surface from its initial state with a kinetic energy dependent on the incident X-ray photon energy and the binding energy of the atomic orbital from which it is originated following the relationship: $E_{kinetic} = E_{photon} - E_{\_binding\text{-}efective\_wf}$, where $E_{kinetic}$ is the Kinetic Energy of the emitted electron, E_{photon} is the energy of the incident photon and $E_{\_binding\text{-}efective\_wf}$ is the effective binding energy of the corresponding atom. The energy and intensity of the emitted photoelectrons can be analysed to identify the elemental and chemical composition in the parts per thousand [1348, 1349]. Photoelectrons originate from depths below 10 nm, and therefore the information obtained is surface-sensitive [1348]. The XPS equipment has to detect electrons, and therefore the sample has to be introduced in a UHV environment. The area illuminated is typically of ~0.5-1 mm when a X-Ray monochromator is used [1348] , meaning that the information obtained correspond to an average on the irradiated area. Typically, best energy resolution that one may have is about 0.4 eV in standard XPS-lab machines. However, this value may be increased to about 0.2 eV in synchrotron radiation XPS facilities.

When analysing graphene based samples there are three main figures that can be extracted from analysis of the XPS spectra: presence of contaminants (or heteroatoms), coverage, and chemical state of the C atoms.

The presence of contaminants (heteroatoms reacting with graphene or other elements) can be derived from a survey spectrum of the sample, i.e. to record in a wide range all the relevant peaks in binding energy. This spectrum usually covers from the Fermi energy to about 50 eV less than the photon energy, and show core-level peaks from all elements on the sample surface. The amount of impurities can be determined by integrating the area of the different levels and comparing the ratio of the different peaks. The analytic expressions for deriving the **coverage** of impurities or graphene patches with respect to a substrate can be found in references [1348, 1349].

The upper spectrum in Fig. IX.46 has been recorded from a clean Pt(111) surface. Only Pt peaks are visible. The middle one belongs to the same sample after SLG growth. In addition to the Pt peaks, a new peak related to the carbon (C1s) appears. Finally, the sample is exposed to air and gets contaminated, mainly with oxygen that binds to SLG as epoxy or hydroxyl groups [785, 875, 1350]. The lower XPS survey spectrum shows in addition to the platinum and carbon peaks the oxygen peak (O1s). This technique is surface-sensitive. Whenever the sample gets something on top, i.e. graphene, oxygen…the intensity of its main peaks decreases. In Fig. IX.46 the Pt4f peaks intensity decrease from the upper spectrum to the lower one, as SLG is grown, and then exposed to air.

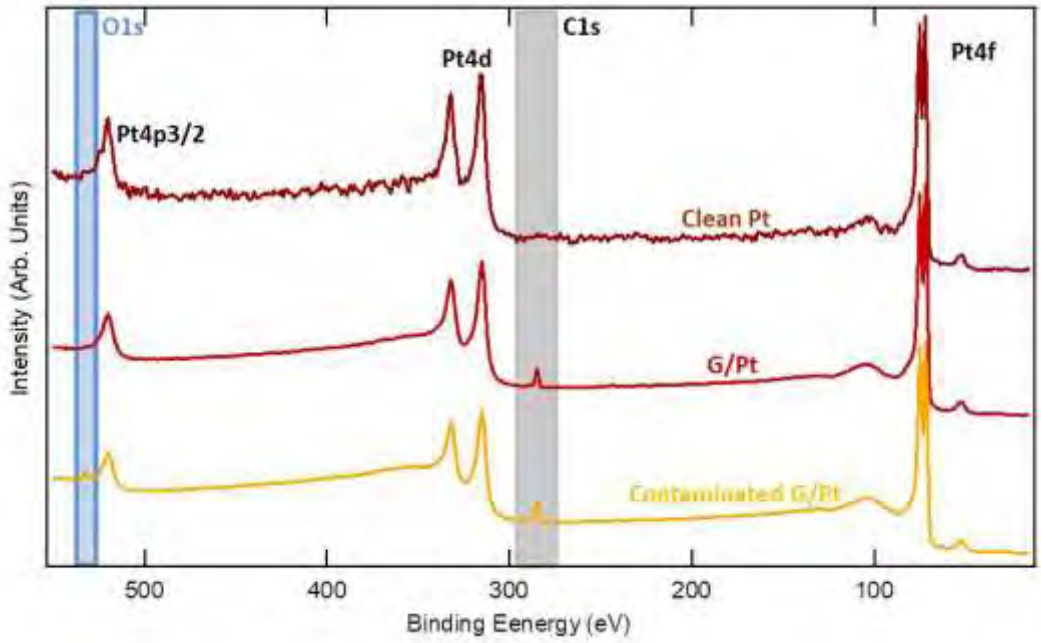

Fig. IX.46. XPS spectra survey of three samples: (top) Pt(111), (middle) SLG/Pt(111), (bottom) contaminated SLG/Pt(111). Grey (blue) area represents the zone where C1s (O1s) related peaks appear.

The chemical state of the carbon atoms of graphene can be also derived from XPS. The characteristic binding energy of C 1s when Carbon is in a sp^2 configuration (either graphene or HOPG) is about 284.5 eV [1351] (the precise value depends on the analyser)[1352]. When SLG is grown on top of substrates, such as metals or semiconductors, the C 1s binding energy might slightly change due to the interaction between the graphene and the substrate [1348]. C-sp^2 is ubiquitous as many contaminants include carbonaceous species that are difficult to discern from graphene.

Importantly, bonding of the C with other atoms leads to different binding energies, and therefore a precise determination of the C1s binding energy may give you the kind of bonding. This is known as core level shift, and most of the values are tabulated [1349]. Thus, C-sp^3 appears at about 285.0 eV [1353-1356]. To appreciate the different components of an XPS peak, a curve fitting shall be performed.

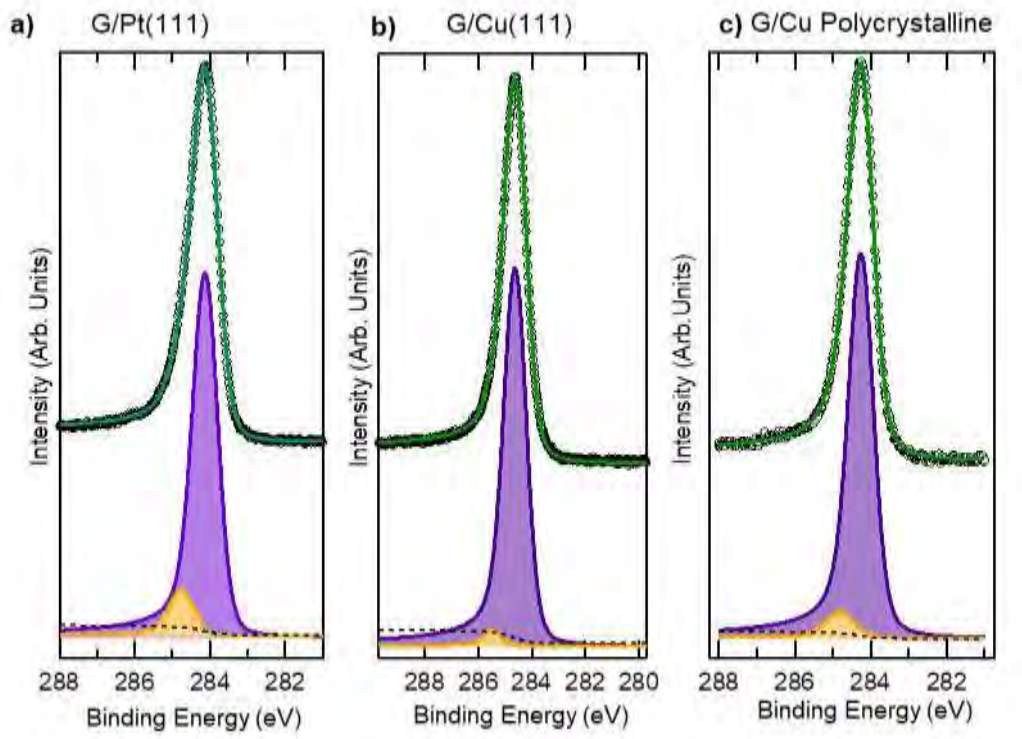

Fig. IX.47. C1s XPS spectra of a) SLG/ Pt(111) b) SLG/Cu(111) and c)SLG/Cu polycrystalline

Fig. IX.47 shows three C1S XPS spectra of SLG grown on different substrates by thermal decomposition of fullerenes in a UHV environment on Pt(111) [875] Cu(111) and polycrystalline Cu. The peaks are fitted with two components. The purple and narrow one is related with C-sp^2. This component is fitted using a Doniach-Sunjic curve, which is the mathematical function that better fits an XPS core level peak [1348]. In this curve, the asymmetry parameter used is 0.068 eV [1348]. The Lorentzian FWHM is about 0.13 eV. The binding energies found for the C-sp^2 are 284.1, 284.6, 284.3 eV for SLG on Pt(111), Cu(111) and polycrystalline Cu respectively. Another small component is needed to complete the fitting, with a binding energy that depends on the substrate. This can be assigned to C-sp^3 [1353-1355].This component appears in defective SLG due to the presence of different domains and grain boundaries [1270]. In Fig. IX.47 the fitted values are: 284.7, 285.4, 284.8 eV for SLG on Pt(111), Cu(111) and polycrystalline Cu. The width of these peaks (0.13 eV) may increase when the graphene surface is damaged, contaminated or oxidized.

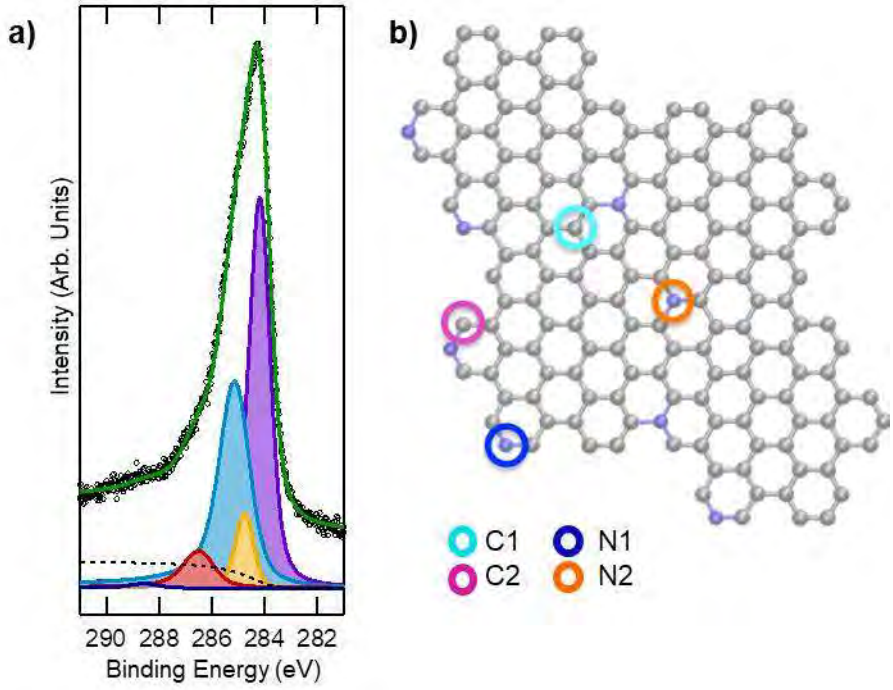

Fig. IX.48 a) C1s XPS spectrum of a SLG/ Pt(111) after exposure to air and water. New components related with epoxy and hydroxyl groups appear as a tail of the main C-sp^2 component. b) Schematic representation of the N and C atomic configuration of heteroatoms on a graphene flake related with the XPS peaks assignments. C1 (light blue): sp^2 C atoms; C2 (purple): C–N pyridine ring; N1 (dark blue): N atoms in the pyridine ring interacting with the metal substrate (copper in this example); N2 (orange): substitutional N atoms in the graphene network. Adapted from [1357].

Fig. IX.48a shows an example C1s peak of a SLG exposed to air and water. The C1s become a broad peak with many components. The purple one at 284.1 corresponds to the C-sp^2 component and the yellow one at 284.7 to the C-sp^3 component (as in the clean sample depicted on Fig. IX.47a. Three new components related to the surface contaminants are also present: the light blue at 285.1 assigned to C-OH, the red one at 286.5 assigned to C-O and the dark blue at 288.5 assigned to C=O [1353, 1358]. They can be fitted using Gaussian-Lorentzians. These epoxy groups (CO bonding or oxidized species) and hydroxyl groups appear as a tail of the main peak at higher binding energies and they are a fingerprint of the "cleanliness" of a graphene sample. A soft annealing in vacuum will remove these type of contaminants. Table IX.III shows typical binding energies of some of the most important oxygenated species (epoxy and hydroxyl) bonded to C atoms. It has to be taken into account that the binding energy may slightly change (within ±0.5 eV) depending on the system or substrate used.

It is important though, not to mistake the contamination of graphene with the graphene oxide. Graphene oxide has been extensively studied [266], among other reasons because it presents a better yielding. A simple method to obtain graphene from graphene oxide consist of reducing it by the use of chemical reducing agents. This process is easily followed by XPS by evaluating the ratio of the component at around 286.5 eV (mainly C–O bonds) with the C-sp^2 [1359].

Heteroatoms. Finally, it is important to remark that in some cases one may be interested in the binding energy not of the C atoms, but of other elements that are covalently linked to graphene. The most important case corresponds to nitrogen heteroatoms. Its binding energy strongly depends on the adsorption configuration inside the graphene network. A scheme of the carbon and nitrogen atoms configuration in relation with the XPS components is shown in Fig. IX.48b. Four possible configurations of the nitrogen and carbon atoms are shown: a carbon atom in an sp^2 configuration (C1, light blue circle), a carbon atom in a pyridine ring (C2, purple circle), a nitrogen atom in the pyridine ring interacting with the metal substrate (copper for this case) (N1, dark blue circle) and a substitutional nitrogen atom in the graphene network (N2, orange circle). The XPS binding energies of these atoms in these particular configurations are resumed and referenced on the Table IX.III.

	C1	C2	N1	N2	R-N-C	C-Metal	sp^3	C-OH	C-O	C=O	O-C=C/C-C=O
Binding Energy (eV)	284.4	285.9	398.0	400.6	399.5	283.2	284.7	285.4	286.7	288.5	290.5
Ref	[1357]	[1357]	[1357]	[1357]	[1115]	[1357]	[875]	[785]	[785]	[785]	[785]

Table IX.III. Reported binding energies of the graphene carbon atoms in different chemical states. C1, C2, N1 and N2 are related with the scheme of Fig. IX.48b and represent the sp^2 carbon atoms(C1), C-N pyridine ring (C2), N atoms in the pyridine ring interacting with the metal (N1)) and the substitutional N atoms in the graphene network(N2), respectively. In addition, binding energies of C-metal, sp^3 configuration, radical-nitrogen, epoxy and hydroxyl groups are also given. It is important to remark that the values may slightly change depending on the substrate.

Epitaxial Graphene grown on SiC

XPS characterization of C-rich SiC(0001) surfaces can be used to extract the degree of graphitization. SiC surfaces prepared in UHV conditions present a series of surface reconstructions depending on the C/Si stoichiometry [1360]. For T>1350 K, Si depletion from the surface eventually leads a reconstruction presenting a (6√3×6√3)R30° LEED pattern [598, 612, 1361-1363]. This is also known as quasi-(6x6), BF or zero layer graphene (ZLG). The atomic structure is normally described as a graphene-like honeycomb carbon mesh highly buckled and covalently bonded to the uppermost Si layer [1364]. This covalent interaction alters the electronic properties of the graphene-like layer and it becomes a semiconductor [545]. The XPS spectrum is presented in Fig IX.49. The lower spectrum is

an overview on a (6√3×6√3)R30° surface. The C1s peak (284.8 eV) presents higher intensity than the two Si-related peaks; Si2p (101.4 eV) and Si2s (152.0 eV) [785, 1349] . The C1s/Si2p ratio is~1.15 for 1486.6 eV, indicating that the surface is carbon-rich [612].

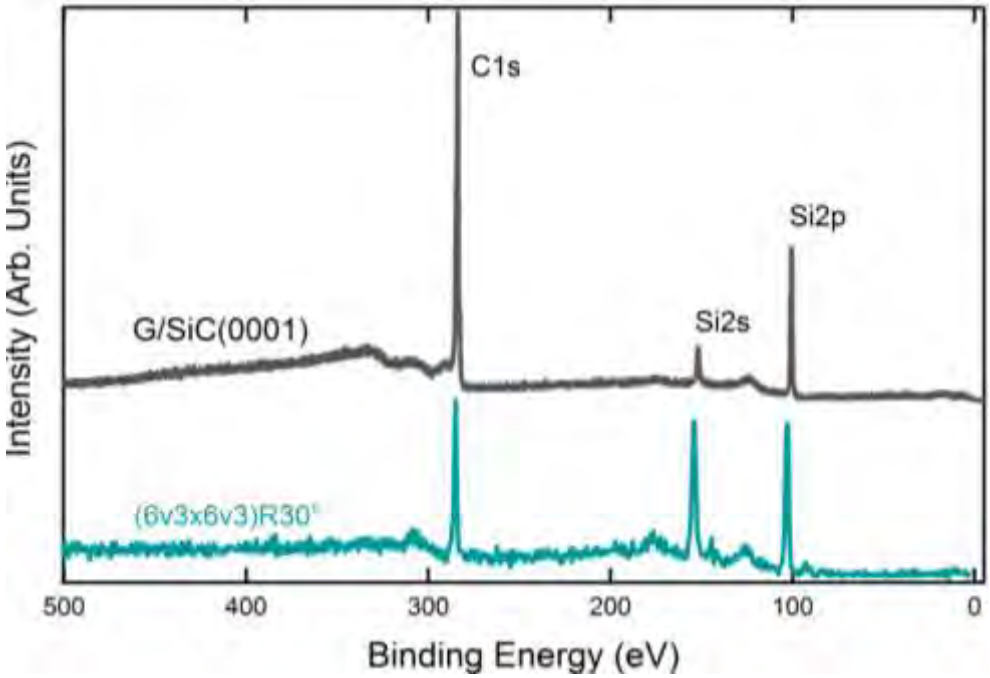

F*ig .IX.49: Lower spectrum: (6√3x6√3)R30° surface using an Al Kα anode (1486.6 eV) as X-ray source. Upper spectrum: synchrotron radiation XPS overview of the SLG/SiC(0001) sample annealed at 1400 K for 600 eV photons.*

A SLG/SiC(0001) spectrum is presented in Fig. IX.49 for comparison. The upper black spectrum corresponds to a synchrotron radiation-based overview of a sample annealed at 1400K recorded with a photon energy of 600 eV [1365] The C1s peak dominates, being the C1s/Si2p ratio 2.53, which indicates a higher carbon concentration on the surface than in the (6√3x6√3)R30. The good resolution of the XPS spectra in Fig. IX.50 allowed to decompose the peaks into their curve-components, which results from a convolution of a purely quantum Lorentzian energy distribution (FWHM, 0.12–0.2 eV) with a Gaussian distribution (FWHM, 0.4–0.7 eV) [1366].

The carbon chemistry is very rich and the interpretation of the C1s spectra is complicated. One could decompose the C1s peak of SLG/SiC(0001) in five components. That at 284.83 eV can be assigned to C-sp^2 atoms, and is the biggest contribution to the C1s core level peak, with 58.2% of the total area. This is used for calibration of the energy width of the Lorentzian and Gaussian widths. The components at lower binding energies (283.98 eV) can be attributed to carbides [1367], due to the C in the SiC bulk [542, 543]. There are three other components at higher binding energies, which can in principle be assigned to different configurations of C atoms in the superficial rearrangement that takes place on surface reconstruction [543]. These can be assigned to surface-related peaks: C-Si 1 at 285.26 eV (orange component in Fig. IX.50a), C-Si 2 at 285.73 eV (pink component in Fig. IX.50 a) and S. C-Si 3 at 286.4 eV (bordeaux component in Fig. IX.50b).

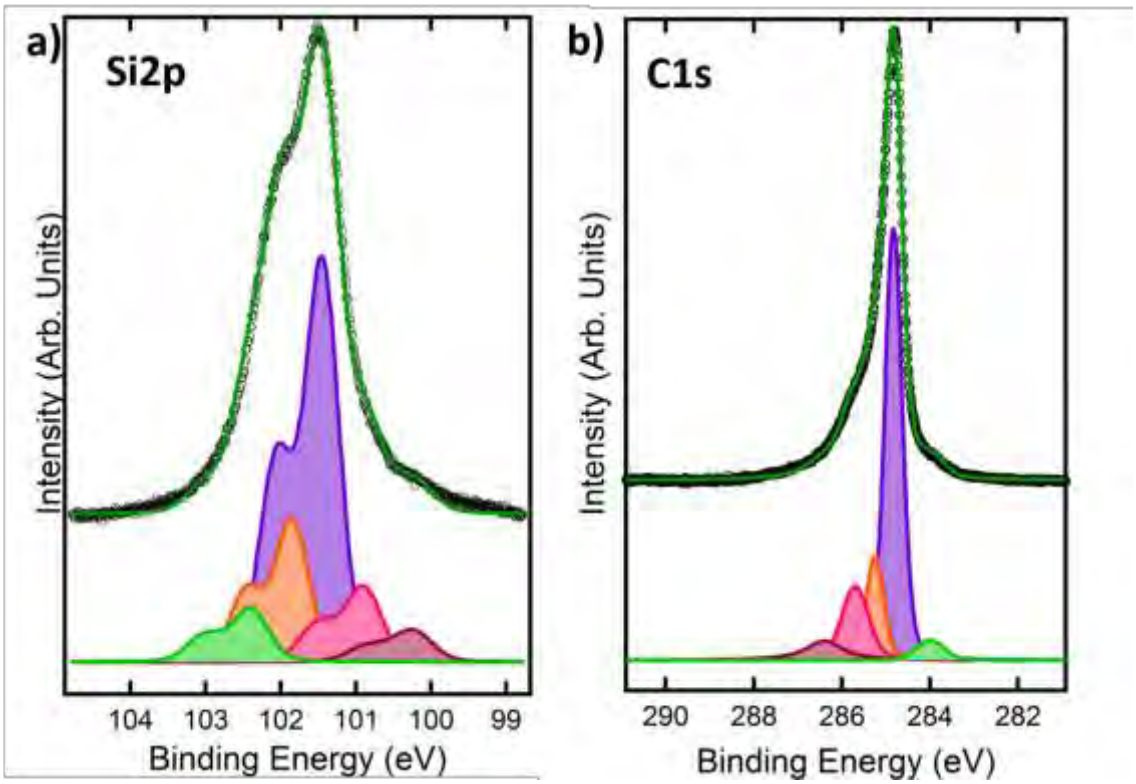

Fig. IX.50: a) XPS Spectrum of Si2p peak of SLG/SiC annealed at 1400K recorded with a photon energy of 150 eV. b) XPS spectrum of C1s peak of SLG/SiC annealed at 1400K recorded at 400 eV.

The Si2p curve can be decomposed in five Si doublets. Based on H adsorption it is possible to distinguish the surface-related from the bulk-related components. Three components present intensity decrease upon H exposition. The intensity of the components at 100.4, 101.45 and 101.85 eV decrease~15% after H exposure, while the other two components at 100.9 and 102.4 eV present a small (3-4%) increase [1367]. This suggests that the components which decrease and those that increase to be related to surface and bulk Si atoms respectively.

ARPES

ARPES is a technique that extracts the information retained by the electrons, emitted from a solid surface upon excitation with a photon. Due to the confinement of the electronic wavefunctions in the (x,y) plane, the band structure of 2d materials can be fully determined through angle-resolved photoemission spectroscopy (ARPES) [1368-1370]. This technique takes advantage of the photoelectric effect [1371], hence ultraviolet or soft X-ray radiation is used to extract electrons from the investigated sample.

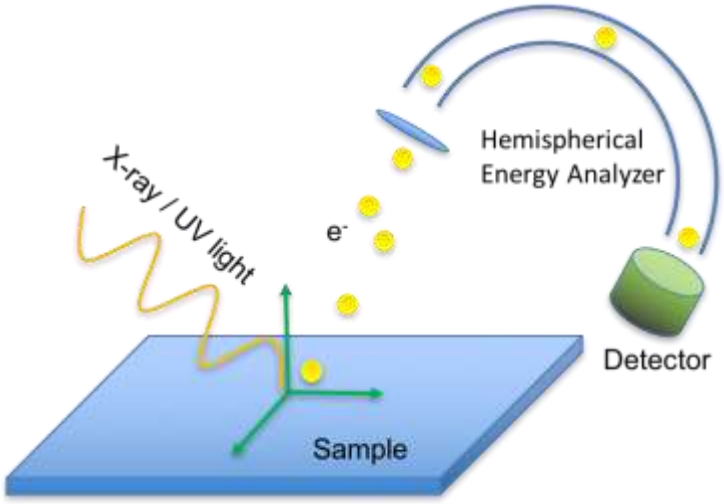

Fig. IX.51. ARPES set up scheme. Electromagnetic radiation provides enough energy to the sample to leave the first layers of the substrate and travel towards the analyzer.

The photons can be generated by laboratory sources, such as He or Hg lamps, or by synchrotron radiation. During the photoemission process, the crystal momentum of the electron inside the material is conserved in th plane parallel to the samples's surfaceAs a consequence, one can easily relate the electron's crystal momentum with the photo emission angle and thereby fully determine the band structure of the material. A typical experimental set-up for ARPES measurement is sketched in Fig. IX.51. The radiation is shone over the sample in a way such that the photon bram and the analyzer lay in the same plane. The photoemitted electrons are collected, within a certain angular acceptance, through a serie of focusing electrostatic lenses and into a hemispherical analyzer. Here, only the electrons with a certain kinetic energy E_0 travel in the middle of the hemispherical capacitor. The width of the energy window about E_0 is called *pass energy* and it is a relevant parameter in determining the energy resolution of the instrument. The other important parameter is the radius of the hemispherical capacitor. Finally, the electrons impinge onto the detector, which in most cases is a fluorescent screen. A charge-coupled device (CCD) camera record the light intensity emitted by the detector. With nowadays detectors it is possible to obtain 2d maps (i.e. E vs. *k*) of the energy dispersion.μ-ARPES

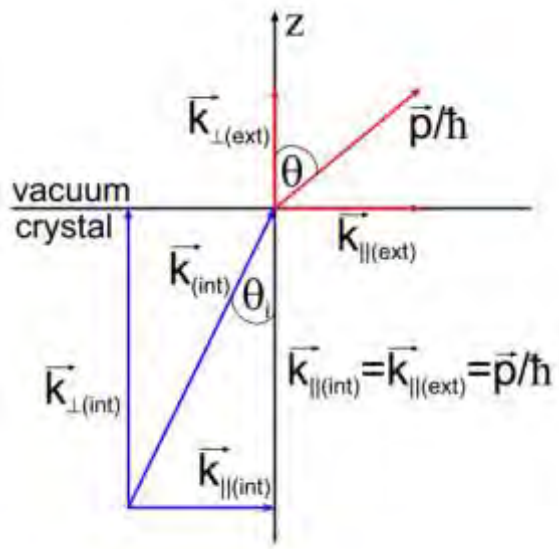

Fig. IX.52. Scheme of the momentum component conservation at the crystal-vacuum interface. The parallel component $\boldsymbol{k}_{||}$ only is conserved.

In the UV, soft X-ray regime, the momentum carried by the photon $p_{ph} = h\upsilon/c$ is negligible compared to the crystal momentum of the electron $\hbar k \gg p_{ph}$, and this ensures that $\mathbf{k}_f = \mathbf{k}_i$. Hence, the von Laue equation $\mathbf{k}_f = \mathbf{k}_i + \mathbf{G}$ is fulfilled, where $\mathbf{G}$ is a base vector of the crystal's reciprocal space. Indeed, experiments are usually performed using photon energy lower than 100 eV, which correspond to a momentum $\frac{p}{\hbar} \simeq 0.05$ Å. In the so-called *sudden approximation,* the electron is extracted instantaneously from the material with no time to interact with the remaining N-1 electrons. This allows us to consider the obtained dispersion as the non-interacting state of the system, or the one particle dispersion. As a consequence, for 2d materials, the emitted photocurrent takes the form:

$$I(\mathbf{k}, E, h\upsilon) \propto \left|M_{i,f}\right|^2 A(\boldsymbol{k}, E) f(E, T) + B \qquad \text{(IX.11)}$$

Where $|M_{i,f}|$ is the matrix element of the transition from the initial (i) to the final (f) state, $A(\boldsymbol{k}, E)$ is the spectral function, $f(E, T)$ is the Fermi-Dirac distribution and *B* is a background term coming from inelastically scattered electrons. The spectral function takes into account the angular dependence of the photo-emitted electrons.

When the electrons leave the material, they end in a free particle state. Considering the scheme in Fig. IX.52 and assuming the conservation of the electron momentum parallel to the surface, the following expression holds:

$$k_{||int} = k_{||ext} = \sqrt{\frac{2mE_{kin}}{\hbar^2}} \sin(\theta) \qquad \text{(IX.12)}$$

Where θ is the emission angle and E_{kin} is the kinetic energy. When considering the perpendicular component, the description is not this simple, since it is not conserved when crossing the crystal surface [1368]. An expression to determine it is the following:

$$k_{\perp int} = \sqrt{\frac{2m}{\hbar^2}}\sqrt{E_{kin}cos^2(\theta) + V_0} \qquad \text{(IX.13)}$$

Where V_0 is the *inner potential*, defined as the energy difference between the vacuum level and the top of the valence band.
Finally, the resolution on the measurement of $k_{||}$ is given by:

$$\Delta k_{||} = k_{||}\sqrt{\left(\frac{\Delta E}{2E_{kin}}\right)^2 + \left(\frac{\Delta\theta}{\tan(\theta)}\right)^2} \qquad \text{(IX.14)}$$

where $\Delta\theta$ is the angular acceptance of the analyzer.

If the electron signal is spin-filtered, e. g. by letting it passing through a Mott detector it is possible to reveal the contribution of a single spin component-projected onto the detector's plane-[1372].on a particular band. This technique is called spin-resolved ARPES (SARPES) and it is fundamental for determining the spin-polarization of electronic bands in materials.
A recent development in ultra-fast lasers gave the opportunity to realize facilities for pump-probe experiments that can access the time scales of the quasiparticle dynamics in solid-state materials. Time-resolved ARPES (Tr-ARPES) is being used more and more to investigate the carrier dynamics in graphene, other 2d materials as well as charge transfer mechanism in vdW heterostructures.

ARPES on graphene and 2d Vertical heterostructures

After almost fifteen years of research, the electronic properties of graphene have essentially no secrets anymore. This is also due to the amount of ARPES measurements that have been carried out on this material. From 2004, ARPES measurements have mapped the dispersion of the π-bands over the entire BZ. The energy loss due to quasiparticle excitation, the electron phonon interaction in the π as well as in the σ bands [626, 1373-1375] were investigated. Graphene on metals [1376] , exfoliated, suspended and graphene nanoribbons [570, 572, 1377] have been measured as well. Perhaps the most investigated graphene with ARPES is epitaxial graphene synthesized on SiC [626, 628, 634, 1373, 1377]. The electronic properties of buffer, mono-, bi and trilayer have been fully characterized by means of ARPES [1378]. Since 2009, also the so-called quasi-free standing graphene on SiC has been deeply investigated [600, 1379, 1380]. Clearly graphene has been the starting point, but this method can be applied also to the study of other 2d materials such as TMDs [1381], their combination in vertical heterostructures [1001, 1382]. The possibility of studying the electronic properties of such a structure allows also for understanding how the layers interact with each other,

giving rise to a new hybrid material. In the following the electronic properties of WS_2 directly grown over epitaxial graphene are reported.

The band structure of WS_2/SLG can be retrieved by means of μ-ARPES on a single WS_2 crystal. μ-ARPES (or micro-spot ARPES) is a technique capable of measuring the electronic properties of a material with a spatial resolution of about a micron. The price for the higher spatial resolution is paid in terms of energy resolution, which is slightly worse. In Fig. IX.53a LEEM image of a single triangular WS_2 crystal on graphene on SiC is shown [1001].

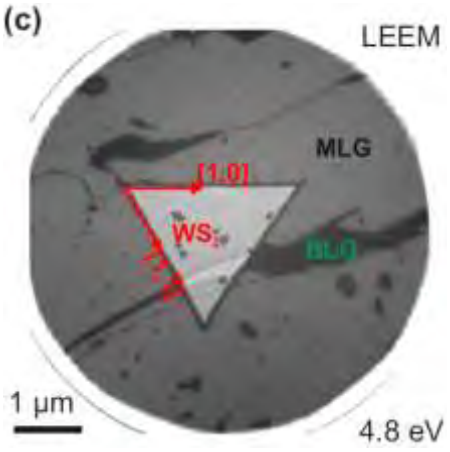

Fig. IX.53 Electron Microscopy micrograph of a single WS_2 crystal. Areas with different contrast are labeled MLG, BLG and WS_2, respectively. Red arrows indicate the crystallographic orientation of WS_2 crystal. Adapted from [1001].

The possibility to directly overlap ARPES measurements with density functional theory (DFT) calculations permits to minimize the error in interpreting the measured signal. Fig IX.54(a) reports the graphene π- and π*-bands measured via μ-ARPES on the crystal shown in Fig. IX.53.The bands are well visible and also highlighted by orange dots, corresponding to the DFT calculated bands on the graphene single cell. Calculated graphene σ-bands are not superimposed as in the experimental data they are not detectable due to their low intensity. The bands visible in belong to WS_2 as also indicated by DFT calculations. Interestingly, at the points where the bands of graphene and WS_2 cross (indicated by green arrows in the panel), no apparent splitting or gap is observed. In order to confirm this finding, DFT calculations were carried out, the result of which is summarized in Fig. IX.54(b), where the bands "unfolded" onto graphene's BZ are displayed for better readability.

When crystals with different lattice parameter are superimposed, they can give rise to a superlattice. When multiples of the different unit cells match in size, they form a supercell which behaves as a new unit cell of a hybrid crystal. This new periodicity in the systems alters the overall band structure opening minigaps in high symmetry points. The smallest coincidence lattice for the WS_2/graphene system was found to be (7 × 7) WS_2 unit cells (u.c.) on (9 × 9) of graphene, as sketched in Fig. IX.54(c). DFT calculations were carried out on this supercell and as a result, no mini-gap opening was predicted for this system, differently to what was recently observed for MoS_2 on graphene [1382]. To better visualize the relation between the graphene π-bands and the WS_2 bands,

constant energy surfaces (CESs) are shown in Fig. IX.54(d), extracted starting from the Fermi surface (FS) at binding energies indicated in the figure. The CESs in this case are small volumes in k-space integrated over about 250 meV, corresponding to the resolution of the instrument. The data were acquired with photon energy 27.5 eV in order to maximize the intensity of the WS_2 bands with respect to graphene.

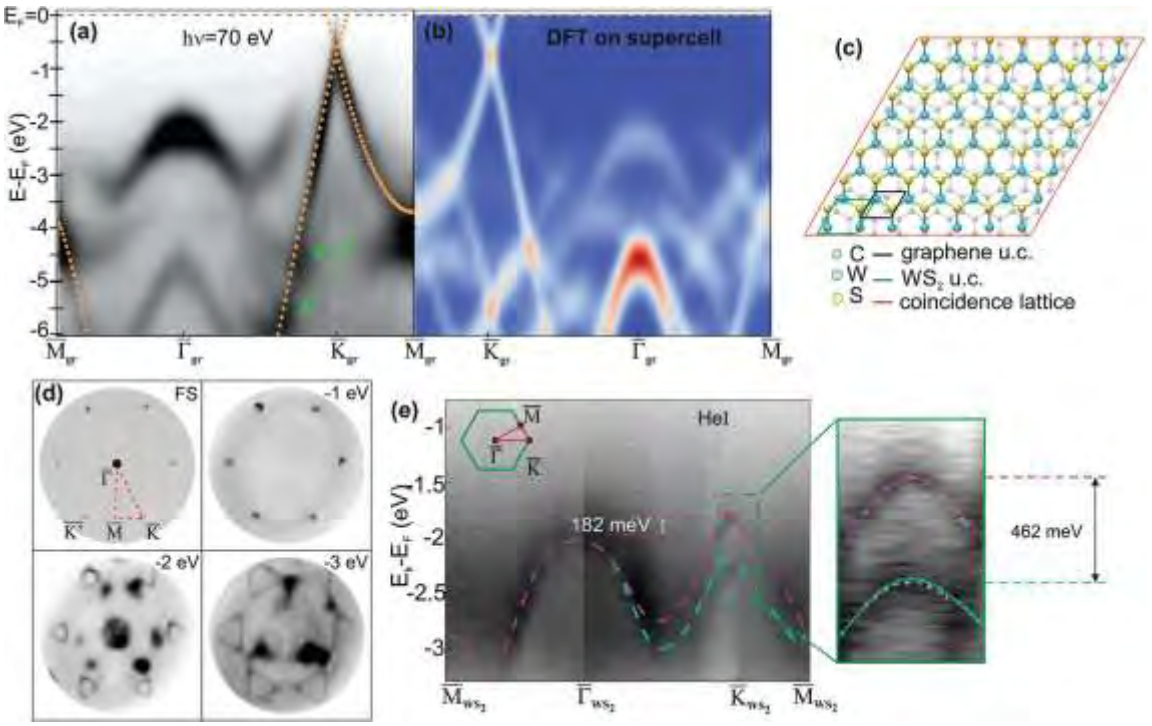

Fig. IX.54: Band structure of WS_2/MLG. (a) μARPES measured on a single WS_2 triangle with photons of 70 eV. (b) Theoretical DFT band structure evaluated on the WS_2/graphene supercell depicted in panel (c) and unfolded into graphene's BZ. (c) Coincidence supercell (7 × 7) over (9 × 9) of WS_2/graphene. (d) Experimental ARPES CESs recorded with p-polarized photons at 27.5 eV (e) Experimental ARPES band structure of WS_2/EG measured with He I light along the path indicated in the inset by the red line. DFT calculated bands including spin–orbit effects are overlapped to the raw data. On the right: zoom-in of the region around $\overline{K}_{WS_2}$(green-dashed line in panel (e)). Both DFT calculated bands and experimental band fit are superimposed to the raw data. The red-dashed line is on the graphene's π-bands. Adapted from [1001] .

We display the results of the ARPES measurements recorded at the Max-Planck Institute for Solid State Research in Stuttgart (Germany) with He I radiation of 21.2 eV in Fig. IX.54(e), together with the DFT-calculated bands including spin–orbit coupling. The image was obtained by scanning the BZ of the system along the red line traced within the green hexagon in the inset. Note that in this image the high symmetry points are for the WS_2 BZ, whereas for panels (a) and (b) we referred to graphene's BZ. Single spectra were measured perpendicular to the red line. We have fitted the experimental data in proximity (±~0.1 $Å^{-1}$) of $\overline{K}$ with a parabolic function in order to extract the effective mass values of the holes. The result along the $\overline{\Gamma}-\overline{K}-\overline{M}$ direction is displayed on the right

side of Fig. IX.54(e), representing the zoom-in of the region framed with a green-dashed line in the panel. We find $m_{h1} \simeq 0.39 m_e$ for the low energy band and $m_{h2} \simeq 0.53 m_e$ for the high energy band, confirming the asymmetry reported in other publications [1383]. The spin–orbit splitting of the WS_2 bands in K was retrieved from integrated energy distribution curves to be 462 ± 5 meV. Notably, this value is about 10% larger than what was measured for monolayer WS_2 on Au(111) and Ag(111) [1384, 1385] and about 7% larger than the highest value reported so far [1385]. The value measured on our system is comparable only with measurements carried out on bulk WS_2 [1381].

IX.3 Electrical characterization

Four probe configuration

The basic electronic properties of a homogeneous metallic diffusive material are captured in the primary parameters: resistivity ρ (Ω.cm), charge density n (cm^{-3}) and electronic mobility μ (cm^2/Vs). For a LM, the resistivity is replaced by the sheet resistance R_S (Ω), i.e the resistance that would have a (homogeneous) sheet of material with equal length and width. For a sheet of thickness t, $R_S = \rho/t$. Similarly the surface charge density n_s (cm^{-2}) is $n_s = n\ t.\ \sigma/(ne) = 1/(n_s e R_S)$, where σ is the conductivity. It is common in the GRM literature for R_S to be written as ρ_{xx}

Resistances are measured in a four-probe configuration, where a current I is applied on 2 probes (source and drain) and the voltage drop V measured on two others following the schemes in Fig.IX.55. The 4-probes configuration removes the contribution to the resistance from contacts, i.e. that of the leads (wires), to the measurement apparatus, and of the metal contacts, so that the measured resistance V/I is intrinsic to the sample. In a linear configuration (Fig. IX.55a and Hall bar Fig. 55b), $R_S = (V_{CD}/I_{AB}).(W/L)$, where W and L are the width of the sheet and distance between the voltage probes C and D, respectively. In a Van der Paw configuration [1386] (Fig. IX.55c), contacts are attached to the edges of a sheet and $R_S = \pi(R_{AB,CD} + R_{BC,DA})/[2Ln(2)].\ f(R_{AB,CD}/R_{BC,DA})$, where $R_{AB,CD}$ is the resistance measured injecting the current between A and B and the voltage probes are C and D; $R_{BC,DA}$ is measured by permutation. The function f is a function of $R_{AB,CD}\ /\ R_{BC,DA}$ only, and satisfies the condition [1386]

$$(R_{AB,CD} + R_{BC,DA})/(R_{AB,CD} + R_{BC,DA}) = f\ \mathrm{arccosh}[\exp((Ln2/f)/2)] \qquad \text{(IX.15)}$$

The function f is plotted in Fig.IX.55f. The Van der Pauw configuration allows measuring a sheet of arbitrary shape, like a cross for instance.

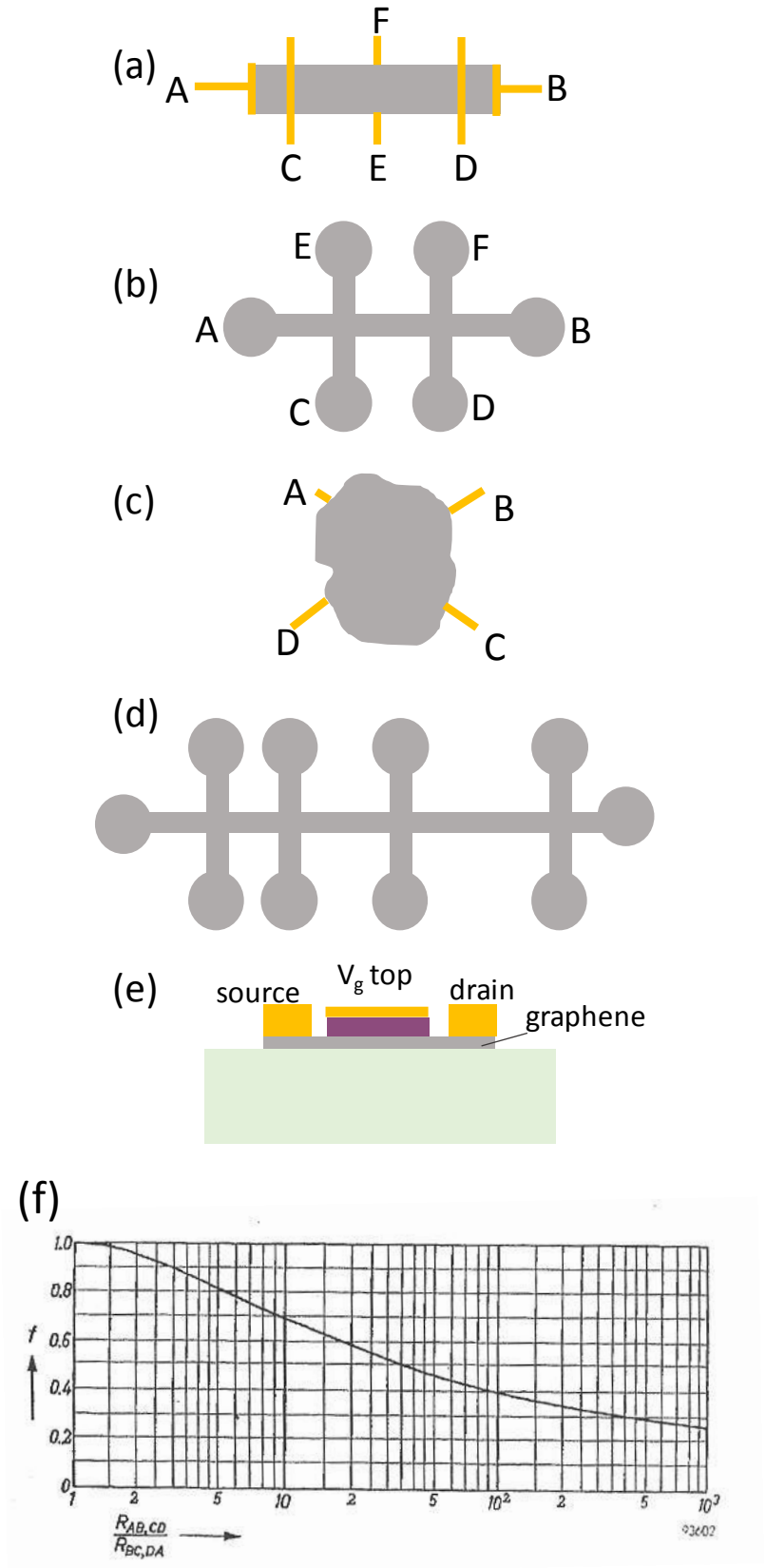

Fig.IX.55. (a) 4-probe configuration. (b) Hall bar. (c) Van der Pauw. (d) TLM configuration; (e) field effect transistor, showing a SLG with a top gate deposited on a dielectric, and source and drain contacts. (f) f coefficient of the Van der Pauw method

Standard measurements techniques [1387] are used to measure the SLG resistance that, is usually in the range a few tens Ω to a few 100 kΩ. In the low current range, low-frequency (typically a few Hz to a few kHz) ac measurements with a lock-in amplifier, either in current or voltage source mode, provide the best signal to noise ratio. I-V characteristics are measured in dc mode, or by recording the current change (I_{ac}) induced by modulating the voltage around a dc bias ($V=V_{dc}+V_{ac}$). In all cases, the current must be kept low enough not to heat the sample, or to induce changes. At cryogenic temperature, typical currents range between nA to hundreds μA. High currents (~mA per μm width) can be used to anneal SLG to clean up impurities [1388, 1389] or to produce narrow constrictions tens of nm wide in suspended SLG [1390].

Ultra-high frequency measurements (>100GHz[1391-1393]) or high precision resistance measurements for quantum Hall effect [564, 588] require specialized equipment and won´t be discussed here.

The charge density is determined either from the Hall effect, or from electrostatic field effect. The Hall voltage V_H is measured perpendicular to both current and magnetic field. Typically Hall bars such as in Fig. IX.55b are used. With the magnetic field B perpendicular to the SLG plane and current from A to B, $V_H=V_{CE} = V_{DF}$. For SLG, $n_S=B/(e\rho_{xy})$, where $\rho_{xy}= (V_H/I)$. In the van de Pauw geometry, current leads and voltage probed are placed in cross configuration, such that $\rho_{xy}= V_{AC, BD} = V_{BD, AC}$ following Fig. IX.55c.

In the simplest approximation, μ is deduced from resistance and charge density measurements : $\mu = \rho_{xy}/(R_{sq} B)$. In the simplest picture of short range scatters, the Boltzmann conductivity σ is independent of energy, i.e. independent of carrier density [1394]. In this picture, the usual definition $\sigma=n_s e\mu$, would give μ with unphysically large values at charge neutrality. In reality, σ varies with n_s, being minimum at and around charge neutrality. This calls for other scattering mechanisms, like charge impurity scattering or resonant scattering [1394]. A better description of the relation between σ and n was given in Refs. [1394, 1395]

$$\sigma=\sigma_{res} + Ke(|n_s/n_{imp}|) \qquad (IX.15)$$

as shown in Fig. IX.56. Here n_{imp} is the charge impurity concentration, K/n_{imp} has the unit of mobility and σ_{res} reflects the fact that SLG conducts even at zero carrier density [1396].

In the previous examples the charge density n is modulated with an electrostatic gate. In principle this is a parallel plate capacitor, with one plate being the gate electrode and the other SLG. Either SLG is deposited on the dielectric or vice-versa. In the former case, the gate below SLG (bottom gate) often consists of a conducting Si (the gate) covered with a dielectric (SiO_2) onto which SLG is deposited. All devices fabricated on the substrate are subjected to the same electric field when a voltage V_g is applied to the Si gate. Top gates are realized by depositing a dielectric (Al_2O_3, HfO, SiN, h-BN, etc) on SLG, for instance by atomic layer deposition (ALD) or thermal evaporation. Sputtering is not recommended since it damages SLG [1397]. This is followed by coating with a metal (Au, Al). Top gates are usually patterned and can be addressed individually to switch one device at a time. The

gate can also be brought close to SLG from the side in the same plane as SLG (side-gate). If the gate itself is also made of SLG, this allows patterning the SLG device and the gate all at once [685, 1398].

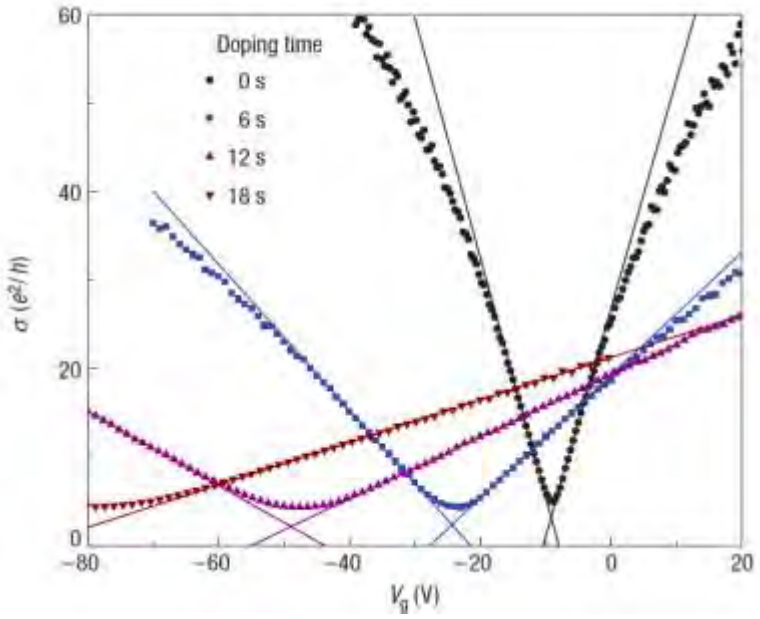

Figure IX.56: The conductivity σ versus gate voltage Vg curves, taken at 20 K in UHV, for a pristine SLG and three different potassium doping concentrations, introducing graphene doping and scattering. Lines are fits to equation (Eq.IX.15) and give the mobility, and the crossing of the lines defines the points of the residual conductivity and the gate voltage at minimum conductivity (σ_{res} , Vg,min) for each data set [1395].

In the top/bottom gate configuration, the simplest assumption gives a charge variation Δn_s induced on SLG as :

$$\Delta n_s=(\varepsilon_0\varepsilon/t_d)V_g \qquad \text{(IX.16)}$$

where ε and t_d are the dielectric constant and thickness of the dielectric. In most FET configurations the SLG channel is provided with only 2-contacts (plus the gate, see Fig. IX.55e), therefore the contact resistance is included in the measurements, which results in underestimating μ. More precise methods have been developed [1399, 1400]. For sufficiently large bias voltage, the charge density may vary along the SLG channel, an even change sign, due to the SLG ambipolar nature, leading to a complex interplay between source-drain voltage and gate voltage (top, bottom or both) [1401]. Eq.(IX.12) does not take into account the variation of chemical potential with charge density, which introduces an extra capacitance term $e^2D(E_F)$ [1402], the so-called quantum capacitance per unit area ($D(E_F)$ is the density of states), which cannot be neglected close to the Dirac point [1402].

n can also be determined from magnetoresistance measurements in high (generally several

Tesla) magnetic fields, and at low (cryogenic) temperature by analyzing the periodic oscillations of the magnetoresistance (Shubnikov de Haas oscillations) as a function of 1/B [88, 574, 1403].

Examples are given in Fig. IX.57 for SLG on SiO_2 and multilayer graphene on 4H-SiC(000-1). The 1/B oscillation period is $B_F = (h/4\pi e)k_F^2$ with $k_F^2 = n\pi$. With increasing field, the oscillations develop into the quantum Hall effect, and the quantification of Hall resistivity also give access to the carrier density [88, 1403]. These measurement techniques can be useful in case of mixed (electron and hole) doping in the vicinity of the Dirac point [1404, 1405].

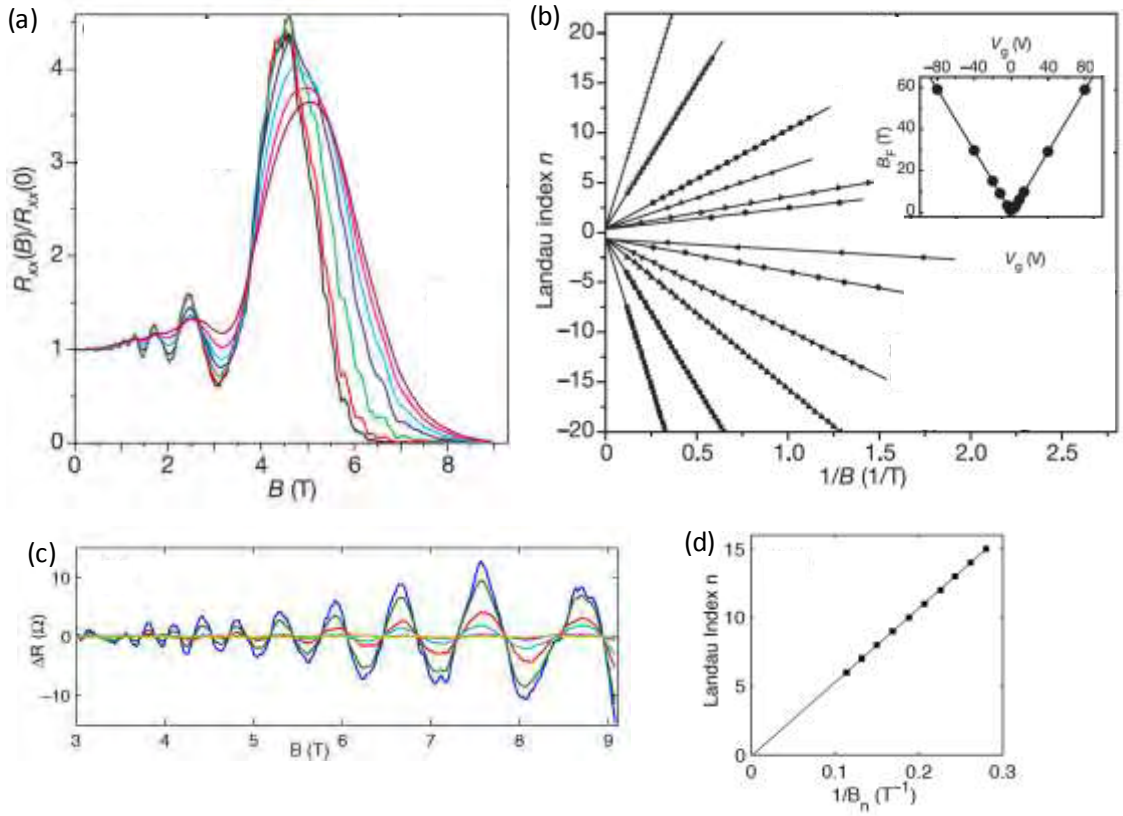

Figure IX.57. Shubnikov de Haas oscillations of the magnetoresistance in (a, b) SLG on SiO_2 [1403] and (c, d) multilayers on 4H-SiC(000-1) (C-face)[1406] for different temperature from 4K to 70K. (b) The minima in ρ_{xx} are plotted as a function of 1/B (so called fan plots) to determine the charge density at a particular gate voltage. (d) same analysis for the data in (c), but plotting the maxima in ρ_{xx}.

In semiconductors a current saturation regime is reached by applying a sufficiently large source-drain voltage, and μ can be deduced from the current saturation value [1407]. However, this regime is difficult to reach in SLG because of the requirement of extremely high source-drain voltages, which will cause inhomogeneity in the carrier densities along the channel [1401, 1408].

Standard electrical measurements require contacts on SLG. Besides the fundamental interest of how to inject from a 3d to a 2d material, from planar (2d) or edge (1d) contacts, while matching energy and momentum (at charge neutrality the SLG Fermi surface is reduced to points in k-space), it is technically difficult to realize contacts to SLG of low (in the 10s Ω) resistance. Because there are no dangling bonds to adhere to, metals like Au tend to bead up on SLG [1409], which requires an

adhesion layer, like Pd, Ti or Cr. Low resistance contacts (50-100Ωμm) are a combination of mechanical adhesion and charge transfer to SLG due to a large metal-SLG work function difference (to increase the SLG conductivity under the contact by heavily doping it) [1410] [1411, 1412]. Metal induced doping can create p-n junctions from the SLG under the contact to the channel, which have to be taken into account in the resistance analysis [1411, 1412].

Contacts are usually defined by lift-off after development of the lithographic resist. Resists commonly used are positive e-beam resist (e.g. 200nm PMMA spun onto 200nm MMA), or photoresist (e.g. S1813~1.8μm thick). Good contacts are obtained with 5-10nm Cr, Pd, Ni or Ti (or combination of these metals, Ti/Pd 2nm/10nm) evaporated on SLG, followed by 30-50nm Au, by e-beam evaporation or thermal evaporation. Contact resistances R_c can be measured by the transfer length method (TLM), see Fig. IX.55d. A SLG strip is provided with a series of contacts. The 2-point resistance $R_{TLM}=R_c(W)+ 2R_s\ L/W$ is measured and plotted as a function of distance L between the contacts, with W the channel width. The advantage of the technique is that it is fast and involves only resistance measurements. However this assumes that all the contacts are the same, and that R_s has a constant value along the graphene channel (i.e, homogeneous scattering, homogeneous gate or bias induced charge density). This may be questionable very close to the contacts due to metal-induced doping. Alternatively, the contact resistance can be measured from Kelvin probe microscopy measurements, by measuring locally with an AFM tip the voltage drop from the contacts to the channel [1413]. The lowest intrinsic contact resistances measured are in the range $\rho_c = R_c.W$ = 50-100 Ωμm [1393]. Ref [1414] developed edge contacts, where lateral contacts inject current through the SLG edges. R_d are of the same order of magnitude [1414]

Deposition of gate dielectrics is a challenge for the same reason that metals do not adhere on SLG. ALD or evaporation of high K dielectrics (Al_2O_3, HfO_2, SiO_2) [1415] or Si_3N_4 [1416] have best RF performances (in terms of cut-off frequency) (see for instance [539] and refs therein and ref [1417], and hBN encapsulation provides protection [989, 1418].

SLG was the first measured LM that was exposed, i.e. not buried at the interface between two semiconductors. While this presents great opportunities (spectroscopy in particular), exposure to the ambient degrades the SLG pristine properties, by doping and scattering by impurities. The transport properties drift with a time constant ~1 hour or so , and are recovered after annealing (e.g.~1 hour at 420K in He [1419]. SLG protection is therefore required (top layer, or measurement in neutral or vacuum environment), unless the exposure provides useful counter doping (like for the measurement of the quantum Hall effect [577]).

SLG is a flexible membrane, therefore the roughness of the substrate matters. Sharp ripples or bubbles introduce field gauge effects [585] [422], equivalent to high magnetic field of up to several hundred Tesla [585], with consequences on transport [422].

It is relevant for graphene nano/microstructures of size LxW to keep in mind that the energy scale in graphene is set by $E = \hbar k v_F = \hbar v_F \sqrt{\frac{n\Pi}{L} + \frac{m\Pi}{W}}$, so that the energy separation between modes in charge neutral SLG is~20K for L=1μm . Therefore, submicrometer structures of SLG at low T (below 3)are effectively quantum dots [572].

1d ballistic transport was measured in SLG ribbons at RT [572]. In that case the nature of the contacts (invasive or not) determines the voltage measured. For invasive contacts the electron flow is interrupted by the voltage probe which somehow then acts like a current injection, and a resistance close to the quantum of conductance $R_q=(e^2/h)^{-1}$ = 25.812 kΩ is measured independent of distance between voltage probes, even in a 4-probe configuration (for a full discussion, see Refs. [572, 1420]).

THz-TDS mapping of electrical properties

The key electronic properties, sheet resistivity, carrier mobility and carrier density, of arbitrary size graphene can be measured quickly, accurately and non-destructively using terahertz time-domain spectroscopy (THz-TDS). Over the past years [1421-1429], this method has been thoroughly benchmarked against van der Pauw electrical measurements (See secton IX.3) with fixed electrodes [1426, 1429] as well as scanning micro four-point probes[1422, 1423].

THz-TDS based electrical characterisation is based on the absorption in the THz frequency range to be highly dependent on the complex-valued and frequency-dependent electrical conductivity [1430]. This is due to the absorption of light in the far-infrared (THz) frequency range being dominated by low-energy intra-band transitions, as opposed to the inter-band transitions that gives rise to graphene's constant absorption of light in the visible spectrum [1431].

The electrical field attenuation caused by the charge carriers in the thin film can be established by dividing the electrical field $\tilde{E}_{\text{graphene}}$ through the sample area, with a reference $\tilde{E}_{\text{ref}}$ from an area without the conducting film, which is then related to the conductivity through [1423]

$$\frac{\tilde{E}_{\text{graphene}}(\omega)}{\tilde{E}_{\text{ref}}(\omega)} = \frac{1+n_{\text{sub}}}{1+n_{\text{sub}}+Z_0\tilde{\sigma}(\omega)} \qquad \text{(IX.17)}$$

where n_{sub} is the refractive index of the substrate, Z_0 is the free-space impedance, and $\tilde{\sigma}(\omega)$ is the frequency-dependent (complex-valued) Drude conductivity,

$$\tilde{\sigma}(\omega) = \frac{\sigma_{\text{dc}}}{1-i\omega\tau} \qquad \text{(IX.18)}$$

The THz radiation is focused into a 300 μm diameter spot, limited by the long wavelength in the THz frequency range, which enables the average sheet conductivity (or resistivity) of a graphene film to be determined. In contrast, electrical measurements measure the device conductance (or resistance), which can differ significantly from the average conductivity for the same device area in case of spatially non-uniform conductivity [1423, 1429].

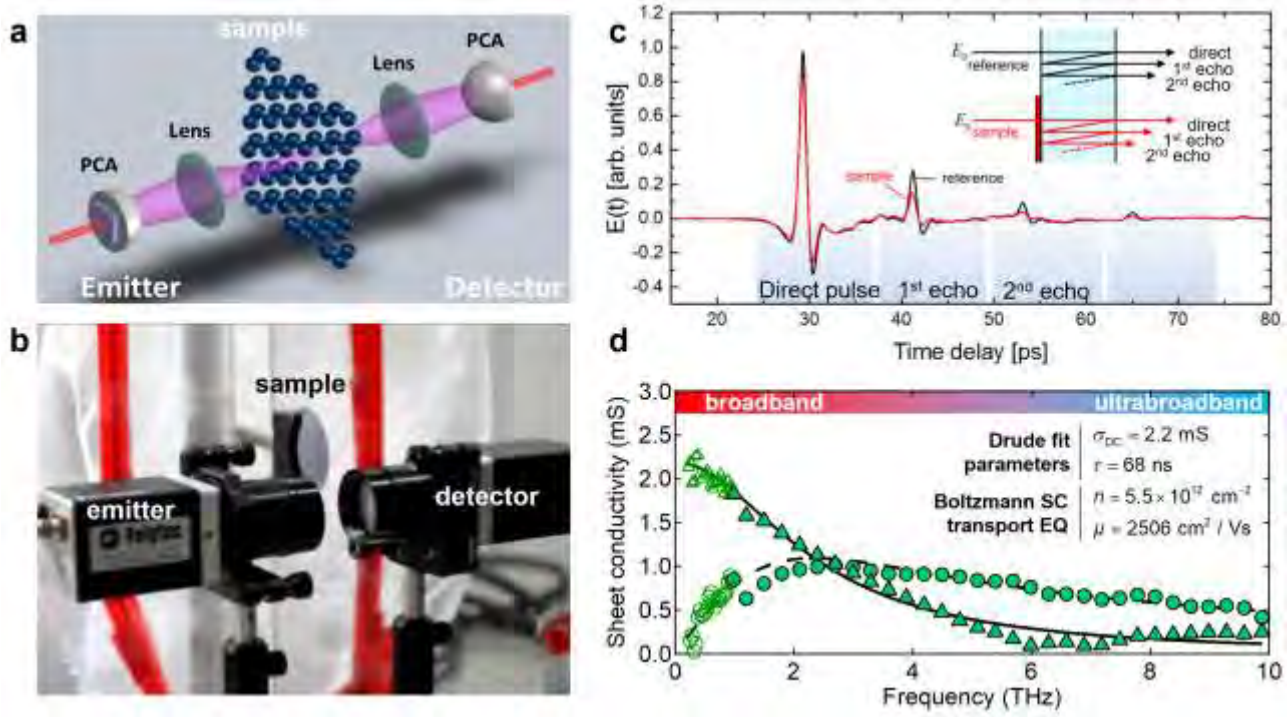

Figure IX.58. (a) Schematic of THz-TDS electrical characterisation setup. (b) Photo of equivalent THz beam line, with a graphene-coated silicon wafer being held by a motorized raster scanner. (c) THz direct pulse and weaker echoes from multiple internal reflections. The black curve is from an uncoated reference area, while the attenuated red curve is attenuated by the conducting sample. (d) Conductivity spectrum of graphene grown on single crystal copper, which closely follows the Drude model (Eq. IX.18). The fitting parameters (σ_{DC}, τ) *can be used to calculate n and μ. For large-area conductivity mapping, commercial spectrometers that cover up to 2-3 THz are used, while a more sophisticated air-THz setup allows spectra up to 15-20 THz to be recorded* [1423].

Figure IX.58(a) shows a conceptual schematic of a THz absorption setup, with a femtosecond laser pulse hitting a photoconductive antenna (PCA). The resulting THz pulse is focused by a lens, and transmitted through a thin conductive film. Finally, after refocusing by another lens, the attenuated THz pulse is picked up by a PCA operating as a detector. Figure IX.58(b) is a photo of a silicon wafer covered with graphene, which is raster scanned across the focal plane of the beam line, while acquiring THz-spectra at a rate of ca. 1 Hz. In Fig. IX.58(c) the time-resolved electrical field is shown.

The initial peak is followed by smaller echo peaks, spaced by the round trip time of flight for internal reflections inside the substrate. Using Eq. (IX.17) the real (green triangles) and imaginary (green circles) parts of the conductivity can be plotted against frequency, and fitting the Drude conductivity (Eq.(IX.18)) yields the low frequency (DC) limit of the conductivity, σ_{DC} , and the momentum relaxation time (elastic scattering time), τ . Under the assumption of diffusive transport, the semiclassical Boltzmann transport equation, $\sigma = (2e^2 / h) k_F v_F \tau$ in combination with the fundamental relation $\sigma = ne\mu$ yields expressions for carrier density *n* and carrier mobility μ that can be calculated from the fitting parameters (σ_{DC}, τ) :

$$\mu = \frac{e^3 {v_F}^2}{\pi \hbar^2} \frac{\tau^2}{\sigma_{DC}} \ , \ n = \frac{\pi \hbar^2}{e^4 {v_F}^2} \frac{\sigma_{DC}^2}{\tau^2} \ , \qquad \text{(IX.19)}$$

where *e* is the electron charge, v_F is the Fermi velocity, and $\hbar$ is the reduced Planck constant. Therefore, the average carrier mobility and carrier density can be spatially mapped with a resolution approximately equal to the THz spotsize $d_{THz} = 300\ \mu m$, by recording a full spectrum in every pixel, and computing Eq. (IX.19) with the Drude fitting parameters.

Figure IX.59(a-c) shows the conductivity map of the same CVD grown graphene film before and after definition of 49 test devices, verifying that the laser ablation / shadow mask device fabrication method has very little impact on the device characteristics due to the complete absence of solvents and resists [1426, 1429]. Panel IX.59(d) and IX.59(e) shows the μ and *n* maps obtained by the methodology described above, with the histograms below showing both the scale and distributions of values within a rectangular zone shown with dark dashed lines. Panel IX.59(f) shows how the method can be used to map the large-scale changes in uniformity of electrical key parameters with growth temperature in a CVD process, showing that higher temperatures tend to give more uniform growth and larger usable areas of the graphene films [1428].

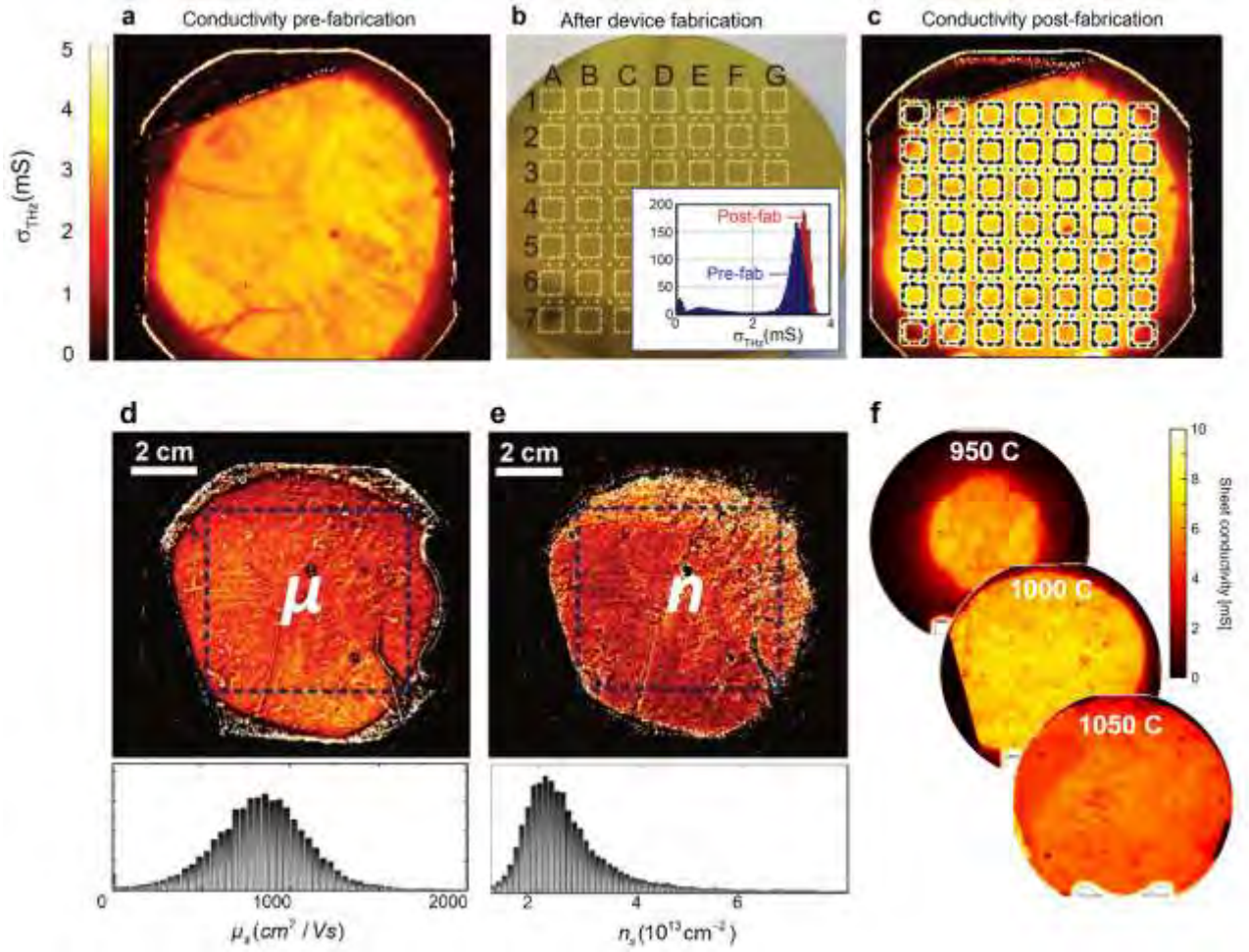

Fig. IX.59. Examples of THz-TDS electrical characterisation of graphene. Conductivity of graphene coated silicon wafer mapped before (a) and after (c) fabrication of 49 electrical test devices, to test how individual process steps affect the conductivity [1428]. (b) Shows the wafer after laser-etching and physical mask deposition of metal contacts [1426]. Histogram (inset) shows the sheet conductivity across the wafer before and after fabrication. (d-e) Carrier mobility and density for a silicon wafer determined by Eqs.(IX.19), with histograms below showing scale and distribution of n and μ [1424]. (f) Investigation of how CVD growth temperatures affect the large-scale uniformity of sheet conductivity of graphene transferred to 4" silicon wafers [1428].

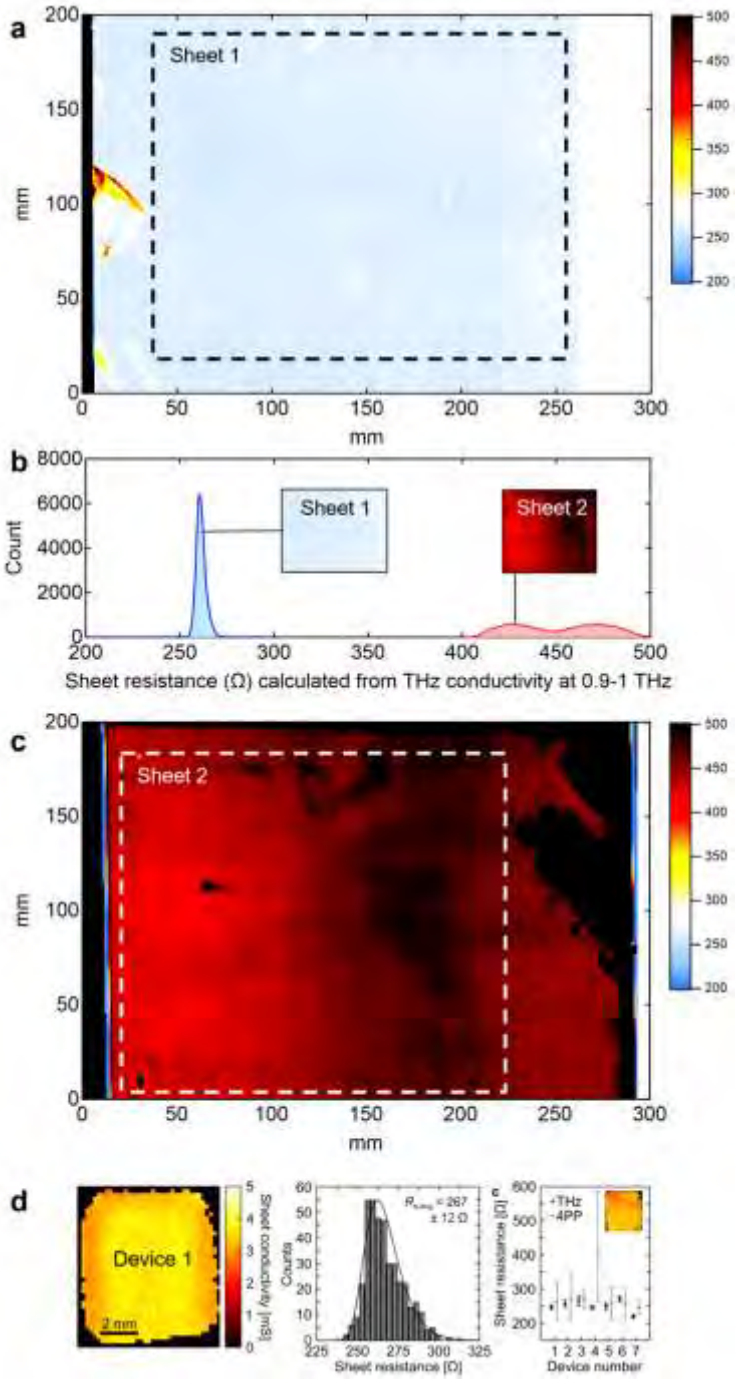

Fig.IX.60. (a) Terahertz resistivity maps (0.9-1.0 THz) of two A4 sized sheets of doped graphene on PET by Chongqing (Institute of Green and Intelligent Technology, Chinese Academy of Science), with high (a) and lower (c) uniformity (color scale is from 200 Ω to 500 Ω). The histograms corresponding to the white dashed rectangles are shown in (b), where sheet 1 shows an exceptionally narrow peak, while sheet 2 exhibits a bimodal distribution. (d) THz conductivity map of a $10\times10\ \mathrm{mm}^2$ *device, which was measured both by THz and van der Pauw measurements. After Drude-fitting, the DC sheet resistance is determined to* $267\pm12\ \Omega$ *for the shown device, as shown in the histogram. The measurements for 7 such devices agree well, except device 4, which had a visible scratch.*

The THz mapping technique can be used for graphene on flexible substrates [1428]. Graphene grown on Cu, transferred to polyethylene terephthalate (PET) and doped by $AuCl_3$ showed

very high uniformity across 15 inch (25x30 cm^2) PET sheets. The THz-resistivity in the frequency range (0.9-1.0 THz) is shown in Figure IX.60(a) and IX.60(b), which is typically within 5-10 % of the DC sheet resistance, as can also be seen by noting the small drop in $\sigma(\omega)$ from 0 to 1.0 THz in Fig IX.58d).

The histogram in Fig IX.60(b) shows a very narrow distribution for sheet 1, and a broader, bimodal peak for sheet 2, consistent with the difference in the visual appearance of the THz resistivity maps (a and c). The histogram of DC sheet resistance obtained after fitting the Drude equation, Eq (IX.18), to every pixel, shows extremely narrow distribution across the ca. 750 cm^2 graphene area (dashed rectangle). Figure IX.60(d) shows a THz map of a cm-sized device with the corresponding histogram of DC sheet resistance values. The sheet resistance obtained by van der Pauw and THz mapping show excellent agreement, however, with larger statistical spread for the THz measurements because of the avoidance of physical contact, and the greater number of measurement points. One of the devices (device 4) had a scratch, which typically offsets electrical measurements in unpredictable ways, while having little impact on the THz-measurements, as discussed in Ref [1428].

THz-TDS electrical characterisation can be done in transmission mode, which is by far the most well-described technique in scientific literature, or in reflection mode. Comparison of THz conductivity maps recorded with transmission (see Fig IX.61**(**a)) with a commercial reflection mode THz-measurement system (DasNano, see Fig IX.61(b)) showed negligible difference [1429], and good agreement with electrical measurements, for the same samples. Despite the large CVD graphene samples not to be encapsulated, the measurements agreed well within the statistical errors, as clear from the conductivity histograms in Fig IX.61(c) and the direct comparison between electrical four point probe sheet conductance with THz sheet conductivity measurements for both transmission and reflection mode systems shown in Fig IX.61(d).

For transmission mode THz-TDS it is important that the carrier substrate has a high resistivity, to reduce the THz absorption in the substrate. The conventional highly doped silicon substrate commonly used as a backgate, can be replaced by a custom-made substrate with a THz-transparent gate [1425] to enable THz-TDS and electrostatic gating on the same samples. The advantage of reflection mode is that there is no need for using high resistive substrates, while transmission mode THz-TDS can measure buried conductive layers at any depth.

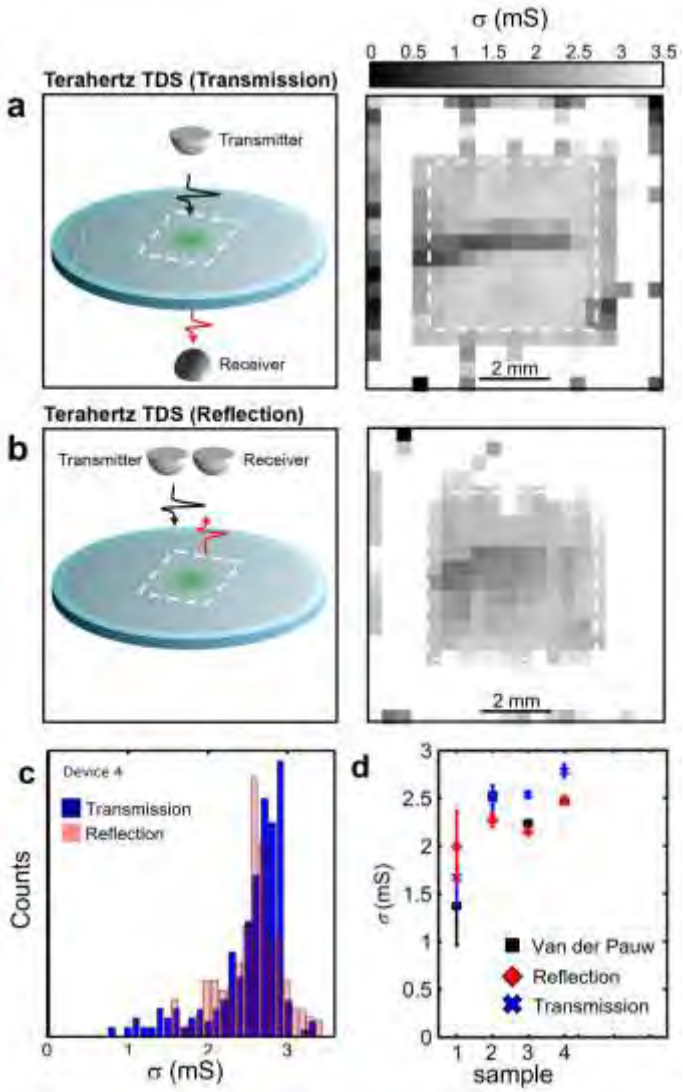

Fig. IX.61. Comparison of transmission (a) and reflection (b) mode measurements on the same four samples, with comparable spatial conductivity pattern and (c) overlapping statistical distributions of measured conductivity values. Similar results were obtained for four studied samples. (d) Direct comparison of van der Pauw four terminal measurements with reflection (diamonds) and transmission (crosses) measurements, showing excellent agreement except sample 1, which was less homogeneous compared to samples 2-4 [1429].

THz-TDS is a fast, clean, powerful and accurate way of measuring the essential transport characteristics of graphene on many substrates. Apart from silicon wafers and PET substrates, the method has been used with success for graphene on SiC and graphene on Ge (on Si). As clear from Fig IX.58(b) there is no limit for the size of samples, as a THz-TDS measurement head could easily be integrated in a roll-to-roll production line, giving instant feedback on the quality of graphene. The technique can also measure buried and encapsulated conducting layers, which provides essential information on the impact of intermediate process steps on the electrical characteristics before device fabrication is possible.

IX.4 Mechanical characterization

GRMs compared to existing materials, combine high stiffness, strength, strin-to-failure and high flexibility [1432]. SLG compared to existing membranes has extremely high ductility as can be stretched up to 30%, however, beyond that point, it fractures in a brittle manner like glass [1433]. However, up to date, experimental evidence under uniaxial tension that confirms fully the above is missing and the above properties have been predicted via theoretical or computational modelling [1432, 1434]. The main reason for the lack of experimental data is associated with the sample quality (and size) and the damage inflicted by handling and subsequent transfer onto the loading devices. For instance, the mechanical exfoliation of bulk graphite crystals produces flakes of at best 100 x 100 μm^2 depending on the substrate interaction [1435].Suspended SLG samples over relatively large areas (around 1 mm^2) as required for classical tensile experiments are difficult to produce [1435]. Wet methods for transferring CVD graphene from a metal substrate to arbitrary target substrates lead to samples with a number of defects such as wrinkles, folds and tears, as well as residues, voids and polymer contaminants that can induce uncertainties in the measurements. Normally, a lot of optimization work has to be done in order to minimize the influence of induced defects and to select the gauge area of the membrane to be tested. Due to limitations posed by the accuracy in force sensing in the nN range and sample gripping techniques, there is a lack of specialized instrumentation for in plane tensile testing of GRMs. This has triggered intense research for applying either AFM based [1432], or thin film metrology techniques [1436] to measure the mechanical properties of GRMs [1432, 1436]. A comparison of the measured mechanical properties with bulk materials is still an open question.

Here, emphasis is given in presenting the measuring techniques which are categorized appropriately in direct and indirect methods of testing. In *direct methods* the force or strain is applied directly to the GRM membrane. In *indirect methods*, Raman spectroscopy can be used for assessing the mechanical response of GRMs supported or embedded into polymers, where the strain is applied by shear forces from the deformed substrate. Other interesting methodologies for applying strain are the budge test and electrostatic actuation will be discussed in below.

AFM Nanoidentation

The elastic properties of suspended SLG can be measured by nanoindentation using an AFM. The samples are made either by exfoliation of bulk graphite or by transferring CVD grown SLG onto pre-patterned substrates with holes or trenches. Usually an AFM tip applies a point load at the center of GRM sheets suspended over a hole on a pre-patterned substrate. Because of the high strength of GRMs, higher than steel and Kevlar [1437],cantilevers with diamond tips are preferable for these experiments. For a doubly clamped SLG ribbon, a wedge indentation tip was used to introduce a uniform tensile strain [1438]. During nanoidenation the force, F, *vs* deformation, δ, of the suspended layer (at the point where the load is applied, Fig. IX.62) is continuously recorded up to fracture. By employing third order elasticity theory and a number of assumptions based on classical membrane

mechanics, the conversion of nanoidentation force-deflection measurements into an axial stress-strain curve for a free standing SLG membrane was attained [1439]. Thus, by this procedure, the 2d Young's modulus, E_{2d}, breaking stress, σ_{2D}^{max}, and strain at break, ε_{max} were estimated [1439]. In order to obtain the corresponding bulk parameters, these quantities were divided by the interlayer spacing in graphite h = 0.335 nm (assumed as SLG thickness) yielding values of Young's modulus of ~1 TPa and of tensile strength of 140 GPa [1439].

As mentioned above, to convert the experimental nanoidentation data to uniaxial stress-strain curves, the GRM is normally modelled as a membrane (thin plate) of negligible bending stiffness and nonlinear elastic properties [1439]. For doubly clamped beam shaped membranes (graphene ribbons GNRs) [1436, 1438] the force-displacement behaviour can be expressed as [1436]:

$$F = \left[30.78w\left(\frac{t}{l}\right)^3 E + \frac{12.32}{l}\sigma_0\right]\delta + tE\frac{8w}{3}\left(\frac{\delta}{l}\right)^3 \qquad \text{(IX.20)}$$

For circular shaped membranes the corresponding relationship is as follows [1439, 1440]:

$$F = \left[\frac{4\pi a}{3(1-\nu^2)}\left(\frac{t}{\alpha}\right)^3 E + \pi\sigma_0\right]\delta + tEq\left(\frac{\delta}{\alpha}\right)^3 \qquad \text{(IX.21)}$$

In Eqs. IX.20, IX.21, σ_0 is the pre-tension present in the membrane due to the preparation procedure, t is the thickness and ν is the Poisson's ratio (for SLG thus is taken as 0.165, the Poisson's ratio for graphite in the basal plane [1439, 1441]). In Eq. IX.20, w,l are the width and length of the GNR, while in Eq. IX.21 a is the hole radius and $q = a/(1.05 - 0.15\nu - 0.16\nu^2)^3$ is a dimensionless constant [1436, 1441]. The microindentation experiment is in essence biaxial. The conversion of biaxial deflection data to uniaxial stress-strain curves by assuming zero bending stiffness is problematic, and not fully representative of true uniaxial tensile loading [1439].

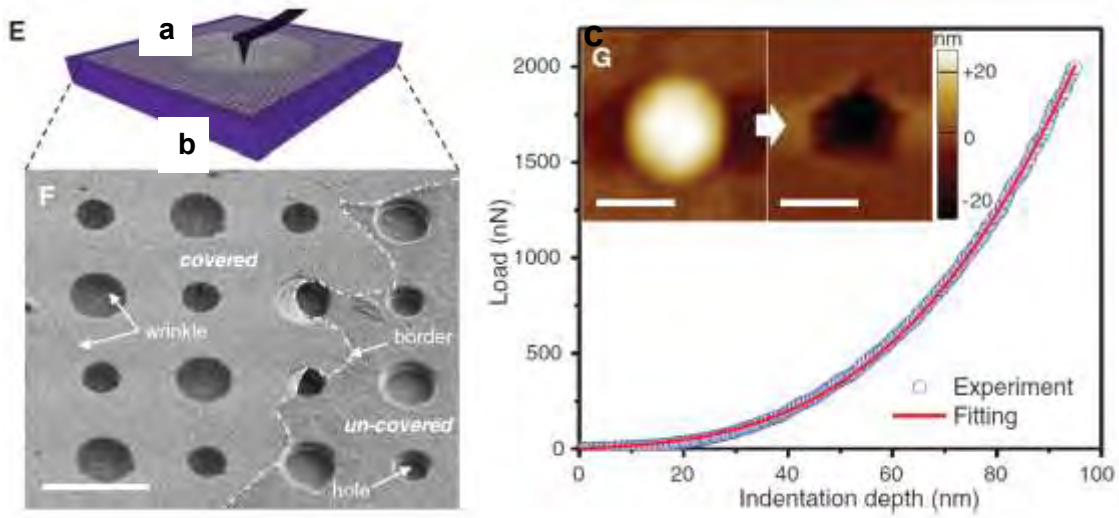

Fig. IX.62 (a) Schematic of the suspended SLG over hole for AFM nanoindentation tests. (b) SEM images of the suspended SLG over holes. The border of the SLG-covered area is indicated by a dashed line. Wrinkles often present in the transferred SLG can be seen. (c) Force-displacement curve of the SGL film in AFM nanoindentation. The red line is a fitting curve to Eq 21 (Inset). The AFM topography images of the suspended SLG before and after fracture. Scale bars in (b) 2 μm and (c) 1 μm Adapted from [1440]

AFM indentation experiments were conducted on epitaxial graphene on SiC [1442] and CVD grown SLG of different grain size [1440]. Ref. [1440] showed that the elastic stiffness of CVD-SLG is similar to that of MC SLG, provided that the sample is free of pleats and ripples.

The mechanical properties of 1L-MoS_2 [1443, 1444] and h-BN [895] were measured by AFM nanoindentation. Similar modelling approaches were pursued for the interpretation of the force-displacement traces. In Table IX.IV the elastic properties of various GRMs measured by AFM nanoidentation techniques are summarized.

Table IX.IV Indicative values of Young modulus and breaking strength for 1L-GRMs measured by AFM nanoidentation

1L-GRM	**E (N/m)**	**Breaking stress, σ_{2D}^{max} (N/m)**	**Strain-at-break (%)**
Graphene (exf.) [1439]	340 (50)	42 (4)	25
Graphene (CVD)	328 (15)	39.5	-
MoS_2 (exf.)	130	16.5	-
MoS_2 (CVD) [1445]	123	-	-
WS_2 (CVD) [1445]	137	-	-
BN[895]	220-510	8.8	-

Bulge testing

The elastic properties of GRMs can be assessed by bulge [1446] or pressurized blister test [1447], commonly applied for thin film testing. The advantage of the bulge test is the ability to measure not only E but also ν, whereas, in the case of AFM nanoidentation, ν should be known in advance (see Eq 21) [1447]. Another advantage is that the stress concentration caused by the AFM tip is avoided by the application of a uniform pressure. Ref.[1448] suspended MC SLG over microcavities (diameter~5 μm) etched in a SiO_2 substrate (Fig IX.63a). The SLG membrane remains flat due to the balance of internal (atmospheric) and external pressures (Fig. IX.63b). It is adhered to the substrate by van der Waals forces and can confine gas molecules (e.g. Nitrogen). The SLG membrane inflates forming a blister, when a pressure difference across its surface is applied (Fig IX.63c). AFM was used to measure the SLG membrane shape. In particular its maximum deflection δ at the center of the blister and its radius α (Fig IX.63d). The deflection can be correlated with the pressure difference, Δp, across the SLG membrane (Fig.IX.63e) using Hencky's solution [1449, 1450] which gives the deformation of the membrane for the geometrically nonlinear response of a clamped circular elastic membrane subjected to a pressure difference Δp provided that the bending stiffness of the membrane is negligible. Therefore, Δp can be written as [1448]:

$$\Delta p = K(\nu) E \, \delta^3/\alpha^4 \qquad \text{(IX.19)}$$

where $K(\nu)$ is a constant that depends on ν [1448].

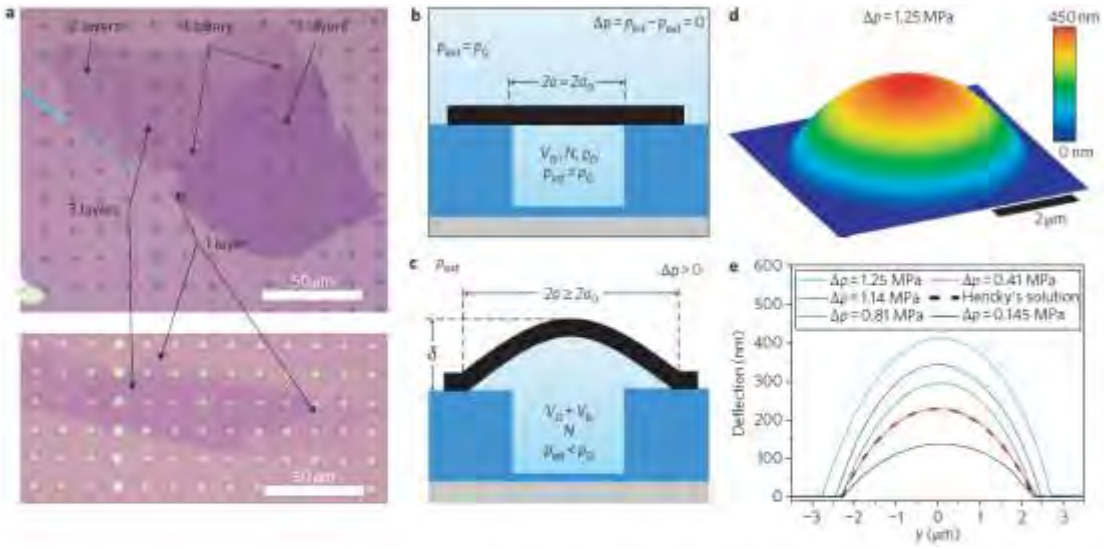

Fig. IX.63 (a) Optical images showing flakes with regions of 2-5L (top) and 1 and 3L (bottom). Schematic illustration of a SLG-sealed microcavity (b) at rest where Δp=0, the pressure inside the microcavity is equal to the external pressure pext, and (c) at higher Δp, (d) an AFM image showing the deformed shape of a SLG membrane with Δp = 1.25 MPa and (e) Deflection versus position for various levels Δp (cyan). The dashed black line is the shape obtained from Hencky's solution for Δp = 0.41 MPa. The deflection is measured by an AFM along a line that passes through the centre of the membrane. Adapted from [1448]

By plotting $K(\nu)\,\delta^3/\alpha^4$ vs Δp, E can be estimated as the slope of the linear dependence. In Fig. IX.64a the experimental data for K(ν) δ^3/α^4 versus *Δp* are shown for SLG. A linear fit to Eq. (IX.22) gives *E* = 347 N/m, in good agreement with the AFM nanoidenatation measurements [1435, 1440]. Ref. [1448] measured E of up to 5LG membranes. The results are summarized in Fig IX.64b and show that E is quantized to the SLG E (347 N m $^{-1}$). These findings are based on a continuum model in which SLG is considered as a membrane with negligible bending stiffness and the crystal is of high structural quality i.e. free of ripples, folds and defects.

Bulge testing has also been used for 1L and ML-MoS_2 as a way to apply biaxial strains upt o 7% for band gap engineering [1451]. The strong adhesion, comparable to solid-liquid adhesion [1448], between 1L-GRMsl and an atomically flat substrate (e.g. SLG/SLG, SLG/BN, MoS_2/MoS_2) results in atomically clean interfaces since any contaminants (water and hydrocarbons) are repelled by the van der Waals forces between the layers forming microbubbles [1452]. These bubbles have constant volume, and their shape is determined by the competition between van der Waals adhesion of the crystal to the substrate and the elastic energy needed to deform it [1453]. In Fig IX.65a, typical force-displacement curves (solid lines) recorded from bubbles of different sizes are presented. The symbols correspond to numerical fits by taking into account the changes in area of contact and the increase in bubble's radius [1453]. The data in Fig. IX.65b correspond to SLG bubbles for which the

fitting curve to the experimental data is drawn by assuming a SLG axial stiffness~420 ± 20N/m [1453]. Similarly, the stiffness of 1L-MoS_2 was estimated as 210 ± 20 N/m. Both values are somewhat higher than those given in Table IV.

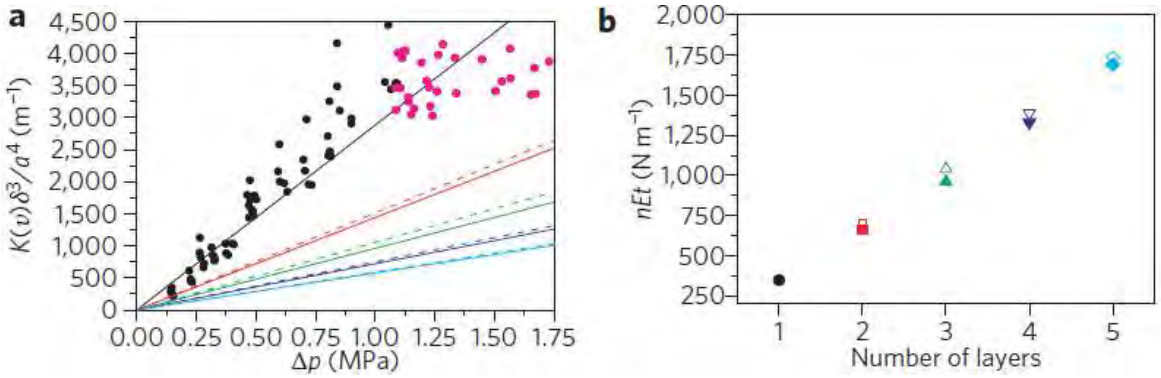

Fig. IX.64. (a) K(y)δ^3/α^4 versus Δp for SLG membranes before delamination (black symbols) and after delamination (magenta) , (b) NEt versus N. Closed shapes are for the fitted lines; open shapes are for NEt, with Et = 347N/m.

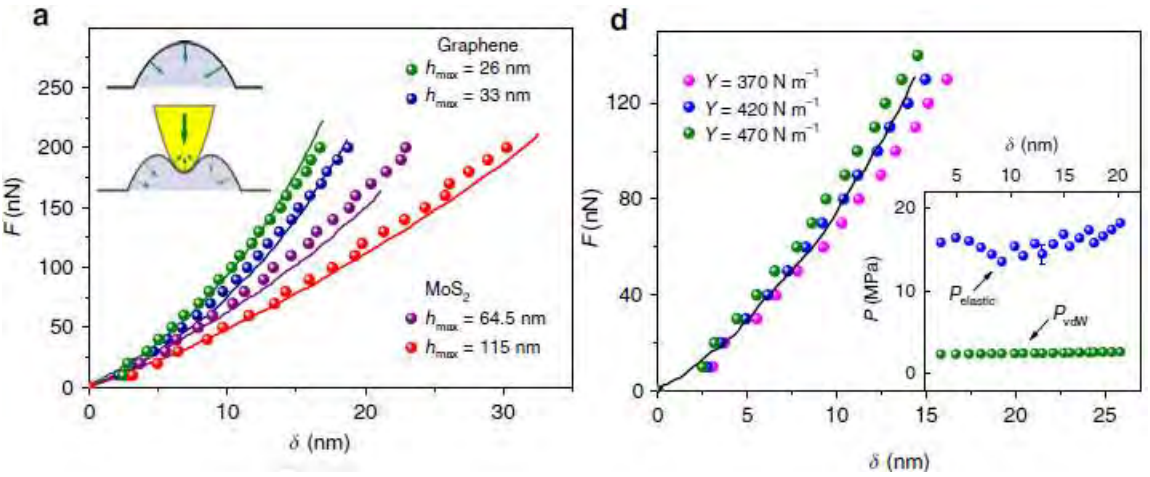

Fig. IX.65 (a) Experimental force-deflection curves (solid lines) and numerical fits (symbols) for two SLG and 1L-MoS_2 bubbles of different sizes. (b) A force-deflection curve (solid curve) and corresponding numerical fits for three E.

Fracture toughness and bending stiffness

Large-scale applications of GRMs, beyond microscale, require the knowledge of fracture toughness, rather than the intrinsic strength, which corresponds to a uniform breaking of atomic bonds in a perfect GRM crystal. Fracture toughness is a property that describes the ability of a material containing a crack or a defect to resist fracture [1454]. The absence of reliable tensile testing devices with force sensing at the pN or nN range and the cumbersome fabrication/ transferring procedure has hindered progress. Thus the direct determination of fracture toughness has been challenging for GRMs. Fracture data for CVD SLG were measured using in situ MEMS-based uniaxial tension devices in a Scanning [1455], Transmission [1456] electron microscopes and AFM nanoidentation [1457, 1458]]. Ref.[1455] conducted in situ tensile testing of centre-cracked CVD SLG

in a SEM and obtained fracture toughness based on the classical Griffith's fracture theory [1459]. Ref. [1455] conducted in situ fracture toughness testing in a HRTEM on MLG having V/U-shaped single-edge notches. For comparative purposes fracture toughness testing on multilayer BN samples was also conducted. Ref. [1460] performed fracture mechanics experiments under uniaxial tension on MC BLG and measured its fracture toughness. In Table V the measured fracture toughness for various SLG and MLG are summarized. The results from multilayer BN are also given for comparative purposes.

Table IX.V.- Fracture toughness of 1L, 2L and MLG

Sample	**Fracture toughness MPa $\sqrt{m}$**	**Mechanical testing/ device**
CVD SLG[1455]	4.00	Tensile/MEMS device (SEM)
BLG[1460]	21.25	Tensile/ MEMS device (SEM)
MLG[1456]	12.00	Tensile/ MEMS device (TEM)
ML-BN[1456]	5.50	Tensile/ MEMS device (TEM)

GRM are modelled as membrane-like materials i.e., with approximately zero bending stiffness [1461]. Therefore, the effect of bending modulus is usually ignored [1439, 1440]. Refs.[1436, 1443] explored the effect of bending modulus as being proportional to the third power of the crystal thickness (see first term in Eq.IX.20) in AFM nanoidenation of MoS_2 crystals with various thicknesses. It was found that the force-displacement curves for the few layer crystals were strongly nonlinear, while for N>10 were linear. This is important when considering membrane-to-plate like transition for N>10. The determination of bending stiffness of either 1L or FL-GRMs has been mainly based on various types of theoretical calculation [1462]. Ab initio or first-principles quantum mechanical calculations and empirical potential calculations were used to determine the bending modulus of SLG [1432, 1462], with higher values (mean value of 1.51 eV) in comparison with those derived by empirical potentials (mean value of 1.12 eV). These models treat SLG as an isotropic body. To introduce anisotropy and to incorporate bending effects, a finite elasticity model has been proposed [1463]. This provides the means to introduce (and handle) additional degrees of freedom through dependence on the shift vector. Continuum mechanics was applied to describe the SLG flexural deformation, leading to a nonlinear von-Karman plate theory with two elastic bending moduli [1432, 1463, 1464]. However, from the experimental point of view, Ref. [1465] criticized the use of the continuum mechanics shell model. By exploring the nm scale rippling of SLG, Ref. [1465] claimed that phenomenology fails to predict correctly E, as well as the SLG thickness of 0.335 nm, since classical continuum plate theory assumes that bending always induces in-plane stretching.

A few attempts have been made to measure experimentally the bending stiffness of FLG and MoS_2 and confirmed the dependence on the third power of thickness in accordance with the membrane theory of shells with pure bending [1462]. Ref.[1466] performed AFM nanoidentation experiments in FLG membranes onto a circular hole, while Ref.[1467], fabricated and measured the

bending stifness of convex-buckled suspended BLG ribbons. By exploiting the abrupt switching from convex to concave geometry of the ribbons, under electrostatic actuation, they measured a bending rigidity~35.5 eV. Ref.[1468] proposed a different experimental approach to measure the bending stiffness of 1L-GRMs. The method is based on atomic mapping of the crystal lattice within a fold by using HRTEM for SLG and scanning TEM imaging for MoS_2 and WSe_2. They confirmed the applicability of the linear elastic shell model and derived the bending rigidity. They found that bending rigidity for TMDs is in the range of 10–16 eV, five to six times that of SLG, in agreement with theory [1469].

Ref.[1470] measured the bending modulus of CVD SLG. They produced cantilever structures (length, 10-100 μm and width, 10 μm) and measured their spring constants by assuming them to be related to the bending rigidity. By using the photon pressure from an infrared laser, the spring constant of the cantilever and consequently the bending rigidity was measured (Fig. IX.66a). Using the thermal fluctuations of the SLG cantilevers and based on the equipartition theorem of classical statistical mechanics, the cantilever spring constant was also measured independently (Fig. IX.66b). As shown in Fig IX.66c both methods yield a high bending stiffness for SLG,~10^3 to 10^4 eV. These values are orders of magnitude higher than 1.2 eV, predicted from simulations [1462] and measurements of the phonon modes in graphite [1471]. This high value is attributed to both thermal and static rippling that stiffen ultrathin crystalline membranes in a manner similar to how a flat sheet of paper becomes more rigid when crumpled [1470].

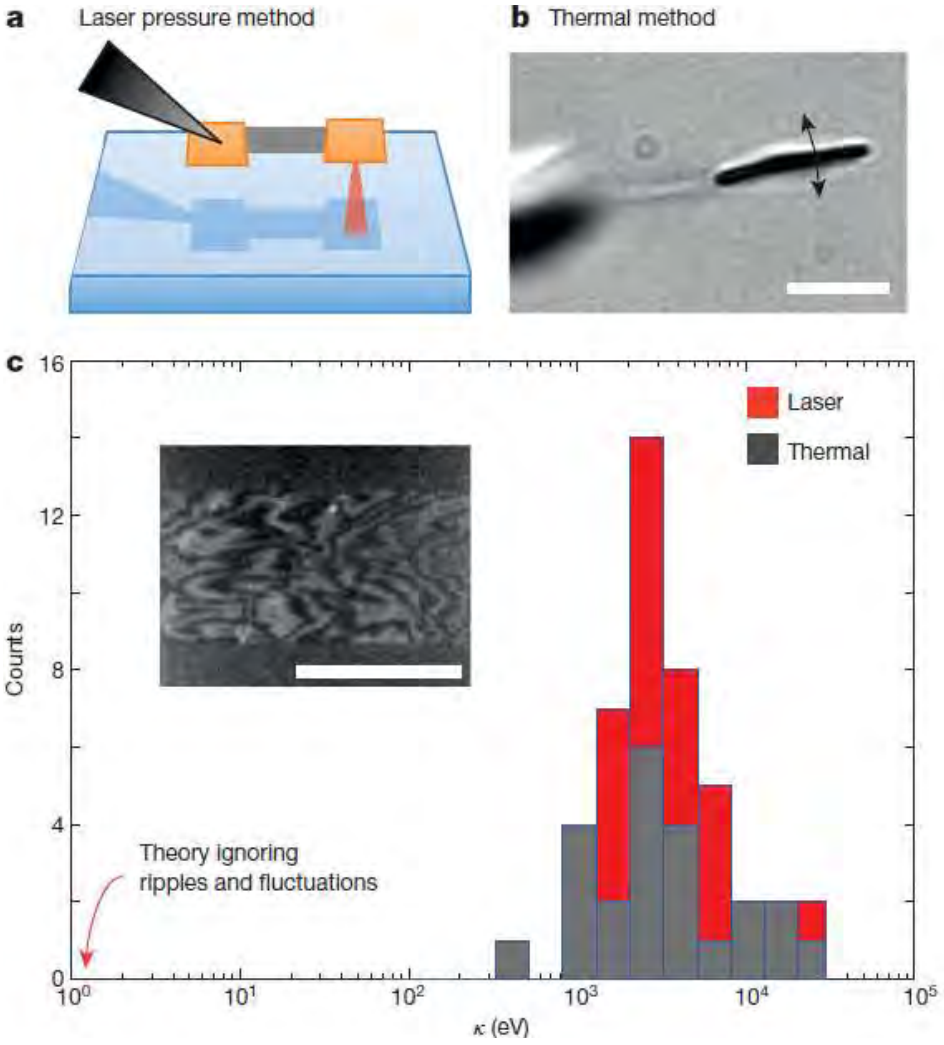

Fig. IX.66. Bending stiffness of SLG by (a) applying controlled forces using an infrared laser and (b) tracking the motion of a rotated device under thermal fluctuations. (c) Stacked histogram of bending stiffness measured by the methods in (a) and (b). The red arrow points to the bending stiffness of ~1.2 eV calculated theoretically. Scale bars are 10 mm. Adapted from [1470].

Raman spectroscopy

Information on GRM mechanical properties may be obtained by Raman spectroscopy in tandem with various types of external loadings (uniaxial, biaxial, hydrostatic, etc) [1472-1475]. Due to the anharmonicity of the interatomic potentials phonon frequencies soften upon tension and harden under compression. As a result, Raman peak positions red (blue) shifted under tensile (compressive) loading. The magnitude of shift depends on the evolved interatomic force constants and the mode eigenvectors relative to the directions of the strain axis. However, in GRM many other effects can shift peaks, e.g. doping [1296], hence caution needs to be taken when using Raman spectroscopy to derive these information.

Several groups investigated the effect of uniaxial strain in tension or compression by bending flexible substrates (e.g. PDMS) or a plastic beams (e.g. PMMA) on which GRMs are deposited without slippage [1307, 1314, 1325, 1476-1483]. The samples can be supported or embedded within a thin

polymer film. In these experiments the application of uniaxial stress/strain leads to the development of interfacial shear between the GRM membrane and the underlying or surrounding polymer, transmitted into a normal stress [1484]. Care should be taken for the examined area of the flake to be free of residual stresses [1484]. Pos(G) is an indicator that the applied strain is transferred to the interatomic bonds, provided one can ensure that other effects, also leading to peak shifts, are not present. In tension, the shift of the main Raman modes is linear up to 1.5 % [1485]. The 2D peak position downshifts with uniaxial strain at a much higher rate of about -60cm^{-1}/% [1307, 1478].An analogous but not as pronounced splitting to two distinct components $2D^-$ and $2D^+$ was observed [1312, 1314] depending on the laser wavelength. The strain-induced splitting and the red shift depend on the strain axis direction relative to the crystallographic axis. The underlining mechanism of the strain depended variation of 2D peak depends on the shifting of the Dirac cones and the anisotropic phonon softening which, in turn, cause alteration in the scatterings paths participating in the double resonance mechanism for the 2D band [1312, 1486-1488].

Under compression by monitoring the Pos(2D) shift of rectangular SLG embedded into polymer flakes of various sizes the critical strain to failure was determined [1482]. These were found to be independent of flake size at a mean value of –0.60% corresponding to a yield stress up to -6 GPa [1481]. CVD SLG can be considerably wrinkled [1489]. Upon uniaxial deformation the Raman response for the 2D band was less than 25% of that of flat exfoliated flakes [1489]. In all cases in which SLG is either supported on or embedded in a polymer matrix, parameters such as the interfacial shear strength, the onset of interfacial sliding and the critical compressive strain to failure may be extracted via in-situ Raman spectroscopy under tensile or compressive loading [1490, 1491].

Raman spectroscopy was also used to investigate SLG bubbles as a function of strain [1309, 1446, 1492]. These are formed by the pressure difference on both sides of SLG during the deposition of flakes over apertures of various size and shape. SLG membranes can support pressures up to 14 bar, corresponding to reversible strains up to 2% [1492]. The advantage of intentionally pressurized membranes is to avoid the influence of the substrate, excluding complications from SLG-substrate interactions. Biaxial strain is essential for the reliable determination of the Grüneisen parameters. Ref. [1493] determined the SLG E by comparing the strain induced on pressurized balloons and the response of the G peak, with numerical simulations. The estimated E as 2.4 and 2.0TPa, much larger than previous values [1439, 1448]. This discrepancy was attributed to the small attainable strain (0.2%), since E may depend on the strain range being larger in small strain ranges.

In Ref.[1479] an effective bending stiffness of SLG embedded into a polymer cantilever was estimated. Flakes of various aspect ratios (length to width) were embedded on the surface of a PMMA bar covered by a 200nm PMMA layer. SLG was modelled as a thin plate and subjected to uniaxial compression [1479]. SLG was buckled at a critical strain determined by the response of the 2D Raman band (Fig IX.67). Pos(2D) relaxed after an abrupt uptake, while the strain at the onset of the Pos(2D) relaxation defines the critical strain for each flake, see Fig IX.67. For flakes with lengths smaller than the critical length (twice the distance it needs for strain to increase to the externally applied value) the externally applied strain is not fully transmitted to the flake [1477, 1484, 1489]. For flake lengths higher than the critical length, the critical strain for buckling is -0.6% [1482]. By

considering the critical buckling strain for an embedded flake in the classical Euler regime [1461, 1479], the effective bending rigidity of SLG fully embedded in a polymer matrix was estimated~70MeV. This means that SLG encapsulation into a matrix affects considerably the resistance of atomic thickness membranes to bending and paves the way for the development of novel composite materials of high intrinsic values of compression strength compared to the conventional ones. This value, however, is six orders of magnitude higher than the value in air and one order of magnitude higher than CVD SLG in water [1470]. This could imply that encapsulation into a matrix or in water, affects considerably the resistance of atomic thickness membranes to bending.

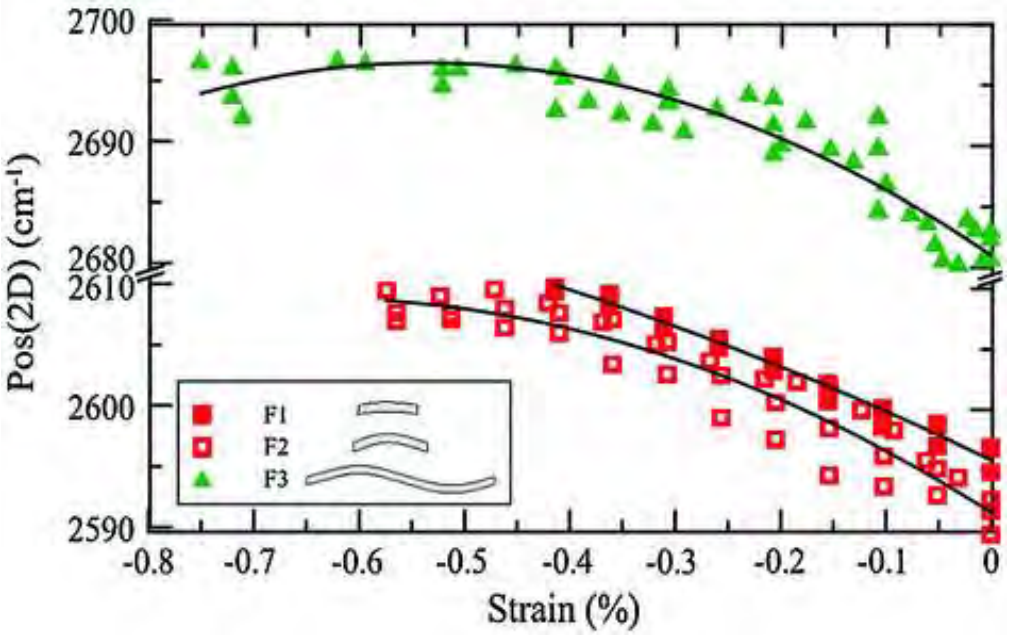

Fig.IX.67 Pos(2D) as a function of uniaxial compressive strain for SLG flakes of various aspect ratios Adapted from [1494]

The bulging test combined with Raman spectroscopy was used by Ref. [1495] on a multireflection model for a SLG-air-Si stack (Fig IX.68a) that takes into account the variation of I(2D) and I(G) (Fig IX.68a). Both oscillate between a minimum and a maximum value which depends on the height of the blister at various pressure differences (Fig IX.68b) [1495]. The enhancement factor of I(D) and I(G) correlated by the multireflection model [1496] with h_{tot}, the total distance between SLG and the underlying Si (Fig IX.68a&c) was used for the metrology of the blister height. Following Hencky's model (Eq. 20), the third power of the height at the centre point of the blister is linearly dependent on the pressure difference across SLG (Fig. IX.68d) resulting in a slope from which the suspended SLG E was estimated as 352 Nm^{-1}, in close agreement with values derived from direct methods (see Table IV).

Instead of using the pressure difference, the bulging test can be also implemented with electrostatic actuation of SLG suspended onto holes with large diameters (7.5 – 30 μm) over a gating chip forming a parallel plate capacitor with an inter-plate distance, *d*, (Fig IX.68a)[1497]. By applying the gating voltage, SLG deflects subjecting to a pressure which defines the radial in plane stress and corresponds to a radial strain. Therefore *E* is estimated (Fig IX.68d). The radial strain depends on the

height of the membrane dome at the centre deflection point which is measured by employing interferometric profilometry (Fig IX.69b). A number of different devices were tested and the estimated *E* are presented in the histogram of Fig. IX.69d and are significantly lower than those from other techniques (Table IX.IV)

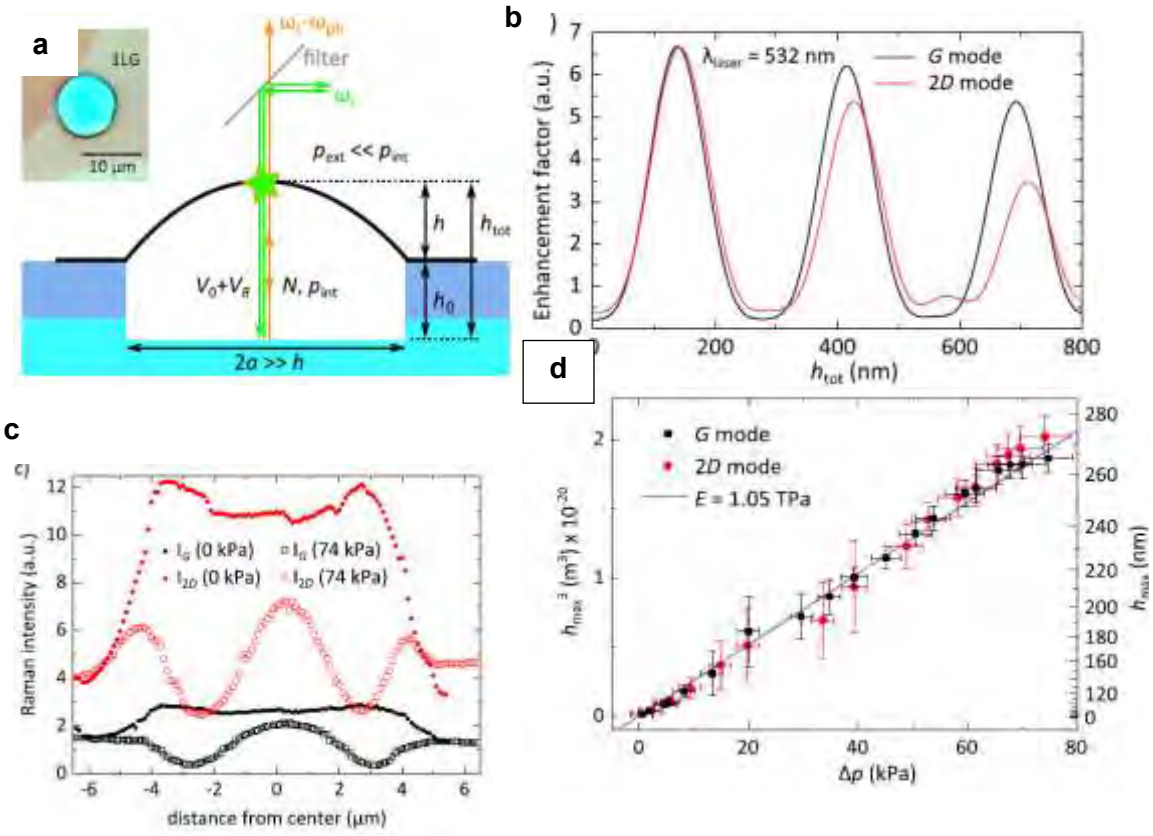

Fig.IX.68: a) Schematic of blister geometry. The optical path of the Raman signal and excitation is also depicted. SLG suspended over the hole(Inset), (b) The enhancement factor for G and 2D. (c) I(G) and I(2D) versus distance from the centre of the hole with SLG at rest (0 kPa) and at a higher pressure difference. (d) Third power of SLG blister at its center versus pressure difference. From the slope of the linear fit, E is determined.

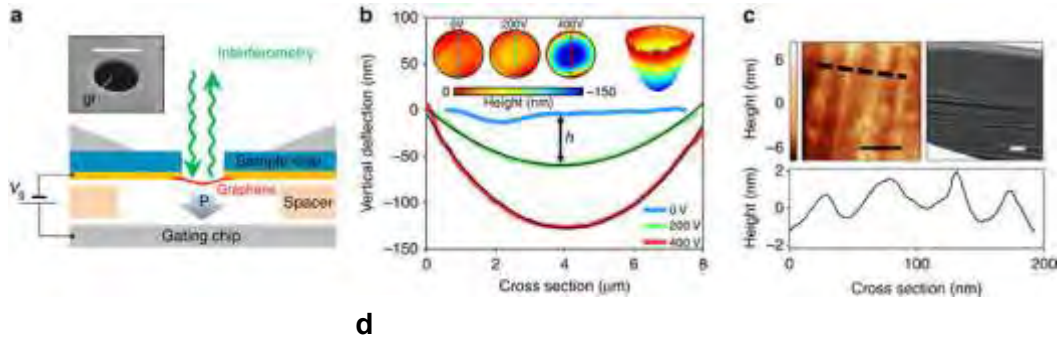

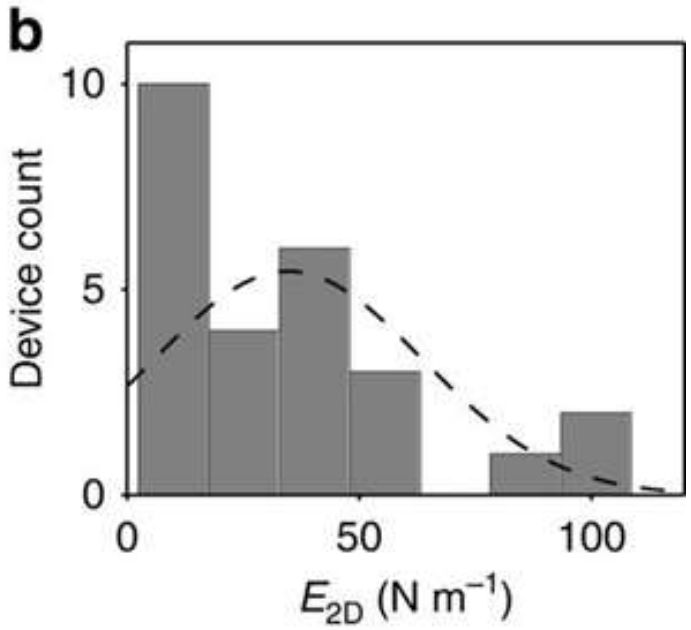

Fig.IX.69 (a) Device schematic. Inset: SEM image of a representative free-standing SLG membrane (scale bar, 8 μm). (b) Cross-sections of SLG membrane at various applied voltages. Height data obtained from interferometric profilometry corresponding to these cross-sections are shown in the inset. Also shown is a 3d view of the data at V_g=400 V. (c) AFM measurements of SLG membrane with nm-scale static wrinkles (left, scale bar, 100 nm). A cross section of the AFM data is shown in the bottom panel. Wrinkling is also evident on the high-angle tilted SEM image (right, scale bar, 1 μm). (d) E Histogram for all measured CVD SLG devices.

Ref.[1498] employed Raman spectroscopy using the aforementioned SLG-sealed micro-chambers under variable external pressure to determine the pressure induced sliding friction between SiO_2 and 1L-, 2L- and 3LG. Tensile radial strain of 0.6% and compressive tangential strain of -0.3% were achieved. A violation of the Amonton's law [1499, 1500] for 1L and 2LG was found. In 3LG, however, the sliding friction is directly proportional to the applied load in accordance with the Amonton's law. This behaviour was attributed the lower bending rigidity of 3LG, enabling higher surface conformation and stronger adhesion.

Several diamond anvil cell experiments were conducted mainly on MC 1L and FLG on Si/SiO_2 or Cu, employing different pressure transmitting media [1308, 1501]. The choice of the transmitting medium e.g. polar (4:1 methanol-ethanol) or non-polar (e.g Fluorinert) is important due to pressure mediated doping that occurs from the substrate. Assuming that SLG follows the pressure-induced substrate contraction, its compression is determined by the bulk modulus of the substrate (140 GPa for Cu [1501]). Ref.[1501] suggested that the expected value of the pressure dependent wavenumber shift is 15 cm^{-1}/GPa (for SiO_2/Si which is more compressible the corresponding value is 21.4 cm^{-1}/GPa). The significant deviation have been ascribed to the non-ideal adherence of graphene on the Cu.

From the applications point of view, it is important to understand how atomically thin membranes can respond to mechanical deformations at the nanoscale. Sample preparation and handling hinders systematic studies, since a defect-free gauge area of the sample is difficult to be placed and gripped onto the loading device. The development of specific instruments with low force sensing and capable of applying in-plane stress in GRM membranes is necessary to capture their full response under axial deformation up to failure and to measure directly the elastic (e.g. stiffness) and inelastic properties (e.g. fracture strength and strain-to-failure). Fundamental questions have been raised on the effects of defects, out-of-plane deformations and wrinkling in either elastic or inelastic properties of GRMs [1458, 1502].Therefore, further experiments are needed in fundamental research in order for novel applications to take the full advantage of these superior properties.

Acknowledgement

We acknowledge funding from the European Commission under the Graphene Flagship from EU Horizon 2020 research and innovation program under grant agreement No. 696656 (GrapheneCore1-Graphene-based disruptive technologies)

References

[1] L. Chen, Y. Hernandez, X. Feng, K. Müllen, From Nanographene and Graphene Nanoribbons to Graphene Sheets: Chemical Synthesis, Angewandte Chemie International Edition, 51 (2012) 7640-7654.
[2] J. Bai, Y. Huang, Fabrication and electrical properties of graphene nanoribbons, Materials Science and Engineering: R: Reports, 70 (2010) 341-353.
[3] L. Ma, J. Wang, F. Ding, Recent Progress and Challenges in Graphene Nanoribbon Synthesis, ChemPhysChem, 14 (2013) 47-54.
[4] M. Terrones, A.R. Botello-Méndez, J. Campos-Delgado, F. López-Urías, Y.I. Vega-Cantú, F.J. Rodríguez-Macías, A.L. Elías, E. Muñoz-Sandoval, A.G. Cano-Márquez, J.-C. Charlier, Graphene and graphite nanoribbons: Morphology, properties, synthesis, defects and applications, Nano Today, 5 (2010) 351-372.
[5] V. Barone, O. Hod, G.E. Scuseria, Electronic Structure and Stability of Semiconducting Graphene Nanoribbons, Nano Letters, 6 (2006) 2748-2754.
[6] K. Wakabayashi, K.-i. Sasaki, T. Nakanishi, T. Enoki, Electronic states of graphene nanoribbons and analytical solutions, Science and Technology of Advanced Materials, 11 (2010) 054504.
[7] K. Nakada, M. Fujita, G. Dresselhaus, M.S. Dresselhaus, Edge state in graphene ribbons: Nanometer size effect and edge shape dependence, Physical Review B, 54 (1996) 17954-17961.
[8] B. Obradovic, R. Kotlyar, F. Heinz, P. Matagne, T. Rakshit, M.D. Giles, M.A. Stettler, D.E. Nikonov, Analysis of graphene nanoribbons as a channel material for field-effect transistors, Applied Physics Letters, 88 (2006) 142102.
[9] J. Wang, R. Zhao, M. Yang, Z. Liu, Z. Liu, Inverse relationship between carrier mobility and bandgap in graphene, The Journal of Chemical Physics, 138 (2013) 084701.

[10] Y.-W. Son, M.L. Cohen, S.G. Louie, Energy Gaps in Graphene Nanoribbons, Physical Review Letters, 97 (2006).
[11] L. Yang, C.-H. Park, Y.-W. Son, M.L. Cohen, S.G. Louie, Quasiparticle Energies and Band Gaps in Graphene Nanoribbons, Physical Review Letters, 99 (2007).
[12] M. Fujita, K. Wakabayashi, K. Nakada, K. Kusakabe, Peculiar Localized State at Zigzag Graphite Edge, Journal of the Physical Society of Japan, 65 (1996) 1920-1923.
[13] J. Cai, P. Ruffieux, R. Jaafar, M. Bieri, T. Braun, S. Blankenburg, M. Muoth, A.P. Seitsonen, M. Saleh, X. Feng, K. Müllen, R. Fasel, Atomically precise bottom-up fabrication of graphene nanoribbons, Nature, 466 (2010) 470-473.
[14] A. Narita, X.-Y. Wang, X. Feng, K. Müllen, New advances in nanographene chemistry, Chemical Society Reviews, 44 (2015) 6616-6643.
[15] X.-Y. Wang, A. Narita, K. Müllen, Precision synthesis versus bulk-scale fabrication of graphenes, Nature Reviews Chemistry, 2 (2017) 0100.
[16] L. Dössel, L. Gherghel, X. Feng, K. Müllen, Graphene Nanoribbons by Chemists: Nanometer-Sized, Soluble, and Defect-Free, Angewandte Chemie International Edition, 50 (2011) 2540-2543.
[17] M.G. Schwab, A. Narita, S. Osella, Y. Hu, A. Maghsoumi, A. Mavrinsky, W. Pisula, C. Castiglioni, M. Tommasini, D. Beljonne, X. Feng, K. Müllen, Bottom-Up Synthesis of Necklace-Like Graphene Nanoribbons, Chemistry - An Asian Journal, 10 (2015) 2134-2138.
[18] X. Yang, X. Dou, A. Rouhanipour, L. Zhi, H.J. Räder, K. Müllen, Two-Dimensional Graphene Nanoribbons, Journal of the American Chemical Society, 130 (2008) 4216-4217.
[19] M.G. Schwab, A. Narita, Y. Hernandez, T. Balandina, K.S. Mali, S. De Feyter, X. Feng, K. Müllen, Structurally Defined Graphene Nanoribbons with High Lateral Extension, Journal of the American Chemical Society, 134 (2012) 18169-18172.
[20] M.D. Watson, A. Fechtenkötter, K. Müllen, Big Is Beautiful−"Aromaticity" Revisited from the Viewpoint of Macromolecular and Supramolecular Benzene Chemistry, Chemical Reviews, 101 (2001) 1267-1300.
[21] J. Wu, W. Pisula, K. Müllen, Graphenes as Potential Material for Electronics, Chemical Reviews, 107 (2007) 718-747.
[22] J.K. Stille, Step-growth polymerization, Journal of Chemical Education, 58 (1981) 862.
[23] W. Zhang, Z. Chen, B. Yang, X.-Y. Wang, R. Berger, A. Narita, G.B. Barin, P. Ruffieux, R. Fasel, X. Feng, H.J. Räder, K. Müllen, Monitoring the On-Surface Synthesis of Graphene Nanoribbons by Mass Spectrometry, Analytical Chemistry, 89 (2017) 7485-7492.
[24] A. Narita, X. Feng, Y. Hernandez, S.A. Jensen, M. Bonn, H. Yang, I.A. Verzhbitskiy, C. Casiraghi, M.R. Hansen, A.H.R. Koch, G. Fytas, O. Ivasenko, B. Li, K.S. Mali, T. Balandina, S. Mahesh, S. De Feyter, K. Müllen, Synthesis of structurally well-defined and liquid-phase-processable graphene nanoribbons, Nature Chemistry, 6 (2013) 126-132.
[25] W.H. Carothers, Polymers and polyfunctionality, Transactions of the Faraday Society, 32 (1936) 39.
[26] G. Odian, Principles of Polymerization, John Wiley & Sons, Inc.2004.
[27] J. Lee, H.-J. Cho, B.-J. Jung, N.S. Cho, H.-K. Shim, Stabilized Blue Luminescent Polyfluorenes: Introducing Polyhedral Oligomeric Silsesquioxane, Macromolecules, 37 (2004) 8523-8529.
[28] S. Setayesh, A.C. Grimsdale, T. Weil, V. Enkelmann, K. Müllen, F. Meghdadi, E.J.W. List, G. Leising, Polyfluorenes with Polyphenylene Dendron Side Chains: Toward Non-Aggregating, Light-Emitting Polymers, Journal of the American Chemical Society, 123 (2001) 946-953.
[29] L. Talirz, P. Ruffieux, R. Fasel, On-Surface Synthesis of Atomically Precise Graphene Nanoribbons, Advanced Materials, 28 (2016) 6222-6231.
[30] H. Zhang, H. Lin, K. Sun, L. Chen, Y. Zagranyarski, N. Aghdassi, S. Duhm, Q. Li, D. Zhong, Y. Li, K. Müllen, H. Fuchs, L. Chi, On-Surface Synthesis of Rylene-Type Graphene Nanoribbons, Journal of the American Chemical Society, 137 (2015) 4022-4025.
[31] L. Talirz, H. Söde, T. Dumslaff, S. Wang, J.R. Sanchez-Valencia, J. Liu, P. Shinde, C.A. Pignedoli, L. Liang, V. Meunier, N.C. Plumb, M. Shi, X. Feng, A. Narita, K. Müllen, R. Fasel, P. Ruffieux, On-Surface

Synthesis and Characterization of 9-Atom Wide Armchair Graphene Nanoribbons, ACS Nano, 11 (2017) 1380-1388.
[32] Y.-C. Chen, D.G. de Oteyza, Z. Pedramrazi, C. Chen, F.R. Fischer, M.F. Crommie, Tuning the Band Gap of Graphene Nanoribbons Synthesized from Molecular Precursors, ACS Nano, 7 (2013) 6123-6128.
[33] G.D. Nguyen, F.M. Toma, T. Cao, Z. Pedramrazi, C. Chen, D.J. Rizzo, T. Joshi, C. Bronner, Y.-C. Chen, M. Favaro, S.G. Louie, F.R. Fischer, M.F. Crommie, Bottom-Up Synthesis ofN= 13 Sulfur-Doped Graphene Nanoribbons, The Journal of Physical Chemistry C, 120 (2016) 2684-2687.
[34] S. Kawai, S. Saito, S. Osumi, S. Yamaguchi, A.S. Foster, P. Spijker, E. Meyer, Atomically controlled substitutional boron-doping of graphene nanoribbons, Nature Communications, 6 (2015) 8098.
[35] R.R. Cloke, T. Marangoni, G.D. Nguyen, T. Joshi, D.J. Rizzo, C. Bronner, T. Cao, S.G. Louie, M.F. Crommie, F.R. Fischer, Site-Specific Substitutional Boron Doping of Semiconducting Armchair Graphene Nanoribbons, Journal of the American Chemical Society, 137 (2015) 8872-8875.
[36] Y. Zhang, Y. Zhang, G. Li, J. Lu, X. Lin, S. Du, R. Berger, X. Feng, K. Müllen, H.-J. Gao, Direct visualization of atomically precise nitrogen-doped graphene nanoribbons, Applied Physics Letters, 105 (2014) 023101.
[37] C. Bronner, S. Stremlau, M. Gille, F. Braße, A. Haase, S. Hecht, P. Tegeder, Aligning the Band Gap of Graphene Nanoribbons by Monomer Doping, Angewandte Chemie International Edition, 52 (2013) 4422-4425.
[38] J. Cai, C.A. Pignedoli, L. Talirz, P. Ruffieux, H. Söde, L. Liang, V. Meunier, R. Berger, R. Li, X. Feng, K. Müllen, R. Fasel, Graphene nanoribbon heterojunctions, Nature Nanotechnology, 9 (2014) 896-900.
[39] T. Marangoni, D. Haberer, D.J. Rizzo, R.R. Cloke, F.R. Fischer, Heterostructures through Divergent Edge Reconstruction in Nitrogen-Doped Segmented Graphene Nanoribbons, Chemistry - A European Journal, 22 (2016) 13037-13040.
[40] P. Ruffieux, S. Wang, B. Yang, C. Sánchez-Sánchez, J. Liu, T. Dienel, L. Talirz, P. Shinde, C.A. Pignedoli, D. Passerone, T. Dumslaff, X. Feng, K. Müllen, R. Fasel, On-surface synthesis of graphene nanoribbons with zigzag edge topology, Nature, 531 (2016) 489-492.
[41] D.G. de Oteyza, A. García-Lekue, M. Vilas-Varela, N. Merino-Díez, E. Carbonell-Sanromà, M. Corso, G. Vasseur, C. Rogero, E. Guitián, J.I. Pascual, J.E. Ortega, Y. Wakayama, D. Peña, Substrate-Independent Growth of Atomically Precise Chiral Graphene Nanoribbons, ACS Nano, 10 (2016) 9000-9008.
[42] L. Grill, K.H. Rieder, F. Moresco, G. Rapenne, S. Stojkovic, X. Bouju, C. Joachim, Rolling a single molecular wheel at the atomic scale, Nature Nanotechnology, 2 (2007) 95-98.
[43] H. Huang, D. Wei, J. Sun, S.L. Wong, Y.P. Feng, A.H.C. Neto, A.T.S. Wee, Spatially Resolved Electronic Structures of Atomically Precise Armchair Graphene Nanoribbons, Scientific Reports, 2 (2012).
[44] A.E.a.N. Greenwood, Chemistry of Elements.
[45] M. Vandescuren, P. Hermet, V. Meunier, L. Henrard, P. Lambin, Theoretical study of the vibrational edge modes in graphene nanoribbons, Physical Review B, 78 (2008).
[46] L. Gross, F. Mohn, N. Moll, P. Liljeroth, G. Meyer, The Chemical Structure of a Molecule Resolved by Atomic Force Microscopy, Science, 325 (2009) 1110-1114.
[47] F.J. Giessibl, Atomic resolution on Si(111)-(7×7) by noncontact atomic force microscopy with a force sensor based on a quartz tuning fork, Applied Physics Letters, 76 (2000) 1470-1472.
[48] L. Bartels, G. Meyer, K.H. Rieder, D. Velic, E. Knoesel, A. Hotzel, M. Wolf, G. Ertl, Dynamics of Electron-Induced Manipulation of Individual CO Molecules on Cu(111), Physical Review Letters, 80 (1998) 2004-2007.
[49] A. Fairbrother, J.-R. Sanchez-Valencia, B. Lauber, I. Shorubalko, P. Ruffieux, T. Hintermann, R. Fasel, High vacuum synthesis and ambient stability of bottom-up graphene nanoribbons, Nanoscale, 9 (2017) 2785-2792.

[50] R. Denk, M. Hohage, P. Zeppenfeld, J. Cai, C.A. Pignedoli, H. Söde, R. Fasel, X. Feng, K. Müllen, S. Wang, D. Prezzi, A. Ferretti, A. Ruini, E. Molinari, P. Ruffieux, Exciton-dominated optical response of ultra-narrow graphene nanoribbons, Nature Communications, 5 (2014).
[51] G. Li, K.-Y. Yoon, X. Zhong, X. Zhu, G. Dong, Efficient Bottom-Up Preparation of Graphene Nanoribbons by Mild Suzuki-Miyaura Polymerization of Simple Triaryl Monomers, Chemistry - A European Journal, 22 (2016) 9116-9120.
[52] P.B. Bennett, Z. Pedramrazi, A. Madani, Y.-C. Chen, D.G. de Oteyza, C. Chen, F.R. Fischer, M.F. Crommie, J. Bokor, Bottom-up graphene nanoribbon field-effect transistors, Applied Physics Letters, 103 (2013) 253114.
[53] P. Angelova, H. Vieker, N.-E. Weber, D. Matei, O. Reimer, I. Meier, S. Kurasch, J. Biskupek, D. Lorbach, K. Wunderlich, L. Chen, A. Terfort, M. Klapper, K. Müllen, U. Kaiser, A. Gölzhäuser, A. Turchanin, A Universal Scheme to Convert Aromatic Molecular Monolayers into Functional Carbon Nanomembranes, ACS Nano, 7 (2013) 6489-6497.
[54] D.G. Matei, N.-E. Weber, S. Kurasch, S. Wundrack, M. Woszczyna, M. Grothe, T. Weimann, F. Ahlers, R. Stosch, U. Kaiser, A. Turchanin, Functional Single-Layer Graphene Sheets from Aromatic Monolayers, Advanced Materials, 25 (2013) 4146-4151.
[55] C.T. Nottbohm, A. Turchanin, A. Beyer, A. Gölzhäuser, Direct e-beam writing of 1 nm thin carbon nanoribbons, Journal of Vacuum Science & Technology B: Microelectronics and Nanometer Structures, 27 (2009) 3059.
[56] C.T. Nottbohm, A. Turchanin, A. Beyer, R. Stosch, A. Gölzhäuser, Mechanically Stacked 1-nm-Thick Carbon Nanosheets: Ultrathin Layered Materials with Tunable Optical, Chemical, and Electrical Properties, Small, 7 (2011) 874-883.
[57] D. Rhinow, N.-E. Weber, A. Turchanin, Atmospheric Pressure, Temperature-Induced Conversion of Organic Monolayers into Nanocrystalline Graphene, The Journal of Physical Chemistry C, 116 (2012) 12295-12303.
[58] A. Turchanin, A. Beyer, C.T. Nottbohm, X. Zhang, R. Stosch, A. Sologubenko, J. Mayer, P. Hinze, T. Weimann, A. Gölzhäuser, One Nanometer Thin Carbon Nanosheets with Tunable Conductivity and Stiffness, Advanced Materials, 21 (2009) 1233-1237.
[59] A. Turchanin, D. Weber, M. Büenfeld, C. Kisielowski, M.V. Fistul, K.B. Efetov, T. Weimann, R. Stosch, J. Mayer, A. Gölzhäuser, Conversion of Self-Assembled Monolayers into Nanocrystalline Graphene: Structure and Electric Transport, ACS Nano, 5 (2011) 3896-3904.
[60] N.-E. Weber, S. Wundrack, R. Stosch, A. Turchanin, Direct Growth of Patterned Graphene, Small, 12 (2016) 1440-1445.
[61] A. Turchanin, A. Gölzhäuser, Carbon Nanomembranes, Advanced Materials, 28 (2016) 6075-6103.
[62] A. Turchanin, D. Käfer, M. El-Desawy, C. Wöll, G. Witte, A. Gölzhäuser, Molecular Mechanisms of Electron-Induced Cross-Linking in Aromatic SAMs, Langmuir, 25 (2009) 7342-7352.
[63] A. Turchanin, M. El-Desawy, A. Gölzhäuser, High thermal stability of cross-linked aromatic self-assembled monolayers: Nanopatterning via selective thermal desorption, Applied Physics Letters, 90 (2007) 053102.
[64] L. Kankate, A. Turchanin, A. Gölzhäuser, On the Release of Hydrogen from the S−H groups in the Formation of Self-Assembled Monolayers of Thiols, Langmuir, 25 (2009) 10435-10438.
[65] D.G. Matei, H. Muzik, A. Gölzhäuser, A. Turchanin, Structural Investigation of 1,1′-Biphenyl-4-thiol Self-Assembled Monolayers on Au(111) by Scanning Tunneling Microscopy and Low-Energy Electron Diffraction, Langmuir, 28 (2012) 13905-13911.
[66] J.C. Love, L.A. Estroff, J.K. Kriebel, R.G. Nuzzo, G.M. Whitesides, Self-Assembled Monolayers of Thiolates on Metals as a Form of Nanotechnology, Chemical Reviews, 105 (2005) 1103-1170.
[67] W. Geyer, V. Stadler, W. Eck, M. Zharnikov, A. Gölzhäuser, M. Grunze, Electron-induced crosslinking of aromatic self-assembled monolayers: Negative resists for nanolithography, Applied Physics Letters, 75 (1999) 2401-2403.
[68] A. Turchanin, A. Gölzhäuser, Carbon nanomembranes from self-assembled monolayers: Functional surfaces without bulk, Progress in Surface Science, 87 (2012) 108-162.

[69] F. Chesneau, H. Hamoudi, B.r. Schüpbach, A. Terfort, M. Zharnikov, Modification of Self-Assembled Monolayers of Perfluoroterphenyl-Substituted Alkanethiols by Low-Energy Electrons, The Journal of Physical Chemistry C, 115 (2011) 4773-4782.
[70] L. Amiaud, J. Houplin, M. Bourdier, V. Humblot, R. Azria, C.M. Pradier, A. Lafosse, Low-energy electron induced resonant loss of aromaticity: consequences on cross-linking in terphenylthiol SAMs, Phys. Chem. Chem. Phys., 16 (2014) 1050-1059.
[71] A. Mrugalla, J. Schnack, Classical molecular dynamics investigations of biphenyl-based carbon nanomembranes, Beilstein Journal of Nanotechnology, 5 (2014) 865-871.
[72] M. Zharnikov, W. Geyer, A. Gölzhäuser, S. Frey, M. Grunze, Modification of alkanethiolate monolayers on Au-substrate by low energy electron irradiation: Alkyl chains and the S/Au interface, Physical Chemistry Chemical Physics, 1 (1999) 3163-3171.
[73] M. Zharnikov, M. Grunze, Modification of thiol-derived self-assembling monolayers by electron and x-ray irradiation: Scientific and lithographic aspects, Journal of Vacuum Science & Technology B: Microelectronics and Nanometer Structures, 20 (2002) 1793.
[74] X. Zhang, H. Vieker, A. Beyer, A. Gölzhäuser, Fabrication of carbon nanomembranes by helium ion beam lithography, Beilstein Journal of Nanotechnology, 5 (2014) 188-194.
[75] A. Turchanin, M. Schnietz, M. El-Desawy, H.H. Solak, C. David, A. Gölzhäuser, Fabrication of Molecular Nanotemplates in Self-Assembled Monolayers by Extreme-Ultraviolet-Induced Chemical Lithography, Small, 3 (2007) 2114-2119.
[76] A. Beyer, A. Turchanin, C.T. Nottbohm, N. Mellech, M. Schnietz, A. Gölzhäuser, Fabrication of metal patterns on freestanding graphenoid nanomembranes, Journal of Vacuum Science & Technology B, Nanotechnology and Microelectronics: Materials, Processing, Measurement, and Phenomena, 28 (2010) C6D5-C6D10.
[77] A.C. Ferrari, D.M. Basko, Raman spectroscopy as a versatile tool for studying the properties of graphene, Nature Nanotechnology, 8 (2013) 235-246.
[78] K. Kim, Z. Lee, W. Regan, C. Kisielowski, M.F. Crommie, A. Zettl, Grain Boundary Mapping in Polycrystalline Graphene, ACS Nano, 5 (2011) 2142-2146.
[79] J.H. Warner, M.H. Rümmeli, T. Gemming, B. Büchner, G.A.D. Briggs, Direct Imaging of Rotational Stacking Faults in Few Layer Graphene, Nano Letters, 9 (2009) 102-106.
[80] J. Kotakoski, A.V. Krasheninnikov, U. Kaiser, J.C. Meyer, From Point Defects in Graphene to Two-Dimensional Amorphous Carbon, Physical Review Letters, 106 (2011).
[81] I. Jung, D.A. Dikin, R.D. Piner, R.S. Ruoff, Tunable Electrical Conductivity of Individual Graphene Oxide Sheets Reduced at “Low” Temperatures, Nano Letters, 8 (2008) 4283-4287.
[82] G. Eda, C. Mattevi, H. Yamaguchi, H. Kim, M. Chhowalla, Insulator to Semimetal Transition in Graphene Oxide, The Journal of Physical Chemistry C, 113 (2009) 15768-15771.
[83] K.P. Loh, Q. Bao, G. Eda, M. Chhowalla, Graphene oxide as a chemically tunable platform for optical applications, Nature Chemistry, 2 (2010) 1015-1024.
[84] K. Parvez, S. Yang, Y. Hernandez, A. Winter, A. Turchanin, X. Feng, K. Müllen, Nitrogen-Doped Graphene and Its Iron-Based Composite As Efficient Electrocatalysts for Oxygen Reduction Reaction, ACS Nano, 6 (2012) 9541-9550.
[85] Z.-S. Wu, A. Winter, L. Chen, Y. Sun, A. Turchanin, X. Feng, K. Müllen, Three-Dimensional Nitrogen and Boron Co-doped Graphene for High-Performance All-Solid-State Supercapacitors, Advanced Materials, 24 (2012) 5130-5135.
[86] A.C. Ferrari, J.C. Meyer, V. Scardaci, C. Casiraghi, M. Lazzeri, F. Mauri, S. Piscanec, D. Jiang, K.S. Novoselov, S. Roth, A.K. Geim, Raman Spectrum of Graphene and Graphene Layers, Physical Review Letters, 97 (2006).
[87] J.C. Meyer, A.K. Geim, M.I. Katsnelson, K.S. Novoselov, D. Obergfell, S. Roth, C. Girit, A. Zettl, On the roughness of single- and bi-layer graphene membranes, Solid State Communications, 143 (2007) 101-109.
[88] K.S. Novoselov, A.K. Geim, S.V. Morozov, D. Jiang, M.I. Katsnelson, I.V. Grigorieva, S.V. Dubonos, A.A. Firsov, Two-dimensional gas of massless Dirac fermions in graphene, Nature, 438 (2005) 197-200.

[89] Y. Wang, Y. Zheng, X. Xu, E. Dubuisson, Q. Bao, J. Lu, K.P. Loh, Electrochemical Delamination of CVD-Grown Graphene Film: Toward the Recyclable Use of Copper Catalyst, ACS Nano, 5 (2011) 9927-9933.
[90] D.-Y. Wang, I.S. Huang, P.-H. Ho, S.-S. Li, Y.-C. Yeh, D.-W. Wang, W.-L. Chen, Y.-Y. Lee, Y.-M. Chang, C.-C. Chen, C.-T. Liang, C.-W. Chen, Clean-Lifting Transfer of Large-area Residual-Free Graphene Films, Advanced Materials, 25 (2013) 4521-4526.
[91] M.J. Lercel, G.F. Redinbo, F.D. Pardo, M. Rooks, R.C. Tiberio, P. Simpson, H.G. Craighead, C.W. Sheen, A.N. Parikh, D.L. Allara, Electron beam lithography with monolayers of alkylthiols and alkylsiloxanes, Journal of Vacuum Science & Technology B: Microelectronics and Nanometer Structures Processing, Measurement, and Phenomena, 12 (1994) 3663-3667.
[92] A.C. Ferrari, F. Bonaccorso, V. Fal'ko, K.S. Novoselov, S. Roche, P. Bøggild, S. Borini, F.H.L. Koppens, V. Palermo, N. Pugno, J.A. Garrido, R. Sordan, A. Bianco, L. Ballerini, M. Prato, E. Lidorikis, J. Kivioja, C. Marinelli, T. Ryhänen, A. Morpurgo, J.N. Coleman, V. Nicolosi, L. Colombo, A. Fert, M. Garcia-Hernandez, A. Bachtold, G.F. Schneider, F. Guinea, C. Dekker, M. Barbone, Z. Sun, C. Galiotis, A.N. Grigorenko, G. Konstantatos, A. Kis, M. Katsnelson, L. Vandersypen, A. Loiseau, V. Morandi, D. Neumaier, E. Treossi, V. Pellegrini, M. Polini, A. Tredicucci, G.M. Williams, B. Hee Hong, J.-H. Ahn, J. Min Kim, H. Zirath, B.J. van Wees, H. van der Zant, L. Occhipinti, A. Di Matteo, I.A. Kinloch, T. Seyller, E. Quesnel, X. Feng, K. Teo, N. Rupesinghe, P. Hakonen, S.R.T. Neil, Q. Tannock, T. Löfwander, J. Kinaret, Science and technology roadmap for graphene, related two-dimensional crystals, and hybrid systems, Nanoscale, 7 (2015) 4598-4810.
[93] A.K. Geim, I.V. Grigorieva, Van der Waals heterostructures, Nature, 499 (2013) 419-425.
[94] Z. Zheng, X. Zhang, C. Neumann, D. Emmrich, A. Winter, H. Vieker, W. Liu, M. Lensen, A. Gölzhäuser, A. Turchanin, Hybrid van der Waals heterostructures of zero-dimensional and two-dimensional materials, Nanoscale, 7 (2015) 13393-13397.
[95] Z. Zheng, C.T. Nottbohm, A. Turchanin, H. Muzik, A. Beyer, M. Heilemann, M. Sauer, A. Gölzhäuser, Janus Nanomembranes: A Generic Platform for Chemistry in Two Dimensions, Angewandte Chemie International Edition, 49 (2010) 8493-8497.
[96] F. Bonaccorso, A. Lombardo, T. Hasan, Z. Sun, L. Colombo, A.C. Ferrari, Production and processing of graphene and 2d crystals, Materials Today, 15 (2012) 564-589.
[97] A.G. Cano-Márquez, F.J. Rodríguez-Macías, J. Campos-Delgado, C.G. Espinosa-González, F. Tristán-López, D. Ramírez-González, D.A. Cullen, D.J. Smith, M. Terrones, Y.I. Vega-Cantú, Ex-MWNTs: Graphene Sheets and Ribbons Produced by Lithium Intercalation and Exfoliation of Carbon Nanotubes, Nano Letters, 9 (2009) 1527-1533.
[98] D.V. Kosynkin, A.L. Higginbotham, A. Sinitskii, J.R. Lomeda, A. Dimiev, B.K. Price, J.M. Tour, Longitudinal unzipping of carbon nanotubes to form graphene nanoribbons, Nature, 458 (2009) 872-876.
[99] H. Varela-Rizo, I. Rodriguez-Pastor, C. Merino, M. Terrones, I. Martin-Gullon, Graphene oxide nanoplatelets of different crystallinity synthesized from helical-ribbon carbon nanofibers and multiwall carbon nanotubes, Journal of Materials Research, 26 (2011) 2632-2641.
[100] Y. Yeon, M.Y. Lee, S.Y. Kim, J. Lee, B. Kim, B. Park, I. In, Production of quasi-2D graphene nanosheets through the solvent exfoliation of pitch-based carbon fiber, Nanotechnology, 26 (2015) 375602.
[101] M. Lee, J. Lee, S.Y. Park, B. Min, B. Kim, I. In, Production of graphene oxide from pitch-based carbon fiber, Scientific Reports, 5 (2015).
[102] C. Botas, P. Álvarez, C. Blanco, R. Santamaría, M. Granda, P. Ares, F. Rodríguez-Reinoso, R. Menéndez, The effect of the parent graphite on the structure of graphene oxide, Carbon, 50 (2012) 275-282.
[103] J.D. Bernal, The Structure of Graphite, Proceedings of the Royal Society A: Mathematical, Physical and Engineering Sciences, 106 (1924) 749-773.
[104] H. Lipson, A.R. Stokes, The Structure of Graphite, Proceedings of the Royal Society A: Mathematical, Physical and Engineering Sciences, 181 (1942) 101-105.

[105] R.E. Franklin, Crystallite Growth in Graphitizing and Non-Graphitizing Carbons, Proceedings of the Royal Society A: Mathematical, Physical and Engineering Sciences, 209 (1951) 196-218.
[106] J.A.G.H. Marsh, in: A.C.S. (Ed.) 14th Biennial Conference on Carbon, Penn State University, USA, 1979, pp. 117.
[107] M.I.R.A. Meyer, Stress Graphitization en Chemistry and Physics of Carbon, Marcel Dekker, Inc: New York1999.
[108] G.C. Loh, D. Baillargeat, Graphitization of amorphous carbon and its transformation pathways, Journal of Applied Physics, 114 (2013) 033534.
[109] F. Rodriguez-Reinoso, Comite internacional para la caracterizacion y la terminologia del carbon, Carbon, 27 (1989) 305-312.
[110] X. Li, C.W. Magnuson, A. Venugopal, R.M. Tromp, J.B. Hannon, E.M. Vogel, L. Colombo, R.S. Ruoff, Large-Area Graphene Single Crystals Grown by Low-Pressure Chemical Vapor Deposition of Methane on Copper, Journal of the American Chemical Society, 133 (2011) 2816-2819.
[111] J.K. Wassei, M. Mecklenburg, J.A. Torres, J.D. Fowler, B.C. Regan, R.B. Kaner, B.H. Weiller, Graphene: Chemical Vapor Deposition of Graphene on Copper from Methane, Ethane and Propane: Evidence for Bilayer Selectivity (Small 9/2012), Small, 8 (2012) 1289-1289.
[112] K.S. Novoselov, D. Jiang, F. Schedin, T.J. Booth, V.V. Khotkevich, S.V. Morozov, A.K. Geim, Two-dimensional atomic crystals, Proceedings of the National Academy of Sciences, 102 (2005) 10451-10453.
[113] Y. Hernandez, V. Nicolosi, M. Lotya, F.M. Blighe, Z. Sun, S. De, I.T. McGovern, B. Holland, M. Byrne, Y.K. Gun'Ko, J.J. Boland, P. Niraj, G. Duesberg, S. Krishnamurthy, R. Goodhue, J. Hutchison, V. Scardaci, A.C. Ferrari, J.N. Coleman, High-yield production of graphene by liquid-phase exfoliation of graphite, Nature Nanotechnology, 3 (2008) 563-568.
[114] C. Botas, A.M. Pérez-Mas, P. Álvarez, R. Santamaría, M. Granda, C. Blanco, R. Menéndez, Optimization of the size and yield of graphene oxide sheets in the exfoliation step, Carbon, 63 (2013) 576-578.
[115] M. Cai, D. Thorpe, D.H. Adamson, H.C. Schniepp, Methods of graphite exfoliation, Journal of Materials Chemistry, 22 (2012) 24992.
[116] A.B. Bourlinos, V. Georgakilas, R. Zboril, T.A. Steriotis, A.K. Stubos, Liquid-Phase Exfoliation of Graphite Towards Solubilized Graphenes, Small, 5 (2009) 1841-1845.
[117] Z. González, C. Botas, C. Blanco, R. Santamaría, M. Granda, P. Álvarez, R. Menéndez, Graphite oxide-based graphene materials as positive electrodes in vanadium redox flow batteries, Journal of Power Sources, 241 (2013) 349-354.
[118] A. Liscio, K. Kouroupis-Agalou, X.D. Betriu, A. Kovtun, E. Treossi, N.M. Pugno, G. De Luca, L. Giorgini, V. Palermo, Evolution of the size and shape of 2D nanosheets during ultrasonic fragmentation, 2D Materials, 4 (2017) 025017.
[119] Z.Y. Xia, S. Pezzini, E. Treossi, G. Giambastiani, F. Corticelli, V. Morandi, A. Zanelli, V. Bellani, V. Palermo, Graphene: The Exfoliation of Graphene in Liquids by Electrochemical, Chemical, and Sonication-Assisted Techniques: A Nanoscale Study (Adv. Funct. Mater. 37/2013), Advanced Functional Materials, 23 (2013) 4756-4756.
[120] P.K.B.a.S. Ghosh, Elements of Prospecting for Non-fuel Mineral Deposits, 1997 ed., Allied Publisher Ltd1997.
[121] W. Peng, H. Li, Y. Hu, Y. Liu, S. Song, Characterisation of reduced graphene oxides prepared from natural flaky, lump and amorphous graphites, Materials Research Bulletin, 78 (2016) 119-127.
[122] W. Peng, H. Li, Y. Hu, Y. Liu, S. Song, Does silicate mineral impurities in natural graphite affect the characteristics of synthesized graphene?, Materials Research Bulletin, 74 (2016) 333-339.
[123] S. Colonna, O. Monticelli, J. Gomez, C. Novara, G. Saracco, A. Fina, Effect of morphology and defectiveness of graphene-related materials on the electrical and thermal conductivity of their polymer nanocomposites, Polymer, 102 (2016) 292-300.
[124] S. Colonna, O. Monticelli, J. Gomez, G. Saracco, A. Fina, Morphology and properties evolution upon ring-opening polymerization during extrusion of cyclic butylene terephthalate and graphene-

related-materials into thermally conductive nanocomposites, European Polymer Journal, 89 (2017) 57-66.
[125] B. Galindo, S.G. Alcolea, J. Gómez, A. Navas, A.O. Murguialday, M.P. Fernandez, R.C. Puelles, Effect of the number of layers of graphene on the electrical properties of TPU polymers, IOP Conference Series: Materials Science and Engineering, 64 (2014) 012008.
[126] J. Gomez, Preparation and processing of large lateral size graphene materialsin epoxy matrix composites,, Graphene Week, Athens, Greece, 2017.
[127] S. Casaluci, M. Gemmi, V. Pellegrini, A. Di Carlo, F. Bonaccorso, Graphene-based large area dye-sensitized solar cell modules, Nanoscale, 8 (2016) 5368-5378.
[128] E. Villaro, Preparación y caracterización de nanocompuestos de grafeno en una suspensión de partículas de PVC (plastisol) Faculta de Ciencias UNED, 2013.
[129] L. Sun, B. Fugetsu, Mass production of graphene oxide from expanded graphite, Materials Letters, 109 (2013) 207-210.
[130] U. Sierra, P. Álvarez, C. Blanco, M. Granda, R. Santamaría, R. Menéndez, New alternatives to graphite for producing graphene materials, Carbon, 93 (2015) 812-818.
[131] U. Sierra, P. Álvarez, C. Blanco, M. Granda, R. Santamaría, R. Menéndez, Cokes of different origin as precursors of graphene oxide, Fuel, 166 (2016) 400-403.
[132] P. Alvarez, N. Díez, R. Santamaría, C. Blanco, R. Menéndez, M. Granda, Novel coal-based precursors for cokes with highly oriented microstructures, Fuel, 95 (2012) 400-406.
[133] A. Oberlin, Carbonization and graphitization, Carbon, 22 (1984) 521-541.
[134] E. Fitzer, K.H. Kochling, H.P. Boehm, H. Marsh, Recommended terminology for the description of carbon as a solid (IUPAC Recommendations 1995), Pure and Applied Chemistry, 67 (1995).
[135] A.E. Del Rio-Castillo, C. Merino, E. Díez-Barra, E. Vázquez, Selective suspension of single layer graphene mechanochemically exfoliated from carbon nanofibres, Nano Research, 7 (2014) 963-972.
[136] B. Lobato, C. Merino, V. Barranco, T.A. Centeno, Large-scale conversion of helical-ribbon carbon nanofibers to a variety of graphene-related materials, RSC Adv., 6 (2016) 57514-57520.
[137] J. Vera-Agullo, H. Varela-Rizo, J.A. Conesa, C. Almansa, C. Merino, I. Martin-Gullon, Evidence for growth mechanism and helix-spiral cone structure of stacked-cup carbon nanofibers, Carbon, 45 (2007) 2751-2758.
[138] B. Lobato, C. Merino, V. Barranco, T.A. Centeno, Large-scale conversion of helical-ribbon carbon nanofibers to a variety of graphene-related materials, RSC Advances, 6 (2016) 57514-57520.
[139] W.S. Hummers, R.E. Offeman, Preparation of Graphitic Oxide, Journal of the American Chemical Society, 80 (1958) 1339-1339.
[140] I.K. Moon, J. Lee, R.S. Ruoff, H. Lee, Reduced graphene oxide by chemical graphitization, Nature Communications, 1 (2010) 1-6.
[141] S. Park, R.S. Ruoff, Chemical methods for the production of graphenes, Nature Nanotechnology, 4 (2009) 217-224.
[142] E. Benavente, M.A. Santa Ana, F. Mendizábal, G. González, Intercalation chemistry of molybdenum disulfide, Coordination Chemistry Reviews, 224 (2002) 87-109.
[143] S. Eigler, A. Hirsch, Chemistry with Graphene and Graphene Oxide—Challenges for Synthetic Chemists, Angewandte Chemie International Edition, 53 (2014) 7720-7738.
[144] E.D. Grayfer, M.N. Kozlova, V.E. Fedorov, Colloidal 2D nanosheets of MoS2 and other transition metal dichalcogenides through liquid-phase exfoliation, Advances in Colloid and Interface Science, 245 (2017) 40-61.
[145] V. Nicolosi, M. Chhowalla, M.G. Kanatzidis, M.S. Strano, J.N. Coleman, Liquid Exfoliation of Layered Materials, Science, 340 (2013) 1420-+.
[146] M. Yi, Z. Shen, A review on mechanical exfoliation for the scalable production of graphene, Journal of Materials Chemistry A, 3 (2015) 11700-11715.
[147] H. Tao, Y. Zhang, Y. Gao, Z. Sun, C. Yan, J. Texter, Scalable exfoliation and dispersion of two-dimensional materials - an update, Physical Chemistry Chemical Physics, 19 (2017) 921-960.
[148] W.S. Hummers, R.E. Offeman, Preparation of graphitic oxide, J. Am. Chem. Soc., 80 (1958) 1339.

[149] A. Ciesielski, P. Samorì, Supramolecular Approaches to Graphene: From Self-Assembly to Molecule-Assisted Liquid-Phase Exfoliation, Advanced Materials, 28 (2016) 6030-6051.
[150] F. Bonaccorso, A. Bartolotta, J.N. Coleman, C. Backes, 2D-Crystal-Based Functional Inks, Advanced Materials, DOI 10.1002/adma.201506410(2016) n/a-n/a.
[151] M. Gutiérrez, A. Henglein, Preparation of colloidal semiconductor solutions of MoS2 and WSe2 via sonication, Ultrasonics, 27 (1989) 259-261.
[152] J. Kang, V.K. Sangwan, J.D. Wood, M.C. Hersam, Solution-Based Processing of Monodisperse Two-Dimensional Nanomaterials, Accounts of Chemical Research, 50 (2017) 943-951.
[153] G. Abellán, C. Martí-Gastaldo, A. Ribera, E. Coronado, Hybrid Materials Based on Magnetic Layered Double Hydroxides: A Molecular Perspective, Accounts of Chemical Research, 48 (2015) 1601-1611.
[154] M. Naguib, V.N. Mochalin, M.W. Barsoum, Y. Gogotsi, 25th Anniversary Article: MXenes: A New Family of Two-Dimensional Materials, Advanced Materials, 26 (2014) 992-1005.
[155] H. Kim, E. Saiz, M. Chhowalla, C. Mattevi, Modeling of the self-limited growth in catalytic chemical vapor deposition of graphene, New Journal of Physics, 15 (2013) 053012.
[156] A. Ciesielski, P. Samori, Graphene via sonication assisted liquid-phase exfoliation, Chemical Society Reviews, 43 (2014) 381-398.
[157] K. Parvez, S. Yang, X. Feng, K. Müllen, Exfoliation of graphene via wet chemical routes, Synthetic Metals, 210 (2015) 123-132.
[158] J.N. Coleman, M. Lotya, A. O'Neill, S.D. Bergin, P.J. King, U. Khan, K. Young, A. Gaucher, S. De, R.J. Smith, I.V. Shvets, S.K. Arora, G. Stanton, H.Y. Kim, K. Lee, G.T. Kim, G.S. Duesberg, T. Hallam, J.J. Boland, J.J. Wang, J.F. Donegan, J.C. Grunlan, G. Moriarty, A. Shmeliov, R.J. Nicholls, J.M. Perkins, E.M. Grieveson, K. Theuwissen, D.W. McComb, P.D. Nellist, V. Nicolosi, Two-Dimensional Nanosheets Produced by Liquid Exfoliation of Layered Materials, Science, 331 (2011) 568-571.
[159] V. Nicolosi, M. Chhowalla, M.G. Kanatzidis, M.S. Strano, J.N. Coleman, Liquid Exfoliation of Layered Materials, Science, 340 (2013) 1226419-1226419.
[160] Y.L. Zhong, Z. Tian, G.P. Simon, D. Li, Scalable production of graphene via wet chemistry: progress and challenges, Materials Today, 18 (2015) 73-78.
[161] K.R. Paton, E. Varrla, C. Backes, R.J. Smith, U. Khan, A. O'Neill, C. Boland, M. Lotya, O.M. Istrate, P. King, T. Higgins, S. Barwich, P. May, P. Puczkarski, I. Ahmed, M. Moebius, H. Pettersson, E. Long, J. Coelho, S.E. O'Brien, E.K. McGuire, B.M. Sanchez, G.S. Duesberg, N. McEvoy, T.J. Pennycook, C. Downing, A. Crossley, V. Nicolosi, J.N. Coleman, Scalable production of large quantities of defect-free few-layer graphene by shear exfoliation in liquids, Nature Materials, 13 (2014) 624-630.
[162] E. Varrla, K.R. Paton, C. Backes, A. Harvey, R.J. Smith, J. McCauley, J.N. Coleman, Turbulence-assisted shear exfoliation of graphene using household detergent and a kitchen blender, Nanoscale, 6 (2014) 11810-11819.
[163] P.G. Karagiannidis, S.A. Hodge, L. Lombardi, F. Tomarchio, N. Decorde, S. Milana, I. Goykhman, Y. Su, S.V. Mesite, D.N. Johnstone, R.K. Leary, P.A. Midgley, N.M. Pugno, F. Torrisi, A.C. Ferrari, Microfluidization of Graphite and Formulation of Graphene-Based Conductive Inks, ACS Nano, 11 (2017) 2742-2755.
[164] V. León, M. Quintana, M.A. Herrero, J.L.G. Fierro, A.d.l. Hoz, M. Prato, E. Vázquez, Few-layer graphenes from ball-milling of graphite with melamine, Chemical Communications, 47 (2011) 10936.
[165] W. Qian, R. Hao, Y. Hou, Y. Tian, C. Shen, H. Gao, X. Liang, Solvothermal-assisted exfoliation process to produce graphene with high yield and high quality, Nano Research, 2 (2009) 706-712.
[166] Z. Tang, J. Zhuang, X. Wang, Exfoliation of Graphene from Graphite and Their Self-Assembly at the Oil−Water Interface, Langmuir, 26 (2010) 9045-9049.
[167] L. Guardia, M.J. Fernandez-Merino, J.I. Paredes, P. Solis-Fernandez, S. Villar-Rodil, A. Martinez-Alonso, J.M.D. Tascon, High-throughput production of pristine graphene in an aqueous dispersion assisted by non-ionic surfactants, Carbon, 49 (2011) 1653-1662.
[168] A.A. Green, M.C. Hersam, Solution Phase Production of Graphene with Controlled Thickness via Density Differentiation, Nano Letters, 9 (2009) 4031-4036.

[169] M. Lotya, Y. Hernandez, P.J. King, R.J. Smith, V. Nicolosi, L.S. Karlsson, F.M. Blighe, S. De, Z. Wang, I.T. McGovern, G.S. Duesberg, J.N. Coleman, Liquid Phase Production of Graphene by Exfoliation of Graphite in Surfactant/Water Solutions, Journal of the American Chemical Society, 131 (2009) 3611-3620.
[170] C. Backes, R.J. Smith, N. McEvoy, N.C. Berner, D. McCloskey, H.C. Nerl, A. O'Neill, P.J. King, T. Higgins, D. Hanlon, N. Scheuschner, J. Maultzsch, L. Houben, G.S. Duesberg, J.F. Donegan, V. Nicolosi, J.N. Coleman, Edge and confinement effects allow in situ measurement of size and thickness of liquid-exfoliated nanosheets, Nature Communications, 5 (2014).
[171] C. Backes, B.M. Szydłowska, A. Harvey, S. Yuan, V. Vega-Mayoral, B.R. Davies, P.-l. Zhao, D. Hanlon, E.J.G. Santos, M.I. Katsnelson, W.J. Blau, C. Gadermaier, J.N. Coleman, Production of Highly Monolayer Enriched Dispersions of Liquid-Exfoliated Nanosheets by Liquid Cascade Centrifugation, ACS Nano, 10 (2016) 1589-1601.
[172] K.P. Lee, N.C. Chromey, R. Culik, J.R. Barnes, P.W. Schneider, Toxicity of N-methyl-2-pyrrolidone (NMP): Teratogenic, subchronic, and two-year inhalation studies, Fundamental and Applied Toxicology, 9 (1987) 222-235.
[173] A. Harvey, C. Backes, Z. Gholamvand, D. Hanlon, D. McAteer, H.C. Nerl, E. McGuire, A. Seral-Ascaso, Q.M. Ramasse, N. McEvoy, S. Winters, N.C. Berner, D. McCloskey, J.F. Donegan, G.S. Duesberg, V. Nicolosi, J.N. Coleman, Preparation of Gallium Sulfide Nanosheets by Liquid Exfoliation and Their Application As Hydrogen Evolution Catalysts, Chemistry of Materials, 27 (2015) 3483-3493.
[174] A. Favron, E. Gaufres, F. Fossard, A.-L. Phaneuf-Lheureux, N.Y.W. Tang, P.L. Levesque, A. Loiseau, R. Leonelli, S. Francoeur, R. Martel, Photooxidation and quantum confinement effects in exfoliated black phosphorus, Nat Mater, 14 (2015) 826-832.
[175] D. Hanlon, C. Backes, E. Doherty, C.S. Cucinotta, N.C. Berner, C. Boland, K. Lee, P. Lynch, Z. Gholamvand, A. Harvey, S. Zhang, K. Wang, G. Moynihan, A. Pokle, Q.M. Ramasse, N. McEvoy, W.J. Blau, J. Wang, G. Abellan, F. Hauke, A. Hirsch, S. Sanvito, D.D. O'Regan, G.S. Duesberg, V. Nicolosi, J.N. Coleman, Liquid Exfoliation of Solvent-Stabilised Few-Layer Black Phosphorus for Applications Beyond Electronics, Nature Communications, 6 (2015) 8563.
[176] Y. Guo, S. Zhou, Y. Bai, J. Zhao, Defects and oxidation of group-III monochalcogenide monolayers, The Journal of Chemical Physics, 147 (2017) 104709.
[177] S. Wang, M. Yi, Z. Shen, The effect of surfactants and their concentration on the liquid exfoliation of graphene, RSC Advances, 6 (2016) 56705-56710.
[178] A. Liscio, K. Kouroupis-Agalou, A. Kovtun, E. Gebremedhn, M. El Garah, W. Rekab, E. Orgiu, L. Giorgini, P. Samorì, D. Beljonne, V. Palermo, Exfoliation of Few-Layer Graphene in Volatile Solvents Using Aromatic Perylene Diimide Derivatives as Surfactants, ChemPlusChem, 82 (2017) 358-367.
[179] A. Schlierf, H.F. Yang, E. Gebremedhn, E. Treossi, L. Ortolani, L.P. Chen, A. Minoia, V. Morandi, P. Samori, C. Casiraghi, D. Beljonne, V. Palermo, Nanoscale insight into the exfoliation mechanism of graphene with organic dyes: effect of charge, dipole and molecular structure, Nanoscale, 5 (2013) 4205-4216.
[180] J.N. Coleman, M. Lotya, A. O'Neill, S.D. Bergin, P.J. King, U. Khan, K. Young, A. Gaucher, S. De, R.J. Smith, I.V. Shvets, S.K. Arora, G. Stanton, H.-Y. Kim, K. Lee, G.T. Kim, G.S. Duesberg, T. Hallam, J.J. Boland, J.J. Wang, J.F. Donegan, J.C. Grunlan, G. Moriarty, A. Shmeliov, R.J. Nicholls, J.M. Perkins, E.M. Grieveson, K. Theuwissen, D.W. McComb, P.D. Nellist, V. Nicolosi, Two-Dimensional Nanosheets Produced by Liquid Exfoliation of Layered Materials, Science, 331 (2011) 568-571.
[181] T. Svedberg, K.O. Pederson, J.H. Bauer, The Ultracentrifuge, Oxford University Press: London, U.K.1940.
[182] C. Hansen, The Three Dimensional Solubility Parameter and Solvent Diffusion Coefficient and Their Importance in Surface Coating Formulation, Danish Technical Press, Copenhagen, 1967.
[183] J.M. Hughes, D. Aherne, J.N. Coleman, Generalizing solubility parameter theory to apply to one- and two-dimensional solutes and to incorporate dipolar interactions, Journal of Applied Polymer Science, 127 (2013) 4483-4491.

[184] J. Shen, Y. He, J. Wu, C. Gao, K. Keyshar, X. Zhang, Y. Yang, M. Ye, R. Vajtai, J. Lou, P.M. Ajayan, Liquid Phase Exfoliation of Two-Dimensional Materials by Directly Probing and Matching Surface Tension Components, Nano Letters, 15 (2015) 5449-5454.
[185] J. Kim, S. Kwon, D.-H. Cho, B. Kang, H. Kwon, Y. Kim, S.O. Park, G.Y. Jung, E. Shin, W.-G. Kim, H. Lee, G.H. Ryu, M. Choi, T.H. Kim, J. Oh, S. Park, S.K. Kwak, S.W. Yoon, D. Byun, Z. Lee, C. Lee, Direct exfoliation and dispersion of two-dimensional materials in pure water via temperature control, Nat Commun, 6 (2015) 9294.
[186] C.Y. Zhi, Y. Bando, C.C. Tang, H. Kuwahara, D. Golberg, Large-Scale Fabrication of Boron Nitride Nanosheets and Their Utilization in Polymeric Composites with Improved Thermal and Mechanical Properties, Advanced Materials, 21 (2009) 2889-+.
[187] D. Hanlon, C. Backes, E. Doherty, C.S. Cucinotta, N.C. Berner, C. Boland, K. Lee, P. Lynch, Z. Gholamvand, A. Harvey, S. Zhang, K. Wang, G. Moynihan, A. Pokle, Q.M. Ramasse, N. McEvoy, W.J. Blau, J. Wang, G. Abellan, F. Hauke, A. Hirsch, S. Sanvito, D.D. O'Regan, G.S. Duesberg, V. Nicolosi, J.N. Coleman, Liquid Exfoliation of Solvent-Stabilised Few-Layer Black Phosphorus for Applications Beyond Electronics, Nature Communications, 6 (2015).
[188] D.J. Finn, M. Lotya, G. Cunningham, R.J. Smith, D. McCloskey, J.F. Donegan, J.N. Coleman, Inkjet deposition of liquid-exfoliated graphene and MoS2 nanosheets for printed device applications, Journal of Materials Chemistry C, 2 (2014) 925-932.
[189] S. Niyogi, M.A. Hamon, D.E. Perea, C.B. Kang, B. Zhao, S.K. Pal, A.E. Wyant, M.E. Itkis, R.C. Haddon, Ultrasonic Dispersions of Single-Walled Carbon Nanotubes, The Journal of Physical Chemistry B, 107 (2003) 8799-8804.
[190] H.C. Yau, M.K. Bayazit, J.H.G. Steinke, M.S.P. Shaffer, Sonochemical degradation of N-methylpyrrolidone and its influence on single walled carbon nanotube dispersion, Chemical Communications, 51 (2015) 16621-16624.
[191] A. Ciesielski, S. Haar, A. Aliprandi, M. El Garah, G. Tregnago, G.F. Cotella, M. El Gemayel, F. Richard, H. Sun, F. Cacialli, F. Bonaccorso, P. Samorì, Modifying the Size of Ultrasound-Induced Liquid-Phase Exfoliated Graphene: From Nanosheets to Nanodots, ACS Nano, 10 (2016) 10768-10777.
[192] H.M. Solomon, B.A. Burgess, G.L. Kennedy, R.E. Staples, 1-methyl-2-pyrrolidone (nmp): reproductive and developmental toxicity study by inhalation in the rat, Drug and Chemical Toxicology, 18 (1995) 271-293.
[193] A. Capasso, A.E. Del Rio Castillo, H. Sun, A. Ansaldo, V. Pellegrini, F. Bonaccorso, Ink-jet printing of graphene for flexible electronics: An environmentally-friendly approach, Solid State Communications, 224 (2015) 53-63.
[194] K.-G. Zhou, N.-N. Mao, H.-X. Wang, Y. Peng, H.-L. Zhang, A Mixed-Solvent Strategy for Efficient Exfoliation of Inorganic Graphene Analogues, Angewandte Chemie International Edition, 50 (2011) 10839-10842.
[195] P. May, U. Khan, J.M. Hughes, J.N. Coleman, Role of Solubility Parameters in Understanding the Steric Stabilization of Exfoliated Two-Dimensional Nanosheets by Adsorbed Polymers, J Phys Chem C, 116 (2012) 11393-11400.
[196] Y.T. Liang, M.C. Hersam, Highly Concentrated Graphene Solutions via Polymer Enhanced Solvent Exfoliation and Iterative Solvent Exchange, J Am Chem Soc, 132 (2010) 17661-17663.
[197] A.B. Bourlinos, V. Georgakilas, R. Zboril, T.A. Steriotis, A.K. Stubos, C. Trapalis, Aqueous-phase exfoliation of graphite in the presence of polyvinylpyrrolidone for the production of water-soluble graphenes, Solid State Commun., 149 (2009) 2172-2176.
[198] W.S. Liu, R. Zhou, D. Zhou, G.G. Ding, J.M. Soah, C.Y. Yue, X.H. Lu, Lignin-assisted direct exfoliation of graphite to graphene in aqueous media and its application in polymer composites, Carbon, 83 (2015) 188-197.
[199] S. Ahadian, M. Estili, V.J. Surya, J. Ramon-Azcon, X.B. Liang, H. Shiku, M. Ramalingam, T. Matsue, Y. Sakka, H. Bae, K. Nakajima, Y. Kawazoe, A. Khademhosseini, Facile and green production of aqueous graphene dispersions for biomedical applications, Nanoscale, 7 (2015) 6436-6443.
[200] F. Irin, M.J. Hansen, R. Bari, D. Parviz, S.D. Metzler, S.K. Bhattacharia, M.J. Green, Adsorption and removal of graphene dispersants, Journal of Colloid and Interface Science, 446 (2015) 282-289.

[201] A. Schlierf, P. Samorì, V. Palermo, Graphene–organic composites for electronics: optical and electronic interactions in vacuum, liquids and thin solid films, Journal of Materials Chemistry C, 2 (2014) 3129.
[202] J.M. Englert, J. Röhrl, C.D. Schmidt, R. Graupner, M. Hundhausen, F. Hauke, A. Hirsch, Soluble Graphene: Generation of Aqueous Graphene Solutions Aided by a Perylenebisimide-Based Bolaamphiphile, Advanced Materials, 21 (2009) 4265-4269.
[203] M. Melucci, M. Durso, M. Zambianchi, E. Treossi, Z.-Y. Xia, I. Manet, G. Giambastiani, L. Ortolani, V. Morandi, F. De Angelis, V. Palermo, Graphene-organic hybrids as processable, tunable platforms for pH-dependent photoemission, obtained by a new modular approach, Journal of Materials Chemistry, 22 (2012) 18237-18243.
[204] M. Melucci, E. Treossi, L. Ortolani, G. Giambastiani, V. Morandi, P. Klar, C. Casiraghi, P. Samorì, V. Palermo, Facile covalent functionalization of graphene oxide using microwaves: bottom-up development of functional graphitic materials, Journal of Materials Chemistry, 20 (2010) 9052.
[205] A. Schlierf, K. Cha, M.G. Schwab, P. Samori, V. Palermo, Exfoliation of graphene with an industrial dye: teaching an old dog new tricks, 2D Materials, 1 (2014) 035006.
[206] H. Yang, F. Withers, E. Gebremedhn, E. Lewis, L. Britnell, A. Felten, V. Palermo, S. Haigh, D. Beljonne, C. Casiraghi, Dielectric nanosheets made by liquid-phase exfoliation in water and their use in graphene-based electronics, 2D Materials, 1 (2014) 011012.
[207] A. Ciesielski, P. Samorì, Supramolecular Approaches to Graphene: From Self-Assembly to Molecule-Assisted Liquid-Phase Exfoliation, Adv. Mater., 28 (2016) 6030-6051.
[208] A. Bianco, Graphene: Safe or Toxic? The Two Faces of the Medal, Angew Chem Int Edit, 52 (2013) 4986-4997.
[209] X.L. Feng, V. Marcon, W. Pisula, M.R. Hansen, J. Kirkpatrick, F. Grozema, D. Andrienko, K. Kremer, K. Müllen, Towards high charge-carrier mobilities by rational design of the shape and periphery of discotics, Nat. Mater., 8 (2009) 421-426.
[210] C. Li, M.Y. Liu, N.G. Pschirer, M. Baumgarten, K. Müllen, Polyphenylene-Based Materials for Organic Photovoltaics, Chem Rev, 110 (2010) 6817-6855.
[211] T. Fujigaya, N. Nakashima, Methodology for homogeneous dispersion of single-walled carbon nanotubes by physical modification, Polym J, 40 (2008) 577-589.
[212] X. Dong, Y. Shi, Y. Zhao, D. Chen, J. Ye, Y. Yao, F. Gao, Z. Ni, T. Yu, Z. Shen, Symmetry breaking of graphene monolayers by molecular decoration, Phys. Rev. Lett., 102 (2009) 135501.
[213] J.-H. Jang, D. Rangappa, Y.-U. Kwon, I. Honma, Direct preparation of 1-PSA modified graphene nanosheets by supercritical fluidic exfoliation and its electrochemical properties, J. Mater. Chem., 21 (2010) 3462-3466.
[214] D. Parviz, S. Das, H.S.T. Ahmed, F. Irin, S. Bhattacharia, M.J. Green, Dispersions of Non-Covalently Functionalized Graphene with Minimal Stabilizer, ACS Nano, 6 (2012) 8857-8867.
[215] L. Zhang, Z.J. Zhang, C.Z. He, L.M. Dai, J. Liu, L.X. Wang, Rationally Designed Surfactants for Few-Layered Graphene Exfoliation: Ionic Groups Attached to Electron-Deficient pi-Conjugated Unit through Alkyl Spacers, Acs Nano, 8 (2014) 6663-6670.
[216] S. Sampath, A.N. Basuray, K.J. Hartlieb, T. Aytun, S.I. Stupp, J.F. Stoddart, Direct Exfoliation of Graphite to Graphene in Aqueous Media with Diazaperopyrenium Dications, Adv. Mater., 25 (2013) 2740–2745.
[217] L.L. Chua, J. Zaumseil, J.F. Chang, E.C.W. Ou, P.K.H. Ho, H. Sirringhaus, R.H. Friend, General observation of n-type field-effect behaviour in organic semiconductors, Nature, 434 (2005) 194-199.
[218] A. Ciesielski, S. Haar, M. El Gemayel, H. Yang, J. Clough, G. Melinte, N. Gobbi, E. Orgiu, M.V. Nardi, G. Ligorio, V. Palermo, N. Koch, O. Ersen, C. Casiraghi, P. Samorì, Liquid-Phase Exfoliation of Graphene Using Intercalating Compounds: A Supramolecular Approach, Angew Chem Int Edit, 53 (2014) 10355–10361.
[219] S. Haar, A. Ciesielski, J. Clough, H. Yang, R. Mazzaro, F. Richard, S. Conti, N. Merstorf, M. Cecchini, V. Morandi, C. Casiraghi, P. Samorì, A supramolecular strategy to leverage the liquid-phase exfoliation of graphene in the presence of surfactants: unraveling the role of the length of fatty acids, Small, 11 (2015) 1691–1702.

[220] S. Haar, M. El Gemayel, Y.Y. Shin, G. Melinte, M.A. Squillaci, O. Ersen, C. Casiraghi, A. Ciesielski, P. Samori, Enhancing the Liquid-Phase Exfoliation of Graphene in Organic Solvents upon Addition of n-Octylbenzene, Sci Rep-Uk, 5 (2015) 16684.
[221] S. Conti, M.G. del Rosso, A. Ciesielski, J. Weippert, A. Bottcher, Y.Y. Shin, G. Melinte, O. Ersen, C. Casiraghi, X.L. Feng, K. Mullen, M.M. Kappes, P. Samori, M. Cecchini, Perchlorination of Coronene Enhances its Propensity for Self-Assembly on Graphene, ChemPhysChem, 17 (2016) 352-357.
[222] M. Döbbelin, A. Ciesielski, S. Haar, S. Osella, M. Bruna, A. Minoia, L. Grisanti, T. Mosciatti, F. Richard, E.A. Prasetyanto, L. De Cola, V. Palermo, R. Mazzaro, V. Morandi, R. Lazzaroni, A.C. Ferrari, D. Beljonne, P. Samorì, Light-enhanced liquid-phase exfoliation and current photoswitching in graphene-azobenzene composites, Nat. Commun., 7 (2016) 11090.
[223] S. Haar, M. Bruna, J.X. Lian, F. Tomarchio, Y. Olivier, R. Mazzaro, V. Morandi, J. Moran, A.C. Ferrari, D. Beljonne, A. Ciesielski, P. Samorì, Liquid-Phase Exfoliation of Graphite into Single- and Few-Layer Graphene with alpha-Functionalized Alkanes, J Phys Chem Lett, 7 (2016) 2714-2721.
[224] K.R. Paton, E. Varrla, C. Backes, R.J. Smith, U. Khan, A. O'Neill, C. Boland, M. Lotya, O.M. Istrate, P. King, T. Higgins, S. Barwich, P. May, P. Puczkarski, I. Ahmed, M. Moebius, H. Pettersson, E. Long, J. Coelho, S.E. O'Brien, E.K. McGuire, B.M. Sanchez, G.S. Duesberg, N. McEvoy, T.J. Pennycook, C. Downing, A. Crossley, V. Nicolosi, J.N. Coleman, Scalable production of large quantities of defect-free few-layer graphene by shear exfoliation in liquids, Nat Mater, 13 (2014) 624-630.
[225] E. Varrla, K.R. Paton, C. Backes, A. Harvey, R.J. Smith, J. McCauley, J.N. Coleman, Turbulence-assisted shear exfoliation of graphene using household detergent and a kitchen blender, Nanoscale, 6 (2014) 11810-11819.
[226] E. Varrla, C. Backes, K.R. Paton, A. Harvey, Z. Gholamvand, J. McCauley, J.N. Coleman, Large-Scale Production of Size-Controlled MoS2 Nanosheets by Shear Exfoliation, Chemistry of Materials, 27 (2015) 1129–1139.
[227] C. Backes, K.R. Paton, D. Hanlon, S. Yuan, M.I. Katsnelson, J. Houston, R.J. Smith, D. McCloskey, J.F. Donegan, J.N. Coleman, Spectroscopic metrics allow in situ measurement of mean size and thickness of liquid-exfoliated few-layer graphene nanosheets, Nanoscale, 8 (2016) 4311-4323.
[228] B. Duncan, C. Perry, Uncancelled hypnotic suggestions: initial studies, The American journal of clinical hypnosis, 19 (1977) 166-176.
[229] D. Hanlon, C. Backes, T.M. Higgins, M. Hughes, A. O'Neill, P. King, N. McEvoy, G.S. Duesberg, B. Mendoza Sanchez, H. Pettersson, V. Nicolosi, J.N. Coleman, Production of Molybdenum Trioxide Nanosheets by Liquid Exfoliation and Their Application in High-Performance Supercapacitors, Chemistry of Materials, 26 (2014) 1751-1763.
[230] A. Harvey, X. He, I.J. Godwin, C. Backes, D. McAteer, N.C. Berner, N. McEvoy, A. Ferguson, A. Shmeliov, M.E.G. Lyons, V. Nicolosi, G.S. Duesberg, J.F. Donegan, J.N. Coleman, Production of Ni(OH)2 nanosheets by liquid phase exfoliation: from optical properties to electrochemical applications, Journal of Materials Chemistry A, 4 (2016) 11046-11059.
[231] U. Khan, A. O'Neill, M. Lotya, S. De, J.N. Coleman, High-Concentration Solvent Exfoliation of Graphene, Small, 6 (2010) 864-871.
[232] M. Lotya, P.J. King, U. Khan, S. De, J.N. Coleman, High-Concentration, Surfactant-Stabilized Graphene Dispersions, ACS Nano, 4 (2010) 3155-3162.
[233] E. Varrla, C. Backes, K.R. Paton, A. Harvey, Z. Gholamvand, J. McCauley, J.N. Coleman, Large-Scale Production of Size-Controlled MoS2Nanosheets by Shear Exfoliation, Chemistry of Materials, 27 (2015) 1129-1139.
[234] M. Ashokkumar, Handbook of Ultrasonics and Sonochemistry, Springer Singapore2016.
[235] A. O'Neill, U. Khan, J.N. Coleman, Preparation of High Concentration Dispersions of Exfoliated MoS2with Increased Flake Size, Chemistry of Materials, 24 (2012) 2414-2421.
[236] C. Backes, D. Hanlon, B.M. Szydlowska, A. Harvey, R.J. Smith, T.M. Higgins, J.N. Coleman, Preparation of Liquid-exfoliated Transition Metal Dichalcogenide Nanosheets with Controlled Size and Thickness: A State of the Art Protocol, Journal of Visualized Experiments, DOI 10.3791/54806(2016).

[237] L. Ueberricke, J.N. Coleman, C. Backes, Robustness of Size Selection and Spectroscopic Size, Thickness and Monolayer Metrics of Liquid-Exfoliated WS2, physica status solidi (b), 254 (2017) n/a-n/a.
[238] E. Varrla, C. Backes, K.R. Paton, A. Harvey, Z. Gholamvand, J. McCauley, J.N. Coleman, Large-Scale Production of Size-Controlled MoS2 Nanosheets by Shear Exfoliation, Chemistry of Materials, 27 (2015) 1129-1139.
[239] T. Panagiotou, S. Mesite, J. Bernard, K. Chomistek, R. Fisher, Production of polymer nanosuspensions using microfluidizerTM processor based processes, NSTI Nanotech, 2008, pp. 688-691.
[240] S. Goldberg, Mechanical/physical methods of cell disruption and tissue homogenization, 2D PAGE: Sample Preparation and Fractionation, DOI (2008) 3-22.
[241] M.I. Corporation, http://www.microfluidicscorp.com/.
[242] T. Lajunen, K. Hisazumi, T. Kanazawa, H. Okada, Y. Seta, M. Yliperttula, A. Urtti, Y. Takashima, Topical drug delivery to retinal pigment epithelium with microfluidizer produced small liposomes, European Journal of Pharmaceutical Sciences, 62 (2014) 23-32.
[243] S.Y. Tang, P. Shridharan, M. Sivakumar, Impact of process parameters in the generation of novel aspirin nanoemulsions – Comparative studies between ultrasound cavitation and microfluidizer, Ultrasonics Sonochemistry, 20 (2013) 485-497.
[244] S.M. Jafari, Y. He, B. Bhandari, Production of sub-micron emulsions by ultrasound and microfluidization techniques, Journal of Food Engineering, 82 (2007) 478-488.
[245] T. Panagiotou, J.M. Bernard, S.V. Mesite, Deagglomeration and dispersion of carbon nanotubes using microfluidizer high shear fluid processors, Nano Science and Technology Institute (NSTI) Conference and Expo Proceedings, 2008, pp. 1-5.
[246] G.A. dos Reis Benatto, B. Roth, M.V. Madsen, M. Hösel, R.R. Søndergaard, M. Jørgensen, F.C. Krebs, Carbon: The Ultimate Electrode Choice for Widely Distributed Polymer Solar Cells, Advanced Energy Materials, 4 (2014) 1400732.
[247] L. Lucera, P. Kubis, F.W. Fecher, C. Bronnbauer, M. Turbiez, K. Forberich, T. Ameri, H.-J. Egelhaaf, C.J. Brabec, Guidelines for Closing the Efficiency Gap between Hero Solar Cells and Roll-To-Roll Printed Modules, Energy Technology, 3 (2015) 373-384.
[248] G. Nisato, D. Lupo, S. Ganz, Organic and Printed Electronics: Fundamentals and Applications, Pan Stanford2016.
[249] X. Huang, T. Leng, X. Zhang, J.C. Chen, K.H. Chang, A.K. Geim, K.S. Novoselov, Z. Hu, Binder-free highly conductive graphene laminate for low cost printed radio frequency applications, Applied Physics Letters, 106 (2015) 203105.
[250] N.J. Welham, V. Berbenni, P.G. Chapman, Effect of extended ball milling on graphite, Journal of Alloys and Compounds, 349 (2003) 255-263.
[251] A. Servant, V. Leon, D. Jasim, L. Methven, P. Limousin, E.V. Fernandez-Pacheco, M. Prato, K. Kostarelos, Graphene-Based Electroresponsive Scaffolds as Polymeric Implants for On-Demand Drug Delivery, Advanced Healthcare Materials, 3 (2014) 1334-1343.
[252] C.M.-E. Gossner, J. Schlundt, P. Ben Embarek, S. Hird, D. Lo-Fo-Wong, J.J.O. Beltran, K.N. Teoh, A. Tritscher, The Melamine Incident: Implications for International Food and Feed Safety, Environmental Health Perspectives, 117 (2009) 1803-1808.
[253] A.M. Rodríguez, A.B. Muñoz-García, O. Crescenzi, E. Vázquez, M. Pavone, Stability of melamine-exfoliated graphene in aqueous media: quantum-mechanical insights at the nanoscale, Phys. Chem. Chem. Phys., 18 (2016) 22203-22209.
[254] A. Mottier, F. Mouchet, C. Laplanche, S. Cadarsi, L. Lagier, J.-C. Arnault, H.A. Girard, V. León, E. Vázquez, C. Sarrieu, É. Pinelli, L. Gauthier, E. Flahaut, Surface Area of Carbon Nanoparticles: A Dose Metric for a More Realistic Ecotoxicological Assessment, Nano Letters, 16 (2016) 3514-3518.
[255] M. Bramini, S. Sacchetti, A. Armirotti, A. Rocchi, E. Vázquez, V. León Castellanos, T. Bandiera, F. Cesca, F. Benfenati, Graphene Oxide Nanosheets Disrupt Lipid Composition, Ca2+Homeostasis, and Synaptic Transmission in Primary Cortical Neurons, ACS Nano, 10 (2016) 7154-7171.

[256] R. Rauti, N. Lozano, V. León, D. Scaini, M. Musto, I. Rago, F.P. Ulloa Severino, A. Fabbro, L. Casalis, E. Vázquez, K. Kostarelos, M. Prato, L. Ballerini, Graphene Oxide Nanosheets Reshape Synaptic Function in Cultured Brain Networks, ACS Nano, 10 (2016) 4459-4471.
[257] T. Friščić, New opportunities for materials synthesis using mechanochemistry, Journal of Materials Chemistry, 20 (2010) 7599.
[258] A.M. Abdelkader, I.A. Kinloch, Mechanochemical Exfoliation of 2D Crystals in Deep Eutectic Solvents, ACS Sustainable Chemistry & Engineering, 4 (2016) 4465-4472.
[259] A.P. Abbott, D. Boothby, G. Capper, D.L. Davies, R.K. Rasheed, Deep Eutectic Solvents Formed between Choline Chloride and Carboxylic Acids: Versatile Alternatives to Ionic Liquids, Journal of the American Chemical Society, 126 (2004) 9142-9147.
[260] Q. Zhang, K. De Oliveira Vigier, S. Royer, F. Jérôme, Deep eutectic solvents: syntheses, properties and applications, Chemical Society Reviews, 41 (2012) 7108.
[261] K. Shahbaz, F.S. Mjalli, G. Vakili-Nezhaad, I.M. AlNashef, A. Asadov, M.M. Farid, Thermogravimetric measurement of deep eutectic solvents vapor pressure, Journal of Molecular Liquids, 222 (2016) 61-66.
[262] C. Ruß, B. König, Low melting mixtures in organic synthesis – an alternative to ionic liquids?, Green Chemistry, 14 (2012) 2969.
[263] Contents, Chemical Society Reviews, 39 (2010) 3339.
[264] E. Treossi, M. Melucci, A. Liscio, M. Gazzano, P. Samorì, V. Palermo, High-Contrast Visualization of Graphene Oxide on Dye-Sensitized Glass, Quartz, and Silicon by Fluorescence Quenching, Journal of the American Chemical Society, 131 (2009) 15576-15577.
[265] H.P. Boehm, A. Clauss, G.O. Fischer, U. Hofmann, Dünnste Kohlenstoff-Folien, Zeitschrift für Naturforschung B, 17 (1962).
[266] D.R. Dreyer, S. Park, C.W. Bielawski, R.S. Ruoff, The chemistry of graphene oxide, Chem. Soc. Rev., 39 (2010) 228-240.
[267] A. Liscio, G.P. Veronese, E. Treossi, F. Suriano, F. Rossella, V. Bellani, R. Rizzoli, P. Samorì, V. Palermo, Charge transport in graphene–polythiophene blends as studied by Kelvin Probe Force Microscopy and transistor characterization, Journal of Materials Chemistry, 21 (2011) 2924.
[268] D.R. Dreyer, S. Park, C.W. Bielawski, R.S. Ruoff, The chemistry of graphene oxide, Chem. Soc. Rev., 39 (2010) 228-240.
[269] D. Chen, H. Feng, J. Li, Graphene Oxide: Preparation, Functionalization, and Electrochemical Applications, Chemical Reviews, 112 (2012) 6027-6053.
[270] Y. Wang, Z. Li, J. Wang, J. Li, Y. Lin, Graphene and graphene oxide: biofunctionalization and applications in biotechnology, Trends in Biotechnology, 29 (2011) 205-212.
[271] C. Zlotea, Y. Oumellal, S.-J. Hwang, C.M. Ghimbeu, P.E. de Jongh, M. Latroche, Ultrasmall MgH2 Nanoparticles Embedded in an Ordered Microporous Carbon Exhibiting Rapid Hydrogen Sorption Kinetics, The Journal of Physical Chemistry C, 119 (2015) 18091-18098.
[272] C. Chung, Y.-K. Kim, D. Shin, S.-R. Ryoo, B.H. Hong, D.-H. Min, Biomedical Applications of Graphene and Graphene Oxide, Accounts of Chemical Research, 46 (2013) 2211-2224.
[273] V. Georgakilas, J.N. Tiwari, K.C. Kemp, J.A. Perman, A.B. Bourlinos, K.S. Kim, R. Zboril, Noncovalent Functionalization of Graphene and Graphene Oxide for Energy Materials, Biosensing, Catalytic, and Biomedical Applications, Chemical Reviews, 116 (2016) 5464-5519.
[274] S.S. Nanda, G.C. Papaefthymiou, D.K. Yi, Functionalization of Graphene Oxide and its Biomedical Applications, Critical Reviews in Solid State and Materials Sciences, 40 (2015) 291-315.
[275] J. Lee, J. Kim, S. Kim, D.-H. Min, Biosensors based on graphene oxide and its biomedical application, Advanced Drug Delivery Reviews, 105 (2016) 275-287.
[276] Y. Liu, X. Dong, P. Chen, Biological and chemical sensors based on graphene materials, Chem. Soc. Rev., 41 (2012) 2283-2307.
[277] M. Kucki, P. Rupper, C. Sarrieu, M. Melucci, E. Treossi, A. Schwarz, V. León, A. Kraegeloh, E. Flahaut, E. Vázquez, V. Palermo, P. Wick, Interaction of graphene-related materials with human intestinal cells: an in vitro approach, Nanoscale, 8 (2016) 8749-8760.

[278] R. Kurapati, J. Russier, M.A. Squillaci, E. Treossi, C. Ménard-Moyon, A.E. Del Rio-Castillo, E. Vazquez, P. Samorì, V. Palermo, A. Bianco, Dispersibility-Dependent Biodegradation of Graphene Oxide by Myeloperoxidase, Small, 11 (2015) 3985-3994.
[279] J. Russier, E. Treossi, A. Scarsi, F. Perrozzi, H. Dumortier, L. Ottaviano, M. Meneghetti, V. Palermo, A. Bianco, Evidencing the mask effect of graphene oxide: a comparative study on primary human and murine phagocytic cells, Nanoscale, 5 (2013) 11234-11247.
[280] S.S. An, S.-Y. Wu, J. Hulme, Current applications of graphene oxide in nanomedicine, International Journal of Nanomedicine, DOI 10.2147/ijn.s88285(2015) 9.
[281] B.C. Brodie, On the Atomic Weight of Graphite, Philosophical Transactions of the Royal Society London, 149 (1859) 249.
[282] L. Staudenmaier, Verfahren zur Darstellung der Graphitsaure, Ber. Deut. Chem.

Ges., 31 (1898) 1481.
[283] D.C. Marcano, D.V. Kosynkin, J.M. Berlin, A. Sinitskii, Z.Z. Sun, A. Slesarev, L.B. Alemany, W. Lu, J.M. Tour, Improved Synthesis of Graphene Oxide, Acs Nano, 4 (2010) 4806-4814.
[284] V.C. Sanchez, A. Jachak, R.H. Hurt, A.B. Kane, Biological Interactions of Graphene-Family Nanomaterials: An Interdisciplinary Review, Chemical Research in Toxicology, 25 (2012) 15-34.
[285] L. De Marzi, L. Ottaviano, F. Perrozzi, M. Nardone, S. Santucci, J. De Lapuente, M. Borras, E. Treossi, V. Palermo, A. Poma, Flake Size-Dependent Cyto And Genotoxic Evaluation Of Graphene Oxide On In Vitro A549, Caco2 And Vero Cell Lines. , Journal of Biological Regulators and Homeostatic Agents, 28 (2014) 281-289.
[286] M. Ardini, G. Golia, P. Passaretti, A. Cimini, G. Pitari, F. Giansanti, L. Di Leandro, L. Ottaviano, F. Perrozzi, S. Santucci, V. Morandi, L. Ortolani, M. Christian, E. Treossi, V. Palermo, F. Angelucci, R. Ippoliti, Supramolecular self-assembly of graphene oxide and metal nanoparticles into stacked multilayers by means of a multitasking protein ring, Nanoscale, 8 (2016) 6739-6753.
[287] S. Panzavolta, B. Bracci, C. Gualandi, M.L. Focarete, E. Treossi, K. Kouroupis-Agalou, K. Rubini, F. Bosia, L. Brely, N.M. Pugno, V. Palermo, A. Bigi, Structural reinforcement and failure analysis in composite nanofibers of graphene oxide and gelatin, Carbon, 78 (2014) 566-577.
[288] N. Morimoto, T. Kubo, Y. Nishina, Tailoring the Oxygen Content of Graphite and Reduced Graphene Oxide for Specific Applications, Scientific Reports, 6 (2016).
[289] L.-C. Tang, Y.-J. Wan, D. Yan, Y.-B. Pei, L. Zhao, Y.-B. Li, L.-B. Wu, J.-X. Jiang, G.-Q. Lai, The effect of graphene dispersion on the mechanical properties of graphene/epoxy composites, Carbon, 60 (2013) 16-27.
[290] G. Wu, W. Gao, GO/rGO as Advanced Materials for Energy Storage and Conversion, Graphene Oxide, Springer International Publishing, 2015, pp. 97-127.
[291] S.Y. Chee, H.L. Poh, C.K. Chua, F. Šaněk, Z. Sofer, M. Pumera, Influence of parent graphite particle size on the electrochemistry of thermally reduced graphene oxide, Physical Chemistry Chemical Physics, 14 (2012) 12794.
[292] J. Gómez, E. Villaro, A. Navas, I. Recio, Testing the influence of the temperature, RH and filler type and content on the universal power law for new reduced graphene oxide TPU composites, Materials Research Express, 4 (2017) 105020.
[293] G. Singh, V. Divakar Botcha, D.S. Sutar, S.S. Talwar, R.S. Srinivasa, S.S. Major, Graphite mediated reduction of graphene oxide monolayer sheets, Carbon, 95 (2015) 843-851.
[294] H. Zhang, Y. Liu, S. Huo, J. Briscoe, W. Tu, O.T. Picot, A. Rezai, E. Bilotti, T. Peijs, Filtration effects of graphene nanoplatelets in resin infusion processes: Problems and possible solutions, Composites Science and Technology, 139 (2017) 138-145.
[295] G. Ambrosetti, C. Grimaldi, I. Balberg, T. Maeder, A. Danani, P. Ryser, Solution of the tunneling-percolation problem in the nanocomposite regime, Physical Review B, 81 (2010).
[296] M. Aleksandrzak, P. Adamski, W. Kukułka, B. Zielinska, E. Mijowska, Effect of graphene thickness on photocatalytic activity of TiO2-graphene nanocomposites, Applied Surface Science, 331 (2015) 193-199.
[297] Graphene-based Energy Devices, Wiley-VCH Verlag GmbH & Co. KGaA2015.

[298] C. Su, K.P. Loh, Carbocatalysts: Graphene Oxide and Its Derivatives, Accounts of Chemical Research, 46 (2013) 2275-2285.
[299] M.E. Casco, A. Morelos-Gómez, S.M. Vega-Díaz, R. Cruz-Silva, F. Tristán-López, H. Muramatsu, T. Hayashi, M. Martínez-Escandell, M. Terrones, M. Endo, F. Rodríguez-Reinoso, J. Silvestre-Albero, CO2 adsorption on crystalline graphitic nanostructures, Journal of CO2 Utilization, 5 (2014) 60-65.
[300] X. Huang, X. Qi, F. Boey, H. Zhang, Graphene-based composites, Chem. Soc. Rev., 41 (2012) 666-686.
[301] I.-Y. Jeon, H.-J. Choi, M. Choi, J.-M. Seo, S.-M. Jung, M.-J. Kim, S. Zhang, L. Zhang, Z. Xia, L. Dai, N. Park, J.-B. Baek, Facile, scalable synthesis of edge-halogenated graphene nanoplatelets as efficient metal-free eletrocatalysts for oxygen reduction reaction, Scientific Reports, 3 (2013).
[302] R. Jabari Seresht, M. Jahanshahi, A. Rashidi, A.A. Ghoreyshi, Synthesize and characterization of graphene nanosheets with high surface area and nano-porous structure, Applied Surface Science, 276 (2013) 672-681.
[303] I.R. J. F. Blanco-Villalba, J. Gómez, Ch. Hübner, Improving the Processability of Graphene Nanoplatelets in Polyamide 6 during Melt Compounding Extrusion, PPS2017, Dresden, Germany, 2017.
[304] S. Park, J. An, J.R. Potts, A. Velamakanni, S. Murali, R.S. Ruoff, Hydrazine-reduction of graphite- and graphene oxide, Carbon, 49 (2011) 3019-3023.
[305] Z. Bo, X. Shuai, S. Mao, H. Yang, J. Qian, J. Chen, J. Yan, K. Cen, Green preparation of reduced graphene oxide for sensing and energy storage applications, Scientific Reports, 4 (2014).
[306] D.R. Dreyer, S. Murali, Y. Zhu, R.S. Ruoff, C.W. Bielawski, Reduction of graphite oxide using alcohols, J. Mater. Chem., 21 (2011) 3443-3447.
[307] M. Agharkar, S. Kochrekar, S. Hidouri, M.A. Azeez, Trends in green reduction of graphene oxides, issues and challenges: A review, Materials Research Bulletin, 59 (2014) 323-328.
[308] S. Sarkar, D. Basak, The reduction of graphene oxide by zinc powder to produce a zinc oxide-reduced graphene oxide hybrid and its superior photocatalytic activity, Chemical Physics Letters, 561-562 (2013) 125-130.
[309] C.K. Chua, M. Pumera, Chemical reduction of graphene oxide: a synthetic chemistry viewpoint, Chem. Soc. Rev., 43 (2014) 291-312.
[310] M.M. Storm, R.E. Johnsen, P. Norby, In situ X-ray powder diffraction studies of the synthesis of graphene oxide and formation of reduced graphene oxide, Journal of Solid State Chemistry, 240 (2016) 49-54.
[311] K. Hu, X. Xie, T. Szkopek, M. Cerruti, Understanding Hydrothermally Reduced Graphene Oxide Hydrogels: From Reaction Products to Hydrogel Properties, Chemistry of Materials, 28 (2016) 1756-1768.
[312] Y. Zhou, Q. Bao, L.A.L. Tang, Y. Zhong, K.P. Loh, Hydrothermal Dehydration for the “Green” Reduction of Exfoliated Graphene Oxide to Graphene and Demonstration of Tunable Optical Limiting Properties, Chemistry of Materials, 21 (2009) 2950-2956.
[313] A. Bagri, C. Mattevi, M. Acik, Y.J. Chabal, M. Chhowalla, V.B. Shenoy, Structural evolution during the reduction of chemically derived graphene oxide, Nature Chemistry, 2 (2010) 581-587.
[314] M. Tortello, S. Colonna, M. Bernal, J. Gomez, M. Pavese, C. Novara, F. Giorgis, M. Maggio, G. Guerra, G. Saracco, R.S. Gonnelli, A. Fina, Effect of thermal annealing on the heat transfer properties of reduced graphite oxide flakes: A nanoscale characterization via scanning thermal microscopy, Carbon, 109 (2016) 390-401.
[315] M. Cheng, R. Yang, L. Zhang, Z. Shi, W. Yang, D. Wang, G. Xie, D. Shi, G. Zhang, Restoration of graphene from graphene oxide by defect repair, Carbon, 50 (2012) 2581-2587.
[316] V. López, R.S. Sundaram, C. Gómez-Navarro, D. Olea, M. Burghard, J. Gómez-Herrero, F. Zamora, K. Kern, Graphene Monolayers: Chemical Vapor Deposition Repair of Graphene Oxide: A Route to Highly-Conductive Graphene Monolayers (Adv. Mater. 46/2009), Advanced Materials, 21 (2009) n/a-n/a.

[317] M. Acik, G. Lee, C. Mattevi, A. Pirkle, R.M. Wallace, M. Chhowalla, K. Cho, Y. Chabal, The Role of Oxygen during Thermal Reduction of Graphene Oxide Studied by Infrared Absorption Spectroscopy, The Journal of Physical Chemistry C, 115 (2011) 19761-19781.
[318] C.-Y. Su, Y. Xu, W. Zhang, J. Zhao, A. Liu, X. Tang, C.-H. Tsai, Y. Huang, L.-J. Li, Highly Efficient Restoration of Graphitic Structure in Graphene Oxide Using Alcohol Vapors, ACS Nano, 4 (2010) 5285-5292.
[319] Z.-l. Wang, D. Xu, Y. Huang, Z. Wu, L.-m. Wang, X.-b. Zhang, Facile, mild and fast thermal-decomposition reduction of graphene oxide in air and its application in high-performance lithium batteries, Chem. Commun., 48 (2012) 976-978.
[320] V. Chabot, D. Higgins, A. Yu, X. Xiao, Z. Chen, J. Zhang, A review of graphene and graphene oxide sponge: material synthesis and applications to energy and the environment, Energy & Environmental Science, 7 (2014) 1564.
[321] M. Wang, X. Duan, Y. Xu, X. Duan, Functional Three-Dimensional Graphene/Polymer Composites, ACS Nano, 10 (2016) 7231-7247.
[322] Z.Y. Xia, D. Wei, E. Anitowska, V. Bellani, L. Ortolani, V. Morandi, M. Gazzano, A. Zanelli, S. Borini, V. Palermo, Electrochemically exfoliated graphene oxide/iron oxide composite foams for lithium storage, produced by simultaneous graphene reduction and Fe(OH)3 condensation, Carbon, 84 (2015) 254-262.
[323] Z.Y. Xia, G. Giambastiani, C. Christodoulou, M.V. Nardi, N. Koch, E. Treossi, V. Bellani, S. Pezzini, F. Corticelli, V. Morandi, A. Zanelli, V. Palermo, Synergic Exfoliation of Graphene with Organic Molecules and Inorganic Ions for the Electrochemical Production of Flexible Electrodes, ChemPlusChem, 79 (2014) 439-446.
[324] J.L. Vickery, A.J. Patil, S. Mann, Fabrication of Graphene-Polymer Nanocomposites With Higher-Order Three-Dimensional Architectures, Advanced Materials, 21 (2009) 2180-2184.
[325] S. Nardecchia, D. Carriazo, M.L. Ferrer, M.C. Gutiérrez, F. del Monte, Three dimensional macroporous architectures and aerogels built of carbon nanotubes and/or graphene: synthesis and applications, Chem. Soc. Rev., 42 (2013) 794-830.
[326] J. Mao, J. Iocozzia, J. Huang, K. Meng, Y. Lai, Z. Lin, Graphene Aerogels for Efficient Energy Storage and Conversion, Energy & Environmental Science, DOI 10.1039/c7ee03031b(2018).
[327] C. Botas, D. Carriazo, G. Singh, T. Rojo, Sn– and SnO2–graphene flexible foams suitable as binder-free anodes for lithium ion batteries, J. Mater. Chem. A, 3 (2015) 13402-13410.
[328] E. Quesnel, F. Roux, F. Emieux, P. Faucherand, E. Kymakis, G. Volonakis, F. Giustino, B. Martín-García, I. Moreels, S.A. Gürsel, A.B. Yurtcan, V.D. Noto, A. Talyzin, I. Baburin, D. Tranca, G. Seifert, L. Crema, G. Speranza, V. Tozzini, P. Bondavalli, G. Pognon, C. Botas, D. Carriazo, G. Singh, T. Rojo, G. Kim, W. Yu, C.P. Grey, V. Pellegrini, Graphene-based technologies for energy applications, challenges and perspectives, 2D Materials, 2 (2015) 030204.
[329] M.C. Gutiérrez, M.L. Ferrer, F. del Monte, Ice-Templated Materials: Sophisticated Structures Exhibiting Enhanced Functionalities Obtained after Unidirectional Freezing and Ice-Segregation-Induced Self-Assembly†, Chemistry of Materials, 20 (2008) 634-648.
[330] C. Botas, D. Carriazo, W. Zhang, T. Rojo, G. Singh, Silicon-Reduced Graphene Oxide Self-Standing Composites Suitable as Binder-Free Anodes for Lithium-Ion Batteries, ACS Applied Materials & Interfaces, 8 (2016) 28800-28808.
[331] J.K. Lee, K.B. Smith, C.M. Hayner, H.H. Kung, Silicon nanoparticles–graphene paper composites for Li ion battery anodes, Chemical Communications, 46 (2010) 2025.
[332] X. Zhou, Y.-X. Yin, L.-J. Wan, Y.-G. Guo, Facile synthesis of silicon nanoparticles inserted into graphene sheets as improved anode materials for lithium-ion batteries, Chemical Communications, 48 (2012) 2198.
[333] C. Botas, D. Carriazo, G. Singh, T. Rojo, Sn– and SnO2–graphene flexible foams suitable as binder-free anodes for lithium ion batteries, Journal of Materials Chemistry A, 3 (2015) 13402-13410.
[334] C. Botas, P. Álvarez, C. Blanco, R. Santamaría, M. Granda, M.D. Gutiérrez, F. Rodríguez-Reinoso, R. Menéndez, Critical temperatures in the synthesis of graphene-like materials by thermal exfoliation–reduction of graphite oxide, Carbon, 52 (2013) 476-485.

[335] G. Li, J. Sun, W. Hou, S. Jiang, Y. Huang, J. Geng, Three-dimensional porous carbon composites containing high sulfur nanoparticle content for high-performance lithium–sulfur batteries, Nature Communications, 7 (2016) 10601.
[336] J. Ajuria, M. Arnaiz, C. Botas, D. Carriazo, R. Mysyk, T. Rojo, A.V. Talyzin, E. Goikolea, Graphene-based lithium ion capacitor with high gravimetric energy and power densities, Journal of Power Sources, 363 (2017) 422-427.
[337] J.M. Englert, K.C. Knirsch, C. Dotzer, B. Butz, F. Hauke, E. Spiecker, A. Hirsch, Functionalization of graphene by electrophilic alkylation of reduced graphite, Chemical Communications, 48 (2012) 5025.
[338] R.A. Schäfer, J.M. Englert, P. Wehrfritz, W. Bauer, F. Hauke, T. Seyller, A. Hirsch, On the Way to Graphane—Pronounced Fluorescence of Polyhydrogenated Graphene, Angewandte Chemie International Edition, 52 (2013) 754-757.
[339] P. Vecera, K. Edelthalhammer, F. Hauke, A. Hirsch, Reductive arylation of graphene: Insights into a reversible carbon allotrope functionalization reaction, Phys Status Solidi B, 251 (2014) 2536-2540.
[340] G. Abellán, M. Schirowski, K. Edelthalhammer, M. Fickert, F. Hauke, A. Hirsch, Unifying Aspects of the Reductive Covalnet Graphene Functionalization, J Am Chem Soc, DOI (2017) under revision.
[341] A. Catheline, L. Ortolani, V. Morandi, M. Melle-Franco, C. Drummond, C. Zakri, A. Penicaud, Solutions of fully exfoliated individual graphene flakes in low boiling point solvents, Soft Matter, 8 (2012) 7882-7887.
[342] A. Pénicaud, C. Drummond, Deconstructing graphite: Graphenide solutions, Accounts of Chemical Research, 46 (2013) 129-137.
[343] K.F. Kelly, W.E. Billups, Synthesis of Soluble Graphite and Graphene, Accounts of Chemical Research, 46 (2013) 4-13.
[344] A. Pénicaud, C. Drummond, Deconstructing Graphite: Graphenide Solutions, Accounts of Chemical Research, 46 (2012) 129-137.
[345] P. Vecera, J. Holzwarth, K.F. Edelthalhammer, U. Mundloch, H. Peterlik, F. Hauke, A. Hirsch, Solvent-driven electron trapping and mass transport in reduced graphites to access perfect graphene, Nat Commun, 7 (2016) 12411.
[346] S.A. Hodge, H.H. Tay, D.B. Anthony, R. Menzel, D.J. Buckley, P.L. Cullen, N.T. Skipper, C.A. Howard, M.S.P. Shaffer, Probing the charging mechanisms of carbon nanomaterial polyelectrolytes, Faraday Discussions, 172 (2014) 311-325.
[347] P. Vecera, J. Holzwarth, K.F. Edelthalhammer, U. Mundloch, H. Peterlik, F. Hauke, A. Hirsch, Solvent-driven electron trapping and mass transport in reduced graphites to access perfect graphene, Nature Communications, 7 (2016) 12411.
[348] G. Bepete, E. Anglaret, L. Ortolani, V. Morandi, K. Huang, A. Pénicaud, C. Drummond, Surfactant-free single-layer graphene in water, Nat Chem, advance online publication (2016).
[349] G. Eda, H. Yamaguchi, D. Voiry, T. Fujita, M. Chen, M. Chhowalla, Photoluminescence from Chemically Exfoliated MoS2, Nano Letters, 11 (2011) 5111-5116.
[350] K.C. Knirsch, N.C. Berner, H.C. Nerl, C.S. Cucinotta, Z. Gholamvand, N. McEvoy, Z. Wang, I. Abramovic, P. Vecera, M. Halik, S. Sanvito, G.S. Duesberg, V. Nicolosi, F. Hauke, A. Hirsch, J.N. Coleman, C. Backes, Basal-Plane Functionalization of Chemically Exfoliated Molybdenum Disulfide by Diazonium Salts, ACS Nano, 9 (2015) 6018-6030.
[351] D. Voiry, A. Goswami, R. Kappera, e. SilvaCecilia de Carvalho Castro, D. Kaplan, T. Fujita, M. Chen, T. Asefa, M. Chhowalla, Covalent functionalization of monolayered transition metal dichalcogenides by phase engineering, Nat Chem, 7 (2015) 45-49.
[352] G. Pagona, C. Bittencourt, R. Arenal, N. Tagmatarchis, Exfoliated semiconducting pure 2H-MoS2and 2H-WS2assisted by chlorosulfonic acid, Chem. Commun., 51 (2015) 12950-12953.
[353] S. Yang, M.R. Lohe, K. Müllen, X. Feng, New-Generation Graphene from Electrochemical Approaches: Production and Applications, Advanced Materials, 28 (2016) 6213-6221.

[354] G. Maccaferri, C. Zanardi, Z.Y. Xia, A. Kovtun, A. Liscio, F. Terzi, V. Palermo, R. Seeber, Systematic study of the correlation between surface chemistry, conductivity and electrocatalytic properties of graphene oxide nanosheets, Carbon, 120 (2017) 165-175.
[355] C.-Y. Su, A.-Y. Lu, Y. Xu, F.-R. Chen, A.N. Khlobystov, L.-J. Li, High-Quality Thin Graphene Films from Fast Electrochemical Exfoliation, ACS Nano, 5 (2011) 2332-2339.
[356] K. Parvez, R. Li, S.R. Puniredd, Y. Hernandez, F. Hinkel, S. Wang, X. Feng, K. Müllen, Electrochemically Exfoliated Graphene as Solution-Processable, Highly Conductive Electrodes for Organic Electronics, ACS Nano, 7 (2013) 3598-3606.
[357] K.S. Rao, J. Sentilnathan, H.-W. Cho, J.-J. Wu, M. Yoshimura, Soft Processing of Graphene Nanosheets by Glycine-Bisulfate Ionic-Complex-Assisted Electrochemical Exfoliation of Graphite for Reduction Catalysis, Advanced Functional Materials, 25 (2014) 298-305.
[358] K. Parvez, Z.-S. Wu, R. Li, X. Liu, R. Graf, X. Feng, K. Müllen, Exfoliation of Graphite into Graphene in Aqueous Solutions of Inorganic Salts, Journal of the American Chemical Society, 136 (2014) 6083-6091.
[359] S. Yang, S. Brüller, Z.-S. Wu, Z. Liu, K. Parvez, R. Dong, F. Richard, P. Samorì, X. Feng, K. Müllen, Organic Radical-Assisted Electrochemical Exfoliation for the Scalable Production of High-Quality Graphene, Journal of the American Chemical Society, 137 (2015) 13927-13932.
[360] J. Wang, K.K. Manga, Q. Bao, K.P. Loh, High-Yield Synthesis of Few-Layer Graphene Flakes through Electrochemical Expansion of Graphite in Propylene Carbonate Electrolyte, Journal of the American Chemical Society, 133 (2011) 8888-8891.
[361] J. Cabana, L. Monconduit, D. Larcher, M.R. Palacín, Beyond Intercalation-Based Li-Ion Batteries: The State of the Art and Challenges of Electrode Materials Reacting Through Conversion Reactions, Advanced Materials, 22 (2010) E170-E192.
[362] T. Ohzuku, Formation of Lithium-Graphite Intercalation Compounds in Nonaqueous Electrolytes and Their Application as a Negative Electrode for a Lithium Ion (Shuttlecock) Cell, Journal of The Electrochemical Society, 140 (1993) 2490.
[363] J.M. Tarascon, M. Armand, Issues and challenges facing rechargeable lithium batteries, Nature, 414 (2001) 359-367.
[364] T.E. Weller, M. Ellerby, S.S. Saxena, R.P. Smith, N.T. Skipper, Superconductivity in the intercalated graphite compounds C6Yb and C6Ca, Nature Physics, 1 (2005) 39-41.
[365] Y.L. Zhong, T.M. Swager, Enhanced Electrochemical Expansion of Graphite forin SituElectrochemical Functionalization, Journal of the American Chemical Society, 134 (2012) 17896-17899.
[366] A.M. Abdelkader, I.A. Kinloch, R.A.W. Dryfe, Continuous Electrochemical Exfoliation of Micrometer-Sized Graphene Using Synergistic Ion Intercalations and Organic Solvents, ACS Applied Materials & Interfaces, 6 (2014) 1632-1639.
[367] P. Yu, Determination of the Lithium Ion Diffusion Coefficient in Graphite, Journal of The Electrochemical Society, 146 (1999) 8.
[368] A.M. Abdelkader, A.J. Cooper, R.A.W. Dryfe, I.A. Kinloch, How to get between the sheets: a review of recent works on the electrochemical exfoliation of graphene materials from bulk graphite, Nanoscale, 7 (2015) 6944-6956.
[369] A.M. Abdelkader, H.V. Patten, Z. Li, Y. Chen, I.A. Kinloch, Electrochemical exfoliation of graphite in quaternary ammonium-based deep eutectic solvents: a route for the mass production of graphane, Nanoscale, 7 (2015) 11386-11392.
[370] A.R. Kamali, J. Feighan, D.J. Fray, Towards large scale preparation of graphene in molten salts and its use in the fabrication of highly toughened alumina ceramics, Faraday Discuss., 190 (2016) 451-470.
[371] A.R. Kamali, D.J. Fray, Large-scale preparation of graphene by high temperature insertion of hydrogen into graphite, Nanoscale, 7 (2015) 11310-11320.
[372] H.-K. Kim, A.R. Kamali, K.C. Roh, K.-B. Kim, D.J. Fray, Dual coexisting interconnected graphene nanostructures for high performance supercapacitor applications, Energy Environ. Sci., 9 (2016) 2249-2256.

[373] A.R. Kamali, Eco-friendly production of high quality low cost graphene and its application in lithium ion batteries, Green Chemistry, 18 (2016) 1952-1964.
[374] Z.Y. Xia, S. Pezzini, E. Treossi, G. Giambastiani, F. Corticelli, V. Morandi, A. Zanelli, V. Bellani, V. Palermo, The Exfoliation of Graphene in Liquids by Electrochemical, Chemical, and Sonication-Assisted Techniques: A Nanoscale Study Advanced Functional Materials, 23 (2013) 4684-4693.
[375] H.L. Zhuang, R.G. Hennig, Computational Discovery, Characterization, and Design of Single-Layer Materials, JOM, 66 (2014) 366-374.
[376] T. Gould, S. Lebègue, T. Björkman, J.F. Dobson, 2D Structures Beyond Graphene, Semiconductors and Semimetals, Elsevier, 2016, pp. 1-33.
[377] S. Lebègue, T. Björkman, M. Klintenberg, R.M. Nieminen, O. Eriksson, Two-Dimensional Materials from Data Filtering andAb InitioCalculations, Physical Review X, 3 (2013).
[378] M. Ashton, J. Paul, S.B. Sinnott, R.G. Hennig, Topology-Scaling Identification of Layered Solids and Stable Exfoliated 2D Materials, Physical Review Letters, 118 (2017).
[379] M.G. Nicolas Mounet, Philippe Schwaller, Andrius Merkys, Ivano E Castelli, Andrea Cepellotti, Giovanni Pizzi, Nicola Marzari, Novel two-dimensional materials from high-throughput computational exfoliation of experimentally known compounds arXiv preprint arXiv:1611.05234, 2016.
[380] H.L. Zhuang, P.R.C. Kent, R.G. Hennig, Strong anisotropy and magnetostriction in the two-dimensional Stoner ferromagnetFe3GeTe2, Physical Review B, 93 (2016).
[381] S. Zhang, Z. Yan, Y. Li, Z. Chen, H. Zeng, Atomically Thin Arsenene and Antimonene: Semimetal-Semiconductor and Indirect-Direct Band-Gap Transitions, Angewandte Chemie, 127 (2015) 3155-3158.
[382] G. Schusteritsch, M. Uhrin, C.J. Pickard, Single-Layered Hittorf's Phosphorus: A Wide-Bandgap High Mobility 2D Material, Nano Letters, 16 (2016) 2975-2980.
[383] S. Cahangirov, M. Topsakal, E. Aktürk, H. Şahin, S. Ciraci, Two- and One-Dimensional Honeycomb Structures of Silicon and Germanium, Physical Review Letters, 102 (2009).
[384] F.A. Rasmussen, K.S. Thygesen, Computational 2D Materials Database: Electronic Structure of Transition-Metal Dichalcogenides and Oxides, The Journal of Physical Chemistry C, 119 (2015) 13169-13183.
[385] C. Ataca, H. Şahin, S. Ciraci, Stable, Single-Layer MX2 Transition-Metal Oxides and Dichalcogenides in a Honeycomb-Like Structure, The Journal of Physical Chemistry C, 116 (2012) 8983-8999.
[386] P. Miró, M. Audiffred, T. Heine, An atlas of two-dimensional materials, Chem. Soc. Rev., 43 (2014) 6537-6554.
[387] S. Bahmann, J. Kortus, EVO—Evolutionary algorithm for crystal structure prediction, Computer Physics Communications, 184 (2013) 1618-1625.
[388] X.-F. Zhou, X. Dong, A.R. Oganov, Q. Zhu, Y. Tian, H.-T. Wang, Semimetallic Two-Dimensional Boron Allotrope with Massless Dirac Fermions, Physical Review Letters, 112 (2014).
[389] B.C. Revard, W.W. Tipton, A. Yesypenko, R.G. Hennig, Grand-canonical evolutionary algorithm for the prediction of two-dimensional materials, Physical Review B, 93 (2016).
[390] W. Luo, Y. Ma, X. Gong, H. Xiang, Prediction of Silicon-Based Layered Structures for Optoelectronic Applications, Journal of the American Chemical Society, 136 (2014) 15992-15997.
[391] X. Luo, J. Yang, H. Liu, X. Wu, Y. Wang, Y. Ma, S.-H. Wei, X. Gong, H. Xiang, Predicting Two-Dimensional Boron–Carbon Compounds by the Global Optimization Method, Journal of the American Chemical Society, 133 (2011) 16285-16290.
[392] J.-H. Yang, Y. Zhang, W.-J. Yin, X.G. Gong, B.I. Yakobson, S.-H. Wei, Two-Dimensional SiS Layers with Promising Electronic and Optoelectronic Properties: Theoretical Prediction, Nano Letters, 16 (2016) 1110-1117.
[393] X. Wu, J. Dai, Y. Zhao, Z. Zhuo, J. Yang, X.C. Zeng, Two-Dimensional Boron Monolayer Sheets, ACS Nano, 6 (2012) 7443-7453.
[394] Z. Zhang, A.J. Mannix, Z. Hu, B. Kiraly, N.P. Guisinger, M.C. Hersam, B.I. Yakobson, Substrate-Induced Nanoscale Undulations of Borophene on Silver, Nano Letters, 16 (2016) 6622-6627.

[395] Z. Zhang, E.S. Penev, B.I. Yakobson, Two-dimensional materials: Polyphony in B flat, Nature Chemistry, 8 (2016) 525-527.
[396] F. Bonaccorso, A. Bartolotta, J.N. Coleman, C. Backes, 2D-Crystal-Based Functional Inks, Adv. Mater., 28 (2016) 6136-6166.
[397] J. Hassoun, F. Bonaccorso, M. Agostini, M. Angelucci, M.G. Betti, R. Cingolani, M. Gemmi, C. Mariani, S. Panero, V. Pellegrini, B. Scrosati, An Advanced Lithium-Ion Battery Based on a Graphene Anode and a Lithium Iron Phosphate Cathode, Nano Letters, 14 (2014) 4901-4906.
[398] J. Kang, S.A. Wells, J.D. Wood, J.-H. Lee, X. Liu, C.R. Ryder, J. Zhu, J.R. Guest, C.A. Husko, M.C. Hersam, Stable aqueous dispersions of optically and electronically active phosphorene, Proceedings of the National Academy of Sciences, 113 (2016) 11688-11693.
[399] J.S. Bunch, Y. Yaish, M. Brink, K. Bolotin, P.L. McEuen, Coulomb Oscillations and Hall Effect in Quasi-2D Graphite Quantum Dots, Nano Letters, 5 (2005) 287-290.
[400] T. Hasan, F. Torrisi, Z. Sun, D. Popa, V. Nicolosi, G. Privitera, F. Bonaccorso, A.C. Ferrari, Solution-phase exfoliation of graphite for ultrafast photonics, physica status solidi (b), 247 (2010) 2953-2957.
[401] L. Liu, Z. Shen, M. Yi, X. Zhang, S. Ma, A green, rapid and size-controlled production of high-quality graphene sheets by hydrodynamic forces, RSC Advances, 4 (2014) 36464.
[402] A. Pattammattel, C.V. Kumar, Kitchen Chemistry 101: Multigram Production of High Quality Biographene in a Blender with Edible Proteins, Advanced Functional Materials, 25 (2015) 7088-7098.
[403] M. Yi, Z. Shen, Kitchen blender for producing high-quality few-layer graphene, Carbon, 78 (2014) 622-626.
[404] C. Damm, T.J. Nacken, W. Peukert, Quantitative evaluation of delamination of graphite by wet media milling, Carbon, 81 (2015) 284-294.
[405] A. Fabbro, D. Scaini, V. León, E. Vázquez, G. Cellot, G. Privitera, L. Lombardi, F. Torrisi, F. Tomarchio, F. Bonaccorso, S. Bosi, A.C. Ferrari, L. Ballerini, M. Prato, Graphene-Based Interfaces Do Not Alter Target Nerve Cells, ACS Nano, 10 (2016) 615-623.
[406] M.A. Ibrahem, T.-w. Lan, J.K. Huang, Y.-Y. Chen, K.-H. Wei, L.-J. Li, C.W. Chu, High quantity and quality few-layers transition metal disulfide nanosheets from wet-milling exfoliation, RSC Advances, 3 (2013) 13193.
[407] C. Knieke, A. Berger, M. Voigt, R.N.K. Taylor, J. Röhrl, W. Peukert, Scalable production of graphene sheets by mechanical delamination, Carbon, 48 (2010) 3196-3204.
[408] Y. Yao, Z. Lin, Z. Li, X. Song, K.-S. Moon, C.-p. Wong, Large-scale production of two-dimensional nanosheets, Journal of Materials Chemistry, 22 (2012) 13494.
[409] W. Zhao, M. Fang, F. Wu, H. Wu, L. Wang, G. Chen, Preparation of graphene by exfoliation of graphite using wet ball milling, Journal of Materials Chemistry, 20 (2010) 5817.
[410] Z. Shen, J. Li, M. Yi, X. Zhang, S. Ma, Preparation of graphene by jet cavitation, Nanotechnology, 22 (2011) 365306.
[411] M. Yi, J. Li, Z. Shen, X. Zhang, S. Ma, Morphology and structure of mono- and few-layer graphene produced by jet cavitation, Applied Physics Letters, 99 (2011) 123112.
[412] M. Yi, Z. Shen, W. Zhang, J. Zhu, L. Liu, S. Liang, X. Zhang, S. Ma, Hydrodynamics-assisted scalable production of boron nitride nanosheets and their application in improving oxygen-atom erosion resistance of polymeric composites, Nanoscale, 5 (2013) 10660.
[413] F. Bonaccorso, M. Zerbetto, A.C. Ferrari, V. Amendola, Sorting Nanoparticles by Centrifugal Fields in Clean Media, The Journal of Physical Chemistry C, 117 (2013) 13217-13229.
[414] M.J. O'Connell, S.M. Bachilo, C.B. Huffman, V.C. Moore, M.S. Strano, E.H. Haroz, K.L. Rialon, P.J. Boul, W.H. Noon, C. Kittrell, J. Ma, R.H. Hauge, R.B. Weisman, R.E. Smalley, Band Gap Fluorescence from Individual Single-Walled Carbon Nanotubes, Science, 297 (2002) 593-596.
[415] T. Hasan, P.H. Tan, F. Bonaccorso, A.G. Rozhin, V. Scardaci, W.I. Milne, A.C. Ferrari, Polymer-Assisted Isolation of Single Wall Carbon Nanotubes in Organic Solvents for Optical-Quality Nanotube−Polymer Composites, The Journal of Physical Chemistry C, 112 (2008) 20227-20232.

[416] O.M. Maragò, P.G. Gucciardi, F. Bonaccorso, G. Calogero, V. Scardaci, A.G. Rozhin, A.C. Ferrari, P.H. Jones, R. Saija, F. Borghese, P. Denti, M.A. Iatì, Optical trapping of carbon nanotubes, Physica E: Low-dimensional Systems and Nanostructures, 40 (2008) 2347-2351.
[417] P.H. Tan, T. Hasan, F. Bonaccorso, V. Scardaci, A.G. Rozhin, W.I. Milne, A.C. Ferrari, Optical properties of nanotube bundles by photoluminescence excitation and absorption spectroscopy, Physica E: Low-dimensional Systems and Nanostructures, 40 (2008) 2352-2359.
[418] O.M. Maragó, F. Bonaccorso, R. Saija, G. Privitera, P.G. Gucciardi, M.A. Iatì, G. Calogero, P.H. Jones, F. Borghese, P. Denti, V. Nicolosi, A.C. Ferrari, Brownian Motion of Graphene, ACS Nano, 4 (2010) 7515-7523.
[419] F. Torrisi, T. Hasan, W. Wu, Z. Sun, A. Lombardo, T.S. Kulmala, G.-W. Hsieh, S. Jung, F. Bonaccorso, P.J. Paul, D. Chu, A.C. Ferrari, Inkjet-Printed Graphene Electronics, ACS Nano, 6 (2012) 2992-3006.
[420] A. Capasso, F. Matteocci, L. Najafi, M. Prato, J. Buha, L. Cinà, V. Pellegrini, A.D. Carlo, F. Bonaccorso, Few-Layer MoS2Flakes as Active Buffer Layer for Stable Perovskite Solar Cells, Advanced Energy Materials, 6 (2016) 1600920.
[421] D. Li, A.E. Del Rio Castillo, H. Jussila, G. Ye, Z. Ren, J. Bai, X. Chen, H. Lipsanen, Z. Sun, F. Bonaccorso, Black phosphorus polycarbonate polymer composite for pulsed fibre lasers, Applied Materials Today, 4 (2016) 17-23.
[422] S.V. Morozov, K.S. Novoselov, M.I. Katsnelson, F. Schedin, L.A. Ponomarenko, D. Jiang, A.K. Geim, Strong suppression of weak localization in graphene, Physical Review Letters, 97 (2006) 016801.
[423] I.S. Khattab, F. Bandarkar, M.A.A. Fakhree, A. Jouyban, Density, viscosity, and surface tension of water+ethanol mixtures from 293 to 323K, Korean Journal of Chemical Engineering, 29 (2012) 812-817.
[424] Z. Gholamvand, D. McAteer, A. Harvey, C. Backes, J.N. Coleman, Electrochemical Applications of Two-Dimensional Nanosheets: The Effect of Nanosheet Length and Thickness, Chemistry of Materials, 28 (2016) 2641-2651.
[425] V. Vega-Mayoral, C. Backes, D. Hanlon, U. Khan, Z. Gholamvand, M. O'Brien, G.S. Duesberg, C. Gadermaier, J.N. Coleman, Photoluminescence from Liquid-Exfoliated WS2 Monomers in Poly(Vinyl Alcohol) Polymer Composites, Advanced Functional Materials, 26 (2016) 1028-1039.
[426] H. Sun, A. Varzi, V. Pellegrini, D.A. Dinh, R. Raccichini, A.E. Del Rio-Castillo, M. Prato, M. Colombo, R. Cingolani, B. Scrosati, S. Passerini, F. Bonaccorso, How much does size really matter? Exploring the limits of graphene as Li ion battery anode material, Solid State Communications, 251 (2017) 88-93.
[427] A.H. Woomer, T.W. Farnsworth, J. Hu, R.A. Wells, C.L. Donley, S.C. Warren, Phosphorene: Synthesis, Scale-Up, and Quantitative Optical Spectroscopy, ACS Nano, 9 (2015) 8869-8884.
[428] S.O. Majekodunmi, A Review on Centrifugation in the Pharmaceutical Industry, American Journal of Biomedical Engineering, 5 (2015) 67-78.
[429] J.W. Williams, K.E. Van Holde, R.L. Baldwin, H. Fujita, The Theory Of Sedimentation Analysis, Chemical Reviews, 58 (1958) 715-744.
[430] L. Bildirici, D. Rickwood, Fractionation of differentiating cells using density perturbation, Journal of Immunological Methods, 240 (2000) 93-99.
[431] D. Patel, D. Rickwood, Optimization of conditions for specific binding of antibody-coated beads to cells, Journal of Immunological Methods, 184 (1995) 71-80.
[432] M.G. Cacace, E.M. Landau, J.J. Ramsden, The Hofmeister series: salt and solvent effects on interfacial phenomena, Quarterly Reviews of Biophysics, 30 (1997) 241-277.
[433] K.D. Collins, M.W. Washabaugh, The Hofmeister effect and the behaviour of water at interfaces, Quarterly Reviews of Biophysics, 18 (1985) 323.
[434] M. Kaminsky, Ion-solvent interaction and the viscosity of strong-electrolyte solutions, Discussions of the Faraday Society, 24 (1957) 171.
[435] D.H. Coombs, N.R.M. Watts, Generating sucrose gradients in three minutes by tilted tube rotation, Analytical Biochemistry, 148 (1985) 254-259.

[436] M.K. Brakke, J.M. Daly, Density-Gradient Centrifugation: Non-Ideal Sedimentation and the Interaction of Major and Minor Components, Science, 148 (1965) 387-389.
[437] R. Cohen, J.-M. Claverie, Sedimentation of generalized systems of interacting particles. II. Active enzyme centrifugation?theory and extensions of its validity range, Biopolymers, 14 (1975) 1701-1716.
[438] G. Smale, J. Sasse, RNA isolation from cartilage using density gradient centrifugation in cesium trifluoroacetate: An RNA preparation technique effective in the presence of high proteoglycan content, Analytical Biochemistry, 203 (1992) 352-356.
[439] M.S. Arnold, A.A. Green, J.F. Hulvat, S.I. Stupp, M.C. Hersam, Sorting carbon nanotubes by electronic structure using density differentiation, Nature Nanotechnology, 1 (2006) 60-65.
[440] M.S. Arnold, S.I. Stupp, M.C. Hersam, Enrichment of Single-Walled Carbon Nanotubes by Diameter in Density Gradients, Nano Letters, 5 (2005) 713-718.
[441] F. Bonaccorso, T. Hasan, P.H. Tan, C. Sciascia, G. Privitera, G. Di Marco, P.G. Gucciardi, A.C. Ferrari, Density Gradient Ultracentrifugation of Nanotubes: Interplay of Bundling and Surfactants Encapsulation, The Journal of Physical Chemistry C, 114 (2010) 17267-17285.
[442] O.V. Vieira, J.A.N. Laranjinha, V.M.C. Madeira, L.M. Almeida, Rapid isolation of low density lipoproteins in a concentrated fraction free from water-soluble plasma antioxidants The Journal of Lipid Research, 37 2715-2721.
[443] F. Bonaccorso, Debundling and Selective Enrichment of SWNTs for Applications in Dye-Sensitized Solar Cells, International Journal of Photoenergy, 2010 (2010) 1-14.
[444] S. Li, F. Zhu, F. Meng, H. Li, L. Wang, J. Zhao, Q. Yue, J. Liu, J. Jia, Separation of graphene oxide by density gradient centrifugation and study on their morphology-dependent electrochemical properties, Journal of Electroanalytical Chemistry, 703 (2013) 135-145.
[445] J. Kang, J.-W.T. Seo, D. Alducin, A. Ponce, M.J. Yacaman, M.C. Hersam, Thickness sorting of two-dimensional transition metal dichalcogenides via copolymer-assisted density gradient ultracentrifugation, Nature Communications, 5 (2014) 5478.
[446] J. Zhu, J. Kang, J. Kang, D. Jariwala, J.D. Wood, J.-W.T. Seo, K.-S. Chen, T.J. Marks, M.C. Hersam, Solution-Processed Dielectrics Based on Thickness-Sorted Two-Dimensional Hexagonal Boron Nitride Nanosheets, Nano Letters, 15 (2015) 7029-7036.
[447] J. Kang, V.K. Sangwan, J.D. Wood, X. Liu, I. Balla, D. Lam, M.C. Hersam, Layer-by-Layer Sorting of Rhenium Disulfide via High-Density Isopycnic Density Gradient Ultracentrifugation, Nano Letters, 16 (2016) 7216-7223.
[448] M.K. Brakke, Zonal separations by density-gradient centrifugation, Archives of Biochemistry and Biophysics, 45 (1953) 275-290.
[449] X. Sun, D. Luo, J. Liu, D.G. Evans, Monodisperse Chemically Modified Graphene Obtained by Density Gradient Ultracentrifugal Rate Separation, ACS Nano, 4 (2010) 3381-3389.
[450] A. Huebler, U. Hahn, W. Beier, N. Lasch, T. Fischer, High volume printing technologies for the production of polymer electronic structures, 2nd International IEEE Conference on Polymers and Adhesives in Microelectronics and Photonics. POLYTRONIC 2002. Conference Proceedings (Cat. No.02EX599), IEEE.
[451] T. Kawahara, Journal of Sol-Gel Science and Technology, 27 (2003) 301-307.
[452] F.K. M. Bergsmann, G. Bauer, R. Domnick, H. Walter, The 46th Annual Technical Conference — Society of the Vacuum Coaters, San Francisco, USA., May 4–8, 2003, 46th Annual Technical Conference Proceedings, 2003, p. 566, 46th Annual Technical Conference Proceedings, 2003, p. 566, DOI (2003) 14.
[453] A. Maaninen, M. Tuomikoski, L. Kivimäki, T. Kololuoma, M. Välimäki, M. Leinonen, M. Känsäkoski, Roll to roll fabrication technologies for optoelectronic and electronic devices and sensors, Integrated Optics: Theory and Applications, SPIE, 2005.
[454] H. Sirringhaus, Device physics and reliability of solution processed organic TFTs. Flexidis Training Workshop, Stuttgart, Germany, 2006., DOI.
[455] M.S. Schrödner, K.; Stohn, R.; Schache H.; Blankenburg, L.; Roth, H., Technologies for Polymer Electronics, Frankfurt, Germany, 2006., DOI.

[456] A. Blayo, B. Pineaux, Printing processes and their potential for RFID printing, Proceedings of the 2005 joint conference on Smart objects and ambient intelligence innovative context-aware services: usages and technologies - sOc-EUSAI '05, ACM Press, 2005.
[457] G.E. Jabbour, R. Radspinner, N. Peyghambarian, Screen printing for the fabrication of organic light-emitting devices, IEEE Journal of Selected Topics in Quantum Electronics, 7 (2001) 769-773.
[458] J. Park, J. Moon, Control of Colloidal Particle Deposit Patterns within Picoliter Droplets Ejected by Ink-Jet Printing, Langmuir, 22 (2006) 3506-3513.
[459] A. Pekarovicova, V. Husovska, Printing Ink Formulations, Printing on Polymers, Elsevier, 2016, pp. 41-55.
[460] The colloidal domain: where physics, chemistry, biology, and technology meet, Choice Reviews Online, 37 (1999) 37-0334-0337-0334.
[461] D.S. Viswanath, T.K. Ghosh, D.H.L. Prasad, N.V.K. Dutt, K.Y. Rani, CORRELATIONS AND ESTIMATION OF PURE LIQUID VISCOSITY, Viscosity of Liquids, Springer Netherlands, pp. 135-405.
[462] N. Willenbacher, K. Georgieva, Rheology of Disperse Systems, Product Design and Engineering, Wiley-VCH Verlag GmbH & Co. KGaA, 2013, pp. 7-49.
[463] P.C. Hiemenz, R. Rajagopalan, Principles of Colloid and Surface Chemistry, CRC Press1997.
[464] J. Garg, B. Poudel, M. Chiesa, J.B. Gordon, J.J. Ma, J.B. Wang, Z.F. Ren, Y.T. Kang, H. Ohtani, J. Nanda, G.H. McKinley, G. Chen, Enhanced thermal conductivity and viscosity of copper nanoparticles in ethylene glycol nanofluid, Journal of Applied Physics, 103 (2008) 074301.
[465] I.M. Mahbubul, R. Saidur, M.A. Amalina, Latest developments on the viscosity of nanofluids, International Journal of Heat and Mass Transfer, 55 (2012) 874-885.
[466] P.C. Mishra, S. Mukherjee, S.K. Nayak, A. Panda, A brief review on viscosity of nanofluids, International Nano Letters, 4 (2014) 109-120.
[467] S. Bose, S.S. Keller, T.S. Alstrøm, A. Boisen, K. Almdal, Process Optimization of Ultrasonic Spray Coating of Polymer Films, Langmuir, 29 (2013) 6911-6919.
[468] L.-L. Xing, J.E. Glass, R.H. Fernando, Spray Application of Waterborne Coatings, ACS Symposium Series, American Chemical Society, 1997, pp. 265-295.
[469] J.W. Owen, N.A. Azarova, M.A. Loth, M. Paradinas, M. Coll, C. Ocal, J.E. Anthony, O.D. Jurchescu, Effect of Processing Parameters on Performance of Spray-Deposited Organic Thin-Film Transistors, Journal of Nanotechnology, 2011 (2011) 1-6.
[470] G. Perfetti, T. Alphazan, P. van Hee, W.J. Wildeboer, G.M.H. Meesters, Relation between surface roughness of free films and process parameters in spray coating, European Journal of Pharmaceutical Sciences, 42 (2011) 262-272.
[471] M. Singh, H.M. Haverinen, P. Dhagat, G.E. Jabbour, Inkjet Printing-Process and Its Applications, Advanced Materials, 22 (2010) 673-685.
[472] V. Bergeron, D. Bonn, J.Y. Martin, L. Vovelle, Nature, 405 (2000) 772-775.
[473] L.C. Squire, An Introduction to Fluid Dynamics. G. K. Batchelor. Cambridge University Press. 1967. 616 pp. Figures. 15s, Journal of the Royal Aeronautical Society, 71 (1967) 801-802.
[474] B.-J. de Gans, E. Kazancioglu, W. Meyer, U.S. Schubert, Ink-jet Printing Polymers and Polymer Libraries Using Micropipettes, Macromolecular Rapid Communications, 25 (2004) 292-296.
[475] H. Dong, W.W. Carr, J.F. Morris, An experimental study of drop-on-demand drop formation, Physics of Fluids, 18 (2006) 072102.
[476] J.E. Fromm, Numerical Calculation of the Fluid Dynamics of Drop-on-Demand Jets, IBM Journal of Research and Development, 28 (1984) 322-333.
[477] W.-K. Hsiao, S.D. Hoath, G.D. Martin, I.M. Hutchings, Ink Jet Printing for Direct Mask Deposition in Printed Circuit Board Fabrication, Journal of Imaging Science and Technology, 53 (2009) 050304.
[478] D. Jang, D. Kim, J. Moon, Influence of Fluid Physical Properties on Ink-Jet Printability, Langmuir, 25 (2009) 2629-2635.
[479] S. Jung, I.M. Hutchings, The impact and spreading of a small liquid drop on a non-porous substrate over an extended time scale, Soft Matter, 8 (2012) 2686.
[480] P. Shin, J. Sung, M.H. Lee, Control of droplet formation for low viscosity fluid by double waveforms applied to a piezoelectric inkjet nozzle, Microelectronics Reliability, 51 (2011) 797-804.

[481] T.H.J. van Osch, J. Perelaer, A.W.M. de Laat, U.S. Schubert, Inkjet Printing of Narrow Conductive Tracks on Untreated Polymeric Substrates, Advanced Materials, 20 (2008) 343-345.
[482] J. Perelaer, B.J. de Gans, U.S. Schubert, Ink-jet Printing and Microwave Sintering of Conductive Silver Tracks, Advanced Materials, 18 (2006) 2101-2104.
[483] P.G. de Gennes, Wetting: statics and dynamics, Reviews of Modern Physics, 57 (1985) 827-863.
[484] R.E. Saunders, B. Derby, Inkjet printing biomaterials for tissue engineering: bioprinting, International Materials Reviews, 59 (2014) 430-448.
[485] J. Baker, D. Deganello, D.T. Gethin, T.M. Watson, Flexographic printing of graphene nanoplatelet ink to replace platinum as counter electrode catalyst in flexible dye sensitised solar cell, Materials Research Innovations, 18 (2014) 86-90.
[486] E.B. Secor, S. Lim, H. Zhang, C.D. Frisbie, L.F. Francis, M.C. Hersam, Gravure Printing of Graphene for Large-area Flexible Electronics, Advanced Materials, 26 (2014) 4533-4538.
[487] K. Yamazaki, Report on 1993 TAPPI Coating Conference, JAPAN TAPPI JOURNAL, 47 (1993) 1213-1222.
[488] Y.-J. Kim, H. Yoo, C.-H. Lee, J.B. Park, H. Baek, M. Kim, G.-C. Yi, Position- and Morphology-Controlled ZnO Nanostructures Grown on Graphene Layers, Advanced Materials, 24 (2012) 5565-5569.
[489] W.J. Hyun, E.B. Secor, G.A. Rojas, M.C. Hersam, L.F. Francis, C.D. Frisbie, All-Printed, Foldable Organic Thin-Film Transistors on Glassine Paper, Advanced Materials, 27 (2015) 7058-7064.
[490] B. Liu, S. Wang, Preparation of patterned biological film for nanolithography, Journal of Biosensors & Bioelectronics, 01 (2012).
[491] M. Qian, T. Feng, H. Ding, L. Lin, H. Li, Y. Chen, Z. Sun, Electron field emission from screen-printed graphene films, Nanotechnology, 20 (2009) 425702.
[492] D.W. Zhang, X.D. Li, H.B. Li, S. Chen, Z. Sun, X.J. Yin, S.M. Huang, Graphene-based counter electrode for dye-sensitized solar cells, Carbon, 49 (2011) 5382-5388.
[493] G. Wróblewski, D. Janczak, Screen printed, transparent, and flexible electrodes based on graphene nanoplatelet pastes, Photonics Applications in Astronomy, Communications, Industry, and High-Energy Physics Experiments 2012, SPIE, 2012.
[494] Y. Xu, M.G. Schwab, A.J. Strudwick, I. Hennig, X. Feng, Z. Wu, K. Müllen, Screen-Printable Thin Film Supercapacitor Device Utilizing Graphene/Polyaniline Inks, Advanced Energy Materials, 3 (2013) 1035-1040.
[495] K. Arapov, E. Rubingh, R. Abbel, J. Laven, G. de With, H. Friedrich, Conductive Screen Printing Inks by Gelation of Graphene Dispersions, Advanced Functional Materials, 26 (2015) 586-593.
[496] R. L. Whistler and J. N. BeMiller, Industrial Gums : Polysaccharides and Their Derivatives Academic Press, 1993, (1993) 558-559.
[497] R. Secco, M. Kostic, J. deBruyn, Fluid Viscosity Measurement, Measurement, Instrumentation, and Sensors Handbook, Second Edition, CRC Press, 2014, pp. 1-31.
[498] T.G. Mezger, The Rheology Handbook: For Users of Rotational and Oscillatory Rheometers, Vincentz Network2006.
[499] A. Benchabane, K. Bekkour, Rheological properties of carboxymethyl cellulose (CMC) solutions, Colloid and Polymer Science, 286 (2008) 1173-1180.
[500] K. Nijenhuis, G. McKinley, S. Spiegelberg, H. Barnes, N. Aksel, L. Heymann, J. Odell, Non-Newtonian Flows, Springer Handbook of Experimental Fluid Mechanics, Springer Berlin Heidelberg, 2007, pp. 619-743.
[501] F. Irgens, Rheology and Non-Newtonian Fluids, Springer International Publishing, 2014.
[502] E.H. deButts, J.A. Hudy, J.H. Elliott, Rheology of Sodium Carboxymethylcellulose Solutions, Industrial & Engineering Chemistry, 49 (1957) 94-98.
[503] J.H. Elliot, A.J. Ganz, Some rheological properties of sodium carboxymethylcellulose solutions and gels, Rheologica Acta, 13 (1974) 670-674.
[504] P. Robaeys, F. Bonaccorso, E. Bourgeois, J. D'Haen, W. Dierckx, W. Dexters, D. Spoltore, J. Drijkoningen, J. Liesenborgs, A. Lombardo, A.C. Ferrari, F. Van Reeth, K. Haenen, J.V. Manca, M.

Nesladek, Enhanced performance of polymer:fullerene bulk heterojunction solar cells upon graphene addition, Applied Physics Letters, 105 (2014) 083306.
[505] L. Hu, H.S. Kim, J.-Y. Lee, P. Peumans, Y. Cui, Scalable Coating and Properties of Transparent, Flexible, Silver Nanowire Electrodes, ACS Nano, 4 (2010) 2955-2963.
[506] B. Dan, G.C. Irvin, M. Pasquali, Continuous and Scalable Fabrication of Transparent Conducting Carbon Nanotube Films, ACS Nano, 3 (2009) 835-843.
[507] Z. Liu, K. Parvez, R. Li, R. Dong, X. Feng, K. Müllen, Transparent Conductive Electrodes from Graphene/PEDOT:PSS Hybrid Inks for Ultrathin Organic Photodetectors, Advanced Materials, 27 (2014) 669-675.
[508] Z. Liu, Z.-S. Wu, S. Yang, R. Dong, X. Feng, K. Müllen, Ultraflexible In-Plane Micro-Supercapacitors by Direct Printing of Solution-Processable Electrochemically Exfoliated Graphene, Advanced Materials, 28 (2016) 2217-2222.
[509] C.A. Zaugg, Z. Sun, V.J. Wittwer, D. Popa, S. Milana, T.S. Kulmala, R.S. Sundaram, M. Mangold, O.D. Sieber, M. Golling, Y. Lee, J.H. Ahn, A.C. Ferrari, U. Keller, Ultrafast and widely tuneable vertical-external-cavity surface-emitting laser, mode-locked by a graphene-integrated distributed Bragg reflector, Opt. Express, 21 (2013) 31548-31559.
[510] V. Bianchi, T. Carey, L. Viti, L. Li, E.H. Linfield, A.G. Davies, A. Tredicucci, D. Yoon, P.G. Karagiannidis, L. Lombardi, F. Tomarchio, A.C. Ferrari, F. Torrisi, M.S. Vitiello, Terahertz saturable absorbers from liquid phase exfoliation of graphite, Nature Communications, 8 (2017) 15763.
[511] T.M. Higgins, D. McAteer, J.C.M. Coelho, B.M. Sanchez, Z. Gholamvand, G. Moriarty, N. McEvoy, N.C. Berner, G.S. Duesberg, V. Nicolosi, J.N. Coleman, Effect of Percolation on the Capacitance of Supercapacitor Electrodes Prepared from Composites of Manganese Dioxide Nanoplatelets and Carbon Nanotubes, ACS Nano, 8 (2014) 9567-9579.
[512] D. McAteer, Z. Gholamvand, N. McEvoy, A. Harvey, E. O'Malley, G.S. Duesberg, J.N. Coleman, Thickness Dependence and Percolation Scaling of Hydrogen Production Rate in MoS2 Nanosheet and Nanosheet-Carbon Nanotube Composite Catalytic Electrodes, ACS Nano, 10 (2016) 672-683.
[513] D. Purdie, D. Popa, V.J. Wittwer, Z. Jiang, F. Torrisi, A.C. Ferrari, Sub-50 fs compressed pulses from a graphene-mode locked fiber laser, CLEO: 2014, OSA, 2014.
[514] Z. Jiang, G.E. Bonacchini, D. Popa, F. Torrisi, A.K. Ott, V.J. Wittwer, D. Purdie, A.C. Ferrari, Graphene saturable absorber power scaling laser, CLEO: 2014, OSA, 2014.
[515] R. Yingying, G. Brown, R. Mary, G. Demetriou, D. Popa, F. Torrisi, A.C. Ferrari, C. Feng, A.K. Kar, 7.8-GHz Graphene-Based 2-μm Monolithic Waveguide Laser, IEEE Journal of Selected Topics in Quantum Electronics, 21 (2015) 395-400.
[516] D.A. Dikin, S. Stankovich, E.J. Zimney, R.D. Piner, G.H.B. Dommett, G. Evmenenko, S.T. Nguyen, R.S. Ruoff, Preparation and characterization of graphene oxide paper, Nature, 448 (2007) 457-460.
[517] D.J. Finn, M. Lotya, G. Cunningham, R.J. Smith, D. McCloskey, J.F. Donegan, J.N. Coleman, Inkjet deposition of liquid-exfoliated graphene and MoS2nanosheets for printed device applications, J. Mater. Chem. C, 2 (2014) 925-932.
[518] B. Kim, S. Jang, M.L. Geier, P.L. Prabhumirashi, M.C. Hersam, A. Dodabalapur, High-Speed, Inkjet-Printed Carbon Nanotube/Zinc Tin Oxide Hybrid Complementary Ring Oscillators, Nano Letters, 14 (2014) 3683-3687.
[519] E.B. Secor, P.L. Prabhumirashi, K. Puntambekar, M.L. Geier, M.C. Hersam, Inkjet Printing of High Conductivity, Flexible Graphene Patterns, The Journal of Physical Chemistry Letters, 4 (2013) 1347-1351.
[520] Novacentrix, http://www.novacentrix.com.
[521] A. Rinaldi, A. Proietti, A. Tamburrano, G. De Bellis, M. Mulattieri, M.S. Sarto, Multilayer Graphene-based films for strain sensing, 14th IEEE International Conference on Nanotechnology, IEEE, 2014.
[522] A. Bessonov, M. Kirikova, S. Haque, I. Gartseev, M.J.A. Bailey, Highly reproducible printable graphite strain gauges for flexible devices, Sensors and Actuators A: Physical, 206 (2014) 75-80.
[523] M.-H. Bao, Capacitive pressure transducers and accelerometers, Micro Mechanical Transducers - Pressure Sensors, Accelerometers and Gyroscopes, Elsevier, 2000, pp. 319-352.

[524] C. Zlebic, L. Zivanov, A. Menicanin, N. Blaz, M. Damnjanovic, Inkjet printed resistive strain gages on flexible substrates, Facta universitatis - series: Electronics and Energetics, 29 (2016) 89-100.
[525] D. McManus, S. Vranic, F. Withers, V. Sanchez-Romaguera, M. Macucci, H. Yang, R. Sorrentino, K. Parvez, S.-K. Son, G. Iannaccone, K. Kostarelos, G. Fiori, C. Casiraghi, Water-based and biocompatible 2D crystal inks for all-inkjet-printed heterostructures, Nature Nanotechnology, 12 (2017) 343.
[526] P. Sommer-Larsen, M. Jørgensen, R.R. Søndergaard, M. Hösel, F.C. Krebs, It is all in the Pattern-High-Efficiency Power Extraction from Polymer Solar Cells through High-Voltage Serial Connection, Energy Technology, 1 (2013) 15-19.
[527] F.C. Krebs, N. Espinosa, M. Hösel, R.R. Søndergaard, M. Jørgensen, 25th Anniversary Article: Rise to Power - OPV-Based Solar Parks, Advanced Materials, 26 (2013) 29-39.
[528] D.H. Lee, J.S. Choi, H. Chae, C.H. Chung, S.M. Cho, Screen-printed white OLED based on polystyrene as a host polymer, Current Applied Physics, 9 (2009) 161-164.
[529] S. Jung, S.D. Hoath, G.D. Martin, I.M. Hutchings, Inkjet Printing Process for Large Area Electronics, Large Area and Flexible Electronics, Wiley-VCH Verlag GmbH & Co. KGaA2015, pp. 315-344.
[530] S. Khan, L. Lorenzelli, R.S. Dahiya, Technologies for Printing Sensors and Electronics Over Large Flexible Substrates: A Review, IEEE Sensors Journal, 15 (2015) 3164-3185.
[531] D. Tobjörk, R. Österbacka, Paper Electronics, Advanced Materials, 23 (2011) 1935-1961.
[532] S. Merilampi, T. Laine-Ma, P. Ruuskanen, The characterization of electrically conductive silver ink patterns on flexible substrates, Microelectronics Reliability, 49 (2009) 782-790.
[533] J.W. Birkenshaw, Printing processes, The Printing Ink Manual, Springer Netherlands, pp. 14-85.
[534] W.J. Hyun, S. Lim, B.Y. Ahn, J.A. Lewis, C.D. Frisbie, L.F. Francis, Screen Printing of Highly Loaded Silver Inks on Plastic Substrates Using Silicon Stencils, ACS Applied Materials & Interfaces, 7 (2015) 12619-12624.
[535] S. Abbott, T. Church, D. Parker, A. Harris, How to be a great Screen printer, in: S. Abbott (Ed.), MacDermid Autotype Ltd, 2008.
[536] Novalia, http://www.audioposter.com/.
[537] V.L. Nguyen, B.G. Shin, D.L. Duong, S.T. Kim, D. Perello, Y.J. Lim, Q.H. Yuan, F. Ding, H.Y. Jeong, H.S. Shin, S.M. Lee, S.H. Chae, Q.A. Vu, S.H. Lee, Y.H. Lee, Seamless Stitching of Graphene Domains on Polished Copper (111) Foil, Advanced Materials, 27 (2014) 1376-1382.
[538] C. Berger, Z.M. Song, T.B. Li, X.B. Li, A.Y. Ogbazghi, R. Feng, Z.T. Dai, A.N. Marchenkov, E.H. Conrad, P.N. First, W.A. De Heer, Ultrathin epitaxial graphite: 2D electron gas properties and a route toward graphene-based nanoelectronics, J Phys Chem B, 108 (2004) 19912-19916.
[539] C. Berger, E.H. Conrad, W.A. de Heer, Epigraphene, in: P. Chiaradia, G. Chiarotti (Eds.) Landolt-Borstein2016.
[540] A.J. Van Bommel, J.E. Crobeen, A. Van Tooren, LEED and Auger electron observations of the SiC(0001) surface, Surf. Sci., 48 (1975) 463-472.
[541] W.A. de Heer, C. Berger, P.N. First, Patterned thin films graphite devices and methods for making the same, US patent 7015142, (provisional Application No.60/477,997 filed June 12 2003, Issued March 21 2006), DOI (provisional Application No.60/477,997 filed June 12 2003, Issued March 21 2006).
[542] C. Virojanadara, M. Syvajarvi, R. Yakimova, L.I. Johansson, A.A. Zakharov, T. Balasubramanian, Homogeneous large-area graphene layer growth on 6H-SiC(0001), Physical Review B, 78 (2008).
[543] K.V. Emtsev, A. Bostwick, K. Horn, J. Jobst, G.L. Kellogg, L. Ley, J.L. McChesney, T. Ohta, S.A. Reshanov, J. Rohrl, E. Rotenberg, A.K. Schmid, D. Waldmann, H.B. Weber, T. Seyller, Towards wafer-size graphene layers by atmospheric pressure graphitization of silicon carbide, Nature Materials, 8 (2009) 203-207.
[544] F. Varchon, R. Feng, J. Hass, X. Li, B. Ngoc Nguyen, C. Naud, P. Mallet, J.-Y. Veuillen, C. Berger, E.H. Conrad, L. Magaud, Electronic structure of epitaxial graphene layers on SiC: effect of the substrate, Physical Review Letters, 99 (2007) 126805

[545] M.S. Nevius, M. Conrad, F. Wang, A. Celis, M.N. Nair, A. Taleb-Ibrahimi, A. Tejeda, E.H. Conrad, Semiconducting Graphene from Highly Ordered Substrate Interactions, Physical Review Letters, 115 (2015) 136802.
[546] K.V. Emtsev, F. Speck, T. Seyller, L. Ley, J.D. Riley, Interaction, growth, and ordering of epitaxial graphene on SiC{0001} surfaces: A comparative photoelectron spectroscopy study, Physical Review B, 77 (2008) 155303
[547] G.M. Rutter, N.P. Guisinger, J.N. Crain, E.A.A. Jarvis, M.D. Stiles, T. Li, P.N. First, J.A. Stroscio, Imaging the interface of epitaxial graphene with silicon carbide via scanning tunneling microscopy, Physical Review B, 76 (2007) 235416.
[548] J. Hass, W.A. de Heer, E.H. Conrad, The growth and morphology of epitaxial multilayer graphene, J Phy C: Cond Mat, 20 (2008) 323202.
[549] W.A. de Heer, C. Berger, M. Ruan, M. Sprinkle, X. Li, Y. Hu, B. Zhang, J. Hankinson, E.H. Conrad, Large area and structured epitaxial graphene produced by confinement controlled sublimation of silicon carbide, Proc Nat Acad Sci, 108 (2011) 16900-16905.
[550] C. Coletti, S. Forti, A. Principi, K.V. Emtsev, A.A. Zakharov, K.M. Daniels, B.K. Daas, M.V.S. Chandrashekhar, T. Ouisse, D. Chaussende, A.H. MacDonald, M. Polini, U. Starke, Revealing the electronic band structure of trilayer graphene on SiC: An angle-resolved photoemission study, Physical Review B, 88 (2013) 155439.
[551] J. Hass, F. Varchon, J.E. Millan-Otoya, M. Sprinkle, N. Sharma, W.A. De Heer, C. Berger, P.N. First, L. Magaud, E.H. Conrad, Why multilayer graphene on 4H-SiC(000(1)over-bar) behaves like a single sheet of graphene, Physical Review Letters, 100 (2008) 125504.
[552] D.L. Miller, K.D. Kubista, G.M. Rutter, M. Ruan, W.A. de Heer, P.N. First, J.A. Stroscio, Structural analysis of multilayer graphene via atomic moireacute interferometry, Physical Review B, 81 (2010) 223108.
[553] M. Hupalo, E.H. Conrad, M.C. Tringides, Growth mechanism for epitaxial graphene on vicinal $6H\text{-SiC}(0001)$ surfaces: A scanning tunneling microscopy study, Physical Review B, 80 (2009) 041401.
[554] V. Borovikov, A. Zangwill, Step-edge instability during epitaxial growth of graphene from SiC(0001), Physical Review B, 80 (2009) 121406 R
[555] T. Ohta, N.C. Bartelt, S. Nie, K. Thurmer, G.L. Kellogg, Role of carbon surface diffusion on the growth of epitaxial graphene on SiC, Physical Review B, 81 (2010) 121411 R
[556] Y. Hu, M. Ruan, Z.L. Guo, R. Dong, J. Palmer, J. Hankinson, C. Berger, W.A. de Heer, Structured epitaxial graphene: growth and properties, J. Phys D, 45 (2012) 154010.
[557] J.K. Hite, M.E. Twigg, J.L. Tedesco, A.L. Friedman, R.L. Myers-Ward, C.R. Eddy, D.K. Gaskill, Epitaxial Graphene Nucleation on C-Face Silicon Carbide, Nano Letters, 11 (2011) 1190-1194.
[558] R. Zhang, Y.L. Dong, W.J. Kong, W.P. Han, P.H. Tan, Z.M. Liao, X.S. Wu, D.P. Yu, Growth of large domain epitaxial graphene on the C-face of SiC, Journal of Applied Physics, 112 (2012) 104307.
[559] G.R. Yazdi, T. Iakimov, R. Yakimova, Epitaxial Graphene on SiC: A Review of Growth and Characterization, Crystals, 6 (2016) 53.
[560] P. Råback, R. Yakimova, M. Syväjärvi, R. Nieminen, E. Janzén, A practical model for estimating the growth rate in sublimation growth of SiC, Materials Science and Engineering: B, 61-62 (1999) 89-92.
[561] R.M. Tromp, J.B. Hannon, Thermodynamics and Kinetics of Graphene Growth on SiC(0001), Physical Review Letters, 102 (2009) 106104.
[562] C. Riedl, U. Starke, J. Bernhardt, M. Franke, K. Heinz, Structural properties of the graphene-SiC(0001) interface as a key for the preparation of homogeneous large-terrace graphene surfaces, Physical Review B, 76 (2007) 245406.
[563] W. Strupinski, K. Grodecki, A. Wysmolek, R. Stepniewski, T. Szkopek, P.E. Gaskell, A. Gruneis, D. Haberer, R. Bozek, J. Krupka, J.M. Baranowski, Graphene Epitaxy by Chemical Vapor Deposition on SiC, Nano Letters, 11 (2011) 1786-1791.
[564] F. Lafont, R. Ribeiro-Palau, D. Kazazis, A. Michon, O. Couturaud, C. Consejo, T. Chassagne, M. Zielinski, M. Portail, B. Jouault, F. Schopfer, W. Poirier, Quantum Hall resistance standards from

graphene grown by chemical vapour deposition on silicon carbide, Nature Communications, 6 (2015) 6806.
[565] M. Ostler, F. Speck, M. Gick, T. Seyller, Automated preparation of high-quality epitaxial graphene on 6H-SiC(0001), Physica Status Solidi B-Basic Solid State Physics, 247 (2010) 2924-2926.
[566] R. Yakimova, C. Virojanadara, D. Gogova, M. Syvajarvi, D. Siche, K. Larsson, L.I. Johansson, Analysis of the Formation Conditions for Large Area Epitaxial Graphene on SiC Substrates, Mater Sci Forum, 645-648 (2010) 565-568.
[567] C. Berger, D. Deniz, J. Gigliotti, J. Palmer, J. Hankinson, Y. Hu, J.-P. Turmaud, R. Puybaret, A. Ougazzaden, A. Sidorov, Z. Jiang, W.A. de Heer, Epitaxial graphene on SiC: 2D sheets, selective growth and nanoribbons, in: C.C. N. Motta, F. Iacopi (Ed.) Growing graphene on semiconductors, PanStanford. arXiv:1611.089372016.
[568] J. Palmer, Pre-growth structures for nanoelectronics of EG on SiC, School of Physics - Georgia Inst. Techn, 2014
[569] N. Camara, J.R. Huntzinger, G. Rius, A. Tiberj, N. Mestres, F. Perez-Murano, P. Godignon, J. Camassel, Anisotropic growth of long isolated graphene ribbons on the C face of graphite-capped 6H-SiC, Physical Review B, 80 (2009) 125410.
[570] M. Sprinkle, M. Ruan, Y. Hu, J. Hankinson, M. Rubio-Roy, B. Zhang, X. Wu, C. Berger, W.A. de Heer, Scalable templated growth of graphene nanoribbons on SiC, Nature Nanotechnology, 5 (2010) 727-731.
[571] M. Ruan, Structured epitaxial graphene for electronics, School of Physics, PhD - Georgia Institute of Technology, Atlanta, 2012.
[572] J. Baringhaus, M. Ruan, F. Edler, A. Tejeda, M. Sicot, A. Taleb-Ibrahimi, A.P. Li, Z.G. Jiang, E.H. Conrad, C. Berger, C. Tegenkamp, W.A. de Heer, Exceptional ballistic transport in epitaxial graphene nanoribbons, Nature, 506 (2014) 349-354.
[573] X. Li, Epitaxial graphene films on SiC: growth, characterization, and devices, School of Physics, PhD, Georgia Institute of Technology, 2008.
[574] C. Berger, Z.M. Song, X.B. Li, X.S. Wu, N. Brown, C. Naud, D. Mayou, T.B. Li, J. Hass, A.N. Marchenkov, E.H. Conrad, P.N. First, W.A. de Heer, Electronic confinement and coherence in patterned epitaxial graphene, Science, 312 (2006) 1191-1196.
[575] J. Maysonnave, S. Huppert, F. Wang, S. Maero, C. Berger, W. de Heer, T.B. Norris, L.A. De Vaulchier, S. Dhillon, J. Tignon, R. Ferreira, J. Mangeney, Terahertz Generation by Dynamical Photon Drag Effect in Graphene Excited by Femtosecond Optical Pulses, Nano Letters, 14 (2014) 5797-5802.
[576] M.L. Sadowski, G. Martinez, M. Potemski, C. Berger, W.A. de Heer, Magnetospectroscopy of epitaxial few-layer graphene, Solid State Communications, 143 (2007) 123-125.
[577] X.S. Wu, Y.K. Hu, M. Ruan, N.K. Madiomanana, J. Hankinson, M. Sprinkle, C. Berger, W.A. de Heer, Half integer quantum Hall effect in high mobility single layer epitaxial graphene, Applied Physics Letters, 95 (2009) 223108.
[578] J. Hass, Structural characterization of epitaxial graphene on silicon carbide, School of Physics, PhD, Georgia Institute of Technology, 2008.
[579] D.L. Miller, K.D. Kubista, G.M. Rutter, M. Ruan, W.A. de Heer, P.N. First, J.A. Stroscio, Observing the Quantization of Zero Mass Carriers in Graphene, Science, 324 (2009) 924-927.
[580] Z.G. Cambaz, G. Yushin, S. Osswald, V. Mochalin, Y. Goyotsi, Noncatalytic synthesis of carbon nanotubes, graphene and graphite on SiC, Carbon, 46 (2008) 841-849.
[581] M. Orlita, C. Faugeras, R. Grill, A. Wysmolek, W. Strupinski, C. Berger, W.A. de Heer, G. Martinez, M. Potemski, Carrier Scattering from Dynamical Magnetoconductivity in Quasineutral Epitaxial Graphene, Physical Review Letters, 107 (2011) 216603.
[582] M. Sprinkle, D. Siegel, Y. Hu, J. Hicks, A. Tejeda, A. Taleb-Ibrahimi, P. Le Fevre, F. Bertran, S. Vizzini, H. Enriquez, S. Chiang, P. Soukiassian, C. Berger, W.A. de Heer, A. Lanzara, E.H. Conrad, First Direct Observation of a Nearly Ideal Graphene Band Structure, Physical Review Letters, 103 (2009) 226803.

[583] W.A. de Heer, C. Berger, X. Wu, Y. Hu, M. Ruan, J. Stroscio, P. First, R. Haddon, B. Piot, C. Faugeras, M. Potemski, Epitaxial Graphene Electronic Structure And Transport J Phys D: Appl Phys, 43 (2010) 374007.
[584] J. Kunc, Y. Hu, J. Palmer, C. Berger, W.A. de Heer, A method to extract pure Raman spectrum of epitaxial graphene on SiC, Applied Physics Letters, 103 (2013) 201911
[585] N. Levy, S.A. Burke, K.L. Meaker, M. Panlasigui, A. Zettl, F. Guinea, A.H.C. Neto, M.F. Crommie, Strain-Induced Pseudo-Magnetic Fields Greater Than 300 Tesla in Graphene Nanobubbles, Science, 329 (2010) 544-547.
[586] M. Orlita, C. Faugeras, P. Plochocka, P. Neugebauer, G. Martinez, D.K. Maude, A.L. Barra, M. Sprinkle, C. Berger, W.A. de Heer, M. Potemski, Approaching the Dirac Point in High-Mobility Multilayer Epitaxial Graphene, Physical Review Letters, 101 (2008) 267601.
[587] M.L. Sadowski, G. Martinez, M. Potemski, C. Berger, W.A. de Heer, Landau level spectroscopy of ultrathin graphite layers, Physical Review Letters, 97 (2006) 266405.
[588] A. Tzalenchuk, S. Lara-Avila, A. Kalaboukhov, S. Paolillo, M. Syvajarvi, R. Yakimova, O. Kazakova, T.J.B.M. Janssen, V. Fal'ko, S. Kubatkin, Towards a quantum resistance standard based on epitaxial graphene, Nature Nanotechnology, 5 (2010) 186-189.
[589] V. Borovikov, A. Zangwill, Step bunching of vicinal 6H-SiC{0001} surfaces, Physical Review B, 79 (2009) 121406(R).
[590] C. Chua, M. Connolly, A. Lartsev, T. Yager, S. Lara-Avila, S. Kubatkin, S. Kopylov, V. Fal'ko, R. Yakimova, R. Pearce, T. Janssen, A. Tzalenchuk, C.G. Smith, Quantum Hall Effect and Quantum Point Contact in Bilayer-Patched Epitaxial Graphene, Nano Letters, 14 (2014) 3369-3373.
[591] A. Michon, S. Vezian, E. Roudon, D. Lefebvre, M. Zielinski, T. Chassagne, M. Portail, Effects of pressure, temperature, and hydrogen during graphene growth on SiC(0001) using propane-hydrogen chemical vapor deposition, Journal of Applied Physics, 113 (2013) 203501.
[592] K. Mattias, P. Davood Momeni, P. Klaus, W. Stefan, S. Rainer, D. Thorsten, G. Martin, B. Jens, A. Johannes, T. Christoph, L. Jakob, S. Thomas, H. Frank, J.A. Franz, W.S. Hans, Comeback of epitaxial graphene for electronics: large-area growth of bilayer-free graphene on SiC, 2D Materials, 3 (2016) 041002.
[593] G.R. Yazdi, R. Vasiliauskas, T. Iakimov, A. Zakharov, M. Syvajarvi, R. Yakimova, Growth of large area monolayer graphene on 3C-SiC and a comparison with other SiC polytypes, Carbon, 57 (2013) 477-484.
[594] R. Yakimova, G.R. Yazdi, private commnication, DOI (2015).
[595] J. Palmer, J. Kunc, Y.K. Hu, J. Hankinson, Z.L. Guo, C. Berger, W.A. De Heer, Controlled epitaxial graphene growth within removable amorphous carbon corrals, Applied Physics Letters, 105 (2014) 023106.
[596] R. Yakimova, unpublished, DOI (2017).
[597] W. Norimatsu, M. Kusunoki, Growth of graphene from SiC{0001} surfaces and its mechanisms, Semicond. Sci. Technol., 29 (2014).
[598] C. Riedl, C. Coletti, T. Iwasaki, A.A. Zakharov, U. Starke, Quasi-Free-Standing Epitaxial Graphene on SiC Obtained by Hydrogen Intercalation, Physical Review Letters, 103 (2009) 246804.
[599] C. Riedl, C. Coletti, T. Iwasaki, U. Starke, Hydrogen intercalation below epitaxial graphene on SiC(0001), Materials Science Forum, 645-648 (2010) 623-628.
[600] C. Coletti, K.V. Emtsev, A.A. Zakharov, T. Ouisse, D. Chaussende, U. Starke, Large area quasi-free standing monolayer graphene on 3C-SiC(111), Applied Physics Letters, 99 (2011) 081904.
[601] M. Kruskopf, K. Pierz, S. Wundrack, R. Stosch, T. Dziomba, C.C. Kalmbach, A. Muller, J. Baringhaus, C. Tegenkamp, F.J. Ahlers, H.W. Schumacher, Epitaxial graphene on SiC: modification of structural and electron transport properties by substrate pretreatment, J Phy C: Cond Mat, 27 (2015) 185303
[602] I.G. Ivanov, J.U. Hassan, T. Iakimov, A.A. Zakharov, R. Yakimova, E. Janzen, Layer-number determination in graphene on SiC by reflectance mapping, Carbon, 77 (2014) 492-500.

[603] N. Camara, B. Jouault, A. Caboni, B. Jabakhanji, W. Desrat, E. Pausas, C. Consejo, N. Mestres, P. Godignon, J. Camassel, Growth of monolayer graphene on 8 degrees off-axis 4H-SiC (000-1) substrates with application to quantum transport devices, Applied Physics Letters, 97 (2010).
[604] C.R. Eddy, D.K. Gaskill, Silicon Carbide as a Platform for Power Electronics, Science, 324 (2009) 1398-1400.
[605] F. Giannazzo, I. Deretzis, G. Nicotra, G. Fisichella, Q.M. Ramasse, C. Spinella, F. Roccaforte, A. La Magna, High resolution study of structural and electronic properties of epitaxial graphene grown on off-axis 4H-SiC (0001), J Cryst Growth, 393 (2014) 150-155.
[606] S. Sonde, F. Giannazzo, J.R. Huntzinger, A. Tiberj, M. Syvajarvi, R. Yakimova, V. Raineri, J. Camassel, Uniformity of Epitaxial Graphene on On-axis and Off-axis SiC Probed by Raman Spectroscopy and Nanoscale Current Mapping, Mater Sci Forum, 645-648 (2010) 607-610.
[607] C. Vecchio, S. Sonde, C. Bongiorno, M. Rambach, R. Yakimova, V. Raineri, F. Giannazzo, Nanoscale structural characterization of epitaxial graphene grown on off-axis 4H-SiC (0001), Nanoscale Res Lett, 6 (2011) 269.
[608] J. Penuelas, A. Ouerghi, D. Lucot, C. David, J. Gierak, H. Estrade-Szwarckopf, C. Andreazza-Vignolle, Surface morphology and characterization of thin graphene films on SiC vicinal substrate, Physical Review B, 79 (2009) 033408.
[609] T. Maassen, J.J. van den Berg, E.H. Huisman, H. Dijkstra, F. Fromm, T. Seyller, B.J. van Wees, Localized States Influence Spin Transport in Epitaxial Graphene, Physical Review Letters, 110 (2013) 067209(067205pp).
[610] I. Shtepliuk, V. Khranovskyy, R. Yakimova, Combining graphene with silicon carbide: synthesis and properties - a review, Semicond. Sci. Technol., 31 (2016) 113004.
[611] F. Speck, J. Jobst, F. Fromm, M. Ostler, D. Waldmann, M. Hundhausen, H.B. Weber, T. Seyller, The quasi-free-standing nature of graphene on H-saturated SiC(0001), Applied Physics Letters, 99 (2011).
[612] C. Riedl, C. Coletti, U. Starke, Structural and electronic properties of epitaxial graphene on SiC(0 0 0 1): a review of growth, characterization, transfer doping and hydrogen intercalation, Journal of Physics D: Applied Physics, 43 (2010) 374009.
[613] M. Ostler, I. Deretzis, S. Mammadov, F. Giannazzo, G. Nicotra, C. Spinella, T. Seyller, A. La Magna, Direct growth of quasi-free-standing epitaxial graphene on nonpolar SiC surfaces, Physical Review B, 88 (2013) 085408.
[614] P. Hens, A.A. Zakharov, T. Iakimov, M. Syvajarvi, R. Yakimova, Large area buffer-free graphene on non-polar (001) cubic silicon carbide, Carbon, 80 (2014) 823-829.
[615] P. Hens, A.A. Zakharov, T. Iakimov, M. Syväjärvi, R. Yakimova, Large area buffer-free graphene on non-polar (001) cubic silicon carbide, Carbon, 80 (2014) 823-829.
[616] B. Jabakhanji, N. Camara, A. Caboni, C. Consejo, B. Jouault, P. Godignon, J. Camassel, Almost free standing Graphene on SiC(000-1) and SiC(11-20), Heterosic & Wasmpe 2011, 711 (2012) 235-241.
[617] A.J. van Bommel, J.E. Crombeen, A. van Tooren, LEED and Auger electron observations of the SiC(0001) surface, Surf. Sci., 48 (1975) 463.
[618] I. Forbeaux, J.M. Themlin, J.M. Debever, Heteroepitaxial graphite on 6H-SiC(0001): Interface formation through conduction-band electronic structure, Physical Review B, 58 (1998) 16396-16406.
[619] I. Forbeaux, J.M. Themlin, A. Charrier, F. Thibaudau, J.M. Debever, Solid-state graphitization mechanisms of silicon carbide 6H–SiC polar faces, Applied Surface Science, 162–163 (2000) 406-412.
[620] U. Starke, Atomic Structure of SiC Surfaces, in: W.J. Choyke, H. Matsunami, G. Pensl (Eds.) Recent major advances in silicon carbide, Springer2003.
[621] I. Deretzis, A. La Magna, Simulating structural transitions with kinetic Monte Carlo: The case of epitaxial graphene on SiC, Physical Review E, 93 (2016) 033304.
[622] B.K. Daas, S.U. Omar, S. Shetu, K.M. Daniels, S. Ma, T.S. Sudarshan, M.V.S. Chandrashekhar, Comparison of Epitaxial Graphene Growth on Polar and Nonpolar 6H-SiC Faces: On the Growth of Multilayer Films, Cryst Growth Des, 12 (2012) 3379-3387.

[623] S. Goler, C. Coletti, V. Piazza, P. Pingue, F. Colangelo, V. Pellegrini, K.V. Emtsev, S. Forti, U. Starke, F. Beltram, S. Heun, Revealing the atomic structure of the buffer layer between SiC(0 0 0 1) and epitaxial graphene, Carbon, 51 (2013) 249-254.
[624] A. Mattausch, O. Pankratov, Ab initio study of graphene on SiC, Physical Review Letters, 99 (2007).
[625] T. Seyller, Epitaxial Graphene on SiC(0001), in: H. Raza (Ed.) Graphene Nanoelectronics: Metrology, Synthesis, Properties and Applications, Springer, Berlin, Heidelberg, 2012, pp. 135-159.
[626] A. Bostwick, T. Ohta, T. Seyller, K. Horn, E. Rotenberg, Quasiparticle dynamics in graphene, Nature Physics, 3 (2007) 36-40.
[627] E. Rollings, G.H. Gweon, S.Y. Zhou, B.S. Mun, J.L. McChesney, B.S. Hussain, A. Fedorov, P.N. First, W.A. de Heer, A. Lanzara, Synthesis and characterization of atomically thin graphite films on a silicon carbide substrate, J Phys Chem Sol, 67 (2006) 2172-2177.
[628] T. Ohta, A. Bostwick, T. Seyller, K. Horn, E. Rotenberg, Controlling the Electronic Structure of Bilayer Graphene, Science, 313 (2006) 951-954.
[629] T. Ohta, A. Bostwick, J.L. McChesney, T. Seyller, K. Horn, E. Rotenberg, Interlayer Interaction and Electronic Screening in Multilayer Graphene Investigated with Angle-Resolved Photoemission Spectroscopy, Physical Review Letters, 98 (2007) 206802.
[630] J. Jobst, D. Waldmann, F. Speck, R. Hirner, D.K. Maude, T. Seyller, H.B. Weber, Quantum oscillations and quantum Hall effect in epitaxial graphene, Physical Review B, 81 (2010) 195434.
[631] J. Jobst, D. Waldmann, F. Speck, R. Hirner, D.K. Maude, T. Seyller, H.B. Weber, Transport properties of high-quality epitaxial graphene on 6H-SiC(0001), Solid State Communications, 151 (2011) 1061-1064.
[632] D. Farías, K.H. Rieder, A.M. Shikin, V.K. Adamchuk, T. Tanaka, C. Oshima, Modification of the surface phonon dispersion of a graphite monolayer adsorbed on Ni(111) caused by intercalation of Yb, Cu and Ag, Surf. Sci., 454–456 (2000) 437-441.
[633] S. Forti, K.V. Emtsev, C. Coletti, A.A. Zakharov, C. Riedl, U. Starke, Large-area homogeneous quasifree standing epitaxial graphene on SiC(0001): Electronic and structural characterization, Physical Review B, 84 (2011) 125449.
[634] A. Bostwick, F. Speck, T. Seyller, K. Horn, M. Polini, R. Asgari, A.H. MacDonald, E. Rotenberg, Observation of Plasmarons in Quasi-Freestanding Doped Graphene, Science, 328 (2010) 999-1002.
[635] C. Virojanadara, A.A. Zakharov, R. Yakimova, L.I. Johansson, Buffer layer free large area bi-layer graphene on SiC(0 0 0 1), Surf. Sci., 604 (2010) L4-L7.
[636] S. Watcharinyanon, C. Virojanadara, J.R. Osiecki, A.A. Zakharov, R. Yakimova, R.I.G. Uhrberg, L.I. Johansson, Hydrogen intercalation of graphene grown on 6H-SiC(0001), Surf. Sci., 605 (2011) 1662-1668.
[637] S. Oida, F.R. McFeely, J.B. Hannon, R.M. Tromp, M. Copel, Z. Chen, Y. Sun, D.B. Farmer, J. Yurkas, Decoupling graphene from SiC(0001) via oxidation, Physical Review B, 82 (2010) 041411R(041414pp).
[638] M.H. Oliveira Jr, T. Schumann, F. Fromm, R. Koch, M. Ostler, M. Ramsteiner, T. Seyller, J.M.J. Lopes, H. Riechert, Formation of high-quality quasi-free-standing bilayer graphene on SiC(0 0 0 1) by oxygen intercalation upon annealing in air, Carbon, 52 (2013) 83-89.
[639] M. Ostler, F. Fromm, R.J. Koch, P. Wehrfritz, F. Speck, H. Vita, S. Böttcher, K. Horn, T. Seyller, Buffer layer free graphene on SiC(0 0 0 1) via interface oxidation in water vapor, Carbon, 70 (2014) 258-265.
[640] M. Ostler, R.J. Koch, F. Speck, F. Fromm, H. Vita, M. Hundhausen, K. Horn, T. Seyller, Decoupling the Graphene Buffer Layer from SiC(0001) via Interface Oxidation, Mater Sci Forum, 717-720 (2012) 649- 652.
[641] A.L. Walter, K.-J. Jeon, A. Bostwick, F. Speck, M. Ostler, T. Seyller, L. Moreschini, Y.S. Kim, Y.J. Chang, K. Horn, E. Rotenberg, Highly p-doped epitaxial graphene obtained by fluorine intercalation, Applied Physics Letters, 98 (2011) 184102.

[642] S.L. Wong, H. Huang, Y. Wang, L. Cao, D. Qi, I. Santoso, W. Chen, A.T.S. Wee, Quasi-Free-Standing Epitaxial Graphene on SiC (0001) by Fluorine Intercalation from a Molecular Source, ACS Nano, 5 (2011) 7662-7668.
[643] Y. Masuda, W. Norimatsu, M. Kusunoki, Formation of a nitride interface in epitaxial graphene on SiC (0001), Physical Review B, 91 (2015).
[644] C. Xia, S. Watcharinyanon, A.A. Zakharov, R. Yakimova, L. Hultman, L.I. Johansson, C. Virojanadara, Si intercalation/deintercalation of graphene on 6H-SiC(0001), Physical Review B, 85 (2012).
[645] F. Wang, K. Shepperd, J. Hicks, M.S. Nevius, H. Tinkey, A. Tejeda, A. Taleb-Ibrahimi, F. Bertran, P. Le Fevre, D.B. Torrance, P.N. First, W.A. de Heer, A.A. Zakharov, E.H. Conrad, Silicon intercalation into the graphene-SiC interface, Physical Review B, 85 (2012) 165449.
[646] K.V. Emtsev, A.A. Zakharov, C. Coletti, S. Forti, U. Starke, Ambipolar doping in quasifree epitaxial graphene on SiC(0001) controlled by Ge intercalation, Physical Review B, 84 (2011) 125423.
[647] J. Baringhaus, A. Stöhr, S. Forti, U. Starke, C. Tegenkamp, Ballistic bipolar junctions in chemically gated graphene ribbons, 5 (2015) 9955.
[648] I. Gierz, T. Suzuki, R.T. Weitz, D.S. Lee, B. Krauss, C. Riedl, U. Starke, H. Höchst, J.H. Smet, C.R. Ast, K. Kern, Electronic decoupling of an epitaxial graphene monolayer by gold intercalation, Physical Review B, 81 (2010) 235408.
[649] B. Premlal, M. Cranney, F. Vonau, D. Aubel, D. Casterman, M.M. De Souza, L. Simon, Surface intercalation of gold underneath a graphene monolayer on SiC(0001) studied by scanning tunneling microscopy and spectroscopy, Applied Physics Letters, 94 (2009) 263115.
[650] P.B. Pillai, M. Desouza, R. Narula, S. Reich, L.Y. Wong, T. Batten, J. Pokorny, Decoupling of epitaxial graphene via gold intercalation probed by dispersive Raman spectroscopy, Journal of Applied Physics, 117 (2015).
[651] D. Marchenko, A. Varykhalov, J. Sánchez-Barriga, T. Seyller, O. Rader, Rashba splitting of 100 meV in Au-intercalated graphene on SiC, Applied Physics Letters, 108 (2016) 172405.
[652] K. Yagyu, T. Tajiri, A. Kohno, K. Takahashi, H. Tochihara, H. Tomokage, T. Suzuki, Fabrication of a single layer graphene by copper intercalation on a SiC(0001) surface, Applied Physics Letters, 104 (2014) 053115.
[653] C. Virojanadara, S. Watcharinyanon, A.A. Zakharov, L.I. Johansson, Epitaxial graphene on 6H-SiC and Li intercalation, Physical Review B, 82 (2010) 205402.
[654] C. Virojanadara, S. Watcharinyanon, A.A. Zakharov, R. Yakimova, L.I. Johansson, Studies of Li intercalation into epitaxial graphene on SiC(0001), Materials Science Forum, 717-720 (2012) 653-656.
[655] C. Xia, S. Watcharinyanon, A.A. Zakharov, L.I. Johansson, R. Yakimova, C. Virojanadara, Detailed studies of Na intercalation on furnace-grown graphene on 6H-SiC(0001), Surf. Sci., 613 (2013) 88-94.
[656] T. Seyller, Hydrogen-saturated SiC-surfaces: Model systems for studies of passivation, reconstruction, and interface formation, 5th European Conference on Silicon Carbide and Related Materials, ECRSCRM2004, 483-485 (2005) 535-540.
[657] T. Seyller, K.V. Emtsev, K. Gao, F. Speck, L. Ley, A. Tadich, L. Broekman, J.D. Riley, R.C.G. Leckey, O. Rader, A. Varykhalov, A.M. Shikin, Structural and electronic properties of graphite layers grown on SiC(0001), Surf. Sci., 600 (2006) 3906-3911.
[658] N. Sieber, B.F. Mantel, T. Seyller, J. Ristein, L. Ley, T. Heller, D.R. Batchelor, D. Schmeisser, Electronic and chemical passivation of hexagonal 6H-SiC surfaces by hydrogen termination, Applied Physics Letters, 78 (2001) 1216-1218.
[659] F. Speck, M. Ostler, J. Röhrl, J. Jobst, D. Waldmann, M. Hundhausen, L. Ley, H.B. Weber, T. Seyller, Quasi-freestanding graphene on SiC(0001), Materials Science Forum, 645-648 (2010) 629-632.
[660] K.M. Daniels, M.M. Jadidi, A.B. Sushkov, A.K. Boyd, A. Nath, H.D. Drew, T.E. Murphy, R.L. Myers-Ward, D.K. Gaskill, Narrow terahertz plasmon resonance of quasi-freestanding bilayer epitaxial graphene, 2016 74th Annual Device Research Conference (DRC), 2016, pp. 1-2.

[661] S. Tanabe, Y. Sekine, H. Kageshima, H. Hibino, Electrical Characterization of Bilayer Graphene Formed by Hydrogen Intercalation of Monolayer Graphene on SiC(0001), Japanese Journal of Applied Physics, 51 (2012) 02BN02.
[662] S. Mammadov, J. Ristein, J. Krone, C. Raidel, M. Wanke, V. Wiesmann, F. Speck, T. Seyller, Work function of graphene multilayers on SiC(0001), 2D Materials, DOI (2017) accepted.
[663] S. Mammadov, J. Ristein, R.J. Koch, M. Ostler, C. Raidel, M. Wanke, R. Vasiliauskas, R. Yakimova, T. Seyller, Polarization doping of graphene on silicon carbide, 2d Materials, 1 (2014) 035003.
[664] J. Ristein, S. Mammadov, T. Seyller, Origin of Doping in Quasi-Free-Standing Graphene on Silicon Carbide, Physical Review Letters, 108 (2012) 246104.
[665] J. Sławińska, H. Aramberri, M.C. Muñoz, J.I. Cerdá, Ab initio study of the relationship between spontaneous polarization and p-type doping in quasi-freestanding graphene on H-passivated SiC surfaces, Carbon, 93 (2015) 88-104.
[666] N. Ferralis, C. Carraro, Evolution of interfacial intercalation chemistry on epitaxial graphene/SiC by surface enhanced Raman spectroscopy, Applied Surface Science, 320 (2014) 441-447.
[667] C. Melios, S. Spencer, A. Shard, W. Strupiński, S.R.P. Silva, O. Kazakova, Surface and interface structure of quasi-free standing graphene on SiC, 2D Materials, 3 (2016) 025023.
[668] J.A. Robinson, M. Hollander, M. LaBella, K.A. Trumbull, R. Cavalero, D.W. Snyder, Epitaxial Graphene Transistors: Enhancing Performance via Hydrogen Intercalation, Nano Letters, 11 (2011) 3875-3880.
[669] T. Ciuk, W. Strupinski, Statistics of epitaxial graphene for Hall effect sensors, Carbon, 93 (2015) 1042-1049.
[670] Y. Murata, T. Mashoff, M. Takamura, S. Tanabe, H. Hibino, F. Beltram, S. Heun, Correlation between morphology and transport properties of quasi-free-standing monolayer graphene, Applied Physics Letters, 105 (2014).
[671] E. Pallecchi, F. Lafont, V. Cavaliere, F. Schopfer, D. Mailly, W. Poirier, A. Ouerghi, High Electron Mobility in Epitaxial Graphene on 4H-SiC(0001) via post-growth annealing under hydrogen, Scientific Reports, 4 (2014) 4558.
[672] S. Tanabe, M. Takamura, Y. Harada, H. Kageshima, H. Hibino, Quantum Hall Effect and Carrier Scattering in Quasi-Free-Standing Monolayer Graphene, Applied Physics Express, 5 (2012) 125101.
[673] S. Tanabe, M. Takamura, Y. Harada, H. Kageshima, H. Hibino, Effects of hydrogen intercalation on transport properties of quasi-free-standing monolayer graphene, Japanese Journal of Applied Physics, 53 (2014).
[674] N. Sieber, Wasserstoff- und Sauerstofftabilisierte 6H-SiC{0001}-Oberflächen - eine Studie Chemischer, Struktureller und Elektronischer Eigenschaften, Friedrich-Alexander-Universität Erlangen-Nürnberg, 2002.
[675] N. Sieber, T. Seyller, L. Ley, D. James, J.D. Riley, R.C.G. Leckey, M. Polcik, Synchrotron x-ray photoelectron spectroscopy study of hydrogen-terminated 6H-SiC{0001} surfaces, Physical Review B, 67 (2003).
[676] J.D. Emery, V.H. Wheeler, J.E. Johns, M.E. McBriarty, B. Detlefs, M.C. Hersam, D.K. Gaskill, M.J. Bedzyk, Structural consequences of hydrogen intercalation of epitaxial graphene on SiC(0001), Applied Physics Letters, 105 (2014) 161602.
[677] I. Deretzis, A.L. Magna, Process simulation of hydrogen intercalation in epitaxial graphene on SiC(0001), Physica Status Solidi (b), 250 (2013) 1478-1482.
[678] F. Fromm, J. M. H. Oliveira, A. Molina-Sánchez, M. Hundhausen, J.M.J. Lopes, H. Riechert, L. Wirtz, T. Seyller, Contribution of the buffer layer to the Raman spectrum of epitaxial graphene on SiC(0001), New Journal of Physics, 15 (2013) 043031.
[679] F. Giannazzo, S. Hertel, A. Albert, A. La Magna, F. Roccaforte, M. Krieger, H.B. Weber, Electrical nanocharacterization of epitaxial graphene/silicon carbide Schottky contacts, in: H. Okumura, H. Harima, T. Kimoto, M. Yoshimoto, H. Watanabe, T. Hatayama, H. Matsuura, T. Funaki, Y. Sano (Eds.) Silicon Carbide and Related Materials 2013, Pts 1 and 2, Trans Tech Publications Ltd, Stafa-Zurich, 2014, pp. 1142-1145.

[680] I. Deretzis, A. La Magna, Role of covalent and metallic intercalation on the electronic properties of epitaxial graphene on SiC(0001), Physical Review B, 84 (2011) 235426.
[681] N.M. Caffrey, R. Armiento, R. Yakimova, I.A. Abrikosov, Charge neutrality in epitaxial graphene on 6H-SiC(0001) via nitrogen intercalation, Physical Review B, 92 (2015).
[682] M. Rubio-Roy, F. Zaman, Y.K. Hu, C. Berger, M.W. Moseley, J.D. Meindl, W.A. de Heer, Structured epitaxial graphene growth on SiC by selective graphitization using a patterned AlN cap, Applied Physics Letters, 96 (2010) 082112.
[683] R. Puybaret, J. Hankinson, J. Palmer, C. Bouvier, A. Ougazzaden, P.L. Voss, C. Berger, W.A. de Heer, Scalable control of graphene growth on 4H-SiC C-face using decomposing silicon nitride masks, J. Phys D, 48 (2015) 152001.
[684] M.Y. Han, J.C. Brant, P. Kim, Electron Transport in Disordered Graphene Nanoribbons, Physical Review Letters, 104 (2010) 056801.
[685] C. Stampfer, S. Fringes, J. Guttinger, F. Molitor, C. Volk, B. Terres, J. Dauber, S. Engels, S. Schnez, A. Jacobsen, S. Droscher, T. Ihn, K. Ensslin, Transport in graphene nanostructures, Front Phys-Beijing, 6 (2011) 271-293.
[686] J. Hicks, A. Tejeda, A. Taleb-Ibrahimi, M.S. Nevius, F. Wang, K. Shepperd, J. Palmer, F. Bertran, P. Le Fevre, J. Kunc, W.A. de Heer, C. Berger, E.H. Conrad, A wide-bandgap metal-semiconductor-metal nanostructure made entirely from graphene, Nature Physics, 9 (2013) 49-54.
[687] R. Yakimova, T. Iakimov, G.R. Yazdi, C. Bouhafs, J. Eriksson, A. Zakharov, A. Boosalis, M. Schubert, V. Darakchieva, Morphological and electronic properties of epitaxial graphene on SiC, Physica B, 439 (2014) 54-59.
[688] M. Ruan, Y. Hu, Z. Guo, R. Dong, J. Palmer, J. Hankinson, C. Berger, W.A. de Heer, Epitaxial graphene on silicon carbide: Introduction to structured graphene, MRS Bulletin, 37 (2012) 1138-1147.
[689] I. Palacio, A. Celis, M.N. Nair, A. Gloter, A. Zobelli, M. Sicot, D. Malterre, M.S. Nevius, W.A. de Heer, C. Berger, E.H. Conrad, A. Taleb-Ibrahimi, A. Tejeda, Atomic Structure of Epitaxial Graphene Sidewall Nanoribbons: Flat Graphene, Miniribbons, and the Confinement Gap, Nano Letters, 15 (2014) 182−189.
[690] W. Norimatsu, M. Kusunoki, Formation process of graphene on SiC (0001), Physica E, 42 (2010) 691-694.
[691] J. Baringhaus, J. Aprojanz, J. Wiegand, D. Laube, M. Halbauer, J. Hubner, M. Oestreich, C. Tegenkamp, Growth and characterization of sidewall graphene nanoribbons, Applied Physics Letters, 106 (2015) 043109(043105pp)
[692] R. Dong, Z.L. Guo, J. Palmer, Y.K. Hu, M. Ruan, J. Hankinson, J. Kunc, S.K. Bhattacharya, C. Berger, W.A. de Heer, Wafer bonding solution to epitaxial graphene-silicon integration, J. Phys D, 47 (2014) 094001 (094008pp).
[693] M. Suemitsu, S. Jiao, H. Fukidome, Y. Tateno, I. Makabe, T. Nakabayashi, Epitaxial graphene formation on 3C-SiC/Si thin films, J. Phys D, 47 (2014) 094016 (094011pp).
[694] V.Y. Aristov, G. Urbanik, K. Kummer, D.V. Vyalikh, O.V. Molodtsova, A.B. Preobrajenski, A.A. Zakharov, C. Hess, T. Hanke, B. Buchner, I. Vobornik, J. Fujii, G. Panaccione, Y.A. Ossipyan, M. Knupfer, Graphene Synthesis on Cubic SiC/Si Wafers. Perspectives for Mass Production of Graphene-Based Electronic Devices, Nano Letters, 10 (2010) 992-995.
[695] A. Ouerghi, M. Ridene, A. Balan, R. Belkhou, A. Barbier, N. Gogneau, M. Portail, A. Michon, S. Latil, P. Jegou, A. Shukla, Sharp interface in epitaxial graphene layers on 3C-SiC(100)/Si(100) wafers, Physical Review B, 83 (2011) 205429.
[696] F. Zarotti, B. Gupta, F. Iacopi, A. Sgarlata, M. Tomellini, N. Motta, Time evolution of graphene growth on SiC as a function of annealing temperature, Carbon, 98 (2016) 307-312.
[697] F. Iacopi, N. Mishra, B.V. Cunning, D. Goding, S. Dimitrijev, R. Brock, R.H. Dauskardt, B. Wood, J. Boeckl, A catalytic alloy approach for graphene on epitaxial SiC on silicon wafers, Journal of Materials Research, 30 (2015) 609-616.
[698] W. Strupinski, K. Grodecki, P. Caban, P. Ciepielewski, I. Jozwik-Biala, J.M. Baranowski, Formation mechanism of graphene buffer layer on SiC(0001), Carbon, 81 (2015) 63-72.

[699] W. Strupinski, Method of graphene manufacturing, PAT-213291; US 9,067,796 B2; JP 5662249; ZL 201180027996.X; Korea 10-1465452; EP 11168749.7, Filed: Jun 7, 2010.
[700] M.E. Weber, Momentum, heat and mass transfer, 2nd edition, C. O. Bennett and J. E. Myers, McGraw-Hill, New York (1974). 810 pages. $17.85, AIChE Journal, 20 (1974) 1037-1037.
[701] T. Ciuk, O. Petruk, A. Kowalik, I. Jozwik, A. Rychter, J. Szmidt, W. Strupinski, Low-noise epitaxial graphene on SiC Hall effect element for commercial applications, Applied Physics Letters, 108 (2016).
[702] M. Tokarczyk, G. Kowalski, M. Możdżonek, J. Borysiuk, R. Stępniewski, W. Strupiński, P. Ciepielewski, J.M. Baranowski, Structural investigations of hydrogenated epitaxial graphene grown on 4H-SiC (0001), Applied Physics Letters, 103 (2013) 241915.
[703] T. Ciuk, S. Cakmakyapan, E. Ozbay, P. Caban, K. Grodecki, A. Krajewska, I. Pasternak, J. Szmidt, W. Strupinski, Step-edge-induced resistance anisotropy in quasi-free-standing bilayer chemical vapor deposition graphene on SiC, Journal of Applied Physics, 116 (2014) 123708.
[704] C. Melios, V. Panchal, C.E. Giusca, W. Strupiński, S.R.P. Silva, O. Kazakova, Carrier type inversion in quasi-free standing graphene: studies of local electronic and structural properties, Scientific Reports, 5 (2015).
[705] O. Habibpour, Z.S. He, W. Strupinski, N. Rorsman, H. Zirath, Wafer scale millimeter-wave integrated circuits based on epitaxial graphene in high data rate communication, Scientific Reports, 7 (2017) 41828.
[706] W. Strupinski, unpublished, DOI (2017).
[707] A. Reina, X. Jia, J. Ho, D. Nezich, H. Son, V. Bulovic, M.S. Dresselhaus, J. Kong, Large Area, Few-Layer Graphene Films on Arbitrary Substrates by Chemical Vapor Deposition, Nano Letters, 9 (2009) 30-35.
[708] X. Li, W. Cai, J. An, S. Kim, J. Nah, D. Yang, R. Piner, A. Velamakanni, I. Jung, E. Tutuc, S.K. Banerjee, L. Colombo, R.S. Ruoff, Large-Area Synthesis of High-Quality and Uniform Graphene Films on Copper Foils, Science, 324 (2009) 1312-1314.
[709] X. Liang, B.A. Sperling, I. Calizo, G. Cheng, C.A. Hacker, Q. Zhang, Y. Obeng, K. Yan, H. Peng, Q. Li, X. Zhu, H. Yuan, A.R. Hight Walker, Z. Liu, L.-m. Peng, C.A. Richter, Toward Clean and Crackless Transfer of Graphene, ACS Nano, 5 (2011) 9144-9153.
[710] W.-H. Lin, T.-H. Chen, J.-K. Chang, J.-I. Taur, Y.-Y. Lo, W.-L. Lee, C.-S. Chang, W.-B. Su, C.-I. Wu, A Direct and Polymer-Free Method for Transferring Graphene Grown by Chemical Vapor Deposition to Any Substrate, ACS Nano, 8 (2014) 1784-1791.
[711] R.B. McLellan, The solubility of carbon in solid gold, copper, and silver, Scripta Metallurgica, 3 (1969) 389-391.
[712] T. Ciuk, I. Pasternak, A. Krajewska, J. Sobieski, P. Caban, J. Szmidt, W. Strupinski, Properties of Chemical Vapor Deposition Graphene Transferred by High-Speed Electrochemical Delamination, The Journal of Physical Chemistry C, 117 (2013) 20833-20837.
[713] D.E.L. P.R. Subramanian, Phase diagrams of binary copper alloys, Monograph series on alloy phase diagrams, ASM International,(1994).
[714] G. Mathieu, S. Guiot, J. Cabané, Solubilite du carbone dans l'argent, le cuivre et l'or, Scripta Metallurgica, 7 (1973) 421-425.
[715] G.A. López, E.J. Mittemeijer, The solubility of C in solid Cu, Scripta Materialia, 51 (2004) 1-5.
[716] P. Trinsoutrot, C. Rabot, H. Vergnes, A. Delamoreanu, A. Zenasni, B. Caussat, High quality graphene synthesized by atmospheric pressure CVD on copper foil, Surface and Coatings Technology, 230 (2013) 87-92.
[717] Y. Hao, M.S. Bharathi, L. Wang, Y. Liu, H. Chen, S. Nie, X. Wang, H. Chou, C. Tan, B. Fallahazad, H. Ramanarayan, C.W. Magnuson, E. Tutuc, B.I. Yakobson, K.F. McCarty, Y.W. Zhang, P. Kim, J. Hone, L. Colombo, R.S. Ruoff, The Role of Surface Oxygen in the Growth of Large Single-Crystal Graphene on Copper, Science, 342 (2013) 720-723.
[718] S. Nie, W. Wu, S. Xing, Q. Yu, J. Bao, S.-s. Pei, K.F. McCarty, Growth from below: bilayer graphene on copper by chemical vapor deposition, New Journal of Physics, 14 (2012) 093028.
[719] V.I. Artyukhov, Y. Liu, B.I. Yakobson, Equilibrium at the edge and atomistic mechanisms of graphene growth, Proceedings of the National Academy of Sciences, 109 (2012) 15136-15140.

[720] I. Vlassiouk, S. Smirnov, M. Regmi, S.P. Surwade, N. Srivastava, R. Feenstra, G. Eres, C. Parish, N. Lavrik, P. Datskos, S. Dai, P. Fulvio, Graphene Nucleation Density on Copper: Fundamental Role of Background Pressure, The Journal of Physical Chemistry C, 117 (2013) 18919-18926.
[721] R.M. Jacobberger, M.S. Arnold, Graphene Growth Dynamics on Epitaxial Copper Thin Films, Chemistry of Materials, 25 (2013) 871-877.
[722] C.-Y. Su, A.-Y. Lu, C.-Y. Wu, Y.-T. Li, K.-K. Liu, W. Zhang, S.-Y. Lin, Z.-Y. Juang, Y.-L. Zhong, F.-R. Chen, L.-J. Li, Direct Formation of Wafer Scale Graphene Thin Layers on Insulating Substrates by Chemical Vapor Deposition, Nano Letters, 11 (2011) 3612-3616.
[723] I. Wlasny, P. Dabrowski, M. Rogala, P.J. Kowalczyk, I. Pasternak, W. Strupinski, J.M. Baranowski, Z. Klusek, Publisher's Note: “Role of graphene defects in corrosion of graphene-coated Cu(111) surface” [Appl. Phys. Lett. 102, 111601 (2013)], Applied Physics Letters, 102 (2013) 149901.
[724] A.T. Murdock, A. Koos, T.B. Britton, L. Houben, T. Batten, T. Zhang, A.J. Wilkinson, R.E. Dunin-Borkowski, C.E. Lekka, N. Grobert, Controlling the Orientation, Edge Geometry, and Thickness of Chemical Vapor Deposition Graphene, ACS Nano, 7 (2013) 1351-1359.
[725] O.V. Yazyev, S.G. Louie, Electronic transport in polycrystalline graphene, Nature Materials, 9 (2010) 806-809.
[726] R. Grantab, V.B. Shenoy, R.S. Ruoff, Anomalous Strength Characteristics of Tilt Grain Boundaries in Graphene, Science, 330 (2010) 946-948.
[727] Z. Luo, Y. Lu, D.W. Singer, M.E. Berck, L.A. Somers, B.R. Goldsmith, A.T.C. Johnson, Effect of Substrate Roughness and Feedstock Concentration on Growth of Wafer-Scale Graphene at Atmospheric Pressure, Chemistry of Materials, 23 (2011) 1441-1447.
[728] I. Vlassiouk, P. Fulvio, H. Meyer, N. Lavrik, S. Dai, P. Datskos, S. Smirnov, Large scale atmospheric pressure chemical vapor deposition of graphene, Carbon, 54 (2013) 58-67.
[729] Z. Yan, J. Lin, Z. Peng, Z. Sun, Y. Zhu, L. Li, C. Xiang, E.L. Samuel, C. Kittrell, J.M. Tour, Toward the Synthesis of Wafer-Scale Single-Crystal Graphene on Copper Foils, ACS Nano, 6 (2012) 9110-9117.
[730] H. Wang, G. Wang, P. Bao, S. Yang, W. Zhu, X. Xie, W.-J. Zhang, Controllable Synthesis of Submillimeter Single-Crystal Monolayer Graphene Domains on Copper Foils by Suppressing Nucleation, Journal of the American Chemical Society, 134 (2012) 3627-3630.
[731] B. Wu, D. Geng, Z. Xu, Y. Guo, L. Huang, Y. Xue, J. Chen, G. Yu, Y. Liu, Self-organized graphene crystal patterns, NPG Asia Materials, 5 (2013) e36.
[732] Z.R. Robinson, E.W. Ong, T.R. Mowll, P. Tyagi, D.K. Gaskill, H. Geisler, C.A. Ventrice, Influence of Chemisorbed Oxygen on the Growth of Graphene on Cu(100) by Chemical Vapor Deposition, The Journal of Physical Chemistry C, 117 (2013) 23919-23927.
[733] V. Miseikis, F. Bianco, J. David, M. Gemmi, V. Pellegrini, M. Romagnoli, C. Coletti, Deterministic patterned growth of high-mobility large-crystal graphene: a path towards wafer scale integration, 2D Materials, 4 (2017) 021004.
[734] Samsung, US.
[735] J.H. Lee, E.K. Lee, W.J. Joo, Y. Jang, B.S. Kim, J.Y. Lim, S.H. Choi, S.J. Ahn, J.R. Ahn, M.H. Park, C.W. Yang, B.L. Choi, S.W. Hwang, D. Whang, Wafer-Scale Growth of Single-Crystal Monolayer Graphene on Reusable Hydrogen-Terminated Germanium, Science, 344 (2014) 286-289.
[736] W.S. Li, Z.P. Wang, Y. Lu, Y.H. Jin, L.H. Yuan, F. Wang, Mechanical and tribological properties of a novel aluminum bronze material for drawing dies, Wear, 261 (2006) 155-163.
[737] V.Y. Berent, Heat-resistant high-conductivity materials, Metal Science and Heat Treatment, 22 (1980) 753-757.
[738] N. Petrone, C.R. Dean, I. Meric, A.M. van der Zande, P.Y. Huang, L. Wang, D. Muller, K.L. Shepard, J. Hone, Chemical Vapor Deposition-Derived Graphene with Electrical Performance of Exfoliated Graphene, Nano Letters, 12 (2012) 2751-2756.
[739] L. Lin, J. Li, H. Ren, A.L. Koh, N. Kang, H. Peng, H.Q. Xu, Z. Liu, Surface Engineering of Copper Foils for Growing Centimeter-Sized Single-Crystalline Graphene, ACS Nano, 10 (2016) 2922-2929.
[740] T. Wu, X. Zhang, Q. Yuan, J. Xue, G. Lu, Z. Liu, H. Wang, H. Wang, F. Ding, Q. Yu, X. Xie, M. Jiang, Fast growth of inch-sized single-crystalline graphene from a controlled single nucleus on Cu–Ni alloys, Nature Materials, 15 (2015) 43-47.

[741] H. Zhou, W.J. Yu, L. Liu, R. Cheng, Y. Chen, X. Huang, Y. Liu, Y. Wang, Y. Huang, X. Duan, Chemical vapour deposition growth of large single crystals of monolayer and bilayer graphene, Nature Communications, 4 (2013).
[742] V. Miseikis, D. Convertino, N. Mishra, M. Gemmi, T. Mashoff, S. Heun, N. Haghighian, F. Bisio, M. Canepa, V. Piazza, C. Coletti, Rapid CVD growth of millimetre-sized single crystal graphene using a cold-wall reactor, 2D Materials, 2 (2015) 014006.
[743] A.O. Musa, T. Akomolafe, M.J. Carter, Production of cuprous oxide, a solar cell material, by thermal oxidation and a study of its physical and electrical properties, Solar Energy Materials and Solar Cells, 51 (1998) 305-316.
[744] L. Gan, Z. Luo, Turning off Hydrogen To Realize Seeded Growth of Subcentimeter Single-Crystal Graphene Grains on Copper, ACS Nano, 7 (2013) 9480-9488.
[745] S.M. Kim, A. Hsu, Y.-H. Lee, M. Dresselhaus, T. Palacios, K.K. Kim, J. Kong, The effect of copper pre-cleaning on graphene synthesis, Nanotechnology, 24 (2013) 365602.
[746] W. Fang, A.L. Hsu, Y. Song, A.G. Birdwell, M. Amani, M. Dubey, M.S. Dresselhaus, T. Palacios, J. Kong, Asymmetric Growth of Bilayer Graphene on Copper Enclosures Using Low-Pressure Chemical Vapor Deposition, ACS Nano, 8 (2014) 6491-6499.
[747] S. Chen, H. Ji, H. Chou, Q. Li, H. Li, J.W. Suk, R. Piner, L. Liao, W. Cai, R.S. Ruoff, Millimeter-Size Single-Crystal Graphene by Suppressing Evaporative Loss of Cu During Low Pressure Chemical Vapor Deposition, Advanced Materials, 25 (2013) 2062-2065.
[748] C.S. Jayanthi, E. Tosatti, L. Pietronero, Surface melting of copper, Physical Review B, 31 (1985) 3456-3459.
[749] L. Banszerus, M. Schmitz, S. Engels, J. Dauber, M. Oellers, F. Haupt, K. Watanabe, T. Taniguchi, B. Beschoten, C. Stampfer, Ultrahigh-mobility graphene devices from chemical vapor deposition on reusable copper, Science Advances, 1 (2015) e1500222-e1500222.
[750] A. Srivastava, C. Galande, L. Ci, L. Song, C. Rai, D. Jariwala, K.F. Kelly, P.M. Ajayan, Novel Liquid Precursor-Based Facile Synthesis of Large-Area Continuous, Single, and Few-Layer Graphene Films, Chemistry of Materials, 22 (2010) 3457-3461.
[751] A. Guermoune, T. Chari, F. Popescu, S.S. Sabri, J. Guillemette, H.S. Skulason, T. Szkopek, M. Siaj, Chemical vapor deposition synthesis of graphene on copper with methanol, ethanol, and propanol precursors, Carbon, 49 (2011) 4204-4210.
[752] Y. Yao, Z. Li, Z. Lin, K.-S. Moon, J. Agar, C. Wong, Controlled Growth of Multilayer, Few-Layer, and Single-Layer Graphene on Metal Substrates, The Journal of Physical Chemistry C, 115 (2011) 5232-5238.
[753] Z. Li, P. Wu, C. Wang, X. Fan, W. Zhang, X. Zhai, C. Zeng, Z. Li, J. Yang, J. Hou, Low-Temperature Growth of Graphene by Chemical Vapor Deposition Using Solid and Liquid Carbon Sources, ACS Nano, 5 (2011) 3385-3390.
[754] B. Zhang, W.H. Lee, R. Piner, I. Kholmanov, Y. Wu, H. Li, H. Ji, R.S. Ruoff, Low-Temperature Chemical Vapor Deposition Growth of Graphene from Toluene on Electropolished Copper Foils, ACS Nano, 6 (2012) 2471-2476.
[755] C. Wirtz, K. Lee, T. Hallam, G.S. Duesberg, Growth optimisation of high quality graphene from ethene at low temperatures, Chemical Physics Letters, 595–596 (2014) 192-196.
[756] J. Chan, A. Venugopal, A. Pirkle, S. McDonnell, D. Hinojos, C.W. Magnuson, R.S. Ruoff, L. Colombo, R.M. Wallace, E.M. Vogel, Reducing Extrinsic Performance-Limiting Factors in Graphene Grown by Chemical Vapor Deposition, ACS Nano, 6 (2012) 3224-3229.
[757] Y.Y. Tan, K.D.G.I. Jayawardena, A.A.D.T. Adikaari, L.W. Tan, J.V. Anguita, S.J. Henley, V. Stolojan, J.D. Carey, S.R.P. Silva, Photo-thermal chemical vapor deposition growth of graphene, Carbon, 50 (2012) 668-673.
[758] L. Huang, Q.H. Chang, G.L. Guo, Y. Liu, Y.Q. Xie, T. Wang, B. Ling, H.F. Yang, Synthesis of high-quality graphene films on nickel foils by rapid thermal chemical vapor deposition, Carbon, 50 (2012) 551-556.
[759] J. Riikonen, W. Kim, C. Li, O. Svensk, S. Arpiainen, M. Kainlauri, H. Lipsanen, Photo-thermal chemical vapor deposition of graphene on copper, Carbon, 62 (2013) 43-50.

[760] W. Kim, C. Li, N. Chekurov, S. Arpiainen, D. Akinwande, H. Lipsanen, J. Riikonen, All-Graphene Three-Terminal-Junction Field-Effect Devices as Rectifiers and Inverters, ACS Nano, 9 (2015) 5666-5674.
[761] J. Ryu, Y. Kim, D. Won, N. Kim, J.S. Park, E.-K. Lee, D. Cho, S.-P. Cho, S.J. Kim, G.H. Ryu, H.-A.S. Shin, Z. Lee, B.H. Hong, S. Cho, Fast Synthesis of High-Performance Graphene Films by Hydrogen-Free Rapid Thermal Chemical Vapor Deposition, ACS Nano, 8 (2014) 950-956.
[762] S. Gsell, M. Fischer, M. Schreck, B. Stritzker, Epitaxial films of metals from the platinum group (Ir, Rh, Pt and Ru) on YSZ-buffered Si(111), J Cryst Growth, 311 (2009) 3731-3736.
[763] P. Zeller, S. Dänhardt, S. Gsell, M. Schreck, J. Wintterlin, Scalable synthesis of graphene on single crystal Ir(111) films, Surf. Sci., 606 (2012) 1475-1480.
[764] A. Hemmi, H. Cun, S. Roth, J. Osterwalder, T. Greber, Low cost photoelectron yield setup for surface process monitoring, Journal of Vacuum Science & Technology A: Vacuum, Surfaces, and Films, 32 (2014) 023202.
[765] G. Lippert, J. Dąbrowski, T. Schroeder, M.A. Schubert, Y. Yamamoto, F. Herziger, J. Maultzsch, J. Baringhaus, C. Tegenkamp, M.C. Asensio, J. Avila, G. Lupina, Graphene grown on Ge(001) from atomic source, Carbon, 75 (2014) 104-112.
[766] V. Di Lecce, R. Grassi, A. Gnudi, E. Gnani, S. Reggiani, G. Baccarani, Graphene-Base Heterojunction Transistor: An Attractive Device for Terahertz Operation, IEEE Transactions on Electron Devices, 60 (2013) 4263-4268.
[767] R.W. Olesinski, G.J. Abbaschian, The C–Ge (Carbon-Germanium) system, Bulletin of Alloy Phase Diagrams, 5 (1984) 484-486.
[768] B. Kiraly, R.M. Jacobberger, A.J. Mannix, G.P. Campbell, M.J. Bedzyk, M.S. Arnold, M.C. Hersam, N.P. Guisinger, Electronic and Mechanical Properties of Graphene–Germanium Interfaces Grown by Chemical Vapor Deposition, Nano Letters, 15 (2015) 7414-7420.
[769] I. Pasternak, P. Dabrowski, P. Ciepielewski, V. Kolkovsky, Z. Klusek, J.M. Baranowski, W. Strupinski, Large-area high-quality graphene on Ge(001)/Si(001) substrates, Nanoscale, 8 (2016) 11241-11247.
[770] I. Pasternak, M. Wesolowski, I. Jozwik, M. Lukosius, G. Lupina, P. Dabrowski, J.M. Baranowski, W. Strupinski, Graphene growth on Ge(100)/Si(100) substrates by CVD method, Scientific Reports, 6 (2016).
[771] R. Hasegawa, T. Kurosawa, T. Yagihashi, Hydrogen Reduction of Germanium Dioxide, Transactions of the Japan Institute of Metals, 13 (1972) 39-44.
[772] M. Zeng, W.-L. Wang, X.-D. Bai, Preparing three-dimensional graphene architectures: Review of recent developments, Chinese Physics B, 22 (2013) 098105.
[773] F. Yavari, Z. Chen, A.V. Thomas, W. Ren, H.-M. Cheng, N. Koratkar, High Sensitivity Gas Detection Using a Macroscopic Three-Dimensional Graphene Foam Network, Scientific Reports, 1 (2011).
[774] Y. Xu, K. Sheng, C. Li, G. Shi, Self-Assembled Graphene Hydrogelviaa One-Step Hydrothermal Process, ACS Nano, 4 (2010) 4324-4330.
[775] P.M. Wilson, G.N. Mbah, T.G. Smith, D. Schmidt, R.Y. Lai, T. Hofmann, A. Sinitskii, Three-dimensional periodic graphene nanostructures, Journal of Materials Chemistry C, 2 (2014) 1879.
[776] W. Chen, Z. Fan, G. Zeng, Z. Lai, Layer-dependent supercapacitance of graphene films grown by chemical vapor deposition on nickel foam, Journal of Power Sources, 225 (2013) 251-256.
[777] N. Li, Q. Zhang, S. Gao, Q. Song, R. Huang, L. Wang, L. Liu, J. Dai, M. Tang, G. Cheng, Three-dimensional graphene foam as a biocompatible and conductive scaffold for neural stem cells, Scientific Reports, 3 (2013).
[778] E. Singh, Z. Chen, F. Houshmand, W. Ren, Y. Peles, H.-M. Cheng, N. Koratkar, Superhydrophobic Graphene Foams, Small, 9 (2012) 75-80.
[779] Y.R. Jeong, H. Park, S.W. Jin, S.Y. Hong, S.-S. Lee, J.S. Ha, Highly Stretchable and Sensitive Strain Sensors Using Fragmentized Graphene Foam, Advanced Functional Materials, 25 (2015) 4228-4236.
[780] X. Li, W. Cai, L. Colombo, R.S. Ruoff, Evolution of Graphene Growth on Ni and Cu by Carbon Isotope Labeling, Nano Letters, 9 (2009) 4268-4272.

[781] L.V. M. Christian, L. Ortolani, F. Liscio, R. Rizzoli, V. Palermo, V. Morandi, , Synthesis of High-Density Graphene Foams Using Nanoparticle Templates,, in: V.O. Morandi, L. (Ed.) GraphITA, .Springer International Publishing, 2017, Bologna.
[782] L. Wang, X. Li, T. Guo, X. Yan, B.K. Tay, Three-dimensional Ni(OH)2 nanoflakes/graphene/nickel foam electrode with high rate capability for supercapacitor applications, International Journal of Hydrogen Energy, 39 (2014) 7876-7884.
[783] S. Drieschner, M. Weber, J. Wohlketzetter, J. Vieten, E. Makrygiannis, B.M. Blaschke, V. Morandi, L. Colombo, F. Bonaccorso, J.A. Garrido, High surface area graphene foams by chemical vapor deposition, 2D Materials, 3 (2016) 045013.
[784] H.W. Kroto, J.R. Heath, S.C. O'Brien, R.F. Curl, R.E. Smalley, C60: Buckminsterfullerene, Nature, 318 (1985) 162-163.
[785] J. Azpeitia, G. Otero-Irurueta, I. Palacio, J.I. Martinez, N. Ruiz del Árbol, G. Santoro, A. Gutiérrez, L. Aballe, M. Foerster, M. Kalbac, V. Vales, F.J. Mompeán, M. García-Hernández, J.A. Martín-Gago, C. Munuera, M.F. López, High-quality PVD graphene growth by fullerene decomposition on Cu foils, Carbon, 119 (2017) 535-543.
[786] A.L. Pinardi, G. Biddau, K. van De Ruit, G. Otero-Irurueta, S. Gardonio, S. Lizzit, R. Schennach, C.F.J. Flipse, M.F. López, J. Méndez, R. Pérez, J.A. Martín-Gago, Vacancy formation on C60/Pt (111): unraveling the complex atomistic mechanism, Nanotechnology, 25 (2014) 385602.
[787] G. Otero, C. González, A.L. Pinardi, P. Merino, S. Gardonio, S. Lizzit, M. Blanco-Rey, K. Van de Ruit, C.F.J. Flipse, J. Méndez, P.L. de Andrés, J.A. Martín-Gago, Ordered Vacancy Network Induced by the Growth of Epitaxial Graphene on Pt(111), Physical Review Letters, 105 (2010).
[788] J.I. Martínez, P. Merino, A.L. Pinardi, O.-I. Gonzalo, M.F. López, J. Méndez, J.A. Martín-Gago, Role of the Pinning Points in epitaxial Graphene Moiré Superstructures on the Pt(111) Surface, Scientific Reports, 6 (2016).
[789] R. Muñoz, C. Gómez-Aleixandre, Review of CVD Synthesis of Graphene, Chemical Vapor Deposition, 19 (2013) 297-322.
[790] Z. Yan, Z. Peng, J.M. Tour, Chemical Vapor Deposition of Graphene Single Crystals, Accounts of Chemical Research, 47 (2014) 1327-1337.
[791] A.J. Martínez-Galera, I.n. Brihuega, J.M. Gómez-Rodríguez, Ethylene Irradiation: A New Route to Grow Graphene on Low Reactivity Metals, Nano Letters, 11 (2011) 3576-3580.
[792] S. Nie, N.C. Bartelt, J.M. Wofford, O.D. Dubon, K.F. McCarty, K. Thürmer, Scanning tunneling microscopy study of graphene on Au(111): Growth mechanisms and substrate interactions, Physical Review B, 85 (2012).
[793] G. Lippert, J. Dabrowski, M. Lemme, C. Marcus, O. Seifarth, G. Lupina, Direct graphene growth on insulator, physica status solidi (b), 248 (2011) 2619-2622.
[794] J.M. Garcia, U. Wurstbauer, A. Levy, L.N. Pfeiffer, A. Pinczuk, A.S. Plaut, L. Wang, C.R. Dean, R. Buizza, A.M. Van Der Zande, J. Hone, K. Watanabe, T. Taniguchi, Graphene growth on h-BN by molecular beam epitaxy, Solid State Communications, 152 (2012) 975-978.
[795] I. Hernández-Rodríguez, J.M. García, J.A. Martín-Gago, P.L. de Andrés, J. Méndez, Graphene growth on Pt(111) and Au(111) using a MBE carbon solid-source, Diamond and Related Materials, 57 (2015) 58-62.
[796] L.N.P.J.M.G. Martinez, Devices with graphene layers, 2008.
[797] L.N. Pfeiffer, Deposition of carbon-containing layers using vitreous carbon source, 2008.
[798] P.J.F. Harris, Structure of non-graphitising carbons, International Materials Reviews, 42 (1997) 206-218.
[799] P.W. J.M.Garcia, “System and methods using a glassy carbon heater”, 2012.
[800] S. Taioli, G. Garberoglio, S. Simonucci, S.a. Beccara, L. Aversa, M. Nardi, R. Verucchi, S. Iannotta, M. Dapor, D. Alfè, Non-adiabatic ab initio molecular dynamics of supersonic beam epitaxy of silicon carbide at room temperature, The Journal of Chemical Physics, 138 (2013) 044701.
[801] R. Verucchi, L. Aversa, M.V. Nardi, S. Taioli, S. a Beccara, D. Alfè, L. Nasi, F. Rossi, G. Salviati, S. Iannotta, Epitaxy of Nanocrystalline Silicon Carbide on Si(111) at Room Temperature, Journal of the American Chemical Society, 134 (2012) 17400-17403.

[802] S. Taioli, Computational study of graphene growth on copper by first-principles and kinetic Monte Carlo calculations, Journal of Molecular Modeling, 20 (2014).
[803] R. Tatti, L. Aversa, R. Verucchi, E. Cavaliere, G. Garberoglio, N.M. Pugno, G. Speranza, S. Taioli, Synthesis of single layer graphene on Cu(111) by C60 supersonic molecular beam epitaxy, RSC Advances, 6 (2016) 37982-37993.
[804] Sun J, Lindvall N, Cole M, Large-area uniform graphene-like thin films grown by chemical vapor deposition directly on silicon nitride, Appl. Phys. Lett, 98 (2011) 252107.
[805] Chen J, Guo Y, Wen Y, Two-Stage Metal-Catalyst-Free Growth of High-Quality Polycrystalline Graphene Films on Silicon Nitride Substrates Adv. Mater., 25 (2013) 992.
[806] Jerng S K, Yu D S, Kim Y S, Nanocrystalline Graphite Growth on Sapphire by Carbon Molecular Beam Epitaxy, J. Phys. Chem. C. , 115 (2011) 4491.
[807] Chen J, Wen Y, Guo Y, Oxygen-Aided Synthesis of Polycrystalline Graphene on Silicon Dioxide Substrates, J Am Chem Soc, 133 (2011).
[808] Rümmeli M H, Bachmatiuk A, Scott A, Direct Low-Temperature Nanographene CVD Synthesis over a Dielectric Insulator ACS Nano, 4 (2010) 4206.
[809] Sun J, Lindvall N, Cole M T, Controllable chemical vapor deposition of large area uniform nanocrystalline graphene directly on silicon dioxide J. Appl. Phys., 111 (2012) 044103.
[810] Song H J, Son M, Park C, Large scale metal-free synthesis of graphene on sapphire and transfer-free device fabrication, Nanoscale, 4 (2012) 3050.
[811] Chen J, e. al., Near-Equilibrium Chemical Vapor Deposition of High-Quality Single-Crystal Graphene Directly on Various Dielectric Substrates Adv. Mater., 26 (2014) 1348.
[812] X. Ding, G. Ding, X. Xie, F. Huang, M. Jiang, Direct growth of few layer graphene on hexagonal boron nitride by chemical vapor deposition, Carbon, 49 (2011) 2522-2525.
[813] Zhang L, Shi Z, Wang Y, Catalyst-free growth of nanographene films on various substrates, Nano Res., 4 (2011) 315.
[814] Medina H, Lin Y-C, Jin C, Metal-Free Growth of Nanographene on Silicon Oxides for Transparent Conducting Applications, Adv. Funct. Mater., 22 (2012) 2123.
[815] R. Muñoz, C. Gómez-Aleixandre, Fast and non-catalytic growth of transparent and conductive graphene-like carbon films on glass at low temperature, Journal of Physics D: Applied Physics, 47 (2013) 045305.
[816] R. Muñoz, C. Munuera, J.I. Martínez, J. Azpeitia, C. Gómez-Aleixandre, M. García-Hernández, Low temperature metal free growth of graphene on insulating substrates by plasma assisted chemical vapor deposition, 2D Materials, 4 (2016) 015009.
[817] Nguyen V L, Lee Y H, Towards Wafer-Scale Monocrystalline Graphene Growth and Characterization, Small, 11 (2015) 3512.
[818] W. Yang, G. Chen, Z. Shi, C.-C. Liu, L. Zhang, G. Xie, M. Cheng, D. Wang, R. Yang, D. Shi, K. Watanabe, T. Taniguchi, Y. Yao, Y. Zhang, G. Zhang, Epitaxial growth of single-domain graphene on hexagonal boron nitride, Nature Materials, 12 (2013) 792-797.
[819] Tang S, Wang H, Zhang Y, Precisely aligned graphene grown on hexagonal boron nitride by catalyst free chemical vapor deposition, Sci. Reports, 3 (2013) 2666.
[820] Zhang L, Shi Z, Liu D, Vapour-phase graphene epitaxy at low temperatures, Nano Res., 5 (2012) 258.
[821] Bo Z, Yang Y, Chen J, Plasma-enhanced chemical vapor deposition synthesis of vertically oriented graphene nanosheets, Nanoscale, 5 (2013) 5180.
[822] Buijnsters J G, Camero M, Gago R, Direct spectroscopic evidence of self-formed C60 inclusions in fullerenelike hydrogenated carbon films, Appl. Phys. Lett., 92 (2008) 141920.
[823] Tamor M A, Vassell W C, Carduner K R, Atomic constraint in hydrogenated "diamond-like" carbon, Appl. Phys. Lett, 58 (1990) 592.
[824] Buijnsters J G, Camero M, Vázquez L, DC substrate bias effects on the physical properties of hydrogenated amorphous carbon films grown by plasma-assisted chemical vapour deposition, Vacuum, 81 (2007) 1412.

[825] Zhang L, Ni M, Liu D, Competitive Growth and Etching of Epitaxial Graphene, J. Phys. Chem. C., 116 (2012) 26929.
[826] Yang R, Zhang L, Wang Y, An Anisotropic Etching Effect in the Graphene Basal Plane, Adv. Mater., 22 (2010) 4014.
[827] Diankov G, Neumann M, Goldhaber-Gordon D, Extreme Monolayer-Selectivity of Hydrogen-Plasma Reactions with Graphene, ACS Nano, 7 (2013) 1324.
[828] Nishijima M, Yoshinobu J, Tsuda H, The adsorption and thermal decomposition of acetylene on Si(100) and vicinal Si(100) 9°, Surf. Sci., 192 (1987) 383.
[829] Riikonen S, Krasheninnikov A V, Halonen L, The role of Stable and Mobile Carbon Adspecies in Copper-Promoted Graphene Growth, J. Phys. Chem. C., 116 (2012) 5802.
[830] Zhang J, Wang Z, Niu T, Elementary Process for CVD Graphene on Cu(110): Size-selective Carbon Clusters, Sci. Reports, 4 (2014) 4431.
[831] M. Cai, R.A. Outlaw, R.A. Quinlan, D. Premathilake, S.M. Butler, J.R. Miller, Fast Response, Vertically Oriented Graphene Nanosheet Electric Double Layer Capacitors Synthesized from C2H2, ACS Nano, 8 (2014) 5873-5882.
[832] J.R. Miller, R.A. Outlaw, B.C. Holloway, Graphene Double-Layer Capacitor with ac Line-Filtering Performance, Science, 329 (2010) 1637-1639.
[833] J.R. Miller, R.A. Outlaw, B.C. Holloway, Graphene electric double layer capacitor with ultra-high-power performance, Electrochimica Acta, 56 (2011) 10443-10449.
[834] T. Kaplas, D. Sharma, Y. Svirko, Few-layer graphene synthesis on a dielectric substrate, Carbon, 50 (2012) 1503-1509.
[835] T. Kaplas, A. Zolotukhin, Y. Svirko, Thickness determination of graphene on metal substrate by reflection spectroscopy, Opt. Express, 19 (2011) 17226.
[836] K.L. Chavez, D.W. Hess, A Novel Method of Etching Copper Oxide Using Acetic Acid, Journal of The Electrochemical Society, 148 (2001) G640.
[837] T. Kaplas, Y. Svirko, Self-assembled graphene on dielectric micro- and nanostructures, Carbon, 70 (2014) 273-278.
[838] J.M. Kosterlitz, D.J. Thouless, Long range order and metastability in two dimensional solids and superfluids. (Application of dislocation theory), Journal of Physics C: Solid State Physics, 5 (1972) L124-L126.
[839] I. Vlassiouk, S. Smirnov, I. Ivanov, P.F. Fulvio, S. Dai, H. Meyer, M. Chi, D. Hensley, P. Datskos, N.V. Lavrik, Electrical and thermal conductivity of low temperature CVD graphene: the effect of disorder, Nanotechnology, 22 (2011) 275716.
[840] R. Kumar, B.R. Mehta, M. Bhatnagar, R. S, S. Mahapatra, S. Salkalachen, P. Jhawar, Graphene as a transparent conducting and surface field layer in planar Si solar cells, Nanoscale Res Lett, 9 (2014) 349.
[841] M. Losurdo, M.M. Giangregorio, P. Capezzuto, G. Bruno, Graphene CVD growth on copper and nickel: role of hydrogen in kinetics and structure, Physical Chemistry Chemical Physics, 13 (2011) 20836.
[842] S. Bhaviripudi, X. Jia, M.S. Dresselhaus, J. Kong, Role of Kinetic Factors in Chemical Vapor Deposition Synthesis of Uniform Large Area Graphene Using Copper Catalyst, Nano Letters, 10 (2010) 4128-4133.
[843] T. Jawhari, A. Roid, J. Casado, Raman spectroscopic characterization of some commercially available carbon black materials, Carbon, 33 (1995) 1561-1565.
[844] T. Kaplas, L. Karvonen, S. Ahmadi, B. Amirsolaimani, S. Mehravar, N. Peyghambarian, K. Kieu, S. Honkanen, H. Lipsanen, Y. Svirko, Optical characterization of directly deposited graphene on a dielectric substrate, Opt. Express, 24 (2016) 2965.
[845] A.B.D. Cassie, S. Baxter, Wettability of porous surfaces, Transactions of the Faraday Society, 40 (1944) 546.
[846] Z. Peng, Z. Yan, Z. Sun, J.M. Tour, Direct Growth of Bilayer Graphene on SiO2Substrates by Carbon Diffusion through Nickel, ACS Nano, 5 (2011) 8241-8247.

[847] J. Kwak, J.H. Chu, J.-K. Choi, S.-D. Park, H. Go, S.Y. Kim, K. Park, S.-D. Kim, Y.-W. Kim, E. Yoon, S. Kodambaka, S.-Y. Kwon, Near room-temperature synthesis of transfer-free graphene films, Nature Communications, 3 (2012) 645.
[848] M. Marchena, D. Janner, T.L. Chen, V. Finazzi, V. Pruneri, Low temperature direct growth of graphene patterns on flexible glass substrates catalysed by a sacrificial ultrathin Ni film, Optical Materials Express, 6 (2016) 2487.
[849] H.-J. Shin, W.M. Choi, S.-M. Yoon, G.H. Han, Y.S. Woo, E.S. Kim, S.J. Chae, X.-S. Li, A. Benayad, D.D. Loc, F. Gunes, Y.H. Lee, J.-Y. Choi, Transfer-Free Growth of Few-Layer Graphene by Self-Assembled Monolayers, Advanced Materials, 23 (2011) 4392-4397.
[850] Z. Sun, Z. Yan, J. Yao, E. Beitler, Y. Zhu, J.M. Tour, Growth of graphene from solid carbon sources, Nature, 468 (2010) 549-552.
[851] C. Mattevi, H. Kim, M. Chhowalla, A review of chemical vapour deposition of graphene on copper, J. Mater. Chem., 21 (2011) 3324-3334.
[852] A.P. ASM Handbook; ASM International: 2002; Vol. 3.
[853] Q. Yu, J. Lian, S. Siriponglert, H. Li, Y.P. Chen, S.-S. Pei, Graphene segregated on Ni surfaces and transferred to insulators, Applied Physics Letters, 93 (2008) 113103.
[854] T. Kaplas, A. Matikainen, T. Nuutinen, S. Suvanto, P. Vahimaa, Y. Svirko, Scalable fabrication of the graphitic substrates for graphene-enhanced Raman spectroscopy, Scientific Reports, 7 (2017).
[855] M.H. Kang, W.I. Milne, M.T. Cole, Doping stability and opto-electronic performance of chemical vapour deposited graphene on transparent flexible substrates, IET Circuits, Devices & Systems, 9 (2015) 39-45.
[856] M.H. Kang, W.I. Milne, M.T. Cole, Temporal Stability of Metal-Chloride-Doped Chemical-Vapour-Deposited Graphene, ChemPhysChem, 17 (2016) 2545-2550.
[857] M.H. Kang, L.O. Prieto López, B. Chen, K. Teo, J.A. Williams, W.I. Milne, M.T. Cole, Mechanical Robustness of Graphene on Flexible Transparent Substrates, ACS Applied Materials & Interfaces, 8 (2016) 22506-22515.
[858] T. Hallam, N.C. Berner, C. Yim, G.S. Duesberg, Strain, Bubbles, Dirt, and Folds: A Study of Graphene Polymer-Assisted Transfer, Advanced Materials Interfaces, 1 (2014) 1400115.
[859] C. Wirtz, N.C. Berner, G.S. Duesberg, Large-Scale Diffusion Barriers from CVD Grown Graphene, Advanced Materials Interfaces, 2 (2015) 1500082.
[860] A. Beyer, H. Vieker, R. Klett, H. Meyer zu Theenhausen, P. Angelova, A. Gölzhäuser, Imaging of carbon nanomembranes with helium ion microscopy, Beilstein Journal of Nanotechnology, 6 (2015) 1712-1720.
[861] X. Zhang, A. Beyer, A. Gölzhäuser, Mechanical characterization of carbon nanomembranes from self-assembled monolayers, Beilstein Journal of Nanotechnology, 2 (2011) 826-833.
[862] T. Taubner, F. Keilmann, R. Hillenbrand, Nanoscale-resolved subsurface imaging by scattering-type near-field optical microscopy, Opt. Express, 13 (2005) 8893.
[863] F.K.a.R. Hillenbrand, Nano-Optics and Near-Field Optical Microscopy, Artech House Publishers, Boston, 2008.
[864] R. Hillenbrand, F. Keilmann, Material-specific mapping of metal/semiconductor/dielectric nanosystems at 10 nm resolution by backscattering near-field optical microscopy, Applied Physics Letters, 80 (2002) 25-27.
[865] R. Hillenbrand, F. Keilmann, Complex Optical Constants on a Subwavelength Scale, Physical Review Letters, 85 (2000) 3029-3032.
[866] T. Taubner, R. Hillenbrand, F. Keilmann, Nanoscale polymer recognition by spectral signature in scattering infrared near-field microscopy, Applied Physics Letters, 85 (2004) 5064-5066.
[867] M.K. Gunde, Vibrational modes in amorphous silicon dioxide, Physica B: Condensed Matter, 292 (2000) 286-295.
[868] F. Huth, A. Govyadinov, S. Amarie, W. Nuansing, F. Keilmann, R. Hillenbrand, Nano-FTIR Absorption Spectroscopy of Molecular Fingerprints at 20 nm Spatial Resolution, Nano Letters, 12 (2012) 3973-3978.

[869] M. Batzill, The surface science of graphene: Metal interfaces, CVD synthesis, nanoribbons, chemical modifications, and defects, Surface Science Reports, 67 (2012) 83-115.
[870] L. Koefoed, M. Kongsfelt, S. Ulstrup, A.G. Čabo, A. Cassidy, P.R. Whelan, M. Bianchi, M. Dendzik, F. Pizzocchero, B. Jørgensen, P. Bøggild, L. Hornekær, P. Hofmann, S.U. Pedersen, K. Daasbjerg, Facile electrochemical transfer of large-area single crystal epitaxial graphene from Ir(1 1 1), Journal of Physics D: Applied Physics, 48 (2015) 115306.
[871] J. Simonet, H. Lund, Electrochemical behaviour of graphite cathodes in the presence of tetraalkylammonium cations, Journal of Electroanalytical Chemistry and Interfacial Electrochemistry, 75 (1977) 719-730.
[872] E. Miniussi, C. Bernard, H.Y. Cun, B. Probst, D. Leuenberger, G. Mette, W.D. Zabka, M. Weinl, M. Haluska, M. Schreck, J. Osterwalder, T. Greber, Fermi surface map of large-scale single-orientation graphene on SiO2, Journal of Physics: Condensed Matter, 29 (2017) 475001.
[873] A. Krajewska, I. Pasternak, G. Sobon, J. Sotor, A. Przewloka, T. Ciuk, J. Sobieski, J. Grzonka, K.M. Abramski, W. Strupinski, Fabrication and applications of multi-layer graphene stack on transparent polymer, Applied Physics Letters, 110 (2017) 041901.
[874] A.M. Gómez-Marín, J. Clavilier, J.M. Feliu, Sequential Pt(111) oxide formation in perchloric acid: An electrochemical study of surface species inter-conversion, Journal of Electroanalytical Chemistry, 688 (2013) 360-370.
[875] I. Palacio, G. Otero-Irurueta, C. Alonso, J.I. Martínez, E. López-Elvira, I. Muñoz-Ochando, H.J. Salavagione, M.F. López, M. García-Hernández, J. Méndez, G.J. Ellis, J.A. Martín-Gago, Chemistry below graphene: Decoupling epitaxial graphene from metals by potential-controlled electrochemical oxidation, Carbon, 129 (2018) 837-846.
[876] X. Feng, S. Maier, M. Salmeron, Water Splits Epitaxial Graphene and Intercalates, Journal of the American Chemical Society, 134 (2012) 5662-5668.
[877] C.G.-A. Alonso, M.C.; Escudero, M. L. , Spain, 2008.
[878] S. Bae, H. Kim, Y. Lee, X. Xu, J.-S. Park, Y. Zheng, J. Balakrishnan, T. Lei, H. Ri Kim, Y.I. Song, Y.-J. Kim, K.S. Kim, B. Özyilmaz, J.-H. Ahn, B.H. Hong, S. Iijima, Roll-to-roll production of 30-inch graphene films for transparent electrodes, Nature Nanotechnology, 5 (2010) 574-578.
[879] L. Banszerus, M. Schmitz, S. Engels, M. Goldsche, K. Watanabe, T. Taniguchi, B. Beschoten, C. Stampfer, Ballistic Transport Exceeding 28 μm in CVD Grown Graphene, Nano Letters, 16 (2016) 1387-1391.
[880] T. Kaplas, A. Bera, A. Matikainen, P. Pääkkönen, H. Lipsanen, Transfer and patterning of chemical vapor deposited graphene by a multifunctional polymer film, Applied Physics Letters, 112 (2018) 073107.
[881] K. Batrakov, P. Kuzhir, S. Maksimenko, A. Paddubskaya, S. Voronovich, P. Lambin, T. Kaplas, Y. Svirko, Flexible transparent graphene/polymer multilayers for efficient electromagnetic field absorption, Scientific Reports, 4 (2014).
[882] R. Kotsilkova, P. Todorov, E. Ivanov, T. Kaplas, Y. Svirko, A. Paddubskaya, P. Kuzhir, Mechanical properties investigation of bilayer graphene/poly(methyl methacrylate) thin films at macro, micro and nanoscale, Carbon, 100 (2016) 355-366.
[883] K. Batrakov, P. Kuzhir, S. Maksimenko, A. Paddubskaya, S. Voronovich, P. Lambin, T. Kaplas, Y. Svirko, Flexible transparent graphene/polymer multilayers for efficient electromagnetic field absorption, Sci Rep, 4 (2014) 7191.
[884] M. Corso, Boron Nitride Nanomesh, Science, 303 (2004) 217-220.
[885] S. Berner, M. Corso, R. Widmer, O. Groening, R. Laskowski, P. Blaha, K. Schwarz, A. Goriachko, H. Over, S. Gsell, M. Schreck, H. Sachdev, T. Greber, J. Osterwalder, Boron Nitride Nanomesh: Functionality from a Corrugated Monolayer, Angewandte Chemie International Edition, 46 (2007) 5115-5119.
[886] A. Hemmi, C. Bernard, H. Cun, S. Roth, M. Klöckner, T. Kälin, M. Weinl, S. Gsell, M. Schreck, J. Osterwalder, T. Greber, High quality single atomic layer deposition of hexagonal boron nitride on single crystalline Rh(111) four-inch wafers, Review of Scientific Instruments, 85 (2014) 035101.

[887] S. Chatterjee, M.J. Kim, D.N. Zakharov, S.M. Kim, E.A. Stach, B. Maruyama, L.G. Sneddon, Syntheses of Boron Nitride Nanotubes from Borazine and Decaborane Molecular Precursors by Catalytic Chemical Vapor Deposition with a Floating Nickel Catalyst, Chemistry of Materials, 24 (2012) 2872-2879.
[888] S.K. Jang, J. Youn, Y.J. Song, S. Lee, Synthesis and Characterization of Hexagonal Boron Nitride as a Gate Dielectric, Scientific Reports, 6 (2016).
[889] A. Gibb, N. Alem, A. Zettl, Low pressure chemical vapor deposition synthesis of hexagonal boron nitride on polycrystalline metal foils, physica status solidi (b), 250 (2013) 2727-2731.
[890] S. Suzuki, H. Hibino, Chemical Vapor Deposition of Hexagonal Boron Nitride, e-Journal of Surface Science and Nanotechnology, 10 (2012) 133-138.
[891] A. Ismach, H. Chou, D.A. Ferrer, Y. Wu, S. McDonnell, H.C. Floresca, A. Covacevich, C. Pope, R. Piner, M.J. Kim, R.M. Wallace, L. Colombo, R.S. Ruoff, Toward the Controlled Synthesis of Hexagonal Boron Nitride Films, ACS Nano, 6 (2012) 6378-6385.
[892] H. Cho, S. Park, D.-I. Won, S.O. Kang, S.-S. Pyo, D.-I. Kim, S.M. Kim, H.C. Kim, M.J. Kim, Growth kinetics of white graphene (h-BN) on a planarised Ni foil surface, Scientific Reports, 5 (2015).
[893] Y.-H. Lee, K.-K. Liu, A.-Y. Lu, C.-Y. Wu, C.-T. Lin, W. Zhang, C.-Y. Su, C.-L. Hsu, T.-W. Lin, K.-H. Wei, Y. Shi, L.-J. Li, Growth selectivity of hexagonal-boron nitride layers on Ni with various crystal orientations, RSC Adv., 2 (2012) 111-115.
[894] H.P. A. Andrieux- Ledier, F. Fossard, N. Dorval and A. Loiseau, under review (2017), DOI.
[895] L. Song, L. Ci, H. Lu, P.B. Sorokin, C. Jin, J. Ni, A.G. Kvashnin, D.G. Kvashnin, J. Lou, B.I. Yakobson, P.M. Ajayan, Large Scale Growth and Characterization of Atomic Hexagonal Boron Nitride Layers, Nano Letters, 10 (2010) 3209-3215.
[896] K.K. Kim, A. Hsu, X. Jia, S.M. Kim, Y. Shi, M. Hofmann, D. Nezich, J.F. Rodriguez-Nieva, M. Dresselhaus, T. Palacios, J. Kong, Synthesis of Monolayer Hexagonal Boron Nitride on Cu Foil Using Chemical Vapor Deposition, Nano Letters, 12 (2011) 161-166.
[897] Y. Shi, C. Hamsen, X. Jia, K.K. Kim, A. Reina, M. Hofmann, A.L. Hsu, K. Zhang, H. Li, Z.-Y. Juang, M.S. Dresselhaus, L.-J. Li, J. Kong, Synthesis of Few-Layer Hexagonal Boron Nitride Thin Film by Chemical Vapor Deposition, Nano Letters, 10 (2010) 4134-4139.
[898] Y. Wen, X. Shang, J. Dong, K. Xu, J. He, C. Jiang, Ultraclean and large-area monolayer hexagonal boron nitride on Cu foil using chemical vapor deposition, Nanotechnology, 26 (2015) 275601.
[899] J.-H. Park, J.C. Park, S.J. Yun, H. Kim, D.H. Luong, S.M. Kim, S.H. Choi, W. Yang, J. Kong, K.K. Kim, Y.H. Lee, Large-Area Monolayer Hexagonal Boron Nitride on Pt Foil, ACS Nano, 8 (2014) 8520-8528.
[900] S. Caneva, R.S. Weatherup, B.C. Bayer, R. Blume, A. Cabrero-Vilatela, P. Braeuninger-Weimer, M.-B. Martin, R. Wang, C. Baehtz, R. Schloegl, J.C. Meyer, S. Hofmann, Controlling Catalyst Bulk Reservoir Effects for Monolayer Hexagonal Boron Nitride CVD, Nano Letters, 16 (2016) 1250-1261.
[901] H. Cun, A. Hemmi, E. Miniussi, C. Bernard, B. Probst, K. Liu, D.T.L. Alexander, A. Kleibert, G. Mette, M. Weinl, M. Schreck, J. Osterwalder, A. Radenovic, T. Greber, Centimeter-Sized Single-Orientation Monolayer Hexagonal Boron Nitride With or Without Nanovoids, Nano Letters, 18 (2018) 1205-1212.
[902] R. Wang, P.R. Whelan, P. Braeuninger-Weimer, S. Tappertzhofen, J.A. Alexander-Webber, Z.A. Van Veldhoven, P.R. Kidambi, B.S. Jessen, T. Booth, P. Bøggild, S. Hofmann, Catalyst Interface Engineering for Improved 2D Film Lift-Off and Transfer, ACS Applied Materials & Interfaces, 8 (2016) 33072-33082.
[903] M. O'Brien, N. McEvoy, T. Hallam, H.-Y. Kim, N.C. Berner, D. Hanlon, K. Lee, J.N. Coleman, G.S. Duesberg, Transition Metal Dichalcogenide Growth via Close Proximity Precursor Supply, Scientific Reports, 4 (2014).
[904] D. Dumcenco, D. Ovchinnikov, K. Marinov, P. Lazić, M. Gibertini, N. Marzari, O.L. Sanchez, Y.-C. Kung, D. Krasnozhon, M.-W. Chen, S. Bertolazzi, P. Gillet, A. Fontcuberta i Morral, A. Radenovic, A. Kis, Large-Area Epitaxial Monolayer MoS2, ACS Nano, 9 (2015) 4611-4620.
[905] S. Najmaei, Z. Liu, W. Zhou, X. Zou, G. Shi, S. Lei, B.I. Yakobson, J.-C. Idrobo, P.M. Ajayan, J. Lou, Vapour phase growth and grain boundary structure of molybdenum disulphide atomic layers, Nature Materials, 12 (2013) 754-759.

[906] A.M. van der Zande, P.Y. Huang, D.A. Chenet, T.C. Berkelbach, Y. You, G.-H. Lee, T.F. Heinz, D.R. Reichman, D.A. Muller, J.C. Hone, Grains and grain boundaries in highly crystalline monolayer molybdenum disulphide, Nature Materials, 12 (2013) 554-561.
[907] H. Kim, D. Dumcenco, M. Frégnaux, A. Benayad, M.-W. Chen, Y.-C. Kung, A. Kis, O. Renault, Free-standing electronic character of monolayerMoS2in van der Waals epitaxy, Physical Review B, 94 (2016).
[908] G. Boxhoorn, A. Jesse, J. Ernsting, A. Oskam, Vapour pressure measurements on M (CO) 5PX3 (M= Cr, Mo, W; X= F, Cl, Br), Thermochimica Acta, 27 (1978) 261-267.
[909] Z. Liu, X. Li, M.R. Close, E.L. Kugler, J.L. Petersen, D.B. Dadyburjor, Screening of Alkali-Promoted Vapor-Phase-Synthesized Molybdenum Sulfide Catalysts for the Production of Alcohols from Synthesis Gas, Industrial & Engineering Chemistry Research, 36 (1997) 3085-3093.
[910] M.R. Close, J.L. Petersen, E.L. Kugler, Synthesis and Characterization of Nanoscale Molybdenum Sulfide Catalysts by Controlled Gas Phase Decomposition of Mo(CO)6and H2S, Inorganic Chemistry, 38 (1999) 1535-1542.
[911] Y. Shi, W. Zhou, A.-Y. Lu, W. Fang, Y.-H. Lee, A.L. Hsu, S.M. Kim, K.K. Kim, H.Y. Yang, L.-J. Li, J.-C. Idrobo, J. Kong, van der Waals Epitaxy of MoS2Layers Using Graphene As Growth Templates, Nano Letters, 12 (2012) 2784-2791.
[912] K. Hara, T. Kojima, H. Kukimoto, Epitaxial Growth of CuGaS2by Metalorganic Chemical Vapor Deposition, Japanese Journal of Applied Physics, 26 (1987) L1107-L1109.
[913] K. Kang, S. Xie, L. Huang, Y. Han, P.Y. Huang, K.F. Mak, C.-J. Kim, D. Muller, J. Park, High-mobility three-atom-thick semiconducting films with wafer-scale homogeneity, Nature, 520 (2015) 656-660.
[914] V. Kranthi Kumar, S. Dhar, T.H. Choudhury, S.A. Shivashankar, S. Raghavan, A predictive approach to CVD of crystalline layers of TMDs: the case of MoS2, Nanoscale, 7 (2015) 7802-7810.
[915] L.K. Tan, B. Liu, J.H. Teng, S. Guo, H.Y. Low, K.P. Loh, Atomic layer deposition of a MoS2film, Nanoscale, 6 (2014) 10584-10588.
[916] J.J. Pyeon, S.H. Kim, D.S. Jeong, S.-H. Baek, C.-Y. Kang, J.-S. Kim, S.K. Kim, Wafer-scale growth of MoS2thin films by atomic layer deposition, Nanoscale, 8 (2016) 10792-10798.
[917] Z. Jin, S. Shin, D.H. Kwon, S.-J. Han, Y.-S. Min, Novel chemical route for atomic layer deposition of MoS2thin film on SiO2/Si substrate, Nanoscale, 6 (2014) 14453-14458.
[918] S. Cadot, O. Renault, M. Frégnaux, D. Rouchon, E. Nolot, K. Szeto, C. Thieuleux, L. Veyre, H. Okuno, F. Martin, E.A. Quadrelli, A novel 2-step ALD route to ultra-thin MoS2 films on SiO2 through a surface organometallic intermediate, Nanoscale, 9 (2017) 538-546.
[919] D.J. Lewis, A.A. Tedstone, X.L. Zhong, E.A. Lewis, A. Rooney, N. Savjani, J.R. Brent, S.J. Haigh, M.G. Burke, C.A. Muryn, J.M. Raftery, C. Warrens, K. West, S. Gaemers, P. O'Brien, Thin Films of Molybdenum Disulfide Doped with Chromium by Aerosol-Assisted Chemical Vapor Deposition (AACVD), Chemistry of Materials, 27 (2015) 1367-1374.
[920] J. Cheon, J.E. Gozum, G.S. Girolami, Chemical Vapor Deposition of MoS2and TiS2Films From the Metal−Organic Precursors Mo(S-t-Bu)4and Ti(S-t-Bu)4, Chemistry of Materials, 9 (1997) 1847-1853.
[921] H. Kim, D. Ovchinnikov, D. Deiana, D. Unuchek, A. Kis, Suppressing Nucleation in Metal–Organic Chemical Vapor Deposition of MoS2 Monolayers by Alkali Metal Halides, Nano Letters, 17 (2017) 5056-5063.
[922] W.-C.J. Wei, M.-H. Lo, Processing and properties of (Mo,Cr) oxycarbides from MOCVD, Applied Organometallic Chemistry, 12 (1998) 201-220.
[923] L.H. Kaplan, F.M. d'Heurle, The Deposition of Molybdenum and Tungsten Films from Vapor Decomposition of Carbonyls, Journal of The Electrochemical Society, 117 (1970) 693.
[924] J.R. Stubbles, F.D. Richardson, Equilibria in the system molybdenum + sulphur + hydrogen, Transactions of the Faraday Society, 56 (1960) 1460.
[925] V.E. Kaloidas, N.G. Papayannakos, Hydrogen production from the decomposition of hydrogen sulphide. Equilibrium studies on the system H2S/ H2/Si, (i = 1,…,8) in the gas phase, International Journal of Hydrogen Energy, 12 (1987) 403-409.

[926] S. Dhar, V. Kranthi Kumar, T.H. Choudhury, S.A. Shivashankar, S. Raghavan, Chemical vapor deposition of MoS2 layers from Mo-S-C-O-H system: thermodynamic modeling and validation, Physical Chemistry Chemical Physics, 18 (2016) 14918-14926.
[927] L.W. Fannin, D.W. Webb, R.H. Pearce, Cause and resolution of problem of erratic and decreasing trimethylindium bubbler delivery rates, J Cryst Growth, 124 (1992) 307-310.
[928] A. Koma, Van der Waals epitaxy for highly lattice-mismatched systems, J Cryst Growth, 201-202 (1999) 236-241.
[929] A. Koma, Van der Waals epitaxy—a new epitaxial growth method for a highly lattice-mismatched system, Thin Solid Films, 216 (1992) 72-76.
[930] D.M. Dobkin, M.K. Zuraw, Principles of Chemical Vapor Deposition, Springer Netherlands2013.
[931] H. Li, H. Wu, S. Yuan, H. Qian, Synthesis and characterization of vertically standing MoS2 nanosheets, Scientific Reports, 6 (2016) 21171.
[932] Y. Yu, C. Li, Y. Liu, L. Su, Y. Zhang, L. Cao, Controlled Scalable Synthesis of Uniform, High-Quality Monolayer and Few-layer MoS2 Films, Scientific Reports, 3 (2013) 1866.
[933] D. Zhu, H. Shu, F. Jiang, D. Lv, V. Asokan, O. Omar, J. Yuan, Z. Zhang, C. Jin, Capture the growth kinetics of CVD growth of two-dimensional MoS2, npj 2D Materials and Applications, 1 (2017) 8.
[934] W. Xuan, Z. Yong Ping, C. Zhi Qian, Effect of MoO 3 constituents on the growth of MoS 2 nanosheets by chemical vapor deposition, Materials Research Express, 3 (2016) 065014.
[935] V.N.E. Robinson, J.L. Robins, Nucleation kinetics of gold deposited onto UHV cleaved surfaces of NaCl and KBr, Thin Solid Films, 20 (1974) 155-175.
[936] H. Kim, C. Mattevi, M.R. Calvo, J.C. Oberg, L. Artiglia, S. Agnoli, C.F. Hirjibehedin, M. Chhowalla, E. Saiz, Activation Energy Paths for Graphene Nucleation and Growth on Cu, ACS Nano, 6 (2012) 3614-3623.
[937] J.J. Pyeon, S.H. Kim, D.S. Jeong, S.-H. Baek, C.-Y. Kang, J.-S. Kim, S.K. Kim, Wafer-scale growth of MoS2 thin films by atomic layer deposition, Nanoscale, 8 (2016) 10792-10798.
[938] M. Marx, S. Nordmann, J. Knoch, C. Franzen, C. Stampfer, D. Andrzejewski, T. Kümmell, G. Bacher, M. Heuken, H. Kalisch, A. Vescan, Large-area MoS2 deposition via MOVPE, J Cryst Growth, 464 (2017) 100-104.
[939] S. Jeong-Gyu, R. Gyeong Hee, K. Youngjun, W. Whang Je, K. Kyung Yong, K. Yongsung, L. Changseung, O. Il-Kwon, P. Jusang, L. Zonghoon, K. Hyungjun, Catalytic chemical vapor deposition of large-area uniform two-dimensional molybdenum disulfide using sodium chloride, Nanotechnology, 28 (2017) 465103.
[940] W. Zhan, X. Yong, W. Haolin, W. Ruixue, N. Tang, Z. Yongjie, S. Jing, J. Teng, Z. Ying, L. Yimin, Y. Mei, W. Weidong, Z. Qing, M. Xiaohua, H. Yue, NaCl-assisted one-step growth of MoS 2 –WS 2 in-plane heterostructures, Nanotechnology, 28 (2017) 325602.
[941] F. Reale, P. Palczynski, I. Amit, G.F. Jones, J.D. Mehew, A. Bacon, N. Ni, P.C. Sherrell, S. Agnoli, M.F. Craciun, S. Russo, C. Mattevi, High-Mobility and High-Optical Quality Atomically Thin WS 2, Scientific Reports, 7 (2017) 14911.
[942] S.L.e. al., Vapor-Liquid-Solid Growth of Monolayer MoS2 Nanoribbons, arXiv:1801.09043 DOI (2018).
[943] J. Chen, X. Zhao, S.J.R. Tan, H. Xu, B. Wu, B. Liu, D. Fu, W. Fu, D. Geng, Y. Liu, W. Liu, W. Tang, L. Li, W. Zhou, T.C. Sum, K.P. Loh, Chemical Vapor Deposition of Large-Size Monolayer MoSe2 Crystals on Molten Glass, Journal of the American Chemical Society, 139 (2017) 1073-1076.
[944] L. Zhang, C. Wang, X.-L. Liu, T. Xu, M. Long, E. Liu, C. Pan, G. Su, J. Zeng, Y. Fu, Y. Wang, Z. Yan, A. Gao, K. Xu, P.-H. Tan, L. Sun, Z. Wang, X. Cui, F. Miao, Damage-free and rapid transfer of CVD-grown two-dimensional transition metal dichalcogenides by dissolving sacrificial water-soluble layers, Nanoscale, 9 (2017) 19124-19130.
[945] S. Boandoh, S.H. Choi, J.-H. Park, S.Y. Park, S. Bang, M.S. Jeong, J.S. Lee, H.J. Kim, W. Yang, J.-Y. Choi, S.M. Kim, K.K. Kim, A Novel and Facile Route to Synthesize Atomic-Layered MoS2 Film for Large-Area Electronics, Small, 13 (2017) 1701306.

[946] P. Yang, X. Zou, Z. Zhang, M. Hong, J. Shi, S. Chen, J. Shu, L. Zhao, S. Jiang, X. Zhou, Y. Huan, C. Xie, P. Gao, Q. Chen, Q. Zhang, Z. Liu, Y. Zhang, Batch production of 6-inch uniform monolayer molybdenum disulfide catalyzed by sodium in glass, Nature Communications, 9 (2018).
[947] J. Chen, X. Zhao, G. Grinblat, Z. Chen, S.J.R. Tan, W. Fu, Z. Ding, I. Abdelwahab, Y. Li, D. Geng, Y. Liu, K. Leng, B. Liu, W. Liu, W. Tang, S.A. Maier, S.J. Pennycook, K.P. Loh, Homoepitaxial Growth of Large-Scale Highly Organized Transition Metal Dichalcogenide Patterns, Advanced Materials, 30 (2017) 1704674.
[948] S.M. Eichfeld, L. Hossain, Y.-C. Lin, A.F. Piasecki, B. Kupp, A.G. Birdwell, R.A. Burke, N. Lu, X. Peng, J. Li, A. Azcatl, S. McDonnell, R.M. Wallace, M.J. Kim, T.S. Mayer, J.M. Redwing, J.A. Robinson, Highly Scalable, Atomically Thin WSe2 Grown via Metal–Organic Chemical Vapor Deposition, ACS Nano, 9 (2015) 2080-2087.
[949] W. Xu, Z. Ye, T. Zhou, B. Zhao, L. Zhu, J. Huang, Low-pressure MOCVD growth of p-type ZnO thin films by using NO as the dopant source, J Cryst Growth, 265 (2004) 133-136.
[950] M. Suzuki, J. Nishio, M. Onomura, C. Hongo, Doping characteristics and electrical properties of Mg-doped AlGaN grown by atmospheric-pressure MOCVD, J Cryst Growth, 189-190 (1998) 511-515.
[951] R. Gatensby, N. McEvoy, K. Lee, T. Hallam, N.C. Berner, E. Rezvani, S. Winters, M. O'Brien, G.S. Duesberg, Controlled synthesis of transition metal dichalcogenide thin films for electronic applications, Applied Surface Science, 297 (2014) 139-146.
[952] R. Gatensby, T. Hallam, K. Lee, N. McEvoy, G.S. Duesberg, Investigations of vapour-phase deposited transition metal dichalcogenide films for future electronic applications, Solid-State Electronics, 125 (2016) 39-51.
[953] K. Lee, R. Gatensby, N. McEvoy, T. Hallam, G.S. Duesberg, High-Performance Sensors Based on Molybdenum Disulfide Thin Films, Advanced Materials, 25 (2013) 6699-6702.
[954] M. O'Brien, K. Lee, R. Morrish, N.C. Berner, N. McEvoy, C.A. Wolden, G.S. Duesberg, Plasma assisted synthesis of WS2 for gas sensing applications, Chemical Physics Letters, 615 (2014) 6-10.
[955] C. Yim, K. Lee, N. McEvoy, M. O'Brien, S. Riazimehr, N.C. Berner, C.P. Cullen, J. Kotakoski, J.C. Meyer, M.C. Lemme, G.S. Duesberg, High-Performance Hybrid Electronic Devices from Layered PtSe2 Films Grown at Low Temperature, ACS Nano, 10 (2016) 9550-9558.
[956] D.A. Bandurin, A.V. Tyurnina, G.L. Yu, A. Mishchenko, V. Zólyomi, S.V. Morozov, R.K. Kumar, R.V. Gorbachev, Z.R. Kudrynskyi, S. Pezzini, Z.D. Kovalyuk, U. Zeitler, K.S. Novoselov, A. Patanè, L. Eaves, I.V. Grigorieva, V.I. Fal'ko, A.K. Geim, Y. Cao, High electron mobility, quantum Hall effect and anomalous optical response in atomically thin InSe, Nat Nano, advance online publication (2016).
[957] W. Huang, L. Gan, H. Li, Y. Ma, T. Zhai, 2D layered group IIIA metal chalcogenides: synthesis, properties and applications in electronics and optoelectronics, CrystEngComm, 18 (2016) 3968-3984.
[958] S. Lei, X. Wang, B. Li, J. Kang, Y. He, A. George, L. Ge, Y. Gong, P. Dong, Z. Jin, G. Brunetto, W. Chen, Z.T. Lin, R. Baines, D.S. Galvao, J. Lou, E. Barrera, K. Banerjee, R. Vajtai, P. Ajayan, Surface functionalization of two-dimensional metal chalcogenides by Lewis acid-base chemistry, Nat Nanotechnol, 11 (2016) 465-471.
[959] S. Lei, F. Wen, L. Ge, S. Najmaei, A. George, Y. Gong, W. Gao, Z. Jin, B. Li, J. Lou, J. Kono, R. Vajtai, P. Ajayan, N.J. Halas, An Atomically Layered InSe Avalanche Photodetector, Nano Lett, 15 (2015) 3048-3055.
[960] G.W. Mudd, S.A. Svatek, L. Hague, O. Makarovsky, Z.R. Kudrynskyi, C.J. Mellor, P.H. Beton, L. Eaves, K.S. Novoselov, Z.D. Kovalyuk, E.E. Vdovin, A.J. Marsden, N.R. Wilson, A. Patane, High broad-band photoresponsivity of mechanically formed InSe-graphene van der Waals heterostructures, Adv Mater, 27 (2015) 3760-3766.
[961] L. Debbichi, O. Eriksson, S. Lebegue, Two-Dimensional Indium Selenides Compounds: An Ab Initio Study, J Phys Chem Lett, 6 (2015) 3098-3103.
[962] D.V. Rybkovskiy, A.V. Osadchy, E.D. Obraztsova, Transition from parabolic to ring-shaped valence band maximum in few-layer GaS, GaSe, and InSe, Physical Review B, 90 (2014).
[963] J.F. Sánchez-Royo, G. Muñoz-Matutano, M. Brotons-Gisbert, J.P. Martínez-Pastor, A. Segura, A. Cantarero, R. Mata, J. Canet-Ferrer, G. Tobias, E. Canadell, J. Marqués-Hueso, B.D. Gerardot,

Electronic structure, optical properties, and lattice dynamics in atomically thin indium selenide flakes, Nano Research, 7 (2014) 1556-1568.
[964] D. Wickramaratne, F. Zahid, R.K. Lake, Electronic and thermoelectric properties of van der Waals materials with ring-shaped valence bands, Journal of Applied Physics, 118 (2015) 075101.
[965] V. Zólyomi, N.D. Drummond, V.I. Fal'ko, Electrons and phonons in single layers of hexagonal indium chalcogenides fromab initiocalculations, Physical Review B, 89 (2014).
[966] G. Han, Z.G. Chen, J. Drennan, J. Zou, Indium selenides: structural characteristics, synthesis and their thermoelectric performances, Small, 10 (2014) 2747-2765.
[967] M. Lin, D. Wu, Y. Zhou, W. Huang, W. Jiang, W. Zheng, S. Zhao, C. Jin, Y. Guo, H. Peng, Z. Liu, Controlled growth of atomically thin In2Se3 flakes by van der Waals epitaxy, J Am Chem Soc, 135 (2013) 13274-13277.
[968] J. Zhou, Q. Zeng, D. Lv, L. Sun, L. Niu, W. Fu, F. Liu, Z. Shen, C. Jin, Z. Liu, Controlled Synthesis of High-Quality Monolayered alpha-In2Se3 via Physical Vapor Deposition, Nano Lett, 15 (2015) 6400-6405.
[969] N. Balakrishnan, C.R. Staddon, E.F. Smith, J. Stec, D. Gay, G.W. Mudd, O. Makarovsky, Z.R. Kudrynskyi, Z.D. Kovalyuk, L. Eaves, A. Patanè, P.H. Beton, Quantum confinement and photoresponsivity ofβ-In2Se3nanosheets grown by physical vapour transport, 2D Materials, 3 (2016) 025030.
[970] S. Zhou, X. Tao, Y. Gu, Thickness-Dependent Thermal Conductivity of Suspended Two-Dimensional Single-Crystal In2Se3Layers Grown by Chemical Vapor Deposition, The Journal of Physical Chemistry C, 120 (2016) 4753-4758.
[971] J. Lauth, F.E.S. Gorris, M. Samadi Khoshkhoo, T. Chassé, W. Friedrich, V. Lebedeva, A. Meyer, C. Klinke, A. Kornowski, M. Scheele, H. Weller, Solution-Processed Two-Dimensional Ultrathin InSe Nanosheets, Chemistry of Materials, 28 (2016) 1728-1736.
[972] X. Tao, Y. Gu, Crystalline-crystalline phase transformation in two-dimensional In2Se3 thin layers, Nano Lett, 13 (2013) 3501-3505.
[973] Y.-T. Huang, C.-W. Huang, Jui-Yuan Chen, Yi-Hsin Ting, Kuo-Chang Lu, Yu-Lun Chueh, W.-W. Wu, Dynamic Observation of Phase Transformation Behaviors in Indium(III) Selenide Nanowire Based Phase Change Memory, ACS Nano, 8 (2014) 9457-9462.
[974] R. B. Jacobs-Gedrim, M. Shanmugam, N. Jain, C. A. Durcan, M. T. Murphy, T. M. Murray, R. J. Matyi, R. L. Moore, B. Yu, Extraordinary Photoresponse in Two-Dimensional In2Se3 Nanosheets, ACS Nano, 8 (2014) 514-521.
[975] G.W. Mudd, S.A. Svatek, T. Ren, A. Patane, O. Makarovsky, L. Eaves, P.H. Beton, Z.D. Kovalyuk, G.V. Lashkarev, Z.R. Kudrynskyi, A.I. Dmitriev, Tuning the bandgap of exfoliated InSe nanosheets by quantum confinement, Adv Mater, 25 (2013) 5714-5718.
[976] Z.D. Kovalyuk, Sydor, O.M., Sydor, O.A., Tkachenko, V.G.; Maksymchuk, I.M.,Dubinko, V.I., Ostapchuk, P.M., J. Mater. Sci. Eng. A 2 (2012) 537–543.
[977] A.P. Bakhtinov, V.B. Boledzyuk, Z.D. Kovalyuk, Z.R. Kudrynskyi, O.S. Lytvyn, A.D. Shevchenko, Magnetic properties and surface morphology of layered In2Se3 crystals intercalated with cobalt, Physics of the Solid State, 55 (2013) 1148-1155.
[978] F. Ke, C. Liu, Y. Gao, J. Zhang, D. Tan, Y. Han, Y. Ma, J. Shu, W. Yang, B. Chen, H.-K. Mao, X.-J. Chen, C. Gao, Interlayer-glide-driven isosymmetric phase transition in compressed In2Se3, Applied Physics Letters, 104 (2014) 212102.
[979] T. Nakayama, M. Hishikawa, Bonding and Optical Anisotropy of Vacancy ordered Ga_2Se_3, Journal of the Physical Society of Japan, 66 (1997) 3887-3892.
[980] J. Zhao, H. Nam, T.H. Ly, S.J. Yun, S. Kim, S. Cho, H. Yang, Y.H. Lee, Chain Vacancies in 2D Crystals, Small, 13 (2016) 1601930.
[981] P.R. Kidambi, R. Blume, J. Kling, J.B. Wagner, C. Baehtz, R.S. Weatherup, R. Schloegl, B.C. Bayer, S. Hofmann, In Situ Observations during Chemical Vapor Deposition of Hexagonal Boron Nitride on Polycrystalline Copper, Chemistry of Materials, 26 (2014) 6380-6392.

[982] J.D. Thomsen, T. Gunst, S.S. Gregersen, L. Gammelgaard, B.S. Jessen, D.M.A. Mackenzie, K. Watanabe, T. Taniguchi, P. Boggild, T.J. Booth, Suppression of intrinsic roughness in encapsulated graphene, Physical Review B, 96 (2017).
[983] G.F. Schneider, V.E. Calado, H. Zandbergen, L.M.K. Vandersypen, C. Dekker, Wedging Transfer of Nanostructures, Nano Letters, 10 (2010) 1912-1916.
[984] X. Cui, G.H. Lee, Y.D. Kim, G. Arefe, P.Y. Huang, C.H. Lee, D.A. Chenet, X. Zhang, L. Wang, F. Ye, F. Pizzocchero, B.S. Jessen, K. Watanabe, T. Taniguchi, D.A. Muller, T. Low, P. Kim, J. Hone, Multi-terminal transport measurements of MoS2 using a van der Waals heterostructure device platform, Nature Nanotechnology, 10 (2015) 534-540.
[985] A. Glaser, S. Surnev, F.P. Netzer, N. Fateh, G.A. Fontalvo, C. Mitterer, Oxidation of vanadium nitride and titanium nitride coatings, Surface Science, 601 (2007) 1153-1159.
[986] K. Kang, S.E. Xie, L.J. Huang, Y.M. Han, P.Y. Huang, K.F. Mak, C.J. Kim, D. Muller, J. Park, High-mobility three-atom-thick semiconducting films with wafer-scale homogeneity, Nature, 520 (2015) 656-660.
[987] J. Wong, D. Jariwala, G. Tagliabue, K. Tat, A.R. Davoyan, M.C. Sherrott, H.A. Atwater, High Photovoltaic Quantum Efficiency in Ultrathin van der Waals Heterostructures, Acs Nano, 11 (2017) 7230-7240.
[988] D. Jariwala, A.R. Dayoyan, G. Tagliabue, M.C. Sherrott, J. Wong, H.A. Atwater, Near-Unity Absorption in van der Waals Semiconductors for Ultrathin Optoelectronics, Nano Letters, 16 (2016) 5482-5487.
[989] C.R. Dean, A.F. Young, I. Meric, C. Lee, L. Wang, S. Sorgenfrei, K. Watanabe, T. Taniguchi, P. Kim, K.L. Shepard, J. Hone, Boron nitride substrates for high-quality graphene electronics, Nature Nanotechnology, 5 (2010) 722-726.
[990] S. Tang, H. Wang, H.S. Wang, Q. Sun, X. Zhang, C. Cong, H. Xie, X. Liu, X. Zhou, F. Huang, X. Chen, T. Yu, F. Ding, X. Xie, M. Jiang, Silane-catalysed fast growth of large single-crystalline graphene on hexagonal boron nitride, Nature Communications, 6 (2015) 6499.
[991] X. Song, T. Gao, Y. Nie, J. Zhuang, J. Sun, D. Ma, J. Shi, Y. Lin, F. Ding, Y. Zhang, Z. Liu, Seed-Assisted Growth of Single-Crystalline Patterned Graphene Domains on Hexagonal Boron Nitride by Chemical Vapor Deposition, Nano Letters, 16 (2016) 6109-6116.
[992] S. Tang, G. Ding, X. Xie, J. Chen, C. Wang, X. Ding, F. Huang, W. Lu, M. Jiang, Nucleation and growth of single crystal graphene on hexagonal boron nitride, Carbon, 50 (2012) 329-331.
[993] N. Mishra, V. Miseikis, D. Convertino, M. Gemmi, V. Piazza, C. Coletti, Rapid and catalyst-free van der Waals epitaxy of graphene on hexagonal boron nitride, Carbon, 96 (2016) 497-502.
[994] A.A. SE Saddow, Advances in silicon carbide processing and applications,, Artech House Publisher2004.
[995] Y. Rong, Y. Fan, A. Leen Koh, A.W. Robertson, K. He, S. Wang, H. Tan, R. Sinclair, J.H. Warner, Controlling sulphur precursor addition for large single crystal domains of WS2, Nanoscale, 6 (2014) 12096-12103.
[996] Q. Fu, W. Wang, L. Yang, J. Huang, J. Zhang, B. Xiang, Controllable synthesis of high quality monolayer WS2 on a SiO2/Si substrate by chemical vapor deposition, RSC Advances, 5 (2015) 15795-15799.
[997] C.E. Giusca, I. Rungger, V. Panchal, C. Melios, Z. Lin, Y.-C. Lin, E. Kahn, A.L. Elías, J.A. Robinson, M. Terrones, O. Kazakova, Excitonic Effects in Tungsten Disulfide Monolayers on Two-Layer Graphene, ACS Nano, 10 (2016) 7840-7846.
[998] G.V. Bianco, M. Losurdo, M.M. Giangregorio, A. Sacchetti, P. Prete, N. Lovergine, P. Capezzuto, G. Bruno, Direct epitaxial CVD synthesis of tungsten disulfide on epitaxial and CVD graphene, RSC Advances, 5 (2015) 98700-98708.
[999] M. Okada, T. Sawazaki, K. Watanabe, T. Taniguch, H. Hibino, H. Shinohara, R. Kitaura, Direct Chemical Vapor Deposition Growth of WS2 Atomic Layers on Hexagonal Boron Nitride, ACS Nano, 8 (2014) 8273-8277.

[1000] A. Rossi, H. Büch, C. Di Rienzo, V. Miseikis, D. Convertino, A. Al-Temimy, V. Voliani, M. Gemmi, V. Piazza, C. Coletti, Scalable synthesis of WS2on graphene and h-BN: an all-2D platform for light-matter transduction, 2D Materials, 3 (2016) 031013.
[1001] S. Forti, A. Rossi, H. Büch, T. Cavallucci, F. Bisio, A. Sala, T.O. Menteş, A. Locatelli, M. Magnozzi, M. Canepa, K. Müller, S. Link, U. Starke, V. Tozzini, C. Coletti, Electronic properties of single-layer tungsten disulfide on epitaxial graphene on silicon carbide, Nanoscale, 9 (2017) 16412-16419.
[1002] H.-Y. Kim, K. Lee, N. McEvoy, C. Yim, G.S. Duesberg, Chemically Modulated Graphene Diodes, Nano Letters, 13 (2013) 2182-2188.
[1003] C. Yim, M. O'Brien, N. McEvoy, S. Riazimehr, H. Schäfer-Eberwein, A. Bablich, R. Pawar, G. Iannaccone, C. Downing, G. Fiori, M.C. Lemme, G.S. Duesberg, Heterojunction Hybrid Devices from Vapor Phase Grown MoS2, Scientific Reports, 4 (2014).
[1004] A. Hirsch, J.M. Englert, F. Hauke, Wet Chemical Functionalization of Graphene, Accounts of Chemical Research, 46 (2013) 87-96.
[1005] P. Huang, L. Jing, H. Zhu, X. Gao, Diazonium Functionalized Graphene: Microstructure, Electric, and Magnetic Properties, Accounts of Chemical Research, 46 (2013) 43-52.
[1006] E. Bekyarova, S. Sarkar, F. Wang, M.E. Itkis, I. Kalinina, X. Tian, R.C. Haddon, Effect of Covalent Chemistry on the Electronic Structure and Properties of Carbon Nanotubes and Graphene, Accounts of Chemical Research, 46 (2013) 65-76.
[1007] E.M. Milner, N.T. Skipper, C.A. Howard, M.S.P. Shaffer, D.J. Buckley, K.A. Rahnejat, P.L. Cullen, R.K. Heenan, P. Lindner, R. Schweins, Structure and Morphology of Charged Graphene Platelets in Solution by Small-Angle Neutron Scattering, Journal of the American Chemical Society, 134 (2012) 8302-8305.
[1008] S.A. Hodge, D.J. Buckley, H.C. Yau, N.T. Skipper, C.A. Howard, M.S.P. Shaffer, Chemical routes to discharging graphenides, Nanoscale, 9 (2017) 3150-3158.
[1009] R.A. Schäfer, D. Dasler, U. Mundloch, F. Hauke, A. Hirsch, Basic Insights into Tunable Graphene Hydrogenation, J Am Chem Soc, 138 (2016) 1647-1652.
[1010] V. Strauss, R.A. Schäfer, F. Hauke, A. Hirsch, D.M. Guldi, Polyhydrogenated Graphene: Excited State Dynamics in Photo- and Electroactive Two-Dimensional Domains, Journal of the American Chemical Society, 137 (2015) 13079-13086.
[1011] R.A. Schäfer, K. Weber, M. Koleśnik-Gray, F. Hauke, V. Krstić, B. Meyer, A. Hirsch, Substrate-Modulated Reductive Graphene Functionalization, Angewandte Chemie International Edition, 55 (2016) 14858-14862.
[1012] K.C. Knirsch, J.M. Englert, C. Dotzer, F. Hauke, A. Hirsch, Screening of the chemical reactivity of three different graphite sources using the formation of reductively alkylated graphene as a model reaction, Chemical Communications, 49 (2013) 10811-10813.
[1013] T. Morishita, A.J. Clancy, M.S.P. Shaffer, Optimised exfoliation conditions enhance isolation and solubility of grafted graphenes from graphite intercalation compounds, Journal of Materials Chemistry A, 2 (2014) 15022-15028.
[1014] F. Hof, R.A. Schäfer, C. Weiss, F. Hauke, A. Hirsch, Novel λ3-Iodane-Based Functionalization of Synthetic Carbon Allotropes (SCAs)—Common Concepts and Quantification of the Degree of Addition, Chem. Eur. J., 20 (2014) 16644-16651.
[1015] J.M. Englert, P. Vecera, K.C. Knirsch, R.A. Schäfer, F. Hauke, A. Hirsch, Scanning-Raman-Microscopy for the Statistical Analysis of Covalently Functionalized Graphene, ACS Nano, 7 (2013) 5472-5482.
[1016] F. Hof, S. Bosch, S. Eigler, F. Hauke, A. Hirsch, New Basic Insight into Reductive Functionalization Sequences of Single Walled Carbon Nanotubes (SWCNTs), Journal of the American Chemical Society, 135 (2013) 18385-18395.
[1017] P. Vecera, J.C. Chacón-Torres, T. Pichler, S. Reich, H.R. Soni, A. Görling, K. Edelthalhammer, H. Peterlik, F. Hauke, A. Hirsch, The First Precise Determination of Graphene Functionalisation by in situ Raman Spectroscopy, Nature Communications, DOI (2017) under revision.
[1018] K.C. Knirsch, R.A. Schäfer, F. Hauke, A. Hirsch, Mono- and Ditopic Bisfunctionalization of Graphene, Angewandte Chemie International Edition, 55 (2016) 5861-5864.

[1019] M. Quintana, E. Vazquez, M. Prato, Organic Functionalization of Graphene in Dispersions, Accounts of Chemical Research, 46 (2013) 138-148.
[1020] G.L.C. Paulus, Q.H. Wang, M.S. Strano, Covalent Electron Transfer Chemistry of Graphene with Diazonium Salts, Accounts of Chemical Research, 46 (2013) 160-170.
[1021] J. Park, M. Yan, Covalent Functionalization of Graphene with Reactive Intermediates, Accounts of Chemical Research, 46 (2013) 181-189.
[1022] N.V. Kozhemyakina, S. Eigler, R.E. Dinnebier, A. Inayat, W. Schwieger, A. Hirsch, Effect of the Structure and Morphology of Natural, Synthetic and Post-processed Graphites on Their Dispersibility and Electronic Properties, Fullerenes, Nanotubes and Carbon Nanostructures, 21 (2013) 804-823.
[1023] A.J. Birch, 117. Reduction by dissolving metals. Part I, Journal of the Chemical Society (Resumed), DOI 10.1039/jr9440000430(1944) 430.
[1024] A.J. Birch, 212. Reduction by dissolving metals. Part II, Journal of the Chemical Society (Resumed), DOI 10.1039/JR9450000809(1945) 809-813.
[1025] A.J. Birch, 119. Reduction by dissolving metals. Part III, Journal of the Chemical Society (Resumed), DOI 10.1039/JR9460000593(1946) 593-597.
[1026] A.J. Birch, 25. Reduction by dissolving metals. Part IV, Journal of the Chemical Society (Resumed), DOI 10.1039/JR9470000102(1947) 102-105.
[1027] J.M. Englert, C. Dotzer, G. Yang, M. Schmid, C. Papp, J.M. Gottfried, H.-P. Steinrück, E. Spiecker, F. Hauke, A. Hirsch, Covalent bulk functionalization of graphene, Nat. Chem., 3 (2011) 279-286.
[1028] M.S. Dresselhaus, G. Dresselhaus, Intercalation compounds of graphite, Advances in Physics, 30 (1981) 139-326.
[1029] K.C. Knirsch, F. Hof, V. Lloret, U. Mundloch, F. Hauke, A. Hirsch, Topology-Driven Reductive Silylation of Synthetic Carbon Allotropes, Journal of the American Chemical Society, 138 (2016) 15642-15647.
[1030] A.J. Clancy, J. Melbourne, M.S.P. Shaffer, A one-step route to solubilised, purified or functionalised single-walled carbon nanotubes, Journal of Materials Chemistry A, 3 (2015) 16708-16715.
[1031] D. Dasler, R.A. Schäfer, M.B. Minameyer, J.F. Hitzenberger, F. Hauke, T. Drewello, A. Hirsch, Direct Covalent Coupling of Porphyrins to Graphene, Journal of the American Chemical Society, 139 (2017) 11760-11765.
[1032] C.K. Chan, T.E. Beechem, T. Ohta, M.T. Brumbach, D.R. Wheeler, K.J. Stevenson, Electrochemically Driven Covalent Functionalization of Graphene from Fluorinated Aryl Iodonium Salts, The Journal of Physical Chemistry C, 117 (2013) 12038-12044.
[1033] F. Hof, F. Hauke, A. Hirsch, Brominated single walled carbon nanotubes as versatile precursors for covalent sidewall functionalization, Chemical Communications, 50 (2014) 6582-6584.
[1034] C.A. Dyke, J.M. Tour, Unbundled and Highly Functionalized Carbon Nanotubes from Aqueous Reactions, Nano Letters, 3 (2003) 1215-1218.
[1035] J. Chattopadhyay, S. Chakraborty, A. Mukherjee, R. Wang, P.S. Engel, W.E. Billups, SET Mechanism in the Functionalization of Single-Walled Carbon Nanotubes, The Journal of Physical Chemistry C, 111 (2007) 17928-17932.
[1036] J. Hioe, H. Zipse, Radical stability and its role in synthesis and catalysis, Organic & Biomolecular Chemistry, 8 (2010) 3609-3617.
[1037] Z. Xia, F. Leonardi, M. Gobbi, Y. Liu, V. Bellani, A. Liscio, A. Kovtun, R. Li, X. Feng, E. Orgiu, P. Samorì, E. Treossi, V. Palermo, Electrochemical Functionalization of Graphene at the Nanoscale with Self-Assembling Diazonium Salts, ACS Nano, 10 (2016) 7125-7134.
[1038] D.R. Dreyer, A.D. Todd, C.W. Bielawski, Harnessing the chemistry of graphene oxide, Chemical Society Reviews, 43 (2014) 5288.
[1039] J. Wang, H.-Z. Geng, Z.-J. Luo, S. Zhang, J. Zhang, J. Liu, H.-J. Yang, S. Ma, B. Sun, Y. Wang, S.-X. Da, Y.-Q. Fu, Preparation, characterization, and chemical-induced hydrophobicity of thermostable amine-modified graphene oxide, RSC Adv., 5 (2015) 105393-105399.

[1040] H. Wu, H. Shi, Y. Wang, X. Jia, C. Tang, J. Zhang, S. Yang, Hyaluronic acid conjugated graphene oxide for targeted drug delivery, Carbon, 69 (2014) 379-389.
[1041] S. Eigler, Y. Hu, Y. Ishii, A. Hirsch, Controlled functionalization of graphene oxide with sodium azide, Nanoscale, 5 (2013) 12136.
[1042] J.U. Lee, W. Lee, J.W. Yi, S.S. Yoon, S.B. Lee, B.M. Jung, B.S. Kim, J.H. Byun, Preparation of highly stacked graphene papers via site-selective functionalization of graphene oxide, Journal of Materials Chemistry A, 1 (2013) 12893.
[1043] Q. Mei, K. Zhang, G. Guan, B. Liu, S. Wang, Z. Zhang, Highly efficient photoluminescent graphene oxide with tunable surface properties, Chemical Communications, 46 (2010) 7319.
[1044] C. Neumann, S. Reichardt, P. Venezuela, M. Drögeler, L. Banszerus, M. Schmitz, K. Watanabe, T. Taniguchi, F. Mauri, B. Beschoten, S.V. Rotkin, C. Stampfer, Raman spectroscopy as probe of nanometre-scale strain variations in graphene, Nature Communications, 6 (2015) 8429.
[1045] H.R. Thomas, A.J. Marsden, M. Walker, N.R. Wilson, J.P. Rourke, Sulfur-Functionalized Graphene Oxide by Epoxide Ring-Opening, Angewandte Chemie International Edition, 53 (2014) 7613-7618.
[1046] S. Wang, P.-J. Chia, L.-L. Chua, L.-H. Zhao, R.-Q. Png, S. Sivaramakrishnan, M. Zhou, R.G.S. Goh, R.H. Friend, A.T.S. Wee, P.K.H. Ho, Band-like Transport in Surface-Functionalized Highly Solution-Processable Graphene Nanosheets, Advanced Materials, 20 (2008) 3440-3446.
[1047] H. Yang, C. Shan, F. Li, D. Han, Q. Zhang, L. Niu, Covalent functionalization of polydisperse chemically-converted graphene sheets with amine-terminated ionic liquid, Chemical Communications, DOI 10.1039/b905085j(2009) 3880.
[1048] I.A. Vacchi, C. Spinato, J. Raya, A. Bianco, C. Ménard-Moyon, Chemical reactivity of graphene oxide towards amines elucidated by solid-state NMR, Nanoscale, 8 (2016) 13714-13721.
[1049] S. Stankovich, D.A. Dikin, R.D. Piner, K.A. Kohlhaas, A. Kleinhammes, Y. Jia, Y. Wu, S.T. Nguyen, R.S. Ruoff, Synthesis of graphene-based nanosheets via chemical reduction of exfoliated graphite oxide, Carbon, 45 (2007) 1558-1565.
[1050] J.-X. Jiang, F. Su, A. Trewin, C.D. Wood, N.L. Campbell, H. Niu, C. Dickinson, A.Y. Ganin, M.J. Rosseinsky, Y.Z. Khimyak, A.I. Cooper, Conjugated Microporous Poly(aryleneethynylene) Networks, Angewandte Chemie International Edition, 47 (2008) 1167-1167.
[1051] F. Bonaccorso, L. Colombo, G.H. Yu, M. Stoller, V. Tozzini, A.C. Ferrari, R.S. Ruoff, V. Pellegrini, Graphene, related two-dimensional crystals, and hybrid systems for energy conversion and storage, Science, 347 (2015).
[1052] A. Peigney, C. Laurent, E. Flahaut, R.R. Bacsa, A. Rousset, Specific surface area of carbon nanotubes and bundles of carbon nanotubes, Carbon, 39 (2001) 507-514.
[1053] M.D. Stoller, S.J. Park, Y.W. Zhu, J.H. An, R.S. Ruoff, Graphene-Based Ultracapacitors, Nano Lett., 8 (2008) 3498-3502.
[1054] Y.W. Zhu, S. Murali, W.W. Cai, X.S. Li, J.W. Suk, J.R. Potts, R.S. Ruoff, Graphene and Graphene Oxide: Synthesis, Properties, and Applications, Adv. Mater., 22 (2010) 3906-3924.
[1055] X.H. Cao, Z.Y. Yin, H. Zhang, Three-dimensional graphene materials: preparation, structures and application in supercapacitors, Energy Environ. Sci., 7 (2014) 1850-1865.
[1056] L.M. Dai, D.W. Chang, J.B. Baek, W. Lu, Carbon Nanomaterials for Advanced Energy Conversion and Storage, Small, 8 (2012) 1130-1166.
[1057] P.M. Sudeep, T.N. Narayanan, A. Ganesan, M.M. Shaijumon, H. Yang, S. Ozden, P.K. Patra, M. Pasquali, R. Vajtai, S. Ganguli, A.K. Roy, M.R. Anantharaman, P.M. Ajayan, Covalently Interconnected Three-Dimensional Graphene Oxide Solids, Acs Nano, 7 (2013) 7034-7040.
[1058] J.W. Burress, S. Gadipelli, J. Ford, J.M. Simmons, W. Zhou, T. Yildirim, Graphene Oxide Framework Materials: Theoretical Predictions and Experimental Results, Angew Chem Int Edit, 49 (2010) 8902-8904.
[1059] T. Tsoufis, G. Tuci, S. Caporali, D. Gournis, G. Giambastiani, p-Xylylenediamine intercalation of graphene oxide for the production of stitched nanostructures with a tailored interlayer spacing, Carbon, 59 (2013) 100-108.

[1060] X.Y. Zhang, A. Ciesielski, F. Richard, P.K. Chen, E.A. Prasetyanto, L. De Cola, P. Samorì, Modular Graphene-Based 3D Covalent Networks: Functional Architectures for Energy Applications, Small, 12 (2016) 1044-1052.
[1061] X. Zhuang, D. Gehrig, N. Forler, H. Liang, M. Wagner, M.R. Hansen, F. Laquai, F. Zhang, X. Feng, Conjugated Microporous Polymers with Dimensionality-Controlled Heterostructures for Green Energy Devices, Advanced Materials, 27 (2015) 3789-3796.
[1062] X. Zhuang, F. Zhang, D. Wu, N. Forler, H. Liang, M. Wagner, D. Gehrig, M.R. Hansen, F. Laquai, X. Feng, Two-Dimensional Sandwich-Type, Graphene-Based Conjugated Microporous Polymers, Angewandte Chemie International Edition, 52 (2013) 9668-9672.
[1063] D.A. Jasim, C. Ménard-Moyon, D. Bégin, A. Bianco, K. Kostarelos, Tissue distribution and urinary excretion of intravenously administered chemically functionalized graphene oxide sheets, Chem. Sci., 6 (2015) 3952-3964.
[1064] Y.-J. Wan, L.-C. Tang, D. Yan, L. Zhao, Y.-B. Li, L.-B. Wu, J.-X. Jiang, G.-Q. Lai, Improved dispersion and interface in the graphene/epoxy composites via a facile surfactant-assisted process, Composites Science and Technology, 82 (2013) 60-68.
[1065] H. Bai, Y. Xu, L. Zhao, C. Li, G. Shi, Non-covalent functionalization of graphene sheets by sulfonated polyaniline, Chemical Communications, DOI 10.1039/b821805f(2009) 1667.
[1066] R. Atif, F. Inam, Reasons and remedies for the agglomeration of multilayered graphene and carbon nanotubes in polymers, Beilstein Journal of Nanotechnology, 7 (2016) 1174-1196.
[1067] M. Bhattacharya, Polymer Nanocomposites—A Comparison between Carbon Nanotubes, Graphene, and Clay as Nanofillers, Materials, 9 (2016) 262.
[1068] J. Wei, T. Vo, F. Inam, Epoxy/graphene nanocomposites – processing and properties: a review, RSC Adv., 5 (2015) 73510-73524.
[1069] H.J. Salavagione, G. Martínez, G. Ellis, Graphene-Based Polymer Nanocomposites, Physics and Applications of Graphene - Experiments, 2011.
[1070] T. Ramanathan, A.A. Abdala, S. Stankovich, D.A. Dikin, M. Herrera-Alonso, R.D. Piner, D.H. Adamson, H.C. Schniepp, X. Chen, R.S. Ruoff, S.T. Nguyen, I.A. Aksay, R.K. Prud'Homme, L.C. Brinson, Functionalized graphene sheets for polymer nanocomposites, Nature Nanotechnology, 3 (2008) 327.
[1071] H. Yang, F. Li, C. Shan, D. Han, Q. Zhang, L. Niu, A. Ivaska, Covalent functionalization of chemically converted graphene sheets via silane and its reinforcement, Journal of Materials Chemistry, 19 (2009) 4632-4638.
[1072] A. Alam, C. Wan, T. McNally, Surface amination of carbon nanoparticles for modification of epoxy resins: plasma-treatment vs. wet-chemistry approach, European Polymer Journal, 87 (2017) 422-448.
[1073] X. Ji, Y. Xu, W. Zhang, L. Cui, J. Liu, Review of functionalization, structure and properties of graphene/polymer composite fibers, Composites Part A: Applied Science and Manufacturing, 87 (2016) 29-45.
[1074] L. Vaisman, H.D. Wagner, G. Marom, The role of surfactants in dispersion of carbon nanotubes, Advances in Colloid and Interface Science, 128-130 (2006) 37-46.
[1075] R. Verdejo, M.M. Bernal, L.J. Romasanta, M.A. Lopez-Manchado, Graphene filled polymer nanocomposites, Journal of Materials Chemistry, 21 (2011) 3301-3310.
[1076] Z. Li, R. Wang, R.J. Young, L. Deng, F. Yang, L. Hao, W. Jiao, W. Liu, Control of the functionality of graphene oxide for its application in epoxy nanocomposites, Polymer, 54 (2013) 6437-6446.
[1077] A.S. Wajid, S. Das, F. Irin, H.S.T. Ahmed, J.L. Shelburne, D. Parviz, R.J. Fullerton, A.F. Jankowski, R.C. Hedden, M.J. Green, Polymer-stabilized graphene dispersions at high concentrations in organic solvents for composite production, Carbon, 50 (2012) 526-534.
[1078] Y.-J. Wan, L.-X. Gong, L.-C. Tang, L.-B. Wu, J.-X. Jiang, Mechanical properties of epoxy composites filled with silane-functionalized graphene oxide, Composites Part A: Applied Science and Manufacturing, 64 (2014) 79-89.
[1079] S. Hou, S. Su, M.L. Kasner, P. Shah, K. Patel, C.J. Madarang, Formation of highly stable dispersions of silane-functionalized reduced graphene oxide, Chemical Physics Letters, 501 (2010) 68-74.

[1080] Functionalization of Graphene, Wiley-VCH Verlag GmbH & Co. KGaA2014.
[1081] V. Georgakilas, M. Otyepka, A.B. Bourlinos, V. Chandra, N. Kim, K.C. Kemp, P. Hobza, R. Zboril, K.S. Kim, Functionalization of Graphene: Covalent and Non-Covalent Approaches, Derivatives and Applications, Chemical Reviews, 112 (2012) 6156-6214.
[1082] B. Yuan, H. Sheng, X. Mu, L. Song, Q. Tai, Y. Shi, K.M. Liew, Y. Hu, Enhanced flame retardancy of polypropylene by melamine-modified graphene oxide, Journal of Materials Science, 50 (2015) 5389-5401.
[1083] M. Xie, H. Lei, Y. Zhang, Y. Xu, S. Shen, Y. Ge, H. Li, J. Xie, Non-covalent modification of graphene oxide nanocomposites with chitosan/dextran and its application in drug delivery, RSC Advances, 6 (2016) 9328-9337.
[1084] Y. Mao, S. Wen, Y. Chen, F. Zhang, P. Panine, T.W. Chan, L. Zhang, Y. Liang, L. Liu, High Performance Graphene Oxide Based Rubber Composites, Scientific Reports, 3 (2013) 2508.
[1085] A.E. Vladár, http://dx.doi.org/10.6028/NIST.SP.1200-17 "Strategies for scanning electron microscopy sample preparation and characterization of multiwall carbon nanotube polymer composites", National Institute of Standards and Technology.
[1086] J.P. Rabe, S. Buchholz, Commensurability and Mobility in 2-Dimensional Molecular-Patterns on Graphite, Science, 253 (1991) 424-427.
[1087] C.S. Boland, U. Khan, C. Backes, A. O'Neill, J. McCauley, S. Duane, R. Shanker, Y. Liu, I. Jurewicz, A.B. Dalton, J.N. Coleman, Sensitive, High-Strain, High-Rate Bodily Motion Sensors Based on Graphene-Rubber Composites, Acs Nano, 8 (2014) 8819-8830.
[1088] M. Grande, G.V. Bianco, M.A. Vincenti, D. de Ceglia, P. Capezzuto, M. Scalora, A. D'Orazio, G. Bruno, Optically Transparent Microwave Polarizer Based On Quasi-Metallic Graphene, 5 (2015) 17083.
[1089] B. Sachs, T.O. Wehling, A. I, M. I, Theory of Doping: Monovalent Adsorbates, Physics and Applications of Graphene - Theory, InTech, 2011.
[1090] F. Karlický, K. Kumara Ramanatha Datta, M. Otyepka, R. Zbořil, Halogenated Graphenes: Rapidly Growing Family of Graphene Derivatives, ACS Nano, 7 (2013) 6434-6464.
[1091] H.L. Poh, P. Šimek, Z. Sofer, M. Pumera, Halogenation of Graphene with Chlorine, Bromine, or Iodine by Exfoliation in a Halogen Atmosphere, Chemistry - A European Journal, 19 (2013) 2655-2662.
[1092] A.E. Mansour, S. Dey, A. Amassian, M.H. Tanielian, Bromination of Graphene: A New Route to Making High Performance Transparent Conducting Electrodes with Low Optical Losses, ACS Applied Materials & Interfaces, 7 (2015) 17692-17699.
[1093] M. Bruna, A.K. Ott, M. Ijäs, D. Yoon, U. Sassi, A.C. Ferrari, Doping Dependence of the Raman Spectrum of Defected Graphene, ACS Nano, 8 (2014) 7432-7441.
[1094] L.G. Cançado, A. Jorio, E.H.M. Ferreira, F. Stavale, C.A. Achete, R.B. Capaz, M.V.O. Moutinho, A. Lombardo, T.S. Kulmala, A.C. Ferrari, Quantifying Defects in Graphene via Raman Spectroscopy at Different Excitation Energies, Nano Letters, 11 (2011) 3190-3196.
[1095] N.C. Berner, S. Winters, C. Backes, C. Yim, K.C. Dumbgen, I. Kaminska, S. Mackowski, A.A. Cafolla, A. Hirsch, G.S. Duesberg, Understanding and optimising the packing density of perylene bisimide layers on CVD-grown graphene, Nanoscale, 7 (2015) 16337-16342.
[1096] X.Q. Tian, J.B. Xu, X.M. Wang, Self-Assembly of PTCDA Ultrathin Films on Graphene: Structural Phase Transition and Charge Transfer Saturation, The Journal of Physical Chemistry C, 114 (2010) 20917-20924.
[1097] H. Huang, S. Chen, X. Gao, W. Chen, A.T.S. Wee, Structural and Electronic Properties of PTCDA Thin Films on Epitaxial Graphene, ACS Nano, 3 (2009) 3431-3436.
[1098] Q.H. Wang, M.C. Hersam, Room-temperature molecular-resolution characterization of self-assembled organic monolayers on epitaxial graphene, Nature Chemistry, 1 (2009) 206.
[1099] S. Winters, N.C. Berner, R. Mishra, K.C. Dumbgen, C. Backes, M. Hegner, A. Hirsch, G.S. Duesberg, On-surface derivatisation of aromatic molecules on graphene: the importance of packing density, Chemical Communications, 51 (2015) 16778-16781.

[1100] M. Woszczyna, A. Winter, M. Grothe, A. Willunat, S. Wundrack, R. Stosch, T. Weimann, F. Ahlers, A. Turchanin, All-Carbon Vertical van der Waals Heterostructures: Non-destructive Functionalization of Graphene for Electronic Applications, Advanced Materials, 26 (2014) 4831-+.
[1101] K.S. Novoselov, A.K. Geim, S.V. Morozov, D. Jiang, M.I. Katsnelson, I.V. Grigorieva, S.V. Dubonos, A.A. Firsov, Two-dimensional gas of massless Dirac fermions in graphene, Nature, 438 (2005) 197.
[1102] Y. Liu, X. Dong, P. Chen, Biological and chemical sensors based on graphene materials, Chemical Society Reviews, 41 (2012) 2283-2307.
[1103] C.K. Chua, M. Pumera, Covalent chemistry on graphene, Chemical Society Reviews, 42 (2013) 3222-3233.
[1104] Z. Sun, S.-i. Kohama, Z. Zhang, J.R. Lomeda, J.M. Tour, Soluble graphene through edge-selective functionalization, Nano Research, 3 (2010) 117-125.
[1105] A. Bellunato, H. Arjmandi Tash, Y. Cesa, G.F. Schneider, Chemistry at the Edge of Graphene, ChemPhysChem, 17 (2016) 785-801.
[1106] F.M. Koehler, A. Jacobsen, K. Ensslin, C. Stampfer, W.J. Stark, Selective Chemical Modification of Graphene Surfaces: Distinction Between Single- and Bilayer Graphene, Small, 6 (2010) 1125-1130.
[1107] J.R. Lomeda, C.D. Doyle, D.V. Kosynkin, W.-F. Hwang, J.M. Tour, Diazonium Functionalization of Surfactant-Wrapped Chemically Converted Graphene Sheets, Journal of the American Chemical Society, 130 (2008) 16201-16206.
[1108] M. Quintana, A. Montellano, A.E. del Rio Castillo, G.V. Tendeloo, C. Bittencourt, M. Prato, Selective organic functionalization of graphene bulk or graphene edges, Chemical Communications, 47 (2011) 9330-9332.
[1109] A. Wang, W. Yu, Z. Huang, F. Zhou, J. Song, Y. Song, L. Long, M.P. Cifuentes, M.G. Humphrey, L. Zhang, J. Shao, C. Zhang, Covalent functionalization of reduced graphene oxide with porphyrin by means of diazonium chemistry for nonlinear optical performance, Scientific Reports, 6 (2016) 23325.
[1110] S. Niyogi, E. Bekyarova, J. Hong, S. Khizroev, C. Berger, W. de Heer, R.C. Haddon, Covalent Chemistry for Graphene Electronics, The Journal of Physical Chemistry Letters, 2 (2011) 2487-2498.
[1111] M.M. Bernal, A.D. Pierro, C. Novara, F. Giorgis, B. Mortazavi, G. Saracco, A. Fina, Edge-grafted molecular junctions between graphene nanoplatelets: applied chemistry to enhance heat transfer in nanomaterials, submitted, DOI (2017).
[1112] M.M. Bernal, C. Novara, S. Colonna, F. Giorgis, A. Fina, In preparation, DOI (2017).
[1113] D.B. Farmer, R. Golizadeh-Mojarad, V. Perebeinos, Y.-M. Lin, G.S. Tulevski, J.C. Tsang, P. Avouris, Chemical Doping and Electron−Hole Conduction Asymmetry in Graphene Devices, Nano Letters, 9 (2009) 388-392.
[1114] D. Bouša, O. Jankovský, D. Sedmidubský, J. Luxa, J. Šturala, M. Pumera, Z. Sofer, Mesomeric Effects of Graphene Modified with Diazonium Salts: Substituent Type and Position Influence its Properties, Chemistry – A European Journal, 21 (2015) 17728-17738.
[1115] R.A. Bueno, J.I. Martínez, R.F. Luccas, N.R. del Árbol, C. Munuera, I. Palacio, F.J. Palomares, K. Lauwaet, S. Thakur, J.M. Baranowski, W. Strupinski, M.F. López, F. Mompean, M. García-Hernández, J.A. Martín-Gago, Highly selective covalent organic functionalization of epitaxial graphene, Nature Communications, 8 (2017) 15306.
[1116] M. Castelaín, G. Martínez, C. Marco, G. Ellis, H.J. Salavagione, Effect of Click-Chemistry Approaches for Graphene Modification on the Electrical, Thermal, and Mechanical Properties of Polyethylene/Graphene Nanocomposites, Macromolecules, 46 (2013) 8980-8987.
[1117] A. Criado, M. Melchionna, S. Marchesan, M. Prato, The Covalent Functionalization of Graphene on Substrates, Angewandte Chemie International Edition, 54 (2015) 10734-10750.
[1118] J.M. Englert, C. Dotzer, G. Yang, M. Schmid, C. Papp, J.M. Gottfried, H.-P. Steinrück, E. Spiecker, F. Hauke, A. Hirsch, Covalent bulk functionalization of graphene, Nature Chemistry, 3 (2011) 279-286.
[1119] M.Z. Hossain, M.A. Walsh, M.C. Hersam, Scanning Tunneling Microscopy, Spectroscopy, and Nanolithography of Epitaxial Graphene Chemically Modified with Aryl Moieties, Journal of the American Chemical Society, 132 (2010) 15399-15403.

[1120] S. Niyogi, E. Bekyarova, M.E. Itkis, H. Zhang, K. Shepperd, J. Hicks, M. Sprinkle, C. Berger, C.N. Lau, W.A. deHeer, E.H. Conrad, R.C. Haddon, Spectroscopy of Covalently Functionalized Graphene, Nano Letters, 10 (2010) 4061-4066.
[1121] M.H. Gass, U. Bangert, A.L. Bleloch, P. Wang, R.R. Nair, A.K. Geim, Free-standing graphene at atomic resolution, Nature Nanotechnology, 3 (2008) 676-681.
[1122] J.C. Meyer, C. Kisielowski, R. Erni, M.D. Rossell, M.F. Crommie, A. Zettl, Direct Imaging of Lattice Atoms and Topological Defects in Graphene Membranes, Nano Letters, 8 (2008) 3582-3586.
[1123] L. Rodrigo, P. Pou, R. Pérez, Graphene monovacancies: Electronic and mechanical properties from large scale ab initio simulations, Carbon, 103 (2016) 200-208.
[1124] M.M. Ugeda, D. Fernández-Torre, I. Brihuega, P. Pou, A.J. Martínez-Galera, R. Pérez, J.M. Gómez-Rodríguez, Point Defects on Graphene on Metals, Physical Review Letters, 107 (2011).
[1125] K.F. Kelly, D. Sarkar, G.D. Hale, S.J. Oldenburg, N.J. Halas, Threefold Electron Scattering on Graphite Observed with C60-Adsorbed STM Tips, Science, 273 (1996) 1371-1373.
[1126] O. Lehtinen, J. Kotakoski, A.V. Krasheninnikov, A. Tolvanen, K. Nordlund, J. Keinonen, Effects of ion bombardment on a two-dimensional target: Atomistic simulations of graphene irradiation, Physical Review B, 81 (2010).
[1127] Q. Li, N. Mahmood, J. Zhu, Y. Hou, S. Sun, Graphene and its composites with nanoparticles for electrochemical energy applications, Nano Today, 9 (2014) 668-683.
[1128] H.C. Choi, M. Shim, S. Bangsaruntip, H. Dai, Spontaneous Reduction of Metal Ions on the Sidewalls of Carbon Nanotubes, Journal of the American Chemical Society, 124 (2002) 9058-9059.
[1129] S. Fogden, C.A. Howard, R.K. Heenan, N.T. Skipper, M.S.P. Shaffer, Scalable Method for the Reductive Dissolution, Purification, and Separation of Single-Walled Carbon Nanotubes, ACS Nano, 6 (2012) 54-62.
[1130] C.A. Howard, H. Thompson, J.C. Wasse, N.T. Skipper, Formation of Giant Solvation Shells around Fulleride Anions in Liquid Ammonia, Journal of the American Chemical Society, 126 (2004) 13228-13229.
[1131] A. Catheline, C. Vallés, C. Drummond, L. Ortolani, V. Morandi, M. Marcaccio, M. Iurlo, F. Paolucci, A. Pénicaud, Graphene solutions, Chemical Communications, 47 (2011) 5470.
[1132] A. Pénicaud, P. Poulin, A. Derré, E. Anglaret, P. Petit, Spontaneous Dissolution of a Single-Wall Carbon Nanotube Salt, Journal of the American Chemical Society, 127 (2005) 8-9.
[1133] S.A. Hodge, S. Fogden, C.A. Howard, N.T. Skipper, M.S.P. Shaffer, Electrochemical Processing of Discrete Single-Walled Carbon Nanotube Anions, ACS Nano, 7 (2013) 1769-1778.
[1134] M.K. Bayazit, A. Suri, K.S. Coleman, Formylation of single-walled carbon nanotubes, Carbon, 48 (2010) 3412-3419.
[1135] K. Chen, C. Ge, J. Li, Phase Formation and Thermodynamic Analysis of Self-propagating High-temperature Synthesis Al–Zr–N System Composites, Journal of Materials Research, 13 (1998) 2610-2613.
[1136] R. Graupner, J. Abraham, D. Wunderlich, A. Vencelová, P. Lauffer, J. Röhrl, M. Hundhausen, L. Ley, A. Hirsch, Nucleophilic−Alkylation−Reoxidation: A Functionalization Sequence for Single-Wall Carbon Nanotubes, Journal of the American Chemical Society, 128 (2006) 6683-6689.
[1137] A. Mukherjee, R. Combs, J. Chattopadhyay, D.W. Abmayr, P.S. Engel, W.E. Billups, Attachment of Nitrogen and Oxygen Centered Radicals to Single-Walled Carbon Nanotube Salts, Chemistry of Materials, 20 (2008) 7339-7343.
[1138] D. Wunderlich, F. Hauke, A. Hirsch, Preferred Functionalization of Metallic and Small-Diameter Single-Walled Carbon Nanotubes by Nucleophilic Addition of Organolithium and -Magnesium Compounds Followed by Reoxidation, Chemistry - A European Journal, 14 (2008) 1607-1614.
[1139] C.A. Howard, M.P.M. Dean, F. Withers, Phonons in potassium-doped graphene: The effects of electron-phonon interactions, dimensionality, and adatom ordering, Physical Review B, 84 (2011).
[1140] S.A. Hodge, H.H. Tay, D.B. Anthony, R. Menzel, D.J. Buckley, P.L. Cullen, N.T. Skipper, C.A. Howard, M.S.P. Shaffer, Probing the charging mechanisms of carbon nanomaterial polyelectrolytes, Faraday Discuss., 172 (2014) 311-325.

[1141] A.J. Bard, L.R. Faulkner, Electrochemical Methods, 2nd ed., John Wiley & Sons, Inc., New York, 2001.
[1142] W. Wei, G. Wang, S. Yang, X. Feng, K. Müllen, Efficient Coupling of Nanoparticles to Electrochemically Exfoliated Graphene, Journal of the American Chemical Society, 137 (2015) 5576-5581.
[1143] Y. Huttel, Gas-Phase Synthesis of Nanoparticles, Wiley-VCH, Weinheim, 2017.
[1144] F. Frank, W. Schulze, B. Tesche, J. Urban, B. Winter, Formation of metal clusters and molecules by means of the gas aggregation technique and characterisation of size distribution, Surf. Sci., 156 90-99.
[1145] D. Llamosa, M. Ruano, L. Martínez, A. Mayoral, E. Roman, M. García-Hernández, Y. Huttel, The ultimate step towards a tailored engineering of core@shell and core@shell@shell nanoparticles, Nanoscale, 6 (2014) 13483-13486.
[1146] L. Martínez, M. Díaz, E. Román, M. Ruano, D. Llamosa P, Y. Huttel, Generation of Nanoparticles with Adjustable Size and Controlled Stoichiometry: Recent Advances, Langmuir, 28 (2012) 11241-11249.
[1147] L. Martínez, A. Mayoral, M. Espiñeira, E. Roman, F.J. Palomares, Y. Huttel, Core@shell, Au@TiOx nanoparticles by gas phase synthesis, Nanoscale, 9 (2017) 6463-6470.
[1148] R. Ferrando, J. Jellinek, R.L. Johnston, Nanoalloys: From Theory to Applications of Alloy Clusters and Nanoparticles, Chemical Reviews, 108 (2008) 845-910.
[1149] R. Ghosh Chaudhuri, S. Paria, Core/Shell Nanoparticles: Classes, Properties, Synthesis Mechanisms, Characterization, and Applications, Chemical Reviews, 112 (2012) 2373-2433.
[1150] D. Pohl, A. Surrey, L. Schultz, B. Rellinghaus, The impact of oxygen on the morphology of gas-phase prepared Au nanoparticles, Applied Physics Letters, 101 (2012) 263105.
[1151] M.A. Garcia, E. Fernandez Pinel, J. de la Venta, A. Quesada, V. Bouzas, J.F. Fernández, J.J. Romero, M.S. Martín González, J.L. Costa-Krämer, Sources of experimental errors in the observation of nanoscale magnetism, Journal of Applied Physics, 105 (2009) 013925.
[1152] M. Ruano, M. Díaz, L. Martínez, E. Navarro, E. Román, M. García-Hernandez, A. Espinosa, C. Ballesteros, R. Fermento, Y. Huttel, Matrix and interaction effects on the magnetic properties of Co nanoparticles embedded in gold and vanadium, Phys. Chem. Chem. Phys., 15 (2013) 316-329.
[1153] S.R. Plant, L. Cao, R.E. Palmer, Atomic Structure Control of Size-Selected Gold Nanoclusters during Formation, Journal of the American Chemical Society, 136 (2014) 7559-7562.
[1154] M. Jordá-Beneyto, F. Suárez-García, D. Lozano-Castelló, D. Cazorla-Amorós, A. Linares-Solano, Hydrogen storage on chemically activated carbons and carbon nanomaterials at high pressures, Carbon, 45 (2007) 293-303.
[1155] A. Züttel, C. Nützenadel, P. Sudan, P. Mauron, C. Emmenegger, S. Rentsch, L. Schlapbach, A. Weidenkaff, T. Kiyobayashi, Hydrogen sorption by carbon nanotubes and other carbon nanostructures, Journal of Alloys and Compounds, 330-332 (2002) 676-682.
[1156] C. Shen, K.-F. Aguey-Zinsou, Nanosized Magnesium Electrochemically Deposited on a Carbon Nanotubes Suspension: Synthesis and Hydrogen Storage, Frontiers in Energy Research, 5 (2017).
[1157] S.-J. Hwang, Y.-S. Chuang, Enhanced hydrogen storage properties of MgH 2 co-catalyzed with zirconium oxide and single-walled carbon nanotubes, Journal of Alloys and Compounds, 664 (2016) 284-290.
[1158] Y. Liu, J. Zou, X. Zeng, X. Wu, H. Tian, W. Ding, J. Wang, A. Walter, Study on hydrogen storage properties of Mg nanoparticles confined in carbon aerogels, International Journal of Hydrogen Energy, 38 (2013) 5302-5308.
[1159] L. Popilevsky, V.M. Skripnyuk, M. Beregovsky, M. Sezen, Y. Amouyal, E. Rabkin, Hydrogen storage and thermal transport properties of pelletized porous Mg-2 wt.% multiwall carbon nanotubes and Mg-2 wt.% graphite composites, International Journal of Hydrogen Energy, 41 (2016) 14461-14474.
[1160] Y. Yürüm, A. Taralp, T.N. Veziroglu, Storage of hydrogen in nanostructured carbon materials, International Journal of Hydrogen Energy, 34 (2009) 3784-3798.

[1161] S. Zhang, A.F. Gross, S.L. Van Atta, M. Lopez, P. Liu, C.C. Ahn, J.J. Vajo, C.M. Jensen, The synthesis and hydrogen storage properties of a MgH2incorporated carbon aerogel scaffold, Nanotechnology, 20 (2009) 204027.
[1162] W. Liu, E. Setijadi, L. Crema, R. Bartali, N. Laidani, K.F. Aguey-Zinsou, G. Speranza, Carbon nanostructures/Mg hybrid materials for hydrogen storage, Diamond and Related Materials, 82 (2018) 19-24.
[1163] K.-F. Aguey-Zinsou, J.-R. Ares-Fernández, Synthesis of Colloidal Magnesium: A Near Room Temperature Store for Hydrogen, Chemistry of Materials, 20 (2008) 376-378.
[1164] Z. Lu, A. Schechter, M. Moshkovich, D. Aurbach, On the electrochemical behavior of magnesium electrodes in polar aprotic electrolyte solutions, Journal of Electroanalytical Chemistry, 466 (1999) 203-217.
[1165] E.J. Setijadi, C. Boyer, K.-F. Aguey-Zinsou, Remarkable hydrogen storage properties for nanocrystalline MgH2 synthesised by the hydrogenolysis of Grignard reagents, Physical Chemistry Chemical Physics, 14 (2012) 11386.
[1166] E.J. Setijadi, C. Boyer, K.-F. Aguey-Zinsou, Switching the thermodynamics of MgH2nanoparticles through polystyrene stabilisation and oxidation, RSC Adv., 4 (2014) 39934.
[1167] W. Liu, K.-F. Aguey-Zinsou, Size effects and hydrogen storage properties of Mg nanoparticles synthesised by an electroless reduction method, Journal of Materials Chemistry A, 2 (2014) 9718.
[1168] E.S. Cho, A.M. Ruminski, S. Aloni, Y.-S. Liu, J. Guo, J.J. Urban, Graphene oxide/metal nanocrystal multilaminates as the atomic limit for safe and selective hydrogen storage, Nature Communications, 7 (2016) 10804.
[1169] G. Liu, Y. Wang, L. Jiao, H. Yuan, Understanding the Role of Few-Layer Graphene Nanosheets in Enhancing the Hydrogen Sorption Kinetics of Magnesium Hydride, ACS Applied Materials & Interfaces, 6 (2014) 11038-11046.
[1170] H. Tachikawa, T. Iyama, H. Kawabata, MD simulation of the interaction of magnesium with graphene, Thin Solid Films, 518 (2009) 877-879.
[1171] R. Liu, Y. Zhao, T. Chu, Theoretical exploration of MgH2and graphene nano-flakes in cyclohexane: proposing a new perspective toward functional hydrogen storage material, Chem. Commun., 51 (2015) 2429-2432.
[1172] V. Tozzini, V. Pellegrini, Prospects for hydrogen storage in graphene, Phys. Chem. Chem. Phys., 15 (2013) 80-89.
[1173] G. Barkhordarian, T. Klassen, R. Bormann, Kinetic investigation of the effect of milling time on the hydrogen sorption reaction of magnesium catalyzed with different Nb2O5 contents, Journal of Alloys and Compounds, 407 (2006) 249-255.
[1174] B. Bogdanović, K. Bohmhammel, B. Christ, A. Reiser, K. Schlichte, R. Vehlen, U. Wolf, Thermodynamic investigation of the magnesium–hydrogen system, Journal of Alloys and Compounds, 282 (1999) 84-92.
[1175] K.-F. Aguey-Zinsou, J.-R. Ares-Fernández, Hydrogen in magnesium: new perspectives toward functional stores, Energy & Environmental Science, 3 (2010) 526.
[1176] J. Graetz, New approaches to hydrogen storage, Chem. Soc. Rev., 38 (2009) 73-82.
[1177] K.C. Kim, B. Dai, J. Karl Johnson, D.S. Sholl, Assessing nanoparticle size effects on metal hydride thermodynamics using the Wulff construction, Nanotechnology, 20 (2009) 204001.
[1178] M. Makarova, Y. Okawa, M. Aono, Selective Adsorption of Thiol Molecules at Sulfur Vacancies on MoS2(0001), Followed by Vacancy Repair via S–C Dissociation, The Journal of Physical Chemistry C, 116 (2012) 22411-22416.
[1179] S.S. Chou, M. De, J. Kim, S. Byun, C. Dykstra, J. Yu, J. Huang, V.P. Dravid, Ligand Conjugation of Chemically Exfoliated MoS2, Journal of the American Chemical Society, 135 (2013) 4584-4587.
[1180] L. Zhou, B. He, Y. Yang, Y. He, Facile approach to surface functionalized MoS2 nanosheets, RSC Advances, 4 (2014) 32570-32578.
[1181] K. Yuan, X. Zhuang, H. Fu, G. Brunklaus, M. Forster, Y. Chen, X. Feng, U. Scherf, Two-Dimensional Core-Shelled Porous Hybrids as Highly Efficient Catalysts for the Oxygen Reduction Reaction, Angew Chem Int Ed, 55 (2016) 6858-6863.

[1182] C. Backes, N.C. Berner, X. Chen, P. Lafargue, P. LaPlace, M. Freeley, G.S. Duesberg, J.N. Coleman, A.R. McDonald, Functionalization of Liquid-Exfoliated Two-Dimensional 2H-MoS2, Angewandte Chemie International Edition, 54 (2015) 2638-2642.
[1183] X. Chen, A.R. McDonald, Functionalization of Two-Dimensional Transition-Metal Dichalcogenides, Advanced Materials, 28 (2016) 5738-5746.
[1184] A. Hirsch, F. Hauke, Post Graphene 2D Chemistry: The Emerging Field of Molybdenum Disulfide and Black Phosphorus Functionalization, Angewandte Chemie International Edition, DOI 10.1002/anie.201708211 n/a-n/a.
[1185] C. Wirtz, T. Hallam, C.P. Cullen, N.C. Berner, M. O'Brien, M. Marcia, A. Hirsch, G.S. Duesberg, Atomic layer deposition on 2D transition metal chalcogenides: layer dependent reactivity and seeding with organic ad-layers, Chemical Communications, 51 (2015) 16553-16556.
[1186] Y.Y. Wang, R.X. Gao, Z.H. Ni, H. He, S.P. Guo, H.P. Yang, C.X. Cong, T. Yu, Thickness identification of two-dimensional materials by optical imaging, Nanotechnology, 23 (2012) 495713.
[1187] A. Castellanos-Gomez, E. Navarro-Moratalla, G. Mokry, J. Quereda, E. Pinilla-Cienfuegos, N. Agraït, H.S. van der Zant, E. Coronado, G.A. Steele, G. Rubio-Bollinger, Fast and reliable identification of atomically thin layers of TaSe2 crystals, Nano Research, 6 (2013) 191-199.
[1188] H. Zhang, F. Ran, X. Shi, X. Fang, S. Wu, Y. Liu, X. Zheng, P. Yang, Y. Liu, L. Wang, Optical thickness identification of transition metal dichalcogenide nanosheets on transparent substrates, Nanotechnology, 28 (2017) 164001.
[1189] H. Li, G. Lu, Z. Yin, Q. He, H. Li, Q. Zhang, H. Zhang, Optical Identification of Single- and Few-Layer MoS2 Sheets, Small, 8 (2012) 682-686.
[1190] P. Blake, E. Hill, A. Castro Neto, K. Novoselov, D. Jiang, R. Yang, T. Booth, A. Geim, Making graphene visible, Applied Physics Letters, 91 (2007) 063124.
[1191] C. Casiraghi, A. Hartschuh, E. Lidorikis, H. Qian, H. Harutyunyan, T. Gokus, K.S. Novoselov, A.C. Ferrari, Rayleigh Imaging of Graphene and Graphene Layers, Nano Letters, 7 (2007) 2711-2717.
[1192] S. Roddaro, P. Pingue, V. Piazza, V. Pellegrini, F. Beltram, The optical visibility of graphene: interference colors of ultrathin graphite on SiO2, Nano letters, 7 (2007) 2707-2710.
[1193] A. Castellanos-Gomez, N. Agraït, G. Rubio-Bollinger, Optical identification of atomically thin dichalcogenide crystals, Applied Physics Letters, 96 (2010) 213116.
[1194] M. Benameur, B. Radisavljevic, J. Heron, S. Sahoo, H. Berger, A. Kis, Visibility of dichalcogenide nanolayers, Nanotechnology, 22 (2011) 125706.
[1195] A. Castellanos-Gomez, M. Wojtaszek, N. Tombros, N. Agraït, B.J. van Wees, G. Rubio-Bollinger, Atomically thin mica flakes and their application as ultrathin insulating substrates for graphene, Small, 7 (2011) 2491-2497.
[1196] P. Ares, F. Zamora, J. Gomez-Herrero, Optical identification of few-layer antimonene crystals, ACS Photonics, 4 (2017) 600-605.
[1197] M. Brotons-Gisbert, D. Andres-Penares, J. Martínez-Pastor, A. Cros, J. Sánchez-Royo, Optical contrast of 2D InSe on SiO2/Si and transparent substrates using bandpass filters, Nanotechnology, 28 (2017) 115706.
[1198] D. Abergel, A. Russell, V.I. Fal'ko, Visibility of graphene flakes on a dielectric substrate, Applied Physics Letters, 91 (2007) 063125.
[1199] A. Castellanos Gómez, Propiedades electrónicas, mecánicas y ópticas de cristales bidimensionales de espesor atómico, PhD Thesis, Universidad Autónoma de Madrid,, ISBN: 978-84-694-5401-5 (2011).
[1200] H. Zhang, Y. Ma, Y. Wan, X. Rong, Z. Xie, W. Wang, L. Dai, Measuring the refractive index of highly crystalline monolayer MoS2 with high confidence, Scientific reports, 5 (2015).
[1201] F. Ghasemi, R. Frisenda, D. Dumcenco, A. Kis, D. Perez de Lara, A. Castellanos-Gomez, High Throughput Characterization of Epitaxially Grown Single-Layer MoS2, Electronics, 6 (2017) 28.
[1202] P. Gant, F. Ghasemi, D. Maeso, C. Munuera, E. López-Elvira, R. Frisenda, D.P. De Lara, G. Rubio-Bollinger, M. Garcia-Hernandez, A. Castellanos-Gomez, Optical contrast and refractive index of natural van der Waals heterostructure nanosheets of franckeite, Beilstein journal of nanotechnology, 8 (2017) 2357.

[1203] A. Castellanos-Gomez, J. Quereda, H.P. van der Meulen, N. Agraït, G. Rubio-Bollinger, Spatially resolved optical absorption spectroscopy of single-and few-layer MoS2 by hyperspectral imaging, Nanotechnology, 27 (2016) 115705.
[1204] G. Rubio-Bollinger, R. Guerrero, D.P. de Lara, J. Quereda, L. Vaquero-Garzon, N. Agraït, R. Bratschitsch, A. Castellanos-Gomez, Enhanced visibility of MoS2, MoSe2, WSe2 and black-phosphorus: making optical identification of 2D semiconductors easier, Electronics, 4 (2015) 847-856.
[1205] W. Zhao, Z. Ghorannevis, L. Chu, M. Toh, C. Kloc, P.-H. Tan, G. Eda, Evolution of electronic structure in atomically thin sheets of WS2 and WSe2, ACS nano, 7 (2012) 791-797.
[1206] K.P. Dhakal, D.L. Duong, J. Lee, H. Nam, M. Kim, M. Kan, Y.H. Lee, J. Kim, Confocal absorption spectral imaging of MoS 2: optical transitions depending on the atomic thickness of intrinsic and chemically doped MoS 2, Nanoscale, 6 (2014) 13028-13035.
[1207] Y. Li, A. Chernikov, X. Zhang, A. Rigosi, H.M. Hill, A.M. van der Zande, D.A. Chenet, E.-M. Shih, J. Hone, T.F. Heinz, Measurement of the optical dielectric function of monolayer transition-metal dichalcogenides: MoS 2, Mo S e 2, WS 2, and WS e 2, Physical Review B, 90 (2014) 205422.
[1208] R. Frisenda, Y. Niu, P. Gant, A.J. Molina-Mendoza, R. Schmidt, R. Bratschitsch, J. Liu, L. Fu, D. Dumcenco, A. Kis, Micro-reflectance and transmittance spectroscopy: a versatile and powerful tool to characterize 2D materials, Journal of Physics D: Applied Physics, 50 (2017) 074002.
[1209] J. Quereda, P. San-Jose, V. Parente, L. Vaquero-Garzon, A.J. Molina-Mendoza, N. Agraït, G. Rubio-Bollinger, F. Guinea, R. Roldán, A. Castellanos-Gomez, Strong Modulation of Optical Properties in Black Phosphorus through Strain-Engineered Rippling, Nano Letters, 16 (2016) 2931-2937.
[1210] Y. Niu, S. Gonzalez-Abad, R. Frisenda, P. Marauhn, M. Drüppel, P. Gant, R. Schmidt, D. Barcons, A.J. Molina-Mendoza, S.M.d. Vasconcellos, R. Bratschitsch, D.P.D. Lara, M. Rohlfing, A. Castellanos-Gomez, Thickness-dependent optical properties of MoS2, MoSe2, WS2 and WSe2, unpublished, DOI (2017).
[1211] K. Kouroupis-Agalou, A. Liscio, E. Treossi, L. Ortolani, V. Morandi, N.M. Pugno, V. Palermo, Fragmentation and exfoliation of 2-dimensional materials: a statistical approach, Nanoscale, 6 (2014) 5926-5933.
[1212] C. Ridings, G.G. Warr, G.G. Andersson, Composition of the outermost layer and concentration depth profiles of ammonium nitrate ionic liquid surfaces, Physical Chemistry Chemical Physics, 14 (2012) 16088-16095.
[1213] P. Nemes-Incze, Z. Osváth, K. Kamarás, L.P. Biró, Anomalies in thickness measurements of graphene and few layer graphite crystals by tapping mode atomic force microscopy, Carbon, 46 (2008) 1435-1442.
[1214] C. Backes, R.J. Smith, N. McEvoy, N.C. Berner, D. McCloskey, H.C. Nerl, A. O'Neill, P.J. King, T. Higgins, D. Hanlon, N. Scheuschner, J. Maultzsch, L. Houben, G.S. Duesberg, J.F. Donegan, V. Nicolosi, J.N. Coleman, Edge and Confinement Effects Allow in situ Measurement of Size and Thickness of Liquid-Exfoliated Nanosheets, Nature Commun., 5 (2014) 4576.
[1215] X. Fan, P. Xu, Y.C. Li, D. Zhou, Y. Sun, M.A.T. Nguyen, M. Terrones, T.E. Mallouk, Controlled Exfoliation of MoS2 Crystals into Trilayer Nanosheets, Journal of the American Chemical Society, 138 (2016) 5143-5149.
[1216] Michael Rubinstein, R.H. Colby, Polymer Physics, Oxford University Press2003.
[1217] J.M. Mativetsky, E. Treossi, E. Orgiu, M. Melucci, G.P. Veronese, P. Samorì, V. Palermo, Local Current Mapping and Patterning of Reduced Graphene Oxide, Journal of the American Chemical Society, 132 (2010) 14130-14136.
[1218] X. Song, F. Hui, K. Gilmore, B. Wang, G. Jing, Z. Fan, E. Grustan-Gutierrez, Y. Shi, L. Lombardi, S.A. Hodge, A.C. Ferrari, M. Lanza, Enhanced piezoelectric effect at the edges of stepped molybdenum disulfide nanosheets, Nanoscale, 9 (2017) 6237-6245.
[1219] S. Sadewasser, M.C. Lux-Steiner, Correct Height Measurement in Noncontact Atomic Force Microscopy, Physical Review Letters, 91 (2003).
[1220] K.M. Yang, J.Y. Chung, M.F. Hsieh, S.S. Ferng, D.S. Lin, T.C. Chiang, Systematic variations in apparent topographic height as measured by noncontact atomic force microscopy, Physical Review B, 74 (2006).

[1221] K.S. Novoselov, Electric Field Effect in Atomically Thin Carbon Films, Science, 306 (2004) 666-669.
[1222] J. Tamayo, R. García, Effects of elastic and inelastic interactions on phase contrast images in tapping-mode scanning force microscopy, Applied Physics Letters, 71 (1997) 2394-2396.
[1223] M. Paradinas, C. Munuera, C. Silien, M. Buck, C. Ocal, Heterogeneous nanotribological response of polymorphic self-assembled monolayers arising from domain and phase dependent friction, Phys. Chem. Chem. Phys., 15 (2013) 1302-1309.
[1224] R. García, Dynamic atomic force microscopy methods, Surface Science Reports, 47 (2002) 197-301.
[1225] R. Wiesendanger, Scanning Probe Microscopy and Spectroscopy, Cambridge University Press1994.
[1226] J. Tamayo, R. García, Deformation, Contact Time, and Phase Contrast in Tapping Mode Scanning Force Microscopy, Langmuir, 12 (1996) 4430-4435.
[1227] R. García, R. Magerle, R. Perez, Nanoscale compositional mapping with gentle forces, Nature Materials, 6 (2007) 405-411.
[1228] A.N. Obraztsov, E.A. Obraztsova, A.V. Tyurnina, A.A. Zolotukhin, Chemical vapor deposition of thin graphite films of nanometer thickness, Carbon, 45 (2007) 2017-2021.
[1229] S. Deng, V. Berry, Wrinkled, rippled and crumpled graphene: an overview of formation mechanism, electronic properties, and applications, Materials Today, 19 (2016) 197-212.
[1230] T. Filleter, J.L. McChesney, A. Bostwick, E. Rotenberg, K.V. Emtsev, T. Seyller, K. Horn, R. Bennewitz, Friction and Dissipation in Epitaxial Graphene Films, Physical Review Letters, 102 (2009).
[1231] B. Vasić, A. Matković, R. Gajić, I. Stanković, Wear properties of graphene edges probed by atomic force microscopy based lateral manipulation, Carbon, 107 (2016) 723-732.
[1232] N.F. Martínez, R. García, Measuring phase shifts and energy dissipation with amplitude modulation atomic force microscopy, Nanotechnology, 17 (2006) S167-S172.
[1233] E. Palacios-Lidón, C. Munuera, C. Ocal, J. Colchero, Contrast inversion in non-contact Dynamic Scanning Force Microscopy: What is high and what is low?, Ultramicroscopy, 110 (2010) 789-800.
[1234] R.W. Carpick, M. Salmeron, Scratching the Surface: Fundamental Investigations of Tribology with Atomic Force Microscopy, Chemical Reviews, 97 (1997) 1163-1194.
[1235] D. Berman, A. Erdemir, A.V. Sumant, Graphene: a new emerging lubricant, Materials Today, 17 (2014) 31-42.
[1236] H.-J. Butt, B. Cappella, M. Kappl, Force measurements with the atomic force microscope: Technique, interpretation and applications, Surface Science Reports, 59 (2005) 1-152.
[1237] B. Cappella, G. Dietler, Force-distance curves by atomic force microscopy, Surface Science Reports, 34 (1999) 1-104.
[1238] O. Kazakova, V. Panchal, T. Burnett, Epitaxial Graphene and Graphene–Based Devices Studied by Electrical Scanning Probe Microscopy, Crystals, 3 (2013) 191-233.
[1239] S. Hormeño, M. Penedo, C.V. Manzano, M. Luna, Gold nanoparticle coated silicon tips for Kelvin probe force microscopy in air, Nanotechnology, 24 (2013) 395701.
[1240] T. Filleter, K.V. Emtsev, T. Seyller, R. Bennewitz, Local work function measurements of epitaxial graphene, Applied Physics Letters, 93 (2008) 133117.
[1241] D. Ziegler, P. Gava, J. Güttinger, F. Molitor, L. Wirtz, M. Lazzeri, A.M. Saitta, A. Stemmer, F. Mauri, C. Stampfer, Variations in the work function of doped single- and few-layer graphene assessed by Kelvin probe force microscopy and density functional theory, Physical Review B, 83 (2011).
[1242] J. Eriksson, R. Pearce, T. Iakimov, C. Virojanadara, D. Gogova, M. Andersson, M. Syväjärvi, A. Lloyd Spetz, R. Yakimova, The influence of substrate morphology on thickness uniformity and unintentional doping of epitaxial graphene on SiC, Applied Physics Letters, 100 (2012) 241607.
[1243] A. Krajewska, K. Oberda, J. Azpeitia, A. Gutierrez, I. Pasternak, M.F. López, Z. Mierczyk, C. Munuera, W. Strupinski, Influence of Au doping on electrical properties of CVD graphene, Carbon, 100 (2016) 625-631.
[1244] M. Nonnenmacher, M.P. O'Boyle, H.K. Wickramasinghe, Kelvin probe force microscopy, Applied Physics Letters, 58 (1991) 2921-2923.

[1245] F. Mohn, L. Gross, N. Moll, G. Meyer, Imaging the charge distribution within a single molecule, Nature Nanotechnology, 7 (2012) 227-231.
[1246] L. Collins, A. Belianinov, S. Somnath, N. Balke, S.V. Kalinin, S. Jesse, Full data acquisition in Kelvin Probe Force Microscopy: Mapping dynamic electric phenomena in real space, Scientific Reports, 6 (2016).
[1247] A. O'Neill, U. Khan, P.N. Nirmalraj, J. Boland, J.N. Coleman, Graphene Dispersion and Exfoliation in Low Boiling Point Solvents, Journal of Physical Chemistry C, 115 (2011) 5422-5428.
[1248] O.D. Scherzer, Die Strahlenschädigung der Objekte als Grenze für die hochauflösende Elektronenmikroskopie, German Bunsen Society for Applied Physical Chemistry, , 1970, pp., 1154-1167.
[1249] R.F. Egerton, P. Li, M. Malac, Radiation damage in the TEM and SEM, Micron, 35 (2004) 399-409.
[1250] U. Kaiser, J. Biskupek, J.C. Meyer, J. Leschner, L. Lechner, H. Rose, M. Stöger-Pollach, A.N. Khlobystov, P. Hartel, H. Müller, M. Haider, S. Eyhusen, G. Benner, Transmission electron microscopy at 20kV for imaging and spectroscopy, Ultramicroscopy, 111 (2011) 1239-1246.
[1251] F.R. Eder, J. Kotakoski, U. Kaiser, J.C. Meyer, A journey from order to disorder — Atom by atom transformation from graphene to a 2D carbon glass, Scientific Reports, 4 (2014).
[1252] F. Banhart, Irradiation effects in carbon nanostructures, Reports on Progress in Physics, 62 (1999) 1181-1221.
[1253] D. Cherns, F.J. Minter, R.S. Nelson, Sputtering in the high voltage electron microscope, Nuclear Instruments and Methods, 132 (1976) 369-376.
[1254] R.F. Egerton, R. McLeod, F. Wang, M. Malac, Basic questions related to electron-induced sputtering in the TEM, Ultramicroscopy, 110 (2010) 991-997.
[1255] K. Suenaga, Y. Iizumi, T. Okazaki, Single atom spectroscopy with reduced delocalization effect using a 30 kV-STEM, The European Physical Journal Applied Physics, 54 (2011) 33508.
[1256] C. Ricolleau, J. Nelayah, T. Oikawa, Y. Kohno, N. Braidy, G. Wang, F. Hue, L. Florea, V. Pierron Bohnes, D. Alloyeau, Performances of an 80–200 kV microscope employing a cold-FEG and an aberration-corrected objective lens, Microscopy, 62 (2012) 283-293.
[1257] O.L. Krivanek, J.P. Ursin, N.J. Bacon, G.J. Corbin, N. Dellby, P. Hrncirik, M.F. Murfitt, C.S. Own, Z.S. Szilagyi, High-energy-resolution monochromator for aberration-corrected scanning transmission electron microscopy/electron energy-loss spectroscopy, Philosophical Transactions of the Royal Society A: Mathematical, Physical and Engineering Sciences, 367 (2009) 3683-3697.
[1258] S. Morishita, M. Mukai, K. Suenaga, H. Sawada, Resolution enhancement in transmission electron microscopy with 60-kV monochromated electron source, Applied Physics Letters, 108 (2016) 013107.
[1259] M. Linck, P. Hartel, S. Uhlemann, F. Kahl, H. Müller, J. Zach, M. Haider, M. Niestadt, M. Bischoff, J. Biskupek, Z. Lee, T. Lehnert, F. Börrnert, H. Rose, U. Kaiser, Chromatic Aberration Correction for Atomic Resolution TEM Imaging from 20 to 80 kV, Physical Review Letters, 117 (2016).
[1260] Z. Lee, J.C. Meyer, H. Rose, U. Kaiser, Optimum HRTEM image contrast at 20kV and 80kV—Exemplified by graphene, Ultramicroscopy, 112 (2012) 39-46.
[1261] R.F. Egerton, Choice of operating voltage for a transmission electron microscope, Ultramicroscopy, 145 (2014) 85-93.
[1262] G. Algara-Siller, O. Lehtinen, A. Turchanin, U. Kaiser, Dry-cleaning of graphene, Applied Physics Letters, 104 (2014) 153115.
[1263] G. Algara-Siller, S. Kurasch, M. Sedighi, O. Lehtinen, U. Kaiser, Publisher's Note: "The pristine atomic structure of MoS2 monolayer protected from electron radiation damage by graphene" [Appl. Phys. Lett. 103, 203107 (2013)], Applied Physics Letters, 103 (2013) 239901.
[1264] T.W. Chamberlain, J. Biskupek, S.T. Skowron, P.A. Bayliss, E. Bichoutskaia, U. Kaiser, A.N. Khlobystov, Transmission Electron Microscopy: Isotope Substitution Extends the Lifetime of Organic Molecules in Transmission Electron Microscopy (Small 5/2015), Small, 11 (2015) 510-510.
[1265] R. Wiesendanger, Related scanning probe methods, Scanning Probe Microscopy and Spectroscopy, Cambridge University Press, pp. 265-288.

[1266] R. Wiesendanger, Applications of scanning probe microscopy and spectroscopy, Scanning Probe Microscopy and Spectroscopy, Cambridge University Press, pp. 289-290.
[1267] P. Merino, L. Rodrigo, A.L. Pinardi, J. Méndez, M.F. López, P. Pou, R. Pérez, J.A. Martín Gago, Sublattice Localized Electronic States in Atomically Resolved Graphene-Pt(111) Edge-Boundaries, ACS Nano, 8 (2014) 3590-3596.
[1268] P. Merino, H. Santos, A.L. Pinardi, L. Chico, J.A. Martin-Gago, Atomically-resolved edge states on surface-nanotemplated graphene explored at room temperature, Nanoscale, 9 (2017) 3905-3911.
[1269] M. Telychko, P. Mutombo, P. Merino, P. Hapala, M. Ondráček, F.C. Bocquet, J. Sforzini, O. Stetsovych, M. Vondráček, P. Jelínek, M. Švec, Electronic and Chemical Properties of Donor, Acceptor Centers in Graphene, ACS Nano, 9 (2015) 9180-9187.
[1270] P. Merino, M. Švec, A.L. Pinardi, G. Otero, J.A. Martín-Gago, Strain-Driven Moiré Superstructures of Epitaxial Graphene on Transition Metal Surfaces, ACS Nano, 5 (2011) 5627-5634.
[1271] P. Lauffer, K.V. Emtsev, R. Graupner, T. Seyller, L. Ley, S.A. Reshanov, H.B. Weber, Atomic and electronic structure of few-layer graphene on SiC(0001) studied with scanning tunneling microscopy and spectroscopy, Physical Review B, 77 (2008).
[1272] F. Varchon, P. Mallet, L. Magaud, J.-Y. Veuillen, Rotational disorder in few-layer graphene films on6H−SiC(000−1): A scanning tunneling microscopy study, Physical Review B, 77 (2008).
[1273] D.L. Nika, A.A. Balandin, Thermal Transport in Graphene, Few-Layer Graphene and Graphene Nanoribbons, Thermal Transport in Low Dimensions, Springer International Publishing, 2016, pp. 339-363.
[1274] X. Xu, L.F.C. Pereira, Y. Wang, J. Wu, K. Zhang, X. Zhao, S. Bae, C. Tinh Bui, R. Xie, J.T.L. Thong, B.H. Hong, K.P. Loh, D. Donadio, B. Li, B. Özyilmaz, Length-dependent thermal conductivity in suspended single-layer graphene, Nature Communications, 5 (2014).
[1275] M.M. Sadeghi, M.T. Pettes, L. Shi, Thermal transport in graphene, Solid State Communications, 152 (2012) 1321-1330.
[1276] A.A. Balandin, Thermal properties of graphene and nanostructured carbon materials, Nature Materials, 10 (2011) 569-581.
[1277] C.Y. Ho, R.W. Powell, P.E. Liley, Thermal Conductivity of the Elements, Journal of Physical and Chemical Reference Data, 1 (1972) 279-421.
[1278] D.L. Nika, A.A. Balandin, Phonons and thermal transport in graphene and graphene-based materials, Reports on Progress in Physics, 80 (2017) 036502.
[1279] J.H. Seol, I. Jo, A.L. Moore, L. Lindsay, Z.H. Aitken, M.T. Pettes, X. Li, Z. Yao, R. Huang, D. Broido, N. Mingo, R.S. Ruoff, L. Shi, Two-Dimensional Phonon Transport in Supported Graphene, Science, 328 (2010) 213-216.
[1280] A.A. Balandin, S. Ghosh, W. Bao, I. Calizo, D. Teweldebrhan, F. Miao, C.N. Lau, Superior Thermal Conductivity of Single-Layer Graphene, Nano Letters, 8 (2008) 902-907.
[1281] A. Majumdar, SCANNING THERMAL MICROSCOPY, Annual Review of Materials Science, 29 (1999) 505-585.
[1282] S. Gomès, A. Assy, P.-O. Chapuis, Scanning thermal microscopy: A review, physica status solidi (a), 212 (2015) 477-494.
[1283] K. Yoon, G. Hwang, J. Chung, H.g. Kim, O. Kwon, K.D. Kihm, J.S. Lee, Measuring the thermal conductivity of residue-free suspended graphene bridge using null point scanning thermal microscopy, Carbon, 76 (2014) 77-83.
[1284] M.E. Pumarol, M.C. Rosamond, P. Tovee, M.C. Petty, D.A. Zeze, V. Falko, O.V. Kolosov, Direct Nanoscale Imaging of Ballistic and Diffusive Thermal Transport in Graphene Nanostructures, Nano Letters, 12 (2012) 2906-2911.
[1285] J. Martinek, P. Klapetek, A.C. Campbell, Methods for topography artifacts compensation in scanning thermal microscopy, Ultramicroscopy, 155 (2015) 55-61.
[1286] M.M. Yovanovich, J.R. Culham, P. Teertstra, Analytical modeling of spreading resistance in flux tubes, half spaces, and compound disks, IEEE Transactions on Components, Packaging, and Manufacturing Technology: Part A, 21 (1998) 168-176.

[1287] F. Menges, H. Riel, A. Stemmer, C. Dimitrakopoulos, B. Gotsmann, Thermal Transport into Graphene through Nanoscopic Contacts, Physical Review Letters, 111 (2013).
[1288] F. Tuinstra, J.L. Koenig, Raman Spectrum of Graphite, The Journal of Chemical Physics, 53 (1970) 1126-1130.
[1289] A.C. Ferrari, J. Robertson, Raman spectroscopy of amorphous, nanostructured, diamond-like carbon, and nanodiamond, Philosophical Transactions of the Royal Society A: Mathematical, Physical and Engineering Sciences, 362 (2004) 2477-2512.
[1290] R. Saito, A.R.T. Nugraha, E.H. Hasdeo, S. Siregar, H. Guo, T. Yang, Ultraviolet Raman spectroscopy of graphene and transition-metal dichalcogenides, physica status solidi (b), 252 (2015) 2363-2374.
[1291] C. Tyborski, F. Herziger, R. Gillen, J. Maultzsch, Beyond double-resonant Raman scattering: Ultraviolet Raman spectroscopy on graphene, graphite, and carbon nanotubes, Physical Review B, 92 (2015).
[1292] P.H. Tan, W.P. Han, W.J. Zhao, Z.H. Wu, K. Chang, H. Wang, Y.F. Wang, N. Bonini, N. Marzari, N. Pugno, G. Savini, A. Lombardo, A.C. Ferrari, The shear mode of multilayer graphene, Nature Materials, 11 (2012) 294-300.
[1293] X. Zhang, W.P. Han, J.B. Wu, S. Milana, Y. Lu, Q.Q. Li, A.C. Ferrari, P.H. Tan, Raman spectroscopy of shear and layer breathing modes in multilayer MoS2, Physical Review B, 87 (2013).
[1294] A.L. Glebov, O. Mokhun, A. Rapaport, S. Vergnole, V. Smirnov, L.B. Glebov, Volume Bragg gratings as ultra-narrow and multiband optical filters, Micro-Optics 2012, SPIE, 2012.
[1295] L.G. Cançado, A. Jorio, E.H. Martins Ferreira, F. Stavale, C.A. Achete, R.B. Capaz, M.V.O. Moutinho, A. Lombardo, T.S. Kulmala, A.C. Ferrari, Quantifying Defects in Graphene via Raman Spectroscopy at Different Excitation Energies, Nano Letters, 11 (2011) 3190-3196.
[1296] A. Das, S. Pisana, B. Chakraborty, S. Piscanec, S.K. Saha, U.V. Waghmare, K.S. Novoselov, H.R. Krishnamurthy, A.K. Geim, A.C. Ferrari, A.K. Sood, Monitoring dopants by Raman scattering in an electrochemically top-gated graphene transistor, Nature Nanotechnology, 3 (2008) 210-215.
[1297] D.M. Basko, S. Piscanec, A.C. Ferrari, Electron-electron interactions and doping dependence of the two-phonon Raman intensity in graphene, Physical Review B, 80 (2009).
[1298] S. Piscanec, M. Lazzeri, F. Mauri, A.C. Ferrari, J. Robertson, Kohn Anomalies and Electron-Phonon Interactions in Graphite, Physical Review Letters, 93 (2004).
[1299] A. Das, B. Chakraborty, S. Piscanec, S. Pisana, A.K. Sood, A.C. Ferrari, Phonon renormalization in doped bilayer graphene, Physical Review B, 79 (2009).
[1300] S. Pisana, M. Lazzeri, C. Casiraghi, K.S. Novoselov, A.K. Geim, A.C. Ferrari, F. Mauri, Breakdown of the adiabatic Born–Oppenheimer approximation in graphene, Nature Materials, 6 (2007) 198-201.
[1301] J. Yan, Y. Zhang, P. Kim, A. Pinczuk, Electric Field Effect Tuning of Electron-Phonon Coupling in Graphene, Physical Review Letters, 98 (2007).
[1302] A.C. Ferrari, J. Robertson, Interpretation of Raman spectra of disordered and amorphous carbon, Physical Review B, 61 (2000) 14095-14107.
[1303] C. Casiraghi, Probing disorder and charged impurities in graphene by Raman spectroscopy, physica status solidi (RRL) - Rapid Research Letters, 3 (2009) 175-177.
[1304] L.G. Cançado, M.A. Pimenta, B.R.A. Neves, M.S.S. Dantas, A. Jorio, Influence of the Atomic Structure on the Raman Spectra of Graphite Edges, Physical Review Letters, 93 (2004).
[1305] C. Casiraghi, S. Pisana, K.S. Novoselov, A.K. Geim, A.C. Ferrari, Raman fingerprint of charged impurities in graphene, Applied Physics Letters, 91 (2007) 233108.
[1306] W. Zhao, P.H. Tan, J. Liu, A.C. Ferrari, Intercalation of Few-Layer Graphite Flakes with FeCl3: Raman Determination of Fermi Level, Layer by Layer Decoupling, and Stability, Journal of the American Chemical Society, 133 (2011) 5941-5946.
[1307] T.M.G. Mohiuddin, A. Lombardo, R.R. Nair, A. Bonetti, G. Savini, R. Jalil, N. Bonini, D.M. Basko, C. Galiotis, N. Marzari, K.S. Novoselov, A.K. Geim, A.C. Ferrari, Uniaxial strain in graphene by Raman spectroscopy:Gpeak splitting, Grüneisen parameters, and sample orientation, Physical Review B, 79 (2009).

[1308] J.E. Proctor, E. Gregoryanz, K.S. Novoselov, M. Lotya, J.N. Coleman, M.P. Halsall, High-pressure Raman spectroscopy of graphene, Physical Review B, 80 (2009).
[1309] J. Zabel, R.R. Nair, A. Ott, T. Georgiou, A.K. Geim, K.S. Novoselov, C. Casiraghi, Raman Spectroscopy of Graphene and Bilayer under Biaxial Strain: Bubbles and Balloons, Nano Letters, 12 (2012) 617-621.
[1310] M. Huang, H. Yan, T.F. Heinz, J. Hone, Probing Strain-Induced Electronic Structure Change in Graphene by Raman Spectroscopy, Nano Letters, 10 (2010) 4074-4079.
[1311] M. Mohr, J. Maultzsch, C. Thomsen, Splitting of the Raman2Dband of graphene subjected to strain, Physical Review B, 82 (2010).
[1312] D. Yoon, Y.-W. Son, H. Cheong, Strain-Dependent Splitting of the Double-Resonance Raman Scattering Band in Graphene, Physical Review Letters, 106 (2011).
[1313] Z.H. Ni, T. Yu, Y.H. Lu, Y.Y. Wang, Y.P. Feng, Z.X. Shen, Uniaxial Strain on Graphene: Raman Spectroscopy Study and Band-Gap Opening, ACS Nano, 2 (2008) 2301-2305.
[1314] M. Huang, H. Yan, C. Chen, D. Song, T.F. Heinz, J. Hone, Phonon softening and crystallographic orientation of strained graphene studied by Raman spectroscopy, Proceedings of the National Academy of Sciences, 106 (2009) 7304-7308.
[1315] T. Kuzuba, K. Era, T. Ishii, T. Sato, A low frequency Raman-active vibration of hexagonal boron nitride, Solid State Communications, 25 (1978) 863-865.
[1316] I. Stenger, L. Schué, M. Boukhicha, B. Berini, B. Plaçais, A. Loiseau, J. Barjon, Low frequency Raman spectroscopy of few-atomic-layer thick hBN crystals, 2D Materials, 4 (2017) 031003.
[1317] L. Schué, I. Stenger, F. Fossard, A. Loiseau, J. Barjon, Characterization methods dedicated to nanometer-thick hBN layers, 2D Materials, 4 (2016) 015028.
[1318] R. Arenal, A.C. Ferrari, S. Reich, L. Wirtz, J.Y. Mevellec, S. Lefrant, A. Rubio, A. Loiseau, Raman Spectroscopy of Single-Wall Boron Nitride Nanotubes, Nano Letters, 6 (2006) 1812-1816.
[1319] R.J. Nemanich, S.A. Solin, R.M. Martin, Light scattering study of boron nitride microcrystals, Physical Review B, 23 (1981) 6348-6356.
[1320] S. Reich, A.C. Ferrari, R. Arenal, A. Loiseau, I. Bello, J. Robertson, Resonant Raman scattering in cubic and hexagonal boron nitride, Physical Review B, 71 (2005).
[1321] B. Chakraborty, A. Bera, D.V.S. Muthu, S. Bhowmick, U.V. Waghmare, A.K. Sood, Symmetry-dependent phonon renormalization in monolayer MoS2transistor, Physical Review B, 85 (2012).
[1322] J. Ribeiro-Soares, R.M. Almeida, E.B. Barros, P.T. Araujo, M.S. Dresselhaus, L.G. Cançado, A. Jorio, Group theory analysis of phonons in two-dimensional transition metal dichalcogenides, Physical Review B, 90 (2014).
[1323] N. Scheuschner, R. Gillen, M. Staiger, J. Maultzsch, Interlayer resonant Raman modes in few-layerMoS2, Physical Review B, 91 (2015).
[1324] S. Mignuzzi, A.J. Pollard, N. Bonini, B. Brennan, I.S. Gilmore, M.A. Pimenta, D. Richards, D. Roy, Effect of disorder on Raman scattering of single-layerMoS2, Physical Review B, 91 (2015).
[1325] H.J. Conley, B. Wang, J.I. Ziegler, R.F. Haglund, S.T. Pantelides, K.I. Bolotin, Bandgap Engineering of Strained Monolayer and Bilayer MoS2, Nano Letters, 13 (2013) 3626-3630.
[1326] J.A. Wilson, A.D. Yoffe, Transition metal dichalcogenides. Discussion and interpretation of the observed optical, electrical, and structural properties, Advances in Physics, 18 (1969) 193-335.
[1327] K.R. Paton, J.N. Coleman, Relating the optical absorption coefficient of nanosheet dispersions to the intrinsic monolayer absorption, Carbon, 107 (2016) 733-738.
[1328] L. Yadgarov, C.L. Choi, A. Sedova, A. Cohen, R. Rosentsveig, O. Bar-Elli, D. Oron, H. Dai, R. Tenne, Dependence of the Absorption and Optical Surface Plasmon Scattering of MoS2 Nanoparticles on Aspect Ratio, Size, and Media, ACS Nano, 8 (2014) 3575-3583.
[1329] K.F. Mak, C. Lee, J. Hone, J. Shan, T.F. Heinz, Atomically thin MoS 2: a new direct-gap semiconductor, Physical Review Letters, 105 (2010) 136805.
[1330] A. Splendiani, L. Sun, Y. Zhang, T. Li, J. Kim, C.-Y. Chim, G. Galli, F. Wang, Emerging photoluminescence in monolayer MoS2, Nano letters, 10 (2010) 1271-1275.
[1331] K. Watanabe, T. Taniguchi, H. Kanda, Direct-bandgap properties and evidence for ultraviolet lasing of hexagonal boron nitride single crystal, Nature Materials, 3 (2004) 404-409.

[1332] P. Jaffrennou, J. Barjon, J.S. Lauret, B. Attal-Trétout, F. Ducastelle, A. Loiseau, Origin of the excitonic recombinations in hexagonal boron nitride by spatially resolved cathodoluminescence spectroscopy, Journal of Applied Physics, 102 (2007) 116102.
[1333] T. Taniguchi, K. Watanabe, Synthesis of high-purity boron nitride single crystals under high pressure by using Ba–BN solvent, J Cryst Growth, 303 (2007) 525-529.
[1334] L. Schué, B. Berini, A.C. Betz, B. Plaçais, F. Ducastelle, J. Barjon, A. Loiseau, Dimensionality effects on the luminescence properties of hBN, Nanoscale, 8 (2016) 6986-6993.
[1335] T. Galvani, F. Paleari, H.P.C. Miranda, A. Molina-Sánchez, L. Wirtz, S. Latil, H. Amara, F. Ducastelle, Excitons in boron nitride single layer, Physical Review B, 94 (2016).
[1336] B. Arnaud, S. Lebègue, P. Rabiller, M. Alouani, Arnaud, Lebègue, Rabiller, and Alouani Reply, Physical Review Letters, 100 (2008).
[1337] K. Watanabe, T. Taniguchi, Jahn-Teller effect on exciton states in hexagonal boron nitride single crystal, Physical Review B, 79 (2009).
[1338] L. Museur, G. Brasse, A. Pierret, S. Maine, B. Attal-Tretout, F. Ducastelle, A. Loiseau, J. Barjon, K. Watanabe, T. Taniguchi, A. Kanaev, Exciton optical transitions in a hexagonal boron nitride single crystal, physica status solidi (RRL) - Rapid Research Letters, 5 (2011) 214-216.
[1339] X.K. Cao, B. Clubine, J.H. Edgar, J.Y. Lin, H.X. Jiang, Two-dimensional excitons in three-dimensional hexagonal boron nitride, Applied Physics Letters, 103 (2013) 191106.
[1340] G. Cassabois, P. Valvin, B. Gil, Hexagonal boron nitride is an indirect bandgap semiconductor, Nature Photonics, 10 (2016) 262-266.
[1341] K. Watanabe, T. Taniguchi, K. Miya, Y. Sato, K. Nakamura, T. Niiyama, M. Taniguchi, Hexagonal boron nitride as a new ultraviolet luminescent material and its application—Fluorescence properties of hBN single-crystal powder, Diamond and Related Materials, 20 (2011) 849-852.
[1342] A. Pierret, J. Loayza, B. Berini, A. Betz, B. Plaçais, F. Ducastelle, J. Barjon, A. Loiseau, Excitonic recombinations inh−BN: From bulk to exfoliated layers, Physical Review B, 89 (2014).
[1343] L. Museur, A. Kanaev, Near band-gap photoluminescence properties of hexagonal boron nitride, Journal of Applied Physics, 103 (2008) 103520.
[1344] M.G. Silly, P. Jaffrennou, J. Barjon, J.S. Lauret, F. Ducastelle, A. Loiseau, E. Obraztsova, B. Attal-Tretout, E. Rosencher, Luminescence properties of hexagonal boron nitride: Cathodoluminescence and photoluminescence spectroscopy measurements, Physical Review B, 75 (2007).
[1345] T.Q.P. Vuong, G. Cassabois, P. Valvin, A. Ouerghi, Y. Chassagneux, C. Voisin, B. Gil, Phonon-Photon Mapping in a Color Center in Hexagonal Boron Nitride, Physical Review Letters, 117 (2016).
[1346] R. Bourrellier, S. Meuret, A. Tararan, O. Stéphan, M. Kociak, L.H.G. Tizei, A. Zobelli, Bright UV Single Photon Emission at Point Defects inh-BN, Nano Letters, 16 (2016) 4317-4321.
[1347] T.T. Tran, C. Elbadawi, D. Totonjian, C.J. Lobo, G. Grosso, H. Moon, D.R. Englund, M.J. Ford, I. Aharonovich, M. Toth, Robust Multicolor Single Photon Emission from Point Defects in Hexagonal Boron Nitride, ACS Nano, 10 (2016) 7331-7338.
[1348] J.E. Castle, Practical surface analysis by Auger and X-ray photoelectron spectroscopy. D. Briggs and M. P. Seah (Editors). John Wiley and Sons Ltd, Chichester, 1983, 533 pp., £44.50, Surface and Interface Analysis, 6 (1984) 302-302.
[1349] B.V.Crist, Handbooks of Monochromatic XPS Spectra, XPS International LLC, , Mountain View, CA, USA, 2005.
[1350] R. Hawaldar, P. Merino, M.R. Correia, I. Bdikin, J. Grácio, J. Méndez, J.A. Martín-Gago, M.K. Singh, Large-area high-throughput synthesis of monolayer graphene sheet by Hot Filament Thermal Chemical Vapor Deposition, Scientific Reports, 2 (2012).
[1351] A.B. Preobrajenski, M.L. Ng, A.S. Vinogradov, N. Mårtensson, Controlling graphene corrugation on lattice-mismatched substrates, Physical Review B, 78 (2008).
[1352] Y.I. N. Ikeo, N. Nimura, M. Sigematsu, T. Tazawa, S. Matsumoto, K. Kojima, and Y. Nagasawa, Handbook of X-ray Photoelectron Spectroscopy, JEOL, 1991.
[1353] G.V. Bianco, M. Losurdo, M.M. Giangregorio, P. Capezzuto, G. Bruno, Exploring and rationalising effective n-doping of large area CVD-graphene by NH3, Physical Chemistry Chemical Physics, 16 (2014) 3632.

[1354] R. Blume, P.R. Kidambi, B.C. Bayer, R.S. Weatherup, Z.-J. Wang, G. Weinberg, M.-G. Willinger, M. Greiner, S. Hofmann, A. Knop-Gericke, R. Schlögl, The influence of intercalated oxygen on the properties of graphene on polycrystalline Cu under various environmental conditions, Phys. Chem. Chem. Phys., 16 (2014) 25989-26003.
[1355] N.A. Vinogradov, K. Schulte, M.L. Ng, A. Mikkelsen, E. Lundgren, N. Mårtensson, A.B. Preobrajenski, Impact of Atomic Oxygen on the Structure of Graphene Formed on Ir(111) and Pt(111), The Journal of Physical Chemistry C, 115 (2011) 9568-9577.
[1356] A. Barinov, O.B. Malcioğlu, S. Fabris, T. Sun, L. Gregoratti, M. Dalmiglio, M. Kiskinova, Initial Stages of Oxidation on Graphitic Surfaces: Photoemission Study and Density Functional Theory Calculations, The Journal of Physical Chemistry C, 113 (2009) 9009-9013.
[1357] I. Palacio, A.L. Pinardi, J.I. Martínez, A. Preobrajenski, A. Cossaro, A. Jancarik, I. Stará, I. Starý, J. Méndez, J.A. Martín-Gago, M.F. López, Spectroscopic characterization of the on-surface induced (cyclo)dehydrogenation of a N-heteroaromatic compound on noble metal surfaces, Physical Chemistry Chemical Physics, 19 (2017) 22454-22461.
[1358] R. Hawaldar, P. Merino, M.R. Correia, I. Bdikin, J. Grácio, J. Méndez, J.A. Martín-Gago, M.K. Singh, Large-area high-throughput synthesis of monolayer graphene sheet by Hot Filament Thermal Chemical Vapor Deposition, Sci Rep, 2 (2012).
[1359] E. Casero, C. Alonso, L. Vázquez, M.D. Petit-Domínguez, A.M. Parra-Alfambra, M. de la Fuente, P. Merino, S. Álvarez-García, A. de Andrés, F. Pariente, E. Lorenzo, Comparative Response of Biosensing Platforms Based on Synthesized Graphene Oxide and Electrochemically Reduced Graphene, Electroanalysis, 25 (2012) 154-165.
[1360] U. Starke, Atomic Structure of Hexagonal SiC Surfaces, physica status solidi (b), 202 (1997) 475-499.
[1361] F. Owman, P. Mårtensson, The SiC(0001)6√3 × 6√3 reconstruction studied with STM and LEED, Surf. Sci., 369 (1996) 126-136.
[1362] F. Varchon, P. Mallet, J.Y. Veuillen, L. Magaud, Ripples in epitaxial graphene on the Si-terminated SiC(0001) surface, Physical Review B, 77 (2008) 235412.
[1363] K.V. Emtsev, F. Speck, T. Seyller, L. Ley, J.D. Riley, Interaction, growth, and ordering of epitaxial graphene on SiC{0001} surfaces: A comparative photoelectron spectroscopy study, Physical Review B, 77 (2008) 155303.
[1364] L.H. de Lima, A. de Siervo, R. Landers, G.A. Viana, A.M.B. Goncalves, R.G. Lacerda, P. Häberle, Atomic surface structure of graphene and its buffer layer on SiC(0001): A chemical-specific photoelectron diffraction approach, Physical Review B, 87 (2013).
[1365] A. Abrami, M. Barnaba, L. Battistello, A. Bianco, B. Brena, G. Cautero, Q.H. Chen, D. Cocco, G. Comelli, S. Contrino, F. DeBona, S. Di Fonzo, C. Fava, P. Finetti, P. Furlan, A. Galimberti, A. Gambitta, D. Giuressi, R. Godnig, W. Jark, S. Lizzit, F. Mazzolini, P. Melpignano, L. Olivi, G. Paolucci, R. Pugliese, S.N. Qian, R. Rosei, G. Sandrin, A. Savoia, R. Sergo, G. Sostero, R. Tommasini, M. Tudor, D. Vivoda, F.Q. Wei, F. Zanini, Super ESCA: First beamline operating at ELETTRA, Review of Scientific Instruments, 66 (1995) 1618-1620.
[1366] G. Zampieri, S. Lizzit, L. Petaccia, A. Goldoni, A. Baraldi, M. Bremholm, J.E. Gayone, S.V. Hoffmann, P. Hofmann, Photoelectron diffraction study of the6H−SiC(0001)3×3R30°reconstruction, Physical Review B, 72 (2005).
[1367] P. Merino, M. Švec, J.I. Martinez, P. Jelinek, P. Lacovig, M. Dalmiglio, S. Lizzit, P. Soukiassian, J. Cernicharo, J.A. Martin-Gago, Graphene etching on SiC grains as a path to interstellar polycyclic aromatic hydrocarbons formation, Nature Communications, 5 (2014).
[1368] A. Damascelli, Probing the Electronic Structure of Complex Systems by ARPES, Physica Scripta, T109 (2004) 61.
[1369] F. Reinert, S. Hüfner, Photoemission spectroscopy—from early days to recent applications, New Journal of Physics, 7 (2005) 97-97.
[1370] F.J. Himpsel, Angle-resolved measurements of the photoemission of electrons in the study of solids, Advances in Physics, 32 (1983) 1-51.

[1371] A. Einstein, Über einen die Erzeugung und Verwandlung des Lichtes betreffenden heuristischen Gesichtspunkt, Annalen der Physik, 322 (1905) 132-148.
[1372] D.J. Huang, J.Y. Lee, J.S. Suen, G.A. Mulhollan, A.B. Andrews, J.L. Erskine, Adapting a compact Mott spin polarimeter to a large commercial electron energy analyzer for spin-polarized electron spectroscopy, Review of Scientific Instruments, 64 (1993) 3474-3479.
[1373] J.L. McChesney, A. Bostwick, T. Ohta, T. Seyller, K. Horn, J. González, E. Rotenberg, Extended van Hove Singularity and Superconducting Instability in Doped Graphene, Physical Review Letters, 104 (2010).
[1374] F. Mazzola, T. Frederiksen, T. Balasubramanian, P. Hofmann, B. Hellsing, J.W. Wells, Strong electron-phonon coupling in the σ band of graphene, Physical Review B, 95 (2017).
[1375] F. Mazzola, J.W. Wells, R. Yakimova, S. Ulstrup, J.A. Miwa, R. Balog, M. Bianchi, M. Leandersson, J. Adell, P. Hofmann, T. Balasubramanian, Publisher's Note: Kinks in theσBand of Graphene Induced by Electron-Phonon Coupling [Phys. Rev. Lett.111, 216806 (2013)], Physical Review Letters, 111 (2013).
[1376] I. Pletikosić, M. Kralj, P. Pervan, R. Brako, J. Coraux, A.T. N'Diaye, C. Busse, T. Michely, Dirac Cones and Minigaps for Graphene on Ir(111), Physical Review Letters, 102 (2009).
[1377] K.V. Emtsev, F. Speck, T. Seyller, L. Ley, J.D. Riley, Interaction, growth, and ordering of epitaxial graphene on SiC{0001} surfaces: A comparative photoelectron spectroscopy study, Phys Rev B, 77 (2008).
[1378] C. Coletti, S. Forti, A. Principi, K.V. Emtsev, A.A. Zakharov, K.M. Daniels, B.K. Daas, M.V.S. Chandrashekhar, T. Ouisse, D. Chaussende, A.H. MacDonald, M. Polini, U. Starke, Revealing the electronic band structure of trilayer graphene on SiC: An angle-resolved photoemission study, Phys Rev B, 88 (2013).
[1379] C. Riedl, C. Coletti, T. Iwasaki, A.A. Zakharov, U. Starke, Quasi-Free-Standing Epitaxial Graphene on SiC Obtained by Hydrogen Intercalation, Phys Rev Lett, 103 (2009).
[1380] S. Forti, K.V. Emtsev, C. Coletti, A.A. Zakharov, C. Riedl, U. Starke, Large-area homogeneous quasifree standing epitaxial graphene on SiC(0001): Electronic and structural characterization, Phys Rev B, 84 (2011).
[1381] H. Yuan, Z. Liu, G. Xu, B. Zhou, S. Wu, D. Dumcenco, K. Yan, Y. Zhang, S.-K. Mo, P. Dudin, V. Kandyba, M. Yablonskikh, A. Barinov, Z. Shen, S. Zhang, Y. Huang, X. Xu, Z. Hussain, H.Y. Hwang, Y. Cui, Y. Chen, Evolution of the Valley Position in Bulk Transition-Metal Chalcogenides and Their Monolayer Limit, Nano Letters, 16 (2016) 4738-4745.
[1382] D. Pierucci, H. Henck, J. Avila, A. Balan, C.H. Naylor, G. Patriarche, Y.J. Dappe, M.G. Silly, F. Sirotti, A.T.C. Johnson, M.C. Asensio, A. Ouerghi, Band Alignment and Minigaps in Monolayer MoS2-Graphene van der Waals Heterostructures, Nano Letters, 16 (2016) 4054-4061.
[1383] M. Dendzik, M. Michiardi, C. Sanders, M. Bianchi, J.A. Miwa, S.S. Grønborg, J.V. Lauritsen, A. Bruix, B. Hammer, P. Hofmann, Growth and electronic structure of epitaxial single-layerWS2on Au(111), Physical Review B, 92 (2015).
[1384] S. Ulstrup, A.G. Čabo, D. Biswas, J.M. Riley, M. Dendzik, C.E. Sanders, M. Bianchi, C. Cacho, D. Matselyukh, R.T. Chapman, E. Springate, P.D.C. King, J.A. Miwa, P. Hofmann, Spin and valley control of free carriers in single-layer WS2, Physical Review B, 95 (2017).
[1385] J. Katoch, S. Ulstrup, R.J. Koch, S. Moser, K.M. McCreary, S. Singh, J. Xu, B.T. Jonker, R.K. Kawakami, A. Bostwick, E. Rotenberg, C. Jozwiak, Giant spin-splitting and gap renormalization driven by trions in single-layer WS2/h-BN heterostructures, Nature Physics, DOI 10.1038/s41567-017-0033-4(2018).
[1386] L.J. van der Pauw, A method for measuring resistivity and Hall effects of disks of arbitrary shape, Philips Res. Reports, 13 (1958) 1-9.
[1387] D.F.A. Edwards, Electronic Measurement Techniques, Butterworth-Heinemann1971.
[1388] J. Moser, A. Barreiro, A. Bachtold, Current-induced cleaning of graphene, Applied Physics Letters, 91 (2007) 163513.
[1389] S. Hertel, F. Kisslinger, J. Jobst, D. Waldmann, M. Krieger, H.B. Weber, Current annealing and electrical breakdown of epitaxial graphene, Applied Physics Letters, 98 (2011) 212109.

[1390] N. Tombros, A. Veligura, J. Junesch, M.H.D. Guimaraes, I.J. Vera-Marun, H.T. Jonkman, B.J. van Wees, Quantized conductance of a suspended graphene nanoconstriction, Nat Phys, 7 (2011) 697-700.
[1391] Y.M. Lin, C. Dimitrakopoulos, K.A. Jenkins, D.B. Farmer, H.Y. Chiu, A. Grill, P. Avouris, 100-GHz Transistors from Wafer-Scale Epitaxial Graphene, Science, 327 (2010) 662-662.
[1392] J.S. Moon, D. Curtis, S. Bui, M. Hu, D.K. Gaskill, J.L. Tedesco, P. Asbeck, G.G. Jernigan, B.L. VanMil, R.L. Myers-Ward, C.R. Eddy, P.M. Campbell, X. Weng, Top-Gated Epitaxial Graphene FETs on Si-Face SiC Wafers With a Peak Transconductance of 600 mS/mm, Ieee Electr Device L, 31 (2010) 260-262.
[1393] Z.L. Guo, R. Dong, P.S. Chakraborty, N. Lourenco, J. Palmer, Y.K. Hu, M. Ruan, J. Hankinson, J. Kunc, J.D. Cressler, C. Berger, W.A. de Heer, Record Maximum Oscillation Frequency in C-Face Epitaxial Graphene Transistors, Nano Letters, 13 (2013) 942-947.
[1394] S. Das Sarma, S. Adam, E.H. Hwang, E. Rossi, Electronic transport in two-dimensional graphene, Review of modern physics, 83 (2011) 407-466.
[1395] J.H. Chen, C. Jang, S. Adam, M.S. Fuhrer, E.D. Williams, M. Ishigami, Charged-impurity scattering in graphene, Nature Physics, 4 (2008) 377-381.
[1396] N.H. Shon, T. Ando, Quantum transport in two-dimensional graphite system, Journal of the Physical Society of Japan, 67 (1998) 2421-2429.
[1397] B. Dlubak, P. Seneor, A. Anane, C. Barraud, C. Deranlot, D. Deneuve, B. Servet, R. Mattana, F. Petroff, A. Fert, Are Al2O3 and MgO tunnel barriers suitable for spin injection in graphene?, Applied Physics Letters, 97 (2010) 092502.
[1398] X. Li, X. Wu, M. Sprinkle, F. Ming, M. Ruan, Y. Hu, C. Berger, W.A. de Heer, Top- and side-gated epitaxial graphene field effect transistors, Phys Status Solidi A, 207 (2010) 286-290.
[1399] S. Kim, J. Nah, I. Jo, D. Shahrjerdi, L. Colombo, Z. Yao, E. Tutuc, S.K. Banerjee, Realization of a high mobility dual-gated graphene field-effect transistor with Al2O3 dielectric, Applied Physics Letters, 94 (2009) 062107.
[1400] H. Zhong, Z.Y. Zhang, H.T. Xu, C.G. Qiu, L.M. Peng, Comparison of mobility extraction methods based on field-effect measurements for graphene, Aip Adv, 5 (2015) 057136.
[1401] I. Meric, M.Y. Han, A.F. Young, B. Ozyilmaz, P. Kim, K.L. Shepard, Current saturation in zero-bandgap, topgated graphene field-effect transistors, Nature Nanotechnology, 3 (2008) 654-659.
[1402] S. Droscher, P. Roulleau, F. Molitor, P. Studerus, C. Stampfer, K. Ensslin, T. Ihn, Quantum capacitance and density of states of graphene, Applied Physics Letters, 96 (2010).
[1403] Y. Zhang, Y.-W. Tan, H.L. Stormer, P. Kim, Experimental observation of the quantum Hall effect and Berry's phase in graphene, Nature, 438 (2005) 201.
[1404] J.M. Poumirol, W. Escoffier, A. Kumar, M. Goiran, B. Raquet, J.M. Broto, Electron-hole coexistence in disordered graphene probed by high-field magneto-transport, New Journal of Physics, 12 (2010) 83006.
[1405] S. Wiedmann, H.J. van Elferen, E.V. Kurganova, M.I. Katsnelson, A.J.M. Giesbers, A. Veligura, B.J. van Wees, R.V. Gorbachev, K.S. Novoselov, J.C. Maan, U. Zeitler, Coexistence of electron and hole transport in graphene, Physical Review B, 84 (2011) 115314.
[1406] W.A. de Heer, C. Berger, X. Wu, P.N. First, E.H. Conrad, X. Li, T. Li, M. Sprinkle, J. Hass, M.L. Sadowski, M. Potemski, G. Martinez, Epitaxial graphene, Solid State Communications, 143 (2007) 92-100.
[1407] F. Schwierz, Graphene transistors, Nature Nanotechnology, 5 (2010) 487.
[1408] V.E. Dorgan, M.H. Bae, E. Pop, Mobility and saturation velocity in graphene on SiO2, Applied Physics Letters, 97 (2010).
[1409] J.A. Robinson, M. LaBella, M. Zhu, M. Hollander, R. Kasarda, Z. Hughes, K. Trumbull, R. Cavalero, D. Snyder, Contacting graphene, Applied Physics Letters, 98 (2011) 053103.
[1410] A.C. Ferney, J. David, A.S. Abhay, K. Wonjae, R. Juha, L. Harri, N. Daniel, A physics-based model of gate-tunable metal–graphene contact resistance benchmarked against experimental data, 2D Materials, 2 (2015) 025006.

[1411] K. Nagashio, A. Toriumi, Density-of-States Limited Contact Resistance in Graphene Field-Effect Transistors, Japanese Journal of Applied Physics, 50 (2011).
[1412] F.N. Xia, V. Perebeinos, Y.M. Lin, Y.Q. Wu, P. Avouris, The origins and limits of metal-graphene junction resistance, Nature Nanotechnology, 6 (2011) 179-184.
[1413] M. Shaygan, M. Otto, A.A. Sagade, C.A. Chavarin, G. Bacher, W. Mertin, D. Neumaier, Low Resistive Edge Contacts to CVD-Grown Graphene Using a CMOS Compatible Metal, Annalen der Physik, 529 (2017) 1600410.
[1414] L. Wang, I. Meric, P.Y. Huang, Q. Gao, Y. Gao, H. Tran, T. Taniguchi, K. Watanabe, L.M. Campos, D.A. Muller, J. Guo, P. Kim, J. Hone, K.L. Shepard, C.R. Dean, One-Dimensional Electrical Contact to a Two-Dimensional Material, Science, 342 (2013) 614-617.
[1415] J.A. Robinson, M. LaBella, K.A. Trumbull, X.J. Weng, R. Cavelero, T. Daniels, Z. Hughes, M. Hollander, M. Fanton, D. Snyder, Epitaxial Graphene Materials Integration: Effects of Dielectric Overlayers on Structural and Electronic Properties, Acs Nano, 4 (2010) 2667-2672.
[1416] Y.Q. Wu, D.B. Farmer, A. Valdes-Garcia, W.J. Zhu, K.A. Jenkins, C. Dimitrakopoulos, P. Avouris, Y.M. Lin, Record High RF Performance for Epitaxial Graphene Transistors, 2011 Ieee International Electron Devices Meeting (Iedm), DOI (2011).
[1417] R. Cheng, J. Bai, L. Liao, H. Zhou, Y. Chen, L. Liu, Y.C. Lin, S. Jiang, Y. Huang, X. Duan, High-frequency self-aligned graphene transistors with transferred gate stacks, Proceedings of the National Academy of Sciences, 109 (2012) 11588-11592.
[1418] A.S. Mayorov, R.V. Gorbachev, S.V. Morozov, L. Britnell, R. Jalil, L.A. Ponomarenko, P. Blake, K.S. Novoselov, K. Watanabe, T. Taniguchi, A.K. Geim, Micrometer-Scale Ballistic Transport in Encapsulated Graphene at Room Temperature, Nano Letters, 11 (2011) 2396-2399.
[1419] J.P. D. Deniz, Y. Hu, Y. Hu, J.-P. Turmaud, V.S. Prudkovskiy, C. Berger, W.A. de Heer unpublished, DOI (2018).
[1420] S. Datta, electronic transport in mesoscopic systems, Cambridge University Press, Cambridge, 1995.
[1421] J.L. Tomaino, A.D. Jameson, J.W. Kevek, M.J. Paul, A.M. van der Zande, R.A. Barton, P.L. McEuen, E.D. Minot, Y.S. Lee, Terahertz imaging and spectroscopy of large-area single-layer graphene, Optics Express, 19 141-146.
[1422] J.D. Buron, D.H. Petersen, P. Boggild, D.G. Cooke, M. Hilke, J. Sun, E. Whiteway, P.F. Nielsen, O. Hansen, A. Yurgens, P.U. Jepsen, Graphene conductance uniformity mapping, Nano letters, 12 (2012) 5074-5081.
[1423] J.D. Buron, F. Pizzocchero, B.S. Jessen, T.J. Booth, P.F. Nielsen, O. Hansen, M. Hilke, E. Whiteway, P.U. Jepsen, P. Boggild, D.H. Petersen, Electrically Continuous Graphene from Single Crystal Copper Verified by Terahertz Conductance Spectroscopy and Micro Four-Point Probe, Nano Letters, 14 (2014) 6348-6355.
[1424] J.D. Buron, D.M.A. Mackenzie, D.H. Petersen, A. Pesquera, A. Centeno, P. Boggild, A. Zurutuza, P.U. Jepsen, Terahertz wafer-scale mobility mapping of graphene on insulating substrates without a gate, Optics Express, 23 (2015) 30721-30729.
[1425] J.D. Buron, F. Pizzocchero, P.U. Jepsen, D.H. Petersen, J.M. Caridad, B.S. Jessen, T.J. Booth, P. Boggild, Graphene mobility mapping, Scientific Reports, 5 (2015) 12305.
[1426] D.M.A. Mackenzie, J.D. Buron, P.R. Whelan, B.S. Jessen, A. Silajdzic, A. Pesquera, A. Centeno, A. Zurutuza, P. Boggild, D.H. Petersen, Fabrication of CVD graphene-based devices via laser ablation for wafer-scale characterization, 2D Materials, 2 (2015) 045003.
[1427] D.M.A. Mackenzie, J.C.D. Buron, P.R. Whelan, J.M. Caridad, M. Bjergfelt, B. L., A. Shivayogimath, A.L. Smitshuysen, J.D. Thomsen, T.J. Booth, L. Gammelgaard, J. Zultak, B.S. Jessen, P. Bøggild, D.H. Petersen, Quality Assessment of CVD Graphene: continuity, uniformity and accuracy of mobility measurements, Nano Research, DOI (2017).
[1428] P. Bøggild, D.M.A. Mackenzie, P.R. Whelan, D.H. Petersen, J.D. Buron, A. Zurutuza, J. Gallop, L. Hao, P.U. Jepsen, Mapping the electrical properties of large-area graphene, 2D Materials, 4 (2017).

[1429] D.M.A. Mackenzie, P.R. Whelan, P. Boggild, P.U. Jepsen, A. Redo-Sanchez, D. Etayo, N. Fabricius, D.H. Petersen, Quality assessment of terahertz time-domain spectroscopy transmission and reflection modes for graphene conductivity mapping, Optics Express, 26 (2018) 9220-9229.
[1430] J. Horng, C.F. Chen, B.S. Geng, C. Girit, Y.B. Zhang, Z. Hao, H.A. Bechtel, M. Martin, A. Zettl, M.F. Crommie, Y.R. Shen, F. Wang, Drude conductivity of Dirac fermions in graphene, Physical Review B, 83 (2011) 165113.
[1431] B. Sensale-Rodriguez, R.S. Yan, L. Liu, D. Jena, H.G. Xing, Graphene for Reconfigurable Terahertz Optoelectronics, Proceedings of the IEEE, 101 (2013) 1705-1716.
[1432] D. Akinwande, C.J. Brennan, J.S. Bunch, P. Egberts, J.R. Felts, H. Gao, R. Huang, J.-S. Kim, T. Li, Y. Li, K.M. Liechti, N. Lu, H.S. Park, E.J. Reed, P. Wang, B.I. Yakobson, T. Zhang, Y.-W. Zhang, Y. Zhou, Y. Zhu, A review on mechanics and mechanical properties of 2D materials—Graphene and beyond, Extreme Mechanics Letters, 13 (2017) 42-77.
[1433] A.K. Geim, Graphene: Status and Prospects, Science, 324 (2009) 1530-1534.
[1434] B. Amorim, A. Cortijo, F. de Juan, A.G. Grushin, F. Guinea, A. Gutiérrez-Rubio, H. Ochoa, V. Parente, R. Roldán, P. San-Jose, J. Schiefele, M. Sturla, M.A.H. Vozmediano, Novel effects of strains in graphene and other two dimensional materials, Physics Reports, 617 (2016) 1-54.
[1435] C.-K. Lee, Y. Hwangbo, S.-M. Kim, S.-K. Lee, S.-M. Lee, S.-S. Kim, K.-S. Kim, H.-J. Lee, B.-I. Choi, C.-K. Song, J.-H. Ahn, J.-H. Kim, Monatomic Chemical-Vapor-Deposited Graphene Membranes Bridge a Half-Millimeter-Scale Gap, ACS Nano, 8 (2014) 2336-2344.
[1436] A. Castellanos-Gomez, V. Singh, H.S.J. van der Zant, G.A. Steele, Mechanics of freely-suspended ultrathin layered materials, Annalen der Physik, 527 (2014) 27-44.
[1437] K.S. Novoselov, Nobel Lecture: Graphene: Materials in the Flatland, Reviews of Modern Physics, 83 (2011) 837-849.
[1438] M. Huang, T.A. Pascal, H. Kim, W.A. Goddard, J.R. Greer, Electronic−Mechanical Coupling in Graphene from in situ Nanoindentation Experiments and Multiscale Atomistic Simulations, Nano Letters, 11 (2011) 1241-1246.
[1439] C. Lee, X. Wei, J.W. Kysar, J. Hone, Measurement of the Elastic Properties and Intrinsic Strength of Monolayer Graphene, Science, 321 (2008) 385-388.
[1440] G.H. Lee, R.C. Cooper, S.J. An, S. Lee, A. van der Zande, N. Petrone, A.G. Hammerberg, C. Lee, B. Crawford, W. Oliver, J.W. Kysar, J. Hone, High-Strength Chemical-Vapor-Deposited Graphene and Grain Boundaries, Science, 340 (2013) 1073-1076.
[1441] O.L. Blakslee, D.G. Proctor, E.J. Seldin, G.B. Spence, T. Weng, Elastic Constants of Compression-Annealed Pyrolytic Graphite, Journal of Applied Physics, 41 (1970) 3373-3382.
[1442] Y. Gao, S. Kim, S. Zhou, H.-C. Chiu, D. Nélias, C. Berger, W. de Heer, L. Polloni, R. Sordan, A. Bongiorno, E. Riedo, Elastic coupling between layers in two-dimensional materials, Nature Materials, 14 (2015) 714.
[1443] A. Castellanos-Gomez, M. Poot, G.A. Steele, H.S.J. van der Zant, N. Agraït, G. Rubio-Bollinger, Elastic Properties of Freely Suspended MoS2Nanosheets, Advanced Materials, 24 (2012) 772-775.
[1444] S. Bertolazzi, J. Brivio, A. Kis, Stretching and Breaking of Ultrathin MoS2, ACS Nano, 5 (2011) 9703-9709.
[1445] K. Liu, Q. Yan, M. Chen, W. Fan, Y. Sun, J. Suh, D. Fu, S. Lee, J. Zhou, S. Tongay, J. Ji, J.B. Neaton, J. Wu, Elastic Properties of Chemical-Vapor-Deposited Monolayer MoS2, WS2, and Their Bilayer Heterostructures, Nano Letters, 14 (2014) 5097-5103.
[1446] T. Georgiou, L. Britnell, P. Blake, R.V. Gorbachev, A. Gholinia, A.K. Geim, C. Casiraghi, K.S. Novoselov, Graphene bubbles with controllable curvature, Applied Physics Letters, 99 (2011) 093103.
[1447] J.J. Vlassak, W.D. Nix, A new bulge test technique for the determination of Young's modulus and Poisson's ratio of thin films, Journal of Materials Research, 7 (1992) 3242-3249.
[1448] S.P. Koenig, N.G. Boddeti, M.L. Dunn, J.S. Bunch, Ultrastrong adhesion of graphene membranes, Nature Nanotechnology, 6 (2011) 543-546.
[1449] H. Hencky, Die Berechnung dünner rechteckiger Platten mit verschwindender Biegungsteifigkeit, ZAMM - Zeitschrift für Angewandte Mathematik und Mechanik, 1 (1921) 81-89.

[1450] K.-T. Wan, Y.-W. Mai, Fracture mechanics of a new blister test with stable crack growth, Acta Metallurgica et Materialia, 43 (1995) 4109-4115.
[1451] R. Yang, J. Lee, S. Ghosh, H. Tang, R.M. Sankaran, C.A. Zorman, P.X.L. Feng, Tuning Optical Signatures of Single- and Few-Layer MoS2 by Blown-Bubble Bulge Straining up to Fracture, Nano Letters, 17 (2017) 4568-4575.
[1452] S.J. Haigh, A. Gholinia, R. Jalil, S. Romani, L. Britnell, D.C. Elias, K.S. Novoselov, L.A. Ponomarenko, A.K. Geim, R. Gorbachev, Cross-sectional imaging of individual layers and buried interfaces of graphene-based heterostructures and superlattices, Nature Materials, 11 (2012) 764-767.
[1453] E. Khestanova, F. Guinea, L. Fumagalli, A.K. Geim, I.V. Grigorieva, Universal shape and pressure inside bubbles appearing in van der Waals heterostructures, Nature Communications, 7 (2016) 12587.
[1454] T.W.P.p. Courtney, Mechanical Behavior of Materials. Chapter 9, , 2005, pp. 433-436.
[1455] P. Zhang, L. Ma, F. Fan, Z. Zeng, C. Peng, P.E. Loya, Z. Liu, Y. Gong, J. Zhang, X. Zhang, P.M. Ajayan, T. Zhu, J. Lou, Fracture toughness of graphene, Nature Communications, 5 (2014).
[1456] X. Wei, S. Xiao, F. Li, D.-M. Tang, Q. Chen, Y. Bando, D. Golberg, Comparative Fracture Toughness of Multilayer Graphenes and Boronitrenes, Nano Letters, 15 (2015) 689-694.
[1457] Y. Hwangbo, C.-K. Lee, S.-M. Kim, J.-H. Kim, K.-S. Kim, B. Jang, H.-J. Lee, S.-K. Lee, S.-S. Kim, J.-H. Ahn, S.-M. Lee, Fracture Characteristics of Monolayer CVD-Graphene, Scientific Reports, 4 (2014).
[1458] G. López-Polín, J. Gómez-Herrero, C. Gómez-Navarro, Confining Crack Propagation in Defective Graphene, Nano Letters, 15 (2015) 2050-2054.
[1459] A.A. Griffith, The Phenomena of Rupture and Flow in Solids, Philosophical Transactions of the Royal Society A: Mathematical, Physical and Engineering Sciences, 221 (1921) 163-198.
[1460] B. Jang, A.E. Mag-isa, J.-H. Kim, B. Kim, H.-J. Lee, C.-S. Oh, T. Sumigawa, T. Kitamura, Uniaxial fracture test of freestanding pristine graphene using in situ tensile tester under scanning electron microscope, Extreme Mechanics Letters, DOI 10.1016/j.eml.2016.11.001(2016).
[1461] S.P. Timoshenko, J.M. Gere, W. Prager, Theory of Elastic Stability, Second Edition, Journal of Applied Mechanics, 29 (1962) 220.
[1462] I.E. Berinskii, A.M. Krivtsov, A.M. Kudarova, Bending stiffness of a graphene sheet, Physical Mesomechanics, 17 (2014) 356-364.
[1463] D. Sfyris, G.I. Sfyris, C. Galiotis, Curvature dependent surface energy for a free standing monolayer graphene: Some closed form solutions of the non-linear theory, International Journal of Non-Linear Mechanics, 67 (2014) 186-197.
[1464] Y. Wei, B. Wang, J. Wu, R. Yang, M.L. Dunn, Bending Rigidity and Gaussian Bending Stiffness of Single-Layered Graphene, Nano Letters, 13 (2013) 26-30.
[1465] L. Tapasztó, T. Dumitrică, S.J. Kim, P. Nemes-Incze, C. Hwang, L.P. Biró, Breakdown of continuum mechanics for nanometre-wavelength rippling of graphene, Nature Physics, 8 (2012) 739-742.
[1466] M. Poot, H.S.J. van der Zant, Nanomechanical properties of few-layer graphene membranes, Applied Physics Letters, 92 (2008) 063111.
[1467] N. Lindahl, D. Midtvedt, J. Svensson, O.A. Nerushev, N. Lindvall, A. Isacsson, E.E.B. Campbell, Determination of the Bending Rigidity of Graphene via Electrostatic Actuation of Buckled Membranes, Nano Letters, 12 (2012) 3526-3531.
[1468] J. Zhao, Q. Deng, T.H. Ly, G.H. Han, G. Sandeep, M.H. Rümmeli, Two-dimensional membrane as elastic shell with proof on the folds revealed by three-dimensional atomic mapping, Nature Communications, 6 (2015) 8935.
[1469] J. Zhao, Q. Deng, T.H. Ly, G.H. Han, G. Sandeep, M.H. Rümmeli, Two-dimensional membrane as elastic shell with proof on the folds revealed by three-dimensional atomic mapping, Nature Communications, 6 (2015).
[1470] M.K. Blees, A.W. Barnard, P.A. Rose, S.P. Roberts, K.L. McGill, P.Y. Huang, A.R. Ruyack, J.W. Kevek, B. Kobrin, D.A. Muller, P.L. McEuen, Graphene kirigami, Nature, 524 (2015) 204-207.

[1471] R. Nicklow, N. Wakabayashi, H.G. Smith, Lattice Dynamics of Pyrolytic Graphite, Physical Review B, 5 (1972) 4951-4962.
[1472] N. Ferralis, Probing mechanical properties of graphene with Raman spectroscopy, Journal of Materials Science, 45 (2010) 5135-5149.
[1473] M.A. Bissett, M. Tsuji, H. Ago, Strain engineering the properties of graphene and other two-dimensional crystals, Physical Chemistry Chemical Physics, 16 (2014) 11124.
[1474] R. Roldán, A. Castellanos-Gomez, E. Cappelluti, F. Guinea, Strain engineering in semiconducting two-dimensional crystals, Journal of Physics: Condensed Matter, 27 (2015) 313201.
[1475] C. Si, Z. Sun, F. Liu, Strain engineering of graphene: a review, Nanoscale, 8 (2016) 3207-3217.
[1476] L. Gong, R.J. Young, I.A. Kinloch, I. Riaz, R. Jalil, K.S. Novoselov, Optimizing the Reinforcement of Polymer-Based Nanocomposites by Graphene, ACS Nano, 6 (2012) 2086-2095.
[1477] L. Gong, I.A. Kinloch, R.J. Young, I. Riaz, R. Jalil, K.S. Novoselov, Interfacial Stress Transfer in a Graphene Monolayer Nanocomposite, Advanced Materials, 22 (2010) 2694-2697.
[1478] G. Tsoukleri, J. Parthenios, K. Papagelis, R. Jalil, A.C. Ferrari, A.K. Geim, K.S. Novoselov, C. Galiotis, Subjecting a Graphene Monolayer to Tension and Compression, Small, 5 (2009) 2397-2402.
[1479] O. Frank, G. Tsoukleri, J. Parthenios, K. Papagelis, I. Riaz, R. Jalil, K.S. Novoselov, C. Galiotis, Compression Behavior of Single-Layer Graphenes, ACS Nano, 4 (2010) 3131-3138.
[1480] O. Frank, M. Bouša, I. Riaz, R. Jalil, K.S. Novoselov, G. Tsoukleri, J. Parthenios, L. Kavan, K. Papagelis, C. Galiotis, Phonon and Structural Changes in Deformed Bernal Stacked Bilayer Graphene, Nano Letters, 12 (2012) 687-693.
[1481] C. Androulidakis, E.N. Koukaras, O. Frank, G. Tsoukleri, D. Sfyris, J. Parthenios, N. Pugno, K. Papagelis, K.S. Novoselov, C. Galiotis, Failure Processes in Embedded Monolayer Graphene under Axial Compression, Scientific Reports, 4 (2014).
[1482] C. Androulidakis, E.N. Koukaras, J. Parthenios, G. Kalosakas, K. Papagelis, C. Galiotis, Graphene flakes under controlled biaxial deformation, Scientific Reports, 5 (2015).
[1483] C. Rice, R.J. Young, R. Zan, U. Bangert, D. Wolverson, T. Georgiou, R. Jalil, K.S. Novoselov, Raman-scattering measurements and first-principles calculations of strain-induced phonon shifts in monolayer MoS2, Physical Review B, 87 (2013).
[1484] G. Anagnostopoulos, C. Androulidakis, E.N. Koukaras, G. Tsoukleri, I. Polyzos, J. Parthenios, K. Papagelis, C. Galiotis, Stress Transfer Mechanisms at the Submicron Level for Graphene/Polymer Systems, ACS Applied Materials & Interfaces, 7 (2015) 4216-4223.
[1485] D.G. Papageorgiou, I.A. Kinloch, R.J. Young, Mechanical properties of graphene and graphene-based nanocomposites, Progress in Materials Science, 90 (2017) 75-127.
[1486] O. Frank, M. Mohr, J. Maultzsch, C. Thomsen, I. Riaz, R. Jalil, K.S. Novoselov, G. Tsoukleri, J. Parthenios, K. Papagelis, L. Kavan, C. Galiotis, Raman 2D-Band Splitting in Graphene: Theory and Experiment, ACS Nano, 5 (2011) 2231-2239.
[1487] M. Mohr, J. Maultzsch, C. Thomsen, Publisher's Note: Splitting of the Raman2Dband of graphene subjected to strain [Phys. Rev. B82, 201409 (2010)], Physical Review B, 82 (2010).
[1488] M. Mohr, K. Papagelis, J. Maultzsch, C. Thomsen, Two-dimensional electronic and vibrational band structure of uniaxially strained graphene fromab initiocalculations, Physical Review B, 80 (2009).
[1489] Z. Li, I.A. Kinloch, R.J. Young, K.S. Novoselov, G. Anagnostopoulos, J. Parthenios, C. Galiotis, K. Papagelis, C.-Y. Lu, L. Britnell, Deformation of Wrinkled Graphene, ACS Nano, 9 (2015) 3917-3925.
[1490] C. Xu, T. Xue, J. Guo, Q. Qin, S. Wu, H. Song, H. Xie, An experimental investigation on the mechanical properties of the interface between large-sized graphene and a flexible substrate, Journal of Applied Physics, 117 (2015) 164301.
[1491] T. Jiang, R. Huang, Y. Zhu, Interfacial Sliding and Buckling of Monolayer Graphene on a Stretchable Substrate, Advanced Functional Materials, 24 (2013) 396-402.
[1492] Y. Shin, M. Lozada-Hidalgo, J.L. Sambricio, I.V. Grigorieva, A.K. Geim, C. Casiraghi, Raman spectroscopy of highly pressurized graphene membranes, Applied Physics Letters, 108 (2016) 221907.

[1493] J.-U. Lee, D. Yoon, H. Cheong, Estimation of Young's Modulus of Graphene by Raman Spectroscopy, Nano Letters, 12 (2012) 4444-4448.
[1494] F.O. Papagelis K, Tsoukleri G, Parthenios J, Novoselov K and Galiotis C Axial Deformation of Monolayer Graphene under Tension and Compression, in: L.O.a.V. Morandi (Ed.) GraphITA 2011, Springer Berlin Heidelberg, Bologna , Italy, 2012, pp. pp 87–97.
[1495] D. Metten, F. Federspiel, M. Romeo, S. Berciaud, All-Optical Blister Test of Suspended Graphene Using Micro-Raman Spectroscopy, Physical Review Applied, 2 (2014).
[1496] D. Yoon, H. Moon, Y.-W. Son, J.S. Choi, B.H. Park, Y.H. Cha, Y.D. Kim, H. Cheong, Interference effect on Raman spectrum of graphene onSiO2/Si, Physical Review B, 80 (2009).
[1497] R.J.T. Nicholl, H.J. Conley, N.V. Lavrik, I. Vlassiouk, Y.S. Puzyrev, V.P. Sreenivas, S.T. Pantelides, K.I. Bolotin, The effect of intrinsic crumpling on the mechanics of free-standing graphene, Nature Communications, 6 (2015) 8789.
[1498] A.L. Kitt, Z. Qi, S. Rémi, H.S. Park, A.K. Swan, B.B. Goldberg, How Graphene Slides: Measurement and Theory of Strain-Dependent Frictional Forces between Graphene and SiO2, Nano Letters, 13 (2013) 2605-2610.
[1499] B. Bhushan, J.N. Israelachvili, U. Landman, Nanotribology: friction, wear and lubrication at the atomic scale, Nature, 374 (1995) 607-616.
[1500] J. Gao, W.D. Luedtke, D. Gourdon, M. Ruths, J.N. Israelachvili, U. Landman, Frictional Forces and Amontons' Law: From the Molecular to the Macroscopic Scale, The Journal of Physical Chemistry B, 108 (2004) 3410-3425.
[1501] K. Filintoglou, N. Papadopoulos, J. Arvanitidis, D. Christofilos, O. Frank, M. Kalbac, J. Parthenios, G. Kalosakas, C. Galiotis, K. Papagelis, Raman spectroscopy of graphene at high pressure: Effects of the substrate and the pressure transmitting media, Physical Review B, 88 (2013).
[1502] A. Zandiatashbar, G.-H. Lee, S.J. An, S. Lee, N. Mathew, M. Terrones, T. Hayashi, C.R. Picu, J. Hone, N. Koratkar, Effect of defects on the intrinsic strength and stiffness of graphene, Nature Communications, 5 (2014).